2019

THE HYDROTHERMAL RARE EARTH ELEMENT MINERALISATION AT THE PERALKALINE CARBONATITE FEN COMPLEX IN NORWAY

Marien, Christian

UNIVERSITY OF PLYMOUTH

THE HYDROTHERMAL RARE EARTH ELEMENT MINERALISATION AT THE PERALKALINE CARBONATITE FEN COMPLEX IN NORWAY

by

CHRISTIAN MARIEN

A thesis submitted to the University of Plymouth

in partial fulfilment for the degree of

DOCTOR OF PHILOSOPHY

School of Geography, Earth and Environmental Sciences

May 2019

ACKNOWLEDGEMENT

First, I would like to thank my supervisors Arjan Dijkstra and Colin Wilkins for their guidance, support and commitment to this project. They accompanied me into the investigated field area in Norway and enthusiastically helped me in every other aspect of my thesis, be it grinding rocks, analysing samples or reading and commenting on conference abstracts and various drafts for this thesis. They gave me the freedom to independently work on my thesis and contribute to many conferences, while at the same time making sure I always had a place to turn to for help and advice. I want to thank them for the trust they put in me. I am grateful for receiving a grant from the NERC Isotope Geosciences Facilities Steering Committee to do geochronology on the REE-mineralisation in cooperation with Simon Tapster. Simon's great work at the NERC Isotope Geosciences laboratory delivered crucial data for this thesis.

A special thanks to Bård Bergfald (CEO) and Paloma Magistrati from Fen Minerals As for their helpful support by providing documents, maps and access to the Tufte Tunnel (Fen Complex). I want to thank Natasha Stephen, Roy Mate, Pete Bond and Glen Harper from Plymouth Electron Microscopy Centre (PEMC) for their support and for letting one of the "dirt people" use their beautiful instruments. Special thanks to Alex Taylor and Geoff Millward of the Consolidated Radio-isotope Facility (CORIF) and Rob Clough, who helped me to analyse the notorious bunch of Rare Earth Elements. I would also like to thank Robert Hall and Marc Davis for their lab support. Thanks to Sam Broom-Fendley for his very helpful comments on this thesis. Thanks to my colleague and friend Wycliff Tupiti for his help in the lab and for the epic table tennis breaks we had together. Furthermore, I would like to thank a special group of pub-academics who helped me during this PhD to not just cherish to good times but also embrace the hard times – especially Gustavo Viegas, Simone Bangis, Guilia Degli Alessandrini, Tom Newton, Hoayda Darkal, Francis Rowney, Scarlett Davies, Alex Dawson and Grant Cole.

Huge thanks to my family and my wife's family who treated every day I was back at home like a holiday and always put unquestionable confidence into my abilities! My biggest thanks and gratitude goes to my wife, Astrid. She gave me the freedom and confidence to go my own way, was always there for me in challenging situations and on top of that served as a smart and rigorous critic of my scientific work. Thanks for being you!

AUTHOR'S DECLARATION

At no time during the registration for the degree of Doctor of Philosophy has the author been registered for any other University award without prior agreement of the Doctoral College Quality Sub-Committee.

Work submitted for this research degree at the University of Plymouth has not formed part of any other degree either at the University of Plymouth or at another establishment.

This study was financed with the aid of a studentship from Plymouth University and a grant from the NERC Isotope Geosciences Facilities Steering Committee of £29,500.

Publications:

Marien, C., Dijkstra, A.H. and Wilkins, C., 2018. The hydrothermal alteration of carbonatite in the Fen Complex, Norway: mineralogy, geochemistry, and implications for rare-earth element resource formation. Mineralogical Magazine, 82(S1): S115-S131.

Presentations at conferences:

Plymouth University Earth Science Research Seminar, 2014, Plymouth, U.K. “From mantle to Ore: The Geological Processes that build a mayor REE-Deposit” (oral presentation)

Goldschmidt2015, Prague, Czech Republic “The gradual transformation from carbonatite to rødbergite and the implication on the REE-Mineral species - case study Bjørndalen, Fen-Complex, Norway” (poster presentation).

Plymouth University Earth Science Research Seminar, 2015, Plymouth, U.K. “The alteration of carbonatite to Rødbergite with respect to the formation of Rare Earth Minerals: Evidence from the Fen-Complex, Norway” (oral presentation).

VMSG 2016, Dublin, Ireland “The Formation of Rødbergite and associated REE Mineralization: from Fen Complex, Norway” (poster presentation).

European Geosciences Union General Assembly 2016, Vienna, Austria “REE mobility during the alteration of Carbonatite and their economic potential” (poster presentation).

2nd European Mineralogical Conference 2016, Rimini, Italy “The hydrothermal alteration of carbonatite in the Fen Complex, Norway: mineralogy, geochemistry, and implications for rare earth element resource formation” (oral presentation).

Early Career Geoscientist Evening – South-West Regional Group 2017, Camborne School of Mines, Exeter, UK “Characterisation of a REE-mineralisation in the Fen Complex – Norway” (oral presentation)

The 2nd conference on European Rare Earth Resources 2017, Santorini, Greece “NEW MINERALOGICAL INSIGHTS INTO THE REE POTENTIAL OF THE FEN COMPLEX, NORWAY” (oral presentation).

Plymouth University Earth Science Research Seminar, 2017, Plymouth, U.K. “50 Shades of Red" - the Rare Earth Mineralisation of the Fen Complex – Norway” (oral presentation).

Goldschmidt2017, Paris, France “NEW INSIGHTS INTO THE REE MINERALISATION OF THE FEN COMPLEX, NORWAY” (oral presentation).

Word count of main body of thesis: 62161

Signed ……..

Date……**17/05/2019** ……

THE HYDROTHERMAL RARE EARTH ELEMENT MINERALISATION AT THE PERALKALINE CARBONATITE FEN COMPLEX IN NORWAY

Christian Marien

ABSTRACT

The Fen Complex in Norway consists of a composite carbonatite-ijolite-pyroxenite diatreme intrusion. Locally, the hydrothermally altered, hematite-rich rock rødbergite exhibited high grades (up to 2.1 wt% REE) of rare earth elements (REE). In order to secure the supply of REE for future technology markets in Europe, it becomes increasingly important to establish potential domestic REE sources like the Fen Complex.

This project aims to develop a model for the carbonatite-hosted hydrothermal REE deposit ('Rødbergite') in the Fen Complex, Norway. SEM and ICP-MS trace element analyses of 73 bulk samples taken along various geological key transects showed the transformation of carbonatite, damtjernite, gneiss and fenite to rødbergite. An alteration mineral assemblage of dolomite, Fe-dolomite, barite, Ba-bearing phlogopite, hematite with accessory apatite, calcite, monazite-(Ce) and quartz replaced the original minerals of the protolith. The transformation to rødbergite is accompanied by an increase in REE concentrations (up to 23-fold) — mainly light REE— and Th. The overall REE concentration of rødbergite varies strongly and depends on the REE concentration of the protolith, density of hydrothermal micro-veins — containing monazite, bastnäsite, synchysite and allanite — and locally apatite relics.

While Th-Pb geochronology of zircons established a robust age for the emplacement of the Fen Complex carbonatite with 550 Ma ± 10 Ma, monazite from rødbergite gave U-Pb and Th-Pb ages of 272 Ma ± 5 Ma and 272 Ma ± 10 Ma respectively. The age of the REE-mineralisation coincides with the Oslo rift formation, which is interpreted as the heat source triggering the hydrothermal formation of rødbergite at the Fen Complex

The major findings are combined in a new ore deposit model for rødbergite that can help to improve exploration strategies in the Fen complex and has implications for carbonatite-hosted hydrothermal REE resources around the world.

CONTENTS

GLOSSARY

The classification of samples used in this thesis is following the International Union of Geological Sciences (IUGS) classification by Le Maitre et al. (2002).

Carbonatite: igneous rock type with more than 50 % of primary carbonate minerals (Le Maitre 2002)

Søvite: coarse carbonatite with **calcite** as dominant carbonate species

Rauhaugite: coarse carbonatite with **dolomite** as dominant carbonate species

Modern classification uses calcite/dolomite/ankerite carbonatite based on the most abundant carbonate species or calcio/magnesio/ferro/natrocarbonatite based on the chemical composition

Brøgger (1921)	Sæther (1957)	Andersen (1984)	Adopted in this Thesis
Søvite	Søvite	Calcite carbonatite	Calcite-Carbonatite
Rauhaugite	Rauhaugite I	Dolomite Carbonatite	Calcite-bearing Dolomite-Carbonatite
			Dolomite-Carbonatite
	Rauhaugite II	Ankerite Ferrocarbonatite	Chlorite-bearing Dolomite-Carbonatite
Rødbergite	Rødbergite	Hematite Carbonatite	Rødbergite

Fenite: the fenite of the Fen Complex is an alkali feldspar-rich rock with a minor concentration of calcite and nepheline plus fine black veins of aegirine, aegirine-augite and arfvedsonite. Apatite, titanite, zircon, pyrite and magnetite are accessory minerals

Fenitisation: alteration/contact metasomatism of country rock due to the intrusion of carbonatite or alkaline rocks. The alteration is caused by alkali-rich fluids which commonly changes the chemical composition of granite or gneiss to the composition of an alkali syenite

Ijolite-pyroxenite series: Nepheline rich rock with or without carbonate and/or alkali feldspar with varying content of mafic components (olivine, aegirine-augite, hornblende, biotite, melanite-garnet and apatite)

Urtite: nepheline > 70 %

Ijolite: nepheline 30 - 70 %

Melteigite: nepheline < 30 %

Vipetoite: calcite bearing pyroxenite with little to none nepheline

Rødbergite: Rødbergite (literally: red rock) is usually defined as a calcite-dolomite carbonatite stained red by disseminated fine crystals of hematite (Andersen, 1984)

Silicocarbonatite: Carbonatites with more than 20 % SiO_2 (Le Maitre 2002)

Kåsenite: leucocratic pyroxene calciocarbonatite (silicate content 40 %: nepheline, apatite and titanite)

Hollaite: melanocratic calcite-rich pyroxenite (silicate content up to 80 %)

Ringite: alkali feldspar (up to 30 %) pyroxene calciocarbonatite with a great mineralogical variety. Probably the result of the assimilation of fenite into carbonatite

Tinguaite: phonolitic dyke with alkali feldspar and nepheline porphyritic texture in a greenish matrix

Ultramafic Lamprophyres: M > 90, inequigranular, olivine and phlogopite macrocrysts and/or phenocrysts, primary carbonate bearing (aillikite, alnöite and damtjernite) (Tappe et al. 2005). The differentiation between UML, kimberlites and orangeites is not possible without chemical analyses from groundmass minerals*!*

Damtjernite (ouachitites is a more felsic variety): UML with nepheline and or alkali feldspar in the groundmass but without melilite

Alnöite: UML with melilite

Aillikite: Carbonate-rich UML without melilite, nepheline and alkali feldspar -> only a detailed chemical analysis of spinels, phlogopite and clinopyroxene makes it distinguishable from kimberlite and orangeite

LIP: Large igneous provinces

OIB: Ocean island basalt

Ulefoss: a small village with approximately 2700 inhabitants

TABLE OF FIGURES

TABLE OF TABLES

1 Introduction

The sustainable economic development of our society depends on the secure supply of raw materials. These raw materials are needed to produce high technology applications. However, most industrialised countries strongly depend on raw material imports, as their domestic raw material deposits and exploitation activities are small (Behrens et al., 2007). The current supply of raw materials comes from a small number of countries and companies (Sievers and Tercero, 2012), which gives them significant power in the raw material market and poses a serious threat to different industries as both higher prices and the limited availability of essential raw materials compromise their competitiveness (Campbell, 2014; Parthemore, 2011).

On 6th October 2010 — one month after the collision of a Chinese fishing trawler with two Japanese Coast Guard patrol boats around the uninhabited islands known as the Senkaku Islands — China responded by restricting the export of Rare Earth Elements (REE) (Agence France-Presse, 2010; Hatch, 2012). The territorial dispute over the Senkaku Islands triggered a price race for REE (Fig. 1-1) and brought the issue of the dependence on critical raw materials into the focus of the media, the political and scientific communities and the economy in general. Before the REE bottleneck situation occurred, our society was largely unaware of the existence, let alone the importance of REE for our everyday life.

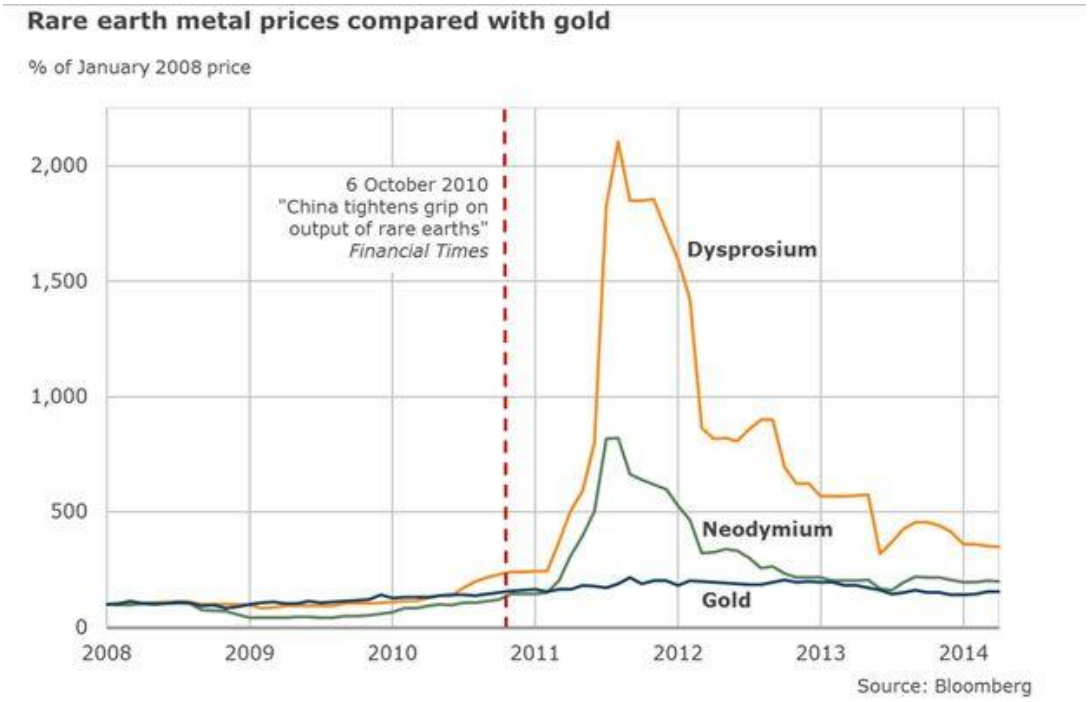

Figure 1-1: Price fluctuation of dysprosium, neodymium and gold relative to their price in January 2008 (Bloomberg, 2015). As a reaction of Chinas decrease in REE export, the price for REE increased sharply in 2011 and in the case of dysprosium increased twenty-fold.

Rare Earth Elements (REE) are a group of elements, which are essential components in a large range of high-technology applications such as smartphones, TV-screens, lasers and catalysts. Their usage in powerful permanent magnets makes them important for wind turbines as well as for electric cars (Wall, 2014). Without REE, modern technology cannot be manufactured, and more importantly, the green revolution cannot be accomplished.

The EU report regarding raw materials classified REE as a critical commodity due to their economic importance and high supply risk (European Commission, 2014) (Fig. 1-2). The National Defence Authorization Act for 2019 of the US-government states for the first time to minimise the purchase of sensitive material, e.g., rare earth magnets from the countries China, Russia, Iran and North Korea and to seek alternate sources of supply as far as possible (Thornberry and Smith, 2018).

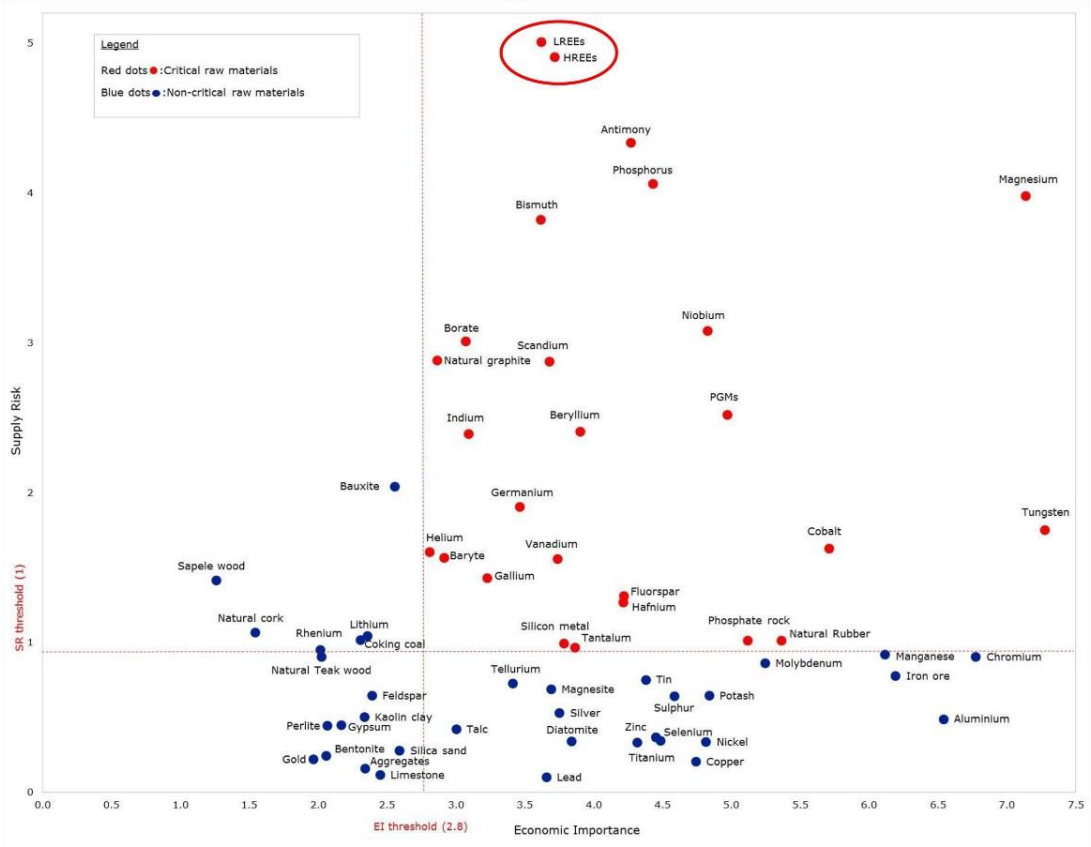

Figure 1-2: Economic importance vs. supply risk of critical raw material (CRM) for the European Market (European Commission, 2017).

In 2010 China was accountable for over 97% of the world's REE production (USGS, 2012). The global production dropped due to reduced domestic production in China. However, new REE mines opened worldwide — most importantly, Mount Weld (Lynas Corp., Australia). Nevertheless, a European REE mining operation would not only be beneficial for the European high technology industry but would also take the environmental and social issues into account, which are caused by the exploitation of raw materials in general (Wall, 2014), and are especially a cause for concern in China. An important part of reaching this ambitious goal is research in order to understand the petrogenesis and mining potential and challenges of known European REE reserves.

The Fen Complex in Norway (Fig. 1-3) is subject of REE exploration since the early 1960s. Recent estimations calculated 84 Mt of Rare Earth Oxides (REO) at 1.08 wt% (inferred resources) and 400 Mt of REO at 0.9 wt% (unconfirmed) for two separate claims respectively (Schiellerup et al., 2017), which makes the Fen Complex one of the largest REE deposits in Europe (Fig. 1-4). Given current demand levels, the estimated amount of REE at the Fen Complex is sufficient to meet worldwide demands of REE for approximately the next 47 years. Despite the ongoing exploration programs, there is still much work to be done before REE can be exploited. This PhD project sets out to undertake a geochemical and mineralogical study of potentially REE-enriched rocks of the Fen Complex, Norway. The data will help to develop a REE-mineralisation model for the Fen Complex, which companies can use to improve the REE exploitation at the Fen Complex and potentially similar deposit types worldwide.

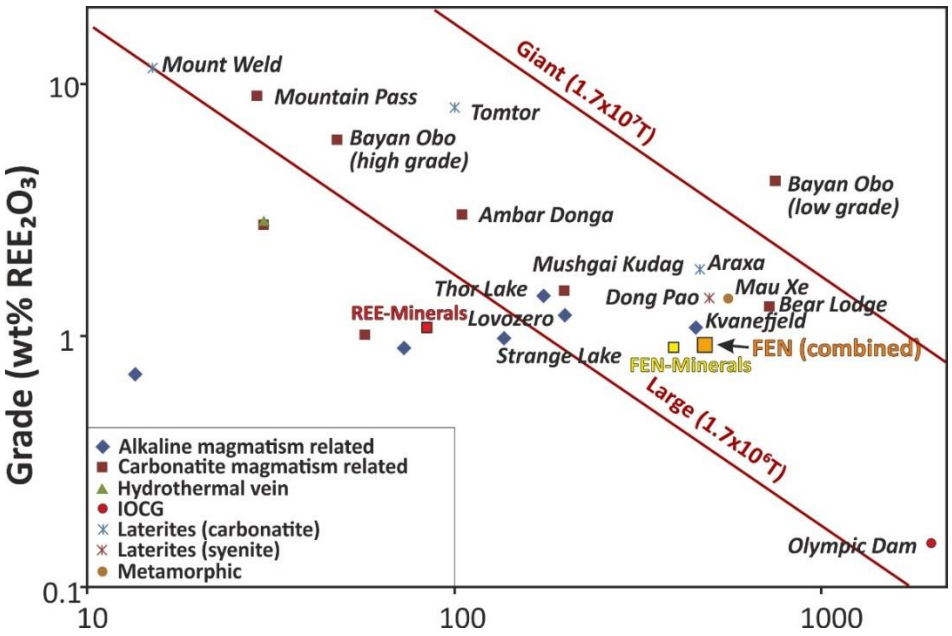

Figure 1-3: REE deposits in REE_2O_3 grade vs. tonnage modified after Smith et al. (2016) using size classification after Laznicka (1999). The two separate claims of REE-Minerals AS and Fen Minerals AS (Schiellerup et al., 2017) are illustrated as well as their combined resources for the Fen Complex.

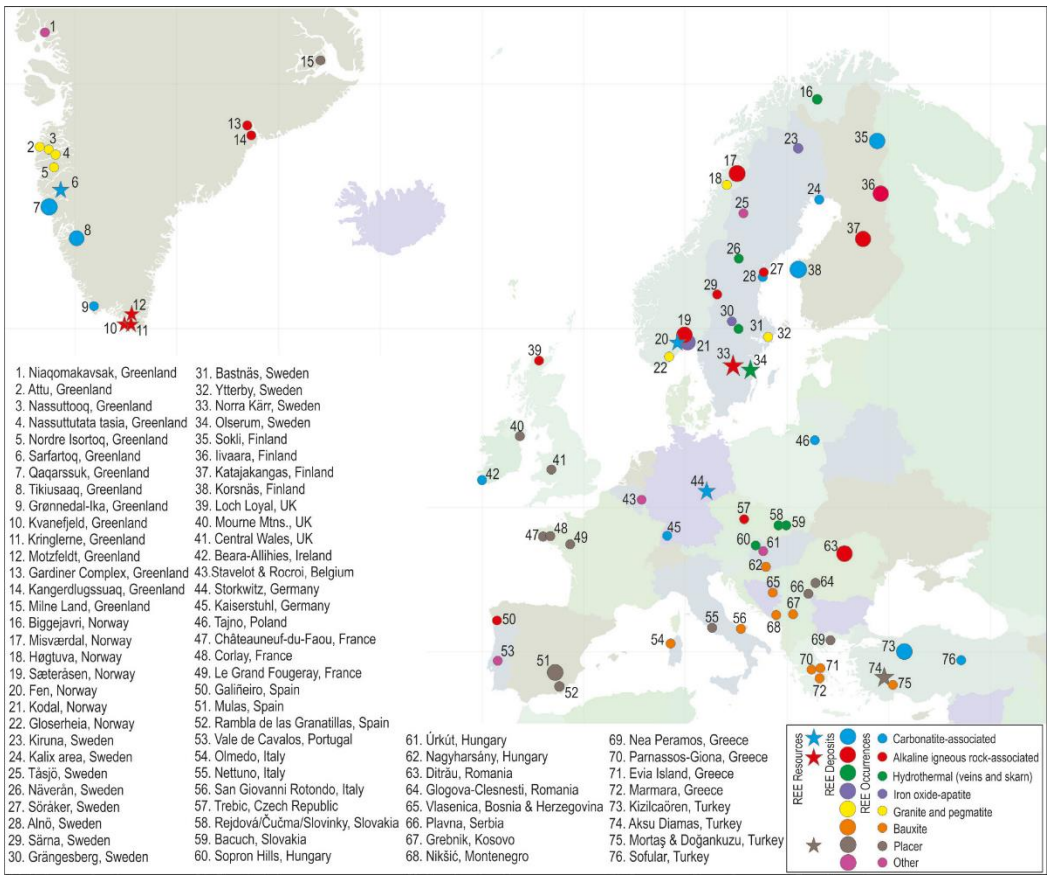

Figure 1-4: REE resources, deposits and occurrences in Europe recognised by the EURARE project *©NERC (Deady et al., 2017)*. The Fen Complex is labelled with number 20.

1.1 Aims and Objectives

The Fen Complex in Norway is host to a variety of uncommon rock types, e.g., carbonatites, highly alkaline silicate rocks such as ijolites, and ultramafic lamprophyres. Carbonatites contain the highest average content of REE of any igneous rock (Cullers and Graf, 1984) and are especially fertile to the formation of REE-deposits. This project proposes a geochemical and mineralogical approach to identify the highest REE-potential amongst the rocks of the Fen Complex and to develop a deep understanding of the underlying REE-ore formation processes. The goal will be to develop a REE-model, which can potentially help to improve REE exploitation at the Fen Complex and similar mineralisation worldwide.

Previous work on the Fen Complex (Schilling, 2013) suggested rødbergite – red hematised carbonate rock – yielded the highest – but often very variable - grades of REE. Associated with high REE concentrations in rødbergite is a higher abundance of radioactive elements, e.g., Th and U, which are a major obstacle for the exploitation of REE resources worldwide. The current models for the formation of rødbergite by Andersen (1989b) and Mitchell & Brunfelt (1975) do not explain the formation of rødbergite in sufficient detail. Although the occurrence of rødbergite specifically was only mentioned for the Fen Complex, there are reports from other localities describing hydrothermal alteration of carbonatite with striking similarities to rødbergite (Groves and Vielreicher, 2001). The occurrence of rødbergite might be rather underrepresented in the literature rather than being unique to the Fen Complex.

Based on these outstanding issues, several **objectives** were defined for this project.

1. To collect representative samples of the major rock types and subsequently analyse them for their REE potential
2. To locate and describe key sections in the field that record the transformation of unaltered carbonatite to rødbergite, and to systematically sample these sections for petrographic and geochemical analysis
3. To carry out a thin section and scanning electron microscopy analysis of samples from the chosen key sections to describe and record the transformation of protolith to rødbergite in terms of mineralogy and texture;
4. To carry out trace element analyses of samples from key transect
5. To find suitable samples/minerals for age dating of the emplacement of the Fen Complex and formation of REE mineralisation
6. To develop a holistic REE ore-deposit model for the Fen Complex.

2 Rare Earth Elements

Rare Earth Elements (REE) are considered the most useful of all trace elements and can be used in igneous, sedimentary, as well as metamorphic petrology (Rollinson, 1993). Their partitioning in igneous systems and their redox behaviour are powerful tools to decipher the petrogenetic history of rocks (Henderson, 1996). Furthermore, REE are of great importance for a variety of high tech applications. This chapter will provide a short introduction into the geochemistry of REE, their economic potential and the general geology associated with REE deposits. It will demonstrate the challenges of supplying the European market with REE and propose the exploitation of domestic REE deposits as part of the solution to overcome REE criticality.

2.1 General

According to the International Union of Pure and Applied Chemistry (IUPAC), REE are a group of 17 elements, combining the 15 lanthanides (lanthanum to lutetium), yttrium and scandium. The traditional usage of the term REE in geology — as it is adopted in this thesis — does not include scandium (Sc) (Henderson, 1996), due to its small ionic radius compared to the other REE, which allows it to substitute relatively easily for smaller ions e.g., Ca^{2+}, Mg^{2+}, Fe^{2+}, Zr^{4+} and Sn^{4+} (Chakhmouradian and Wall, 2012; Wall, 2014). Geochemists further subdivide REE into Light Rare Earth Elements (LREE) and Heavy Rare Earth Elements (HREE). There is disagreement amongst authors on the specific definition of these groups.

Table 2-1: List of Rare Earth Elements with further subdivision into the groups of LREE and HREE.

Atomic number	Name	Symbol	
57	Lanthanum	La	Light Rare Earth Elements (LREE)
58	Cerium	Ce	
59	Praseodymium	Pr	
60	Neodymium	Nd	
61	Promethium	Pm	
62	Samarium	Sm	
63	Europium	Eu	
64	Gadolinium	Gd	Heavy Rare Earth Elements (HREE)
65	Terbium	Tb	
66	Dysprosium	Dy	
67	Holmium	Ho	
68	Erbium	Er	
69	Thulium	Tm	
70	Ytterbium	Yb	
71	Lutetium	Lu	
39	Yttrium	Y	

In this thesis, the group of LREE incorporates the elements lanthanum (La) to europium (Eu) and the group of HREE incorporates gadolinium (Gd) to lutetium (Lu). Yttrium (Y) is grouped with HREE due to its similar chemical properties (Tab. 2-1). Contrary to their name, most of the REE are rather abundant in the continental crust — based on elemental concentration after Rudnick and Gao (2003). Cerium (Ce), the most abundant REE, has an average concentration of 63 ppm in the upper continental crust, which is more abundant than commonly used metals, e.g., copper (28 ppm) or nickel (47 ppm). HREE are generally less abundant than LREE and Lu is the least abundant REE with a concentration of 310 ppb in the upper continental crust. Nevertheless, this is significantly more abundant than silver (53 ppb) and gold (1.5 ppb). However, deposits of REE-minerals are rare, which explains the “Rare” in Rare Earth Element. “Earth” is an old word for oxide and indicates that REE are preferentially found as oxides rather than metals (Wall, 2014).

REE are a group of elements with similar chemical behaviour. Differences in their chemical behaviour are subtle between rare earths of close atomic number (e.g., La57 and Ce58) and increase systematically with a growing difference in atomic numbers (Rollinson, 1993). The outer electron configuration of La is $[Xe]5d^16s^2$, which means 3 electrons can participate in chemical reactions. The next element of the lanthanides, Ce, adds one electron in the 4f sub-shell $[Xe]4f^15d^16s^2$, as do all the following lanthanides. The 4f shell can incorporate 14 electrons; hence, the lanthanides are comprised of 14 elements plus La. The electrons of the 4f shell are shielded by the outer 5d and 6s orbitals and do not normally participate in chemical reactions in geological environments — except for Ce. Hence, the ionic charge stays 3+, and the increasing number of electrons does not change the chemical properties of the element significantly. Therefore, REE occur in natural systems as a group and do not tend to concentrate individually (Chakhmouradian and Wall, 2012). The only exception for the trivalent state of REE is Ce, also existing in a tetravalent state and Eu in a divalent state. As Ce and Eu have different charges and ionic radii (Fig. 2-1), their partitioning between phases varies strongly compared to the other REE.

Increase in the number of protons within lanthanides, while in general maintaining a constant configuration of the outer electron shell, causes a systematic smooth change in the ionic radii from La to Lu (1.18 to 0.97 Å for coordination 8; (Shannon, 1976)). This change is referred to as the lanthanide contraction, which is the main reason for the slight differentiation among REE (Fig. 2-1). While the change from one REE to the neighbouring REE is very subtle, it has a more significant impact between REE with a greater difference in atomic numbers, e.g., La and Lu. The subdivision between LREE and HREE is due to these incremental changes and differences in abundance.

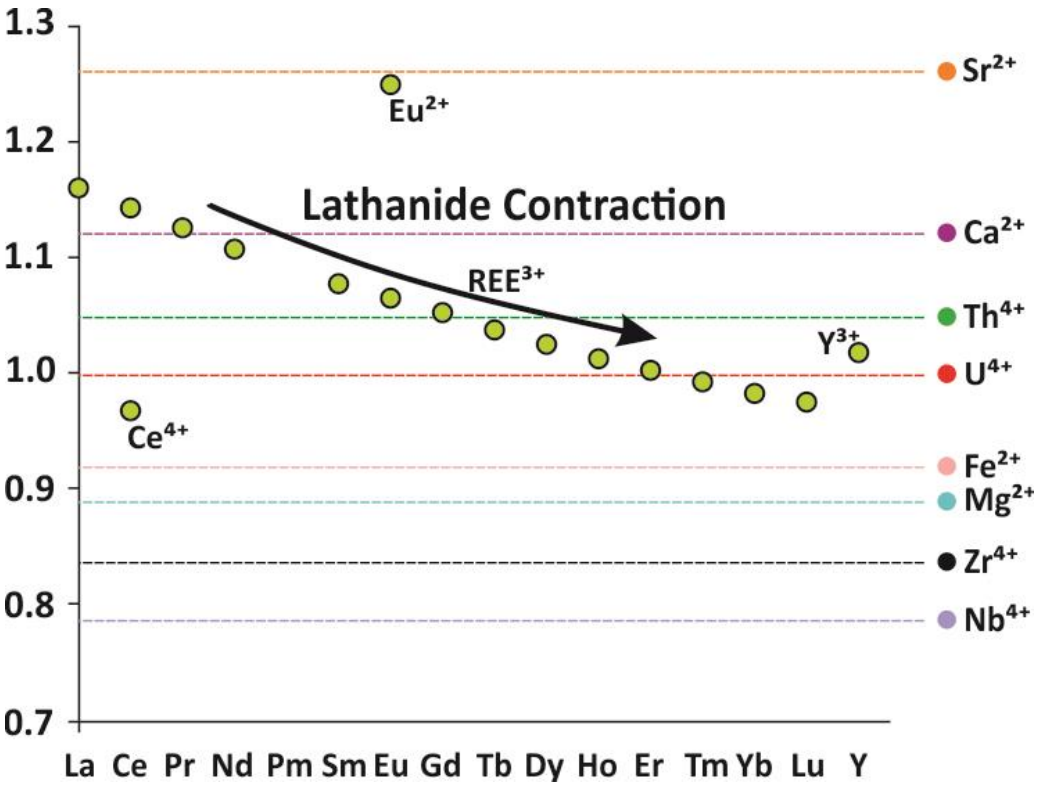

Figure 2-1: Ionic radii of the trivalent rare earth elements REE^{3+}, Eu^{2+} and Ce^{4+} versus the ionic radii of Sr^{2+}, Ca^{2+}, Th^{4+}, U^{4+}, Fe^{2+}, Mg^{2+}, Zr^{4+} and Nb^{4+}. The systematic decrease of the ionic radii is named Lanthanide contraction (Henderson, 1996).

Occasionally the group of Middle Rare Earth Elements (MREE), which encompasses the elements from Sm – Ho, is introduced to differentiate the REE even further (Rollinson, 1993).

REE concentrations are normalised against a common reference standard, which in this thesis is the average CI chondrite data after McDonough and Sun (1995). Chondrites are the least fractionated rock in the Solar System, which makes them ideal reference standards. The normalisation of REE against chondrite values identifies any REE fractionation and nullifies the Oddo-Harkins effect (Rollinson, 1993), which describes that elements with even atomic number are more abundant than adjacent elements with smaller or larger odd atomic numbers. Normalised values are denoted with a subscript “N” and are presented in a concentration vs. atomic number diagram,

expressed as a logarithm to the base 10 of the normalised value. Because of the gradual lanthanide contraction, and therefore the gradual change in chemical and physical behaviour, the REE pattern of the curve is generally smooth. As a result, for the presence of a tetravalent state in Ce and the divalent state in Eu, the normalised concentration of Ce and Eu frequently differ from the expected trend line for the REE concentration. This difference can be expressed in the ratio Eu/Eu* and Ce/Ce* respectively. Eu* and Ce* are the geometrical means of the neighbouring REE:

$Eu^* = \sqrt{(Sm_N * Gd_N)}$

$Ce^* = \sqrt{(La_N * Pr_N)}$

The ratios Eu/Eu* and Ce/Ce* are called cerium anomaly and europium anomaly respectively. Both of these ratios are sensitive to the redox conditions of the system. The speciation of Ce and Eu under different physical conditions, e.g., p, T, fO_2, pH and Eh in combination with different ligands, e.g., Cl^-, SO_4^{2-}, PO_4^{3-} is still poorly constrained. However, these anomalies mainly depend on the redox conditions during the fractionation process, although T and complexation reactions seem to play an important role as well (Liu et al., 2017). Experimental and empirical evidence demonstrate that fractionation of feldspar results in a Eu anomaly in the residual melt (Bédard, 2006).

The shape of chondrite-normalised profiles reflects variation in the REE budget. The ratio of $(La/Yb)_N$ quantifies the tilt of the curve with respect to the x-axis and the ratio $(Dy/Yb)_N$ is occasionally used to determine whether the REE profile maintains a uniform slope or shows downwards bulging in the middle, which locally occurs in igneous rocks (Chakhmouradian et al., 2017).

2.2 Economic Importance

REE are essential to a range of high-tech applications, such as catalysts for fluid cracking, components in highly adapted glass and alloys, yttrium-aluminium-garnet lasers (YAG-laser), permanent neodymium-iron-boron (NdFeB) magnets for wind turbines, special ceramics and military weapons (Charalampides et al., 2015). At the moment, the greatest demand is for dysprosium (Dy), neodymium (Nd) and praseodymium (Pr), europium (Eu), terbium (Tb) and Y (Charalampides et al., 2015; Wall, 2014). Ce, La and Y are part of a matured market that is driven by the growth of the general economy. Dy, Nd and Pr are used in the high growth permanent magnet sector, which is essential for batteries of electric cars, generators for automobiles and wind turbines. The permanent magnet sector has an annual growth rate of 8-10 % (Charalampides et al., 2015). This development is likely to continue because the shift of the European industry towards a low carbon industry with renewable energy technologies requires the input of REE. One of the driving forces will be the future growth of the market for hybrid electric vehicles (HEV) and electric vehicles (EV), which in turn will drive the demand for NdFeB magnets. Demand for the most critical REE — Nd, Pr and Dy — is forecasted to increase between 2016 and 2026 by 4.7 % per year for Nd and Pr, and 5 % for Dy (Roskill, 2016).

Due to their similar chemical properties, REE are concentrated together in deposits and are therefore mined together. Naturally, the demand for individual REE does not reflect the natural abundance of these elements in their deposits, which creates the so-called “balance problem” (Binnemans and Jones, 2015). A deposit enriched in LREE will produce a high amount of valuable Nd but will automatically produce even more Ce and La, which are not needed in the same quantity as Nd. In response, the REE industry tries to either find new ways to apply REE, which are available in excess or reduce the amount

of REE, which are high in demand. For instance, researchers from the Fraunhofer Society were able to reduce the amount of Nd in permanent magnets to 20% of their original composition by replacing it largely with Ce (Fraunhofer IMWS, 2018). One particular case is thorium (Th). Although Th is not a REE, it is commonly associated with REE deposit due to being a high-field-strength element (HFSE) with similar chemical properties to REE. Th-mineral concentrates are a radioactive waste product, which is an issue for future REE operations. The problem is somehow ironic because once REE were a waste product of Th mining and scientists tried to find commercial applications for the REE leftovers. This demonstrates how the importance and value of materials changes in time driven by the available technology and the needs of society. Therefore only the combination of new technology — Th-molten salt reactor — diversification of REE resources, recycling and urban mining, substitution, reduced use and new high-volume application (Binnemans and Jones, 2015) will solve the balance problem in the future.

The development of new specialised technologies increased the demand for REE, and the mining production grew from 64,500 tonnes in 1996 to 130,000 tonnes in 2017 (USGS, 1996; USGS, 2017). Most REE are currently coming from a small number of deposits, e.g., Bayan Obo in China; Mount Weld in Australia; Lovozero in Russia; heavy mineral sands in India and ion-adsorption-clay deposits in China. In 2017, China was the largest producer of REE worldwide with 105,000 t of REE, which corresponds to a market share of over 80%. Besides China's monopoly in REE mining, China managed to control all aspects of the supply chain — from mining to separating and purifying the REE to producing powerful REE-magnets. Using 50 % of the world's REE production, China is the largest consumer of REE worldwide (USGS, 2017). It is not just a monopoly of a commodity but also a monopoly of technology and knowledge. Considering the strategic

importance of REE for present and future technologies, concerns about the dependence on Chinese sources and about the sustainability and long-term security of supplies have been highlighted at national and international levels (British Geological Survey, 2012; DERA, 2017; European Commission, 2014; European Commission, 2016; U.S. Department of Energy, 2011). REE have been widely cited as a critical material with the highest supply risk. To overcome the issue of its dependency on China, the EU started a variety of different programs for a better understanding of geological REE resources and production processes, e.g., EURARE. EURARE's objective is to develop a sustainable exploitation scheme for Europe's Rare Earth ore deposits (Deady et al., 2017).

2.3 REE-Deposits

REE can be concentrated in all the major rock types (igneous, metamorphic and sedimentary) in various settings (Orris and Grauch, 2002). The two main categories for REE-deposits are; high-temperature deposits including carbonatites, alkaline igneous rocks and their associated hydrothermal systems and low-temperature deposits such as placers, bauxites, laterites and ion-adsorption-clays (Fig. 2-2). However, the most important deposits worldwide are associated with carbonatites and peralkaline silicate rocks (Chakhmouradian and Zaitsev, 2012; Goodenough et al., 2017; Wall, 2014). Bayan Obo and Maoniuping in China, Mt Weld in Australia and Mountain Pass mine in the USA are all associated with carbonatite magmatism (Goodenough et al., 2017).

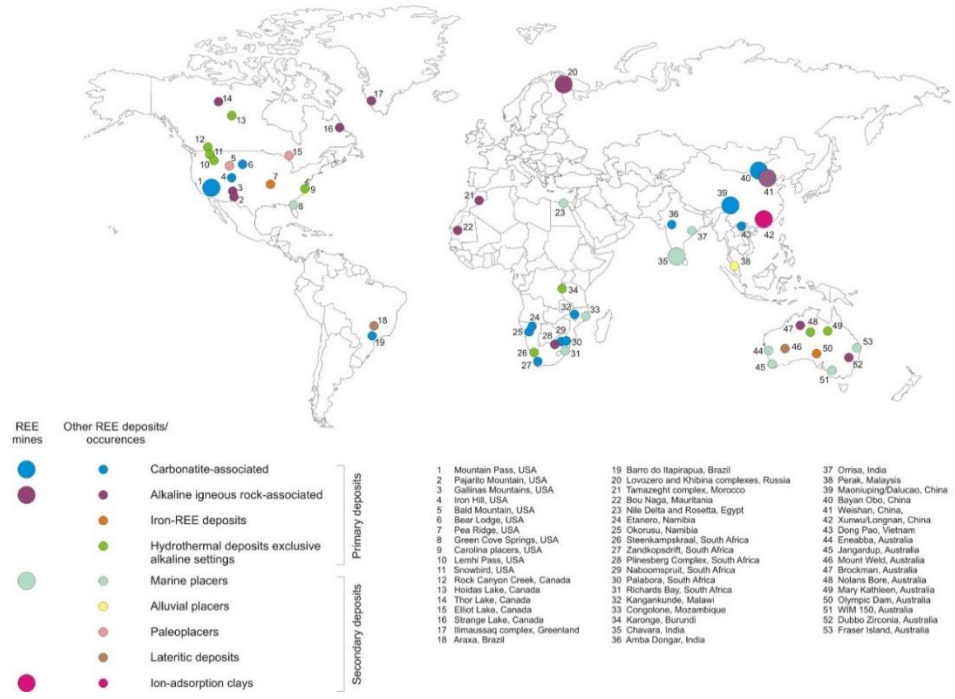

Figure 2-2: Global distribution of REE deposits divided into nine major deposit types (British Geological Survey, 2011).

Carbonatites are igneous rocks with a modal amount of primary (magmatic) carbonate minerals of > 50 % (Le Maitre et al., 2002). The Bayan Obo Fe–REE–Niobium (Nb) deposit in China is the largest REE deposits in the world with an estimated high-grade reserve of 48 Mt at 6 wt% of Rare Earth Oxides (REO) (Drew et al., 1990). Dolomite marble and banded ores of Fe- and REE-minerals are the hosts of the high-grade REE zones. The low-grade ore zone is associated with massive magnetite and hematite with an estimated resource of 750 Mt at 4.1 wt% REO (Smith et al., 2015). Bayan Obo is primarily a Fe mine exploiting Nb and REE as by-products. The deposit still has significant resources of 1500 Mt at 35 wt% Fe (Drew et al., 1990) and 1 Mt at 0.13 wt% Nb_2O_3 (Chao et al., 1997). The annual production of REO at Bayan Obo is 55,000 t (Long et al., 2010), which means that 42 % of the world production of REE are mined as a by-product from one region in China. The REE-mineralisation is strongly LREE enriched (Fan et al., 2016) and primarily hosted in bastnäsite and monazite.

The origin of the host dolomite and banded ores of Fe- and REE-minerals are still subject of ongoing debate. The ore originally formed around 1.3 Ga — associated with sedimentary carbonates and carbonatite dykes — and was deformed several times, metamorphosed and hydrothermally overprinted, culminating in the Caledonian subduction of the Mongolian Plate under the North China Craton from 450 to 420 Ma (Smith et al., 2015). This multitude of processes caused a remobilisation of the original Fe and REE mineralisation and a resetting of the isotope signature. Smith et al. (2015) identified the key for the exceptional metal concentration of the Bayan Obo area exactly in the described complex geological history of multiple stages of alkaline, HFSE-rich metasomatic fluid flow.

Besides the current carbonatite associated mining operations, which are responsible of the majority of the world production of REE, there are a few carbonatite complexes which are the focus of current REE exploration e.g., Kangankunde in Malawi (Lynas Corporation Ltd., 2007), Tomtor in Russia (Kravchenko and Pokrovsky, 1995), Wigu Hill in Tanzania (Montero Mining & Exploration Ltd., 2018) and Fen in Norway (21st North, 2014a). The current focus on carbonatite deposits will increase the earlier discussed balance problem even further (Goodenough et al., 2017) with an oversupply of La and Ce.

Peralkaline rocks are, besides carbonatites, another important source for REE. In peralkaline rocks, the concentration of Na and K together exceeds the concentration of Al (Le Maitre et al., 2002). The excess of alkali metals is expressed in the formation of characteristic minerals rich in K or Na, e.g., aegirine (Na-pyroxene) and riebeckite (Na-amphibole) (Bailey, 1989). Peralkaline intrusions are either silica undersaturated (nepheline syenites) or silica oversaturated (peralkaline granites). Silica undersaturated

(peralkaline nepheline syenite) intrusions show a greater REE deposit potential than saturated intrusions. Especially agpaitic intrusions, which are known for REE enrichment by purely magmatic processes (Goodenough et al., 2017). This agpaitic group of peralkaline nepheline syenites contains complex Na-K-Ca-(Fe)-silicates — rich in Ti or Zr — including most of the HFSE, instead of more common minerals such as zircon, titanite, ilmenite or Ti-bearing magnetite. If these complex Na-K-Ca-(Fe)-silicates, e.g., eudialyte, aenigmatite and astrophyllite are present, then the rock is called an agpaitic peralkaline nepheline syenite in contrast to a zircon bearing miaskitic peralkaline nepheline syenite (Le Maitre et al., 2002; Marks et al., 2011). The only active REE mine in peralkaline rocks is at the agpaitic nepheline syenite complex Lovozero in Russia, where REE are extracted from the mineral loparite — a REE-bearing perovskite (Kogarko et al., 2002). Several of the European agpaitic nepheline syenite complexes are currently explored for REE, including Ilímaussaq, Motzfeld and Kvanefjeld in Greenland and Norra Kärr in Sweden (Goodenough et al., 2016).

REE enriched peralkaline deposits are characterised by large volumes but generally low concentrations (< 1 wt%) of REO. In contrast to carbonatites, they show much flatter REE patterns with a distinct negative Eu anomaly. The exploitation of the peralkaline prospect in Greenland would be sufficient to meet the European demand for HREE but insufficient for the supply of La and Ce (Machacek and Kalvig, 2016). This could cancel out the balance problem caused by the exploitation of carbonatites. A smart combination of two or more deposits from carbonatites and peralkaline igneous rocks with a limited and controlled production should meet the demands of the European industry. Additionally, peralkaline deposits have low Th and uranium (U) concentrations (Goodenough et al., 2017; Wall et al., 2017). On the other hand, peralkaline deposits

yield the mineralogically most diverse and complex assemblages of all rock types — over 550 minerals are present in Lovozero and Khibiny alone (Arzamastsev et al., 2008). This diverse mineralogy makes every REE deposit unique, which requires a complex and expensive development of individual processing routes for each deposit (Wall, 2014). The geological setting for carbonatite and peralkaline silicate rocks is similar, and composite intrusions of syenite and carbonatite suggest a link between those two rock types by either by extreme differentiation (Wyllie and Tuttle, 1960) or liquid-liquid immiscibility (Lee and Wyllie, 1998)

One prominent example of a low-temperature REE deposit type are the ion adsorption clays deposits of the Nanling area in China (Kanazawa and Kamitani, 2006). The deposits formed due to intense lateritic weathering of REE enriched granites. Although the grades are relatively low (< 4,000 ppm REO) compared to carbonatites or peralkaline rocks, the REE can be easily removed from the clay surface of the weathered granite by using ammonium sulphate (Goodenough et al., 2017; Moldoveanu and Papangelakis, 2012). Weathered horizons with significant size and more than 500 ppm of exchangeable REE are already considered ore (Bao and Zhao, 2008). Despite their low REE concentration, ion-adsorption clays make up 35% of China's REE production and 80% of the world's HREE production (Yang et al., 2013). These deposits are the principal source of HREE in the world and therefore, yield great economic power. This type of deposit was considered to be unique for southern China (Kanazawa and Kamitani, 2006) but research over the last decade identified similar deposits outside of China e.g., Serra Verde in Brazil and Tantalus in Madagascar — although they do not necessarily show the same enrichment in HREE (Moldoveanu and Papangelakis, 2016).

Many of the carbonatite and peralkaline REE deposits exhibit a hydrothermal overprint, which leads to the further enrichment of their already magmatically enriched REE concentration. Well known examples for hydrothermally overprinted REE deposits are the giant Bayan Obo Fe-REE-Nb deposit in China (Smith et al., 2015; Yang et al., 2009), Browns Range in Western Australia (Cook et al., 2013), Gallinas Mountains deposit in New Mexico, USA (Williams-Jones et al., 2000) and Strange Lake in Canada (Salvi and Williams-Jones, 1996). Hydrothermal fluids can carry large amounts of REE (1300 ppm in Banks et al. (1994)) and to understand the mobility of REE in hydrothermal fluids is important for understanding the formation of REE deposits in general.

2.4 REE-Mining and Processing

There are many challenges when it comes to the processing of REE-mineral bearing ores and their separation into the individual REE (Wall et al., 2017). Although there are more than 250 known REE-minerals — not counting REE-bearing minerals like apatite — an economically successful extraction of REE was only accomplished for monazite, xenotime and bastnäsite so far (Jordens et al., 2013; Tyler, 2004). Bastnäsite is one of 34 identified REE-fluorocarbonates minerals (Owens et al., 2018). Other members of REE-fluorocarbonate group with a potential economic application are synchysite and parisite. They are common REE-minerals in carbonatites and have a similar structure to bastnäsite. Nevertheless, mineral processing techniques used for bastnäsite do not work the same for other REE-fluorocarbonates. For instance, bastnäsite is paramagnetic while synchysite is diamagnetic (Al Ali, 2016), which means bastnäsite mineral processing cannot be applied to synchysite in the same way. As long as there is no economically viable way of extracting REE from other REE-fluorocarbonates than bastnäsite, they

cannot be considered as actual ore minerals. However, the zeta potential — can be used to deduce surface properties, which are important for mineral flotation — of parisite and bastnäsite are similar, which justifies a similar approach in mineral processing (Owens et al., 2018). This highlights the importance of the mineralogy of a potential REE deposit along with the less meaningful REE grade of the rock and the individual concentrations of economically more important REE, e.g., Dy or Nd. The amount of Th in REE ores is a major obstacle for REE mining (Wall et al., 2017) as was seen by the strong opposition Lynas Corp. had to face for opening up its extraction and separation facility LAMP in Malaysia (Ali, 2014).

According to Goodenough et al. (2017) secondary monazite in weathered carbonatites appears to be the favourable ore mineral for REE processing. Secondary (postmagmatic) monazite contains lower concentrations of Th and U than primary magmatic monazite and can benefit from the already established processing routes for monazite. Additionally, REE extraction as a by-product is a potential way of generating a rapid supply of REE. For instance, REE concentrations in red mud from aluminium productions would be a potential solution. The REE concentration is generally less than 1 wt% in red mud (Binnemans et al., 2015) but the volume of stockpiled red mud is more than 2.7 billion tonnes (Klauber et al., 2011). The fertiliser production from apatite or the Fe-extraction from Kiruna type mineralisation, are also promising alternative resources for the production of REE as a by-product (Al-Thyabat and Zhang, 2015; Binnemans et al., 2015). Additionally, the majority of carbonatites mined in the past were exploited for other commodities than REE (Woolley and Kjarsgaard, 2008a), which demonstrates their versatile economic value.

3 Carbonatites

Carbonatites are igneous rocks with a modal amount of primary (magmatic) carbonate minerals of > 50 % (Le Maitre et al., 2002). They are the magmatic rocks with the highest Rare Earth Element (REE) concentration, which commonly exceeds 1 wt% (Bühn, 2001; Hornig-Kjarsgaard, 1998). The high REE grade of carbonatites relative to other potential REE deposits means that there is less area to be disturbed by mining for the same amount of REE, which makes carbonatites more environmentally friendly than other low REE grade deposits, e.g. peralkaline rocks (Wall et al., 2017). Mining of deposits associated with carbonatites secures the major part of the annual REE demand.

3.1 Beginning of Carbonatite Research

The first mention of a carbonatite in the scientific literature was in 1846. The rock was described as a “kristallinen gangähnlichen Karbonatgesteins” — German for crystalline dyke-like carbonate rock (Verwoerd, 1966). The rock specimen was collected from the Kaiserstuhl volcano, which is nowadays known for its carbonatite dykes and tephra. A similar rock from the island Alnö — type locality for the ultramafic lamprophyre, alnöite — was described as a pyrochlore-bearing marble (Högbom, 1895). Although the rock was classified as a contact metamorphic product, a magmatic origin for the calcite was posited (Högbom, 1895). The monography “IGNEOUS ROCKS AND THEIR ORIGIN” (Daly, 1914) mentioned the undoubtedly primary origin of calcite in various magmatic rocks. The concept of magmatic calcite was further developed to the idea of carbonatite magma by Brøgger (1921) about the Fen Complex in Norway, and a new nomenclature regarding carbonatite and associated rocks was established. Rock type denotations like

søvite and fenite are still part of the scientific nomenclature. The origin of carbonatite magma was explained with the assimilation of large amounts of carbonates by a silicate magma and subsequent differentiation to a CO_2-rich and SiO_2-poor magma composition (Brøgger, 1921). Melting experiments showed a minimum temperature of 1339°C to melt calcite (Smith and Adams, 1923), which was used as an argument against the potential existence of carbonatite magma. Nevertheless, the discovery of many carbonatites worldwide — especially in the Chilwa-Alkali-Province — seemed to prove the existence of carbonatite magma. Eventually, experiments demonstrated the theoretical existence of carbonatite magma (Wyllie and Tuttle, 1960). Depending on the pressure (2.7 MPa – 400 MPa), the potential minimum temperature for the system CaO-CO_2-H_2O was calculated to be between 640°C and 685°C. In the same year, nature produced the ultimate proof with the first scientifically documented eruption of Oldoinyo Lengai — the only active carbonatite volcano in the world (Dawson, 1962). Since then, hundreds of new carbonatite complexes where discovered and their economic and scientific potential is the focus of many scientific endeavours.

3.2 Origin and Classification of Carbonatites

In theory, there are three ways to generate a carbonatite magma (Bell et al., 1998):

a) carbonatitic melts can derive from carbonate-silicate melts (e.g., nephelinite melts) by **liquid immiscibility** (Hamilton et al., 1979; Potter et al., 2017). Liquid immiscibility is the coexistence of two or more liquid phases and occurs when the sum of the free energies of the different liquid phases is smaller than the free energy of their mixture (Freestone, 1989). Liquid immiscibility is the commonly accepted mechanism to explain the presence of the natrocarbonatite at the

Oldoinyo Lengai in Tanzania (Sharygin et al., 2012). Crystallisation and alteration often masked the process of liquid immiscibility in older carbonatites. Therefore, eruptions of the Oldoinyo Lengai are a unique opportunity to learn more about this process in a carbonatite magma. For the eruption in 1993, Potter et al. (2017) identified a multi-stage liquid immiscibility between silicate, carbonatite, fluoride and halide phases — even a carbonate-carbonate unmixing was identified.

b) Carbonatite melt can originate from very low degrees of **partial melting** of mantle lherzolite, which directly produces a primitive carbonatite melt. Experimental data from Dalton and Presnall (1998) show that melting of model lherzolite with a CO_2 content of 0.15 wt% produces a continues magma with a composition ranging from carbonatite to ultramafic lamprophyre to kimberlite magma. The different types of magma are generated by changing the degree of partial melting from 0 to 1 %.

c) **Fractional crystallisation** of silicate phases leads to the concentrating of immobile elements and molecules like CO_2. For instance, the fractional crystallisation of nepheline, sodic pyroxene and melanite can produce silicate-free natrocarbonatite from a silicate-bearing natrocarbonatite, similar to the melt observed at the Oldoinyo Lengai (Petibon et al., 1998). Weidendorfer et al. (2016) demonstrated in the case of Brava Island that fractional crystallisation of Si-undersaturated primitive alkaline magmas leads to silicate melts evolving into the silicate-carbonatite melt miscibility gap. The fractional crystallisation of olivine and augitic clinopyroxene increases alkalis without increasing SiO_2.

Continuous fractionation of oxides (perovskite, titanomagnetite) and augitic clinopyroxene will lead to liquid immiscibility (f > 50%), providing the CO_2 concentration is high enough. Additionally, the saturation in alkali feldspathoids or feldspars will prohibit liquid immiscibility.

Based on phase equilibrium experiments, liquid immiscibility, as well as partial melting and fractional crystallisation, can produce carbonatite melts. All three processes are supported by integrated petrological studies, which indicate the existence of carbonatites with different paths of origin (Bell et al., 1998).

The source of carbonatites remains unclear and isotopic work from the last decades suggests that carbonatite melts can be generated in the lithosphere (Bell et al., 1982), the sub-lithospheric mantle (Bell and Simonetti, 2009) or show a mixed origin (Simonetti et al., 1998) (Fig. 3-1). According to Bell and Simonetti (2009), radiogenic and stable isotope data from carbonatites worldwide are consistent and point to a sub-lithospheric source for their parental melts. The melting process is associated with either asthenospheric upwelling or a more deep-seated activity (plume).

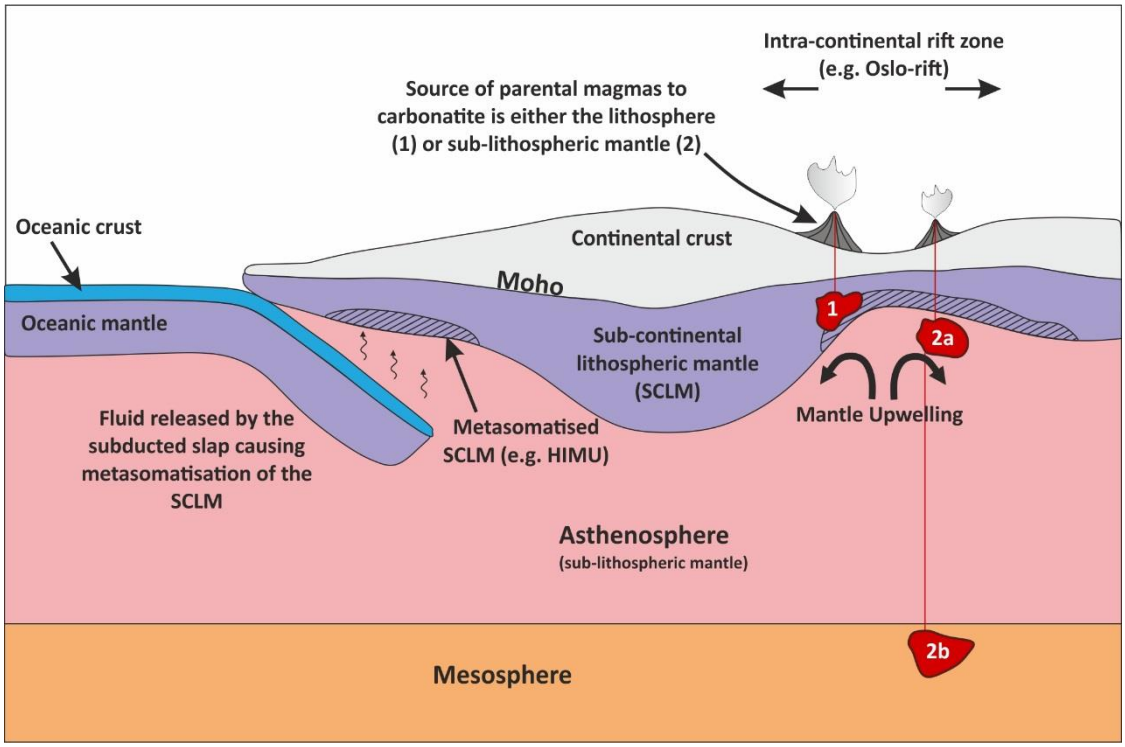

Figure 3-1: Schematic diagram to illustrate the two principal source region for carbonatite magmatism. According to Bell and Simonetti (2009), the source region for carbonatitic magmatism is either within the lithosphere (1), the sub-lithospheric mantle (2) or in both. Based on experiments by Dalou et al. (2009) suggest a possible generation of carbonatitic magma in the Mesosphere (2b). Additionally, the figure depicts the main process of mantle metasomatism by fluids from the subducted slab.

The evidence listed by Bell and Simonetti (2009), which links the carbonated melts (parental melts to carbonatite) to the sub-lithospheric mantle are:

a) The association of carbonatites with Large Igneous Provinces (LIPs), e.g., Deccan and Parana
b) Carbonatites with primitive noble gas isotopic signatures
c) Radiogenic isotope ratios similar to Ocean Island Basalts (OIBs)
d) The uniform, time-integrated Rb/Sr and Sm/Nd development lines for Sr and Nd isotopic data for carbonatites from the Superior Province, Canada, and the Kola Peninsula, Russia.

Additionally, modelling studies show that a very low degree of partial melting is not sufficient to explain the high degree of incompatible elements in carbonatite and peralkaline rocks. The source rock has to be metasomatically enriched (Fig. 3-1) in incompatible elements prior to partial melting (Arzamastsev et al., 2001). The metasomatic enrichment of the lithospheric mantle is most certainly associated with fluids rising from subducted slabs (Goodenough et al., 2014). The involvement of recycled crust in the petrogenesis of extrusive carbonatites has been questioned (Stoppa and Schiazza, 2013). However, experimental studies demonstrate that carbonatite or kimberlitic melts can be produced by melting of carbonated eclogite (Hammouda et al., 2009).

The publication “Carbonatites and Carbonatites and Carbonatites” (Mitchell, 2005) discusses the issues of classifying genetically different carbonatites and establishes a classification based on associated rock types, so-called “clans”, and distinguishes between carbonite sensu stricto, bona fide, sensu lato and pseudocarbonatites (Fig. 3-2). A variation in the source region for carbonatite parental magma, as described by Bell and Simonetti (2009), is plausible if you take multiple modes of origins into account The group of primary magmatic carbonatites (sensu stricto) comprises carbonatites associated with the nephelinite clan, melilite clan, aillikite association and peralkaline nephelinite - natrocarbonatites association (Mitchell, 2005).

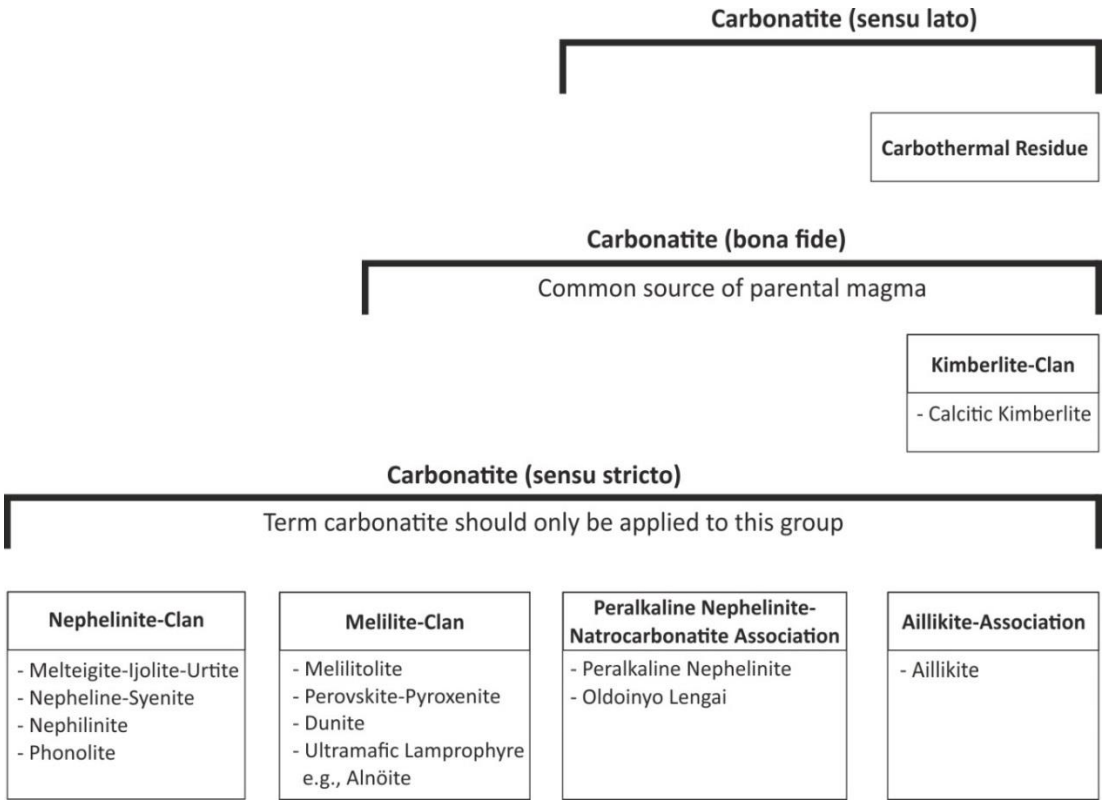

Figure 3-2: Carbonatite classification after Mitchell (2005).

Carbonatite bona fide additionally include carbonatites associated with kimberlites. These late-stage differentiates of kimberlite are recommended to be classified as calcite kimberlite to avoid that other types of carbonatites are mistakenly considered potential targets for diamond exploration (Mitchell, 2005). Carbonatites sensu lato include carbothermal residues from a wide range of magmatic rocks. Carbothermal carbonatites are precipitated at the subsolidus temperature from a CO_2-H_2O fluid that can be rich in CO_2 (carbothermal) or H_2O (hydrothermal). Carbonatite magmas, as well as alkaline silicate magmas, can generate carbothermal carbonatites (Woolley and Kjarsgaard, 2008b). A variety of sodic and potassic alkaline silicate rocks can produce late stage carbohydrothermal fluids, which can precipitate a variety of carbonate and silicate minerals to form carbothermal carbonatites (Mitchell, 2005). The mineral assemblage associated with carbothermal processes typically comprises calcite ± barite ± fluorite ±

quartz ± sulphides ± K-feldspar ± zeolites (Woolley and Kjarsgaard, 2008b). Late stage events involving carbothermal fluids typically concentrate REE, Sr and Ba but not niobium (Nb). The concentration of these elements results in the formation of Sr-, Ba-, and REE-bearing carbonates (Mitchell, 2005; Wall and Mariano, 1996). Although these hydrothermal fluids are important for REE-mineralisation, it is suggested to use the term "carbothermal residue" rather than "carbonatite (sensu stricto)" (Mitchell, 2005). Another group of carbonate-rich rocks (pseudocarbonatites) formed by anatectic melting of crustal rocks should not be considered carbonatites at all. The classification after Mitchell (2005) classifies carbonatite based on their genetic component and differentiates between three major groups of mineralogical similar rock types. However, within the sensu stricto carbonatite group —carbonatites in the purest sense — carbonatites of the nephelinite clan and melilite clan can be generated by partial melting, fractional crystallisation and liquid immiscibility. In an attempt to classify carbonatites based on their clan association, which indirectly groups carbonatites with the same origin, the classification after Mitchell (2005) created a group of sensu stricto carbonatites including at least ten differently generated carbonatites.

The classification of the International Union of Geological Sciences (IUGS) is simpler, and carbonatites are classified by the dominant carbonate mineral, e.g., calcite-carbonatite. If the carbonate species cannot be identified, the carbonatite is classified chemically (Fig. 3-3). Note that based on the classification after Mitchell (2005) and the IUGS classification, the world's only exponent of an active carbonatite volcano — the Oldoinyo Lengai — cannot be included and requires its own category (natrocarbonatite).

Rock contains > 50% modal carbonates			
Main carbonate mineral is known		Carbonate minerals are too fine-grained or in complex solid solution to be accurately determined	
Calcite	-> **Calcite-carbonatite** (coarse: sovite; fine: alvikite)	SiO_2 < 20% + CaO > 80%	-> **Calciocarbonatite**
Dolomite	-> **Dolomite-carbonatite** (beforsite)	SiO_2 < 20% + CaO < 80% $MgO/(FeO+Fe_2O_3+MnO) > 1$	-> **Magnesiocarbonatite**
Fe-rich carbonate	-> **Ferrocarbonatite**	SiO_2 < 20% + CaO < 80% $MgO/(FeO+Fe_2O_3+MnO) < 1$	-> **Ferrocarbonatite**
Na, K, Ca carbonates	-> **Natrocarbonatite**	SiO_2 > 20%	-> **Silicocarbonatite**

Figure 3-3: Carbonatite classification according to the IUGS (Le Maitre et al., 2002).

The classification after Woolley and Kjarsgaard (2008b) classify carbonatites, similar to Mitchell (2005), based on their associated rock types (Fig. 3-4).

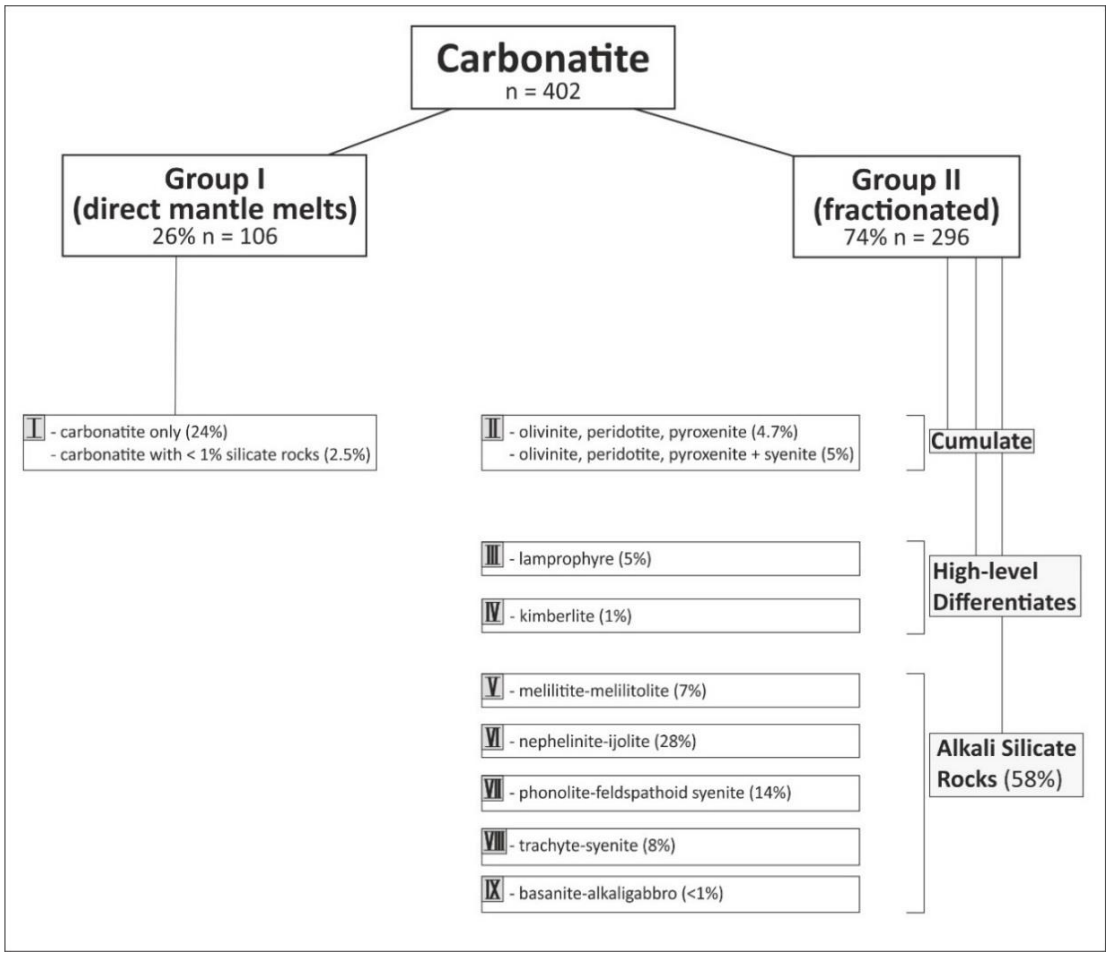

Figure 3-4: Carbonatite classification after Woolley and Kjarsgaard (2008b). The Fen Complex belongs to Group VI, which accounts for 28% of all carbonatites in the world.

The classification after Woolley and Kjarsgaard (2008b) divides carbonatites into magmatic carbonatites and carbothermal carbonatites. Carbothermal carbonatites are related to fluids from either carbonatite magmas or alkaline silicate magmas and can be distinguished from magmatic carbonatites based on their mineralogy and texture. Magmatic carbonatites make up for 84 % of the classified carbonatite occurrences and are of two principal groups: those generated directly in the mantle and those that have evolved from a silicate magma. The group of direct mantle melts make up 26 % of magmatic carbonatites and include the group of carbonatites (only) and carbonatite with less than 1% silicate rocks. Additionally, to the absence of mantle-derived silicate rock, which is precluding an origin from high-level differentiation for the carbonatites, there is strong evidence for these carbonatites to be true mantle melts. As pointed out earlier experimental studies showed the possibility that such melts exist (Dalton and Presnall, 1998). Further evidence is the presence of mantle xenoliths and xenocrysts in several extrusive diatreme-like carbonatite bodies and a mantle isotopic signature of the carbonatite bodies (Gittins and Harmer, 2003; Gittins et al., 2005). The other group of carbonatites — carbonatites evolved from a silicate magma — consist of eight different silicate rock associations, which further classified based on their genetic relation (Woolley and Kjarsgaard, 2008b). The ultramafic dunite, peridotite, pyroxenite ± syenite association is considered to represent a cumulate deposit fractionated from a parental magma. However, evidence from carbonatites and silicate rocks (e.g., nephelinite-ijolite association) show that these cumulates are generated by both magmas, which makes the origin of the cumulate unclear. Carbonatites associated with lamprophyre and kimberlite are regarded products of high-level differentiation processes. Over 50 % of all magmatic carbonatites are associated with one of the five alkaline silicate rock groups

— melilitite-melilitolite, nepheline-ijolite, phonolite-feldspathoidal syenite, trachyte-syenite and basanite-alkaligabbro. For most of these alkaline rocks, melting of a metasomatised mantle material is necessary (Menzies and Murthy, 1980; Pilet et al., 2008) — a similar theory is widely accepted to produce carbonatite (Jones et al., 2013). The change in the degree of partial melting or the type of mantle metasomatism triggers the formation of different types of magmatic rocks (Mitchell, 2005). Additionally, alkali silicate rocks can evolve into each other by fractional crystallisation (Woolley and Kjarsgaard, 2008b). The final formation of carbonatite melts from these silicate melts is the result of liquid immiscibility, fractional crystallisation or a combination of both processes.

Carbonatite associated with the group's "carbonatite only", "lamprophyres", "nephelinite" and "melilite" have sublithospheric signature, while carbonatites associated with shallower alkali silicate magmatism (e.g., phonolite, trachyte and basanite), can have a lithospheric signature as well as sublithospheric signature depending on the magmatic history.

The majority of the scientific community, including Mitchell (2005), believe in a genetic implication between carbonatites and their associated silicate rocks — most commonly nephelinites, ijolites, phonolites and nepheline syenites (Woolley and Kjarsgaard, 2008b). Gittins and Harmer (2003), on the other hand, argue that the association of carbonatite and silicate rocks is spatial rather than genetic. Commonly, the isotopic data does not indicate a genetic relationship and occasionally, proves the opposite (Gittins and Harmer, 2003). Silicate magma uses the same conduits as the carbonatite magma on their way to the crust. Therefore, according to Gittins and Harmer (2003), the silicate rocks should be referred to as "accompanying" rather than "associated". While this must

be true for the carbonatites without any associated silicate rocks, there is evidence showing a genetic relation between silicate rocks and carbonatites. The presence of interlayered tuffs of nephelinite and carbonatite shows a genetic relation between alkaline rocks and carbonatites (Woolley and Kjarsgaard, 2008b). Additionally, many carbonatite-silicate complexes show the emplacement of relatively minor amounts of young carbonatite in the centre of the complex or carbonatite ring dykes in the outer rim of the complex. This geometry of many carbonatite complexes is highly unlikely to be the product of magmatism, which uses the same magma pathways. The geometry, timing and volume strongly suggest a differentiation mechanism in these types of complexes. Additionally, studies from the Oldoinyo Lengai strongly indicate magma unmixing as the major process for the formation of the natrocarbonatite (Potter et al., 2017).

In summary, one must be aware of the differences between pseudocarbonatites, carbothermal carbonatites and magmatic carbonatites. There is strong evidence for one group of magmatic carbonatites to be derived directly from the mantle and another group of carbonatites to be the product of differentiation processes of specific rock types (n=8). However, although carbonatites in a silicate-carbonatite complex are likely to be associated with the silicate rocks, they can also accompany these rocks by using the same conduit. Considerable information about the geochemistry, mineralogy and texture of the carbonatite-silicate rocks has to be acquired before a proper classification is justified, and every carbonatite occurrence has to be discussed individually. To simplify the issue of classification, the IUGS classification is applied for the general rock description, and the classification after Woolley and Kjarsgaard (2008b) is restricted to a genetic discussion of carbonatites.

3.3 Spatial and Temporal Distribution

Over the last decades, there has been a steady increase in identified carbonatite complexes from 200 in the 60s, to 330 in the late 1980s (Woolley, 1989) to currently 527 known occurrences worldwide (Woolley and Kjarsgaard, 2008a) (Fig. 3-5).

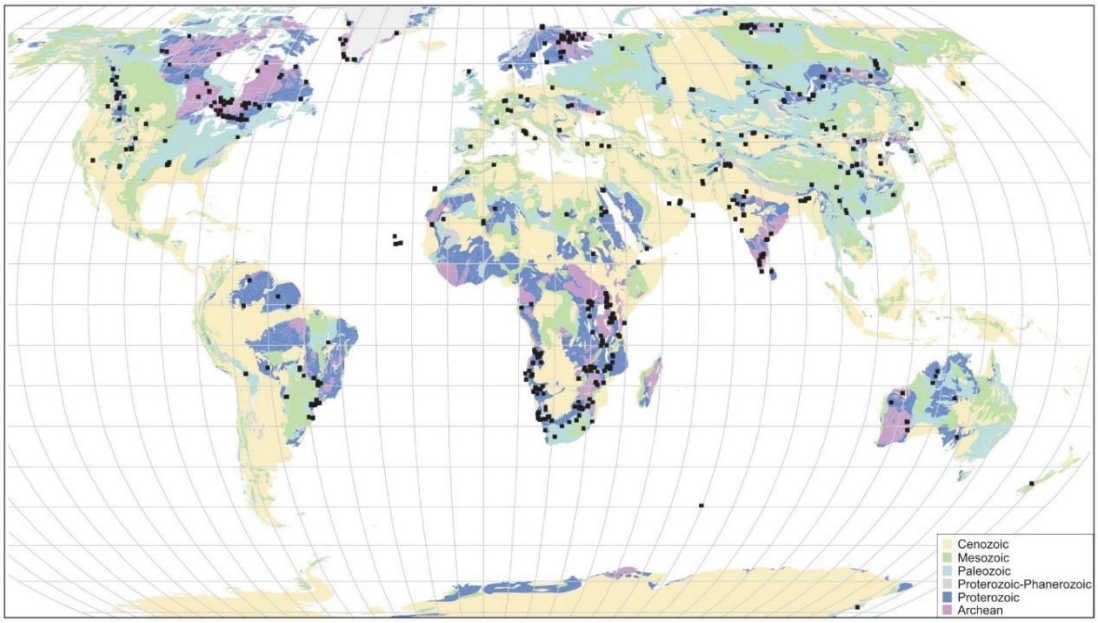

Figure 3-5: Geological world map showing all the known carbonatite localities (n = 527) in 2008 (Woolley and Kjarsgaard, 2008a).

Carbonatites are associated with dome structures, especially at an extensional intracontinental rift setting formed either by pull-apart tectonics or by asthenospheric upwelling (Chakhmouradian and Zaitsev, 2012). Thinning of the continental lithosphere during extension leads to a decompressional melting of the mantle and generates various melts, e.g., carbonatite and peralkaline magmas. The extensional setting in which carbonatite magmatism occurs is not limited to continental extension but can be widened to post-orogenic settings (Chakhmouradian et al., 2008).

The majority of carbonatites are located on relatively stable intraplate areas with an affinity to Precambrian rocks (Woolley and Kjarsgaard, 2008a). Although carbonatites rarely occur in a mountain belt, there is a spatial and temporal relationship to orogenic

processes with clustering of complexes along with defined areas outside of the orogenic belt (Woolley, 1989). A subordinate number of carbonatites are directly associated with oceanic fracture zones. The emplacement of carbonatites is along rifts, graben, crustal lineaments and transcurrent fault systems, which are major lithospheric structures providing pathways for magma to rise into the crust. At times, these deep structures are reactivated, which explains the episodic emplacement of carbonatites at the same locality — carbonatite magmatism at the Kapuskasing structure ranges from 1900 Ma to 1000 Ma (Bell et al., 1987). This ongoing magmatism of over 900 Ma favours magmatism controlled by structures in the underlying lithosphere (Woolley and Bailey, 2012). The post-Archean alkaline magmatism in West Greenland lead to the formation of carbonatites, kimberlites and ultramafic lamprophyres in three distinct but proximal regions within a period of approximately 1 Ga — Mesoproterozoic (1284–1209 Ma), Neoproterozoic (604–555 Ma) and Jurassic (165–155 Ma) (Secher et al., 2009). Protracted magmatism is common for carbonatite complexes, i.e. ultramafic dykes and carbonatite at Aillik Bay (590 Ma – 555 Ma) (Tappe, 2006).

The number of carbonatite intrusions exhibits an exponential increase in time, from the late Archaeon Era to the Cenozoic Era. This results in an accumulation of carbonatites in certain geographical areas and a correlation with generally larger orogenic and tectonic events (Woolley, 1989). The increase in carbonatite activity over time could be partly due to a preservation bias. Nevertheless, the number of Phanerozoic carbonatites in Precambrian rocks exceeds by far the number of Precambrian carbonatites. Modelling of the progressive modification of the mantle demonstrates the increase in the metasomatised mantle from the Archean onwards to a more metasomatised Proterozoic mantle source (Griffin et al., 2003). The reason for the increase in

carbonatite intrusions over time might be the increased proportion of metasomatically enriched lithosphere due to ongoing subduction processes (Woolley and Kjarsgaard, 2008a).

Although more than half of the dated carbonatites are younger than Precambrian, they still preferably occur in Precambrian rocks (Woolley and Kjarsgaard, 2008a), which could be an effect of the difference in thickness between Precambrian lithosphere and younger lithosphere. The thickness of continental lithosphere varies strongly and depends on its age and mechanisms of its formation. Most post-Archean lithosphere is between 100 and 200 km thick, whereas Archean lithosphere commonly exceeds 200 km (Condie, 2016). A thicker lithosphere prevents the migration of metasomatic fluids and helps to concentrate these fluids on the root of the lithosphere (Woolley and Kjarsgaard, 2008a). Additionally, an older lithosphere is also more likely to have experienced metasomatic events. The roots of Archean cratons can reach temperatures which are higher than those of well-mixed mantle (Michaut et al., 2009). This results in partial melting and the formation of carbonatite or nephelinite melts, especially in areas of strong metasomatism. The Canary and Cape Verde hot spots are the only hot spots producing oceanic carbonatites, and both have a lithospheric thickness of 90 km — the maximum thickness of oceanic lithosphere (Humphreys and Niu, 2009; Weidendorfer et al., 2016). Although the setting is different, it highlights the favourable formation of carbonatite in relatively thick lithosphere. In the case of partial melting of a metasomatised mantle, in order to produce either carbonatite magma or silica-undersaturated parental carbonatite magma the question of a conduit to reach the crustal level of emplacement remains. The common association of carbonatite with deep-seated faults is not a coincidence because they provide an effective pathway for

these migrating melts. The distribution of carbonatites in Precambrian rock is not random, and clusters are preferentially along or close to borders of these Precambrian rock units. This spatial association could be due to the easier ascent of magmas at these borders. The thickness of cratons generally declines towards the rims and deep-seated sutures or transform faults at the borders are marking the welding points of different terranes/micro terranes. This makes terrane borders optimal pathways for migrating melts, which originated at the root of a lithospheric keel.

3.4 Mineralogical and Geochemical Characteristic

Carbonate minerals are, by definition, the major component of carbonatites and consist of up to > 90 modal % in carbonate cumulates (Xu et al., 2007). The dominant carbonate species are calcite and dolomite-ankerite (Woolley and Kempe, 1989). The evolution of carbonatites is complex and involves a variety of postmagmatic processes, e.g., exsolution, subsolidus re-equilibration of igneous minerals, hydrothermal crystallisation, recrystallisation, isotopic resetting, grain abrasion, fragmentation, comminution, dissolution and tectonic mobilisation (Chakhmouradian et al., 2015b). Chakhmouradian et al. (2015b) point out that carbonatites are significantly more susceptible to change of their original magmatic texture than silicate rocks. For example, the brittle-ductile transition of a fine-grained calcite marble will occur at P<1kbar at ambient T (Fredrich et al., 1989). As a result, the original igneous texture is normally not preserved, and the carbonatite texture exhibits a juxtaposition of different petrographic characteristics.

Depending on the melt composition (Na, Ca, Mg, CO_2 and H_2O), the earliest carbonate phases are calcite, dolomite, nyerereite and gregoryite (Mitchell and Kjarsgaard, 2010).

Calcite — $Ca(CO_3)$

The early calcite is most likely to have a large amount of Mg and will undergo exsolution with decreasing T to Mg-poor calcite and dolomite (Chakhmouradian et al., 2015b). Vice versa, the exsolution of calcite from Ca-rich dolomite is unlikely because of the chemically narrow dolomite field. The crystallisation of calcite will increase the Mg concentration in the magma, which triggers the precipitation of dolomite. Eutectic-based graphic intergrowth of carbonate and non-carbonate minerals is rare but does occur (Chakhmouradian et al., 2015b). Zoning of calcite and dolomite is common. Dolomite develops Fe-rich rims and the capacity for calcite to include other elements decreases due to cooling. Calcite forms only limited solid solutions with Mg, Fe and Mn. The incorporation of trivalent ions is even more complicated and requires a coupled substitution to balance the charge. Nevertheless, REE enrichment in calcite can reach up to 2000 ppm (Chakhmouradian et al., 2016). The incorporation of tetravalent ions is even harder than the incorporation of trivalent ions; hence the concentration of Zr, Th and U tends to be less than 1 ppm (Chakhmouradian et al., 2016).

Dolomite-Ankerite — $CaMg(CO_3)_2$ - $CaFe(CO_3)_2$

The substitution of Fe^{2+}, Mg^{2+} and Mn^{2+} is common in mineral systems due to their similar charge/size ratio. Most natural dolomite $CaMg(CO_3)_2$ contains minor amounts of Fe (up to 2 mol%) and traces of Mn (Gregg et al., 2015). Dolomite forms a solid solution with the Fe endmember ankerite $CaFe(CO_3)_2$ and Mn endmember kutnahorite $CaMn(CO_3)_2$. In this PhD thesis, only trace amounts of Mn were analysed in dolomite-group minerals. Hence the focus for the following classification lies on the ankerite-dolomite series. There is no accepted universal definition for the compositional

boundaries between ankerite and dolomite. However, the International Mineralogical Association guidelines propose that solid solutions are classified using the "dominant-constitute rule" (Hatert and Burke, 2008) better known as the "50% rule" (Nickel, 1992). Therefore, Ankerite sensu stricto, as part of the ankerite-dolomite series, has to have more Fe atoms per formula unit (a.p.f.u.) than Mg a.p.f.u. (> 18 wt% FeO or 50 mol% $CaFe(CO_3)_2$). This is rare to find in carbonatites and seems to be restricted to late-stage postmagmatic mineral assemblages (Chakhmouradian et al., 2015b). As a result, most of the described ankerite from literature is, in fact, dolomite or ferroan dolomite. Ferroan dolomite is not universally defined either and sometimes used interchangeably with ankerite (Reeder and Dollase, 1989). In this study, ferroan dolomite is used to describe dolomite distinctly enriched in Fe with more than 2 mol% of $FeCO_3$, according to Tucker and Wright (1990).

Apatite — $Ca_5(PO_4)_3(F,OH,Cl)$

Hence, in apatite, the dominant anion contributes the prefix fluor-, hydroxyl- or chlor-. The structure of apatite allows a great range of substitution, which in turn can even change the normal hexagonal symmetry of apatite. Apatite is the most common non-carbonate mineral in carbonatitic rocks with an average of 6 wt% (Chakhmouradian et al., 2017) but its modal content can reach up to 90 % in cumulate rocks of the magmatic origin or hydrothermally formed quartz-apatite rocks (Broom-Fendley et al., 2016). Locally, carbonatites are associated with apatite-rich rocks (up to 70%) ± magnetite, (tetra-ferri)-phlogopite, forsterite, baddeleyite and pyrochlore. These apatite-rich rocks are of economic importance and are called phoscorite — also known as camaforite or the forsterite-free variety nelsonite (Cordeiro et al., 2010; Giebel et al., 2017; Haggerty

and Fung, 2006; Krasnova et al., 2004). Primitive carbonatite melts experimentally produced by low degree partial melting of carbonate-phosphate bearing lherzolite can incorporate up to ~20 wt.% P_2O_5 (Ryabchikov and Hamilton, 1993). However, experimental studies of natural dolomitic melts equilibrated with apatite show a lower concentration of 7.6 – 10.8 wt.% P_2O_5 (Guzmics et al., 2008). Apatite incorporates significant amounts of REE, which changes the distribution of REE, occasionally causing a decoupling of Y^{3+} and Ho^{3+} (Broom-Fendley et al., 2017a; Chakhmouradian et al., 2017). The REE partitioning between apatite and carbonate-rich melts is not established, and experimental studies give contradictory results (Hammouda et al., 2010; Klemme and Dalpé, 2003). However, calculated REE partitioning coefficients between natural apatite and their host carbonatite show REE are compatible in apatite with Middle Rare Earth Elements (MREE) having the highest compatibility (Brassinnes et al., 2005). According to Chakhmouradian et al. (2017), the absence of a general trend for the evolution of trace elements in apatite could be the result of different proportions of coprecipitated minerals, e.g., calcite, dolomite, amphibole, zircon, pyrochlore, columbite, monticellite, andradite and titanite. Apatite usually crystallises early in the magmatic history of a carbonatite due to the relatively low solubility of P_2O_5, together with magnetite, olivine and clinopyroxene (Chakhmouradian et al., 2008; Le Bas, 1989). The continued formation of carbonates maintains the residual melt saturation of P_2O_5, which allows the formation of apatite until the late-stage mineralisation events (Gittins, 1989). If the parental carbonatite magma is saturated in P_2O_5, apatite (or monazite) crystallises, and the bulk of REE will be removed early in the evolutionary stage. The fractionation of large quantities of calcite will enrich the residual liquid in REE. If the amount of fractionated apatite remains small compared to the amount of calcite, REE-

fluorocarbonates can become a stable liquidus phase (Xu et al., 2010). Classically, apatite crystals exhibit an increase of REE from the core to the rim of the crystal, which is contrary to what could be expected from the partitioning behaviour of REE between apatite and carbonatite magma. Possibly, the coprecipitation of non-phosphate mineral with a low D_{REE} causes an increase of P and REE in the remaining melt and triggers the precipitation of REE-rich apatite. Another potential explanation for REE-rich apatite rims is a mechanism behind the incorporation of REE in apatite. The incorporation of REE^{3+} into the mineral structure of fluorapatite requires a coupled substitution to keep the charge in apatite balanced. According to Hammouda et al. (2010), the REE compatibility depends on the Si content of apatite. REE are compatible in Apatite containing 3.5-5 wt% SiO_2 and incompatible in Apatite with 0.2 wt% SiO_2. The incorporation of Si in apatite is one way to keep the charge in apatite balanced:

$$REE^{3+} + SiO^{4-} = Ca^{2+} + PO_4^{3-}$$ (Pan and Fleet, 1995)

Therefore, the higher concentrations of REE in the outer rim of apatite might be a result of a higher Si content in the magma, which therefore enables the increased incorporation of REE in apatite. Locally apatite becomes the main carrier of REE and in extreme cases can incorporate up to 8.3 wt% of REE (Hogarth, 1989).

Geochemical characteristics

Carbonate-rich magmas generated by partial melting of carbonated peridotite, from 2 GPa to at least 7 GPa, are dolomitic with a Ca/(Ca + Mg) ratio between 0.7 and 0.5 (Wyllie and Lee, 1998). During the ascent of carbonatitic melts, they are likely to react with the surrounding mantle and become more calcitic in composition. This process is called metasomatic wehrlitization (Wyllie and Lee, 1998). The evolution of primitive carbonatitic magma to higher $CaCO_3$ composition is increased by degassing and fractionation of magnetite and forsterite (Chakhmouradian et al., 2015b). Compared to basaltic magma, silica undersaturated magmas and carbonatite magmas show a strong enrichment of LREE and a greater degree of fractionation between LREE and HREE, which implies a very low degree of partial melting (< 1%) for their parental magma (Chakhmouradian and Zaitsev, 2012). The origin of the LREE enrichment in carbonatites is part of an ongoing debate. Hornig-Kjarsgaard (1998) suggest that the LREE-enrichment is inherent from the parental magma and is produced during partial melting because the crystallisation of most of the minerals does not change the REE pattern. Minerals like calcite, dolomite and apatite do not preferentially incorporate REE, and minerals which preferably incorporate certain REE occur in an insignificant quantity (e.g. pyrochlore) (Fig. 3-6A). Ionov and Harmer (2002) on the contrary identified a significant difference between LREE enrichment in calcite phenocrysts and LREE of later interstitial calcite crystals, which means that fractional crystallisation has to be an effective and necessary process to increase LREE enrichment in carbonatites (Fig. 3-6B).

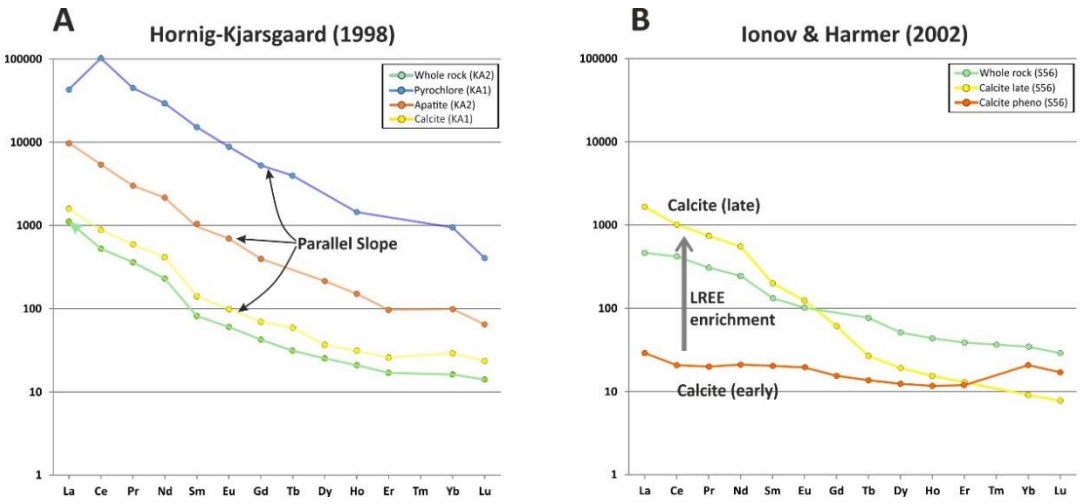

Figure 3-6: REE concentrations normalised to CI1-chondrite values from McDonough and Sun (1995). A) Normalised REE values for whole rock, pyrochlore, apatite and calcite from the Kaiserstuhl carbonatite. The negative slope of the graph indicates an enrichment in LREE relative to HREE. However, the parallel slope of the different phases and whole rock data indicates that fractional crystallisation has not caused the LREE enrichment (Hornig-Kjarsgaard, 1998). B) Normalised REE values for whole rock, early calcite phenocryst and late interstitial calcite from the Spitskop Carbonatite. Early calcite has a flat REE curve, while later interstitial calcite has a steeper curve. The strong LREE enrichment in interstitial calcite relative to early calcite phenocryst indicates that fractional crystallisation has played a significant role in producing this pattern (Ionov and Harmer, 2002).

Bühn (2001) modelled REE fractionation for a carbonite melt for various amounts of precipitating calcite, fluorapatite and clinopyroxene. Results were coherent with enrichment and slope of chondrite-normalised REE plots of actual carbonatites. However, some pristine mantle-derived carbonatites show a strong LREE enrichment, which indicates that fractional crystallisation is not necessary to produce a strong LREE enrichment signature. Although the different levels of LREE for pristine carbonatite could be due to the source material and melting conditions. Additionally, the dismissal of fractional crystallisation as a potent process for LREE does not automatically mean that LREE enrichment must be inherent by the parental magma because other processes like immiscibility in relation to the pressure can change the REE pattern significantly (Moine et al., 2004). Xu et al. (2010) showed that monazite could be part of early precipitation, which in turn would change the REE composition of the evolving melt drastically. Besides REE, trace element distribution diagrams normalised to the primitive

mantle composition show in general negative anomalies for Pb, Zr and Hf in calcite carbonatite worldwide (Nelson et al., 1988; Woolley and Kempe, 1989).

3.5 Petrology of Carbonatites

Carbonatite complexes exhibit the same magmatic features — lava, tephra, diatreme, dykes, ring-dykes, sills, ring complexes — as silicate complexes (Barker, 1989). The main difference is the smaller size and shorter magmatic life span of the carbonatite magmatism. Common textures in carbonatites are polygonal texture, rounded autoliths of disaggregated cumulate, classic igneous texture, spinifex texture, randomly oriented laths to irregularly shaped grains of variable size either as a granular fabric or interstitially(Barker, 1989). Carbonatites usually make up the smallest proportion in a composite magmatic complex. Furthermore, they form at a late stage in the magmatic history of the complex either in the centre of the complex or as outer ring-dykes (Verwoerd, 1966). SiO_2-undersaturated alkali silicates from the nephelinite clan or melilite clan are normally forming the main part of a composite intrusion. Carbonatites do not cause a contact metamorphic reaction of the surrounding country rock due to their relatively low T. Nevertheless, carbonatite magmas are highly enriched in chemically aggressive alkalis and typically form an alkali metasomatic halo — called fenite. Fenitisation exhibits in comparison to other alkali metasomatic events a pronounced deficiency of SiO_2. Plutonic carbonatites commonly grade into a variety of meso- to melanocratic cumulate rocks dominated by apatite, silicate or oxides (Chakhmouradian et al., 2015a). It is because of the ultralow viscosity and generally low density (≤ 2.6 g/cm^3) of carbonatitic melts (Kono et al., 2014), that the formation of cumulate layers is enabled (Dobson et al., 1996).

3.6 REE-Rich Carbonatites

Carbonatites are enriched in large-ion lithophile elements (LILE) and high-field-strength elements (HFSE), and form minerals especially high in these elements. Some of these minerals — e.g., bastnäsite, monazite, apatite, pyrochlore, fluorite, baddeleyite, thorite, and uraninite — were economically exploited in the past for REE, P, Nb, Fe, Zr, Th, U and F. In addition, Cu, fluorite, vermiculite and limestone were mined and by-products such as Ta, Ag, Au and PGEs were utilized (Woolley and Kjarsgaard, 2008a).

Carbonatites have the highest REE concentration of all magmatic rocks and are the major source for REE mining (Cullers and Graf, 1984). In most carbonatites, REE are primarily incorporated in rock-forming minerals such as calcite, dolomite, apatite and silicates (Hornig-Kjarsgaard, 1998). REE concentrations, as well as REE-minerals, are commonly enriched in magnesiocarbonatite and ferrocarbonatite that may be either igneous or carbohydrothermal rocks (Ruberti et al., 2008; Wall and Mariano, 1996). REE behave as incompatible elements in a carbonatite magma, and REE concentration generally increases from a primitive calciocarbonatite (0.45 wt%) to magnesiocarbonatite (0.50 wt%) to an evolved ferrocarbonatites (1.29 wt%) (Woolley, 1989). Although the formation of magmatic REE-minerals is possible, for example, bastnäsite in Mountain Pass or monazite in Miaoya, it is a rare exception (Mariano, 1989; Wall and Mariano, 1996; Xu et al., 2010). Experimental data from Wyllie et al. (1996) demonstrates an initially low REE concentration in the magma, which is dispersed among the major rock-forming minerals so that a REE mineralisation does not develop in this early stage. The presence of hydrothermal REE minerals, e.g., REE-fluorocarbonates, monazite and ancylite as veins or fine-grained polycrystalline clusters (Marien, 2014) in interstitial fillings are most common for carbonatites (Wall and

Mariano, 1996). REE are amongst the least soluble trace elements and are considered to be immobile during low-grade metamorphism, weathering and hydrothermal alteration (Rollinson, 1993). This is however, in conflict with the majority of REE-deposits, which have a clear hydrothermal origin. Humphris (1984) emphasised that one must be careful with interpreting REE in highly altered rocks because of the incompletely immobile nature of REE. Since the 1990s considerable evidence has been accumulated — for elevated REE concentration in hydrothermally altered rocks, REE-bearing minerals in fluid inclusions and REE deposits of hydrothermal origin — showing the possibility for REE to be mobilized by crustal fluids (Broom-Fendley et al., 2017a; Dowman et al., 2018; Marien, 2014; Migdisov et al., 2009). Since then the physicochemical controls on REE mobility have been subject of multiple experiments, which highlight the mobility of REE complexes with chloride, fluoride, sulphate and hydroxide ligands (Migdisov and Williams-Jones, 2014; Williams-Jones and Migdisov, 2014; Williams-Jones et al., 2012).

4 Fen Complex

The Fen Complex is located in the southern part of Norway, ca. 120 km SW of Oslo, in proximity to the small town of Ulefoss and 12 km outside of the Oslo Graben (Fig 4-1). It is a composite intrusion of Ediacaran age (578±24 Ma Rb-Sr isochron age (Dahlgren, 1994) and 583±15 Ma Ar/Ar age (Meert et al., 1998)) comprising of peralkaline silica undersaturated rocks and carbonatites, which intruded into the 1105 Ma old Telemark Gneiss. Rødbergite is one of the petrological units of the Fen Complex with the highest concentration of Rare Earth Elements (REE) (Andersen, 1984; Andersen, 1989b; Bergstøl and Svinndal, 1960; Marien et al., 2018; Schilling, 2013). The focus of this thesis is to create an improved REE-mineralisation model for the formation of rødbergite, which in turn will support mining companies to conduct their REE exploration at Fen in a more effective way. This chapter will provide an overview of the regional and local geological setting of the Fen Complex and will help the reader to familiarise themselves with the uncommon rock types of the Fen Complex.

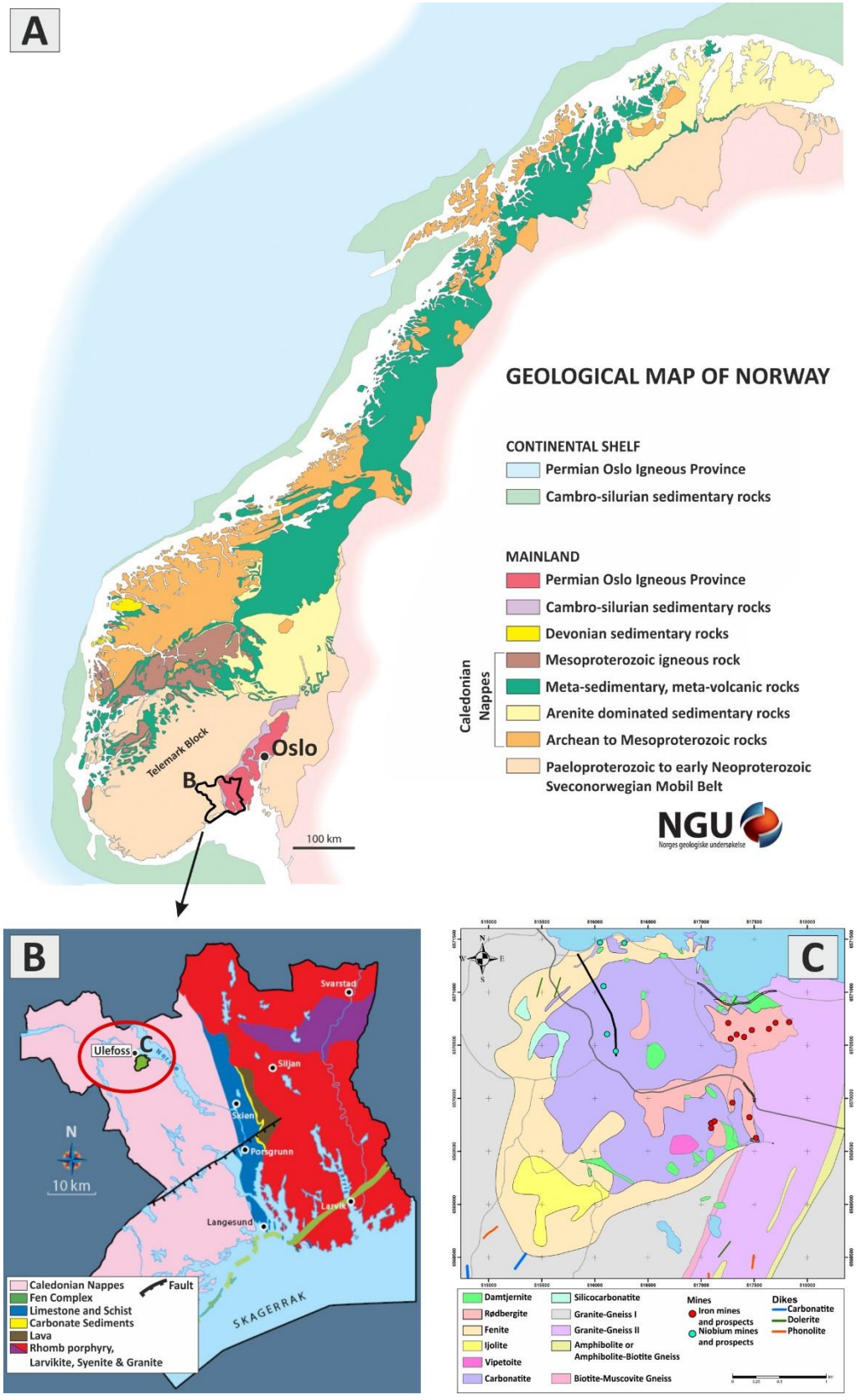

Figure 4-1: A) Simplified geological map of Norway with the rocks of the Oslo rift in red. The Fen Complex is within the outline of map B (NGU, 2017). B) Geological map of the counties Vestfold and Telemark, illustrating the Fen Complex (green) proximal to Ulefoss (Gea Norvegica Geopark, 2018) C) Simplified geological map of the Fen Complex modified after Bergstøl and Svinndal (1960) with minor incorporation of features from Ihlen et al. (2014) modified after Dahlgren (2004).

4.1 The Discovery of the Fen Complex and Subsequent Work

The Fen Complex was part of ongoing Fe-ore exploitation from 1652 to 1927 (Vogt, 1910). The unique peralkaline rock association of the Fen Complex was first scientifically described by Brøgger (1921). Based on the observation made at the Fen Complex, the concept of carbonatite magma was formulated, and a range of new rock types was defined. Although the carbonatite classification introduced by Brøgger (1921) is now to a large extent superseded (and therefore not applied in this thesis), it is necessary to be familiar with rock names like søvite and rauhaugite, which have their type locality in the Fen Complex — please see the rock glossary for further information or chapter 4.4.

Bowen (1924) and Sæther (1957) were opposing the theory of carbonatitic magma and argued that the carbonatites of the Fen Complex are the product of metasomatic replacement of the silicate rocks by carbonate-rich fluids. Other authors postulated a connection to the Oslo magmatism, either in the form of contact metamorphism or as a differentiate from the Oslo magmas (Tomkeieff, 1958). A genetic connection between the Fen Complex and the Oslo-rift magmas was later on falsified by Faul et al. (1959) using K-Ar geochronology on biotite resulting in a Precambrian age for the Fen Complex. (Friedrichsen, 1968)The calculated formation temperatures of 600 – 700°C for søvite (calcite carbonatite) and rauhaugite (dolomite carbonatite) supported a magmatic origin of the Fen carbonatites. The formation temperature of ~200°C for rødbergite indicated a metasomatic formation instead (Friedrichsen, 1968). By the early 70s, the magmatic origin of carbonatite at the Fen Complex and the Precambrian to Cambrian age of the complex (530-600 Ma) was generally accepted by the scientific community (Poorter, 1972). Since then the Fen Complex has been the focus of continuous research and especially Ramberg (1973), Mitchell and Brunfelt (1974); (1975), Griffin and Taylor

(1975) and Andersen (1984); (1986; 1991) contributed much to the general understanding of the Fen Complex.

4.2 The Geological Setting of Scandinavia

The geological history of Norwegian rocks is a long and complex story of continental growth through plate accretion during multiple orogenic processes and rifting events. In the context of this PhD-thesis, the geological setting is an essential framework to understand the formation of the Fen Complex.

The Creation of Fennoscandia (3.5 Ga – 1.85 Ga)

The geological creation of the oldest rocks from the microcontinent Fennoscandia (Fig. 4-2), which Norway is a part of, dates back to the Paleoarchean, ca. 3.5–3.2 Ga (Slabunov et al., 2006).

Fennoscandia was largely formed through the accretion of terrane blocks with an interim rifting event during 3.1 Ga – 2.7 Ga and 1.95 Ga – 1.85 Ga (Bogdanova et al., 2008; Lahtinen et al., 2005)

Formation of the East European Craton (ca. 1.85 Ga)

After 1.85 Ga, Fennoscandia started to collide with Volgo-Sarmatia to create the East European Craton (ECC) (Fig. 4-2). The Volyn-Orsha and Mid-Russian aulacogens outline the suture between these two microcontinents.

ECC as Part of Columbia (ca. 1.7 Ga – 1.4 Ga)

At 1.7 Ga the EEC became part of the supercontinent Columbia (Karlstrom et al., 2001) and grew between 1.73 and 1.48 Ga through the accretion of three NS-trending crustal belts on its southwest rim. First the Eastern Segment between the Protogine Zone in the east and the Mylonite Zone in the west (Bogdanova et al., 2008), second the Idefjorden

terrane west of the Mylonite Zone and third the Telemarkia terrane which, is separated from the Idefjorden terrane by the small Bamble and Kongsberg terranes (Bingen et al., 2005) (Fig. 4-3).

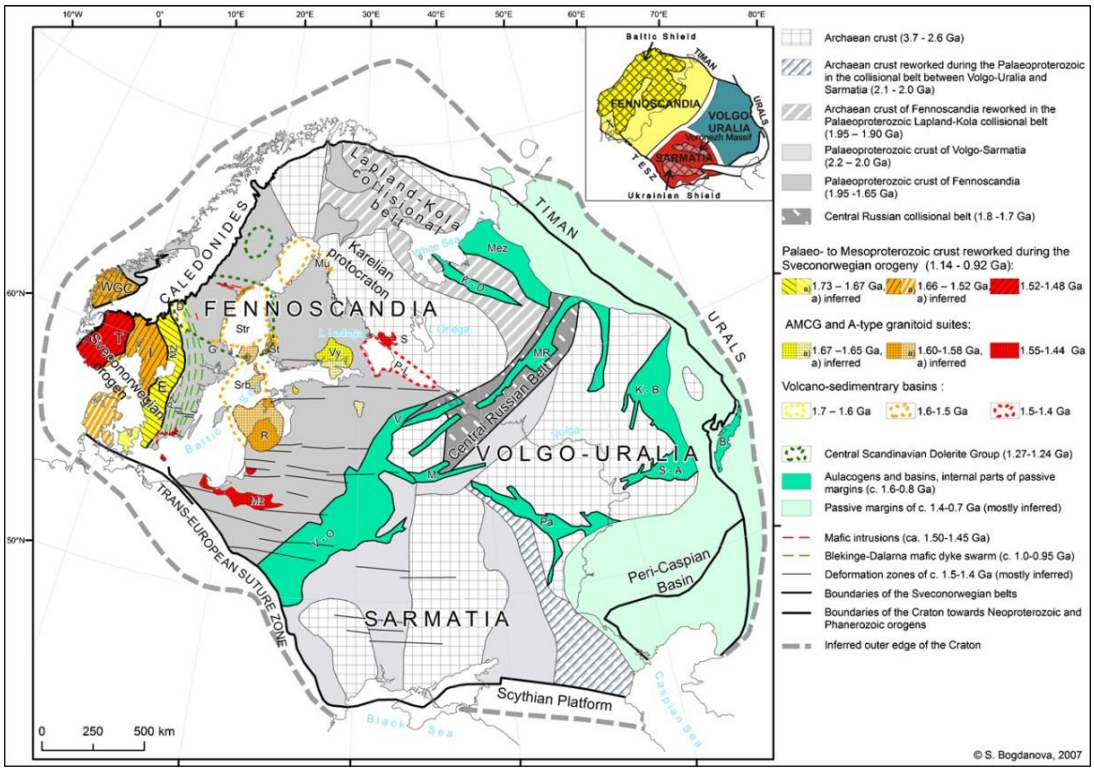

Figure 4-2: Late Paleoproterozoic to Early Neoproterozoic tectonic complexes in the East European Craton (Baltica) (Bogdanova et al., 2008) . B, Bashkirian uplift (S. Urals); D, Dala basin; E, Eastern Segment; G, Gävle graben; **I, Idefjorden terrane**; K-B, Kama-Belsk aulacogen; K-D, Kandalaksha-Dvina graben; M, Moscow graben; Mez, Mezen rifts; MR, Mid-Russian aulacogen; Mu, Muhos graben; MZ, Mylonite Zone; Mz, Mazury igneous complex; Pa, Pachelma aulacogen; P-L, Pasha-Ladoga graben; PZ, Protogine; Zone R, Riga pluton; **T, Telemarkia**; S, Salmi pluton; S-A, Sernovodsk-Abdulino aulacogen; St, Satakunta graben; Srb, Strombus basin; Str, Strömmingsbådan basin; V, Valday graben; V-O, Volyn-Orsha aulacogen; Vy, Vyborg pluton; WGC, Western Gneiss Complex.

Between 1.5 and 1.4 Ga a range of igneous events, metamorphism and structural deformation occurred that are the result of the collision of the EEC with Amazonia. The so-called Danopolonian Orogeny caused extensive EW faulting in large parts of southern Fennoscandia and adjoining parts of Sarmatia (Bogdanova et al., 2001). Around 1.4 Ga the supercontinent Columbia broke apart, and a predominantly extensional setting occurred in the formation of aulacogens and bimodal magmatism in large parts,

especially in the eastern ECC. The gabbro-tonalite Tromøy complex in the Bamble terrane formed between 1.20 and 1.18 Ga. As a remnant of an island arc, it represents a subduction-related setting right before the start or the Sveconorwegian Orogeny.

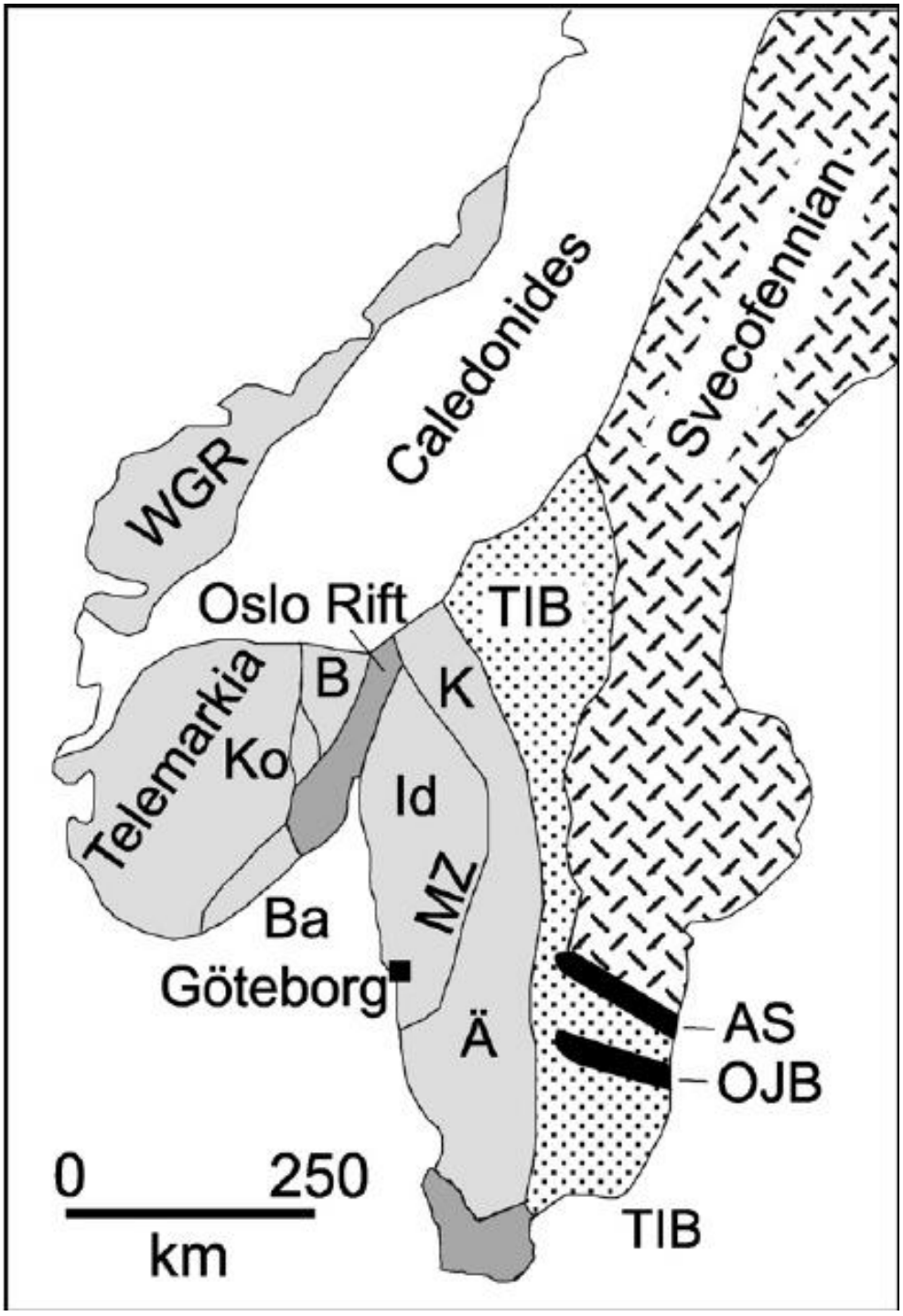

Figure 4-3: Main Precambrian units of SW Scandinavia (Åhäll and Connelly, 2008). Askersund suite (AS), Oskarshamn-Jönköping Belt (OJB), Transscandinavian Igneous Belt (TIB), Klarälven-Ätran segment (K and Ä), Idefjorden terrane (Id), Western Gneiss Region (WGR) and Telemarkia terrane. B, Ba and Ko mark the Begna, Bamble and Kongsberg terranes, and MZ the Mylonite Zone.

Sveconorwegian Orogeny (1140 Ma – 900 Ma)

The Sveconorwegian belt developed during the Grenvillian-Sveconorwegian orogeny between 1140 and 900 Ma as the result of a collision of Baltica and possibly Amazonia (Viola et al., 2011). The Grenvillian-Sveconorwegian orogeny is part of large-scale mountain building processes, which finally produced the supercontinent Rodinia (McMenamin and McMenamin, 1990). During the Sveconorwegian Orogeny, the Bamble terrane and Kongsberg terrane were thrusted onto Telemarkia, developing strong NE-SW trending structural grain in the Bamble terrane (Henderson and Ihlen, 2004). The main collision event caused widespread regional metamorphism within the Telemarkia and Idefjorden terranes. General N-S to NW-SE trending shear zones were developed due to transpression and formation of a nappe complex (Bogdanova et al., 2008). The final Sveconorwegian convergence is associated with a major deformation in the Mylonite Zone and crustal melting of Telemarkia (Bogdanova et al., 2008). Locally, the eastern part of the Sveconorwegian belt contains relics of eclogite, which represent deeply buried Fennoscandian crust during the height of the orogenic process. Already during the time of the Sveconorwegian orogeny in the SW, parts of the EEC passive continental margins showed incipient features of break-up and subsequent rifting of the EEC occurred throughout the Cryogenian (Pease et al., 2008).

The Breakup of Rodinia (620 Ma – 550 Ma)

The breakup of Baltica from supercontinent Rodinia started around ca. 620-550 Ma, with the opening of the Iapetus Ocean between Baltica and Laurentia (Pease et al., 2008).

Caledonian Orogeny (490 Ma – 390 Ma)

During the early Ordovician, the Caledonian orogeny starts with the subduction of the Iapetus Ocean under Baltica and reaches its final stage with the collision between Baltica and Laurentia in the mid-Silurian to early Devonian (Gee et al., 2008). The continent collision resulted in the partial melting of the underthrusted plate (Baltica) and an E and W-vergent thrust system was established. Today most of the basement in southern Norway consists of the lower part of the orogenic belt, which contains material from both the closed Iapetus Ocean and proto-Baltica (Gee et al., 2008)

Oslo rift (308 Ma – 245 Ma)

The Oslo rift is part of a prolonged period of extensional faulting and volcanism in NW Europe during the late Carboniferous and Permian. According to Larsen et al. (2008), the rift was formed by lithospheric stretching initiated during the last stage — the consolidations stage or tectonic collapse (Wilson et al., 2004) — of the Variscan orogeny. Over a period of 65 Ma, the Oslo rift went through six stages of magmatic and tectonic activity (Larsen et al., 2008). The entire Oslo rift is 500 km long and is limited to the S by the Sorgenfrei-Tornquist zone. The classic Oslo Graben is composed of two grabens — Akershus and Vestfold — and has a length of 220 km with a width of 60 km. The Oslo Graben is characterised by a large volume of volcanic material similar to the East African rift zone (Larsen et al., 2008) — known for its high concentration of carbonatites. Neumann et al. (2004) describe at least two mantle sources involved in the melting processes of the Oslo rift. The eruption of Skien basalt and Brunlanes basalt in the southern part of the Oslo rift mark the earliest magmatic activity. These silica undersaturated magmas of basanite, melilites and nephelinites are highly alkaline-rich lavas with the isotopic signature of a metasomatically enriched mantle — HIMU (high-

μ). They are generated by a low degree of partial melting of the asthenosphere, which was subsequently modified by the lithospheric mantle and crustal components (Neumann et al., 2004). The involvement of a potential plume has been indicated (Wilson et al., 2004). The magmatic sequence is just 12 km away from the Fen Complex, and the carbonatitic magmatism of the Fen Complex is seen as the cause of the HIMU signature of the mantle in this area (Neumann et al., 2004).

Uplift of Scandinavia (65 Ma – today)

Extension persisted and the mid-Norwegian margin experienced several periods of rifting since the formation of the Caledonides culminating in the final break-up and subsequent opening of the North Atlantic Ocean ca. 56 Ma ago (Eldholm et al., 1989; Mosar et al., 2002). The topographic evolution of Norway is controversial and likely to be the result of glacio-isostatic rebound and a tectonic component — most likely associated with the Alpine orogeny (Anell et al., 2009; Mörner, 1977).

4.3 Origin of the Fen Complex

Several geological events mentioned in chapter 4.2 play an important role in the formation of the Fen Complex.

Tectonic Setting

The Fen Complex is located at the eastern part of the Telemarkia terrane close to the former Bamble (25 km), Kongsberg (40 km) and Idefjorden terranes (80 km) (Fig. 4-3). The contact zones between those terranes are marked by deep and extensive shear zones — Kristiansand-Porsgrunn Shear Zone, Saggrenda-Sokna Shear Zone and Vardefjell Shear Zone (Fig. 4-4)—, which were created during the Sveconorwegian orogeny (Ebbing et al., 2005; Starmer, 1993). Like most of the carbonatite and alkaline

complexes in the Fennoscandian Shield, the Fen Complex is associated with deep fracture zones (Brøgger, 1921). These kinds of deep-seated shear zones tend to be reactivated repeatedly over time and the presence of the Oslo rift indicates that under a certain stress field, the area is prone to rifting — a typical tectonic setting for the formation of carbonatites (e.g. East African Rift System) (Woolley, 1989).

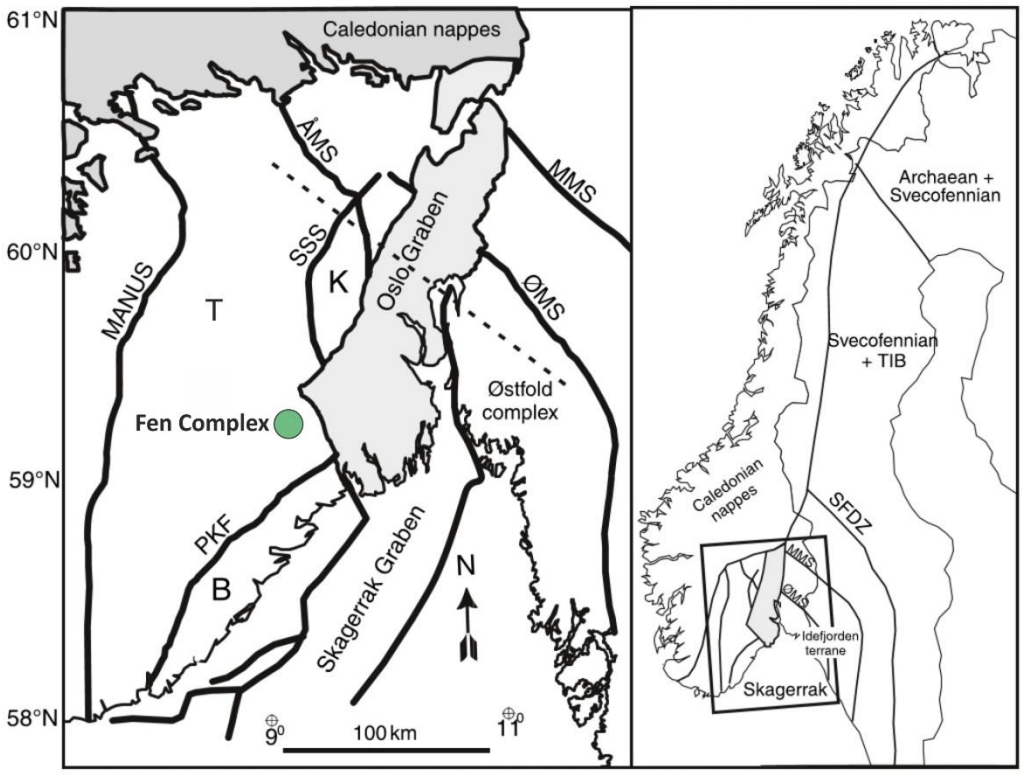

Figure 4-4: Structural map of the Oslo Rift, surrounding terranes and the Fen Complex (green circle) modified after Ebbing et al. (2005). T, Telemark sector; K, Kongsberg sector; B, Bamble sector; SFDZ, Sveconorwegian frontal deformation zone; SSS, Saggrenda-Sokne shear zone; MMS, Mjøsa-Magun mylonite zone; ØMS, Ørje mylonite zone; A ˚ MS, A ˚ mot-Vardefjell shear zone; PKF, Porsgrunn-Kristiansand shear zone; MANUS, Mandal-Ustaoset Fault; TIB, Transcandinavian Igneous Belt.

Besides the association with major faults, there is evidence for a link with areas of higher seismic activity and elongated gravity anomalies (Ramberg, 1973). Carbonatite complexes like Fen occur in areas of thinner lithosphere compared to the rest of Fennoscandia (Heincke et al., 2008; Meert et al., 1998; Tappe, 2006). The thinning of

crust can be observed specifically in the Oslo Graben and in varies graben of the Kola Peninsula, where a positive gravity anomaly has been interpreted as a result of crustal thinning (Ramberg, 1973). Additionally, the Vestfold Graben and the Skagerrak Graben significantly disrupt the geometry of the Oslo rift. Both graben are mechanically connected via the Langesund Accommodation Zone (LAZ) (Larsen et al., 2008). Lake Norsjø and the Fen Complex are located in the extension to the LAZ. The elongated geometry of Lake Norsjø indicates the propagation of the LAZ or a similar kind fault zone. The Fen Complex is located at the intersection of the extended NW-SE striking LAZ and the NNE-SSW striking Oslo rift (Larsen et al., 2008; Ramberg, 1973). Carbonatites are typically associated with the intersection of two fault systems (Woolley, 1989). The Oslo rift follows the contact shear zone of the terranes Telemarkia, Idefjorden, Kongsberg and Bamble (Fig. 4-4) partly. Although the Fen Complex is older than the Oslo rift, the Oslo rift fault zones are likely to be partly reactivated zones of structural weakness, which might have already worked as a conduit for the parental magma of the Fen Complex in the past. The link to deep tectonic structures indicates a common deep magmatic process for the Oslo Graben and the Fen Complex.

In summary, the Fen Complex is in an area located at the intersection of two major deep-seated fault zones, which can be partly traced back to Precambrian terrane borders. The NE-SW trending Oslo Graben and the presumed extension of the NW-SE trending Danish-Polish depression mark the former terrane boundaries. These fault zones were reactivated multiple times and showed a clear tendency for rifting. The formation of carbonatite is typically associated with these characteristics (refer to chapter 3.3).

Mantle Source

In chapter 3.2, the presence of a metasomatised mantle as the source for carbonatite magmatism is highlighted (Arzamastsev et al., 2001). Lherzolite nodules from Fen damtjernites coming from just below the base of the continental crust close to 33 – 34 km and support the mantle origin of the Fen magmatism (Griffin, 1973). Reported mantle garnet xenocrysts in the damtjernite (Dahlgren, personal communication) suggest a depth >60-85 km – the depth where garnet becomes stable in a lherzolitic mantle rock at the mantle solidus (Wood et al., 2013). The subduction of oceanic crust is a potential mechanism to change the mantle chemistry (Goodenough et al., 2014; Woolley and Kjarsgaard, 2008b). There are several reasons to assume that the mantle source of the Fen Complex was such a metasomatised lithospheric mantle: Most parts of the Telemarkia, Bamble, Kongsberg and Idefjorden terranes were formed in an active continental margin setting (Bingen et al., 2005); Relics of eclogite prove the subduction of fluid into the mantle (Bogdanova et al., 2008); The HIMU signature of the early Oslo graben magma, proximal to the Fen Complex prove the presence of a metasomatised mantle region underneath a larger part of the Telemarkia, Bamble and Idefjorden continental crust (Neumann et al., 2004). The carbonatitic magmatism of the Fen Complex is seen as the reason for the HIMU signature of the mantle in this area (Neumann et al., 2004). Regarding the general small volume of carbonatite magma in complexes around the world, it is questionable whether carbonatitic magmatism could alter a mantle source to the degree that would have a significant effect on the isotopic signature of voluminous basaltic magma produced by partial melting of this altered mantle. The HIMU signature of the early Oslo graben magma is rather an indication of the regional metasomatised mantle signature and the geological processes able to melt

this mantle source and conduit the magma to the upper crustal level. The HIMU mantle was the source for the carbonatite magma rather than the result of it. The HIMU mantle was also the source of alkali-rich nephelinites of the Oslo Graben, which essentially represent the volcanic equivalent of the plutonic ijolite rock suite. Besides carbonatites, peralkaline ijolites (urtite-ijolite-melteigite) comprise a major part of the Fen Complex and are often considered to represent the parental magma for carbonatites in general (Woolley and Kjarsgaard, 2008b). A dyke located 50 km north of the Fen Complex and mineralogically resembling damtjernite was dated by a 2-point Rb-Sr mineral isochron at 324 ± 4 Ma (Dahlgren, 1994). This indicates the presence of comparable magmatism in the same area, over 275 Ma after the emplacement of the Fen Complex and shortly before the Oslo rifting started (Larsen et al., 2008; Meert et al., 1998).

The periodical reoccurring of HIMU signature magmatism; and mineralogical and geochemical anomalous magmatism strongly indicates the source of this magmatism to be a Precambrian HIMU reservoir within the sub-continental lithospheric mantle (Fig. 3-1 (1)).

Emplacement

The area around the Fen complex is characterised by a high density of deep fault zones and a potentially metasomatically altered lithospheric mantle, which promotes the formation of parental melt to carbonatite and enables the ascend of mantle-derived melt into the crust. The parental carbonatite magma is originated by a low degree of partial melting of the HIMU reservoir and subsequent ascending of the parental magma along the deep-seated fault zones created during the Sveconorwegian Orogeny. The event, which finally triggered the generation and the emplacement of the Fen Complex,

is the opening of the Iapetus Ocean (620 Ma) (Pease et al., 2008). The actual emplacement of the Fen Complex happened during a minor extensional activity during the drift phase and separation of Baltica and Greenland (Meert et al., 1998). More than 50 satellite intrusions of co-genetic damtjernite occurred in an area of 1500 km^2 around the Fen Complex (Dahlgren, 1994).

4.4 Rock Types of the Fen Complex

The Fen Complex is host to a carbonatite-ijolite rock association, which belongs to the nephelinite–ijolite association of Woolley and Kjarsgaard (2008b). This is the most common group among the magmatic carbonatites. The various rock bodies show steep inward dipping and sharply contrasted densities (Ramberg, 1973).

4.4.1 Carbonatite

The central part of the complex consists of carbonatite rocks, which are surrounded by an incomplete ring of mixed calcite-silicate rocks (Fig. 4-5). Carbonatite accounts for 60 % of the outcrop at the Fen Complex and based on old mining, prospection continues to at least 250 m depth (Ramberg, 1973). According to Brøgger (1921), there are two types of intrusive carbonatite — søvite (calcite-carbonatite) and rauhaugite (dolomite-carbonatite). Over time, researchers have used different classifications for carbonatite rocks of the Fen Complex. To avoid any confusion, please refer to the glossary. The main søvite body consists of steeply dipping white bands of søvite alternating with dark mica-rich carbonate-silicate rocks and fenites (Ramberg, 1973) (Fig. 4-6). The bands are varying in thickness from 10 cm to several metres. Concentric and radial carbonatite dykes can be observed universally in the complex and country rocks. The average

mineral composition for søvite (calcite-carbonatite) given by Brøgger (1921) is calcite, apatite (8%), manganophyllite (Mn-rich biotite), biotite, tremolite-hornblende (blue), microlite (pyrochlore group), schlieren of magnetite and pyrite. Rauhaugite (dolomite-carbonatite) is composed of dolomite and apatite with minor proportions of pyrite, feldspar and barite. In rauhaugite, manganophyllite is absent, and the amount of apatite is 0 – 5%. Quartz, albite, barite and chlorite are late- or postmagmatic.

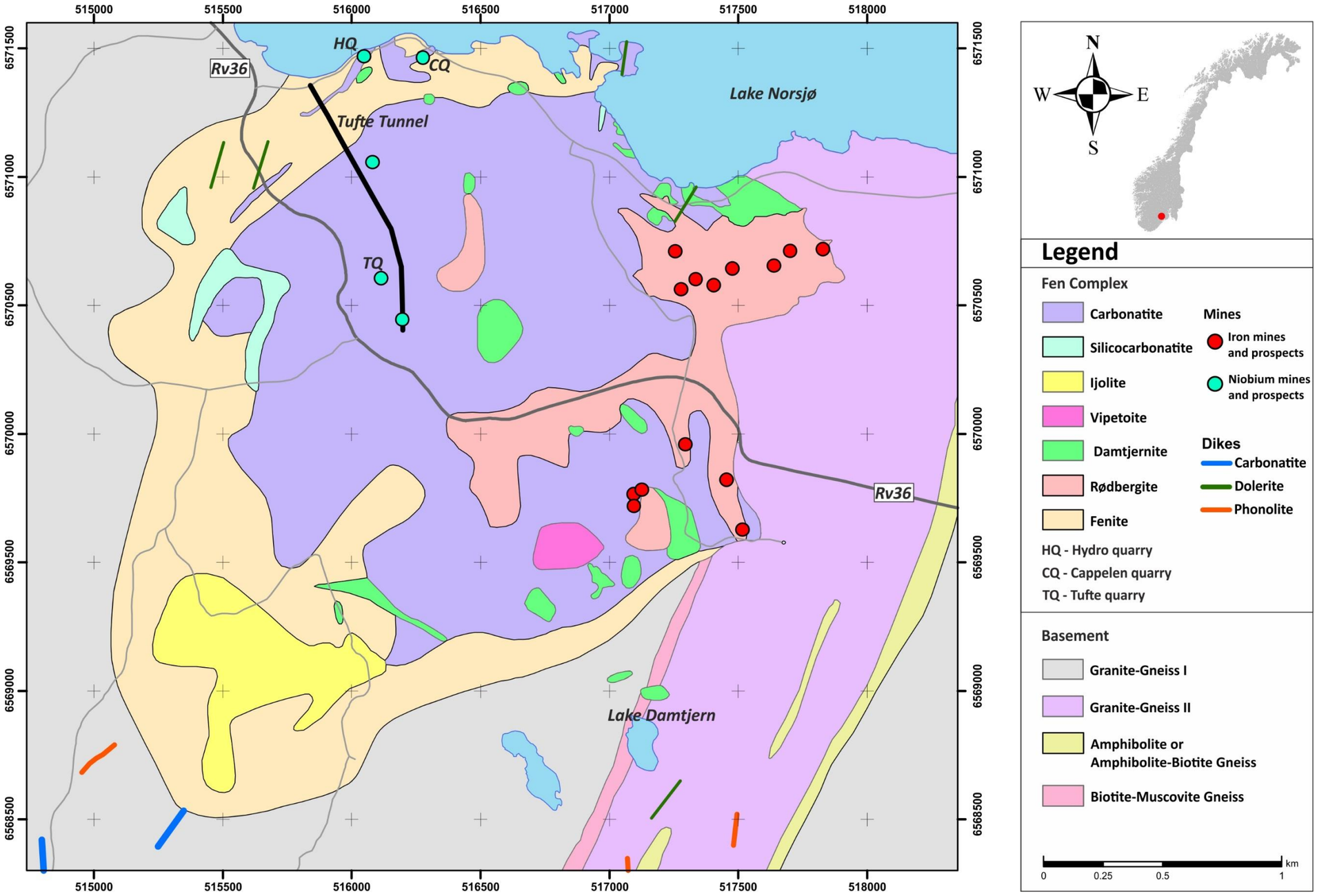

Figure 4-5: Simplified geological map modified after Bergstøl and Svinndal (1960) with minor incorporation of features from Ihlen et al. (2014) modified after Dahlgren (2004). The Bjørndalen, Fen Road and Gruveåsen transects are marked on the map.

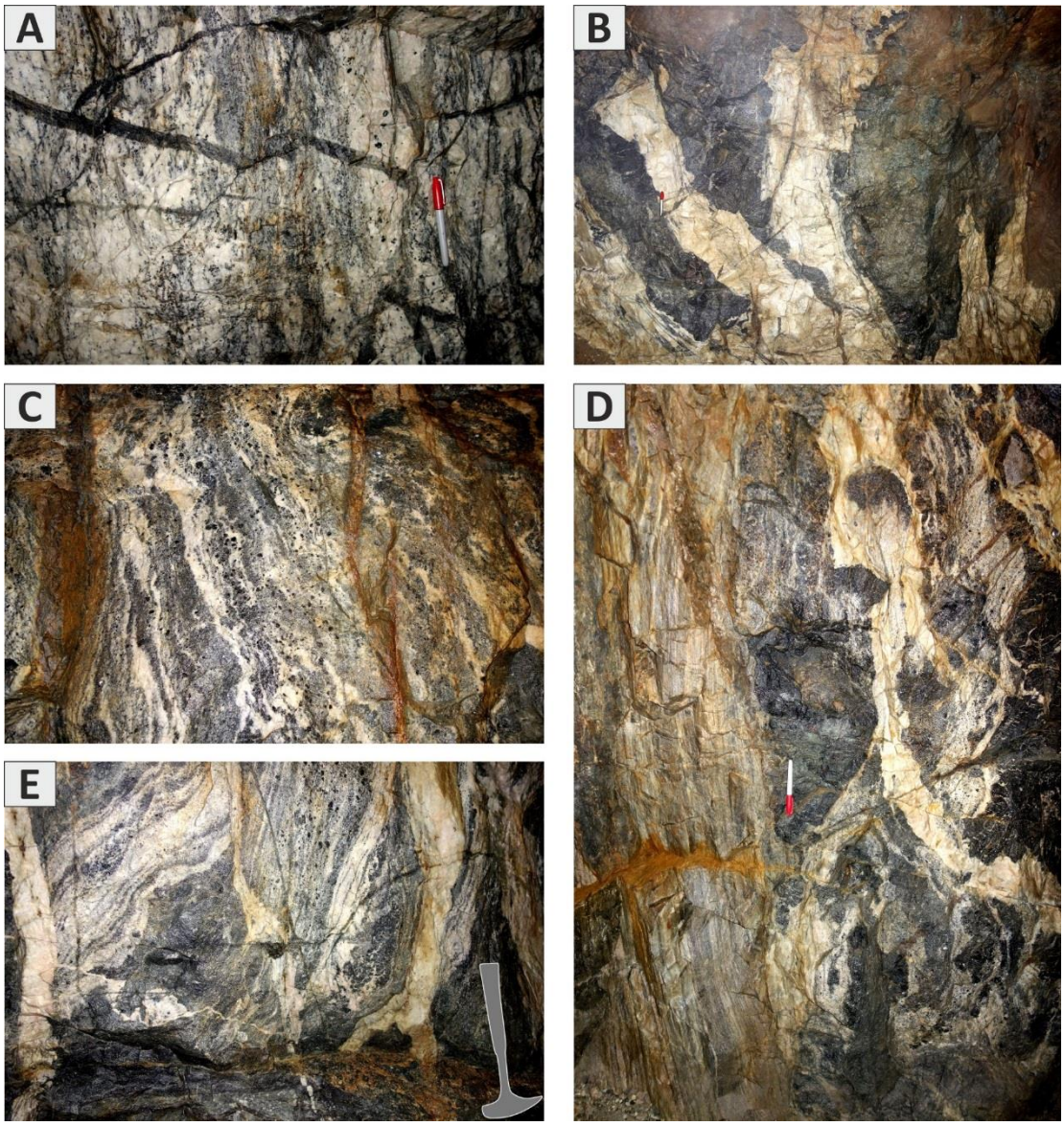

Figure 4-6: Photos from Tufte tunnel of the old Nb-mine are showing rocks with different proportions of carbonatite (white) and silicate (black bands) layers. These vertical layers range in thickness from <1 mm (A) to 0.5 m (B). (C) Clusters of phlogopite phenocryst are present in white and black layers and resemble optically damtjernite phlogopites. (D) Large lumps of black silicate rocks are cut by white carbonatite dykes and are adjacent to finely laminated silicate-carbonatite rocks. (E) Locally fine laminated silicate-carbonatite rocks and dark coloured silicate rocks are part of a breccia surrounded by bands of white carbonatite and cut by later carbonatite dykes.

Carbonates in rauhaugite comprise of >75 % dolomite and <25 % calcite, and vice versa for søvite. Rauhaugite is a dense, yellow-whitish rock with occasional rusty coloured, irregular veins and makes up the largest part of the eastern Fen Complex (Brøgger, 1921). Locally rauhaugite is mixed with greenish to blackish chlorite-carbonate rock,

which Brøgger (1921) defines as an alteration product of the ijolite rock series. Later authors defined this chlorite-carbonate rock as a variety of rauhaugite (ferrocarbonatite or rauhaugite II), which is irregular, spotty and veined and occasionally brecciated (Andersen, 1984; Sæther, 1957). The chlorite-carbonatite rock has a higher concentration of Fe and contains magnetite deposits, which were exploited for Fe — the old Rauhaug mine was such a deposit (Sæther, 1957). Additionally, the rock contains minor amounts of quartz, rutile, barite, barian feldspar, allanite, monazite and synchysite (Andersen, 1984). The white-yellowish varieties of rauhaugite occur in the søvite-dominated part of the complex, near the hamlets of Tufte and Vipeto, as ENE striking dykes of 0.5 to 10 m thickness. They are interlayered with søvite and show gradual contact zones between each other (Sæther, 1957). The rauhaugite dykes show the same mode of occurrence as the søvite dykes; they are associated with, and run parallel to the margins and layering within the søvite complex. Based on the similarities in fabric, orientation and mode of occurrence, Sæther (1957) proposed a similar mode of origin for søvite and the white-yellowish variety of rauhaugite dykes. In contrast, the chlorite-carbonate rock (ferrocarbonatite or rauhaugite II, please refer to glossary) was described as a metasomatic product formed in-situ by carbonisation of silicate rocks, preferentially damtjernite (Sæther, 1957).

4.4.1 Rødbergite

Rødbergite (literally: red rock) of the Fen Complex is defined as a calcite-dolomite carbonatite stained red by disseminated fine crystals of hematite (Andersen, 1984). Rødbergite was originally described by Vogt (1910) as a metasomatised iron limestone surrounding veins of hematite/magnetite ore and grading into Fe-rich calcite limestone.

According to Sæther (1957), rødbergite contains calcite, ankerite and hematite with minor proportions of chlorite, quartz, albite and barite. Rødbergite displays a heterogeneous irregular microstructure with intimate intergrowth of constituent minerals and strongly sutured boundaries between coarser grains (Andersen, 1984). Calcite and dolomite occur in fine intergrowths, and ankerite is present in the form of relics of resorbed grains (Andersen, 1984).

The largest volumes of rødbergite are in the eastern part of the Fen Complex — in the area surrounding the Gruveåsen hill (Fig. 4-5). Locally, smaller bodies of rødbergite occur throughout the Fen Complex (Andersen, 1984). Additionally, there is evidence for a reddish hematised rock type outside of the Fen Complex, which might represent a similar hematisation event (Andersen, 1989a).

Iron-ore, which is most of the time surrounded by rødbergite, is found in veins, lenses or dyke-like bodies (Sæther, 1957). These veins have a width of a few centimetres to several metres and are up to 100 m in length (Andersen, 1983; Vogt, 1910). Because of the former extensive mining of the Fe-ore and a thick cover of vegetation and soil in the area, only a few surface outcrops are accessible. The mining activities left deep, long and narrow pits which show an en-echelon structural pattern and have a preferred orientation of NNW to NW (Andersen, 1983) (Fig. 4-7). The Fe-ore was exploited in open pits as well as in underground mines, where operations reached a level of 225 m below the water level of Lake Norsjø (Fig. 4-8) (Andersen, 1983). The concentration of iron in the Fe-vein surrounding rødbergite ranged between 15% and 30% and was not regarded as economically exploitable (Brøgger, 1921).

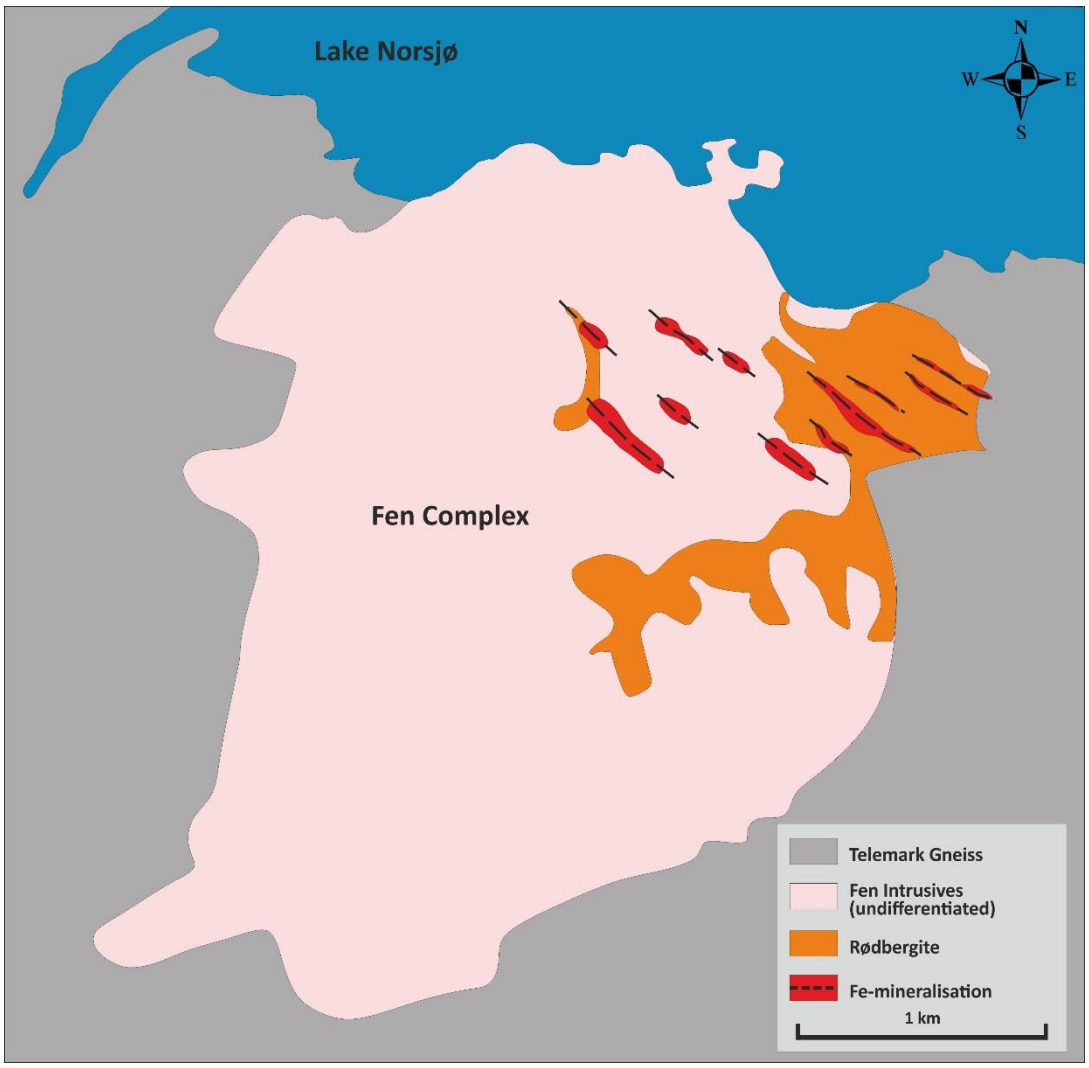

Figure 4-7: Simplified geological map of the Fen Complex showing the extent of rødbergite and the distribution of Fe-ore zones modified after Sæther (1957). The long axes of the Fe-mineralisation are all aligned towards NW.

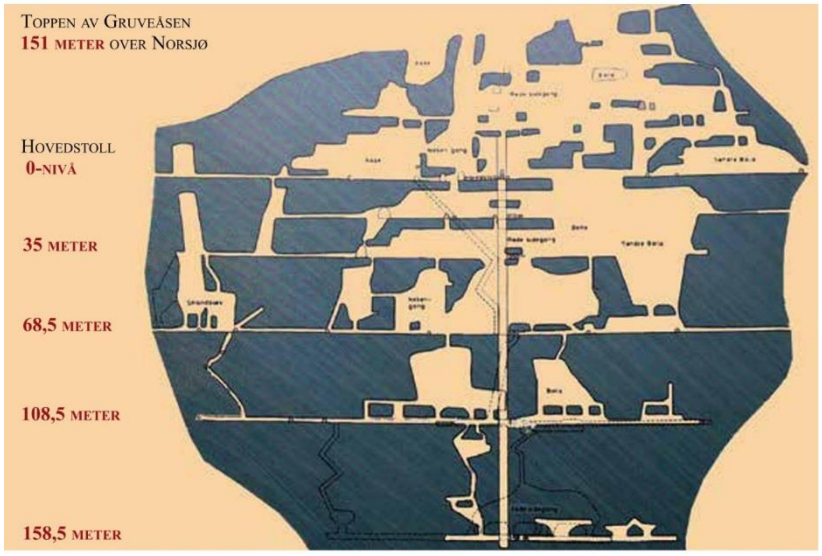

Figure 4-8: Cross section of the central part of Gruveåsen (Aksnes and Årtveit, 2014), showing the depth and extension of the most prominent mining cavities. The deepest level of this cross-section is 158.5 m below the water level of Lake Norsjø.

Formation of Rødbergite

The origin of rødbergite has been previously widely discussed in the literature. Earlier publications concluded that rødbergite is a metasomatic product of carbonatite caused by intense entry of ferric iron into the system (Barth and Ramberg, 1966; Brøgger, 1921; Sæther, 1957). Mitchell and Brunfelt (1975) suggest that rødbergite is a metasomatised transformation of damtjernite, which gradually altered into rauhaugite and finally rødbergite. Locally, silicate-rich varieties of ferrocarbonatite with chlorite phenocrysts represent a potential transitional rock type between damtjernite and ferrocarbonatite (Andersen, 1983; Andersen, 1984). A more detailed study of damtjernite and ferrocarbonatite convinced Andersen and Qvale (1986) of a co-genetic relationship between ferrocarbonatite and damtjernite due to their simultaneous emplacement at Gruveåsen and gradual transition into each other. Andersen (1983) stated that there was no need for a substantial introduction of Fe to a carbonatite as proclaimed by earlier authors (Barth and Ramberg, 1966; Brøgger, 1921; Sæther, 1957) and that the hematite ore associated with the rødbergite was formed by the oxidation of pre-existing magnetite-pyrite ore, which is associated with unaltered carbonatite. Andersen (1984) suggests rødbergite was formed by the replacement of older ferrocarbonatites (rauhaugite II) by an oxidising fluid along zones of intense fracturing. The original mineral assemblage of ferrocarbonatite (ankerite + calcite + magnetite ± pyrite ± ilmenite) was replaced by a rødbergite mineral paragenesis of calcite, dolomite and hematite, and accessory phases like quartz, chlorite, apatite, Ba- and REE phases remained stable. The position for REE minerals in the crystallisation sequence in ferrocarbonatite is not clear as REE minerals are found in the matrix and crosscutting veins (Andersen, 1984). According to Andersen (1984), the replacement of ferrocarbonatite by rødbergite is

postdated only by a crosscutting ferrocarbonatite dyke with rødbergite xenoliths in the main adit of the Fen iron mine. Hematite is evenly distributed within the carbonates in the form of microinclusions (Andersen, 1984) and was formed by the exsolution of an iron-bearing carbonate:

$$\text{Ankerite} + O_2 \rightarrow \text{hematite} + \text{calcite} + \text{dolomite} + CO_2$$

Andersen (1984) argued that the homogenous distribution of Fe in rødbergite could not simply be produced by a penetrating fluid because of the time-integrated water/rock ratio, which would have to be unrealistically high. Furthermore, an iron-bearing solution would have to stay in equilibrium with the carbonates for a prolonged time. However, the pH of any iron-bearing fluid would be low enough to cause the dissolution of the carbonates and rather precipitate massive hematite at the reaction front than finely disseminated hematite along the entire rock sequence. Therefore, Andersen (1984) argued that a local enrichment of hematite reflects the dissolution of carbonates rather than an introduction of Fe. The breakdown of magnetite, pyrite and ilmenite supplied additional Fe.

The decrease of $\delta^{18}O$ and increase of $\delta^{13}C$ values from ferrocarbonatite to rødbergite are interpreted by Andersen (1984) as the result of an interaction of the rock with hydrothermal fluid at temperatures below 300°C, which is in accordance to the calculated T (200°C) of Friedrichsen (1968). The oxygen fugacity during the alteration increased due to the influx of oxidising groundwater. Initial oxygen fugacity below the hematite-magnetite (HM) buffer caused Fe and Mg mobilisation. As the oxygen fugacity increased above the HM buffer, Fe formed hematite, while Mg and Ca were leached

(Andersen, 1987b). The oxidation of pyrite caused a decrease in pH and triggered the dissolution of carbonate minerals and a loss of as much as 70 Vol% of material that led to a local enrichment of insoluble phases, e.g. hematite and REE-minerals. Because of high $^{87}Sr/^{86}Sr$ values, Andersen (1984) suggested that the fluid has to have passed a reservoir rich in radiogenic Sr, such as the surrounding Precambrian gneisses (Fig. 4-5). The relatively low whole-rock strontium concentrations are the result of the removal of Sr during the hydrothermal alteration. Rødbergite displays many areas of small-scale disequilibria such as relics. A whole rock equilibrium for rødbergite, therefore, cannot be assumed (Andersen, 1984).

While carbonate minerals were dissolved during the formation of rødbergite, the REE-minerals (monazite-(Ce) and synchysite-(Ce)) survived the alteration process, according to Andersen (1986). Nevertheless, LREE preferential partitioning into the hydrothermal fluid, which caused a decrease of La/Sm ratios during oxidation. Fluoride ions increased the mobility of lighter REE and are the reason for the LREE depletion during the hydrothermal alteration (Andersen, 1986). MREE, Y and Th were the least soluble elements and were strongly enriched in the solid residue (Andersen, 1984; Andersen, 1987b). In contrast, Mitchell and Brunfelt (1975) reported an extreme LREE enrichment in rødbergite, which they suggested is strongly connected to a volatile process of REE enrichment.

4.4.2 Urtite-Ijolite-Melteigite-(Vipetoite)

Rocks of the urtite-ijolite-melteigite are the most common silicate rocks of the Fen Complex. They occur mainly in the SW of the complex and account for 9 % of the outcrop area (Ramberg, 1973) (Fig. 4-5). They consist of **nepheline** and **pyroxene** (aegirine-

augite) ± calcite, alkali feldspar, olivine, amphibole, biotite, melanite and apatite (Brøgger, 1921). They are classified on the bases of their content of nepheline in: Urtite > 70 % of nepheline, ijolite for 30 – 70 % and melteigite with < 30 % (Le Maitre et al., 2002). Ijolitic rocks are the oldest intrusives in the Fen Complex and are the main source for fenitisation (Griffin and Taylor, 1975). In the south of the Complex is a small body of nepheline bearing alkali pyroxenite called vipetoite — originally misspelt by Brøgger (1921) as vibetoite — which represents a rock with more than 90 % of Ti-augite and minor amounts of nepheline, hornblende, biotite, calcite and albite (Brøgger, 1921). A more common term for a nepheline-bearing (±titanomagnetite, apatite, perovskite and melanite) alkali pyroxenite is jacupirangite (Le Maitre et al., 2002). Ultramafic bodies are part of more than 60 % of the carbonatite complexes in nephelinite–ijolite association and are generally interpreted as cumulates (Woolley and Kjarsgaard, 2008b). Nevertheless, ultramafic cumulates can be a product of carbonatite as well as urtite-ijolite-melteigite magmatism.

4.4.3 Silicocarbonatite

Rocks, which represent the solidification of a carbonatite-silicate melt are located in the western part of the Fen Complex, close to the old church ruin at Holla (Brøgger, 1921; Ramberg, 1973). Silicocarbonatites show strong indications of an initial mingling process in the form of silicate and carbonate schlieren(Brøgger, 1921). Brøgger (1921) assumed the silicate magma to be of ijolitic chemistry due to the similarity in mineral composition. Silicocarbonatites show a gradual transition from a more carbonatite-rich rock with up to 57 % of calcite and 34 % of silicate, to a silicate-rich variety with 15 % of calcite and 72 % of silicate (Brøgger, 1921). Rocks with more than 55 % of calcite are named

kåsenite, and the more silicate-rich variety is referred to as hollaite (Brøgger, 1921). The main minerals are calcite, pyroxene, muscovite and cancrinite (pseudomorph after nepheline), apatite and melanite with minor proportions of biotite, chlorite, sphene, magnetite, ilmenite and pyrite (Brøgger, 1921). For all silicocarbonatites varieties at Fen — formed of a carbonatite-ijolite-melteigite magma mixture — three minerals are distinctive: green **pyroxene** (aegirine-augite), **calcite** ± **nepheline** (mostly replaced by cancrinite). Occasionally the rocks exhibit a graphic intergrowth texture of silicates and carbonate minerals indicating a eutectic composition (Brøgger, 1921).

4.4.4 Damtjernite

Damtjernite belongs to the group of ultramafic lamprophyre (UML), which is defined by the following characteristics: M (percentage of mafic minerals) > 90, porphyritic, with olivine and phlogopite macrocrysts and/or phenocrysts and magmatic carbonate (Tappe et al., 2005). According to the extended classification of Le Maitre et al. (2002) by Tappe et al. (2005), the group of UML is further subdivided into damtjernite, alnöite and aillikite. Damtjernite contains nepheline and/or alkali feldspar and can be distinguished from alnöite by the absence of melilite. Damtjernite occurs in several separate bodies within and outside of the Fen Complex (Dahlgren, 1994). The Fen Complex damtjernite is a porphyritic ultramafic rock consisting of megacrysts of biotite, amphibole, pyroxene and olivine in a matrix of the same minerals plus nepheline, microcline, albite and calcite (ocelli, ankerite) (Ramberg, 1973).

The composition is inhomogeneous due to the presence of xenoliths in various proportions — in some cases, xenoliths are the major component. Xenoliths range from fenites, gneisses, granites, lherzolite nodules to rounded barkevikite (Fe-hornblende)

(Griffin, 1973). Griffin (1973) showed that the lherzolite nodules in damtjernite equilibrated at pressures of 10-13 kb at 1200 – 1250 °C, which implies a mantle origin for the damtjernite. Locally, damtjernite shows signs of repeated fragmentation.

A more homogeneous equivalent of the Fen Complex damtjernite occurs outside the complex with a sharp contact to the wall rock (Dahlgren, 1994). Andersen (1984) describes a silicate-rich carbonatite in the Gruveåsen road section with subhedral laths of chloritised biotite suggesting a genetic link to damtjernite. Based on the presence of carbonate ocelli, Griffin and Taylor (1975) postulated that rauhaugite might be an immiscible melt separated from a damtjernite melt. Rather than the formation of rauhaugite as a derivative of damtjernite, Sæther (1957) suggested damtjernite was subsequently metasomatised by a magnesium-rich carbonatite magma to rauhaugite and rødbergite. Note that Sæther (1957), Griffin and Taylor (1975) as well as Andersen (1984) suggest a genetic link between damtjernite and rauhaugite.

4.4.5 Telemark Gneiss

The country rock of the Fen Complex is the c. 1.1 Ga Ma old Telemark Gneiss. The rock is a heterogeneous medium-grained, migmatitic hornblende-biotite gneiss of the amphibolite facies with minor intercalations of amphibolite (Verschure and Maijer, 2005). According to Verschure and Maijer (2005), the Telemark gneiss has approximately equal amounts of quartz, microcline and oligoclase with roughly 10 % of mafic minerals, e.g., biotite and green hornblende. Accessory minerals are opaques, apatite, metamict allanite, titanite and zircon. The gneissosity is indicated by a preferred orientation of biotite and hornblende. The protolith of the Telemark gneisses formed during the accretion of Telemarkia on Baltica around 1.7 Ga – 1.5 Ga, was

metamorphosed by the Sveconorwegian orogeny (1140 Ma – 900 Ma) and was later intruded by post-orogenic granites roughly at 0.9 Ga (Verschure and Maijer, 2005). Towards the contact zone to the Fen Complex, the gneiss exhibits a gradual replacement of the original biotite, hornblende and quartz by aggregates of Na-pyroxene and Na-amphibole. Additionally, microcline is replaced by mesoperthite and chessboard albite, and oligoclase shows signs of saussuritisation and in severe cases replacement by albite. Accompanied by the increasing alteration is a gradual brecciation of the country rock (Verschure and Maijer, 2005).

Brøgger named the metasomatism of the country rock due to the emplacement of the Fen Complex “fenitisation” and the product “fenite”.

4.4.6 Fenite

The intrusion of carbonatites and alkaline rocks typically causes a metasomatic alteration of the country rock. The alteration product is termed fenite, after the type locality of the Fen Complex (Brøgger, 1921). During the fractional crystallisation and cooling of a carbonatite or alkaline intrusive body, typically alkali- and volatile-rich fluids separate from the main magma and infiltrate into the surrounding host rock. The aureole can reach from centimetres (Marien, 2014) to several kilometres in scale (Elliott et al., 2018). The hot and very reactive fenitisation fluids typically produce K-feldspar, albite, alkali pyroxene and/or alkali amphibole. Depending on several parameters, e.g. fluid temperature, pressure and composition in combination with protolith mineralogy, permeability and structure, the mineral assemblage can vary significantly.

The variability and complexity of fenitisation are reflected in the numerous names and classifications for fenites throughout the literature (Verwoerd, 1966). Fenites are divided into two general groups:

Na-rich fenites: albite, Na-amphibole (arfvedsonite, riebeckite, ferro-richterite, and soda tremolite), Na-pyroxene (aegirine-augite) -> aureole is deep, large and early

K-rich fenites: K-feldspar, microcline, phlogopite -> aureole is shallow, smaller, late and intensely brecciated

Other minerals: quartz, iron oxides, ilmenite, apatite, calcite

Another reason for the variable nature of fenites is the different mobility of potassium and sodium. Sodium is considerably less mobile than potassium and therefore creates an earlier, deeper, hotter and wider Na-rich zone followed by a later, shallower, cooler and narrower K-rich zone. Potassium fenites are often brecciated, which underlines the idea of a shallower and cooler formation under more brittle conditions (Elliott et al., 2018; Rubie and Gunter, 1983). The fenite fluid is a former constituent of the magma and is therefore important for reconstructing the chemical composition of the original magma reservoir (Le Bas, 2008). Additionally, the link between the chemical composition of the fenite fluid and the adjacent intrusive body can be potentially utilised as an exploration tool (Dowman et al., 2018; Elliott et al., 2018).

The fenitisation at Fen happened in at least two stages first producing a fenite aureole of 700 m in size and the second aureole of > 1,500 m in width (Verschure and Maijer, 2005) — this is far beyond the 200 m zone observed by former authors, e.g. Brøgger

(1921), Sæther (1957). The method which was used by Verschure and Maijer (2005) to map the extent of the aureole is based on the petrographical modification of the rock due to fenitisation which is correlated with chemical composition and Rb-Sr isotopes. The Rb-Sr isotopes systematic, relative to a completely unfenitised Telemark gneiss sample, was used to map the chemical alteration — this detection limit cannot be accomplished with classical fieldwork and thin section microscopy as done by earlier researchers, who used the alteration of annite to map the extent of the fenite aureole (Brøgger, 1921). The two metasomatic events were caused by the intrusion of both the carbonatite and alkaline rocks (Kresten and Morogan, 1986). According to Brøgger (1921), the fenitisation of the Precambrian granite adjacent to the melteigite-ijolite-urtite sequence caused: quartz replacement by albite, biotite replacement by aegirine, orthoclase transformation into microperthite and albite and oligoclase transformation into albite. The final product is an alkali feldspar-aegirine rock. The chemical composition of the fenite strongly varies, and none of the elements can be used as a simple tool to determine the grade of fenitisation. Nevertheless, general trends for the major elements are a decline for SiO_2 and an increase in Na_2O, K_2O, Fe_2O_3, MnO, MgO, CaO and possibly P_2O_5 with fenitisation. Carbonatites have a lower concentration of K_2O and Na_2O than unfenitised Telemark gneiss, and ijolitic rocks have lower concentrations of K_2O than unfenitised Telemark gneiss (Kresten and Morogan, 1986). An alkali metasomatism caused by a source with fewer alkalis than the protolith seems to be a paradox. The reason for this might be that the alkalis were completely expelled during the solidification of carbonatite (to a lesser degree in case of the ijolitic rocks). The alkali contents of the Oldoinyo Lengai — the only active carbonatite volcano — are so high that the Oldoinyo Lengai has its own category in carbonatite classification, which

matches with none of the other 526 carbonatites worldwide (Dawson et al., 1987; Woolley and Kjarsgaard, 2008b). It is likely that the carbonatites at Fen and the rest of the world are not representing their original magmatic chemical composition anymore and mostly lost their alkali content due to processes like fenitisation, alteration or weathering. Brøgger (1921) mentions the occurrence of independent fenite dykes in the melteigite group. The rheomorphic behaviour of the fenite might be a result of partial melting of the protolith due to fluxing of volatiles. The potential mobilisation of fenite remains a controversial topic. The occurrence of fenite is mainly restricted to the western part of the Fen complex. The fenite and Telemark gneisses are pierced by bodies of autoclastic breccias, tinguaite and damtjernite.

4.5 The Architecture of the Fen Complex

The gravity model and interpretation are based on Ramberg (1973). The concentric shape of the gravity lines suggests a pipe-like downward extension of the complex to at least 15 km. The pipe widens at depth or exhibits a significant increase in density. The explosive character of carbonatite emplacement suggests an excess of volatiles, which is likely to be achieved in large vertical magma chambers in tectonically stable shield areas (Sæther, 1957). The surface area of the Fen Complex, which is largely dominated by carbonatites, has an average density of 2.9 g/cm^3 and stands out against the surrounding gneiss with 2.67 g/cm^3. The overall density of the whole pipe is with 3.1 g/cm^3 significantly higher. This indicates that carbonatites represent only the volatile end fraction accumulated in the upper part of a long vertical magma chamber and do not extend to more than 0.5 – 1 km below the present erosional level. The root is probably an alkaline ultramafic ring complex comprised of denser rock, e.g. vipetoite or

damtjernite. The eroded top of the Fen Complex might have originally been nephelinite (Mitchell and Brunfelt, 1975) and carbonatite volcanoes.

4.6 Genetic relations

After Sæther (1957) the intrusion of the main complex happed in two distinct sequences. The initial one comprised rocks of the ijolite-urtite-series, silicocarbonatites and carbonatites (dominantly søvite, minor rauhaugite dykes type I). The intrusion of the first series caused an intense fenitisation of the granitic Telemark gneisses at the western margin. The rocks of the ijolitic series have higher $^{87}Sr/^{88}Sr$ ratios than søvite. Therefore the carbonatite melt cannot be a residual differentiation product of a carbonated ijolitic magma as it would have inherited the high $^{87}Sr/^{88}Sr$ ratios of the parental silicate magma (Mitchell and Crocket, 1972). Mitchell and Crocket (1972) considered the formation of the ijolitic sequence by the mixing of carbonatite magma with rheomorphic fenite. The second sequence is comprised of damtjernite, rauhaugite II and rødbergite. Sæther (1957) indicated that damtjernite was subsequently altered by a carbonate-rich solution to rauhaugite II and finally to rødbergite. The Sr isotopic signature of damtjernite negates a simple relation to søvite. The isotopic signature of rauhaugite II and rødbergite could be the result of a damtjernite alteration with a carbonate solution with a high $^{87}Sr/^{86}Sr$ ratio and the removal of Rb by this solution (Mitchell and Crocket, 1972).

4.7 Exploitation and Exploration at the Fen Complex

Fe/(F): The hematite deposits in the eastern part of the complex were exploited for almost 300 years — between 1656 and 1925 — mining roughly 1 Mt of Fe-ore (Vogt, 1918). By far the most ore was mined on Gruveåsen, and only a small quantity was gained from numerous small pits at Fen Farm, Rauhaug, Vipeto, the stream valley east of Søve and Torsnes. Most ore bodies consist of hematite, but subordinate magnetite bodies were mined for instance at Rauhaug. The largest unmined area of magnetite mineralisation is located between Oygard and Skippervoll and is described as a magnetite impregnation with up to 0.1 Mt of ore (Sæther, 1957). Fluorite was occasionally mined in smaller quantities in the Fen iron mines (Vogt, 1918).

Ca: The first signs of limestone (carbonatite) mining date back to the 11th century (Aksnes and Årtveit, 2014). Carbonatite was mainly used for decoration of churches and as an additive in iron production. The Søve dyke close to Lake Norsjø was exploited between 1910 and 1920 to produce lime nitrate fertiliser. Eventually, the production stopped due to relatively high Fe-concentration in the søvite.

P: In the early 1940s, the Norwegian government wanted to secure the production of apatite-based fertiliser and started to explore the “Hydro” carbonatite dyke at the embankment of lake Norsjø (Aksnes and Årtveit, 2014). Later on, the German occupation force shifted the focus to Nb, which was crucial for their “Wunderwaffen” programme.

Nb: The Germans never managed to start the production of Nb (Aksnes and Årtveit, 2014). However, exploration just stopped briefly because the government of the USA pressured the Norwegian government to start producing Nb for the American nuclear and military industry. In 1953, mining operations started at the Cappelen quarry. Later

on, it was discovered that the Cappelen carbonatite vein was cut off by a fault and operation had to go underground to follow the vein (Aksnes and Årtveit, 2014). Further on the construction of a 900 m long tunnel was initiated (Tuftestollen) from lake Norsjø to the central part of the søvite area. From 1953 to 1965, 3000 t of Niobium and 350 t of Ferro-Niobium were produced from the pyrochlore-bearing søvite body (Hydro) (Aksnes and Årtveit, 2014).

REE: Norsk Bergverk A/S continued prospecting for Nb and discovered an area high in radioactivity due to a high concentration of Th, and U to a lesser extent. At the same time, Norsk Bergverk A/S demonstrated that the Th-mineralisation correlates with a high concentration of REE. Exploration work conducted by the Norwegian Geological Survey (NGU) in the 60s and 70s gathered information on the REE mineralisation and concluded that a major REE deposit was located close to the historic Fen mining area (21st NORTH, 2014b). The area coincides mainly with rødbergite (Schilling, 2013). A radiometric survey was carried out by the NGU in order to map areas of high radiation (Heincke et al., 2008). The eastern part of the Fen complex is enriched in Th and to a lesser extent in U (Schilling, 2013). There seems to be a general correlation between areas of higher radiation and REE mineralisation. Several Norwegian junior companies started to claim parts of the Fen Complex in the last two decades. Since the REE price raced up in the early 2010s, the exploration work intensified with Fen Mineral AS claiming the largest part of the central and western part of Fen and REE Mineral AS obtaining the exploration rights to the eastern part of the complex.

4.8 The Potential REE-Ore Rødbergite

The general increasing trend in REE concentration for the rock types at the Fen Complex is ijolite-damtjernite < søvite-rauhaugite < rødbergite. Carbonatites + carbonate-rich rocks show the highest REE concentrations. Within the group of carbonatites, the commonly observed trend for REE increase is from Ca < Mg < Fe (Woolley and Kempe, 1989). The exploration campaign conducted by the NGU in the 60s and 70s demonstrated an increase of REE concentration towards the east of the Fen Complex with a maximum in the Gruveåsen area. During this campaign, three drill holes in the Gruveåsen area with a total length of 510.35 m exhibit an average grade of Rare Earth Oxides (REO) of 1.03 wt%, 1.06 wt% and 1.32 wt% respectively. The drill cores mainly comprised rauhaugite and rødbergite ± damtjernite. Recent analytical work confirms rødbergite as the rock type with the highest average concentration of REE within the Fen Complex (21st North, 2014a; Marien et al., 2016b). Additionally, rauhaugite demonstrated a high average concentration of REE as well.

The NGU conducted beneficiation tests, which showed low recovery rates of REE due to the fine grain size of the REE-minerals. Another obstacle in the economic exploitation of the REE mineralisation is Th, which is a major hindrance in REE exploitation all over the world. A close association of REE with Th would preclude any REE exploitation at the Fen Complex. According to the chemical data from the NGU, both rødbergite and rauhaugite do show a significant variation in REE contents within a few meters (21st North, 2011; Svinndal, 1967; Svinndal, 1968; Svinndal, 1973) and although Th is generally enriched in rødbergite and rauhaugite, it is not necessarily enriched in REE. Additionally, the mineralisation history of REE-minerals within carbonatite, the presence of REE-mineral

bearing veins and the preferential enrichment of LREE, MREE and HREE during rødbergitisation is controversial and poorly constrained.

To understand the REE-mineralisation process in detail, this thesis takes a close look at the mineralogical and chemical changes occurring during the formation of rødbergite, which enhances the REE concentration due to passive enrichment during dissolution processes. A detailed observation will help to build a new REE-model based on the Andersen-model (Andersen, 1983; Andersen, 1984; Andersen, 1986; Andersen, 1987b; Andersen, 1989b). Although rødbergite was thought to be unique to the Fen Complex (Barth and Ramberg, 1966; Sæther, 1957) there is evidence for a common late-stage Fe-rich fluid alteration associated with carbonatite complexes all over the world (e.g., Drew et al. (1990); Maravic and Morteani (1980); Onuonga et al. (1997); Secher and Larsen (1980)). A more accurate and detailed model has the potential to improve REE-exploration campaigns at the Fen Complex as well as in similar carbonatite complexes worldwide.

5 Methods

The following chapter summarises the practices, techniques and instruments, which were used to characterise the mineralogy and geochemistry of rock specimens from the Fen Complex in order to understand the underlying REE-mineralisation processes.

5.1 Fieldwork

At the beginning of April 2015, a 10-day reconnaissance field trip to the Fen Complex was carried out. During this field trip, 94 samples from 44 localities were collected from all the major rock types previously mapped in the area (Appendix I; Fig. 5-1). Rødbergite became a major target for the sampling campaign since reports about the Fen Complex highlighted the high concentration of REE in this rock type (21st North, 2011; Mitchell and Brunfelt, 1975; Schilling, 2013).

Twenty-eight samples of rødbergite and rødbergite-related rocks were collected. Most of the samples came from two different localities: Gruveåsen and Bjørndalen (Fig. 5-1). Gruveåsen is an old iron-mining district in the northeastern part of the Fen Complex and the primary exposure of rødbergite within the Fen complex. The area is mainly covered with forest, but remnants of former mining activity in the form of deep narrow excavations and adits where iron ore was removed are conspicuous. Samples were mainly collected from the remaining unexploited wall rock, supplemented by loose specimens from the vicinity of old mines.

The Bjørndalen study area is located in the eastern part of the Fen Complex, and this area has played a key role in our project in understanding the transformation from carbonatite to rødbergite (Fig. 5-1; UTM 32V 517541 6569595). The site displays the

gradual alteration from an unaltered carbonatite to a rødbergite on a relatively short distance of 30 m along a dirt road to a water tank.

A number of 16 representative samples were taken along the so-called **Bjørndalen transect** in order to study the progressive change from an unaltered carbonatite to a highly altered rødbergite in detail. The samples were chosen in such a way that the main varieties of rock types (e.g. colour, colour patterns/distribution, type of minerals, crystal size, veins, fractures), were represented and the distance between sampling points was less than 7 m.

Several other rødbergite samples were collected from smaller outcrops (< 1m) within the eastern part of the Fen Complex. Another focus of the sampling strategy was damtjernite – an ultramafic lamprophyre – that was described to contain mantle xenoliths (Griffin, 1973; Griffin and Taylor, 1975). In order to learn more about the mantle as the initial REE source for the Fen Complex, damtjernite samples were collected from different locations. Throughout the project, the focus entirely shifted to understanding the complex REE mineralisation, and thus the work on damtjernite was put on hold.

The second and final field trip was undertaken in July 2016. During this 10-day field trip, 152 samples from 34 localities were collected (Appendix I; Fig. 5-1). REE concentrations of rock samples collected during the first field trip confirmed rødbergite to be one of the most promising rock types regarding high REE concentrations (Marien et al., 2016a). The objective of the second field trip was, therefore, to sample transects of rødbergite in a variety of localities to obtain a general understanding of the whole range of REE-mineralisation within rødbergite. Additional 13 samples were taken from Bjørndalen transect, which decreased the maximum distance between two sampling

points of less than 2.5 m and helped to fathom the extent of alteration zones in greater detail. A similar site to the Bjørndalen transect is located along the Rv36 road leading from Porsgrunn to Ulefoss just before entering the Fen municipality (UTM 32V 517477 6570053). This locality is referred to as Fen Road transect (Fig. 5-1). Nineteen samples were collected across the Fen transect, including samples of chloritised granite-gneiss, carbonatite, rødbergite, fluorite mineralised rocks and rødbergite veins. Similar to the Bjørndalen transect, the Fen Road samples were chosen in such a way that the main varieties of rock types (e.g. colour, colour patterns/distribution, type of minerals, crystal size, veins, fractures), were covered and the distance between sampling points was less than 7 m within the zone of alteration and less than 15 m in more homogenous lithofacies distal to the alteration.

The Grønvoldvegen road runs along the northern boundary of the Gruveåsen mining district along Lake Norsjø and gives insight into the chemical and mineralogical changes occurring due to the formation of rødbergite on a larger scale (Fig. 5-1). On a length of ca. 850 m, 37 samples were collected from a variety of rocks, e.g., carbonatites, rødbergite, hematite-rich rock, damtjernite, dolerite, fenite and gneiss. Additionally, hematite-ore samples were taken within the centre of the Gruveåsen mining area. In intervals with continuous outcrop, one sample was taken roughly every 10 m. In case the section could not be properly represented due to lithofacies changes, the distance between two sample points was adjusted accordingly. The longest section without a possibility to sample was ca. 100 m in length. Additional hematite-ore samples were taken within the centre of the Gruveåsen mining area.

A sampling campaign in the Tufte tunnel was commissioned by Fen Minerals AS during the second field trip. Representative samples were taken approximately every 50 m

inside the Tufte tunnel. The geochemical and mineralogical characterisation of these samples was done separately and has not become part of this thesis, except one sample for the geochronology.

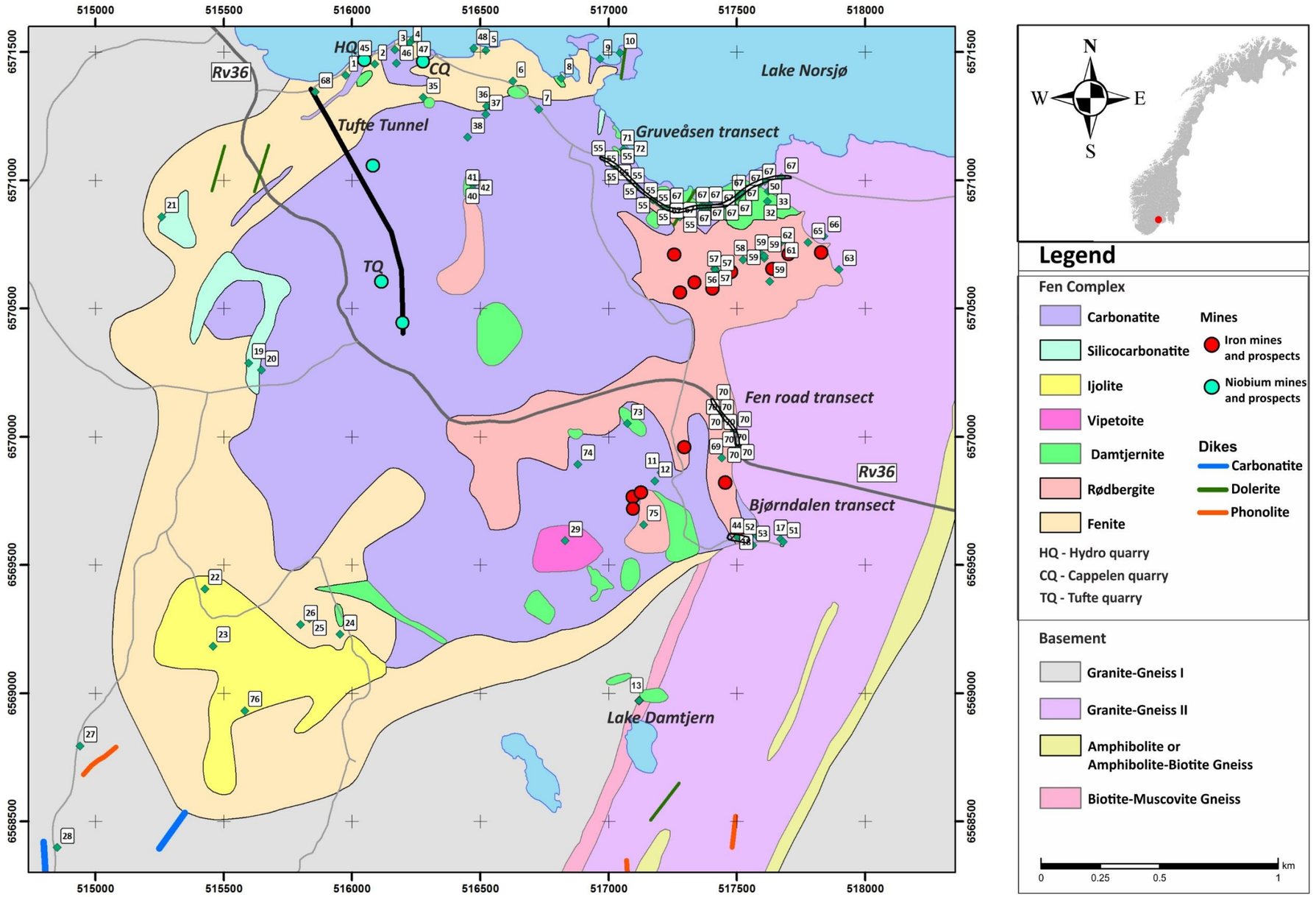

Figure 5-1: Simplified geological map modified after Bergstøl and Svinndal (1960) with the incorporation of minor features from Ihlen et al. (2014) modified after Dahlgren (2004). Sample points with location number are marked. Samples taken along a transect on the same day have the same location number, e.g. western Gruveåsen transect. Samples taken at the same site but not on the same day have different location numbers.

5.2 Sampling and Sample Preparation

Samples (n = 247) were collected in the field and named according to the following system: XX-YY-ZZ. The name of each sample is composed of the two last digits of the sampling year (XX-), an on-going sequence of sample numbers for that respective year (YY-) and a project abbreviation FE (Fen Complex, ZZ). Following this logic, the first sample from 2015 has the name 15-01-FE, and the first sample from 2016 has the name 16-01-FE. The sample code for the samples taken in the commission of Fen Minerals AS is "TS" for Tufte tunnel followed by the metre mark indicating where along the Tufte tunnel the sample was taken, e.g. TS100. A list of all samples is located in the Appendix I. Sample reduction is illustrated in Appendix II.

5.2.1 Local rules for working with radioactive material

An Airborne gamma-ray spectrometer survey, was conducted by the NGU in 2006, and high concentration for thorium and significant concentrations of uranium were measured within the Fen Complex (Heincke et al., 2008). Therefore, generic local rules for working with geological samples containing naturally occurring radioactive material were written, which, after minor editing by Dr Alex Taylor and Prof. William Blake, were adopted by the School of Geography, Earth and Environmental Sciences. These rules helped to ensure safe working procedures with sample material from the Fen Complex and provided a way to quantify and limit exposure to radioactive material.

5.2.2 Sample preparation

For a more detailed description of the sample preparation process, please refer to Appendix III. In the laboratory, the samples were cut perpendicular to the texture of interest. A batch of 26 samples from the first field trip was used to produce thin sections of the major lithotypes with a standard thickness of 30 µm. Optical microscopy was of limited use for this project due to the small grain size and unfamiliar microscopic properties of the prevalent REE-minerals. Therefore, the Scanning Electron Microscope became essential for the mineralogical and textural characterisation of the samples. After the initial use of thin sections, the majority of the samples were prepared as polished blocks, which is less time consuming and more cost effective.

The first step of producing a polished block was to put a sample chip in a mould, covered in a mix of liquid resin (EPO Flo resin) and a liquid hardener (EPO Flo hardener). The curing process stopped after two days, and the block was stepwise polished to a final grain size of 1 µm.

Rock powder for geochemical analysis with XRF or ICPMS was produced from ca. 100 g of representative rock material. First, the sample was crushed using a bench-top jaw-crusher with adjustable aluminium-oxide ceramic plates. The crushed sample was milled to a fine powder using the Retsch RS 100 vibratory disc mill, with an agate ring-and-puck mill (for the last stage of the project a tungsten-carbide (WC) ring-and-puck mill was used) to obtain a fine powder of less than 30 µm particle size.

Before working on a polished block or thin section using the SEM, the polished sample surface was coated with a thin film (ca. 15 nm) of carbon in order to create a conducting surface.

5.3 Scanning Electron Microscope (SEM)

5.3.1 SEM principles

A SEM is a type of electron microscope where a sample surface is scanned with a focused electron beam to create an image of the sample (Fig. 5-2). While the electron beam scans in a raster scan over a specific area (frame) of the sample surface, the interaction of the electron beam with the sample surface produces a range of signals. These signals are combined with the position of the electron beam to produce an image. In this study, only the secondary electron (SE) signal, the backscattered electron (BSE) signal and the characteristic X-rays were used. The part of the sample from which these signals are generated from is the so-called interaction volume.

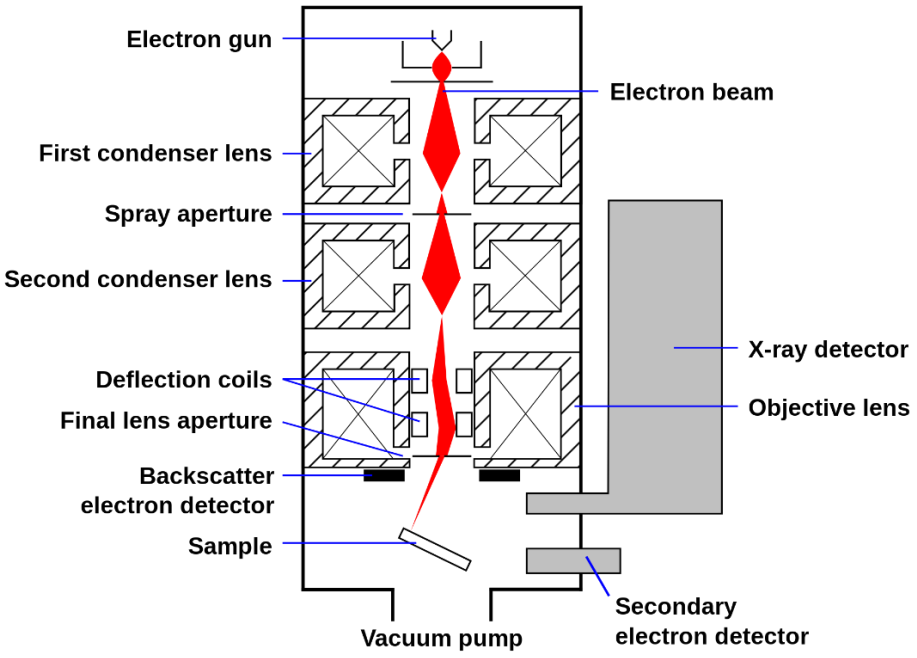

Figure 5-2: Schematic diagram of a Scanning Electron Microscope (SEM) with an Backscatter Electron Detector (BSE) and an Secondary Electron Detector (SE) (Steff and ARTE, 2015)

The interaction volume can be described with the electron range, which is the radius of the hemisphere constructed from the entry point of the electron beam to a certain

range incorporating a specific fraction of the electron trajectories, for example 90 % (Goldstein et al., 2003). The electron range for 90 % of the electron trajectories — given an accelerating voltage of 20 kV and a spot size of 10 nm — is for typical selection of carbonatite forming minerals less than 2700 nm (Fig. 5-3; Fig. 5-4).

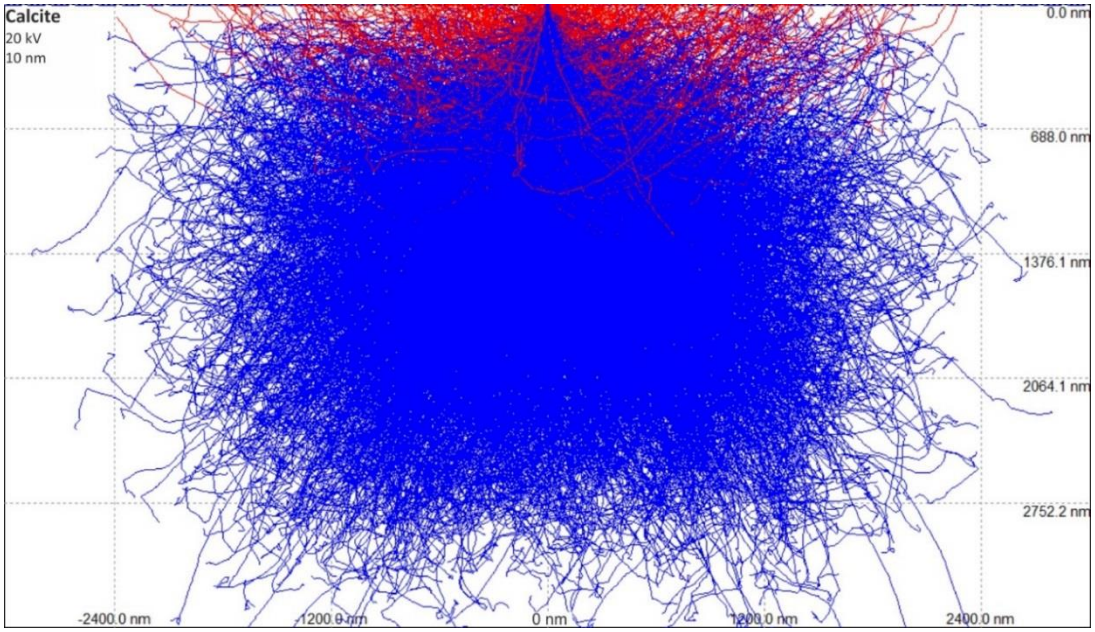

Figure 5-3: Monte Carlo simulation of electron paths for 20 kV electrons in calcite using a spot size of 10nm. Paths of BSE are in red; those of absorbed electrons are in blue. This model was run using the software Casino 2.5.1.0 (Couture, 2000).

SE, BSE and characteristic X-rays are generated from different parts of the interaction volume. Generally, the depth of SE is with 5 – 50 nm much shallower compared to the depth of BSE and characteristic X-rays (Liao, 2018). The Monte Carlo electron trajectory simulations visualised individual electrons, which penetrated the calcite sample up to 1300 nm before the electron reversed its course and returned to the sample surface to escape as a backscattered electron (Fig. 5-3). The sampling depth of BSE is a significant fraction of the electron range — in case of carbon (low atomic number) 95% of all BSE have a sampling depth of less than 63 % of the total penetration depth in contrast to

gold (high atomic number) where 95% of all BSE have a sampling depth of less than 29.5 % of the total penetration depth (Goldstein et al., 2003). The BSE signal is therefore not just representing the surface information like the SE signal but is also influenced by hidden features such as the inclusion of for example high-density minerals, e.g. thorite inclusion below the surface of low-density matrix of calcite. The volume from which characteristic x-rays emanating is always slightly smaller than the actual interaction volume and depends on the critical excitation energy of the sample material (Friel and Lyman, 2006; Goldstein et al., 2003). The different depth and volumes of SE, BSE and characteristic x-rays are important for the resolution of these signal. The spatial resolution of a signal is an expression of the maximal depth of their production. SE have therefore, the highest spatial resolution and are used to image the fine surface structure of samples. The spatial resolution, which depends on the geometry and range of their interaction volume, for BSE is at least two magnitudes less than for SE (50 nm x 50 nm) and slightly better than the resolution of characteristic x-rays. Especially high beam energy in combination with low-density material increases the interaction volume and decreases the spatial resolution for BSE and characteristic x-ray signals. This is especially important for heterogeneous materials. Therefore, for accurate analysis, the specimen must be homogeneous over the electron range (Goldstein et al., 2003).

The electron source for the electron beam is traditionally an electron gun with a W-filament cathode. Alternatively, a field emission gun (FEG) can be used as a cold-cathode or a Schottky type.

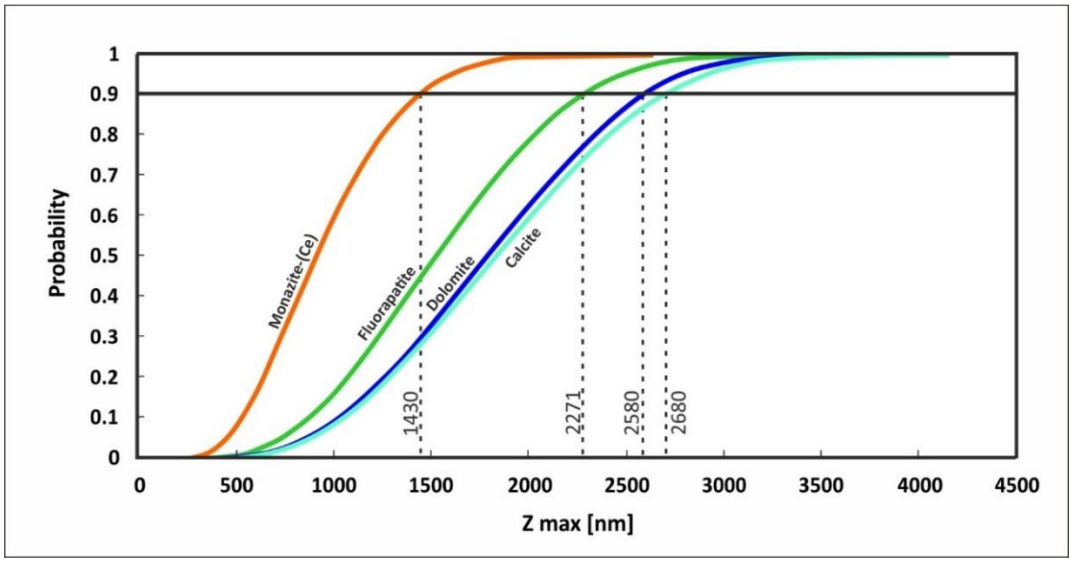

Figure 5-4: Cumulative probability plot for the maximum penetration depth Z max for monazite-(Ce), fluorapatite, dolomite and calcite. The results are based on the Monte Carlo method using the program CASINO V. 2.5.1.0 (Couture, 2000). For the simulation the following parameters were used: acceleration voltage of 20 keV, the spot size of 10 nm and density for monazite-(Ce) 5.34 g/cm^3, fluorapatite 3.2 g/cm^3, dolomite 2.876 g/cm^3 and calcite 2.715 g/cm^3. The most important parameters for the simulation are acceleration voltage and density of the material. The spot size of the electron beam has only a minor influence, and a variation between 10 and 100 nm does not have a significant effect on the interaction volume.

A Schottky field emission gun can produce a more stable electron beam than a W-filament electronic gun, which is advantageous for longer acquisition runs (Claverie and Mouis, 2012). Additionally, the resolution of the FEGSEM is much better due to having a smaller source size with a higher electron density (Joy, 1991).

The accelerating voltage between the electron source (cathode) and the anode is typically between 500 V – 30 kV creating an oriented electronic beam. The higher the acceleration voltage, the higher is the energy of the electron beam. It is generally a trade-off between high-count rate and shorter acquisition time with a higher acceleration voltage, and a better resolution and preservation of the sample with a lower acceleration voltage. Additionally, in order to produce characteristic x-rays, the ionisation energy of the inner electron, which is called critical excitation energy, has to be overcome by the energy of the beam electrons (Goldstein et al., 2003). This aspect will be explained in more detail in chapter 5.3.4. The beam current is controlled by the

condenser lenses and has to be balanced between high beam current for enhanced contrast and faster analysis and low beam current for high resolution and preservation of the sample.

On the way through the column, a range of condenser, lenses and deflection coils or plates are focussing the electronic beam and adjusting the diameter of the beam. The last set of lenses can change the position of the electron beam in a specific x and y-direction, creating the typical rectangular raster of the scan. The sample itself can be moved in x, y and z-direction. The z-axis is the distance between the final lens and the sample surface. The distance between the final lens and the focus point is referred to as working distance. The sample is in focus if z equals the working distance. The current that finally impinges on the sample is called the probe current, which is responsible for the generated signal.

The resolution depends on the size of the electron spot and the size of the interaction volume, which both depending on various parameters (e.g. sample material and energy of the electron beam). The highest spatial resolution of commercial SEM is less than 1 nm for SE signals.

The scan itself consists of a series of discrete locations to which the beam is addressed (Goldstein et al., 2003). The pixel represents the area to which one beam signal is transferred to on the monitor. The magnification is given by the length of the scan in relation to the length of the scan on the computer screen. Because the size of a pixel (represented on the specimen surface) also depends on the magnification, the resolution is also influenced by the magnification. For a specific magnification, images are considered to be in sharpest focus, if the signal produced by the beam at one location only corresponds to a single pixel (Goldstein et al., 2003). The duration that the

electron beam remains in the centre of each 'spot' is called dwell time. An image resolution of 1024 x 768 multiplied with a dwell time of 70 µs for each pixel results in an acquisition time of 55 s for one frame. The quality of the image can be improved by running multiple scans of the same frame.

5.3.2 Backscattered electrons (BSE)

The standard operating mode with the SEM was **backscattered electron (BSE)** imaging in a magnification range of 25 to 10000 times. The BSE signal is the result of an elastic event in which an electron from the electron beam interacts with the electric field of an atom within the interaction volume of the sample (Goldstein et al., 2003). During this elastic event, the electron is redirected without a significant transfer of energy. If the scattered electron deflects out of the sample back into the vacuum chamber, the electron is classified as a backscattered electron (BSE) and can be detected by the BSE-detector. The energy distribution of BSE has a maximum close to the initial energy before the electron-specimen interaction happened and tails of exponentially to lower energies. Detected electrons with an energy below 50 eV are not considered to be BSE anymore but SE instead (Goldstein et al., 2003). The energy of SE is very low compared to BSE, with a maximum of around 10 eV. Therefore the energy of SE and BSE show almost separate distribution. The intensity of the BSE signal from an analysed spot is transferred into a greyscale coloured pixel. Elements with a high atomic mass are more likely to elastically reflect an incoming electron, hence compounds (minerals) with a high mean atomic number (z) generating a stronger BSE signal transferred into a whiter a colour compared to darker compounds (minerals) with a low mean atomic number. BSE imaging can be very helpful to find small minerals with a high mean z compared to the

surrounding groundmass. For instance, REE-fluorocarbonates, which are typical REE minerals in carbonatites, often have small crystal sizes and share similar optical characteristics with calcite and dolomite. It is therefore hard to distinguish REE-fluorocarbonates from the surrounding carbonate groundmass using a petrographic microscope. Since REE are heavier elements than Ca, C or O, minerals like REE-fluorocarbonates have a relatively high mean z; hence appear much brighter in BSE images, than the surrounding carbonates, making it easier to spot them. Areas of interest were captured with a high-resolution BSE image (2048x1536) and dwell time of 35 µs. BSE imaging followed by X-ray spectroscopy point analysis is a powerful tool to find and classify minerals.

Additionally, the BSE image, in combination with Corel PHOTO-PAINT X7, was used to estimate the porosity of a sample (Fig.5-5). The contrast of a BSE image was changed to obtain a b/w image with pores being black and the rest of the image in white. Subsequently, the histogram of Corel PHOTO-PAINT X7 was used to identify the percentage of black in the image, which corresponds the percentage of porosity in the BSE image. This procedure was carried out for six representative samples from the Bjørndalen transect.

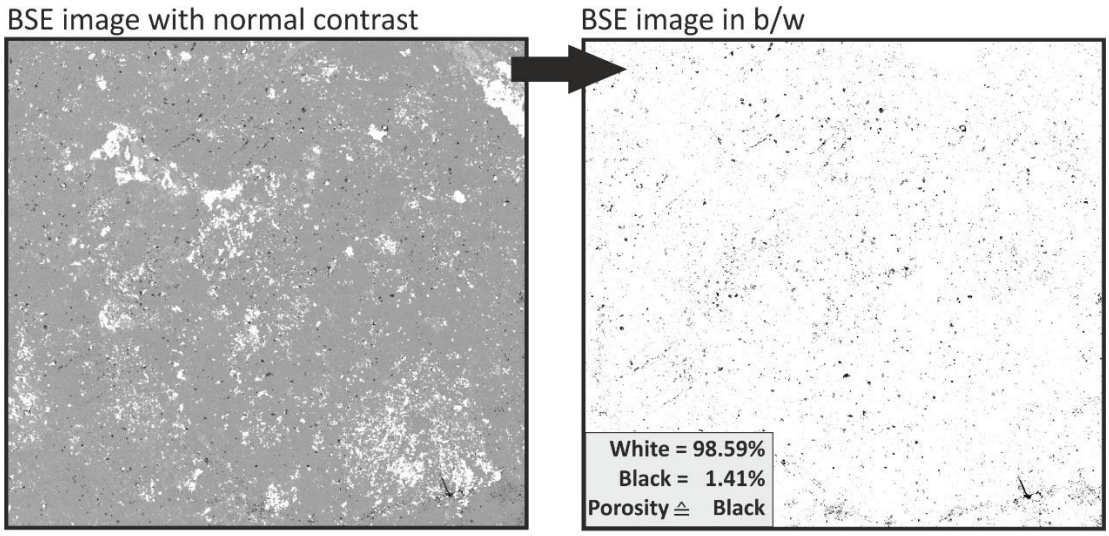

Figure 5-5: The contrast of the BSE image on the left was changed to create the right b/w image. Pores are coloured in black while sample material appears in white. The percentage of black in the image equals the amount of porosity of the sample.

5.3.3 Energy dispersive X-ray spectroscopy (EDS)

Characteristic X-rays are produced by electron beam expulsion of an electron from the specimen. If the vacancy in an atomic orbital is filled with an electron from a higher orbital, the difference in energy between these two orbitals can be emitted in the form of X-rays. The energy level of orbitals is element specific, so the energy difference causes X-rays with a specific energy (keV), hence the name characteristic X-rays. The ionisation energy of the inner electron, which is called critical excitation energy, has to be overcome by the energy of the beam electrons (Goldstein et al., 2003) in order to expulse the electron. However, the efficient generation of X-rays requires the energy of the electron beam to be at least 1.5 (optimum value is ca. 2.7) as much as the critical excitation energy (ammrf, 2014). The energy of the prominent characteristic x-rays (L-line) for Nd, Sm, Tb and Ho lies between 4.5 keV and 9 keV (Fowler et al., 2017). According to Bearden (1967), the critical ionisation energy of Lu is with 9.249 keV (LIII-line) the highest among the REE. Therefore, a reliable analysis of lanthanides requires a

minimum of 15 kV. These characteristic X-rays can be detected by either energy dispersive (ED) or wavelength dispersive (WD) detectors. For this project, an ED-detector was used to analyse the number and energy of the emitted X-rays. Detected X-ray energy is converted into a voltage signal, which is further processed and then displayed in the form of intensity peaks. The EDS can be used to identify elements present in the interaction volume and to estimate their relative concentration. Every element from boron to uranium can be detected simultaneously.

The EDS was used in combination with a BSE image. BSE images show different mineral phases in various greyscales. To analyse a mineral phase, a point target was set on live BSE image of the minerals using the software Aztec from Oxford Instruments. The result shows a spectrum of the analysed point and the chemical composition of this point. Figure 5-6 illustrates the spectrum of barite, which is a common mineral among the analysed carbonatite samples. The software AZtec does the peak identification and chemical composition of the point analysis automatically. The EDS analysis was calibrated with internal standards and gave a semi-quantitative chemical analysis of the relative concentration of major elements. The spectrum was checked for peak overlaps, which might disguise small quantities of unidentified elements, and missing elements were added accordingly. The chemical composition of the point analysis was given as at% and wt% normalised to 100. The chemical composition in at% was used for the stoichiometric calculation to identify the analysed mineral (Tab. 5-1). The Key EDS-SEM analyses are summarised in the appendix **V EDS-SEM Analysis**. The precision of the EDS analysis depends on the element and matrices but generally lies between 0.1 and 0.5 wt%. The accuracy is not possible to determine exactly because geological standards have not been used. Nevertheless, according to the formula of barite ($BaSO_4$), it is

possible to calculate the expected values for the elements. The deviation from the true value is less than 20 %, and elements with high z are generally overrepresented (Tab. 5-1). The final mineral identification was made using the at% of the spectrum in combination with other important information like geological setting, rock type, macroscopic and microscopic observation, paragenesis, texture and mineral habitus.

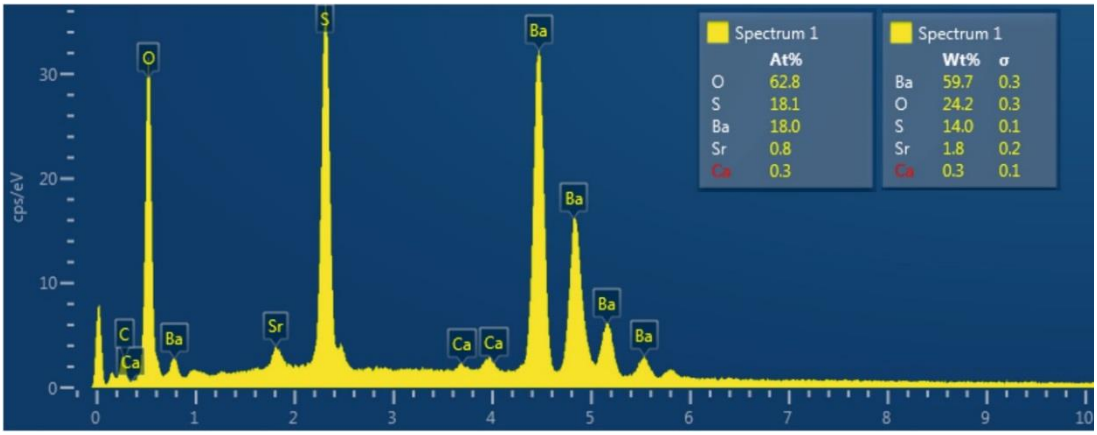

Figure 5-6: Spectrum from an EDS-SEM point analysis with the energy of x-ray photons on the x-axes and counts per second divided by the energy of the photon on the y-axes. Based on the chemical composition of the analysis, which is given in at% and wt%, the mineral is identified as barite.

Table 5-1: Element concentration of ideal barite compared to the element concentration analysed by an EDS point analysis of real barite (Fig. 5-6).

	$Barite_{ideal}$ [at%]	$Barite_{real}$ [at%]	Error [%]
O	66.0	62.8	4.8
S	16.0	18.1	-13.1
Ba+Sr	16.0	18.8	-17.5

The elements H, Li and Be cannot be detected, which has been to taken into account for mineral identification. Additionally, because all the samples were carbon coated, C was excluded from the list of detectable elements, which has to be considered for C bearing

minerals, e.g. carbonates. Nevertheless, this will not affect the relative ratio of other elements, which allows differentiating between different carbonate minerals.

Although this technique helps to identify minerals and especially small quantities of tiny minerals, it can lead to focus too much on an unrepresentative area of the sample and rely solely on the ability to distinguish phases using EDS. In order to gain a better overview, it is possible to use the EDS for the entire image using multiple point analysis, giving each element a colour and combining these points to generate a 2D map – one map for each element, or a combined map based on several elements. Multiple EDS maps can be stitched together to create a larger map. This technique is called Large Area Mapping (LAM) and can produce a coloured EDS-map of the entire sample.

5.3.4 Large Area Mapping (LAM)

Large Area Mapping (LAM) is a very powerful tool to detect less abundant mineral phases in the sample and show texture and element/mineral variations on a larger scale. The electron beam scans a defined area and obtains EDS spectra by mapping point after point creating an EDS map. Different elements are displayed in different colours creating a coloured 2D map of each element and a combined map of every selected element. Multiple fields of view were measured in sequence – frame after frame – and were then stitched together to create a larger map. Doing a LAM is always a trade-off between time and data size vs. spatial and spectral resolution. To improve accuracy the magnification of every frame, the dwell time, image resolution and several scans across the same frame can be increased, resulting in increased measurement time and file size. Because LAM is a time-consuming process and does not need any supervision, it was generally done overnight. The EDS run was set up for to a magnification of 100x, 400

frames, three repeating scans, image resolution of 1024 x 1024 pixels and 70 µs dwell. The setting for the BSE image run were 100x, 400 frames, one scan, image resolution of 512 x 512 pixels and 35 µs dwell. After the acquisition, the single frames were stitched together and montaged. The montaging equalises the colouration of the individual EDS maps and creates a large EDS map. The size of these files is considerably large (ca. 10 Gb) and can make further data processing time-consuming. Although increasing the number of scans or dwell time results in increased acquisition time, it does not affect the file size and can be used to produce a higher quality map. Occasionally weekend runs were used to measure multiple (up to 5) samples one after another.

5.3.5 JEOL FE-SEM 7001

Mineral identification and textural analysis of thin sections and polished blocks were carried out using the JEOL FE-SEM 7001 at the Plymouth Electron Microscopy Centre. The JEOL FE-SEM 7001 is an ultra-high resolution instrument equipped with a Schottky field emission gun. The instrument is equipped with an Oxford Instruments EDS detector and software, designed for point analysis and acquisition of large-area mosaics of elemental maps. EDS data was acquired using an acceleration voltage of 15 or 20 kV, a beam current of 11 nA and a working distance of 10 mm. Acquisition and data processing was carried out using Oxford Instruments' Aztec software. A combination of back-scattered electron imaging, EDS X-ray point analysis, and EDS X-ray mapping was used to identify the chemical composition, size, shape and texture of the mineral phases. The single sided copper tape was used on four different points to provide a conducting contact between the sample surface and the sample holder. The sample holder for polished blocks can fit five blocks at the same time, which makes the sample loading

very effective. On the downside, it takes more time to reach the vacuum conditions when more samples are in the vacuum chamber. Especially for automated large area mapping, this was taken into consideration. At least 2 h before starting the automated run the samples had to be loaded into the vacuum chamber to ensure enough time for the vacuum to build up. The method of using liquid nitrogen to cool the vacuum chamber and force the vacuum to build faster turned out not to be sustainable because the vacuum chamber would eventually warm up again, which in return could cause the vacuum to collapse, producing large-area EDS mosaics with gaps and artefacts. A high-resolution scan of every sample was done in advance and used as a map to navigate on the sample during measurements.

5.4 Geochemical analysis

The geochemical analysis of the Fen Complex samples is one of the pillars of this thesis. Gaining a reliable element concentration, especially for REE, was a fundamental requirement to understand the REE mineralisation processes and to preselect key samples for the SEM. Although EDS-SEM delivers quantitative analysis for most elements of the periodic table, the geochemical data acquisition was carried out using inductively coupled plasma mass spectrometry (ICPMS) — an initial attempt using X-ray Fluorescence did not work out. The detection limit of EDS-SEM depends on various variables and lies roughly between 0.1 wt% and 1 wt%. The detection limit for ICPMS is orders of magnitudes lower and commonly enables to detect trace element concentration of less than 1 ppb. To account for all REE and other important trace elements fully, EDS-SEM analysis was not precise enough. Another advantage is that geochemical analysis with ICPMS produces a representative element concentration of

the whole sample, which can be used for whole rock geochemistry contrary to mineral composition acquired by EDS-SEM point analysis. Although LAM-EDS mapping can identify chemical distribution on a larger scale, it is not precise enough for qualitative reliable whole rock geochemistry. Additionally, using the SEM produces data from a 2D slice of rock, which might not be representative for the whole sample. EDS-SEM is designed and developed to identify chemical composition on a small-scale, e.g. chemical composition of a mineral and not designed to acquire data for whole rock geochemistry, especially for trace elements.

The first sample batch (n=15) was sent away to a professional geochemistry lab at the Ocean and Earth Science, National Oceanography Centre Southampton for trace and isotope analysis ($^{87}Sr/^{86}Sr$ and $^{143}Nd/^{144}Nd$). Rare earth element (REE) concentration, as well as a selection of other elements (Hf, Nb, Ta, Th, U, and Zr), were measured in a conventional multi-acid (HNO_3, HCl, and HF) solution using the ICP-MS. The lab reported various degrees of precipitation in some solutions. A complete digestion of the sample is important for gaining a reliable REE concentrations and is challenging in the presence of refractory minerals such as zircon, which can contain a significant amount of HREE in its crystal lattice. In order to try out alternative methods for geochemical analysis, the decision was made to utilise the facilities at Plymouth University. One way to avoid problems with dissolution and reprecipitation is by using an analytical method that does not require samples digestion to begin with, i.e., XRF.

5.4.1 X-ray Fluorescence

X-ray Fluorescence (XRF) is one possibility of producing quantitative bulk-rock analysis without any digestion. In this PhD project for the PANalytical Wavelength Dispersive **X-Ray Fluorescence** Spectrometer (WD-XRF; Axios Max) from the ISO-certified Consolidated Radio-isotope Facility (CORiF) at Plymouth University was used.

5.4.1.1 XRF Principles

XRF spectrometry is based on the detection of characteristic radiation from an atom after being exited by X-rays. If the incoming radiation has enough energy, it can expel electrons from an inner orbital of an atom. When an electron from the outer orbital jumps in to fill the gap, the energy difference of those two orbitals is emitted as X-rays. The wavelength of these secondary X-rays is characteristic of the element it was emitted from, and the intensity of the X-ray is proportional to the element concentration in the sample (Rollinson, 1993). Similar to the SEM, these X-rays can be measured by an ED-detector or further separated by crystals of a WD-detector, which allows a better resolution. Although the detection limit of the XRF is higher compared to ICPMS analysis, the XRF has many advantages, e.g. analysing of a solid sample is possible, no upper detection limit, which makes it possible to analyse trace and major elements at the same time. Although this is possible, trace elements are generally analysed using press pellets while major elements are analysed using fused beads.

5.4.1.2 Pressed pellets

The process of making pressed pellets involves pressing a powder-wax mixture under high pressure to a solid pellet. The particle size of the sample should be less than 30 µm. Grinding is normally combined with homogenising wax and the sample. Wax is needed as a binding agent to hold the press pellet together. In this project, because the powder was already created, mixing of wax and sample was done in a shaker. Centrifuge tubes were filled with 10 g of sample, 2.5 g of wax and three agate balls and shaken by hand for 1 min. Afterwards, the centrifuge vial was put in the mechanical shaker and shaken for another hour. The next step was to fill the powder into an aluminium cup and apply pressure of 200 kN by using a sample press. The maximum pressure was held for a couple of seconds and then released again. After this last step, the pressed pellet was stored in a petri dish and was ready to be analysed.

5.4.1.3 Fused beads

In order to make a fused bead, 9.0000 g of Lithium tetra/metaborate, 0.9000 g of ammonium nitrate and 0.9000 g of sample material was funnelled into a Pt-crucible. Lithium tetra/meta borate serves as a flux in the melting process and ammonium nitrate-was used as an oxidising agent. Afterwards, the Pt-crucible was loaded into a special furnace and heated up to 1050°C. Following this, the melt in the Pt-crucible was automatically poured into a Pt-disk and cooled down to form a glass bead. After the Pt-crucibles cooled down, they were placed in a beaker with citric acid for cleaning. Following, the beaker was transferred into an ultrasonic warm water bath and heated up to 70°C.

5.4.1.4 XRF analysis

REE-1 Certified Reference Material (Strange Lake REE-Nb ore, Natural Resources Canada) was part of the analytical procedure and showed the reliability for major element analysis, whereas the concentration of trace elements and especially REE showed a significant error with respect to the certified values. The issue is likely due to the high REE concentration that probably lies outside of the calibration curve of the instrument. To this point, the issue with the REE concentration could not be fixed, and no data acquired with the XRF was used for this PhD-project. Sodium peroxide sintering digestion with Inductively Coupled Plasma Mass Spectrometry was tested as an alternative analytical procedure for analysing trace element concentration.

5.4.2 Inductively coupled plasma mass spectrometry (ICP-MS)

Analysing a sample using an ICP-MS requires the sample to be completely dissolved into solution. The risk of incomplete digestion with a conventional multi-acid (HNO_3, HCl, HF) digestion as it was described before, led to an alternative fusion technique, sodium peroxide sintering.

5.4.2.1 ICP-MS principles

An ICP-MS instrument is a combination of an Inductively Coupled Plasma (ICP) and a mass spectrometer (MS) (Fig. 5-7) — the principal mode of operation is described after Thomas (2013).

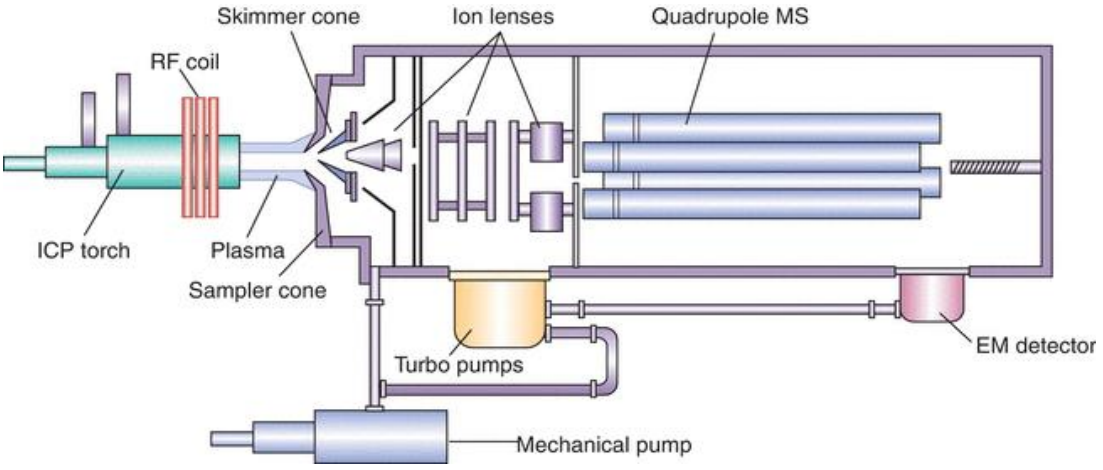

Figure 5-7: Schematic diagram of an Inductive Coupled Plasma Mass Spectrometry (ICPMS) instrument with a quadrupole mass filter (BIOCHEMISTRY, 2017).

The ICP torch produces a plasma, which can reach temperatures of 6000 – 10000 K. The argon plasma of the ICP torch is generated by inductive heating of a radio-frequency coil and ignited by a high-frequency spark. The sample solution is injected as an aerosol from a nebuliser into an argon plasma (Rollinson, 1993). The high temperature of the argon torch causes the sample to ionise. The ions then pass through a small hole in the sampler cone into a vacuum chamber. After passing the skimmer cone, the ions are directed by electrostatic lenses into the MS. Once the ions enter the MS, a magnetic field separates the ions by their mass-to-charge ratio, which causes the ions to hit the detector at different times. Typically, a quadrupole filter is used to increase the resolution of the ICPMS drastically. The quadrupole filter consists of 4 rods to which alternating AC and DC voltage is applied. Certain frequencies only allow specific ions to pass through the filter and hit the detector at a given moment. However, some interferences can still cause issues because of the similar masses of, for instance, ^{87}Sr = 86.90889 amu and ^{87}Rb = 86.90918 amu (Evans and Giglio, 1993). This effect is called isobaric interference and can be limited via the instrumental approach or using a mathematical strategy of

subtraction the contribution of interfering isotopes from measurements of non-interfering isotopes (Meija and Caruso, 2004).

Sodium peroxide sintering

Before using the ICPMS for analysis, the sample has to be fully dissolved. Because the conventional multi-acid (HNO_3, HCl, HF) digestions could not completely dissolve the sample material, it was worth trying an alternative procedure. Sodium peroxide sintering after Bokhari and Meisel (2016) was tested, and rock material like granite dissolved completely without using HF.

For the sintering and dissolving process, the following chemicals were used: analytical reagent-grade sodium peroxide (ACS ISO Merck KGaA, Darmstadt), HCl, HNO_3 and Milli-Q water (resistivity = 18.2 MΩcm at 25°C). Sintering was carried out in 8 ml high purity Ni crucibles from Camlabs. In preparation for sintering sample material, the Ni crucibles were cleaned with one teaspoon of NaOH and heated to 380 °C for 45 min. The heating produced a thin protective layer of NiO on top of the metallic Ni. After the crucibles cooled down, they were put in a Teflon beaker filled with Milli-Q, where they soaked in the basic solution overnight.

Sample sintering preparation started by mixing 100 mg of finely milled sample powder with 600 mg of fine milled N_2O_2 in high purity Ni crucibles using a wooden toothpick. The powder mix was then heated for 120 min at 480 °C in a conventional muffle oven. The process of weighing before heating was done as quickly as possible to prevent the reaction of the hygroscopic Na_2O_2 with air moisture, which would have introduced an added uncertainty with respect to sample mass and make sintering less effective. After cooling down, the outer sidewall of the crucibles was cleaned using Milli-Q water to

prevent any contamination with material from the furnace. The crucibles were then transferred into 100 ml PTFE beakers, and ultrapure water was added dropwise to dissolve the sinter cake. After the reaction stopped, the crucibles were tilted over, placed on a hot magnetic stirring plate, and heated at ca. 90 °C (set up to 160 °C to compensate the heat resistance of PTFE beaker) for about 20 min with a magnetic rotation of ca. 60 rpm. The addition of a magnetic bar is not necessary due to the magnetic properties of the Ni-crucibles, which spin for themselves. The content of the crucible and PTFE beaker were transferred into a 50 ml centrifuge vial. The Ni crucibles were filled with Milli-Q water, and 1 ml of 10% HCl was added to the crucible to dissolve any remaining residue. Since the reaction attacks the Ni crucible, it should not be longer than necessary to keep the Ni contamination of the solution as low as possible. The dissolved content of the Ni crucible was added into the centrifuge vial. Once the reaction in the vial finishes, the vials were filled up and closed. The undissolved residue was separated from the supernatant via centrifugation (10 min at 2500 rpm). The clear supernatant was poured back into the beaker, and the undissolved residue was treated with 1 ml of 70% HNO_3 and 3 ml of 10% HCl and left overnight to react. In case any residue remained, this step was repeated. If residue was left after the repetition residue was treated with 1 ml of 70% HNO_3 and 2 ml of 37% HCl. After this step, normally, no residue was present. Occasionally, if a sample was treated with 37% HCl too early and before adding 70% HNO_3 cloudy precipitation of amorphous silica occurred (confirmed with SEM). Once silica was formed, there was no way of dissolving it again, and the precipitation had to be filtered out to prevent a cloaking of the ICP-MS.

After dissolving and residue, the clear sample solutions were stepwise made up to the mark in a 100-ml volumetric flask with Milli-Q water to give the solution enough time

equilibrate to the higher pH. In case of the formation of new precipitation, more acid was added to have a slightly more acid solution then it needed to be. This was done to ensure the dissolution of the whole sample material while keeping the total amounts of ions in the solution as low as possible. The final solution had an effective dilution of ca. 1000 times and was transferred into plastic bottles for storage and transportation.

The cleaning process involved a rigorous rinsing with deionised water and soaking of the PTFE beakers, glassware and tweezers in 2% solution of HNO_3 for at least two days followed by rinsing with deionised water and a final rinsing with Milli-Q water. Ni crucibles were cleaned with NaOH as described before. Every batch of samples included at least three procedure blanks, two digestions of REES1 Certified Reference Material (Strange Lake REE-Nb ore, Natural Resources Canada) or OREAS 461 Certified Reference Material (carbonatite supergene REE-Nb ore, Mount Weld, Australia) and one acid blank.

5.4.2.2 ICPMS analysis

The solutions obtained with sodium peroxide sintering were analysed for trace elements using the quadrupole VG PQ3 ICP-MS in the trace metal laboratory at Plymouth University. The preparation of the ICPMS run included three different steps:

a) Preparation of the sample solution

20 µl of the internal standard was added into a 15 ml centrifuge tube before adding 5 ml of the sample solution. The solution was shaken to ensure a homogenous mix of the two liquids. The internal standard is made up of 10 mg/l of In and Ir and helps to correct for instrumental drift. The procedure blanks are especially important because they are used to calibrate the In and Ir signal at the beginning of each run.

b) Making of single element standards

The presence of signal interferences happens when two isotopes of different elements are having the same mass (isobaric) or the combination of two or more isotopes from different elements combined having the same mass (polyatomic). In both cases, the isotopes are indistinguishable based on their m/z ratio and the resulting signal will be a combination of both signals.

The inference effects between REE and Ba are usually minimal and can be neglected. Most of the samples happened to be extremely enriched in LREE and Ba relative to HREE. Under these circumstances, interference can affect the concentration of HREE, which has to be taken into account. In order to investigate the effect LREE and Ba have on the concentration of HREE, single element standards were made for La, Ce, Nd, Pr and Ba. The single element standard for La, for example, was created by taking a 25 ml volumetric flask and pipetting 1.25 ml of 10,000 mg/l La solution and filling it up with groundmass solution. From this 500 mg/l La solution, 1.25 ml and 0.25 ml were put into 25 ml volumetric flasks and filled up with groundmass solution to make up the calibration solutions 2.5 µg/l and 0.5 µg/l respectively. From the 2.5 mg/l La solution, 0.5 ml and 0.05 ml were put into 25 ml volumetric flasks and filled up with groundmass solution to make up the calibration solutions 0.05 µg/l and 0.005 µg/l respectively. The other single element standards were made in the same way. No internal standard had to be added.

c) Making of the calibration standards

The calibration solutions contain all the elements of interest (REE, Pb, Sc, Y, Nb, Ta, U, Th, Zr, Hf) and include the full range of these elements as they can be expected from the sample material. In order to prepare the calibration solution more efficiently, two stock

solutions - A and B - were prepared first. Stock A was prepared in a 25 ml volumetric flask by pipetting 2.5 ml of 1,000 mg/l V solution and 0.25 ml of 10,000 g/l Zr, Pb, U, Sc, Th and Y solutions. The flask was then filled up to the mark with 2 % HNO_3. Stock B was prepared in a 25 ml volumetric flask by pipetting 2.5 ml of 1,000 mg/l Hf, Nb and Ta solutions. A few drops of 37 % HCl were added to the flask to secure the stability of stock B in a low pH environment. Finally, the flask was filled up to the mark with 2 % HNO_3. The concentration of each element in stock A and B was 100 mg/l, the same as the individual REE in the REE standard solution. In order to prepare the calibration solution, multiple step dilution had to be performed. In order to avoid cross-contamination 3 ml of stock A, B and REE were poured into individual centrifuge tubes. The calibration solution for 5,000 µg/l, 1,000 µg/l and 100 µg/l were prepared by pipetting 1.25 ml, 0.25 ml and 0.025 ml respectively into 25 ml volumetric flasks and filling up with groundmass solution. Additionally, 100 µl of internal standard (Ir+In) was added. From the 1,000 µg/l calibration solution, 0.25 ml and 0.025 ml were put into 25 ml volumetric flasks and filled up with groundmass solution to make up the calibration solutions of 10 µg/l and 1 µg/l respectively. From the 100 µg/l calibration solution, 0.125 ml and 0.025 ml were put into 25 ml volumetric flasks and filled up with groundmass solution to make up the calibration solutions 0.5 µg/l and 0.1 µg/l respectively. At last 100 µl of internal standard (Ir+In) was added to the calibration solutions 10 µg/l, 1 µg/l, 0.5 µg/l and 0.1 µg/l. The full range of trace elements in the calibration solution is, therefore between 0.1 ppb and 5,000 ppb. In case the concentration of one element in a sample solution might be above 5,000 ppb, the sample was diluted by a factor of 10 and measured again.

After preparing all the necessary solutions, runs were started in a specific order starting with the calibration standard, then the single element standards, followed by the

procedure and acid blank and the sample solution. Each measurement was executed three times, and the software calculated a mean automatically. After each sample, a cleaning run with 2% HNO_3 helped to eliminate any stuck material in the instrument. After 10 samples, a check run with one of the lower concentration calibration standards was done.

5.4.2.3 ICPMS data processing

After data was checked by Dr Rob Clough and Christian Marien the data sheet was extracted as an excel file. Total procedural blanks were analysed to have approx. 0.5 ppb for Ce but less than 0.2 ppb for the other REE, typically 0.025-0.002 ppb for Eu-Lu, which shows a very low degree of REE contamination during the sodium peroxide and ICPMS sample preparation and measurement. The detection limit was calculated for every ICPMS run with 3* standard deviation (confidence level of 99%) of the procedure blank (Tab. 5-2) The precision of the analysis is represented as the relative standard deviation (RSD) was calculated by the standard deviation of each analysis divided by the mean of analysed concentration and was generally <1%. The accuracy calculated as relative error of the measured CRM values in (with respect to certified values of the trace element concentrations, estimated by repeated analysis of the REE-1 CRM, were typically <15% (Tab. 5-2).

Table 5-2: ICPMS analysis of sample 15-94-FE with a selection of trace elements, showing the most important statistical variables — detection limit, RSD (expression of precision) and relative error (expression of accuracy).

		139La	140Ce	157Gd	159Tb	172Yb	175Lu	232Th	238U
Total Procedure Blank	mean value (ppb)	0.36	1.41	0.07	0.01	0.07	0.01	0.42	0.02
	sigma (ppb)	0.33	1.32	0.07	0.02	0.11	0.01	0.28	0.02
	detection limit (ppb)	0.99	3.95	0.21	0.05	0.33	0.04	0.85	0.05
Sample 15-94-Fe	c (ppb)	2678.00	5161.00	141.60	15.37	42.57	5.86	919.60	21.63
(dilution factor = 1010.1)	c blank corrected (ppb)	2677.64	5159.59	141.53	15.36	42.50	5.85	919.18	21.61
	c dilution corrected (ppm)	2704.77	5211.88	142.96	15.51	42.93	5.91	928.49	21.83
	s (ppb)	1.94	18.39	0.57	0.03	0.20	0.01	1.93	0.01
	RSD (%)	0.07	0.36	0.40	0.16	0.46	0.22	0.21	0.03
REES1 CRM	mean c (ppm)	1655.70	3807.51	452.66	123.63	797.27	105.29	834.00	157.64
(Strange Lake REESNb ore)	s (ppm)	65.87	159.56	15.96	4.72	32.49	3.98	19.59	6.76
(n=4)	Reported CRM values (ppm)	1661.00	3960.00	433.00	106.20	678.00	92.40	719.00	137.00
	relative error (%)	-0.32	-3.85	4.54	16.42	17.59	13.95	15.99	15.07

The single element data showed interferences between the LREE and HREE, but most of the interferences could be avoided by a judicious choice of the mass on which the concentration of the element in question was measured. As it turned out, only Ce and Nd caused significant overlaps that could not be resolved analytically. These interferences were corrected off-line by using the standard solutions of Ce and Nd spanning the full range of expected concentrations. For example, $^{140}Ce^{16}O$ was causing an overlap for the signal of ^{156}Gd. The signal of ^{156}Gd in the single element Ce standard derives from the Gd concentration of the matrix solution (acid and Milli-Q water) plus the signal interference of CeO on ^{156}Gd. After subtracting the mean procedural blank concentration from the Gd concentration, the rest is caused by interference of CeO. This effect was measured for four different concentrations of Ce to identify the relation between the concentration of Ce and relative interference with Gd. The final subtraction value [%] was calculated as the mean of the Gd concentration relative to the Ce concentration for the four different Ce concentrations. This is possible because the data points were showing a linear trend (R^2=1) (Fig. 5-8). Other elements were measured via their interference free isotopes. In order to obtain final values for the element

concentration, the procedural blank was subtracted from the samples, the interference was subtracted, and the dilution factor was multiplied.

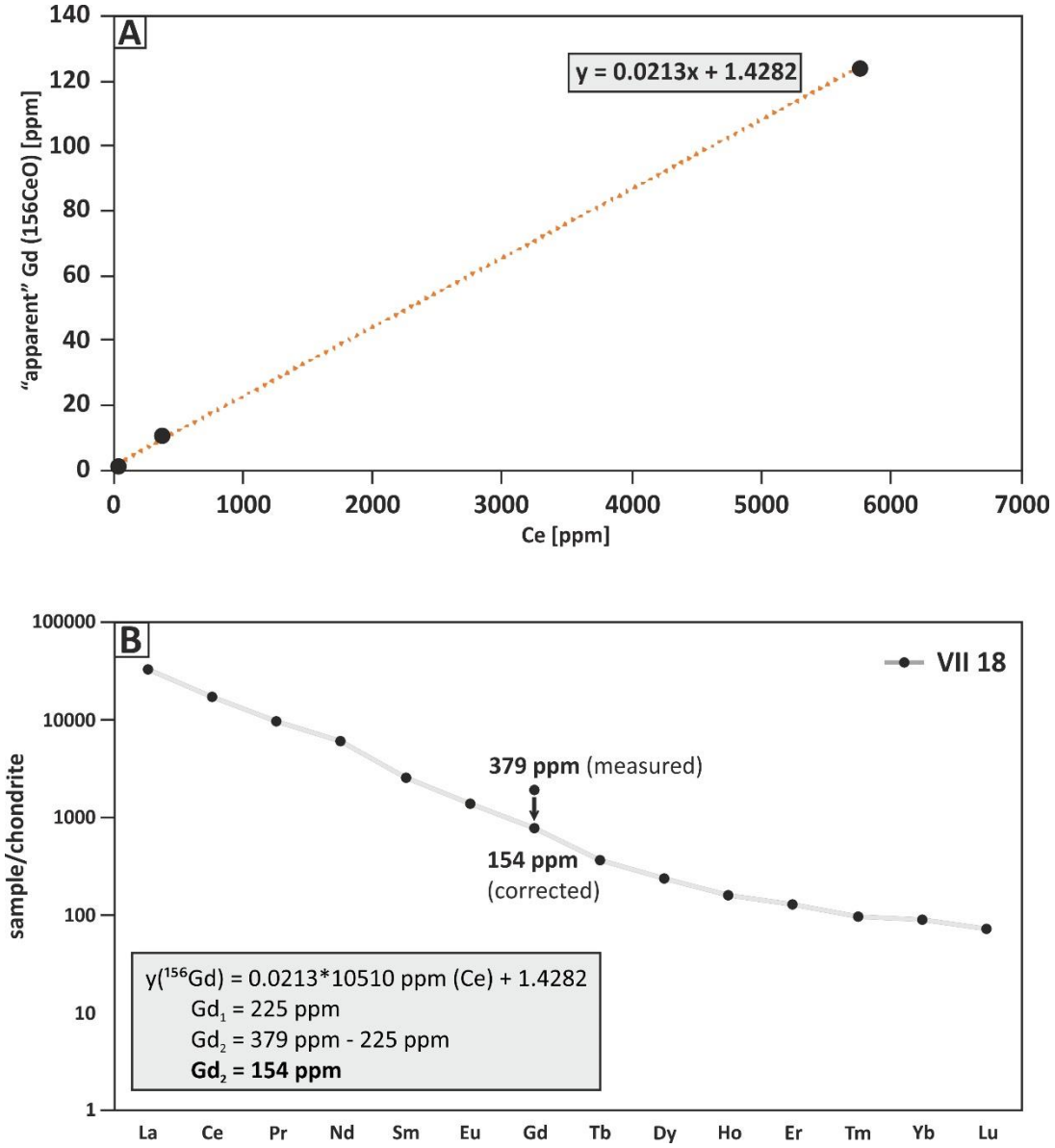

Figure 5-8: Plot A) The concentration of ^{156}Gd as a function of Ce concentration in three single element aqueous solution of Ce. Because the solution (minus blank) does not contain any significant Gd, the ^{156}Gd signal is produced entirely by ^{156}CeO interference. The function of the trendline can be used to correct for ^{156}Gd in a sample produced by ^{156}CeO interference. Plot B) REE concentrations normalised to CI1-chondrite values from McDonough and Sun (1995) illustrates that without a CeO interference correction, Gd would cause a strong positive anomaly, which cannot happen naturally. The corrected value of Gd_2 (154 ppm) using the function of the trendline in plot A fits the curve much better. Gd_1 = Gd signal caused by CeO interference; Gd_2 = real Gd signal after correction.

6 Bjørndalen transect

This chapter will focus on the mineralogy, texture and geochemistry of rock samples from the Bjørndalen transect. The purpose of this chapter is to show the distribution of the rare-earth elements (REE) along the transect and to establish a descriptive and inferred petrogenetic link between the REE mineralisation and the process of rødbergitisation (hydrothermal alteration with red colouration by disseminated Fe-oxides). Thorium (Th) is commonly associated with REE-mineralisation and is one of the major obstacles for a profitable REE-exploitation, as it leads to a radioactive mine waste product. Therefore, the distribution and mineralisation of Th will be part of the discussion. Furthermore, this chapter will explain the underlying ore-forming processes at Fen and establish a REE-mineralisation model for the Bjørndalen transect.

This study has been published in the journal Mineralogical Magazine as Marien et al. (2018), therefore most of the content of this chapter is shared with the publication. Nevertheless, this chapter incorporates additional figures, is largely rewritten and contains new SEM and ICPMS analysis. The Bjørndalen transect (UTM 32V 517541 6569595) located in the SE of the Fen Complex (Fig. 5-1) is a suited introductory site for understanding the processes of rødbergitisation in detail. The transect is relatively well exposed and displays the full range of rock types from unaltered carbonatite to a highly altered rødbergite within a short distance of only 30 m (Fig. 6-1A). For a detailed description of the sampling procedure, please refer to chapter 5. The term transitional rødbergite was established to describe rocks that are between carbonatite and rødbergite in terms of their optical evidence for alteration (Fig. 6-1B). The most noticeable change during alteration is in colour, from white-grey through yellowish-ochre to a rich red — hence the name rødbergite (Norwegian for “red rock”) — this

colour spectrum is illustrated in Fig. 6-1C. Additionally, transitional rødbergite and rødbergite have a higher density of veins and show a grain size reduction relative to the unaltered carbonatite.

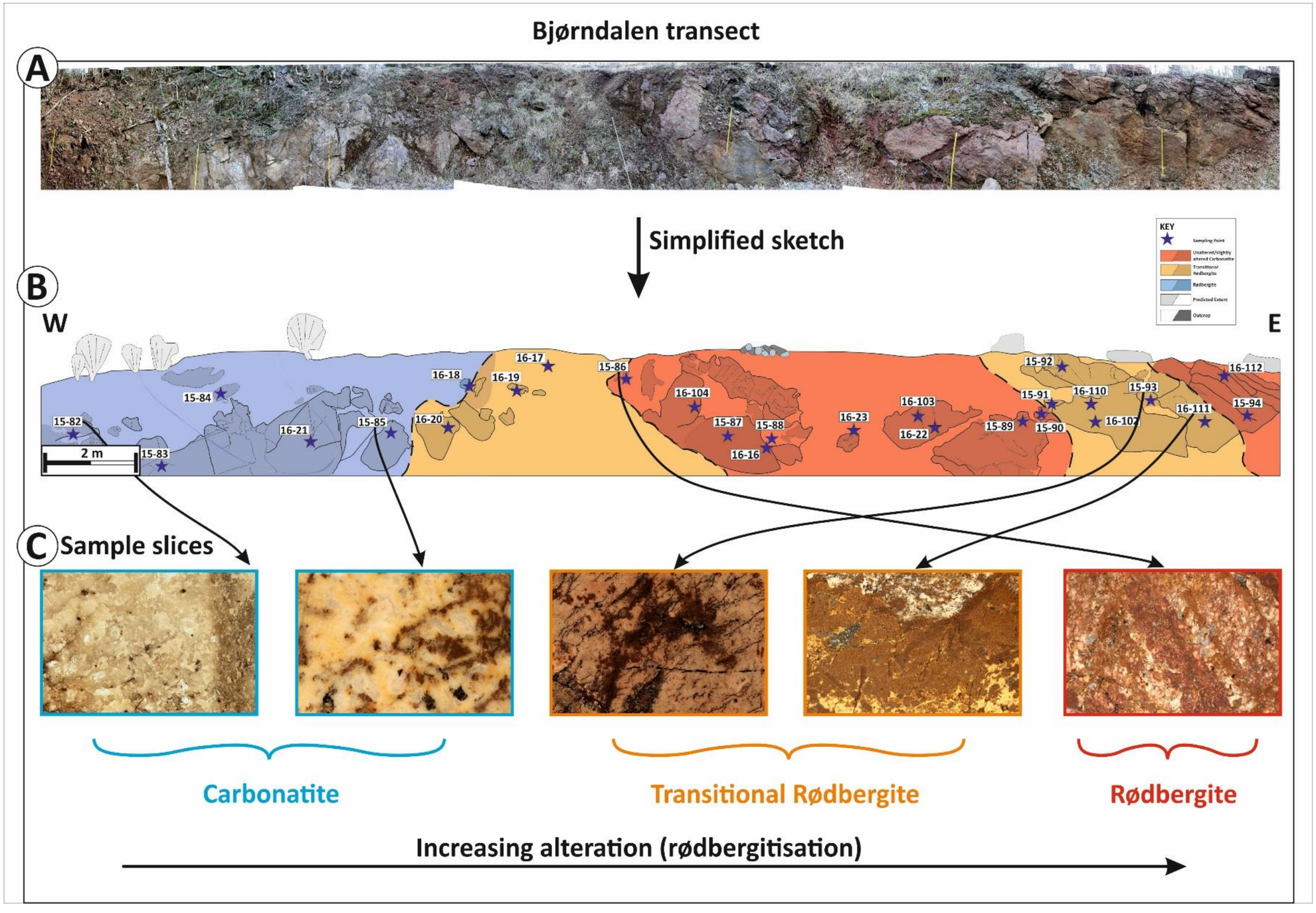

***Figure 6-1**: (A)* Stitched photograph of the Bjørndalen transect. (B) Classification of the Bjørndalen transect into unaltered carbonatite (blue), transitional rødbergite (yellow) and rødbergite (red). The actual outcrop of the alteration zone is highlighted by shading. Sampling locations are marked as blue stars. (C) Representative samples of the alteration zones show the variation in colour and texture across the Bjørndalen transect.

6.1 Rock types

The Bjørndalen transect comprises the three major rock types: unaltered carbonatite, transitional rødbergite and rødbergite. Unaltered carbonatite makes up the western part of the transect, followed by two zones of transitional rødbergite surrounding a central zone of rødbergite and a small strip of rødbergite at the eastern end of the transect (Fig. 6-1B).

6.1.1 Calcite-bearing Dolomite-Carbonatite

The carbonatite from the Bjørndalen transect is a calcite-bearing dolomite-carbonatite with little to no apparent alteration, a white to grey colour with darker spots of opaque minerals and a grain size of approximately 2 mm (Fig. 6-2).

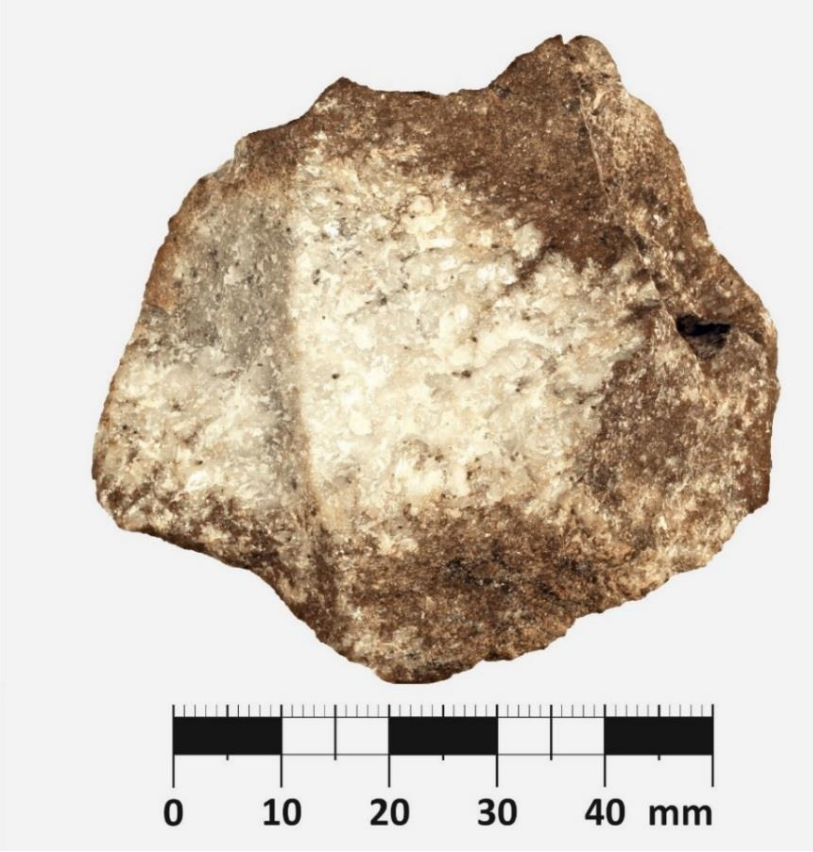

Figure 6-2: Photograph of sample 15-82-FE as a representative sample for unaltered carbonatites. The centre of the sample is relatively unaltered while the outer surface displays signs of alteration or weathering.

The principal minerals, determined based on optical properties and mineral chemical composition by means of EDS analysis, are (in order of decreasing overall modal abundance): dolomite, calcite, apatite, pyrite, magnetite, columbite and zircon, with accessory quartz, barite, pyrochlore, fluorite, synchysite-(Ce) and monazite-(Ce).

Locally, the calcite-bearing dolomite-carbonatite displays a banded texture of whitish carbonate-rich layers and grey blueish apatite rich layers with most of the opaque minerals concentrating in the apatite rich layer (Fig. 6-3, Fig. 6-4).

Although carbonates appear as uniformly sized crystals (~2 mm grain size) in hand specimen (Fig. 6-2), a microscopic analysis shows an irregular fine intergrowth of calcite and dolomite (Fig. 6-4).

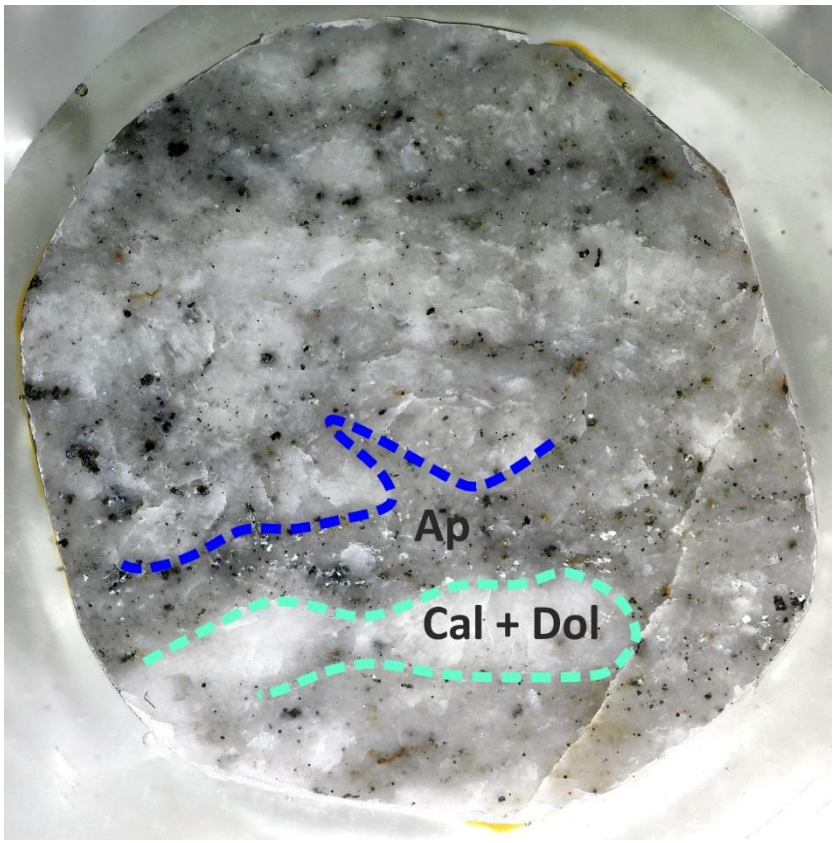

Figure 6-3: Scan of a polished block (Ø = 3 cm) from the same sample displayed in Figure 1.2 (15-82-FE). The blue-grey areas have a high amount of apatite (Ap) whereas the white layers are almost entirely made of calcite (Cal) and dolomite (Dol).

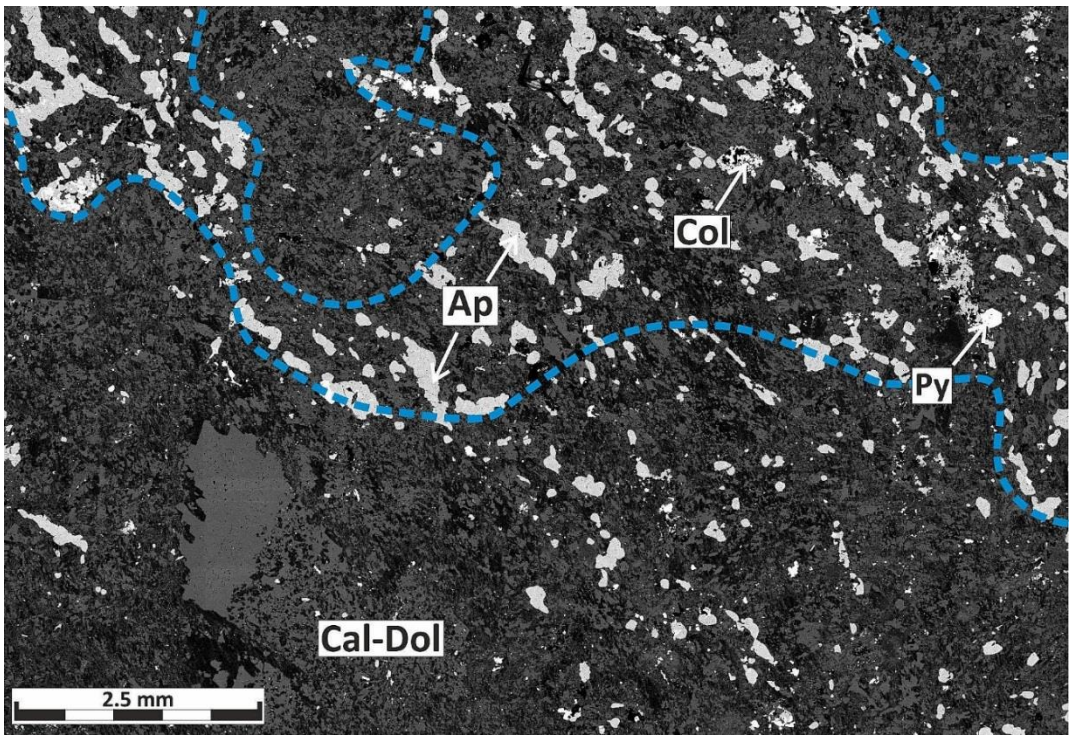

Figure 6-4: BSE-SEM image of an unaltered carbonatite (15-82-FE). Note the complex irregular intergrowth of calcite and dolomite in the groundmass and a distinct zone/layer of apatite (blue dashed line). The elongated polycrystalline apatites show a preferred orientation. Ap – Apatite, Cal – Calcite, Col – Columbite, Dol – Dolomite and Py – Pyrite.

Apatite is the most common non-carbonate mineral and typically occurs as subhedral lozenge-shaped crystals or aggregates, with a preferred orientation (Fig. 6-4). Pyrite is frequently present as aggregates (>0.5 mm) of subhedral pyrites intergrown with calcite, fluorite and REE-fluorocarbonates (Fig. 6-5) or in the form of individual euhedral cubes (0.5 mm). Columbite forms equidimensional crystals (~ 0.5 mm) and occasionally has a poikilitic texture with inclusions of apatite phenocrysts (Fig. 6-6). A small number of large zircons (2 mm) used for radiometric geochronology of the carbonatite formation — for more information, please refer to chapter 9. These zircons are euhedral aggregates with a poikilitic texture and distinct pressure shadows of dolomite (Fig. 6-7). The main mineral hosts for REE are the REE-fluorocarbonates: synchysite-(Ce) and parisite-(Ce).

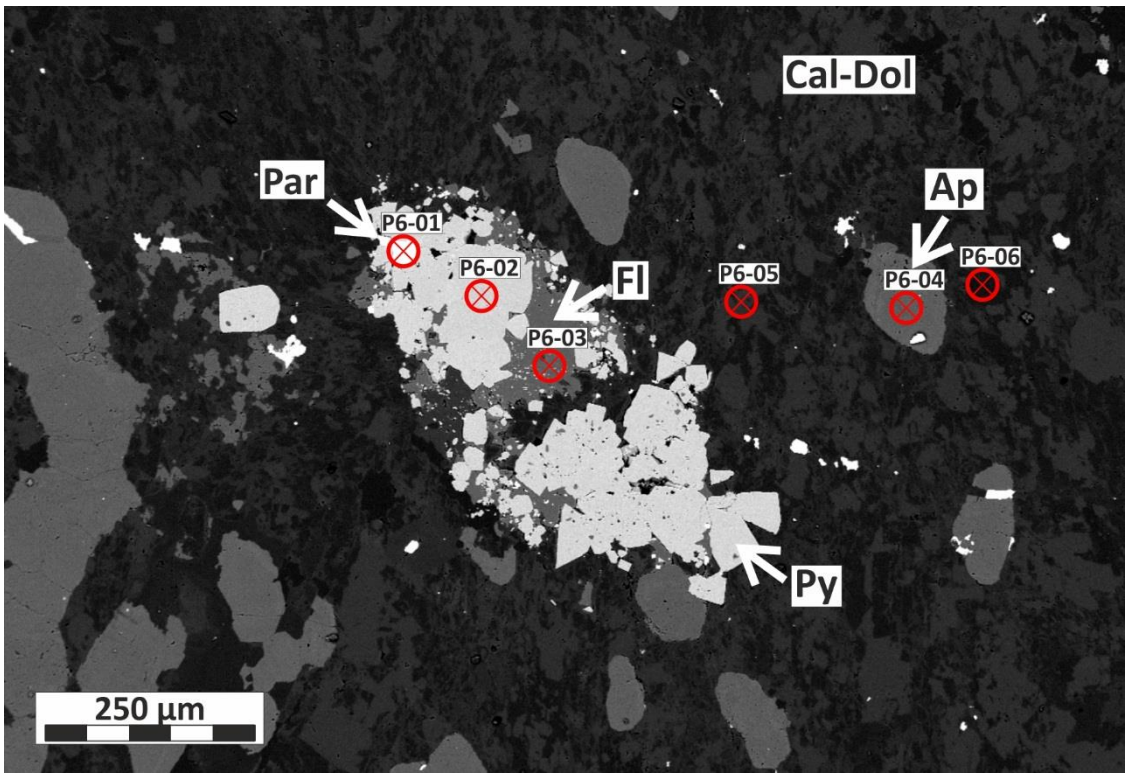

Figure 6-5: BSE-SEM image of a pyrite cluster with minor amounts of fluorite and parisite-(Ce) in an unaltered carbonatite (15-82-FE). Ap – Apatite, Cal – Calcite, Dol – Dolomite, Fl – Fluorite, Par – Parisite-(Ce) and Py – Pyrite.

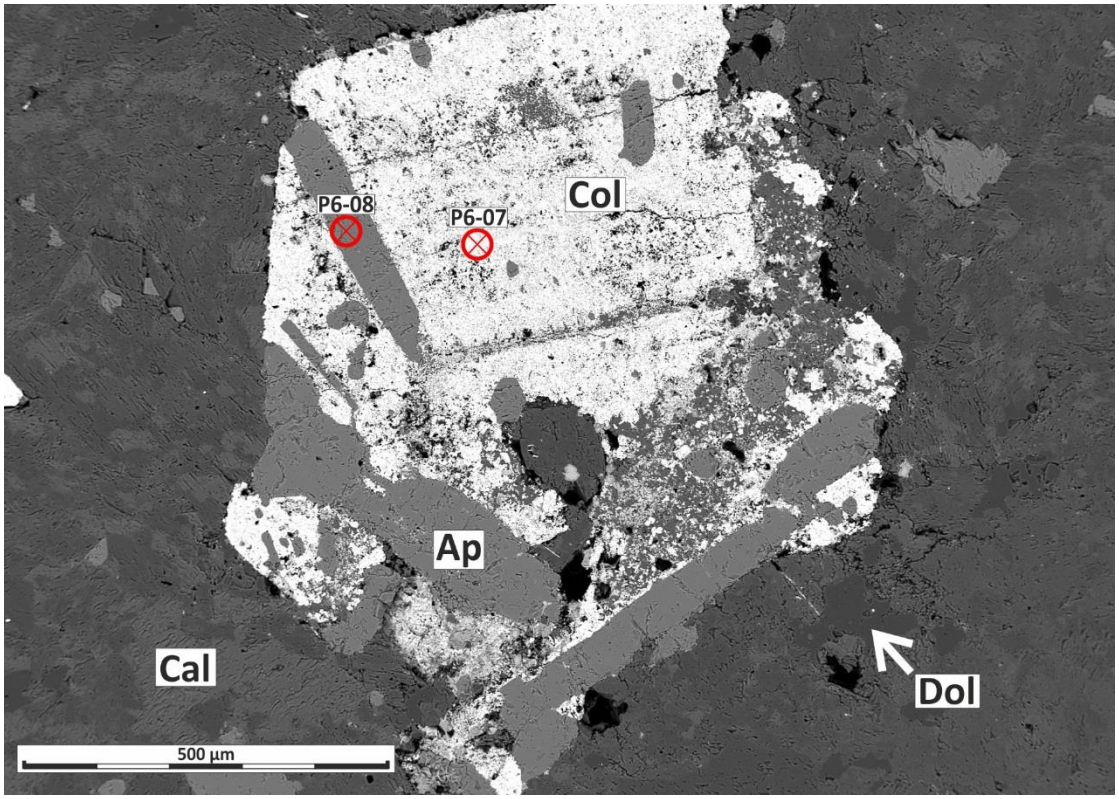

Figure 6-6: BSE-SEM image of a hypidiomorphic columbite phenocryst with inclusions of prismatic apatite crystals, which are significantly larger than the apatite crystals within the groundmass. The columbite crystal displays signs of zonation (15-83-FE). Ap – Apatite, Cal – Calcite, Col – Columbite and Dol – Dolomite.

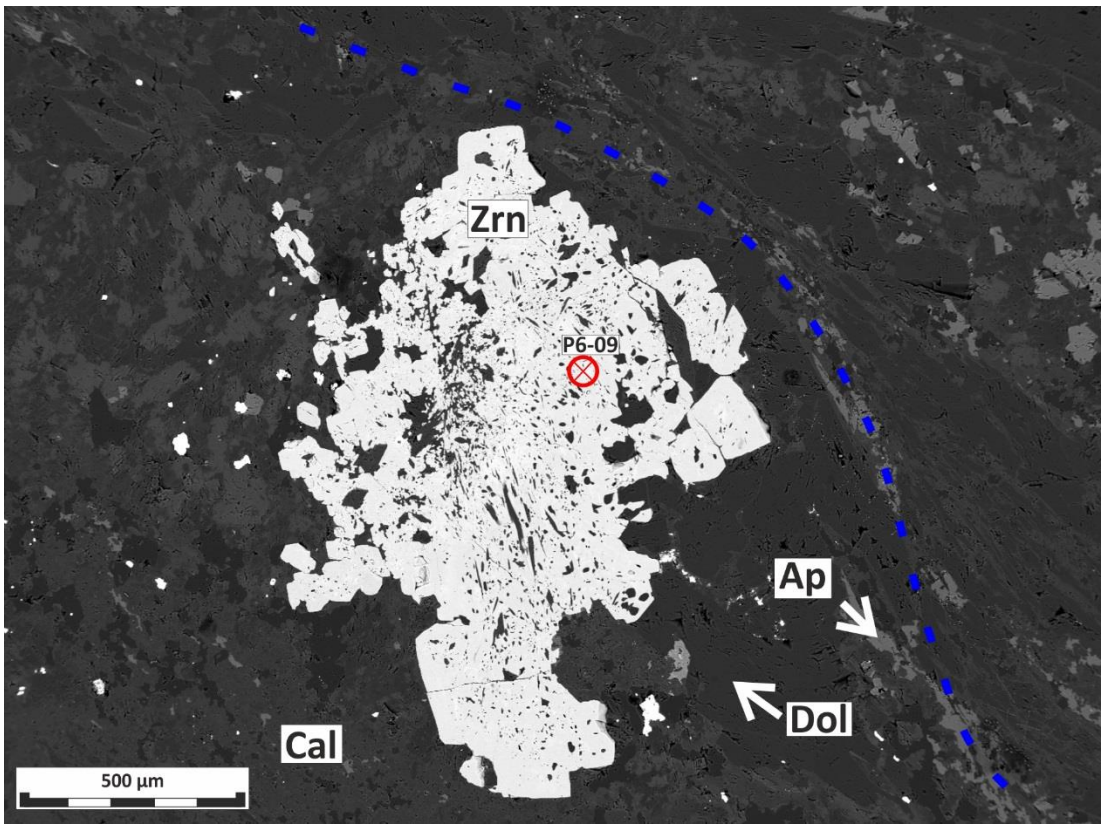

Figure 6-7: BSE-SEM image of a large poikilitic zircon with dolomite inclusions (unaltered carbonatite: 15-82-FE). There is a flow pattern of carbonate minerals and an apatite layer around the zircon phenocryst (blue dashed line) with coarsely crystallised dolomite in the pressure shadow of the zircon. Ap – Apatite, Cal – Calcite, Dol – Dolomite and Zrn – Zircon.

Besides being a minor component in pyrite aggregates (Fig. 6-5), REE-fluorocarbonates occur in veins, as small inclusions (5-20 µm) in calcite, dolomite and apatite as well as in the form of larger anhedral grains (20-50 µm) in intergrowth with barite (Fig. 6-8). To minor extent, monazite-(Ce) is present as small inclusions (<2.5 µm) in apatite, and pyrochlore (Fig. 6-9).

Some areas of the carbonatite have undergone incipient alteration in the form of dark-coloured Fe-oxide, which preferentially occurs along with fractures and grain boundaries (Fig. 6-10). The fine-grained calcite surrounding the Fe-oxide alteration shows a speckled appearance in BSE images, caused by fine disseminated Fe-oxides.

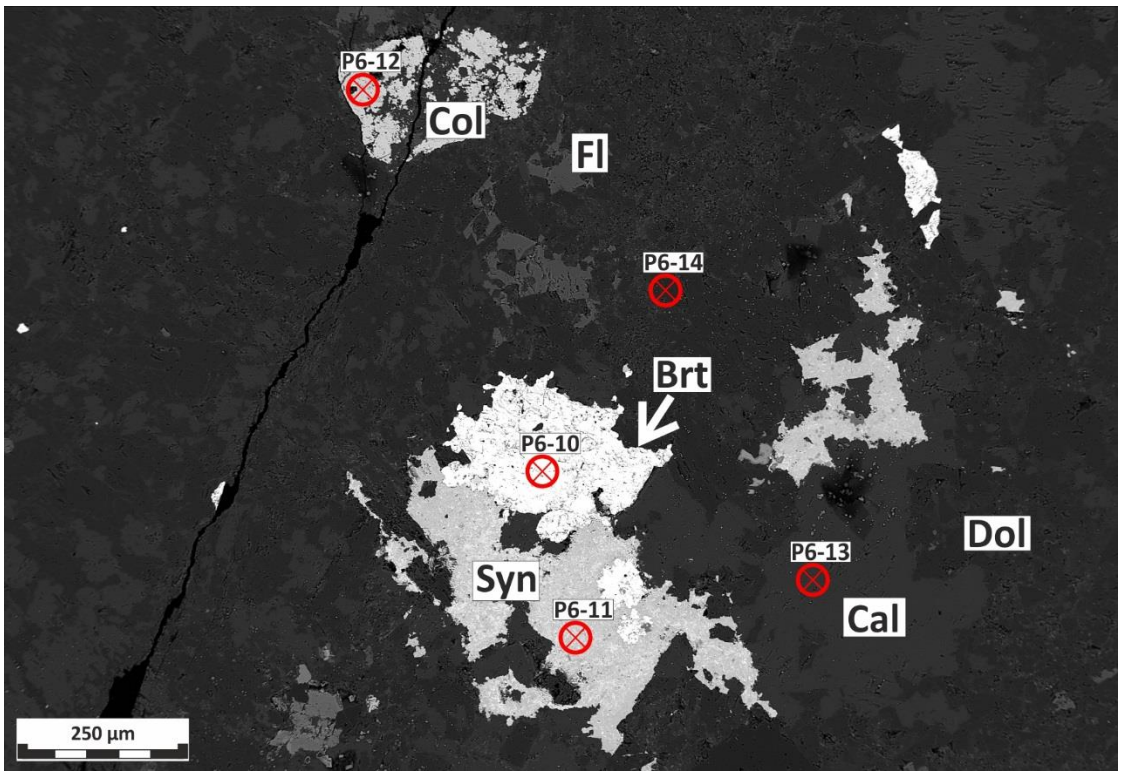

Figure 6-8: BSE-SEM image shows a xenomorphic cluster of synchysite-(Ce) and barite in an unaltered carbonatite (15-83-FE). Brt – Barite, Cal – Calcite, Col – Columbite, Dol – Dolomite, Fl – Fluorite, and Syn – Synchysite-(Ce).

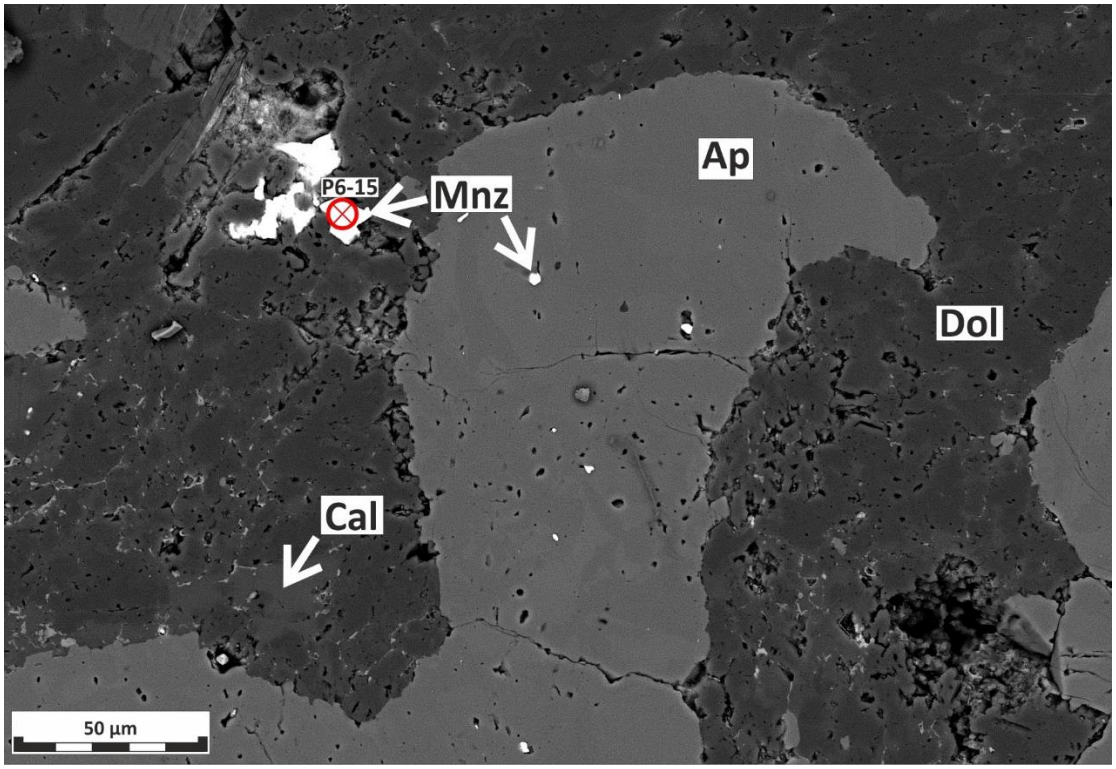

Figure 6-9: BSE-SEM image illustrate micro (<3 µm) monazite-(Ce) inclusion in apatite as well as larger (20 µm) crystals in the groundmass of an unaltered carbonatite (15-85-FE). Ap – Apatite, Cal – Calcite, Dol – Dolomite and Mnz – Monazite-(Ce).

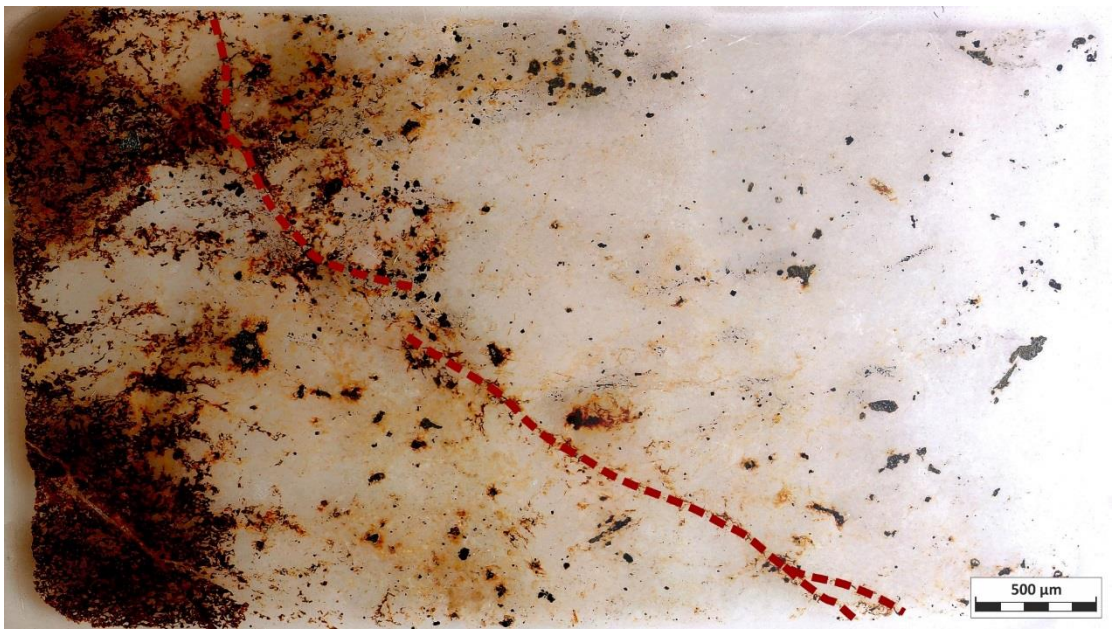

Figure 6-10: Thin section scan of an unaltered carbonatite (15-82-FE). The left-hand side of the thin section shows initial alteration of the carbonatite along cracks (major crack is highlighted by the red dashed line) in the form of Fe-oxide precipitation, while the right-hand side shows little to no signs of alteration.

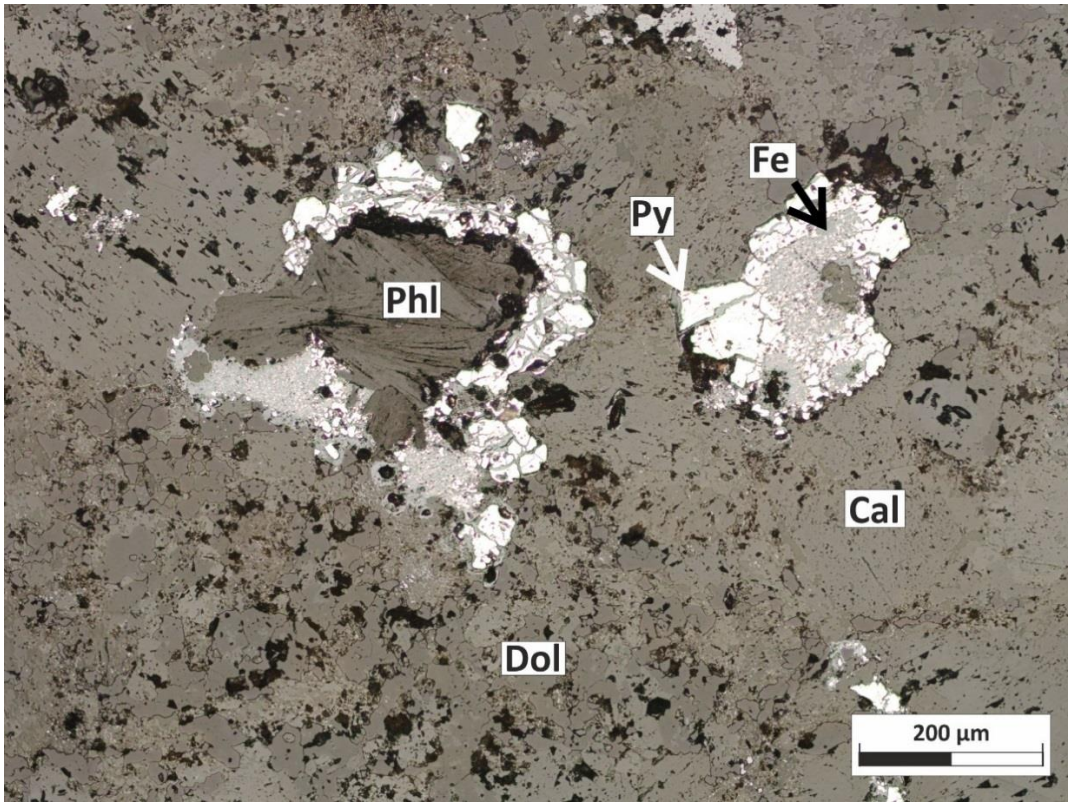

Figure 6-11: Reflective light image of an unaltered carbonatite (15-82-FE) shows the mosaic replacement of pyrite by Fe-oxide. This illustrates the first stage of the rødbergitisation process. Cal – Calcite, Dol – Dolomite, Fe – Fe-oxide, Py – Pyrite and Phl – Phlogopite.

Pyrite is the most susceptible mineral to this incipient alteration and shows a mosaic texture resembling that of a breccia (Fig. 6-11, Fig. 6-12A).

Nevertheless, pyrite is not the only mineral being replaced by Fe-oxide. The only occurrence of REE-fluorocarbonates in the slightly altered part of the carbonatite is within pyrite aggregates (Fig. 6-12). The irregular shape and crosscutting features of the REE-fluorocarbonates indicate the replacement of the REE-fluorocarbonates by Fe-oxide (Fig. 6-12B).

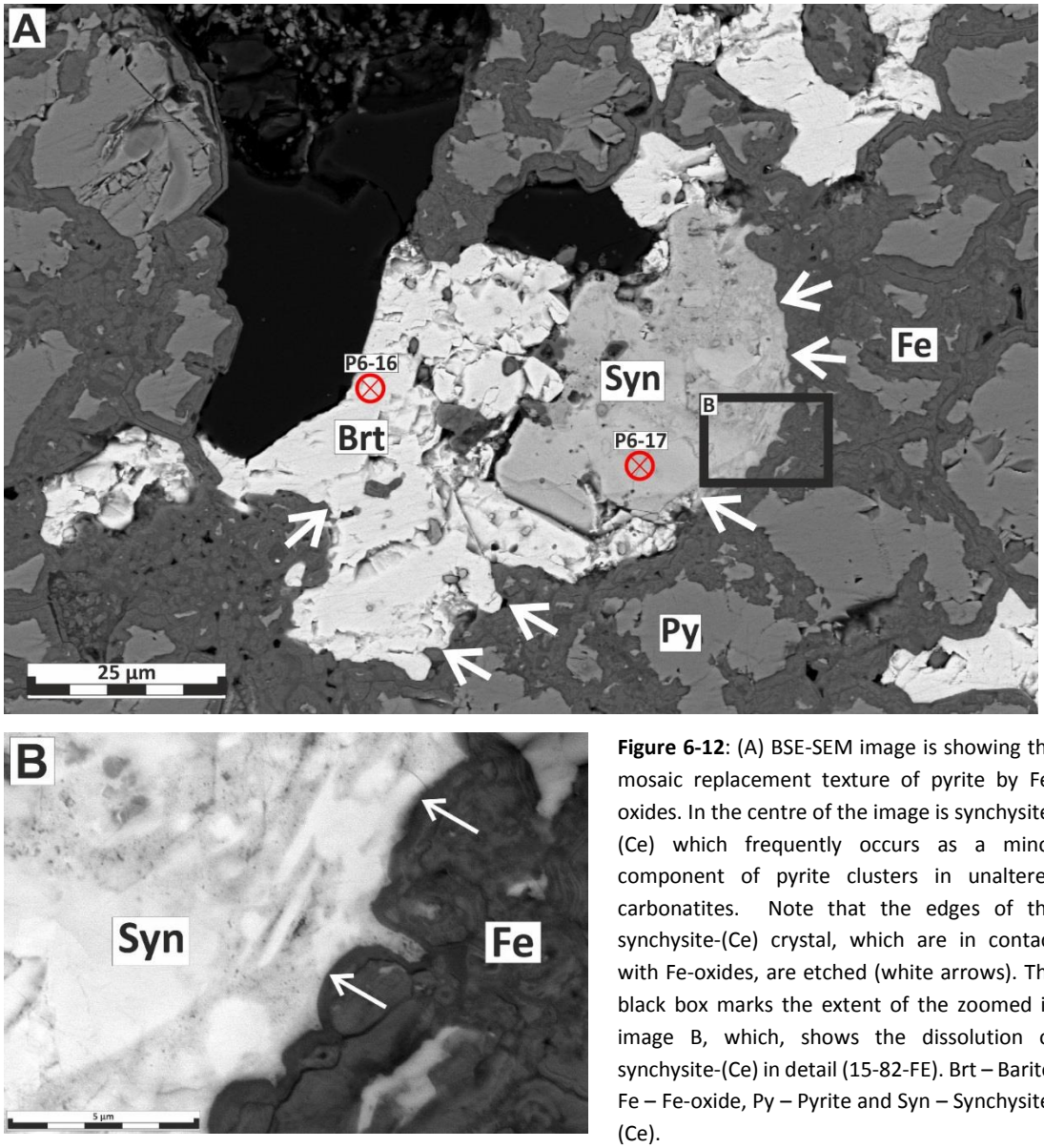

Figure 6-12: (A) BSE-SEM image is showing the mosaic replacement texture of pyrite by Fe-oxides. In the centre of the image is synchysite-(Ce) which frequently occurs as a minor component of pyrite clusters in unaltered carbonatites. Note that the edges of the synchysite-(Ce) crystal, which are in contact with Fe-oxides, are etched (white arrows). The black box marks the extent of the zoomed in image B, which, shows the dissolution of synchysite-(Ce) in detail (15-82-FE). Brt – Barite, Fe – Fe-oxide, Py – Pyrite and Syn – Synchysite-(Ce).

6.1.2 Transitional rødbergite

Transitional rødbergite is a massive calcite bearing dolomite-carbonatite and intermediate between unaltered grey carbonatite and highly altered red rødbergite. The more intense rødbergitisation caused a colouration ranging from greyish to ochre, red and brownish of irregularly shaped patches (Fig. 6-1C; Fig. 6-13). Additionally, some samples show multiple generations of veins and different types of aggregates. These features are further discussed in chapter 6.1.4 Veins and 6.1.5 Relics.

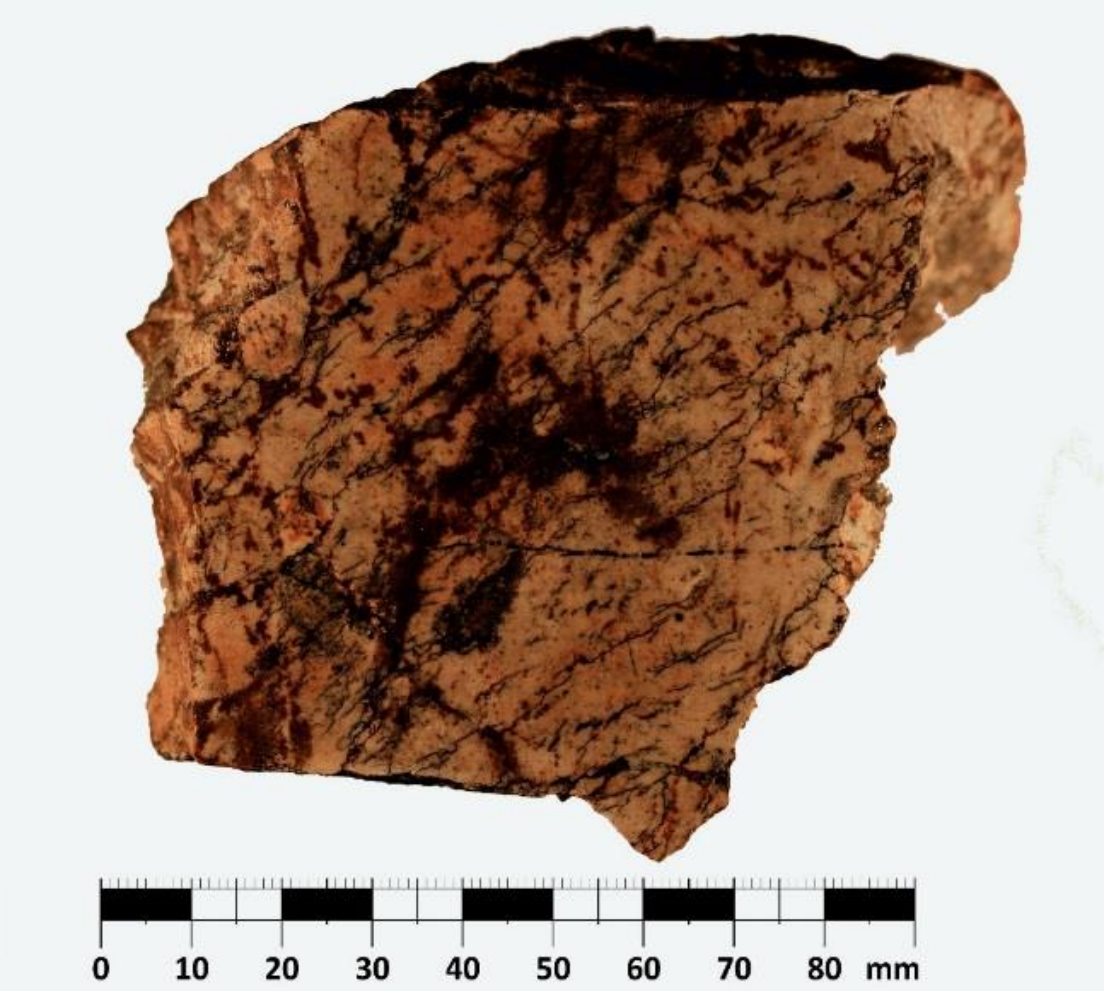

Figure 6-13: Photograph of a transitional rødbergite (15-93-FE). The hand specimen displays patches of different beige, orange and brown colours together with two visible vein generations.

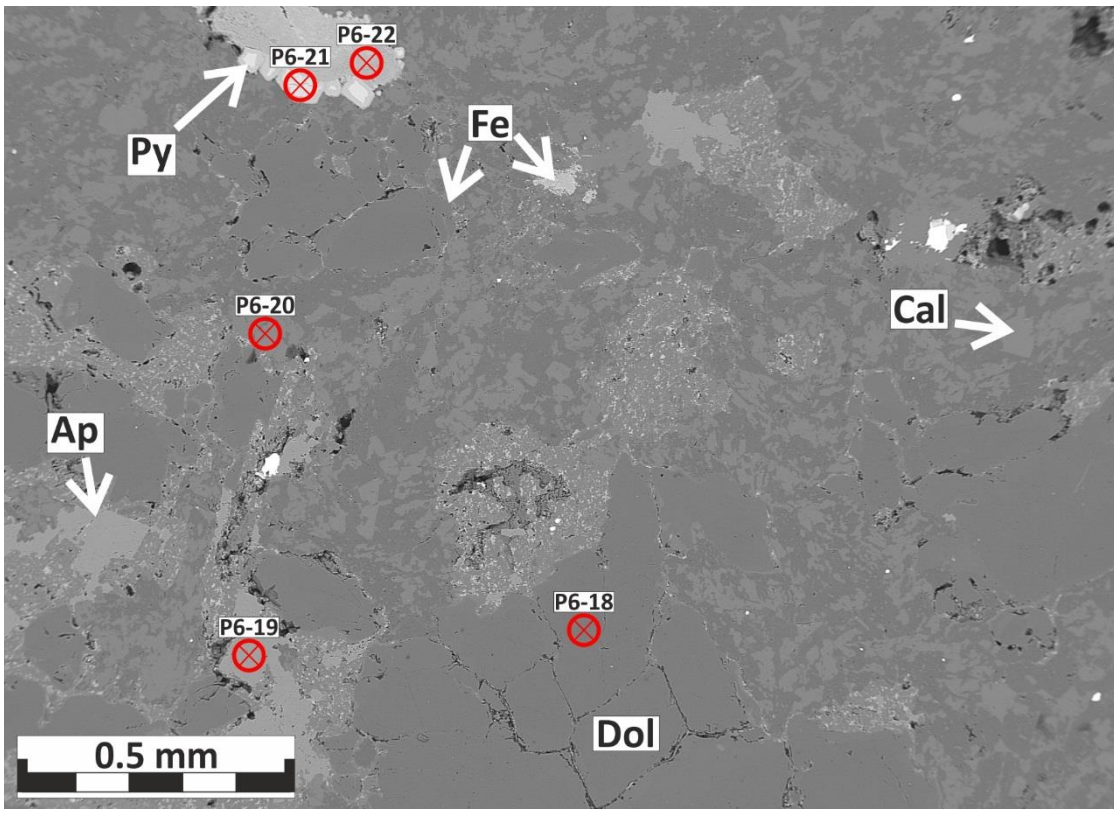

Figure 6-14: BSE-SEM image of a transitional rødbergite showing similar mineral composition and textures to unaltered carbonatite, e.g. the irregular intergrowth of calcite and dolomite in the groundmass (16-19-FE). Note the increasing proportion of small (< 5 µm) inclusions of Fe-oxides (brighter grey) in groundmass calcite and almost complete replacement of pyrite, indicating the progressing rødbergitisation. Ap – Apatite, Cal – Calcite, Dol – Dolomite, Fe – Fe-oxide and Py – Pyrite.

The main minerals in the transitional rødbergite are dolomite and calcite as irregular fine-grained intergrowths as well as medium-grained dolomite aggregates (Fig. 6-14). Accessory minerals in declining order are barite, barian phlogopite, apatite, quartz, pyrite, monazite-(Ce) and synchysite-(Ce) (Fig. 6-14; Fig. 6-15). Barite is evenly distributed in the groundmass as well as in veins, ranging from 50 µm to 1 mm (Fig. 6-15). Barian phlogopite is less abundant than barite and is more commonly restricted to veins or surrounding groundmass. The precipitation of Fe-oxide along grain boundaries and fractures is more pronounced than in unaltered carbonatite (Fig. 6-14; Fig. 6-15; Fig 6-16). Fe-oxide commonly occurs in calcite but rarely in dolomite.

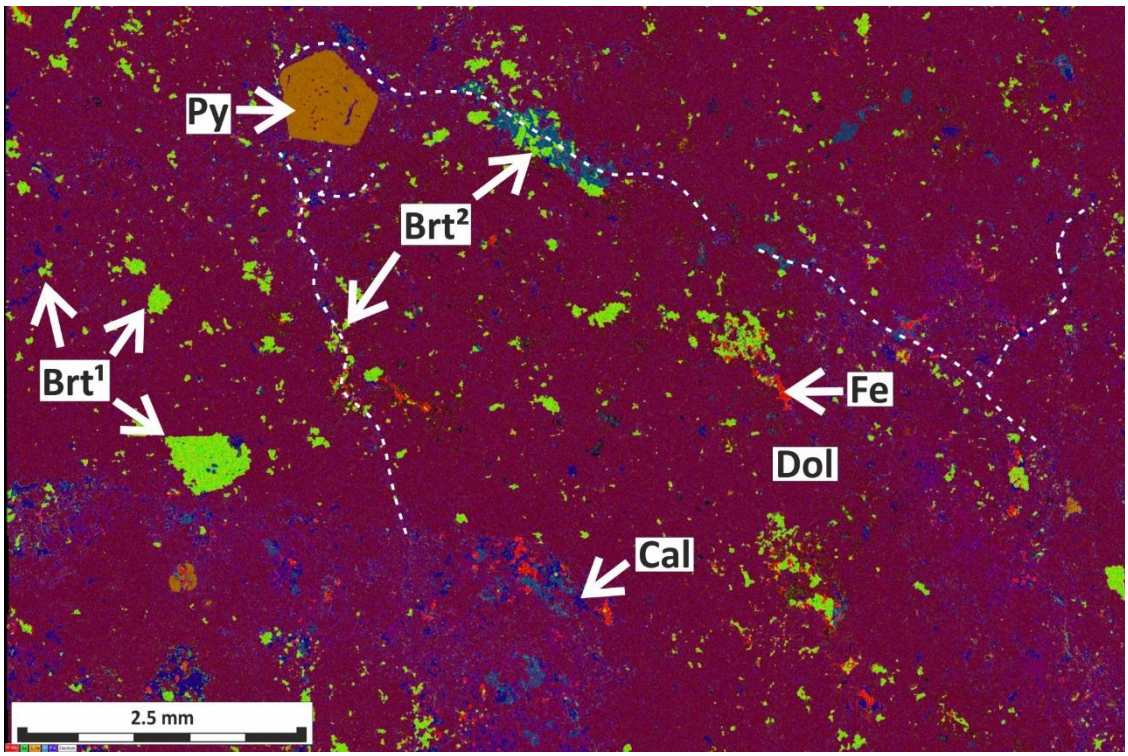

Figure 6-15: Combined EDS element map shows a representative section of a transitional rødbergite with barite homogenously distributed in the groundmass of the rock (Brt^1) as well as incorporated in small veinlets (Brt^2), which are partly highlighted by a dashed white line (15-91-FE). Ap – Apatite, Brt – Barite, Cal – Calcite, Dol – Dolomite, Fe – Fe-oxide and Py – Pyrite.

Occasionally, Fe-oxide is in a fine intergrowth with monazite-(Ce), which is the main REE carrier in transitional rødbergite (Fig. 6-16). Coarser grains (> 200 µm) of monazite-(Ce) are intergrown with barite (Fig. 6-17). Part of the larger monazite-(Ce) grains exhibit a halo of calcite and minor postmagmatic apatite (Fig. 6-18). Locally, monazite replaces apatite-forming high concentrations of monazite around larger apatite relics (chapter 6.1.5).

The overall REE budget is mainly influenced by the presence of monazite-(Ce) and to a lesser degree by allanite and REE-fluorocarbonates from allanite veins (chapter 6.1.4). Besides being a minor component of allanite veins, synchysite-(Ce) also occurs, similarly to monazite-(Ce), in intergrowth with barite (Fig. 6-19) and infilling fractures with Fe-

oxide (Fig. 6-20). The EDS-SEM rarely detected HREE minerals due to the low concentration of these elements in carbonatites.

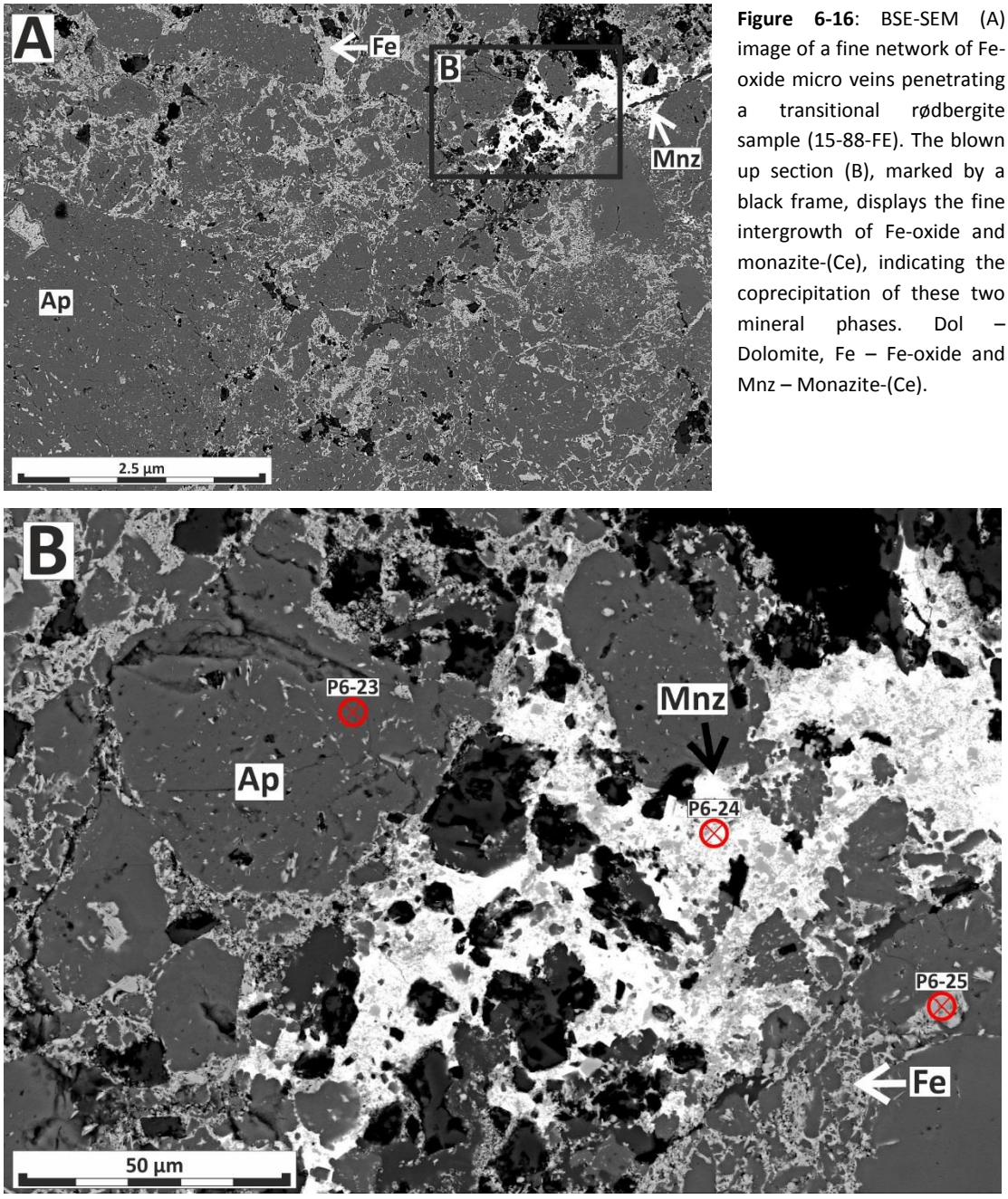

Figure 6-16: BSE-SEM (A) image of a fine network of Fe-oxide micro veins penetrating a transitional rødbergite sample (15-88-FE). The blown up section (B), marked by a black frame, displays the fine intergrowth of Fe-oxide and monazite-(Ce), indicating the coprecipitation of these two mineral phases. Dol – Dolomite, Fe – Fe-oxide and Mnz – Monazite-(Ce).

A single example of a zircon-xenotime-(Y) fine crystalline mixed phase occurs as part of a Fe-oxide veinlet, filling cracks and surrounding a monazite-(Ce) crystal (Fig. 6-21).

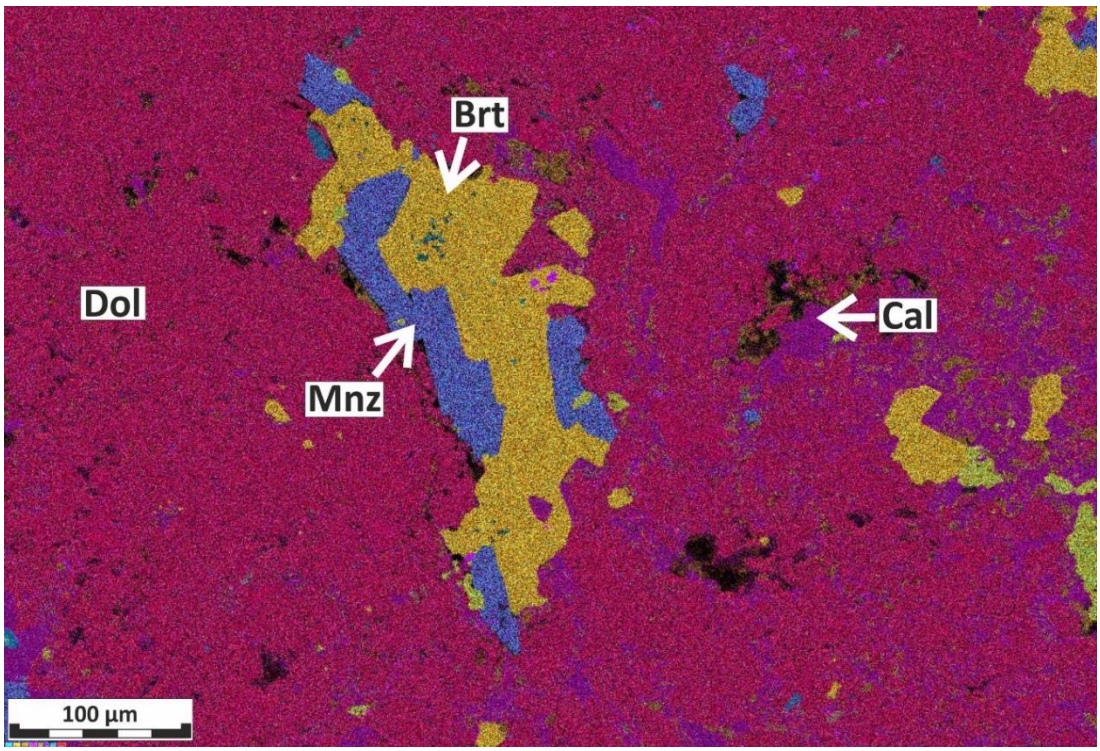

Figure 6-17: Combined EDS element maps illustrate the intergrowth of coarse hypidiomorphic barite and monazite-(Ce) (15-91-FE). EDS maps are especially helpful to distinguish between monazite-(Ce) and barite because both minerals display a similar grey tone in the BSE-SEM image. Brt – Barite, Cal – Calcite, Dol – Dolomite and Mnz – Monazite-(Ce).

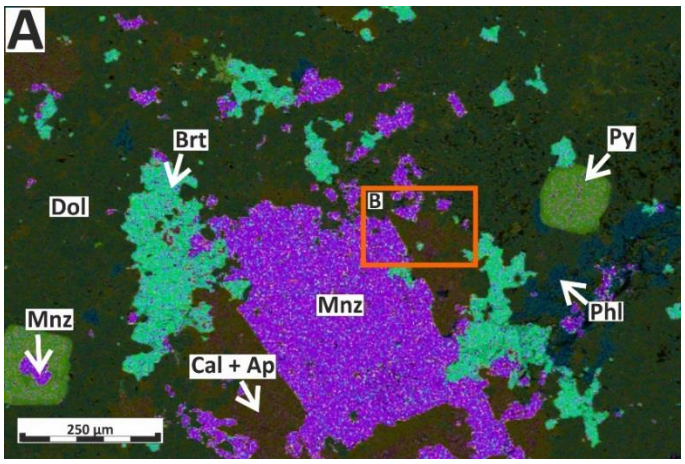

Figure 6-18: A) Combined EDS element maps of coarse hypidiomorphic monazite-(Ce) with barite in a groundmass of calcite and apatite (15-92-FE). Note the pyrite cube with a monazite core in the left corner of the picture. B) The blown up BSE-SEM image, which is marked by the orange frame, shows homogenous idiomorphic to hypidiomorphic apatite crystals in a groundmass of inclusion free calcite. Ap – Apatite, Brt – Barite, Cal – Calcite, Dol – Dolomite, Mnz – Monazite-(Ce), Phl – Phlogopite and Py – Pyrite.

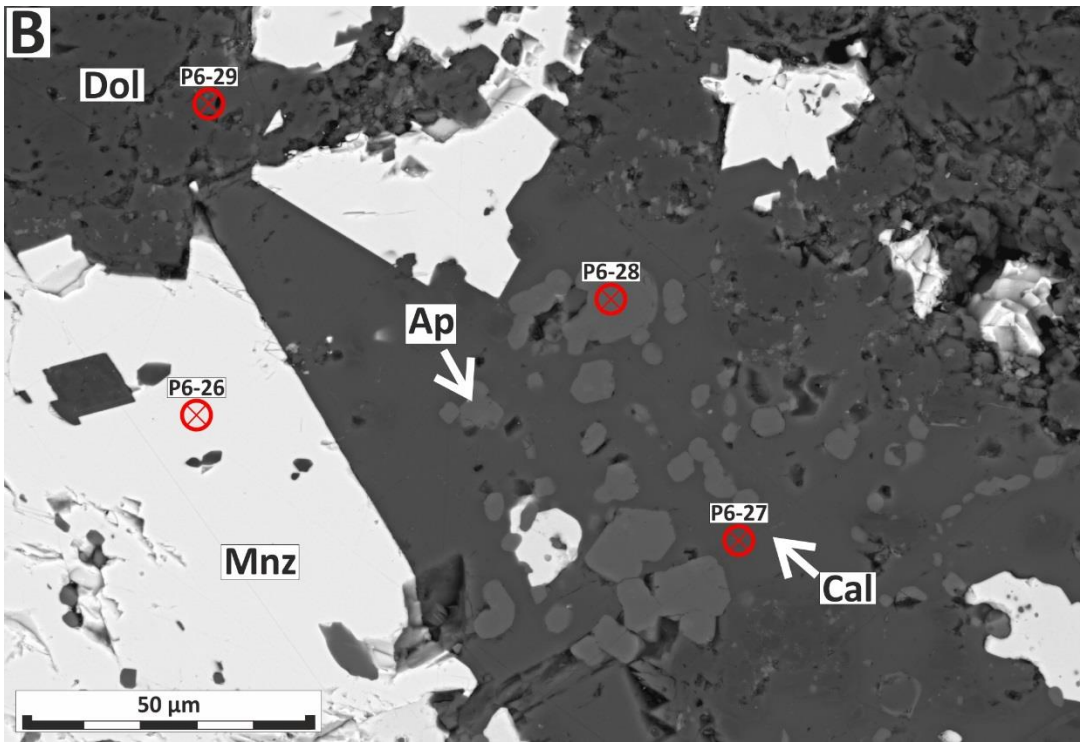

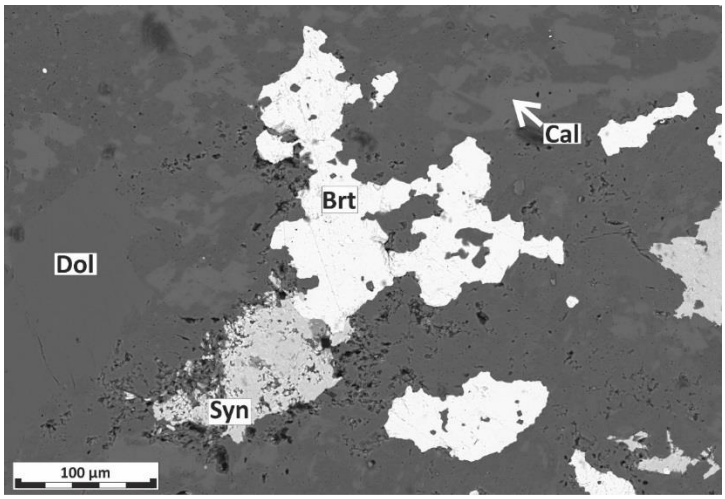

Figure 6-19: BSE-SEM image of xenomorphic barite cluster in an intergrowth with synchysite-(Ce).The same texture is common for barite and monazite-(Ce) (16-19-FE). Brt – Barite, Cal – Calcite, Dol – Dolomite and Syn – Synchysite-(Ce).

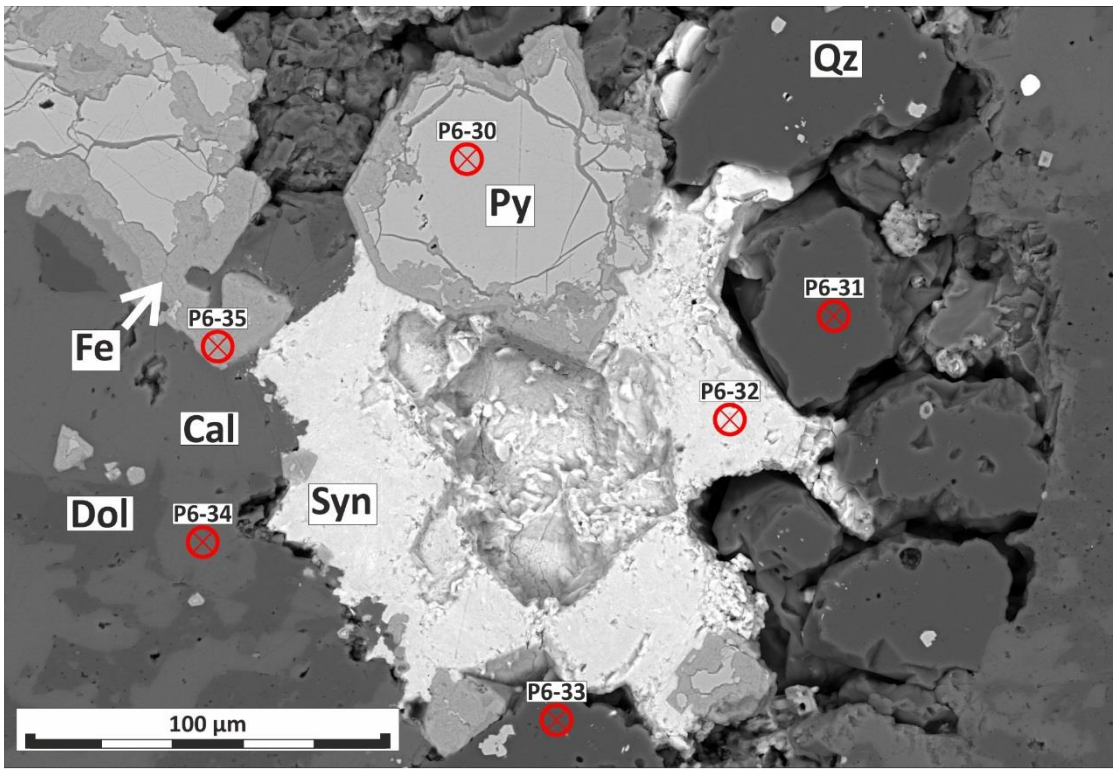

Figure 6-20: BSE-SEM image of a partly oxidised pyrite in a calcite-dolomite groundmass. Note synchysite-(Ce) in the intercrystalline space between quartz and growing around the partly oxidised pyrites (16-19-FE). Cal – Calcite, Dol – Dolomite, Fe – Fe-oxide, Py – Pyrite, Qz - Quartz and Syn – Synchysite-(Ce).

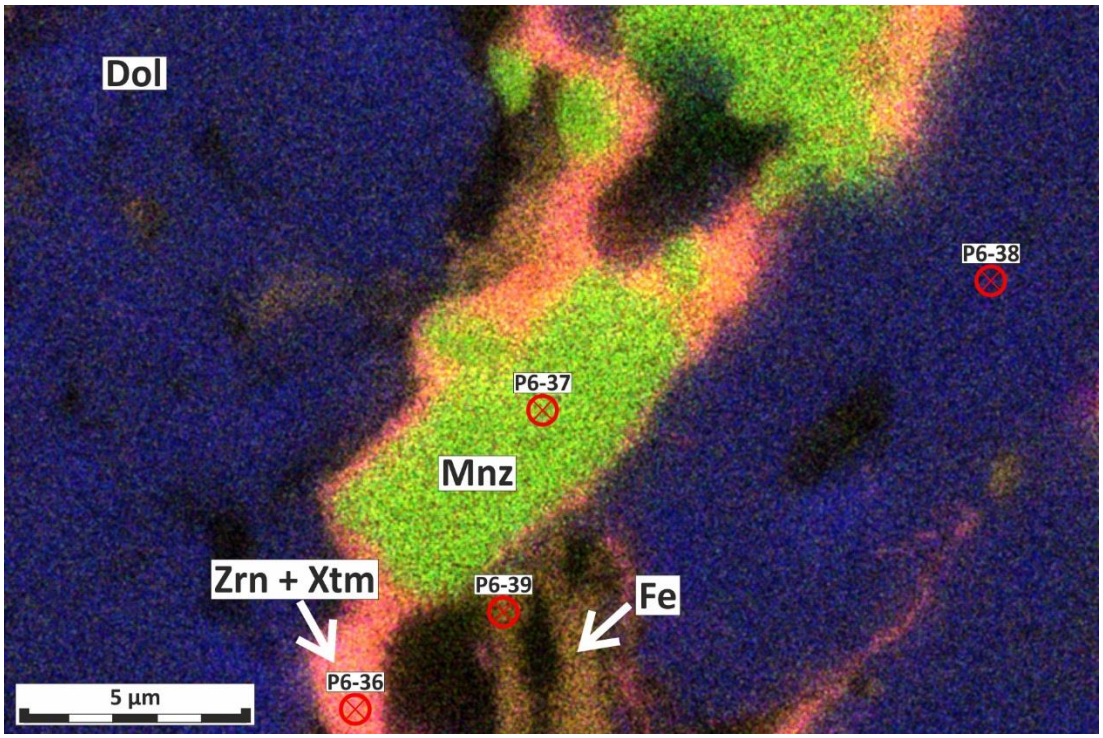

Figure 6-21: Combined EDS element maps showing hydrothermal monazite-(Ce) and hematite mineralisation. Monazite-(Ce) is surrounded by a later phase of zircon and xenotime-(Y). Whether it is a solid solution between zircon and xenotime-(Y) or a fine intergrowth of both phases cannot be determined (15-91-FE). Dol – Dolomite, Fe – Fe-oxide, Mnz – Monazite-(Ce), Xtm – Xenotime-(Y) and Zrn – Zircon.

6.1.3 Rødbergite

Figure 6-22: Photograph of a representative rødbergite sample (15-89-FE). The heterogeneous colouration and texture of the transitional rødbergite are replaced by a more homogeneous red colouration.

Rødbergite is an intensely altered massive carbonatite (Fig. 6-22). The fine crystalline carbonate groundmass is coloured in different shades of red and ranges from a homogenous colour to a heterogeneous mix of different red coloured schlieren. Average Porosity, determined from a large area mapping scanning electron microscopy image, is less than 2% (Fig. 5-5). Rødbergite consists of a varying proportion of dolomite, ferroan dolomite, barite, calcite, barian phlogopite, Fe-oxides, apatite with accessory monazite-(Ce), quartz, pyrite and barian orthoclase.

The groundmass comprises euhedral to anhedral dolomite surrounded by a network of calcite grains with small hematite inclusions (Fig. 6-23). While some parts of the groundmass display finely intergrown calcite and dolomite, other parts have coarser crystal sizes and show evidence for the replacement of dolomite by calcite.

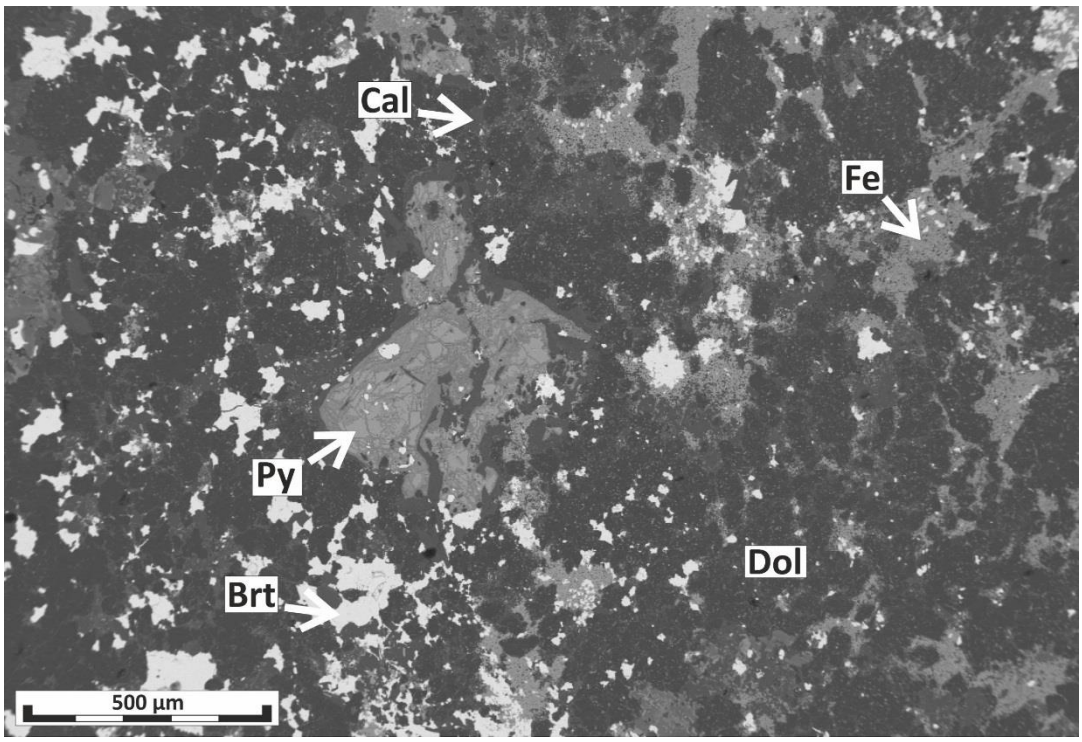

Figure 6-23: BSE-SEM image showing the dolomitic groundmass of a rødbergite sample with high proportions of barite and Fe-oxides. Fe-oxide intergrown with calcite is permeating the rødbergite via a network of veinlets. The pyrite in the centre of the image is largely replaced by hematite (15-89-FE). Brt – Barite, Cal – Calcite, Dol – Dolomite, Fe – Fe-oxide and Py – Pyrite.

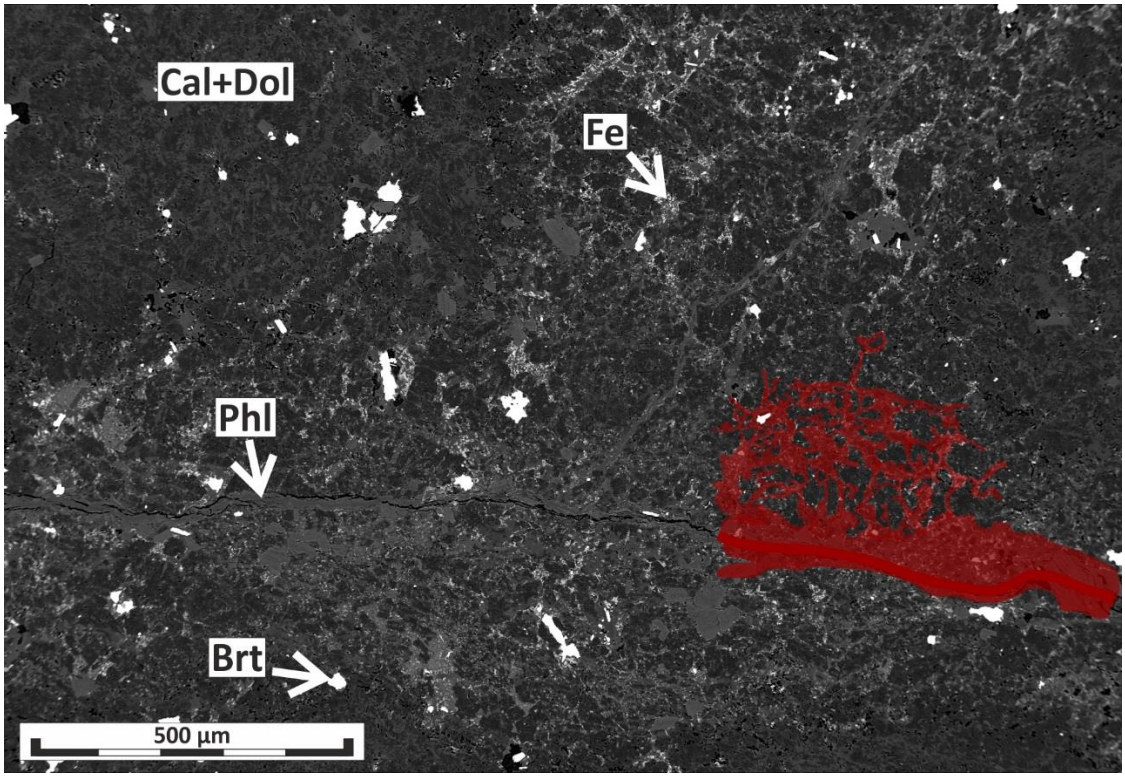

Figure 6-24: BSE-SEM image showing the impregnation of Fe-oxides and calcite along a vein (red colouration) and migrating through crystal boundaries into the carbonate groundmass (15-90-FE).Brt – Barite, Cal – Calcite, Dol – Dolomite, Fe – Fe-oxide and Phl – Phlogopite.

Emanating from fractures, a wide network of fine crystalline barite and Fe-oxide penetrates the carbonatite along grain boundaries, locally forming 20 % of the total rock volume (Fig. 6-24). Barite typically forms large agglomerates (~ 500 µm) with barian orthoclase, barian phlogopite and monazite-(Ce) (Fig. 6-25). Irregularly shaped barite-phlogopite patches (0.2–2 mm) contain clusters of euhedral to subhedral blade-shaped phlogopite (100 µm) (Fig. 6-26). Both phlogopite and barite are unaltered and contain few or no inclusions of hematite. Euhedral crystals of pyrite of up to 2 cm in size occur in rødbergite and show signs of replacement by hematite, with minor amounts of carbonate, barite and monazite-(Ce) (Fig. 6-27). Monazite-(Ce) is the most common REE- carrier in rødbergite and is commonly part of a fine intergrowth of barite and hematite precipitating along grain boundaries or replacing apatite grains (Fig. 6-28, Fig. 6-29 & Fig. 6-30). Locally, REE-fluorocarbonates are neighbouring monazite-(Ce) and occur in the same Fe-oxide-calcite veinlets as monazite-(Ce) (Fig. 6-31). Similar to the mineralisation styles of monazite-(Ce), synchysite-(Ce) also occurs as part of barite-barian orthoclase clusters (Fig. 6-32). REE-fluorocarbonates frequently display a cluster of thin fibrous sheets similar to sheaves of straw (Fig. 6-33).

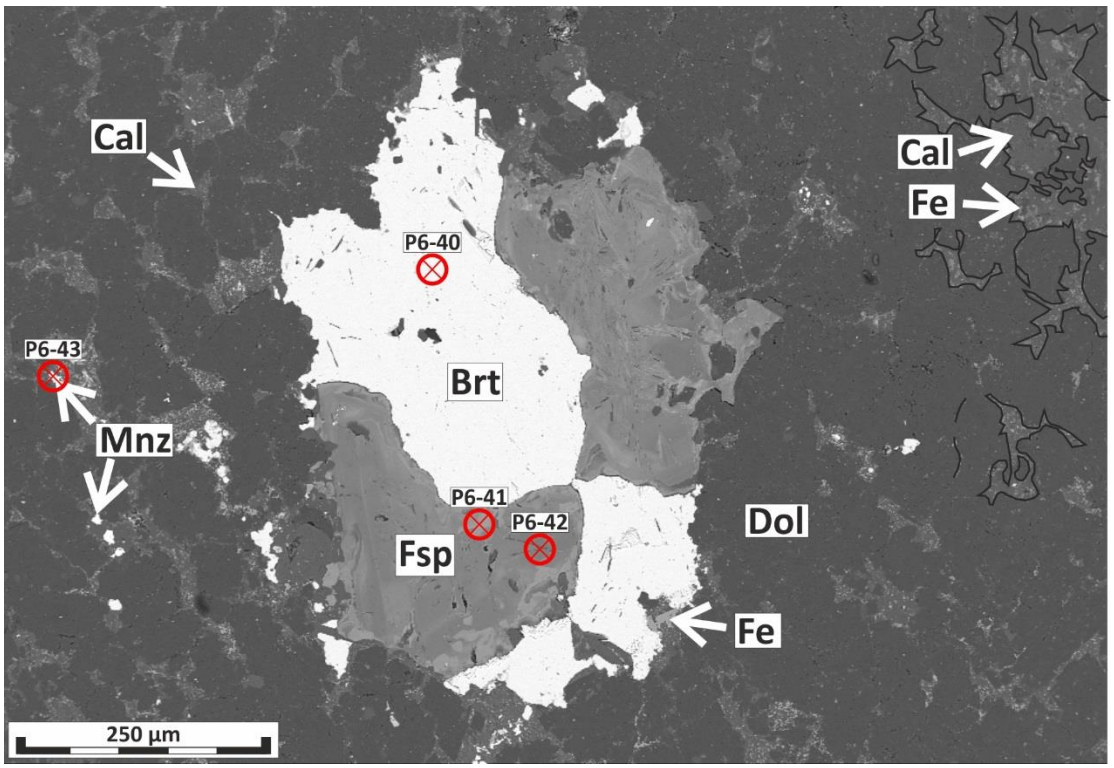

Figure 6-25: BSE-SEM image of a dolomite (dark grey) groundmass with a fine network of calcite (grey) with Fe-oxide (bright grey) inclusions and occasionally monazite-(Ce) (very bright grey). A black line in the upper right corner of the image highlights the calcite network with Fe-oxide inclusions. In the centre of the image, there is an aggregate comprising two opposing sectors of barite and two sectors of barian orthoclase, which are typical for a rødbergite mineral assemblage. Barian orthoclase is commonly associated with rødbergitisation in the Bjørndalen transect (15-89-FE). Brt – Barite, Dol – Dolomite, Fe – Fe-oxide, Fsp – Barian Orthoclase and Mnz – Monazite-(Ce).

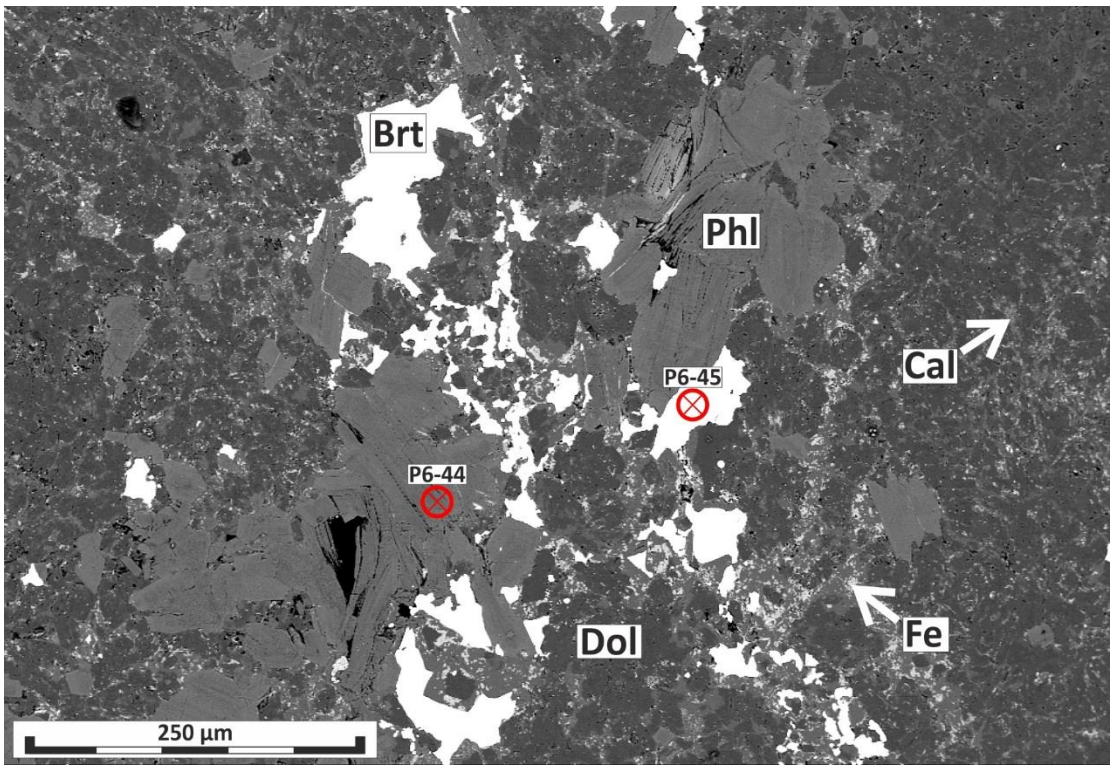

Figure 6-26: BSE-SEM image of a barite-phlogopite cluster along barian phlogopite, calcite, Fe-oxide-vein. Note the fine network of calcite and Fe-oxide surrounding the centre of the image (15-90-FE).Brt – Barite, Cal – Calcite, Dol – Dolomite, Fe – Fe-oxide and Phl – Phlogopite.

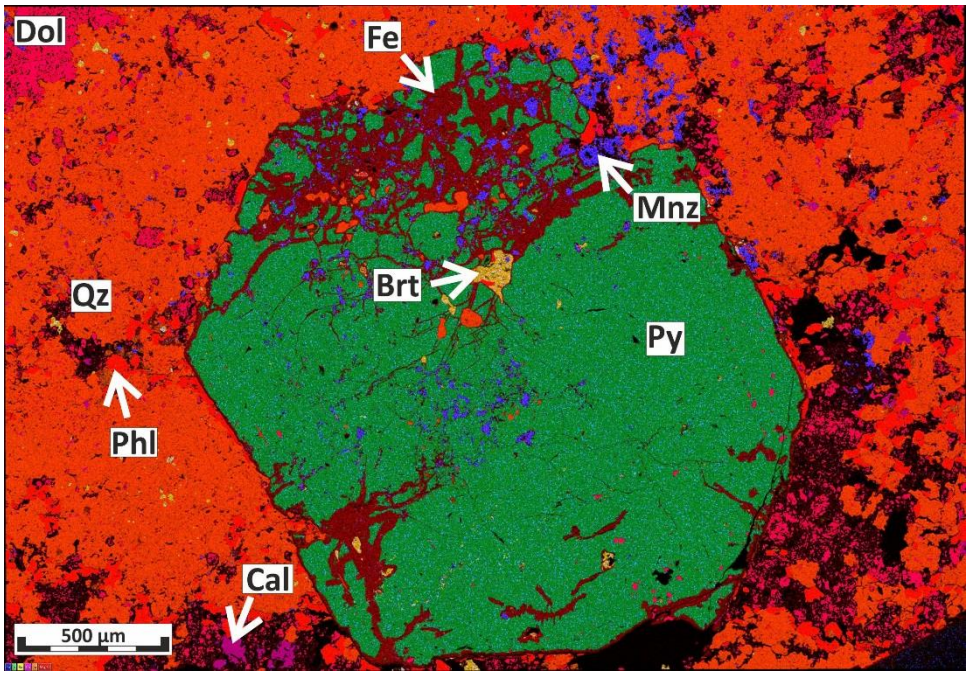

Figure 6-27: Combined EDS element map of large hypidiomorphic pyrite partly replaced by a mix of monazite-(Ce), Fe-oxide, barite and quartz. Note the high proportion of monazite-(Ce) as part of the alteration mineral assemblage. Monazite-(Ce) inclusions (blue) are present in the seemingly unaltered centre of the pyrite (15-94-FE). Brt – Barite, Cal – Calcite, Dol – Dolomite, Fe – Fe-oxide, Mnz – Monazite-(Ce), Phl – Phlogopite, Py – Pyrite and Qz – Quartz.

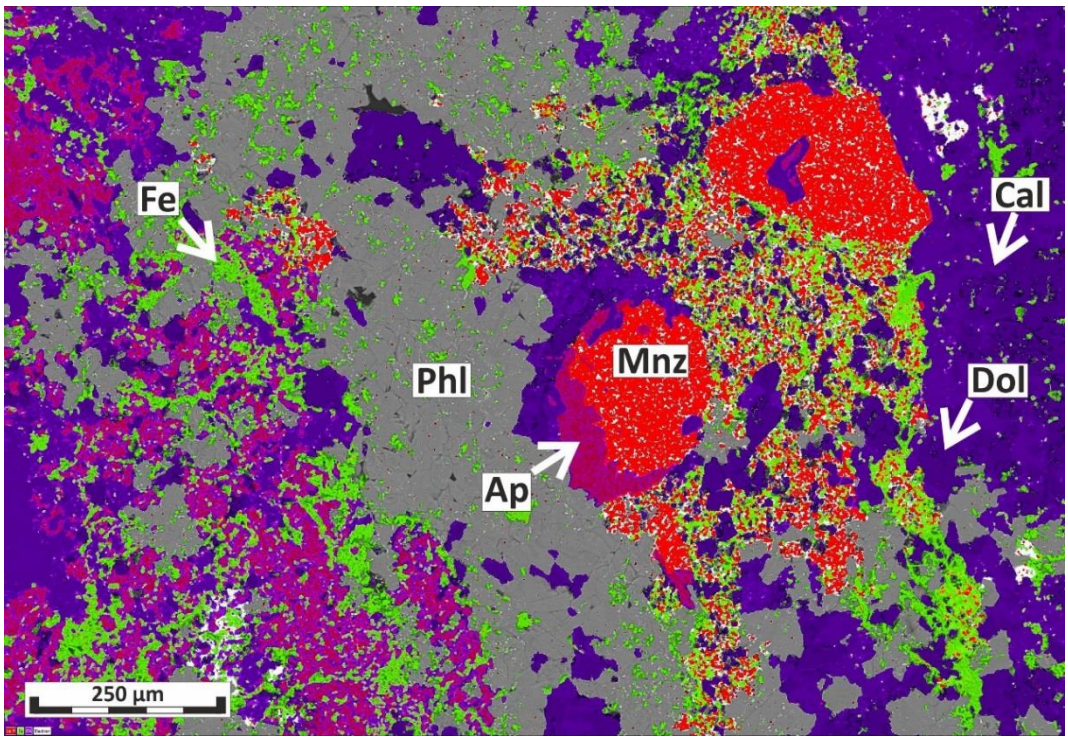

Figure 6-28: Combined EDS element map showing the dispersed distribution of Fe-oxide (green). The red coloured monazite-(Ce) is in intergrowth with Fe-oxide and is concentrated around apatite, replacing parts of the apatite crystals (15-88-FE).Ap – Apatite, Cal – Calcite, Dol – Dolomite, Fe – Fe-oxide, Mnz – Monazite-(Ce) and Phl – Phlogopite.

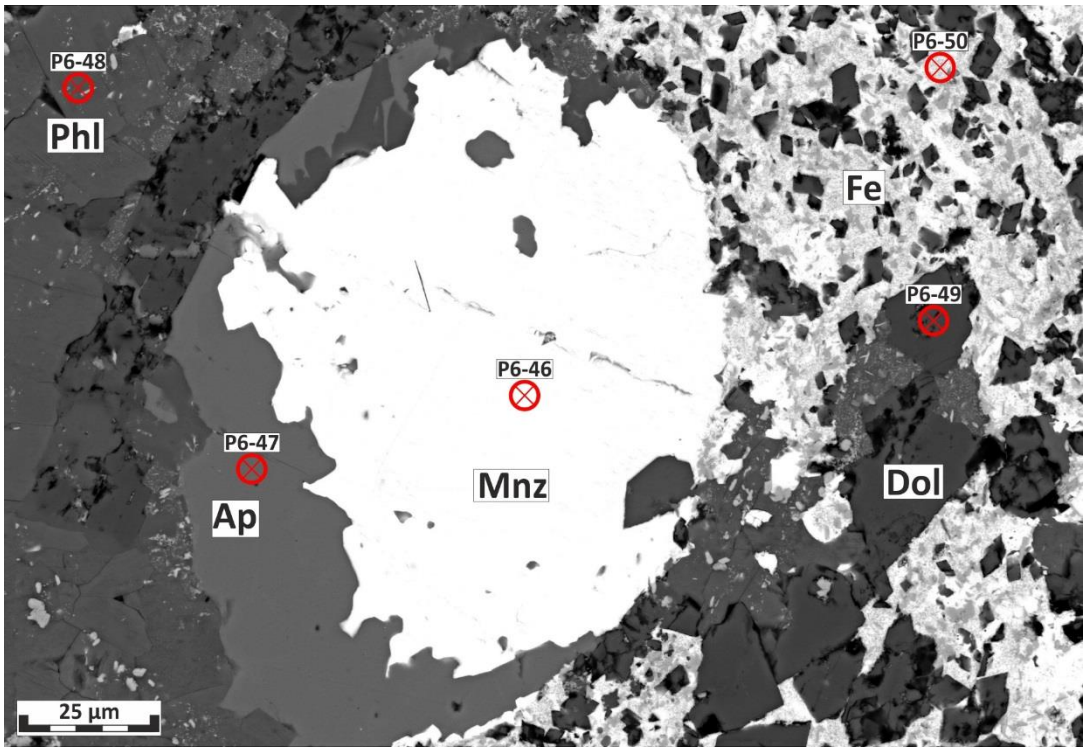

Figure 6-29: BSE-SEM image showing the fine intergrowth of Fe-oxide and monazite-(Ce) around an apatite crystal, which is to a large portion replaced by monazite-(Ce) (15-88-FE). Ap – Apatite, Cal – Calcite, Dol – Dolomite, Fe – Fe-oxide and Mnz – Monazite-(Ce).

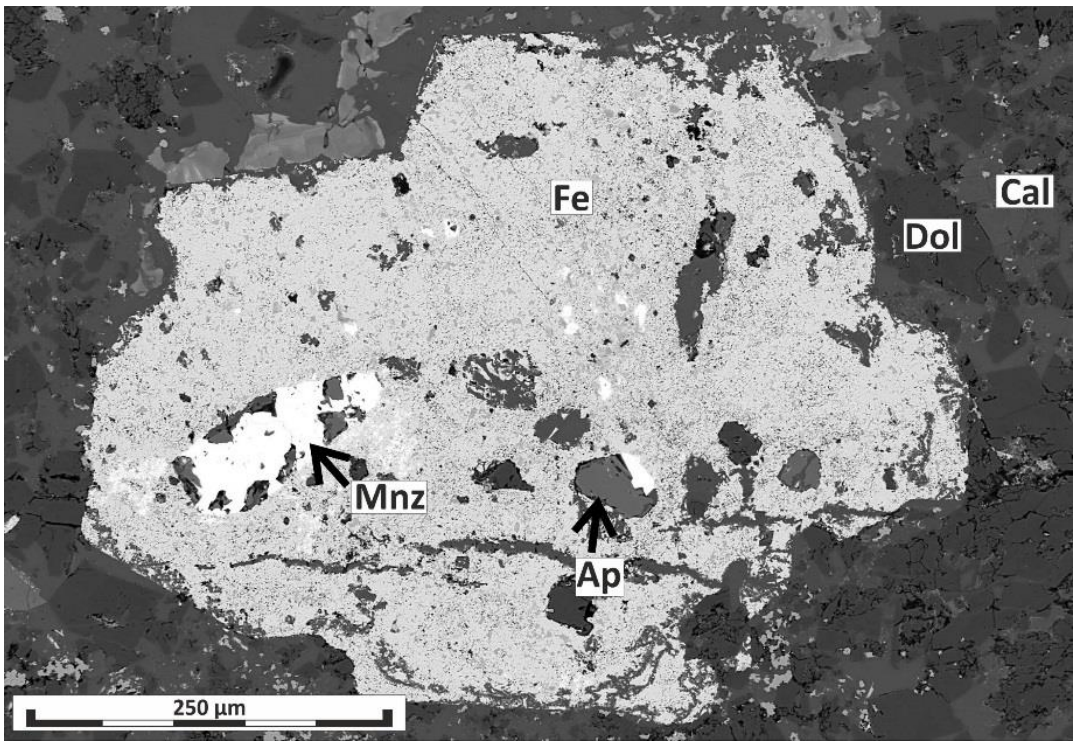

Figure 6-30: BSE-SEM image of a large (Ø 750 µm) Fe-oxide aggregate with inclusions of apatite. One part of the apatite crystal is largely replaced by monazite while other apatites are not affected (15-88-FE). Ap – Apatite, Cal – Calcite, Dol – Dolomite, Fe – Fe-oxide and Mnz – Monazite-(Ce).

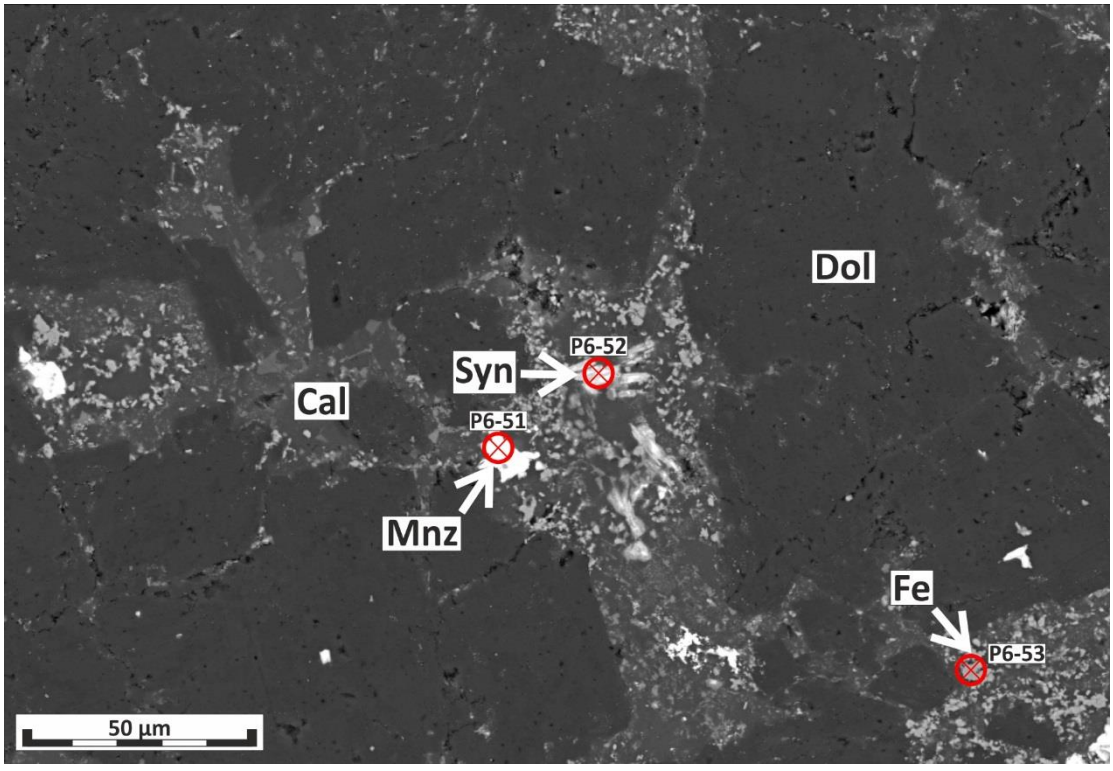

Figure 6-31: BSE-SEM image showing the replacement of dolomite groundmass by calcite. Besides the omnipresent inclusions of Fe-oxides in the calcite vein, spatially associated monazite-(Ce) and synchysite-(Ce) crystals are present (15-89-FE).Cal – Calcite, Dol – Dolomite, Fe – Fe-oxide, Mnz – Monazite-(Ce) and Syn – Synchysite-(Ce).

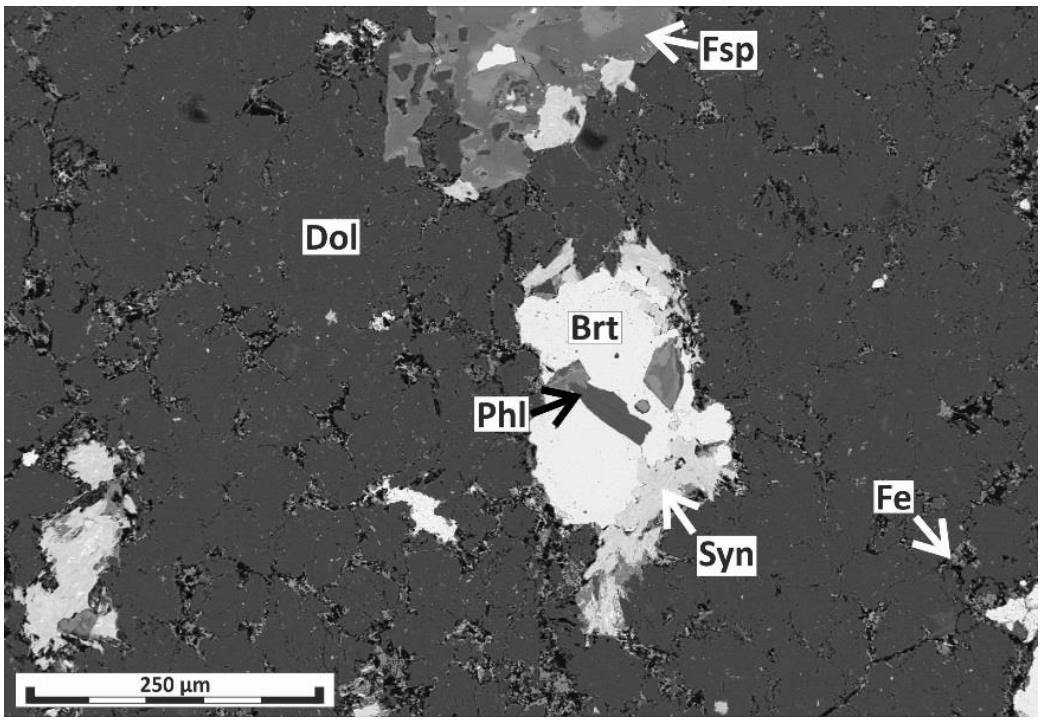

Figure 6-32: BSE-SEM image showing a cluster of barite, synchysite-(Ce), phlogopite and barian orthoclase (15-89-FE). This mineral assemblage indicates that monazite-(Ce) — the main REE-host in rødbergite — can be substituted by synchysite under the right physicochemical conditions. Brt – Barite, Dol – Dolomite, Fe – Fe-oxide, Fsp – Barian Orthoclase and Syn – Synchysite-(Ce).

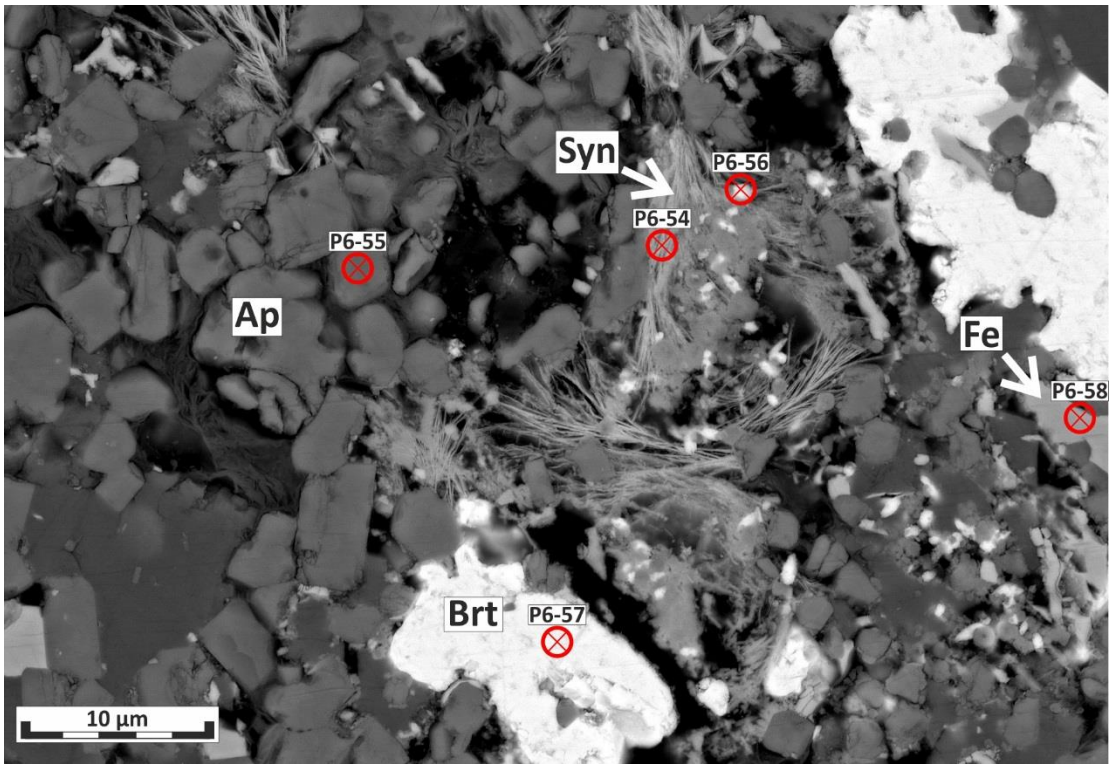

Figure 6-33: BSE-SEM image of a section of an apatite relic showing fibrous sheets of Synchysite-(Ce) together with very small (<0.5 µm) Nb-minerals filling pore space between apatite, barite and Fe-oxide (15-90-FE). Ap – Apatite, Brt – Barite, Fe – Fe-oxide and Syn – Synchysite-(Ce).

6.1.4 Veins

Veins are present in every zone of the Bjørndalen transect in varying density and mineral composition. Some of the vein types contain REE-minerals and are therefore important for the overall REE budget along the Bjørndalen transect.

Veins occur in the unaltered carbonatite (Fig. 6-34) but are significantly less abundant compared to transitional rødbergite and rødbergite. Cross-cutting relationships indicate two vein generations. The younger veins are entirely made of calcite while older veins comprise ferroan dolomite and barite with minor amounts of quartz, REE-fluorocarbonates, barian phlogopite and pyrite. While the eastern transitional rødbergite has almost no veining, the western transitional rødbergite shows a high density of veins with two veins per cm^2 (Fig. 6-1). Three different micro-vein types are present in the eastern transitional rødbergite (Fig. 6-35).

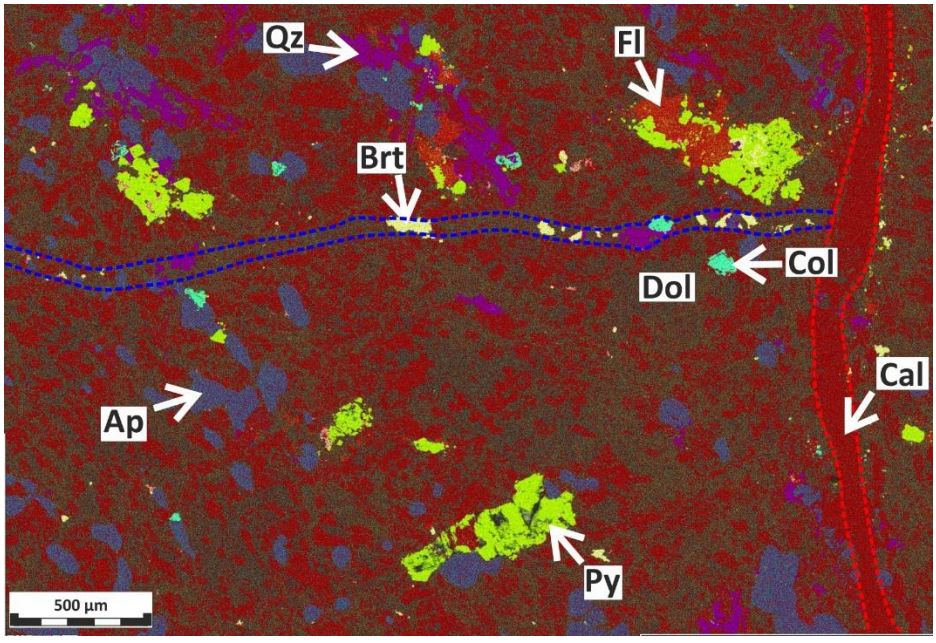

Figure 6-34: Combined EDS element maps show a representative section of an unaltered carbonatite (15-82-FE). Fe-dolomite-barite veins with minor amounts of quartz, REE-fluorocarbonates, barian phlogopite and pyrite (blue dashed line) are crosscut by a calcite vein (red dashed line). Note the irregular fine intergrowth of calcite and dolomite, pyrite-fluorite clusters, elongated apatite crystals with preferred orientation and two cross-cutting veins. Ap – Apatite, Brt – Barite, Cal – Calcite, Col – Columbite, Dol – Dolomite, Fl – Fluorite, Py – Pyrite and Oz – Quartz.

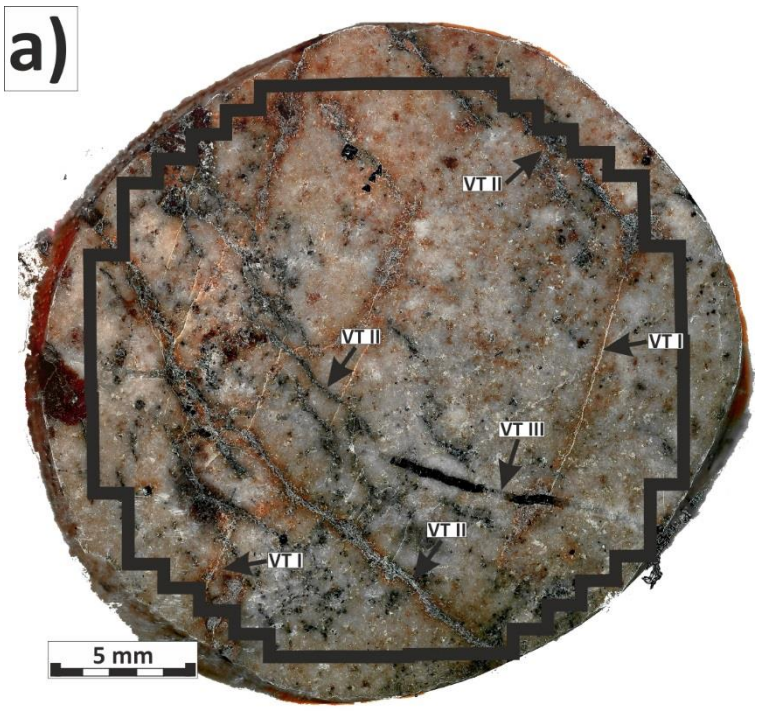

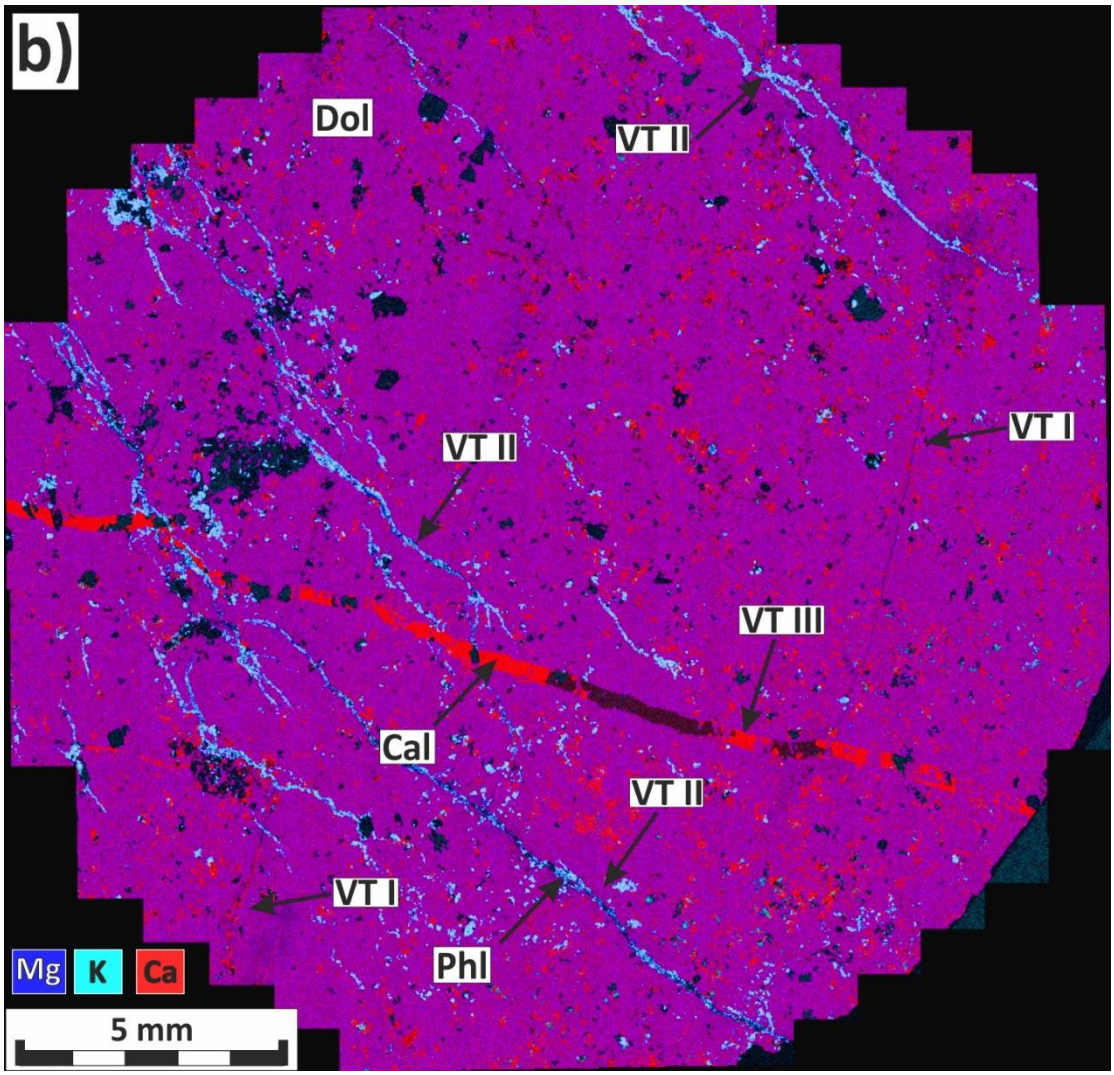

Figure 6-35: a) The image shows a polished block of transitional rødbergite (15-93-FE). Three different generations of veins are marked as VT I, VT II and VT III. b) Large-area EDS mapping of the area marked by the black frame in image a). The VT II and III are easily distinguishable due to their different mineral composition. Cal – Calcite, Dol – Dolomite and Phl – Phlogopite.

The vein generations are numbered based on the observed crosscutting relations in the studied transect. **Fe-oxide veins (Vein type I)** are thin (10 µm) straight veins of Fe-oxide and clay minerals. **Barite-phlogopite veins (Vein type II)** consist of barian phlogopite, barite ± monazite-(Ce), chlorite and hematite. Monazite-(Ce) grains (100 µm x 30 µm) are either enclosed by barian phlogopite or intergrown with Fe-oxides. Irregular patches of monazite-(Ce) occur within the groundmass proximal to the barite-phlogopite veins (Fig. 6-36). Barite-phlogopite veins are the most common veins in transitional rødbergite and are parallel to each other but occasionally branch and display an undulating to en-echelon pattern (Fig. 6-35). The EDS-BSE elemental maps reveal a mild halo of higher Ca concentrations in carbonates near barite-phlogopite veins.

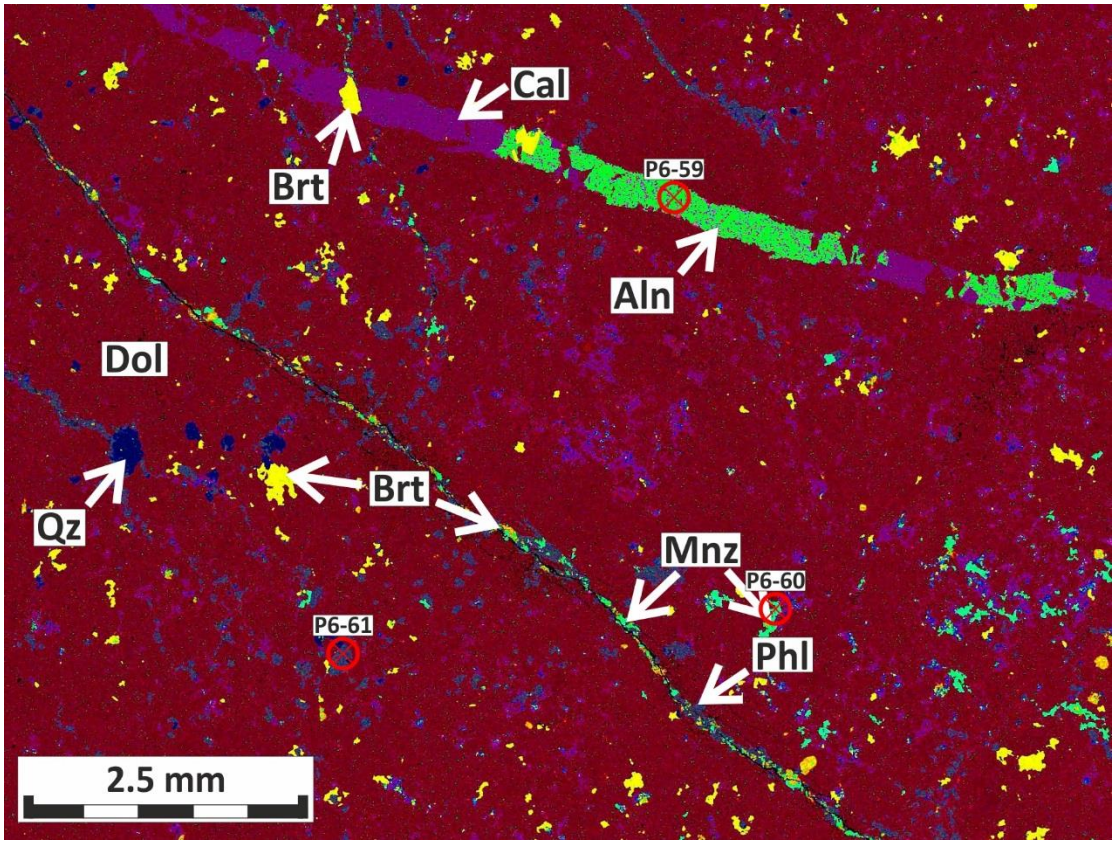

Figure 6-36: Combined large-area EDS mosaic of a section of Figure 1-14. Two veins belonging to VT II and VT III are visible in the image. REE-minerals in these veins are coloured in neon green, highlighting allanite and monazite-(Ce) as part of their mineral assemblage (15-93-FE). Aln – Allanite, Brt – Barite, Cal – Calcite, Dol – Dolomite, Mnz – Monazite-(Ce) , Phl – Phlogopite and Qz – Quartz.

Pyrite occurs as euhedral cubes close to barite-phlogopite veins. Partly barite-phlogopite veins engulf older patches of quartz-barite aggregates. Barite-Phlogopite veins are very common in western transitional rocks and appear to a lesser degree in rødbergite as well. The younger ferroan dolomite–barite vein, described for the unaltered carbonatite, has a very similar mineral composition to the barite-phlogopite vein and is most likely a variation with synchysite-(Ce) instead of monazite-(Ce). **Allanite veins (Vein type III)** consist of calcite with minor amounts of barite, dolomite, coarse-grained allanite (0.3 mm x 2 mm) and rarely coarse-grained synchysite-(Ce). The allanite veins are significantly thicker (300 μm) than vein type I and II and represent the youngest generation of these three vein types.

A variety of rødbergite samples displays red coloured apatite veins up to 3 mm across (Fig. 6-37). The red colouration is the result of small (< 5 μm) Fe-oxide crystals evenly dispersed within the apatite. Around the red apatite veins, a halo of coarser subhedral calcite, dolomite and barite occurs. The red apatite veins are brecciated by smaller barite-calcite-dolomite-hematite veins, which locally crosscut the apatite vein but typically follow along the centre of the vein, which is partly replaced by barite. In one case, the apatite vein is in contact with oriented magmatic apatite crystals (Fig. 6-37C). The red apatite from the vein engulfs part of the apatite crystal without disrupting its position or replacing the apatite crystal. Therefore, it is possible that the apatite vein did not cause any displacement and developed through chemical replacement along a crack leaving the magmatic apatite crystals undisturbed.

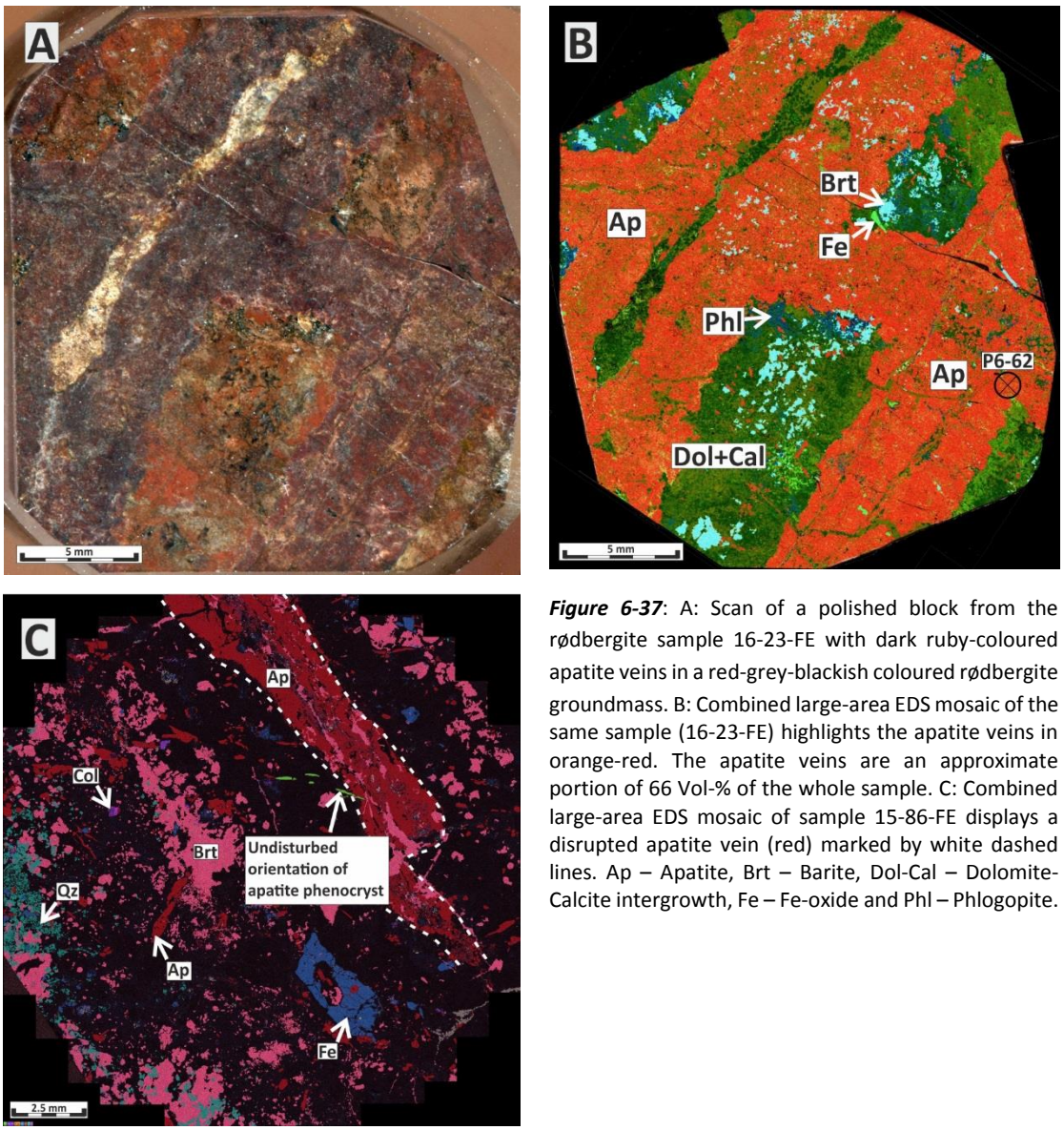

Figure 6-37: A: Scan of a polished block from the rødbergite sample 16-23-FE with dark ruby-coloured apatite veins in a red-grey-blackish coloured rødbergite groundmass. B: Combined large-area EDS mosaic of the same sample (16-23-FE) highlights the apatite veins in orange-red. The apatite veins are an approximate portion of 66 Vol-% of the whole sample. C: Combined large-area EDS mosaic of sample 15-86-FE displays a disrupted apatite vein (red) marked by white dashed lines. Ap – Apatite, Brt – Barite, Dol-Cal – Dolomite-Calcite intergrowth, Fe – Fe-oxide and Phl – Phlogopite.

6.1.5 Apatite-Relics

Occasionally, transitional rødbergite (Fig. 6-38) and rødbergite (Fig. 6-39) samples display prominent rounded elliptical inclusions (5 – 20 mm) of apatite and dolomite with minor amounts of barite, barian phlogopite, monazite-(Ce), calcite and hematite. Apatite is a common early crystallisation product in carbonatitic magmas and occurs in layers, frequently disrupted by magmatic and postmagmatic processes.

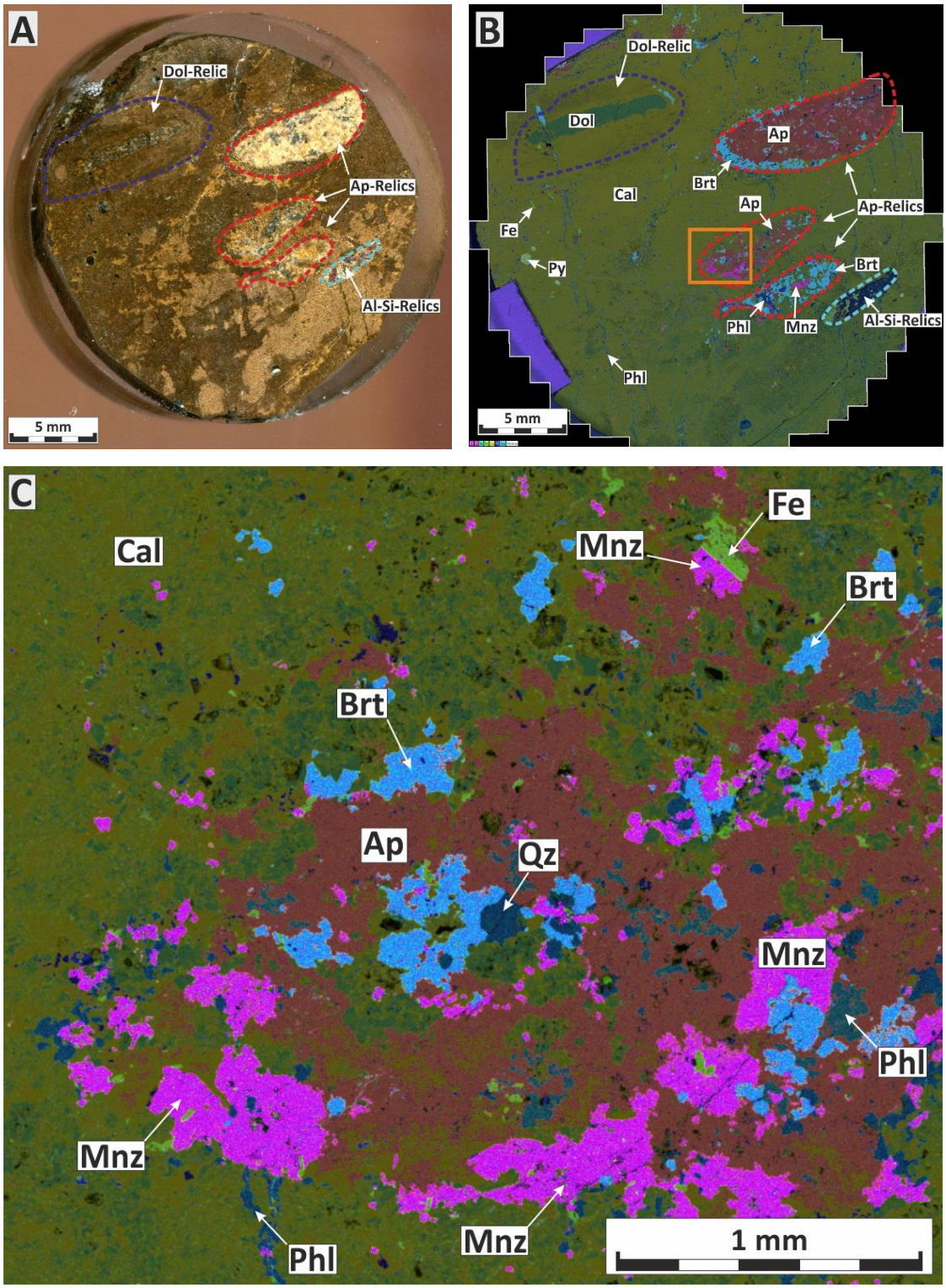

Figure 6-38: (A) Scan of polished block showing a transitional rødbergite with apatite-, dolomite- and aluminium silicate-relics (16-111-FE). (B) Combined EDS element maps of the same image (A). (C) A blown up section of the image (B) marked by the orange box. There is a high concentration of monazite-(Ce) around the apatite relic together with barite, phlogopite, quartz and hematite. Ap – Apatite, Brt – Barite, Cal – Calcite, Dol – Dolomite, Fe – Fe-oxide, Mnz – Monazite-(Ce), Phl – Phlogopite, Py - Pyrite and Qz – Quartz.

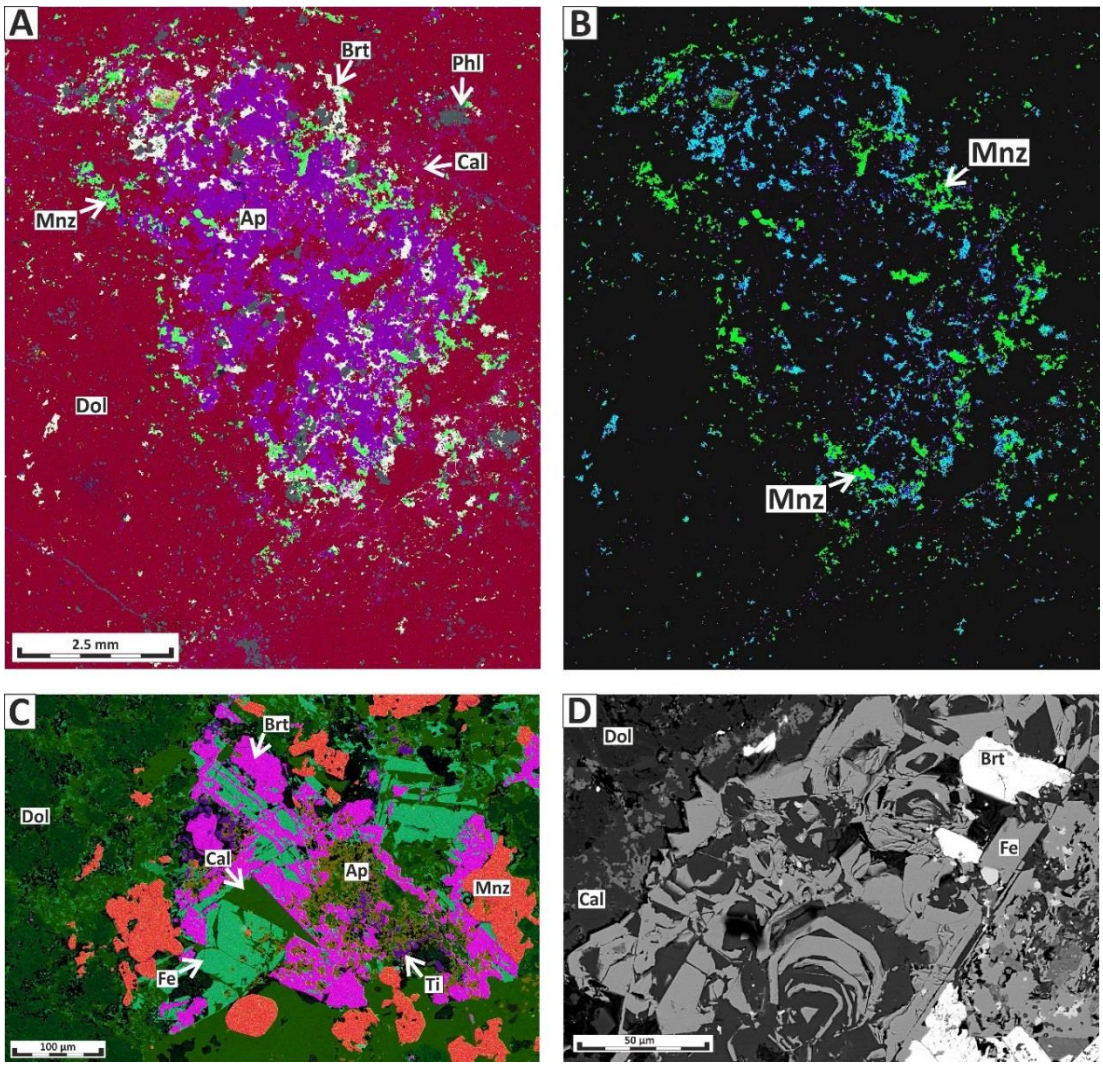

Figure 6-39: Varies images showing the mineralogical composition and texture of apatite relics (A) Combined large-area EDS mosaic of a rødbergite sample showing apatite (purple) relics in a groundmass of dolomite (red) infiltrated by a fine network of barite-phlogopite veins. (B) Combined large-area EDS mosaic of the same picture with modified colours for the elements to specifically highlight the concentration of monazite-(Ce) (neon green) around and within the apatite relic. (C) Combined EDS element map of the outer rim of an apatite relics from the same sample with the alteration mineral assemblage of hematite hopper crystals in intergrowth with barite, calcite, rutile and a high concentration of hypidiomorphic monazite-(Ce). (D) BSE-SEM image showing the basal section of a hematite hopper crystal as part of an apatite relic (15-90-FE). Ap – Apatite, Brt – Barite, Cal – Calcite, Dol – Dolomite and Fe – Fe-oxide, Mnz – Monazite-(Ce) and Phl – Phlogopite.

These layers are generally interpreted as cumulates (Chakhmouradian et al., 2017; Hornig-Kjarsgaard, 1998; Ihlen et al., 2014). Andersen (1987a) and Schilling (2013) also describe apatite cumulate inclusions in calcite carbonatites of the Fen Complex. Similar apatite inclusions are in samples from the unaltered carbonatite and have partly survived the rødbergitisation event as apatite-rich relics. The central part of apatite

relics is mainly made of polycrystalline apatite relic with dendritic patches of dolomite, barite and barian phlogopite (Fig. 6-38). Scattered large hopper crystals of hematite occur in some of these relics (Fig. 6-39D). The apatite relics are partly replaced, and the amount of alteration minerals increases towards the rim. The rim itself is completely replaced by an alteration mineral assemblage (Fig. 6-39C) with a high concentration of hydrothermal monazite-(Ce) of up to ~20 Vol-% in the outer 500-µm layer (Fig. 6-38C, Fig. 6-38B). Similar to the earlier-described REE-mineralisation in fractures, veins and patches (Fig. 6-16; Fig. 6-17; Fig. 6-18; Fig. 6-28), monazite-(Ce) is often intergrown with barite. A halo of calcite is detectable near monazite-(Ce) crystals.

Locally, Barite-Phlogopite veins are in contact with apatite relics, which triggered the preferred precipitation of monazite-(Ce) from the vein fluid along with the apatite relic (Fig. 42A). The formation of hydrothermal monazite at the expense of apatite is a commonly observed feature in carbonatites and is caused by the interaction of carbonatite with hydrothermal fluids (Chakhmouradian and Mitchell, 1998; Giebel et al., 2017; Moore et al., 2015; Smith et al., 1999). This highlights the importance of barite-phlogopite veins as an essential feeder system for monazite.

6.2 Geochemical results

The progressive rødbergitisation of the Bjørndalen transect is visible at outcrop scale from the change in colour (reddening) and texture (grain size reduction) of the rock. This visible change during rødbergitisation of the carbonatite is associated with a systematic change of the whole-rock chemical composition. This chapter will focus on the distribution of Rare Earth Elements (REE) and thorium (Th) along the Bjørndalen transect (Fig. 6-40).

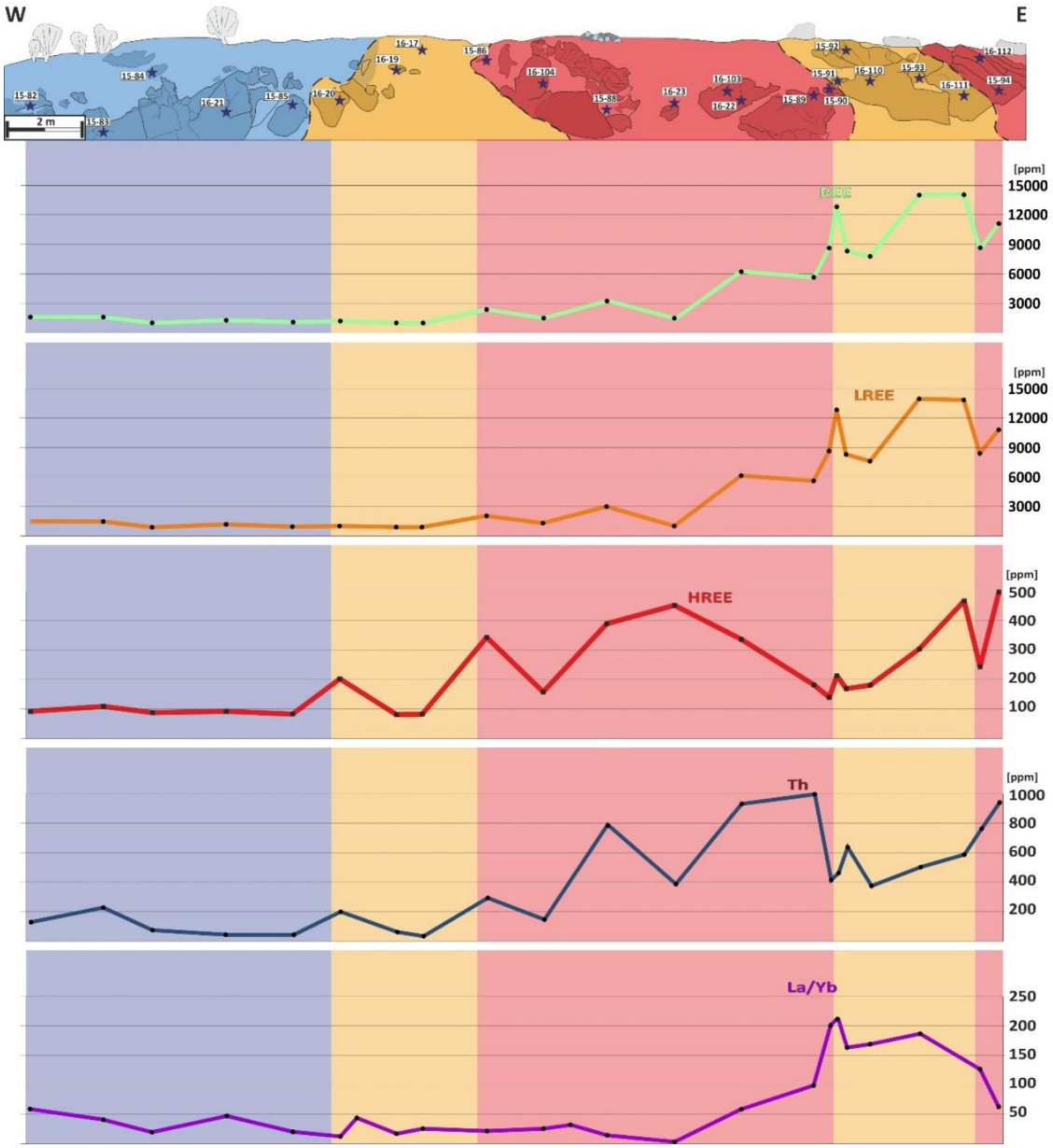

Figure 6-40: Sketch of the Bjørndalen transect, which is divided into three different alteration zones: rødbergite (red), transitional rødbergite (yellow) and unaltered or very weakly altered carbonatite (blue).For each sampling point, the concentration for REE, LREE, HREE and Th is plotted exactly below the sampling location. Additionally, the bottommost plot shows the ratios of La/Yb as an indicator for LREE to HREE fractionation.

On average, the unaltered carbonatites within the Bjørndalen transect contain a low concentration of REE (≤1600 ppm) and Th (≤220 ppm). Transitional rødbergite shows a large variation in REE concentration. The western transitional rødbergites have the lowest REE concentration within the transect (≤1000 ppm), whereas the eastern transitional rødbergites contain the highest concentration of REE within the whole

Bjørndalen transect (≤16,000 ppm). Although the western and eastern transitional rødbergites are optically very similar, the eastern transitional rødbergites exhibit a high density of REE mineral bearing micro-veins (type I-III; Fig 6-35; Fig. 6-36). Fully transformed rødbergite is enriched in REE (1200–11,000 ppm) and has the highest concentration of Th within the transect (≤1000 ppm).

Figure 6-40 shows the concentration of REE, LREE, HREE, Th and La/Yb ratio for each sample relative to the sample position along the transect. The graphs for REE, LREE and La/Yb are similar with a maximum at the eastern transitional rødbergite. This peak of REE and LREE corresponds to higher amounts of monazite-(Ce) bearing veins (vein type II; Fig 6-35; Fig. 6-36). Besides increasing the concentration of REE, Monazite-(Ce) separates LREE and HREE much more efficiently than apatite or calcite and therefore causes higher La/Yb ratios (Chakhmouradian et al., 2016). Unlike LREE, the graphs of HREE and Th show a maximum in central rødbergite — with up to 500 ppm HREE. Samples (16-23-FE) enriched in HREE correlate with high amounts (~65 Vol-%) of red apatite veins (Fig. 6-37). In cases where the REE budget is mainly influenced by apatite rather than monazite, lower La/Yb ratios are the result. This is in agreement with the REE partitioning of monazite and apatite, which produces significantly flatter REE pattern in apatite compared to the steep LREE enriched REE pattern of monazite (Brassinnes et al., 2005; Chakhmouradian et al., 2017; Chen et al., 2017). In cases where monazite is replaced by apatite, LREE are preferentially leached, which results in a relative enrichment in HREE (Smith et al., 2018).

The chondrite-normalised data plot (Fig. 6-41) shows a similar picture with an overall LREE-dominated distribution, which is typical for magmatic rocks in general and carbonatite in particular.

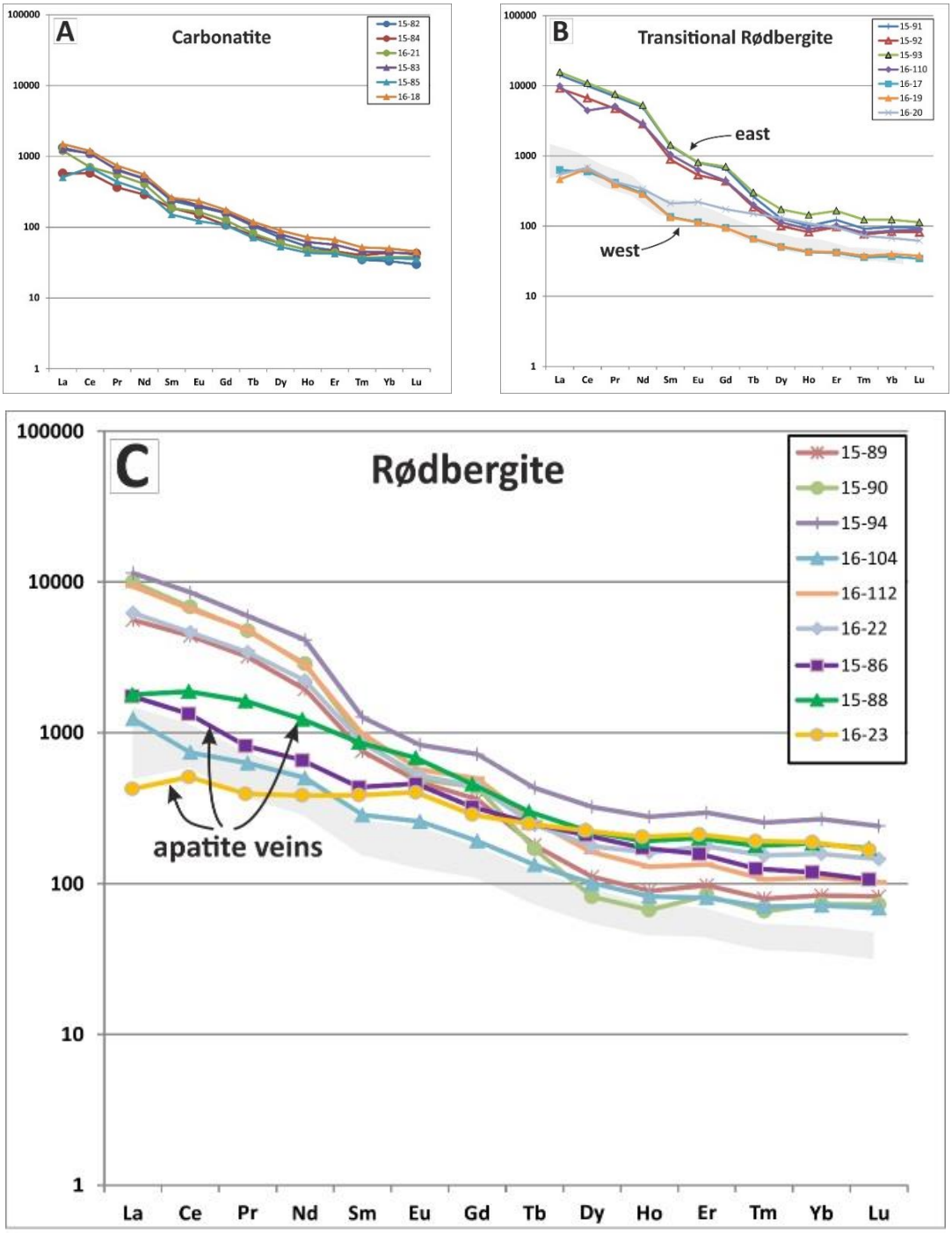

Figure 6-41: REE concentrations normalised to CI1-chondrite values from McDonough and Sun (1995).A) Igneous carbonatites show a relative enrichment of LREE to HREE with a moderately decreasing slope towards HREE. The range of carbonatite curves from A is displayed as a grey area in plot B and C for comparison. B) Transitional rødbergite samples show two distinctly different groups. One group of samples have a similar REE distribution to the unaltered carbonatites and belong to the western transitional zone. The sample 16-20-FE shows a slight HREE enrichment. The second group in the diagram has a much higher concentration of LREE and a slightly higher concentration of HREE and belongs to the eastern transitional rødbergite. The slope of the curve is much steeper, and the curve has a slightly irregular shape. C) Rødbergite samples show a range of REE patterns with some samples (apatite veins) having a flat HREE slope and relatively high HREE concentrations not accompanied by large LREE enrichments compared to unaltered carbonatites. Other rødbergite samples show a strong LREE enrichment similar to the eastern veined transitional rødbergites, but with generally higher concentrations of HREE.

Samples dominated by monazite-(Ce), e.g., the eastern transitional rødbergite, show the highest values of LREE with a very steep slope. On the contrary, the REE pattern of sample 16-23-FE is influenced by the presence of apatite, showing a flat curve with high absolute HREE concentrations (Fig. 6-41).

The element distribution in the Bjørndalen transect produces a zonation with Th and HREE concentrated in rødbergite at the centre of the alteration zone, and LREE locally concentrated in transitional rødbergite with a high vein density.

6.3 Discussion

In this subchapter, the geochemistry of the transect is linked with the mineralogy to create a deeper understanding of the REE mineralisation forming processes. Prior to this, the focus will be on the alteration of the unaltered mineral composition and on the important definition of what “unaltered” actually means.

6.3.1 Original and alteration mineral assemblage

There is clear textural evidence that the minerals of the unaltered carbonatite (e.g. pyrite, synchysite-(Ce) and apatite) are systematically replaced by an alteration mineral assemblage (e.g., hematite, monazite-(Ce), barite, phlogopite, quartz, calcite, barian orthoclase and allanite)e.g. the breakdown of pyrite and replacement by hematite (Fig. 6-11; Fig. 6-12; Fig. 6-23); the breakdown of synchysite-(Ce) and replacement by hematite (Fig. 6-12); the replacement of apatite and apatite relics by an alteration mineral assemblage of monazite-(Ce) and minor amounts of barite, phlogopite, calcite and hematite (Fig. 6-28; Fig. 6-29; Fig.6-38; Fig. 6-39); the precipitation of a network of hematite with minor amounts of calcite and monazite-(Ce) within the original dolomite-

calcite groundmass (Fig. 6-10; Fig.6-16; Fig. 6-23; Fig. 6-24; Fig. 6-25; Fig. 6-31); the increasing amount barite (Fig. 6-15; Fig. 6-23; Fig. 6-25), quartz (Fig. 6-27), barian orthoclase (Fig. 6-25) and phlogopite (Fig. 6-26) with progressing rødbergitisation; veins with various amounts of phlogopite, barite, allanite, synchysite-(Ce), calcite and quartz (Fig. 6-24, Fig. 6-36).

However, it is important to understand that even pristine carbonatite (unaltered) is likely to have experienced postmagmatic alteration. As pointed out in chapter 3, carbonatites are significantly more susceptible to changes in their original magmatic texture than silicate rocks, and their evolution commonly involves a variety of post-magmatic processes, including exsolution and subsolidus re-equilibration with carbothermal-derived fluids (Broom-Fendley et al., 2016; Chakhmouradian et al., 2015b). Because the focus of this thesis lies on the rødbergitisation process, the term 'unaltered carbonatite' used here includes rocks affected by early post-magmatic processes before the rødbergitisation. The unaltered carbonatite of the Bjørndalen transect is no exception and displays signs of postmagmatic processes (Fig. 6-4).

As argued by Andersen (1989b) and as will be shown in chapter 6.3.6, the hydrothermal event causing the formation of rødbergite involves an intense reaction of carbonatite with an oxidising, at least partly external, fluid. The formation of rødbergite discussed here therefore goes beyond the classic early post-magmatic processes of exsolution and subsolidus re-equilibration in carbonatites.

One of the most obvious non-magmatic textures in the unaltered carbonatite is the fine-grained intergrowth of calcite and dolomite in the groundmass (Fig. 6-4). This is a common observation in carbonatites and is likely to be the product of post-magmatic dolomitisation. According to Chakhmouradian et al. (2016), dolomite has a much smaller

capacity to incorporate REE into its structure compared with calcite (up to 2000 ppm REE). During dolomitisation, the excess REE are released, which could have served as an initial REE source, forming the accessory REE-fluorocarbonates in the unaltered carbonatite. The pyrite-fluorite-REE-fluorocarbonate cluster shows textural evidence of a postmagmatic origin (Fig. 6-5). However, these clusters are part of the unaltered carbonatite, which is being attacked by the rødbergitisation fluid, and more importantly, cannot be seen in transitional rødbergites and rødbergites. Therefore, it is likely that these clusters are either the product of postmagmatic processes or alteration caused by an early/distant rødbergitisation fluid.

The main minerals of the Bjørndalen carbonatite – dolomite, calcite, apatite, magnetite, pyrite and columbite – are considered as the unaltered mineral assemblage. They are typically part of an "unaltered" mineral assemblage in carbonatites in the Fen Complex and worldwide (Woolley and Kempe, 1989). Some of the textures provide supporting evidence of their original magmatic nature. For example, the lozenge-shaped, oriented apatite relics show evidence for a magmatic/late magmatic segregation (Fig. 6-4). This segregation is not seen in any rødbergite samples and can be better explained by cumulate forming processes in the carbonatitic magma reservoir (Chakhmouradian et al., 2017). Therefore, the segregation is considered to have happened before the rødbergitisation. Columbite locally contains inclusions of apatite, which are not coming from the surrounding groundmass due to their different shape and size (Fig. 6-6). This indicates columbite was formed at an earlier magmatic stage (cumulate) and was incorporated in the carbonatitic magma during ascent. On the other hand, there is textural evidence that the accessory minerals in the unaltered carbonatite, e.g. barite and quartz formed in a hydrothermal environment. These minerals are part of vein

mineral assemblages in the unaltered carbonatite (Fig. 6-34) as well as part of the rødbergitisation alteration mineral assemblage (Fig. 6-15; Fig. 6-23; Fig. 6-25; Fig. 6-27), and therefore indicate a postmagmatic origin in the unaltered carbonatite. Based on the available evidence, it is not possible to tell if they are the result of post-magmatic processes or the remote alteration halo of the rødbergitisation. REE-fluorocarbonates, which are the dominant REE carrier in the unaltered carbonatites (Fig. 6-5; Fig 6-8), show similar textures. Amongst the four described forms (inclusion, intergrowth, vein and pyrite-aggregate) only the small inclusions of REE-fluorocarbonates in minerals of the unaltered assemblage are, without a doubt, prior to the rødbergitisation.

The presence of a fine network of Fe-oxide veins along carbonate grain boundaries are signs of initial alteration of carbonatite (Fig. 6-10; Fig. 6-14). Although REE-fluorocarbonates are dissolved and replaced by Fe-oxides during initial rødbergitisation (Fig. 6-12B), REE-fluorocarbonates, e.g. in pyrite clusters could result from a distant early rødbergitisation halo, which is not easily distinguished by red Fe-oxide precipitation. As the amount of fine disseminated Fe-oxide between grain boundaries increases, it produces a stronger red colouration in the rock, hence the name rødbergite. The alteration includes oxidation (of magnetite and pyrite to Fe-oxides), recrystallisation and replacement of unaltered mineral assemblage, leading to alteration mineral assemblage of ferroan dolomite, barite, barian phlogopite, calcite and hematite minor monazite-(Ce), quartz, pyrite and barian orthoclase and accessory REE-fluorocarbonates and allanite (Fig. 6-15; Fig.6-23; Fig. 6-27; Fig. 6-36).

6.3.2 Hydrothermal REE-mineralisation

As REE-fluorocarbonates are replaced by the initial rødbergitisation of unaltered carbonatite (Fig. 6.12), monazite-(Ce) becomes the most common REE-carrier in transitional rødbergite (Fig. 6-16, Fig. 6-17, Fig. 6-18, Fig. 6-21, Fig. 6-38) and rødbergite (Fig. 6-25, Fig. 6-27, Fig. 6-28, Fig. 6-29, Fig. 6-30, Fig. 6-39). Monazite-(Ce) is part of the alteration mineral assemblage of hematite, calcite, barite and barian phlogopite and occurs in three different forms: (a) in monazite-(Ce) veins and veinlets (Fig. 6-16, Fig. 6-25, Fig. 6-27, Fig. 6-28, Fig. 6-31, Fig. 6-36), (b) in the groundmass (Fig. 6-17, Fig. 6-18, Fig. 6-36) and (c) around apatite-dolomite relics and apatite grains (Fig. 6-28, Fig. 6-29, Fig. 6-30, Fig. 6-38, Fig. 6-39). During the penetration of the carbonatite by the rødbergitisation fluid, hematite, barite, phlogopite and carbonates precipitated together with minor monazite-(Ce) in the form of (a) veins and (b) in interstitial grain boundary spaces within the groundmass. This explains the intergrowth of monazite-(Ce) with barite (Fig. 6-17; Fig. 6-18; Fig. 6-36; Fig. 6-42), barian phlogopite (Fig. 6-36; Fig. 6-42) and hematite (Fig. 6-16; Fig. 6-25; Fig. 6-28) in monazite veins as well as in the groundmass. The concentration of hydrothermal monazite-(Ce) on the outer rim of apatite-dolomite relics in rødbergite (Fig. 6-39) and transitional rødbergite (Fig. 6-38) is the result of the apatite-replacement reaction (Fig. 6-42). When the rødbergitisation fluid came in contact with apatite, the REE preferentially precipitated as monazite-(Ce), by either partial or full replacement of apatite (Fig. 6-28; Fig. 6-29; Fig. 6-30).

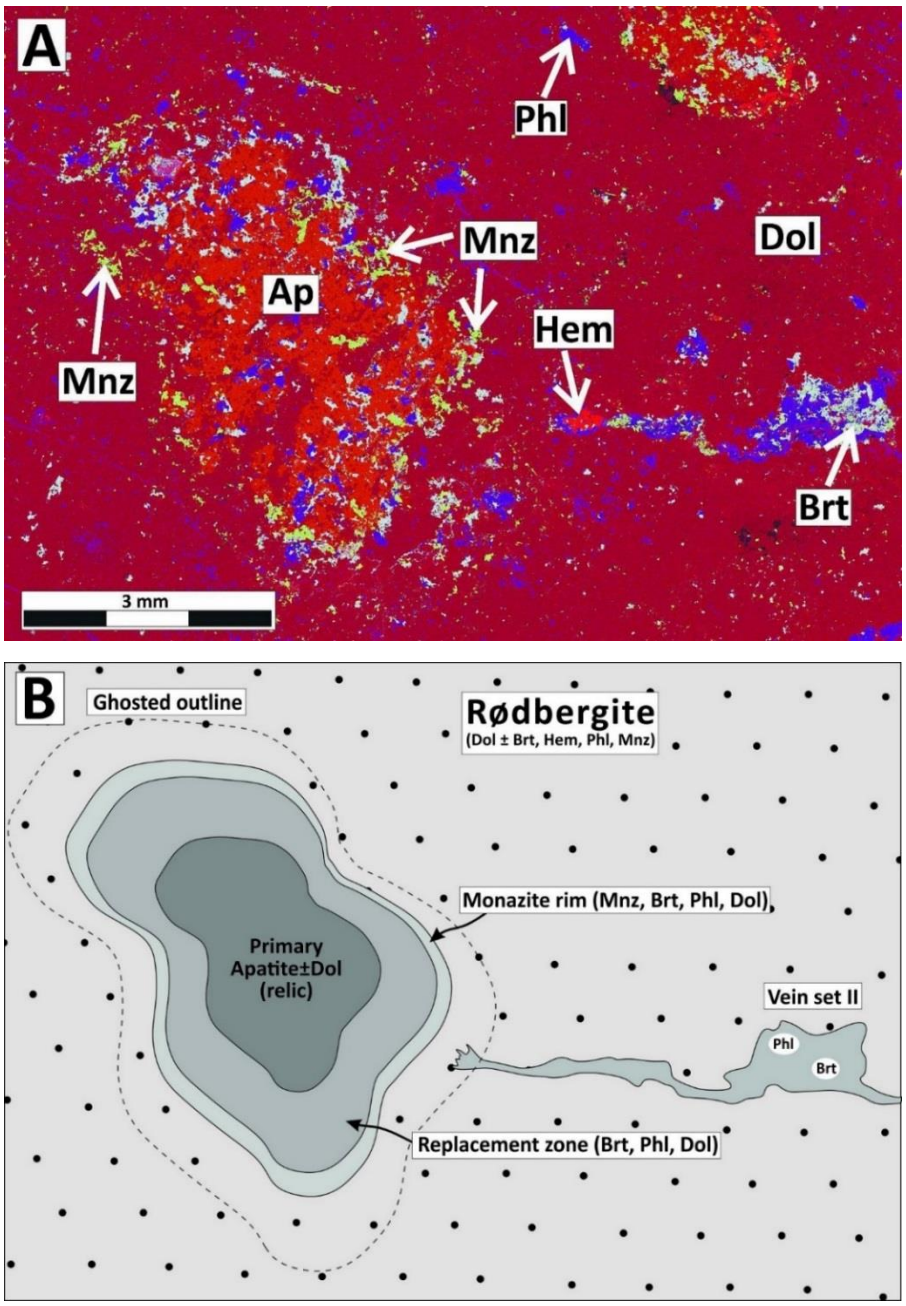

Figure 6-42: Combined large-area EDS mosaic and a schematic line drawing of an 'apatite trap' for REE-mineralisation in rødbergite (sample 15-90-FE). A) Combined large-area EDS mosaic of a rødbergite illustrates the distribution of monazite-(Ce) (green-yellow) on the outer rim of an apatite relic from an unaltered apatite-inclusion-bearing carbonatite, partly replaced during rødbergitisation. There is a rootless barite-phlogopite vein (set II) – a possible feeder fracture – to the right of the apatite relic. Mineral abbreviations: Ap – apatite, Phl – phlogopite, Brt – barite, Hem – hematite, Mnz – monazite-(Ce). B) Schematic diagram showing the replacement of the apatite relic. Transport of the replacement fluid occurred along set II veins, which are comprised of barite, phlogopite ± hematite and monazite-(Ce). The concentration of replacement minerals, e.g., monazite-(Ce), trace a ghost outline. The outer rim of the apatite relic is significantly enriched in monazite-(Ce) plus barite, phlogopite and dolomite. The replacement zone is a mix of apatite relics and hydrothermal minerals like barite and phlogopite. The core of the apatite relic consists mainly of apatite and dolomite.

Hence apatite, and in particular the apatite-rich relics, acted as a REE 'trap' during the formation of rødbergite. The source of the REE is, in all three cases, the rødbergitisation fluid. The zone of transitional rødbergite with the highest concentration of REE (Fig. 6-40) also has the highest density of veining (Fig. 6-13). The fully-transformed rødbergite has, in general, a lower density of veins and there is an analogy with replacement skarn deposits where the margins of replacements are characterised by vein skarn (feeder fractures), whereas massive skarn shows no clear vein assemblage (Kim et al., 2015).

Minor carriers of REE are allanite and REE-fluorocarbonates. Allanite only occurs as part of allanite vein type III in transitional rødbergite (Fig. 6-36). The allanite vein postdates the main hematisation and represents an evolved feeder structure —please refer to chapter 6.1.4 for more details. REE-fluorocarbonates are rarely part of transitional rødbergite and rødbergite. They occur, occasionally in veinlets of hematite-calcite with monazite-(Ce) (Fig, 6-31), in interstitial groundmass space intergrown with, e.g. barite (Fig. 6-19, Fig. 6-32). Therefore, it is possible that the rødbergitisation fluid, out of which monazite-(Ce) precipitates, is also able to precipitate REE-fluorocarbonates under the right physicochemical conditions. Occasionally, allanite veins show the precipitation of REE-fluorocarbonates. Monazite-(Ce) is the only REE-mineral that concentrates around apatite relics ("apatite trap") (Fig. 6-42), due to the unique nature of the replacement reaction.

6.3.3 REE stability in the hydrothermal fluid of the Bjørndalen transect

The breakdown of REE-fluorocarbonates in igneous carbonatites (Fig. 6-12) and the strong enrichment of REE in rødbergite (Fig. 6-40) — by formation of hydrothermal REE-minerals in the groundmass (Fig. 6-17), in veins (Fig. 6-16, Fig. 6-36) and around apatite

“traps” (Fig. 6-29, Fig. 6-39) — is evidence for solubility and mobility of REE in the rødbergitisation fluids. The REE are relatively insoluble in aqueous solution due to their high charge and high ionic potential and are therefore considered to be immobile elements during hydrothermal alteration (White, 2013). Nevertheless, under the right conditions, REE can undergo complexing with preferentially “hard” ligands and become mobile elements. Several experimental studies have emphasized the important role of fluoride, sulphate and chloride ligands to form stable REE complexes in hydrothermal fluids at 200–400 °C in geological environments (Williams-Jones and Migdisov, 2014; Williams-Jones et al., 2012), with REE-sulphate complexes dominating at temperatures >300 °C in weakly acidic fluids (Migdisov and Williams-Jones, 2014). The ubiquitous presence of barite as part of the alteration mineral assemblage in rødbergite (Fig. 6-15; Fig. 6-23), including in the monazite and allanite veins (Fig 6-36), suggests an important role for sulphate complexes in REE mobilisation. Additionally, experimental studies have shown that sulphate inhibits the formation of monazite from fluorapatite (Harlov and Förster, 2004), which highlights the importance of barite precipitation coupled to monazite-(Ce) formation (Feng et al., 2016). Sulphate was released by the breakdown of sulfides in unaltered carbonatites (Fig. 6-11, Fig. 6-27) through the reaction with oxidising hydrothermal fluid.

Experimental studies have further demonstrated that the stabilities of REE-fluoride, -sulphate and -chloride complexes decrease strongly with decreasing temperature and increasing pH (Migdisov and Williams-Jones, 2014; Williams-Jones and Migdisov, 2014; Williams-Jones et al., 2012). Therefore, cooling of the hydrothermal fluid, or reaction with carbonate host rocks leading to a pH-increase in the fluid, are potential geological mechanisms for triggering precipitation of REE-minerals from aqueous solutions. Of

particular relevance to the Bjørndalen transect is the experimental evidence that fluid-rock reactions of fluorine- and sulphate-bearing aqueous fluids with phosphate-rich host rock is a highly effective trigger for the destabilisation of the aqueous REE-complexes, resulting in the precipitation of REE-phosphate minerals such as monazite-(Ce) (Louvel et al., 2015; Migdisov and Williams-Jones, 2014). This mechanism fully explains the textural evidence that relics of apatite layers acted as a trap for REE via the crystallisation of monazite-(Ce) in rødbergite (Fig. 6-38; Fig. 6-39; Fig. 6-42) in the Bjørndalen transect.

6.3.4 LREE and HREE decoupling

The mobilisation of the REE, as discussed in the previous chapter 6.3.3 is variable within the group of REE because the radii of the REE are variable (Fig. 2-1). The HREE have sufficiently small radii that they can substitute in common minerals (e.g. garnet that can concentrate the HREE relative to the LREE in a garnet-bearing rock). The geochemical results of the Bjørndalen transect show clear evidence for a decoupling of LREE and HREE during the formation of rødbergite, and monazite-(Ce) and allanite veins. While some rødbergite samples show a concentration of HREE relative to LREE (Fig, 6-40), the majority of the REE mineralised samples shows a tendency towards high La/Yb ratios (Fig. 6-41). Experimental work has shown that at temperatures >150 °C, aqueous LREE-complexes are generally more stable than HREE-complexes, in particular, those involving fluoride as the dominant transporting ligand (Williams-Jones et al., 2012). This means that HREE first drop out of solution when aqueous REE-complexes are destabilised and that LREE remain in solution longer and are transported over longer distances compared to HREE. For instance, Williams-Jones et al. (2012) showed how a temperature drop of a REE-bearing fluid in a feeder vein system resulted in a distinct

fractionation of REE, with the LREE being transported further along the feeder veins, down the temperature gradient (Fig. 6-43). Therefore, the observed LREE-HREE decoupling and the concentration of HREE in the central rødbergite (Fig. 6-40) in the Bjørndalen transect can be explained by their relative immobility compared to LREE. HREE precipitated in the area of strongest alteration (rødbergite), whereas LREE remained in solution and migrated further away from the centre of alteration domain, into the alteration halo (now represented by the transitional rødbergites). The hydrothermal monazite and allanite micro-veins are an inherent part of the rødbergite formation process. Areas with a high abundance of these veins (possible feeder fractures), as in the eastern transitional rødbergite zone, show the strongest enrichment of LREE in the bulk rock samples. Additionally, red apatite veins influence the La/Yb ratio (Fig. 6-37). Samples with a high amount of red apatite veins show the lowest La/Yb ratios within the Bjørndalen transect (Fig. 6-23; Fig. 6-40). This is likely due to the portioning curve of apatite, which combines two overlapping portioning curves for the Ca1 site and Ca2 site. The resulting portioning curve is almost flat, with a slight maximum for the MREE (Chakhmouradian et al., 2017). The relatively even portioning of REE into apatite would result in relatively low La/Yb ratios. Another potential mechanism could be the preferential depletion of LREE from apatite by fluids as it was described for apatite from IOCG and IOA deposits (Krneta et al., 2017b). Apatite with such a LREE depletion commonly shows inclusions of the overprinting fluid in the form of hematite and or sericite (Krneta et al., 2017a). The red colouration of the apatite veins caused by hematite inclusion (Fig. 6-23) could be an indication of such a hydrothermal LREE depletion process.

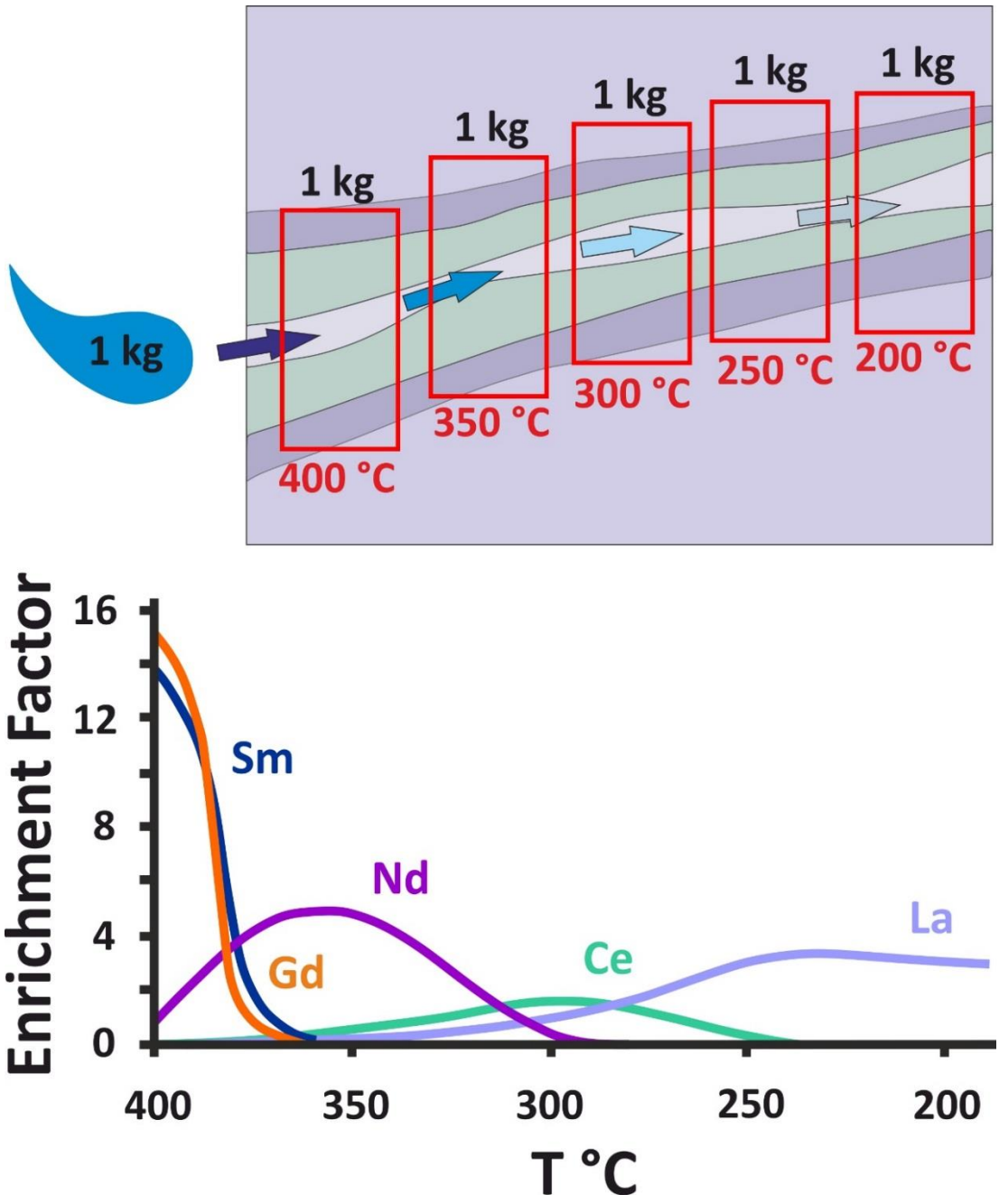

Figure 6-43: Sketch is redrawn from Williams-Jones et al. (2012) to illustrate the different mobility of REE with respect to fluid temperature.(A) Progressing interaction of 1 kg of nepheline syenite (100 ppm Phosphate) with fluid containing 10 wt% NaCl, 500 ppm F and 50 ppm of La, Ce, Nd, Sm and Gd. During a constant pressure of 500 bar and initial pH of 4.5, the fluid temperature cooled down from 400 °C to 200 °C. (B) Fractionation of individual REE after interaction of the rock with five aliquots of fluid. The enrichment factor is defined as $(REE/\Sigma REE)_{Rock}/(REE/\Sigma REE)_{initial\ solution}$. Note the tendency of heavier REE, e.g. Sm and Gd to stay closer to a hotter centre of fluid interaction than lighter REE (La, Ce and Nd), similar to HREE close to the centre of rødbergitisation in the Bjørndalen transect.

6.3.5 Th enrichment during rødbergitisation

Thorium is one of the major obstacles for REE exploitation. Th is enriched in rødbergite along the Bjørndalen transect in a similar pattern like REE (Fig. 6-40). HREE and Th are enriched in rødbergite, relative to transitional rødbergite and unaltered carbonatite. Th is hosted in Th-minerals (thorite) and Th-bearing minerals (e.g. monazite-(Ce) – P6-15, P6-37, P6-43; synchysite-(Ce) – P6-11, P6-32, P6-52), as part of the alteration mineral assemblage associated with the rødbergitisation. The main Th host in the unaltered carbonatite is REE-fluorocarbonate (P6-11 in Fig. 6-8). The Th concentration in monazite-(Ce), found in the monazite veins in the transitional rødbergite, is mainly below the detection limit of the EDS SEM (<0.5 wt%) and samples that show a significant LREE concentration due to a high density of REE-mineral bearing veins do not show elevated Th concentrations (Fig. 6-40). This indicates that Th was less mobile than LREE and precipitated earlier, together with HREE, in the centre of the alteration domain.

6.3.6 Nature of the hydrothermal fluids of the Bjørndalen transect

A comparison between the original and alteration mineral assemblages described in chapter 6.3.1 suggests that the hydrothermal fluids involved in the formation of hematite-barite-rich rødbergite and the observed REE enrichment, were more oxidised than the unaltered magnetite-pyrite-bearing carbonatites; this oxidised character of the fluid must have been acquired outside of the Fen Complex. Furthermore, Andersen (1984) presented strontium and oxygen isotopic evidence to show that fluids involved in rødbergite formation had high $^{87}Sr/^{86}Sr$ ratios and elevated $\delta^{18}O$. This suggests that the fluids involved in the REE mineralisation in the Fen Complex were not simply evolved melt-like hydrous fluids; such late-magmatic fluids often play a critical role in producing

high grades in REE-resources (Bodeving et al., 2017; Broom-Fendley et al., 2017b; Duraiswami and Shaikh, 2014; Smith et al., 2016; Wall and Mariano, 1996). Instead, the rødbergite fluids were hydrothermal and had at least partly equilibrated with Precambrian quartzofeldspathic gneisses outside of the Fen Complex, and possibly with groundwater (Andersen, 1984). REE are highly mobile in such fluids, producing REE-mineralisation well outside of their magmatic source rock. This has been demonstrated for carbonatites, e.g. Kangankunde (Broom-Fendley et al., 2017b; Wall and Mariano, 1996), as well as for peralkaline complexes, e.g. Strange Lake (Gysi and Williams-Jones, 2013). Sediment-hosted replacement-type carbonatite REE deposits, e.g. Bayan Obo (Campbell and Henderson, 1997; Wu, 2008; Smith et al., 2015), breccia-hosted Fe-Cu-Au-REE deposits, e.g. Olympic Dam (Groves and Vielreicher, 2001; McPhie et al., 2011; Oreskes and Einaudi, 1990), and unconformity-type REE ± U deposits, e.g., Athabasca Basin (Fayek and Kyser, 1997) are examples of even more distal deposits for which a link with fluids sourced by igneous carbonatite at depth have been proposed. Especially the REE mineralisation of Mount Weld shows indications of similar processes with a horizon of monazite within carbonatite laterite produced by groundwater alteration of apatite (Lottermoser, 1990; Smith et al., 2016).

It is important to realise that the rødbergitisation process is happening in multiple stages as can be seen by the various generations of veins associated with the rødbergitisation (please refer to chapter 6.1.4 and Fig. 6-35; Fig. 6-36). The difference in vein mineral assemblage (monazite-(Ce), allanite and REE-fluorocarbonate) is evidence for the physicochemical change of the hydrothermal fluid during the rødbergitisation. A range of variables can change during the hydrothermal alteration of the carbonatite, which is effectively an equilibration process of carbonatite with hydrothermal fluid. The

temperature of the fluid alters as well as chemical composition, Eh, pH and fO_2 due to mineral dissolution and reprecipitation. The intergrowth of REE-fluorocarbonates with barite and hematite, similar to monazite-(Ce)-mineralisation, shows the close stability fields of these REE minerals. Additionally, shifts in the redox potential of the hydrothermal fluid occurred. The general oxidising nature of the fluid caused the breakdown of pyrite in the unaltered carbonatite and formation of barite and Fe-oxides during the rødbergitisation. The presence of euhedral pyrite crystals, some of which display inclusions of monazite-(Ce), indicate the formation of hydrothermal pyrite (Fig. 6-18). Although the alteration fluid mainly caused oxidation and formation of monazite-(Ce), there must have been occasions when REE-fluorocarbonates were formed, or reduction (pyrite formation) occurred during alteration.

6.3.7 Rare Earth mineralisation model for Bjørndalen transect

As already pointed out in Marien et al. (2018), the described findings of this thesis are not fully consistent with the existing model of Andersen (1984; 1986) for the REE mineralisation in rødbergite of the Fen Complex. Therefore, this chapter will introduce a new model involving parts of the Andersen model in unison with new observations from the Bjørndalen transect.

A key element of the existing model by Andersen involves a progressive residual enrichment of insoluble REE-minerals by leaching and removal of the carbonate minerals during hydrothermal alteration (Andersen, 1984). Please refer to chapter 4 for a complete summary of Andersen's model. Andersen's model and the present model both propose alteration with post-magmatic oxidising hydrothermal fluids, which equilibrated with rocks outside of the Fen Complex. However, there are three main

reasons why the REE concentration cannot solely be explained by a residual enrichment of magmatic REE-minerals:

a) The main REE carrier-mineral changes from REE-fluorocarbonates in the unaltered carbonatite (Fig. 6-5; Fig. 6-8; Fig. 6-12), to monazite-(Ce) in the transitional rødbergite (Fig. 6-16; Fig. 6-17, Fig. 6-18) and rødbergite (Fig. 6-28; Fig. 6-29). In Andersen's REE-mineralisation model, this must be due to a change of rock units from a REE-fluorocarbonate-rich carbonatite to a monazite-(Ce)-rich carbonatite. However, the evidence presented in chapter 6.1 and further discussed in 6.3.1 clearly show the dissolution of REE-fluorocarbonates in unaltered carbonatites (Fig. 6-12) and formation of hydrothermal monazite-(Ce) as the major REE host in transitional rødbergite (Fig. 6-16) and rødbergite (Fig. 6-28). The change of the REE host mineral is therefore not because of a change in rock units but rather a dissolution and reprecipitation process of REE minerals triggered by a hydrothermal fluid. The REE minerals do not remain stable during this process, as would be required by the Andersen model.

b) Monazite-(Ce) in the transitional rødbergite and rødbergite is predominantly found in a network of fine veins (Fig. 6-16; Fig. 6-28) and is common where these veins are in contact or closely associated with apatite-dolomite relics of unaltered carbonatite as a result of the replacement of apatite by monazite-(Ce) (Fig. 6-42), with the relic apatite acting as a REE-trap. These textures are not present in unaltered carbonatite and require REE to be transported in a fluid phase.

c) Geochemical analysis of samples from the Bjørndalen transect showed REE enrichment by more than an order of magnitude from carbonatite to rødbergite (Fig. 6-40). This would require a major volume reduction by 90% in order to concentrate the supposed stable REE minerals and would be predicted to be accompanied by the

formation of porous rocks with cavernous mineral assemblages (Chakhmouradian et al., 2015b), as well as collapse breccias. No field evidence for extensive brecciation (Andersen, 1987a) (Fig. 6-13; Fig. 6-22), or formation of highly porous, vug-rich rocks (Fig. 5-5) is apparent in the Bjørndalen transect.

The new general model for the formation of rødbergite in the studied transect at Bjørndalen is consistent with the findings (Fig. 6-44). The model involves leaching of REE-fluorocarbonates from unaltered carbonatites by highly oxidising, fluorine and sulphate-rich fluids, and transport, reprecipitation and concentration of REE in new hydrothermal REE minerals, mainly monazite-(Ce). These zones of extensive fluid-rock interaction are marked by rødbergite, surrounded by alteration halos of transitional rødbergite. The progressive alteration of carbonatite to rødbergite in the Bjørndalen transect (Fig. 6-1) by an oxidising hydrothermal fluid caused the breakdown of REE-fluorocarbonates in unaltered carbonatite (Fig. 6-12) and precipitation of hydrothermal monazite-(Ce) along a fine, pervasive, irregular network of micro veins and around apatite-dolomite relics from unaltered carbonatite, where monazite-(Ce) is replacing apatite (Fig. 6-16; Fig. 6-28).

The newly formed monazite-(Ce) together with multiple generations of monazite-, allanite- and REE-fluorocarbonate-bearing veins account for the REE enrichment in rødbergite and transitional rødbergite samples by an order of magnitude relative to the unaltered carbonatite (Fig. 6-40). The relative enrichment of HREE, LREE and Th are variable throughout the Bjørndalen transect due to different element mobilities and the density of the REE-vein networks, which cause the development of overlapping zones of enrichment, with Th and HREE-rich zones being closer to the centre of alteration than the LREE-rich zone found in the alteration halo (Fig. 6-40).

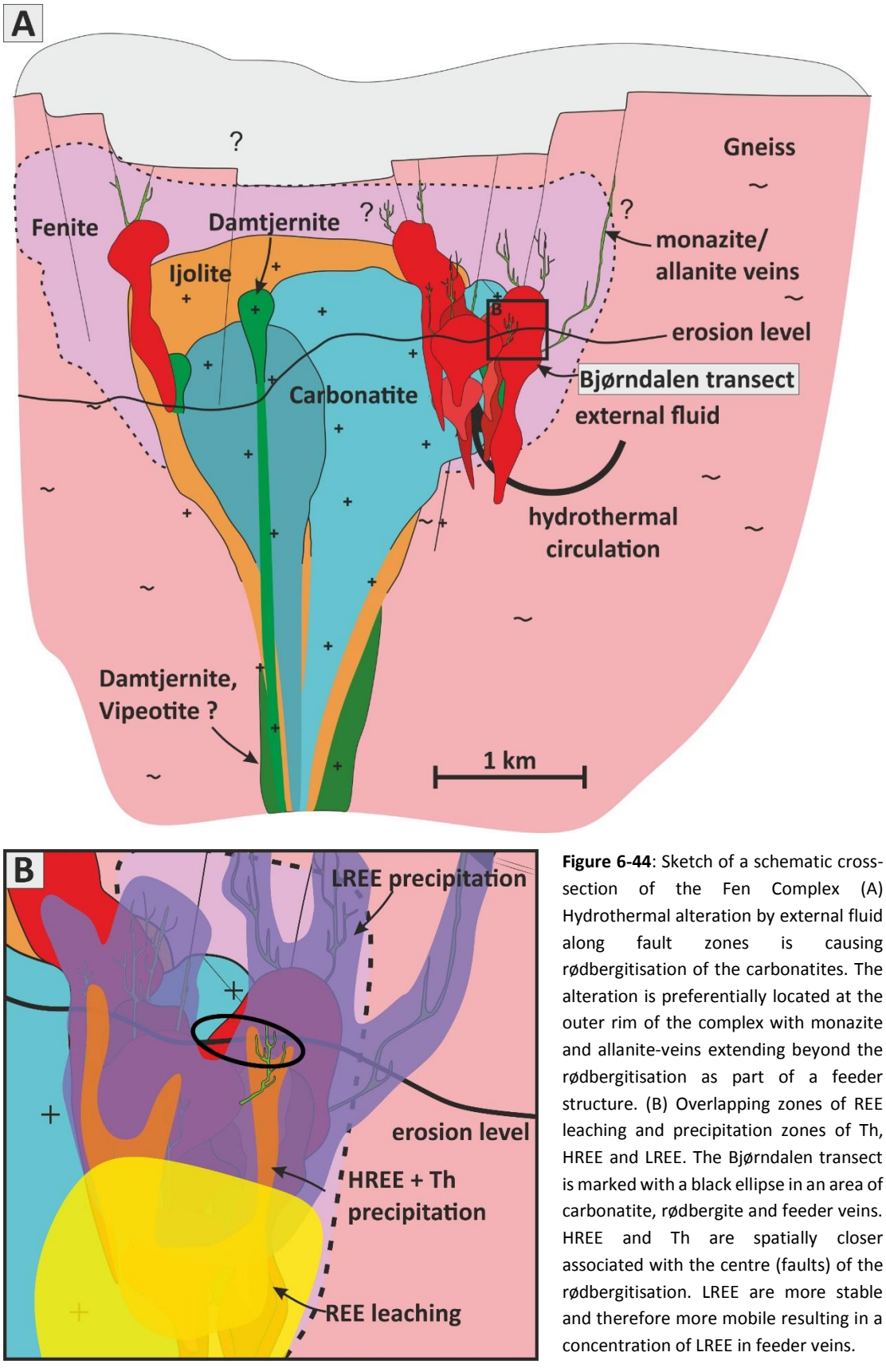

Figure 6-44: Sketch of a schematic cross-section of the Fen Complex (A) Hydrothermal alteration by external fluid along fault zones is causing rødbergitisation of the carbonatites. The alteration is preferentially located at the outer rim of the complex with monazite and allanite-veins extending beyond the rødbergitisation as part of a feeder structure. (B) Overlapping zones of REE leaching and precipitation zones of Th, HREE and LREE. The Bjørndalen transect is marked with a black ellipse in an area of carbonatite, rødbergite and feeder veins. HREE and Th are spatially closer associated with the centre (faults) of the rødbergitisation. LREE are more stable and therefore more mobile resulting in a concentration of LREE in feeder veins.

The newly proposed model for REE-mineralisation in the rødbergite has significant implications for a REE exploration strategy. The model predicts the existence of separate zones of HREE, LREE and Th enrichment throughout the Fen Complex. The selective exploitation of HREE and LREE without high Th concentrations (generally considered an undesirable element in REE exploitation) can now be better assessed. Moreover, LREE potentially form an enriched halo further away from the centre of alteration than expected. Because passive enrichment of REE minerals from unaltered carbonatites is not the cause for the REE mineralisation, the alteration fluid must have contained REE. Therefore, any lithotype in the complex (e.g., damtjernite or fenite) that was exposed to the same rødbergite-forming fluid is a potential exploration target.

6.4 Conclusion

Results of the study of the Bjørndalen transect reported in this chapter show that detailed mineralogical and geochemical investigations of the progressive transformation of unaltered carbonatite to rødbergite are essential to gain a deeper understanding of the REE-mineralisation process in the Fen Complex. There are four major key points:

(i) The progressive alteration is associated with a 10-fold enrichment of REE in the altered samples relative to the unaltered carbonatite (Fig. 6-40). The main cause of this enrichment is the precipitation of hydrothermal monazite-(Ce) in the groundmass, and the occurrence of monazite- and allanite micro-veins, all associated with the rødbergite-forming process (Fig. 6-16; Fig. 6-28, Fig. 6-38).

(ii) The breakdown of REE-fluorocarbonates in unaltered carbonatites (Fig. 6-12) and the formation of monazite-bearing rødbergite (Fig. 6-16; Fig. 6-28) are caused by the

interaction between carbonatite and an oxidising aqueous hydrothermal fluid, in which REE were mobile.

(iii) Locally, hydrothermal monazite-(Ce) is concentrated around apatite-rich relics in rødbergite (Fig. 6-38; Fig. 6-39, Fig. 6-42). These apatite-rich relics acted as a trap for REE by triggering the precipitation of monazite-(Ce), a mechanism predicted by physical-chemical experiments.

(iv) In addition to the enrichment of REE, the formation of rødbergite is also associated with an increased concentration of Th. However, there is evidence for partial decoupling of LREE, HREE and Th in the Bjørndalen transect, and the formation of separate zones of LREE, HREE and Th enrichment (Fig. 6-40).

Based on the model for rødbergite formation by Andersen (1984), the new model can explain all the reported features and has significant implications for future REE exploration strategies. The model predicts the existence of separate zones of LREE, HREE and Th enrichment throughout the Fen Complex and highlights the importance of apatite-rich relics and REE-mineral veining for high-grade REE ore. If the REE mineralisation mechanism from the Bjørndalen transect are unique to the Bjørndalen transect or transferrable to the rest of the Fen Complex, is discussed in chapter 10.

7 Fen Road transect

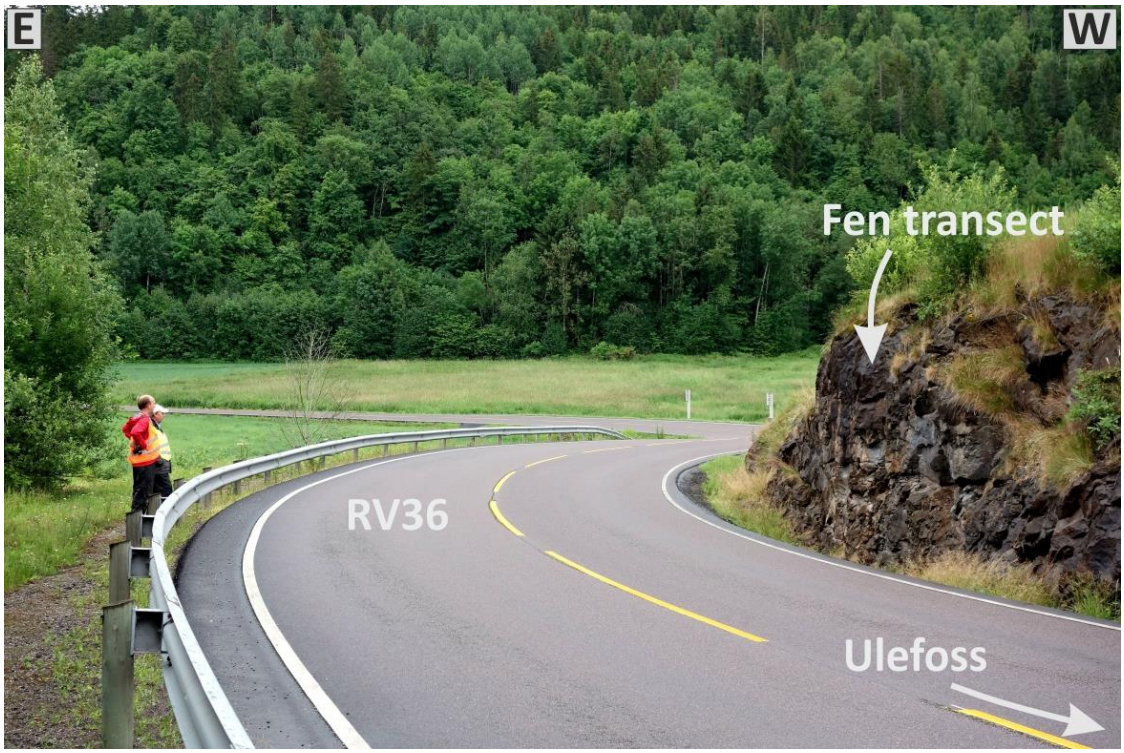

Figure 7-1: Photo of the Fen transect which is located alongside the road RV36 leading from Skien to Ulefoss.

This chapter describes and explains the mineralogy, texture and geochemistry of rock samples from the Fen Road transect (Fig. 7-1). Similar to the previous chapter, the focus lies on the distribution of the rare-earth elements (REE), the prominent REE-minerals and the genetic link between postmagmatic petrological processes (e.g., rødbergitisation) and the REE mineralisation and distribution of Th. The Fen Road transect is treated as an individual system initially, but results and conclusions will be compared to those from the Bjørndalen transect (please refer to chapter 6).

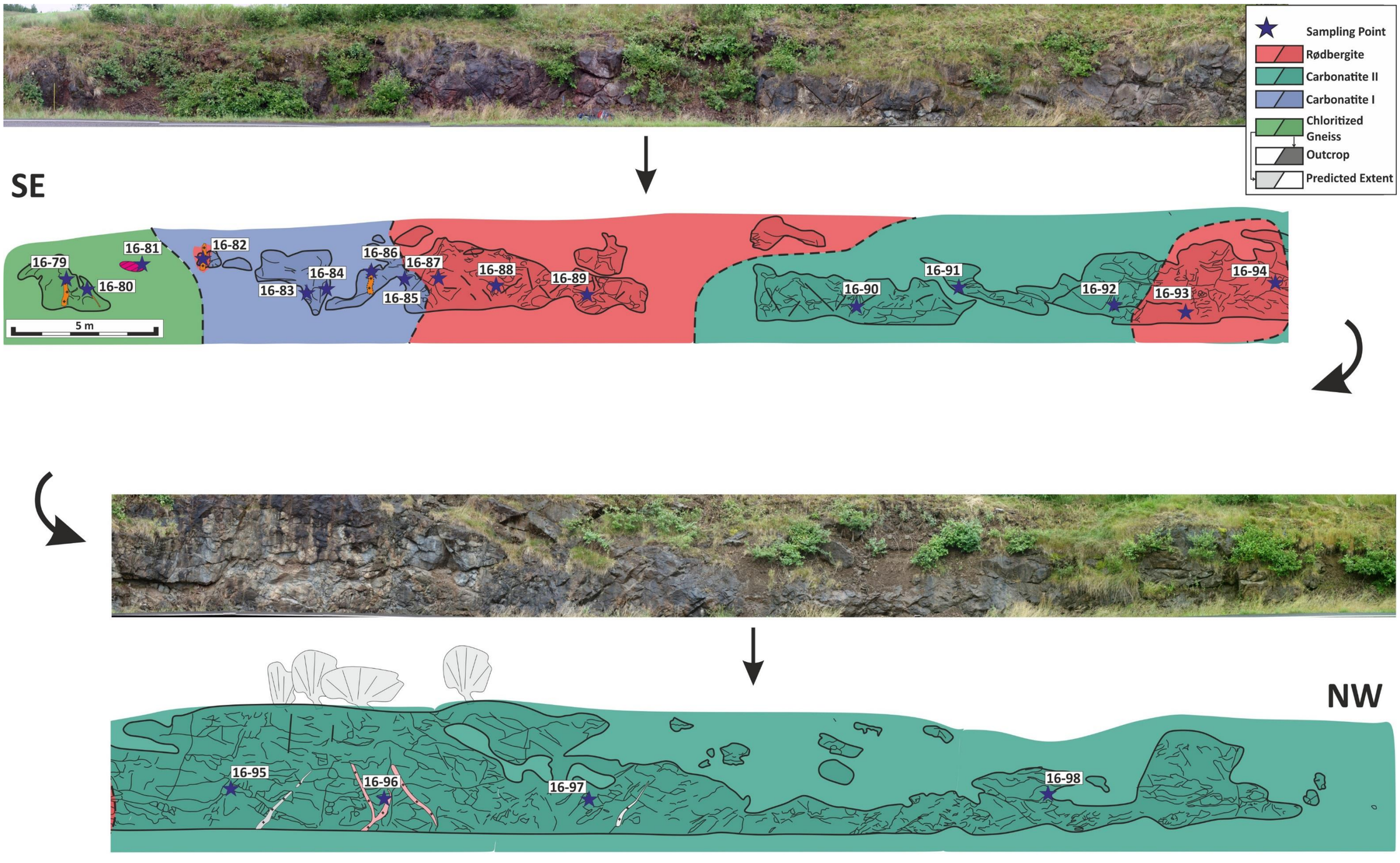

Figure 7-2: Stitched photograph of the Fen transect with a corresponding classification sketch right . Starting in the SE, the Fen transect is divided into chloritised granitic gneiss, dolomite carbonatite, rødbergite and chlorite-bearing dolomite carbonatite. Blue stars mark samples (n = 20) from the Fen Road transect. Large saw cutting marks from a former exploration campaign are illustrated as thick black lines.

7.1 Rock types

The SE end of the Fen transect starts with a narrow zone of chloritised granitic gneiss (green), followed by unaltered carbonatite (blue), then rødbergite (red) and the largest part of the Fen Road transect comprises of carbonatite II (turquoise) (Fig. 7-2). The following section summarises the main observations for these rock types. The mineral composition of the different lithotypes of the Fen Road transect is illustrated in Tab. 7-1.

Table 7-1: Summary table of the identified minerals at the Fen Road transect and their approximate proportion in the different lithotypes. The three samples of dolomite-carbonatite are listed separately and exhibit a natural variation in the mineral assemblage. Mineral proportion symbols: xxx - >20 Vol%; xx – 5-20 Vol%; x – 1-5 Vol%; o - < 1 Vol%.

Minerals	Chloritised Granitic Gneiss	Fluorite-rich Carbonatite	Dolomite-Carbonatite			Chlorite-bearing Dolomite-	Rødbergite	Rødbergite Vein
			16-84-FE	16-96-FE	16-85-FE			
Calcite	x	x					xx	xxx
Dolomite		xx	xxx	xxx	xxx		xx	
Ferroan-Dolomite			xx	xxx	xx	xxx	xx	
Ankerite	xx			o		o		
Apatite	x	xx	xx	x	x	xx	x	o
Barite	o	x	x	x	x	x		o
Chlorite	xxx				o	xx		o
Fe-oxide				o	o	xx	x	xx
Quartz	xxx	x		xx	o	x	o	x
Pyrite	o	x	x	xx	x	x	o	xx
Bastnäsite-(Ce)				o	o	o		
Synchisite-(Ce)		o	o	o	o	o		o
Monazite-(Ce)					o		o	x
Fluorite		xxx		o		o		
Columbite	o		o					
Albite	o				o			
Zircon	o							
Rutile	o					o		
Sphalerite	o							
Barian Orthoclase							o	o

7.1.1 Chloritised Granitic Gneiss

Chloritised granitic gneiss is a relatively dark coloured rock type with irregular shaped pinkish areas, surrounded by chlorite veins (Fig. 7-3).

Figure 7-3: Scan of a chloritised granitic gneiss polished block (Ø = 3 cm) from sample 16-80-FE. Chlorite dominates the dark areas while the pinkish patches are a mix of fine-grained quartz, calcite and apatite.

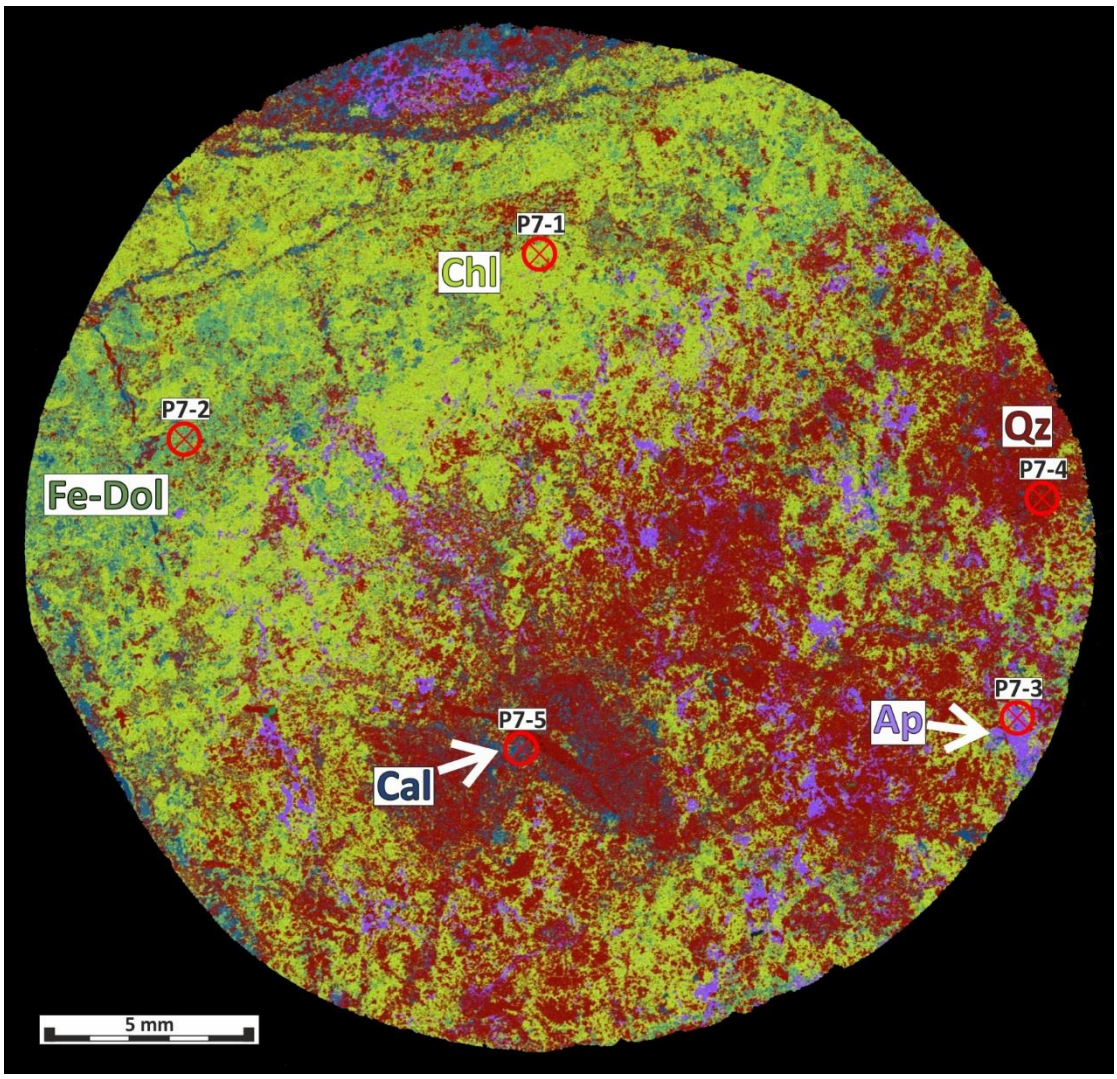

Figure 7-4: Combined large-area EDS mosaic of sample 16-80-FE in Fig. 7.3. There are two main areas visible, a chlorite-rich yellow area and a quartz-rich red area. The yellow area represents a chlorite-rich vein cutting through the quartz dominated chloritised granitic gneiss in red. Ap – Apatite, Cal – Calcite, Chl – Chlorite, Fe-Dol – Fe-Dolomite and Qz – Quartz.

The main minerals (Tab. 7-1) in the chloritised gneiss are chlorite, quartz, apatite and calcite, which occur in a complex fine-grained intergrowth (Fig. 7-4). Chlorite causes the dark colouration of the rock. The pinkish patches show a higher concentration of quartz, calcite and apatite. Black veins of chlorite and ferroan dolomite (Vein type 1 (V1) – please refer to chapter 7.1.7) crosscut the chloritised granitic gneiss.

Accessory minerals are barite, albite, zircon, columbite, TiO_2, pyrite and sphalerite; the latter is a minor component of a thin quartz vein (Vein type 2 (V2) – please refer to chapter 7.1.7). Zircons appear in chloritised gneiss as fractured subhedral crystals (Fig. 7-5) which is a distinctly different texture compared to the round poikilitic grains in chlorite veins. REE-minerals or REE-bearing minerals are not present in chloritised granitic gneiss. The obliteration of the original texture and mineralogy of the protolith makes a proper classification problematic. During the field campaign, the rock was first classified as a fenite because of the brecciated texture with pinkish patches (Fig. 7-3). The classification as chloritised granitic gneiss is supported by the fact that chlorite is rather uncommon as the main mineral in fenites (please refer to chapter 3). Additionally, there is no alkali-rich mineral (e.g., arfvedsonite, riebeckite, aegirine-augite, K-feldspar or phlogopite) — commonly present in fenites (Elliott et al., 2018) — with the chloritised granitic gneiss.

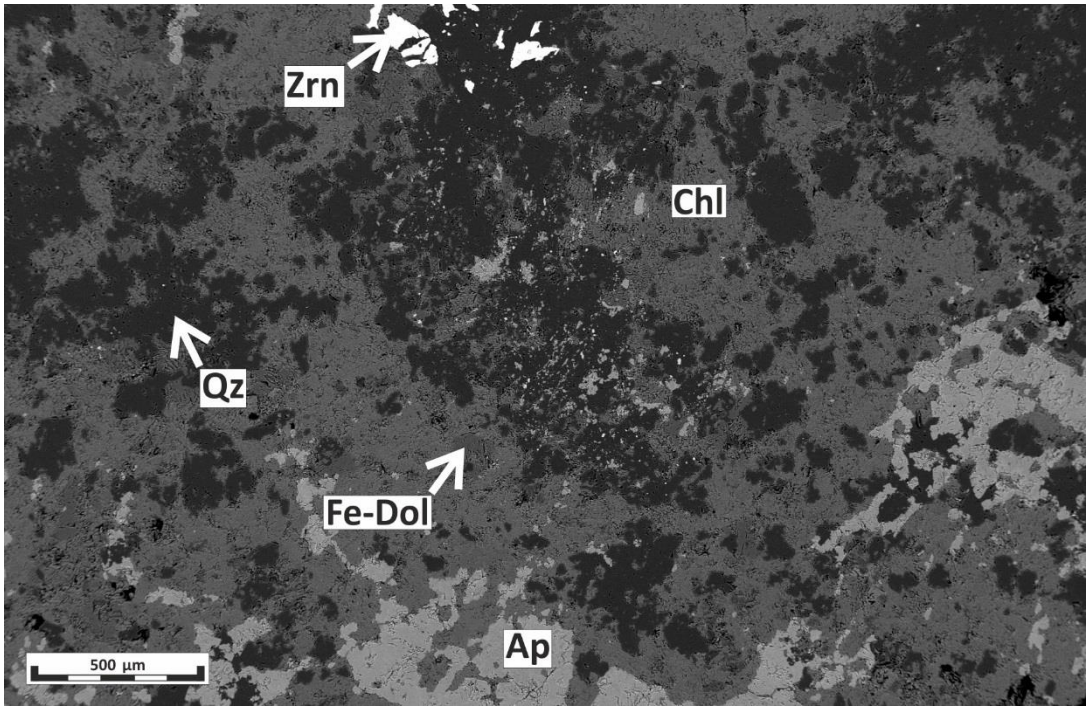

Figure 7-5: BSE-SEM image of chloritised granitic gneiss groundmass comprised of a complex heterogeneous intergrowth of chlorite (Chl), Fe-dolomite (Fe-Dol), apatite (Ap) and quartz (Qz). Zircons (Zrn) occurs as fractured anhedral crystals (16-80-FE).

Additionally, Andersen (1984; 1987 & 1989) described a chloritised granitic gneiss in the eastern part of the Fen Complex postdating the fenitisation and linking it with the A3 metasomatism (chapter 4). According to Andersen (1989a), the A3 metasomatic event was caused by groundwater-derived hydrothermal fluids infiltrating the eastern part of Fen and is seen as the reason for rødbergitisation of ferrocarbonatite.

7.1.2 Fluorite-rich Carbonatite

Fluorite mineralisation in the Fen transect occurs in the contact zone between chloritised granitic gneiss and unaltered carbonatite (Tab. 7-1). The fluorite mineralisation is visible due to its strong purple colouration (Fig. 7-6).

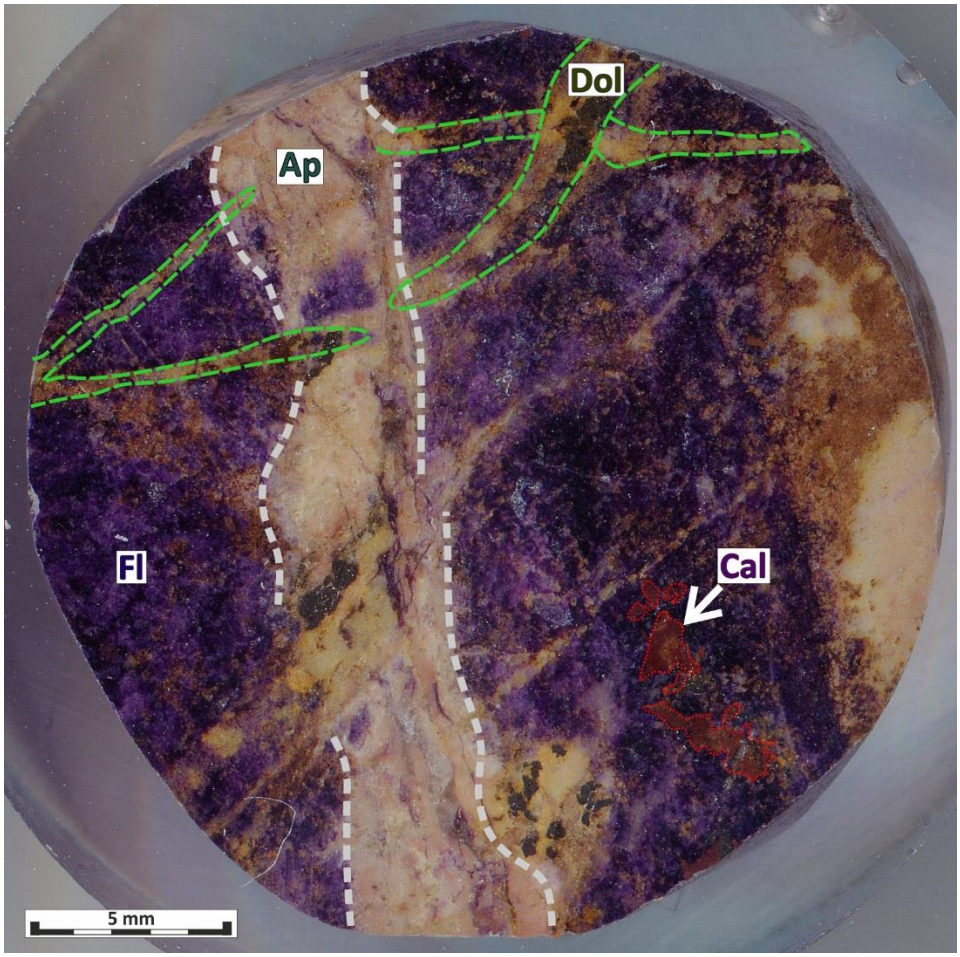

Figure 7-6: Scan of a polished block (Ø = 3 cm) showing fluorite mineralisation (purple) crosscut by two different vein generations (16-81-FE). Clusters of calcite-REE-fluorocarbonates are highlighted (transparent red area). Ap – Apatite, Cal – Calcite, Dol – Dolomite and Fl – Fluorite.

Additionally, the rock type exhibits brown to whitish coloured relics of dolomite and multiple white to ochre coloured veins. The groundmass is mainly composed of fluorite with 5-10 Vol% of dolomite and barite. The dolomite crystals show a weak preferred orientation, are homogeneously distributed within the fluorite groundmass (Fig. 7-7) and are not associated with a vein. Furthermore, the texture of dolomite crystals resembles the texture of dolomite from carbonatite I (please refer to chapter 7.1.3).

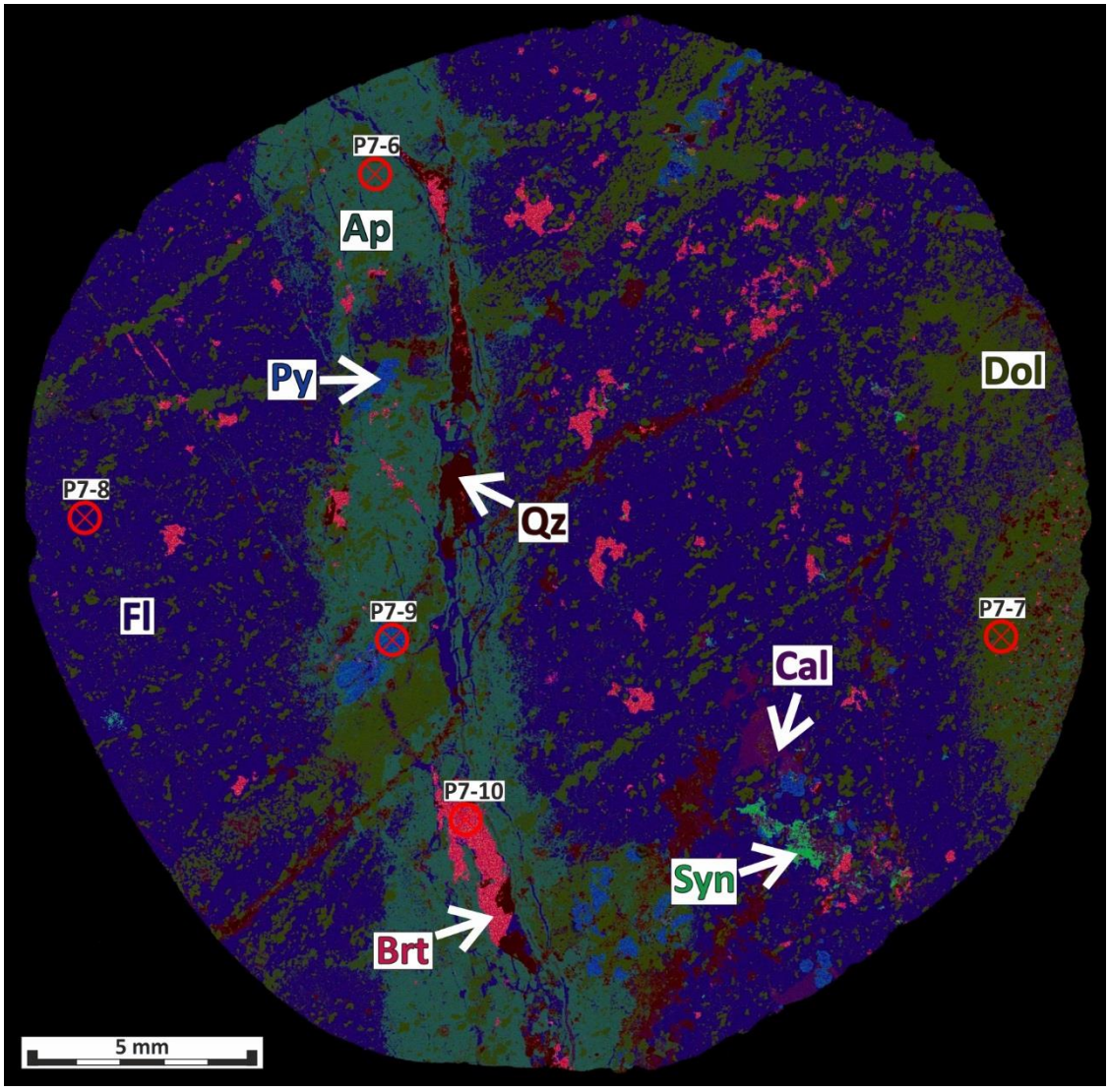

Figure 7-7: The combined large-area EDS mosaic of Fig. 7.6 reveals a complex genetic history of the fluorite mineralisation with an apatite vein, dolomite-quartz vein and barite-quartz vein cross-cutting the fluorite mineralised zone (16-81-FE). Brt – Barite, Cal – Calcite, Dol – Dolomite, Fl – Fluorite, Py – Pyrite, Qz – Quartz and Syn – Synchysite-(Ce).

Barite, on the other hand, forms irregular clusters with spatial affinity to veins and is, therefore, part of the alteration mineral assemblage. The whitish apatite vein (Vein type 3 (V3) – please refer to chapter 7.1.7) is up to 5 mm thick (Fig. 7-6). A detailed EDS-BSE map reveals a thin central part of barite, quartz and apatite within the apatite vein (Fig. 7-8). The outer rim of the apatite vein shows relics of groundmass dolomite, which indicates the formation of a vein salvage as opposed to a fracture-filling vein. Minor amounts of fine-grained synchysite-(Ce) are in the centre of the vein, intergrown with barite and quartz. The second set of whitish-yellowish veins (Vein type 4 (V4) – please refer to chapter 7.1.7) of 0.5 to 2 mm thickness can be distinguished (Fig. 7-6). The second set of veins comprises dolomite with minor quartz and sporadic pyrite clusters (Fig. 7-7, Fig. 7-8).

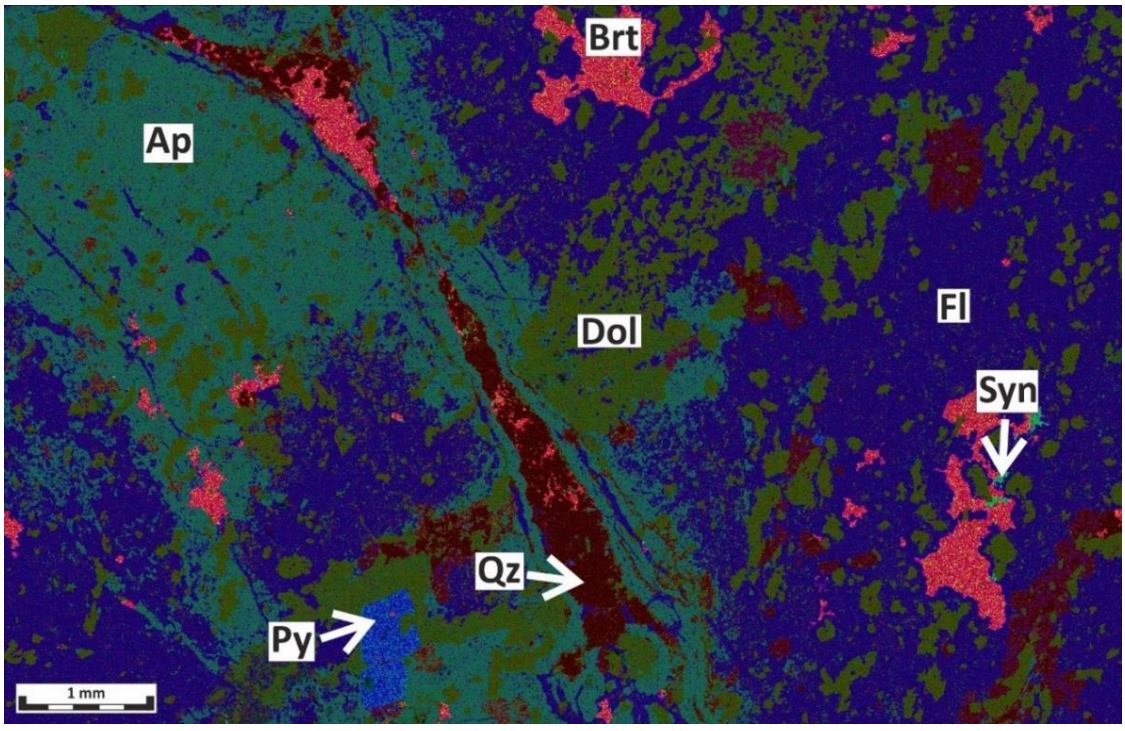

Figure 7-8: A blown-up section of the combined large-area EDS mosaic shows an area where all the main vein types are visible. The apatite vein is several mm wide with a homogenous distribution of dolomite crystals. Dolomite veins are discontinuous, with varying thickness and cross-cut the apatite vein. The quartz-barite vein runs along the centre of the apatite vein and cross-cuts the dolomite veins. A small amount of synchysite-(Ce) is associated with the barite clusters and the quartz-barite vein (16-81-FE). Ap – Apatite, Brt – Barite, Dol – Dolomite, Fl – Fluorite, Py - Pyrite and Qz – Quartz.

The dolomite vein seems to cross cut the apatite veins for the most part but does not cut through the central part of barite and quartz

Red coloured clusters of calcite-synchysite-(Ce) are randomly distributed within the fluorite groundmass (Fig. 7-6) with no apparent genetic relationship to the apatite or dolomite veins (Fig. 7-7). These clusters are up to 2 mm in size and have the highest concentration of REE minerals in the fluorite sample (Fig. 7-9). Synchysite-(Ce) and calcite are in a complex intergrowth, which indicates co-precipitation of the two mineral phases (Fig. 7-10; Fig. 7-11).

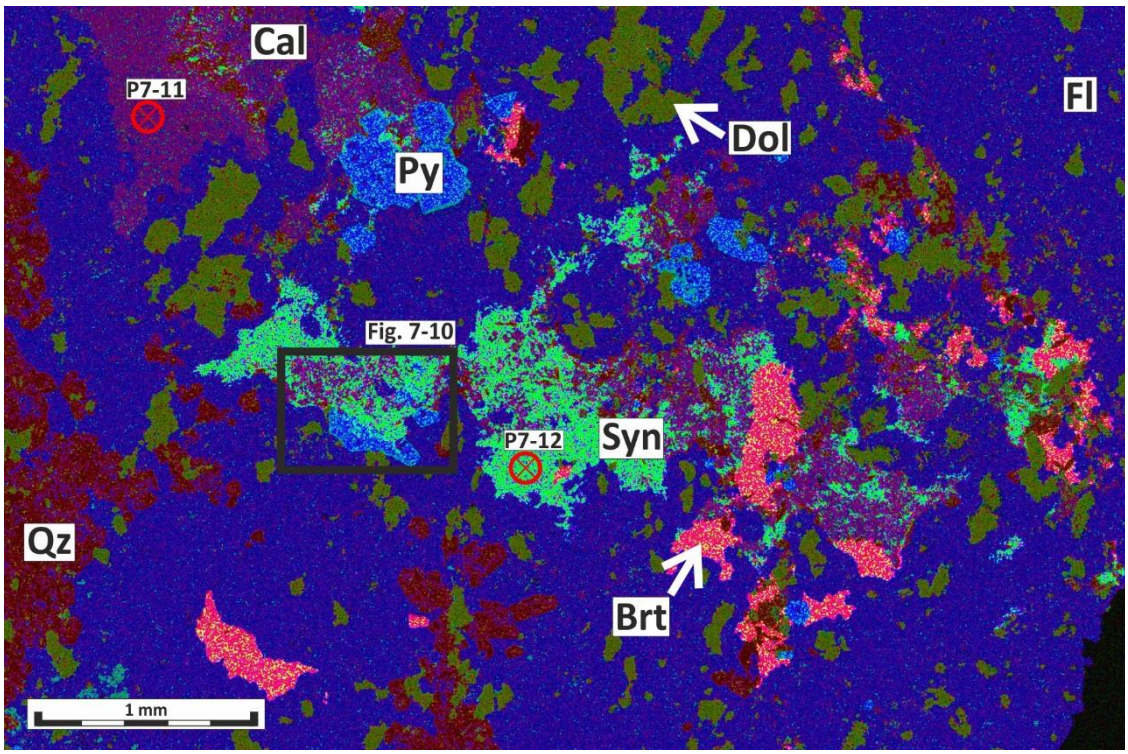

Figure 7-9: A blown up section of the combined large-area EDS mosaic (Fig 7.7), showing a complex intergrowth of synchysite-(Ce) and calcite (16-81-FE).Ap – Apatite, Brt – Barite, Cal – Calcite, Dol – Dolomite, Fl – Fluorite, Py – Pyrite, Qz – Quartz and Syn – Synchysite-(Ce).

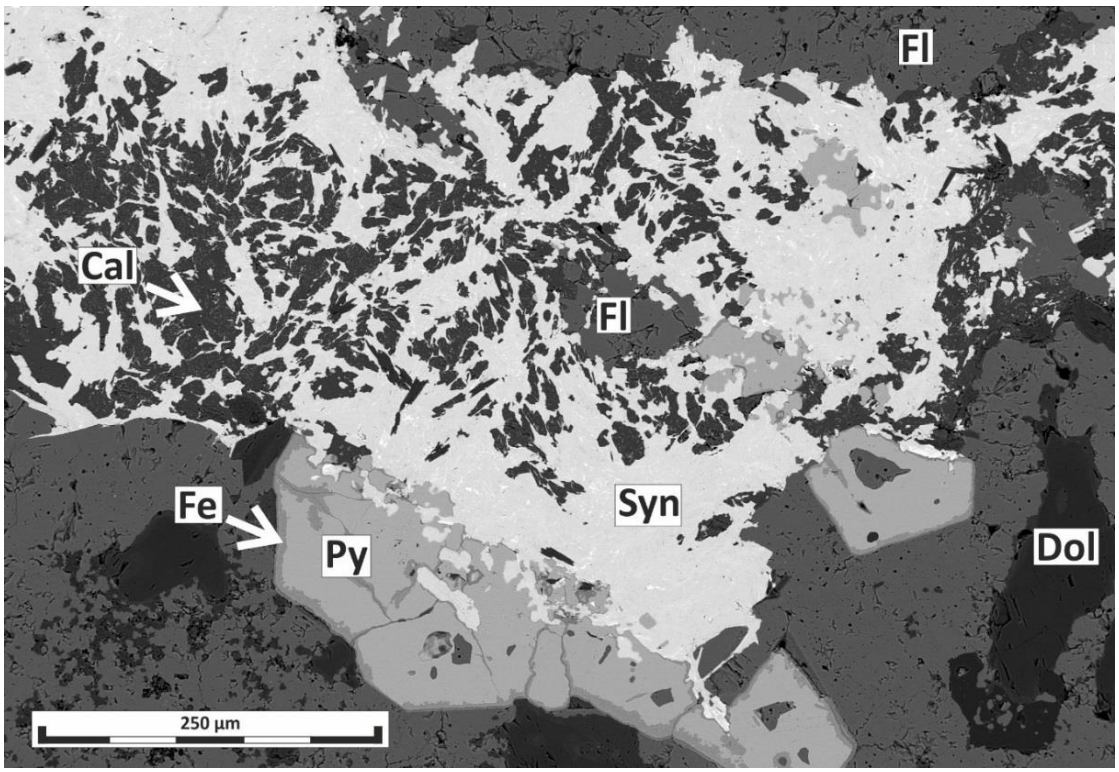

Figure 7-10: A blown-up BSE-SEM image section of the combined large-area EDS mosaic (Fig 7.9), showing the replacement of fluorite and pyrite by the synchysite-(Ce) – calcite cluster (16-81-FE). Ap – Apatite, Brt – Barite, Cal – Calcite, Dol – Dolomite, Fl – Fluorite, Py – Pyrite, Qz – Quartz and Syn – Synchysite-(Ce).

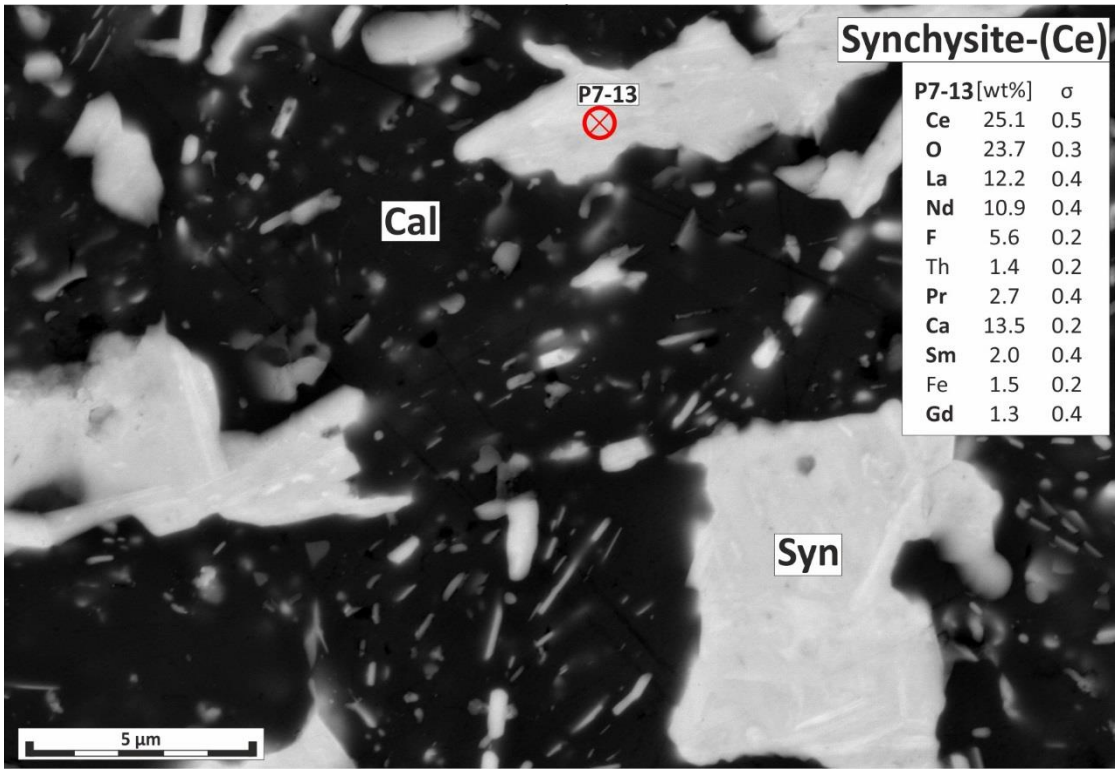

Figure 7-11: A blown-up BSE-SEM image section (Fig 7.10), showing the complex intergrowth of synchysite-(Ce) and calcite (16-81-FE). Cal – Calcite and Syn – Synchysite-(Ce).

7.1.3 Dolomite-Carbonatite

Dolomite-carbonatite shows no sign of rødbergitisation (Fig. 7-12A) or is weakly influenced in contact with rødbergitised other lithotypes (Fig. 7-12B). Dolomite-carbonatite mainly comprises of ferroan dolomite, dolomite, apatite, and pyrite with minor amounts of barite, quartz, columbite, Fe-oxide and REE-fluorocarbonates (Tab. 7-1; Fig. 7-13).

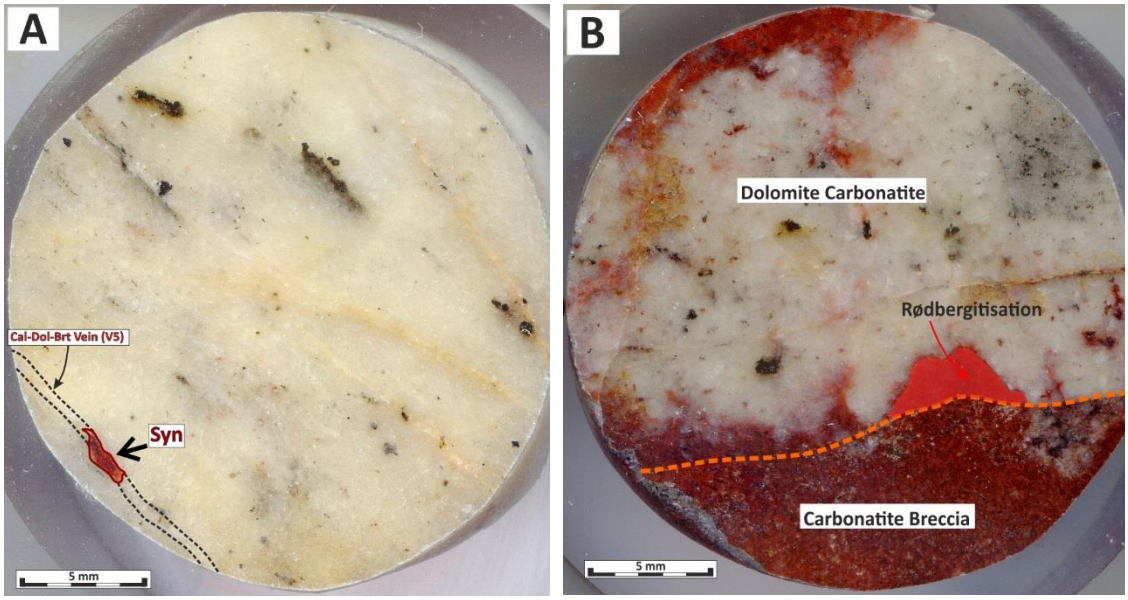

Figure 7-12: A: Scan of a polished block (Ø = 3 cm) of an unaltered carbonatite with white carbonate and greyer translucent apatite (16-84-FE). The opaque minerals, e.g., pyrite, are showing a preferred orientation. B: Scan of a polished block of an unaltered dolomite-carbonatite in sharp contact with a heterogeneous carbonatite breccia, which is mineralogically similar to the chlorite-bearing dolomite carbonatite (16-85-FE). The carbonatite breccia has a red colouration due to rødbergitisation. The precipitation of Fe-oxide stops almost completely at the contact between both carbonatites marked by a dashed orange line.

Apatite forms weakly undulating elongated aggregates and disrupted layers with a strong preferred orientation (Fig. 7-13; Fig. 7-14). Pyrite forms subhedral to euhedral cubes that are solitary or part of elongated aggregates with similar orientations as the apatite layers (Fig. 7-13).

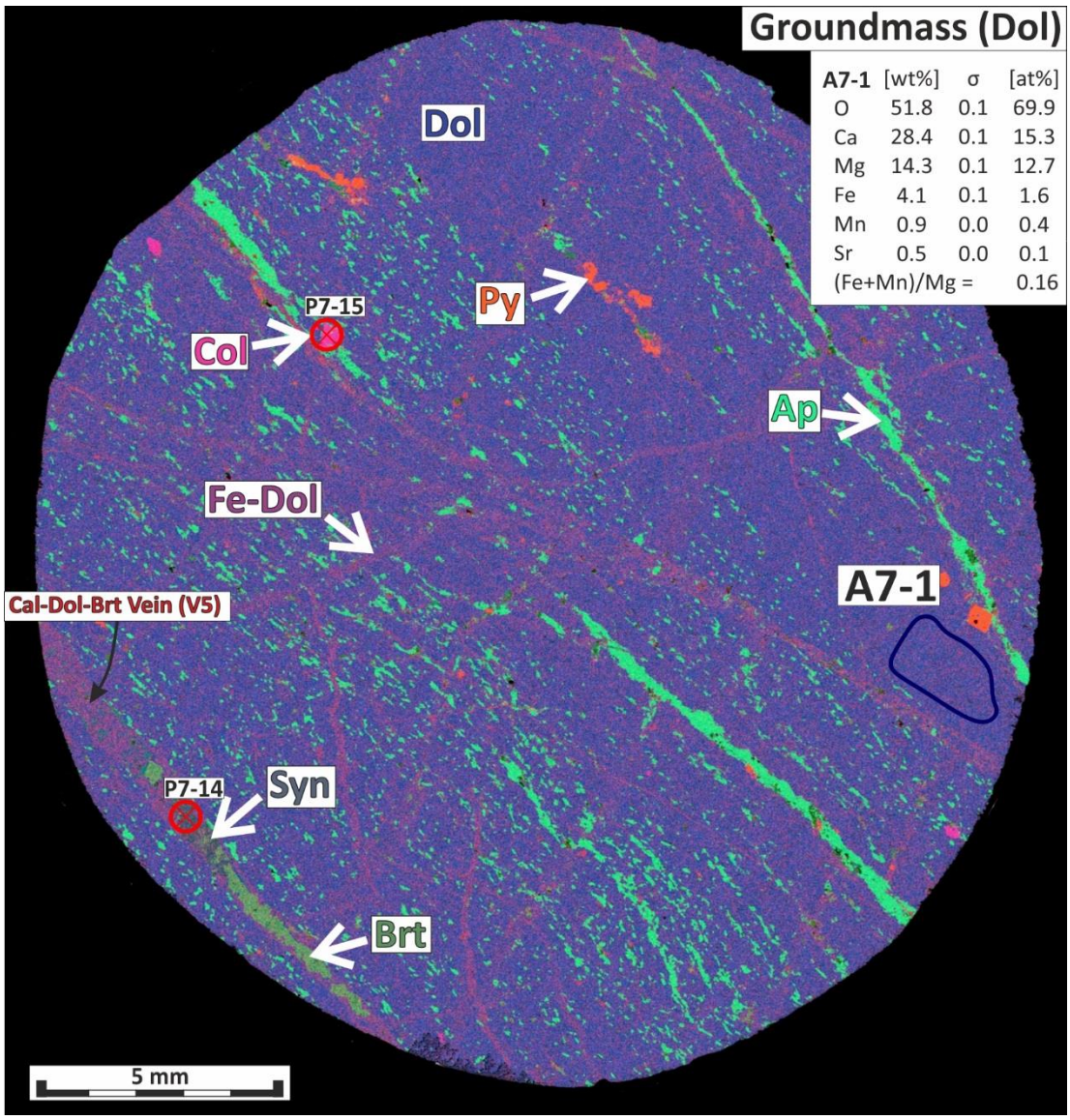

Figure 7-13: The combined large-area EDS mosaic of Fig. 7.12A shows undulating apatite layers with preferred orientation in a groundmass of dolomite. The apatite layers are internally disrupted and cross-cut by an irregular network of ferroan dolomite veins. The chemical composition of the dolomite groundmass — A7-1 (marked with a blue line) — was reconstructed for a homogeneous area using the EDS-LAM (16-84-FE). Ap – Apatite, Brt – Barite, Col – Columbite, Dol – Dolomite, Fe-Dol – Ferroan Dolomite, Py – Pyrite and Syn – Synchysite-(Ce).

A network of randomly oriented ferroan dolomitic to ankeritic veins (Vein type 10 (V10) – please refer to chapter 7.1.7) cut through the dolomitic to ferroan dolomitic groundmass (Fig. 7-13; Fig. 7-14; Fig. 7-15). The Fe concentration of the carbonate minerals in veins is always higher than the Fe concentration of the groundmass carbonates. The density of these Fe-rich carbonate vein networks varies, and veins can make up to 20 Vol% of the sample (Fig. 7-15).

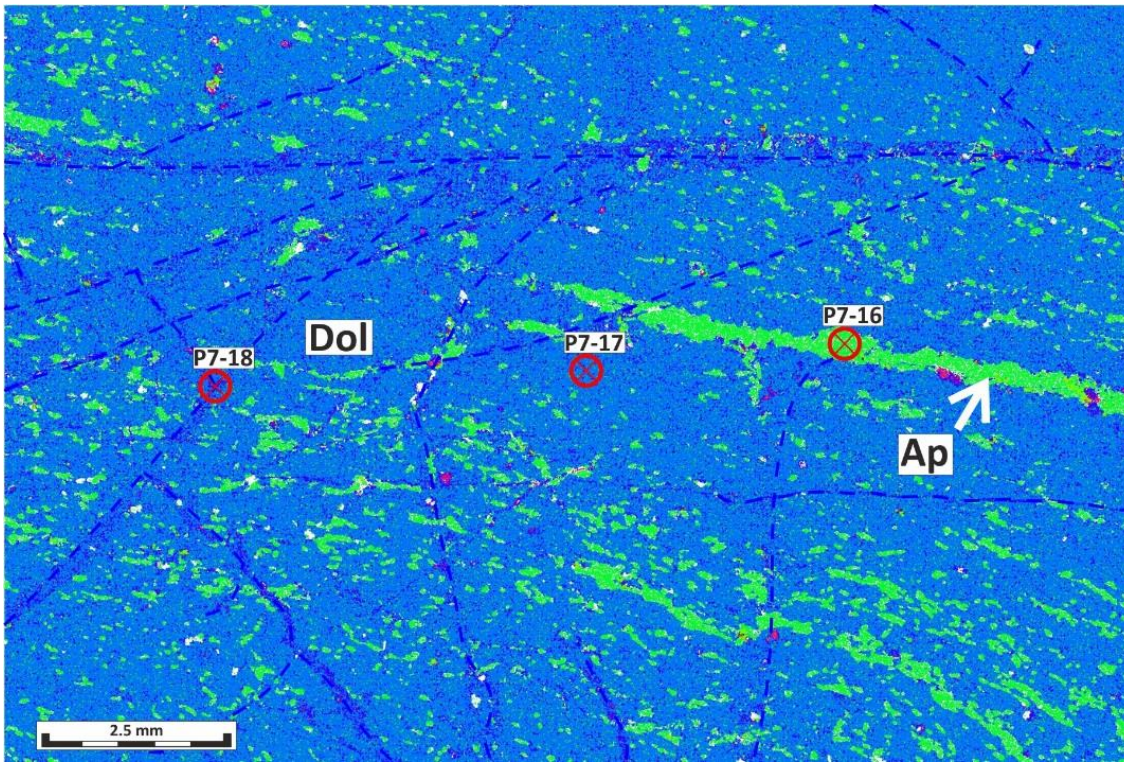

Figure 7-14: The enlarged view of Fig. 7.13 illustrates the undulating apatite layers and highlights the network of ferroan dolomite veins with dashed blue lines (16-84-FE). Ap – Apatite and Dol – Dolomite.

Besides the fine network of Fe-dolomite veinlets (V10), there are four other vein types. Calcite-dolomite-barite veins (V5) with a significant amount of red coloured synchysite-(Ce) (Fig. 7-13). Quartz veins (V6) with an irregular intergrowth of quartz, hematite, barite, apatite and REE-fluorocarbonates (Fig. 7-15; Fig. 7-16). Pyrite-ankerite veins (V7) comprising euhedral pyrite in a groundmass of ankerite and quartz with subordinate amounts of REE-fluorocarbonates (Fig. 7-15; Fig. 7-17). Apatite-barite veins (V8) with minor amounts of quartz, apatite, chlorite, monazite-(Ce) and REE-fluorocarbonates (Fig. 7-18; Fig. 7-19; Fig. 7-20; Fig. 7-21). Please refer to chapter 7.1.7 for more information on the different vein types.

The concentration of barite in the dolomite-carbonatite groundmass significantly increased towards the contact with rødbergite (Fig. 7-18). Chlorite occurs intergrown with irregular-shaped apatite (V8) as well as barite (Fig. 7-19). Similar to barite, the chlorite concentration increases towards the contact with rødbergite (Fig. 7-18).

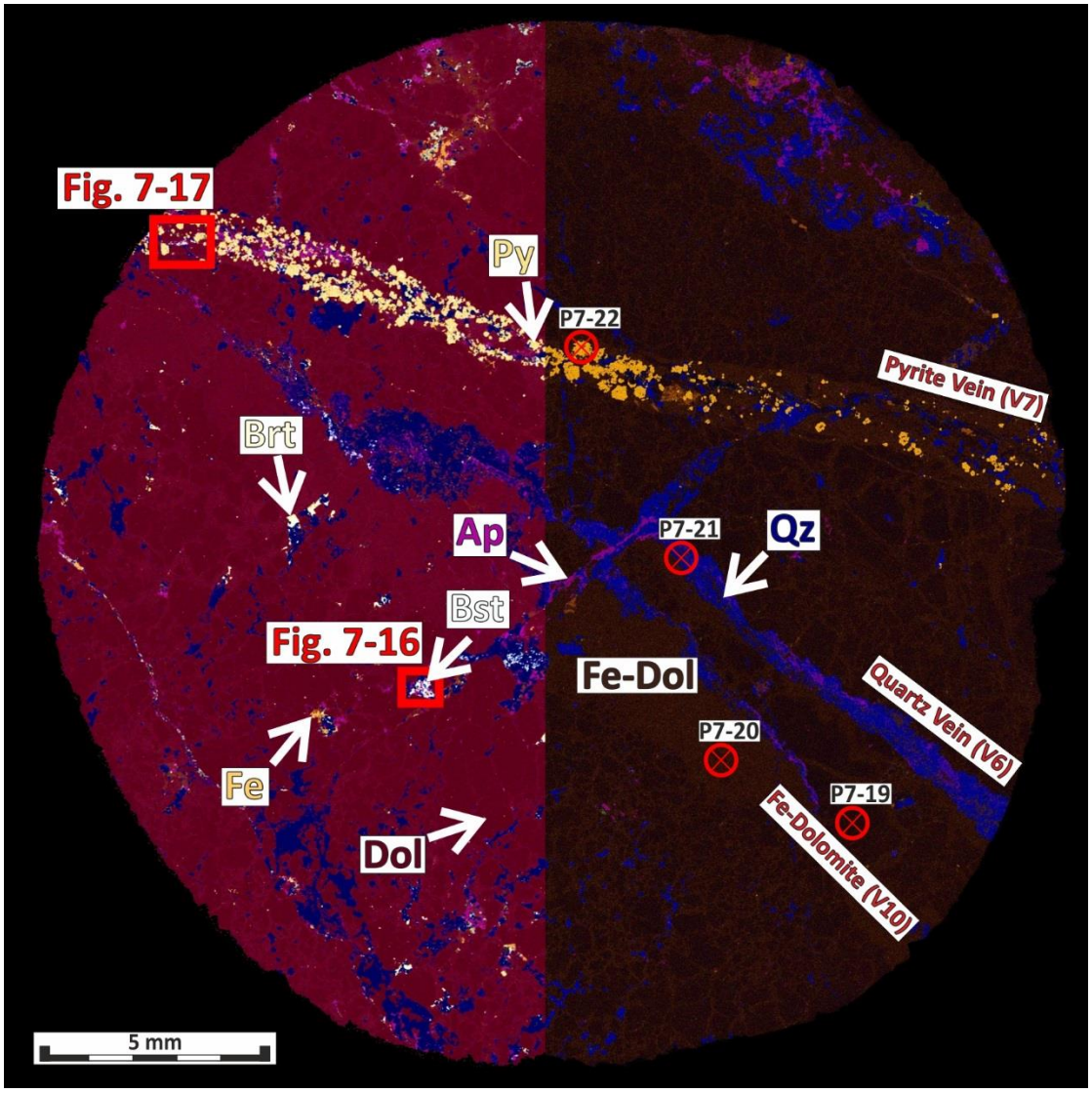

Figure 7-15: The combined large-area EDS with two different colour settings. The left part of the image is the standard colouration, and the right part has a different colour set to highlight the network of ferroan dolomite veinlets (16-96-FE). Pyrite- (V7), quartz- (V6) and Fe-dolomite veins (V10) are annotated. Additionally, Fig. 7-16 and Fig. 7-17 are marked by a red frame. Ap – Apatite, Brt – Barite, Bst – Bastnäsite, Dol – Dolomite, Fe – Fe-oxide, Fe-Dol – Ferroan Dolomite, Py – Pyrite and Qz – Quartz.

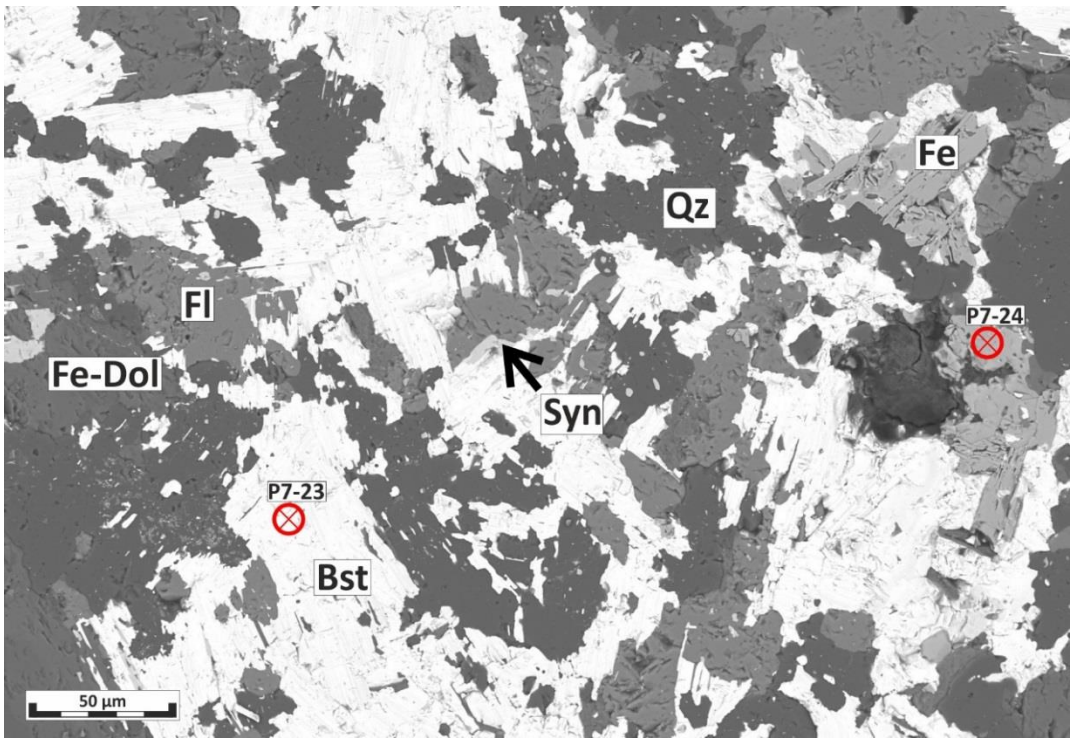

Figure 7-16: A magnified BSE-SEM section of a quartz vein (V6) showing a cluster of bastnäsite-(Ce), fluorite, quartz and hypidiomorphic blades of Fe-oxide (16-96-FE). Ap – Apatite, Bst – Bastnäsite-(Ce), Fe – Fe-oxide, Fe-Dol – Fe-Dolomite, Qz – Quartz and Syn – Synchysite-(Ce).

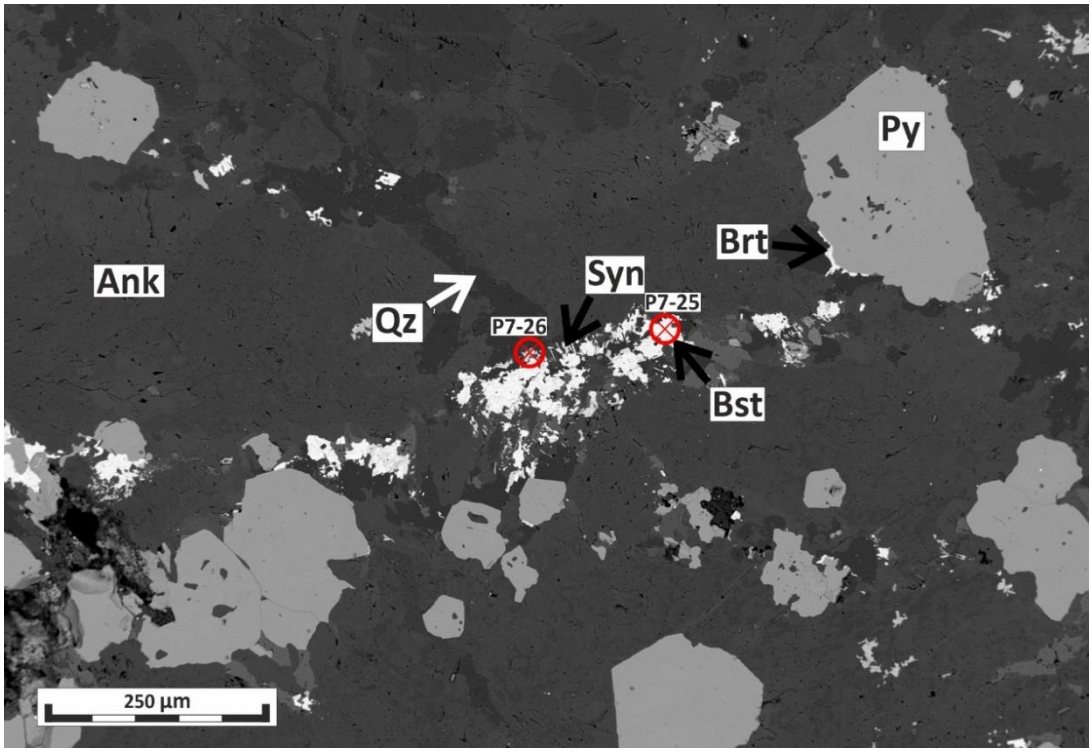

Figure 7-17: A magnified BSE-SEM section of a pyrite vein (V7) showing bastnäsite-(Ce)-synchysite-(Ce) aggregates as minor component of the vein assemblage (16-96-FE). Ank – Ankerite, Brt – Barite, Bst – Bastnäsite-(Ce), Py – Pyrite, Qz – Quartz and Syn – Synchysite-(Ce).

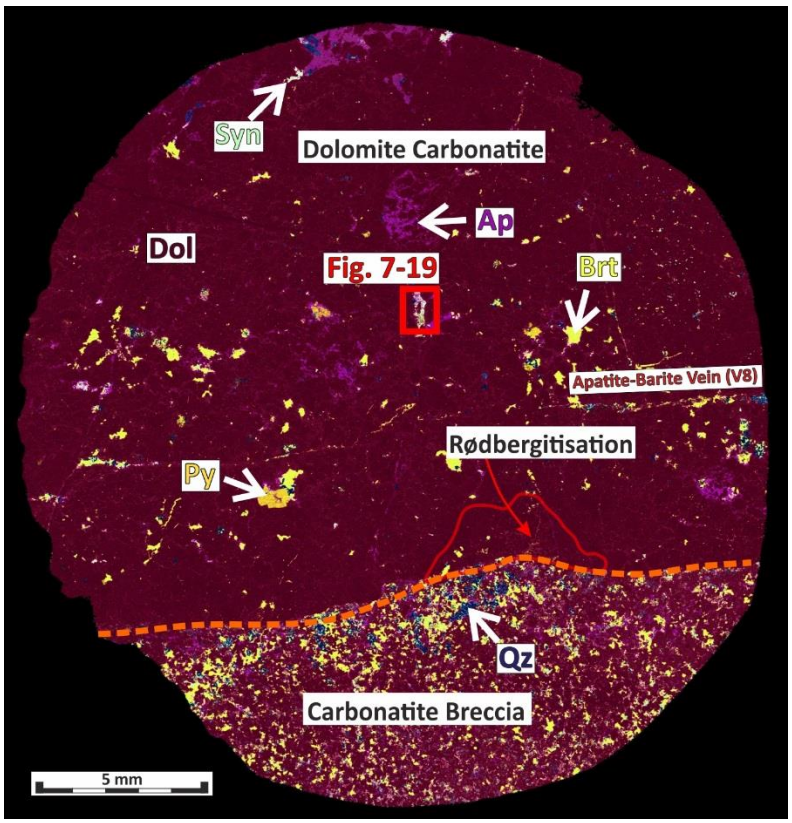

Figure 7-18: The combined large-area EDS mosaic of Fig. 7.12B. The heterogeneous carbonatite breccia is characterised by smaller crystal size and a higher proportion of non-carbonate phases, barite in particular. The dolomite-carbonate has a higher concentration of hydrothermal barite proximal to the carbonatite breccia (16-85-FE). Apatite-barite veins (V8) are annotated, and a red frame marks Fig. 7-19, which represents a synchysite-(Ce)-rich section of V8. Ap – Apatite, Brt – Barite, Dol – Dolomite, Py – Pyrite, Qz – Quartz and Syn – Synchysite-(Ce).

Depending on the sample, the most dominant REE mineral is either synchysite-(Ce) or bastnäsite-(Ce). Synchysite-(Ce) forms elongated clusters in intergrowth with chlorite (Fig. 7-19; Fig. 7-20). These clusters are up to 3 mm long and are in loose association with apatite-barite veins (V8) and Fe-dolomite veinlets (V10). Locally, synchysite-(Ce) is replaced by monazite-(Ce) and barite (Fig. 7-21). Red clusters (0.5 x 2.0 mm) of synchysite-barite are part of calcite-dolomite-barite veins (V5) (Fig. 7-12A). Bastnäsite-(Ce) occurs in quartz veins (V6) (Fig. 7-15; Fig. 7-16) and pyrite veins (V7) (Fig. 7-15; Fig. 7-17) — individual crystals in quartz veins are generally less than 200 µm in size (Fig. 7-16).

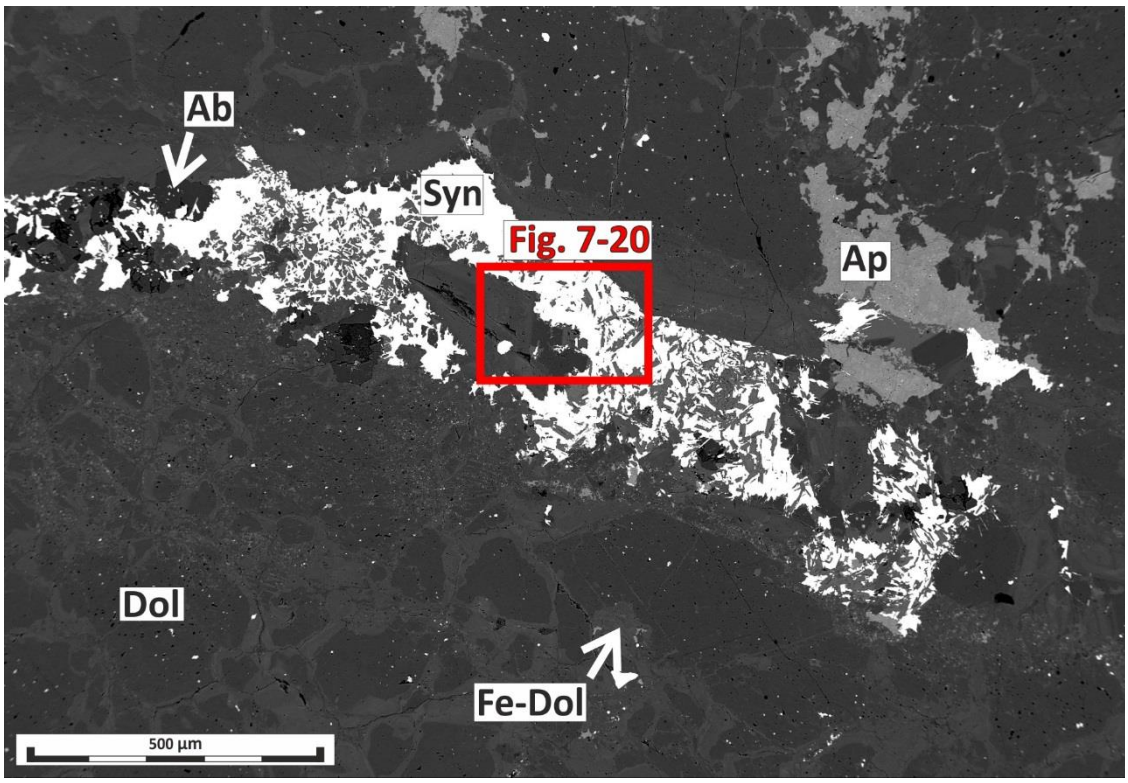

Figure 7-19: A magnified BSE-SEM section of Fig. 7-18 is showing a synchysite-(Ce) cluster as part of an apatite-barite vein (V8) within dolomite-carbonatite (16-85-FE). Note the brecciation of the dolomite groundmass by a fine network of ferroan dolomite (V10). Ab – Albite, Ap – Apatite, Dol – Dolomite, Fe-Dol – Ferroan Dolomite and Syn – Synchysite-(Ce).

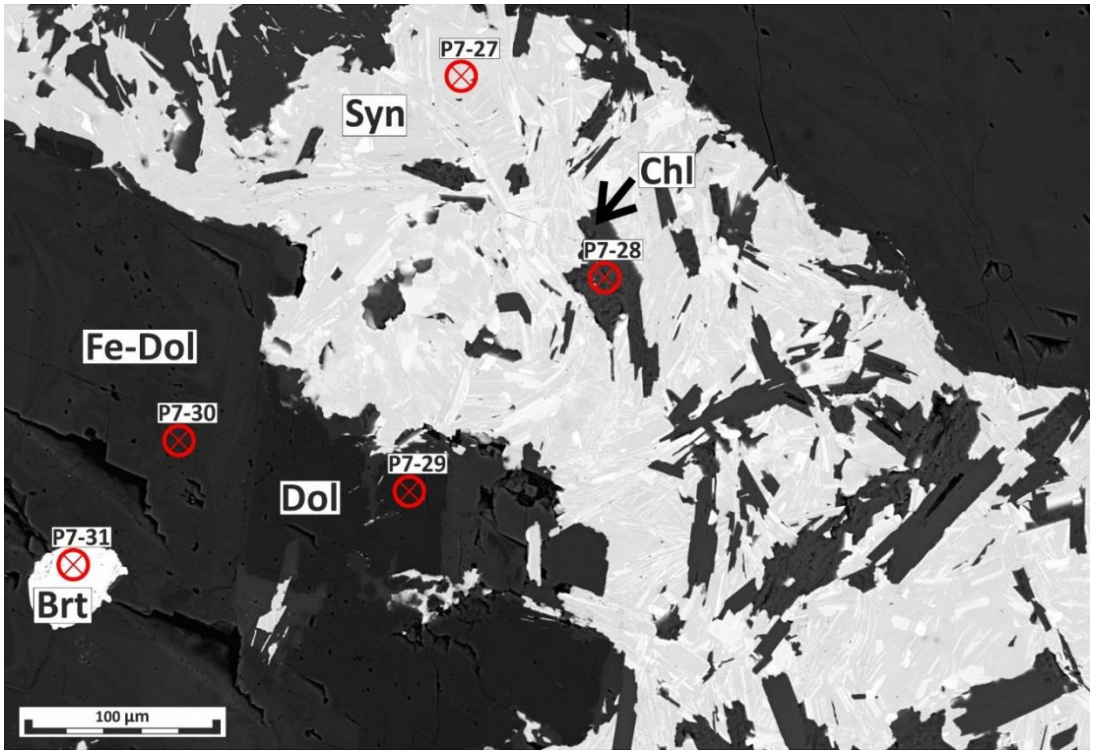

Figure 7-20: A magnified BSE-SEM section of Fig. 7-19 is illustrating the intergrowth of synchysite-(Ce) and hypidiomorphic chlorite blades as part of an apatite-barite vein (V8) (16-85-FE). Brt – Barite, Chl – Chlorite, Dol – Dolomite, Fe-Dol – Ferroan Dolomite and Syn – Synchysite-(Ce).

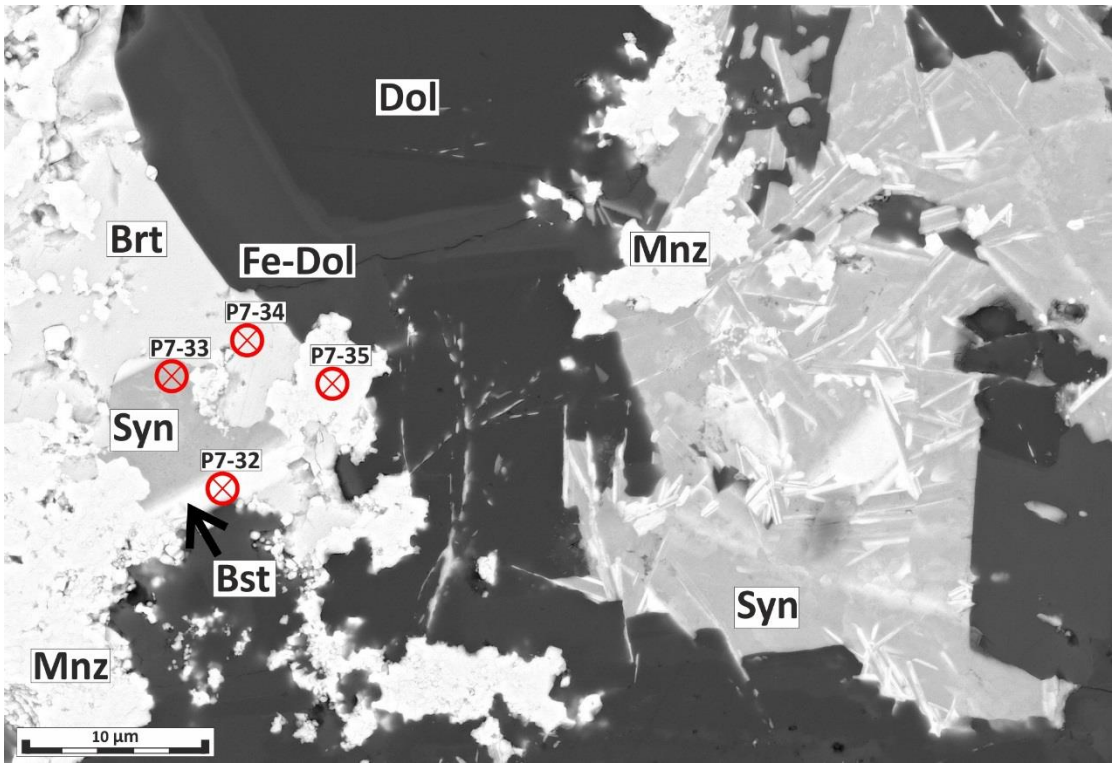

Figure 7-21: A BSE-SEM image of a sheet-like synchysite-(Ce) with minor bastnäsite-(Ce). The REE-fluorocarbonates are being replaced by barite and monazite-(Ce) aggregates. (16-85-FE). Brt – Barite, Bst – Bastnäsite-(Ce), Dol – Dolomite, Fe-Dol – Ferroan Dolomite, Mnz – Monazite-(Ce) and Syn – Synchysite-(Ce).

7.1.4 Chlorite-bearing Dolomite-Carbonatite

Figure 7-22: Scan of a polished block of a heterogeneous chlorite-bearing dolomite-carbonatite (16-95-FE).

The second carbonatite variety is a dark coloured chlorite-bearing dolomite-carbonatite with little or no sign of rødbergitisation (Fig. 7-22). The mineral composition is similar to the dolomite-carbonatite (Tab. 7-1) with a significantly higher amount of chlorite and higher Fe concentration of the ferroan dolomite —

$$\left(\frac{Fe+Mn}{Mg}\right)_{\text{dolomite-carbonatite}} = 0.16 \; < \; \left(\frac{Fe+Mn}{Mg}\right)_{\substack{\text{chlorite-bearing}\\ \text{dolomite-carbonatite}}} = 0.48$$

(A7-1; Fig. 7-13; A7-2; Fig. 7-23). Chlorite-bearing dolomite-carbonatite is comprised of ferroan dolomite, ankerite, chlorite, apatite, Fe-oxides, quartz, pyrite with minor amounts of fluorite, barite, bastnäsite-(Ce) and synchysite-(Ce) (Tab.7-1).

Hydrothermal apatite occurs as irregularly shaped clusters (ø ca. 1 cm) intergrown with chlorite and Fe-oxide (Fig. 7-23). These clusters have a poikilitic texture with inclusions of ferroan dolomite. Locally, apatite relics thin out and become part of a quartz vein (V9 – please refer to chapter 7.1.7). Pyrite is present in the form of euhedral to subhedral solitary cubes and aggregates (Fig.7-23). Clusters of Fe-oxide (< ø 0.3 cm) show a poikilitic texture comparable to the apatite clusters. Additionally, they have inclusions of small barite crystals (< 5 µm) and are in intergrowth with ankerite (7-24).

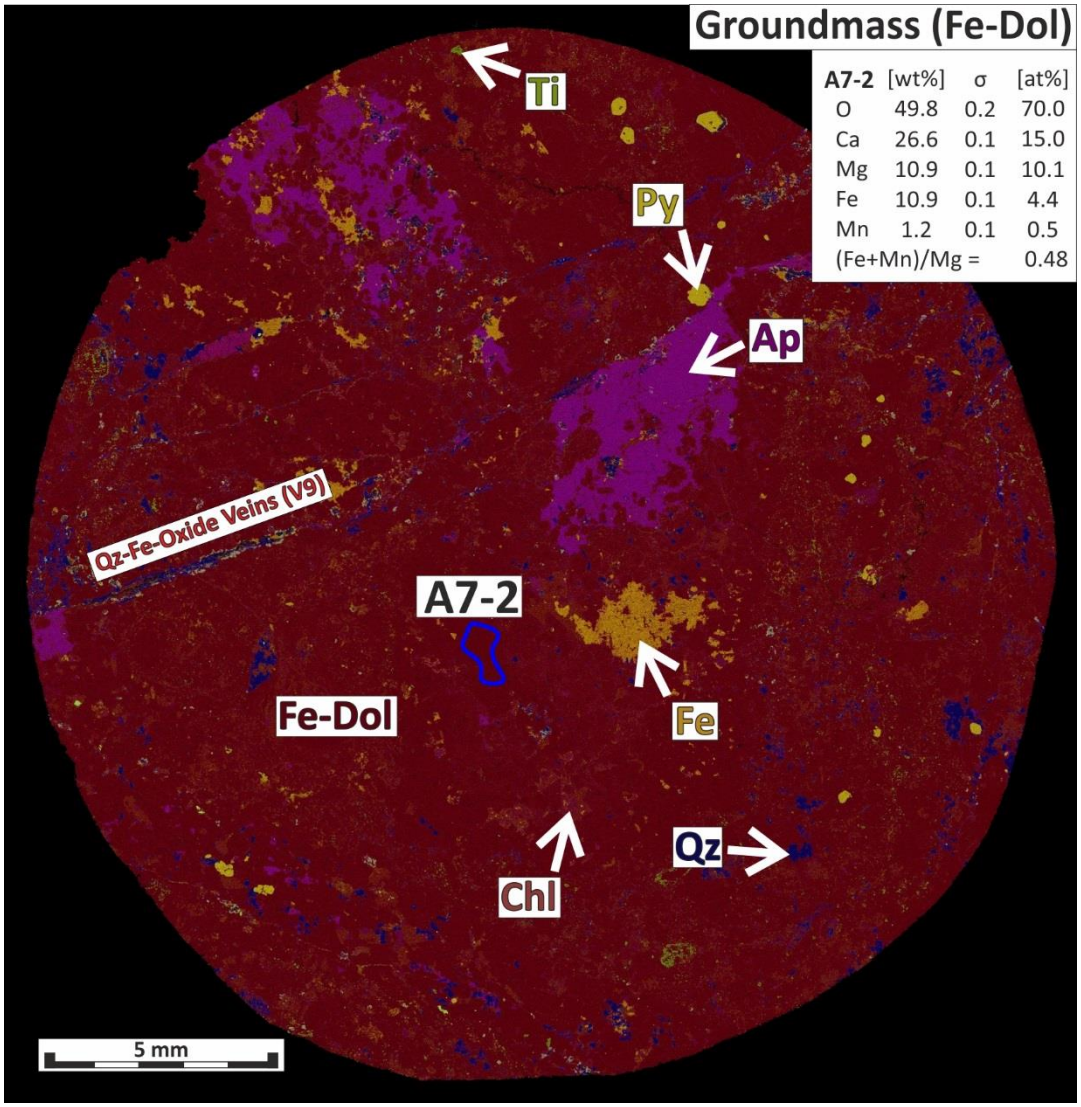

Figure 7-23: The combined large-area EDS mosaic of Fig. 7.25 (16-95-FE).The chemical composition of the ferroan dolomite groundmass — A7-2 (marked with a blue line) — was reconstructed for a homogeneous area using the EDS-LAM. Ap – Apatite, Chl – Chlorite, Fe – Fe-oxide, Fe-Dol – Ferroan Dolomite, Py – Pyrite, Qz – Quartz and Ti – Ti-oxide.

Chlorite with minor quartz and barite has precipitated as a fine network in interstitial areas permeating through the whole rock, resulting in the dark colouration of the carbonatite. Chlorite-bearing dolomite-carbonatite is cross-cut by parallel veinlets (V9), containing quartz, hematite, chlorite, apatite and barite (Fig. 7-23). The dominant REE minerals are bastnäsite-(Ce) and synchysite-(Ce) in the form of stacked sheets in variable proportions of the individual minerals (Fig. 7-24; Fig. 7-25). These stacks are 50 – 200 µm

in size with a subhedral shape and show clear signs of alteration. Some crystals have a poikilitic texture with a high concentration of apatite inclusions (Fig. 7-26, Fig. 7-27).

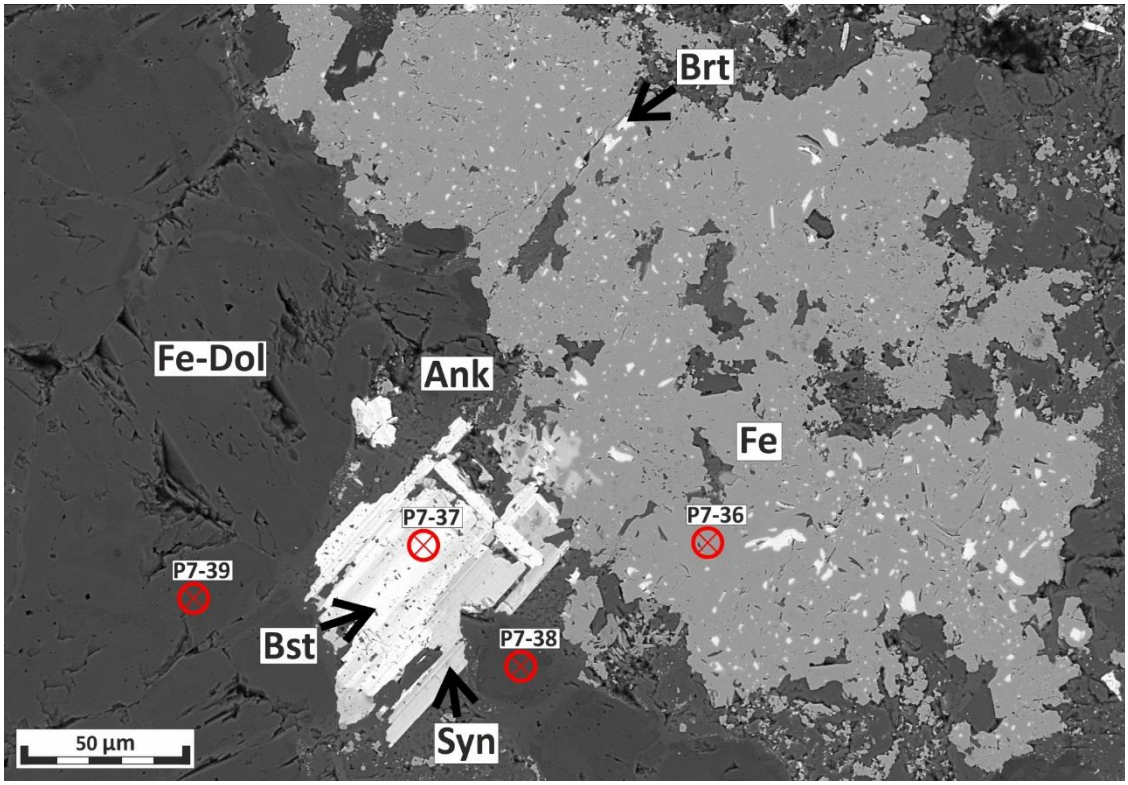

Figure 7-24: A BSE-SEM image of sheeted bastnäsite-(Ce) - synchysite-(Ce) crystal in the vicinity of an Fe-oxide cluster with small (<5 µm) barite inclusions. The stack of REE-fluorocarbonates displays straight edges as well as rigid edges indicating partially replacement by the surrounding groundmass (16-95-FE). Ank – Ankerite, Bst – Bastnäsite-(Ce), Brt – Barite, Fe – Fe-oxide, Fe-Dol – Ferroan Dolomite and Syn – Synchysite-(Ce).

In turn, the apatite inclusions contain Fe-oxide inclusions. The shape and texture are distinctly different from the other forms of REE-fluorocarbonates described in the Fen transect and the Bjørndalen transect. REE-fluorocarbonates are in proximity or direct contact with Fe-oxides and are surrounded by ankerite as part of the Fe-oxide mineral assemblage, which is distinctly different from the ferroan dolomite groundmass of the carbonatite (Fig. 7-24).

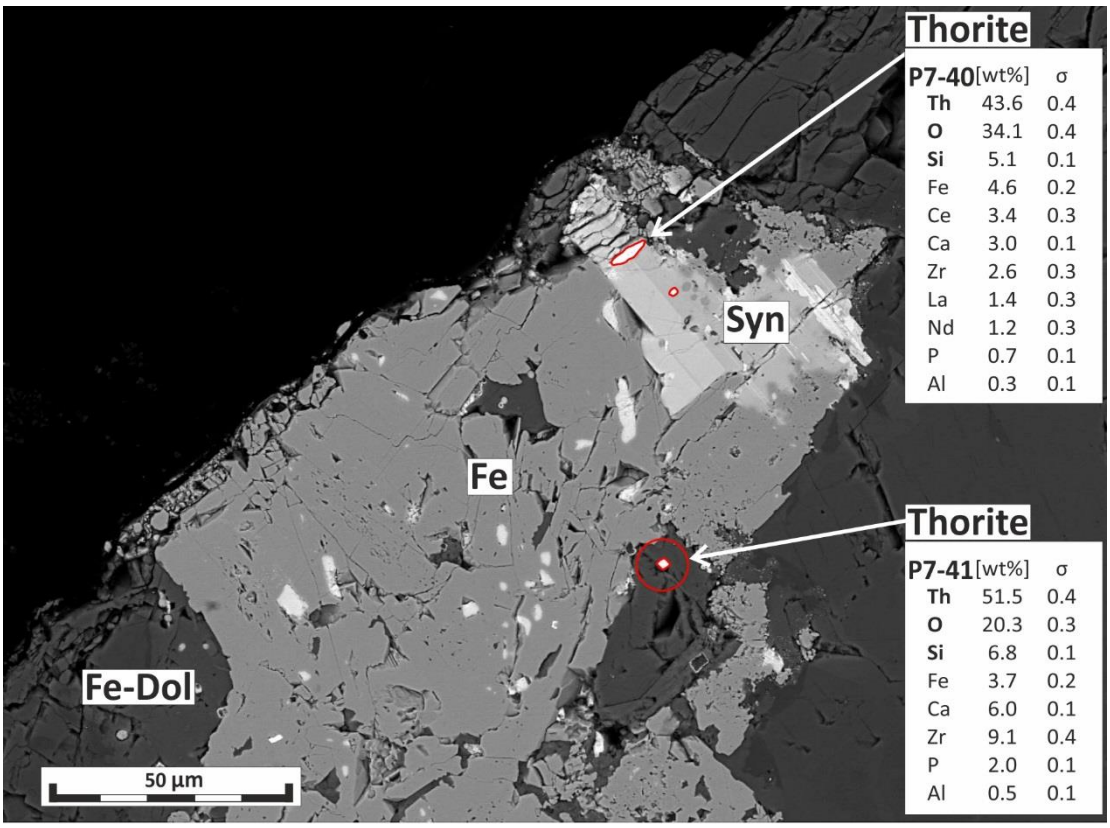

Figure 7-25: A BSE-SEM image of Fe-oxide cluster with a sheeted bastnäsite-(Ce) - synchysite-(Ce) crystal (50 x 75 µm) and many irregulars formed pieces of smaller (50 x 75 µm) REE-fluorocarbonates. Thorite occurs as small idiomorphic crystals within the ferroan dolomite groundmass and as an inclusion with the REE-fluorocarbonates. The EDS point analysis of thorite shows impurities of Fe, REE and Ca from the surrounding minerals.

The REE-fluorocarbonate crystals show a euhedral shape towards the hydrothermal Fe-oxide-ankerite assemblage and a completely irregular shape towards the ferroan dolomite groundmass (Fig. 7-24). Occasionally, bastnäsite-(Ce) and synchysite-(Ce) contain 1 – 5 wt% of Th and inclusions of thorite (Fig. 7-25).

Thorite is the only Th-mineral present at the Fen Road transect and occurs either as idiomorphic cubes (< 2 µm) or as inclusion in REE-fluorocarbonates (0.5 – 10 µm) (Fig. 7-27). Thorite is associated with the alteration mineral paragenesis of Fe-oxide, chlorite and REE-fluorocarbonate.

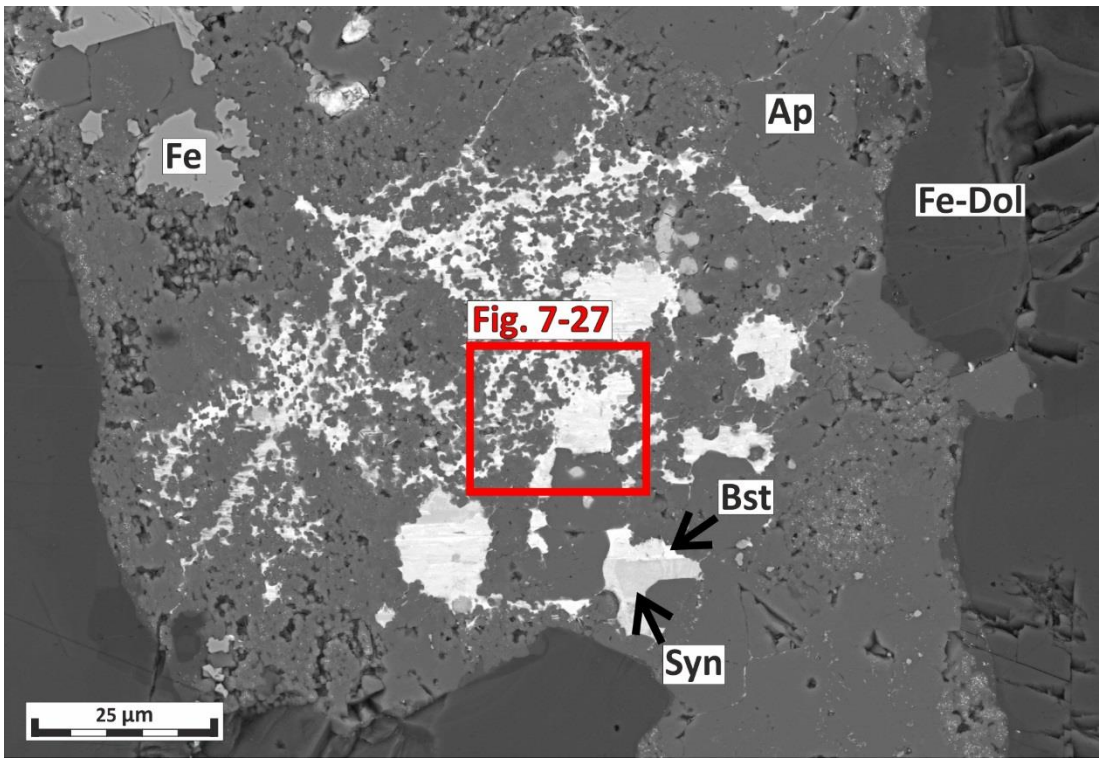

Figure 7-26: A BSE-SEM image of bastnäsite-(Ce) with minor synchysite-(Ce) within an apatite vein. The outline of the REE-fluorocarbonates is rigid, and the crystal partially displays a Swiss-cheese texture (16-95-FE). Ap – Apatite, Bst – Bastnäsite-(Ce), Fe – Fe-oxide, Fe-Dol – Ferroan Dolomite and Syn – Synchysite-(Ce).

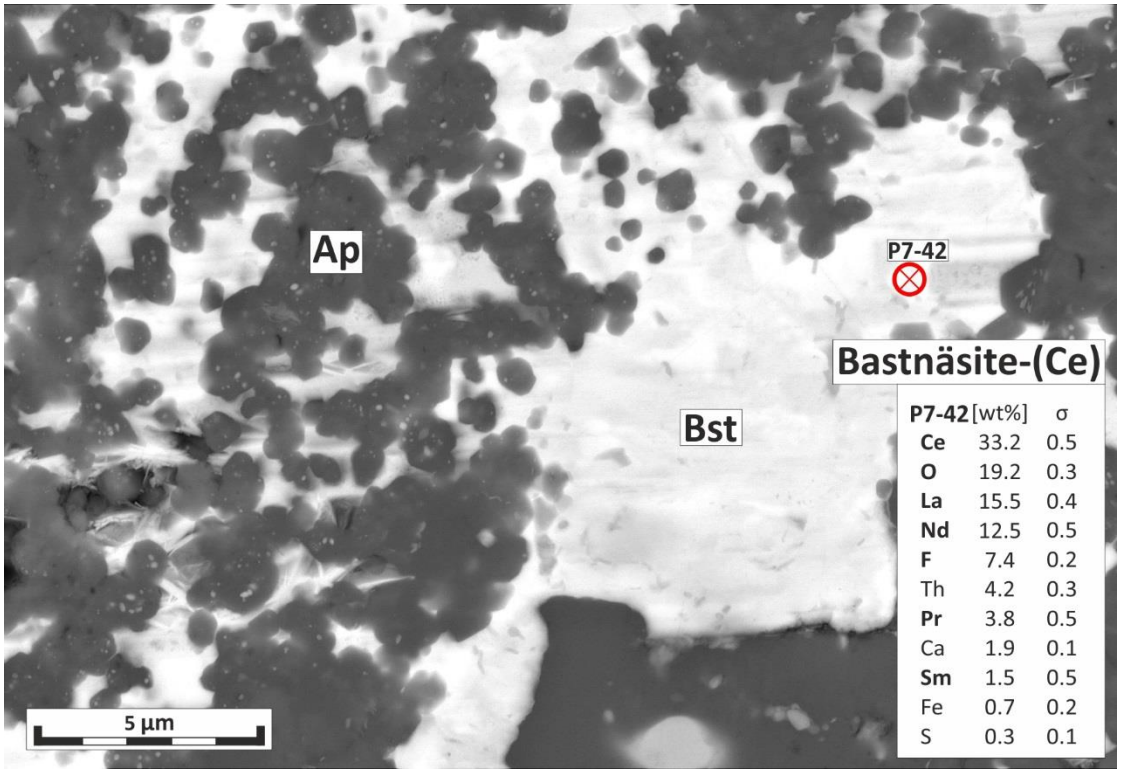

Figure 7-27: The enlarged BSE-SEM image of Fig. 7-26 reveals the poikilitic texture of bastnäsite-(Ce) with inclusions of idiomorphic small (< 2 µm) apatite crystals (16-95-FE). The EDS analysis of bastnäsite-(Ce) in P7-42 reveals a Th concentration of 4.2 wt%. Ap – Apatite and Bst – Bastnäsite-(Ce).

7.1.5 Rødbergite

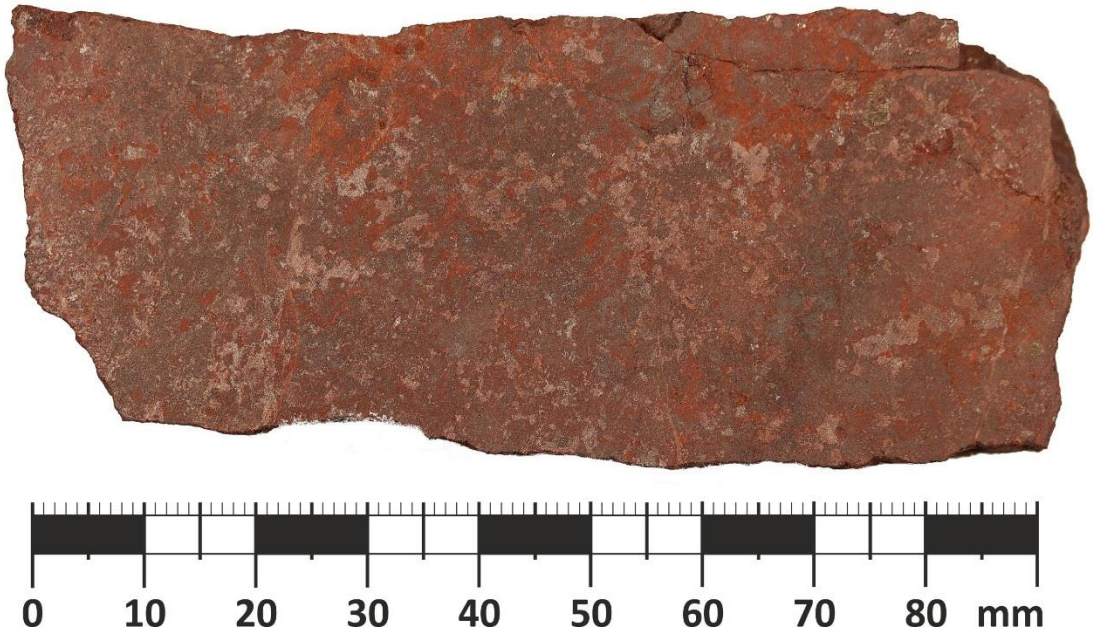

Figure 7-28: Photo of a røbergite hand specimen with different shades of red (16-89-FE).

The protolith of Fen Road rødbergite is carbonatite. The intense Fe-oxide alteration (rødbergitisation) caused a strong colouration in multiple shades of red (Fig. 7-28). The different coloured patches intertwine and mingle in irregular to schlieren-type shape. Relics of pinkish carbonatite are common in rødbergite samples. The contact between rødbergitised carbonatite breccia and dolomite carbonatite is sharp (Fig. 7-12B), with no sign of the formation of transitional rødbergite. Zones enriched in hydrothermal barite outside of the rødbergitisation front show that the effect of alteration goes beyond the visible red precipitation of Fe-oxide (Fig. 7-18).

7.1.6 Rødbergite Veins

Rødbergite veins (V11 – please refer to chapter 7.1.7) occur in chloritised granitic gneiss (Fig. 7-29), dolomite-carbonatite and chlorite-bearing dolomite-carbonatite. They stand out due to their red colouration induced by Fe-oxide inclusions and Fe-oxide clusters within the veins (Tab. 7-1; Fig. 7-30; Fig. 7-31). Besides Fe-oxide, they consist of variable proportions of quartz, calcite, pyrite and monazite-(Ce) with minor chlorite, apatite, barite, barian orthoclase, synchysite-(Ce) and thorite (Tab. 7-1).

Rødbergite veins are composed of a fine intergrowth of calcite and quartz (Fig. 7-32). Pyrite crystals form euhedral to subhedral cubes between 0.25 – 1.00 mm in size (Fig. 7-31, Fig. 7-32) and occur within the rødbergite vein groundmass as well as several centimetres into the host rock. Although some samples of rødbergite contain euhedral pyrite, the concentration tends to be significantly lower than in rødbergite veins.

Figure 7-29: Field photo of a heterogenous vein of rødbergititic and chloritic parts within chloritised granitic gneiss (16-79-FE).

Figure 7-30: Photo of hand specimen of a rødbergitic vein cutting through heterogenous chlorite-bearing dolomite- carbonatite (15-79-FE). The contact zone exhibits a higher pyrite concentration than carbonatite further away from the rødbergite vein.

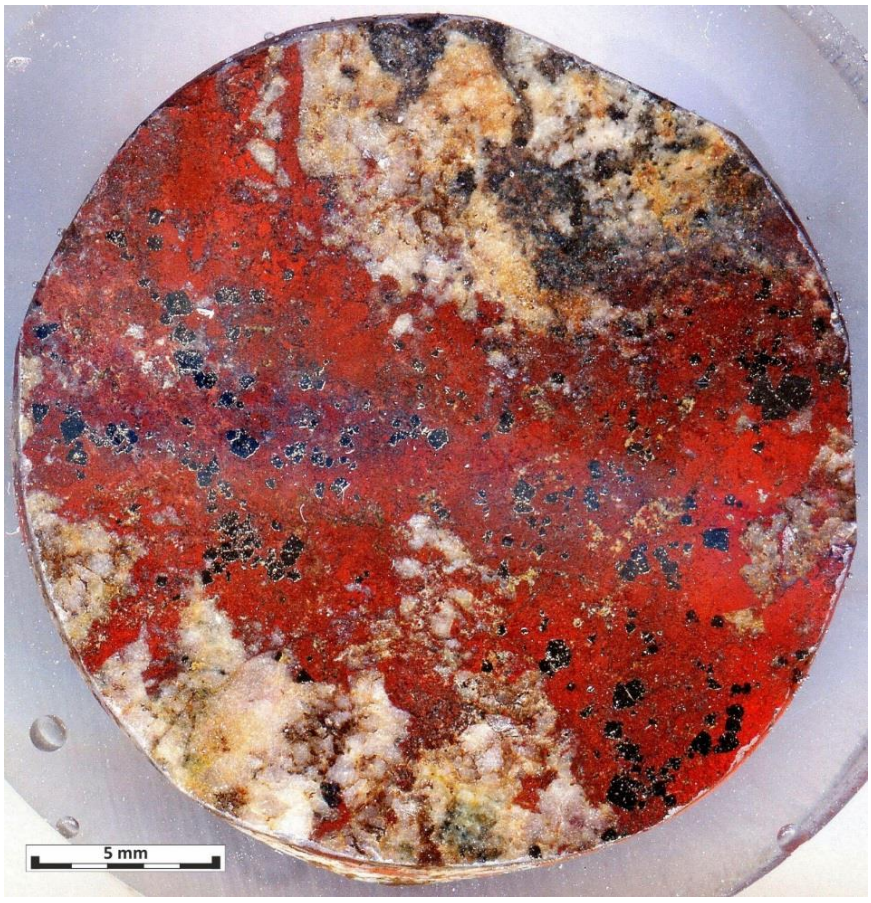

Figure 7-31: Photograph of a polished block of a red rødbergite vein with dark reflecting idiomorphic pyrites (16-82-FE).

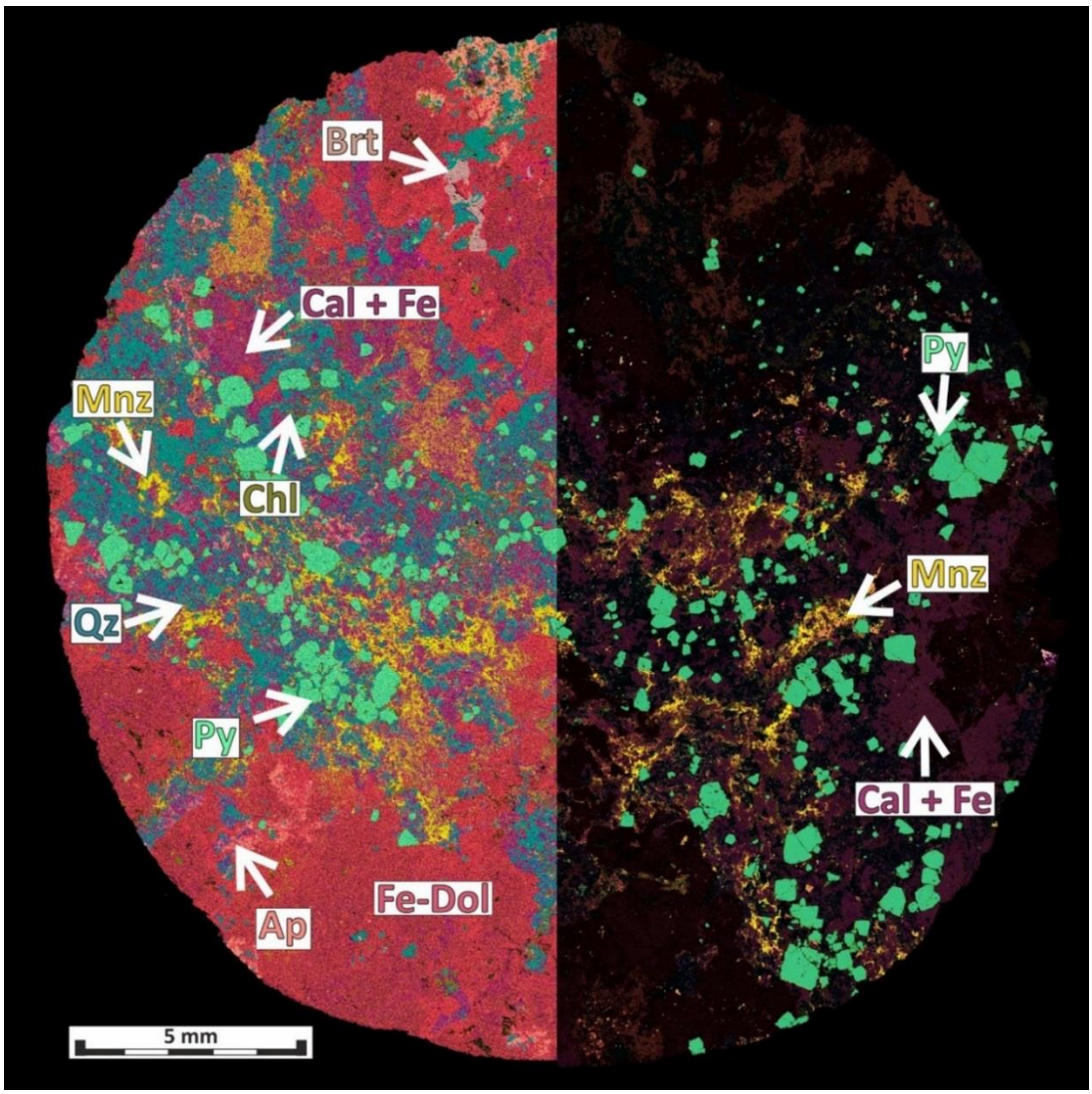

Figure 7-32: The combined large-area EDS mosaic of Fig. 7-31. The left part of the image illustrates mineral phases of the vein, and the right part highlights the distribution of monazite-(Ce) (yellow) within the vein (16-82-FE). Ap – Apatite, Brt – Barite, Cal – Calcite, Chl – Chlorite, Fe – Fe-oxide, Fe-Dol – Ferroan Dolomite, Mnz – Monazite-(Ce), Py – Pyrite and Qz – Quartz.

Rødbergite veins contain a high concentration of monazite-(Ce) (Fig. 7-32; Fig. 7-33), which is associated with the highest concentration of REE within the Fen transect with up to 20000 ppm. Monazite-(Ce) contains an average Th concentration of 3 wt%. The individual crystal size of monazite-(Ce) is between 2.5 and 20 µm, but the individual monazite-(Ce) crystals regularly form larger aggregates (1 mm) (Fig. 7-33; Fig. 7-34; Fig. 7-35).

Locally, monazite-(Ce) engulfs crystals of synchysite-(Ce), but more commonly forms crystals along the grain boundaries of quartz and calcite (Fig. 7-33; Fig. 7-34), and occasionally is intergrown with chlorite surrounded by calcite (Fig. 7-34; Fig. 7-35). SEM-EDX point analyses of groundmass calcite show a high concentration of Fe. Nevertheless, Fe concentrations are not high enough to match the mineral composition of ankerite or siderite. The cause for the detectable concentration of Fe is a high density of homogenously distributed tiny (< 500 nm) Fe-oxide inclusions within the calcite (Fig. 7-35). Calcite without inclusions occurs as small cross-cutting veinlets (Fig. 7-34). The contact between the rødbergite vein and the host rock is sharp to irregular with only a narrow zone of mild alteration of the host rock mineralogy caused by the rødbergite vein. The most common Th-bearing mineral is monazite-(Ce), with a Th concentration between 0.5 – 1.0 wt% (Fig. 7-33).

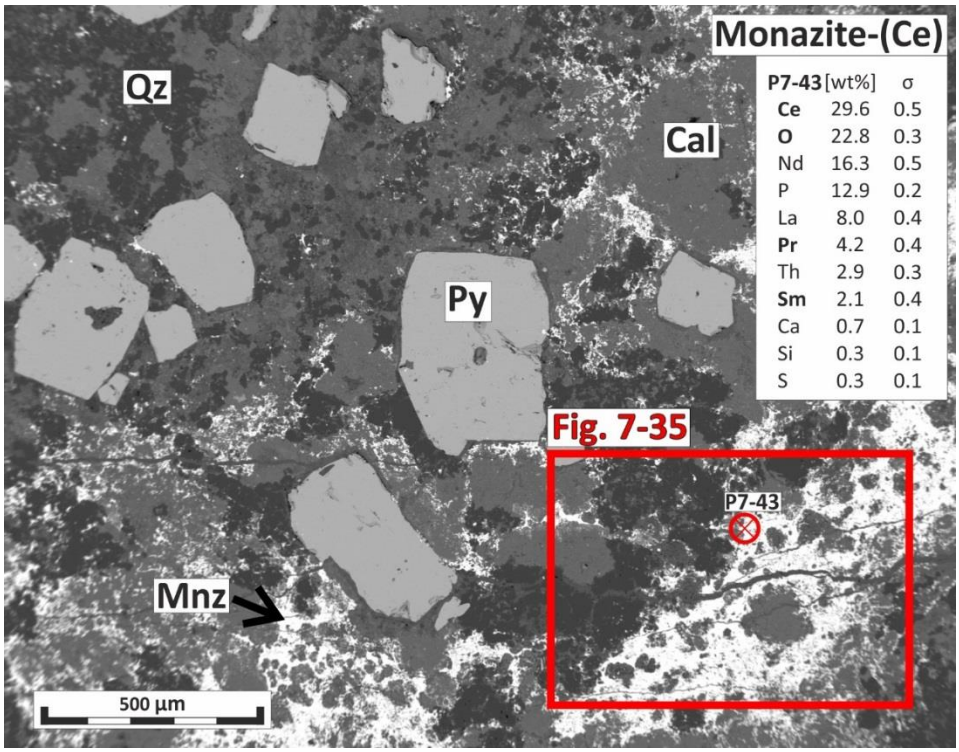

Figure 7-33: A BSE-SEM image of a rødbergite vein with large idiomorphic pyrites in a groundmass of quartz and calcite. Monazite-(Ce) is the very bright phase, which penetrates the rødbergite vein through a fine network of micro veins (16-82-FE). The EDS analysis of monazite-(Ce) in P7-43 shows a Th concentration of 2.9 wt%. Cal – Calcite, Py – Pyrite, Mnz – Monazite-(Ce) and Qz – Quartz.

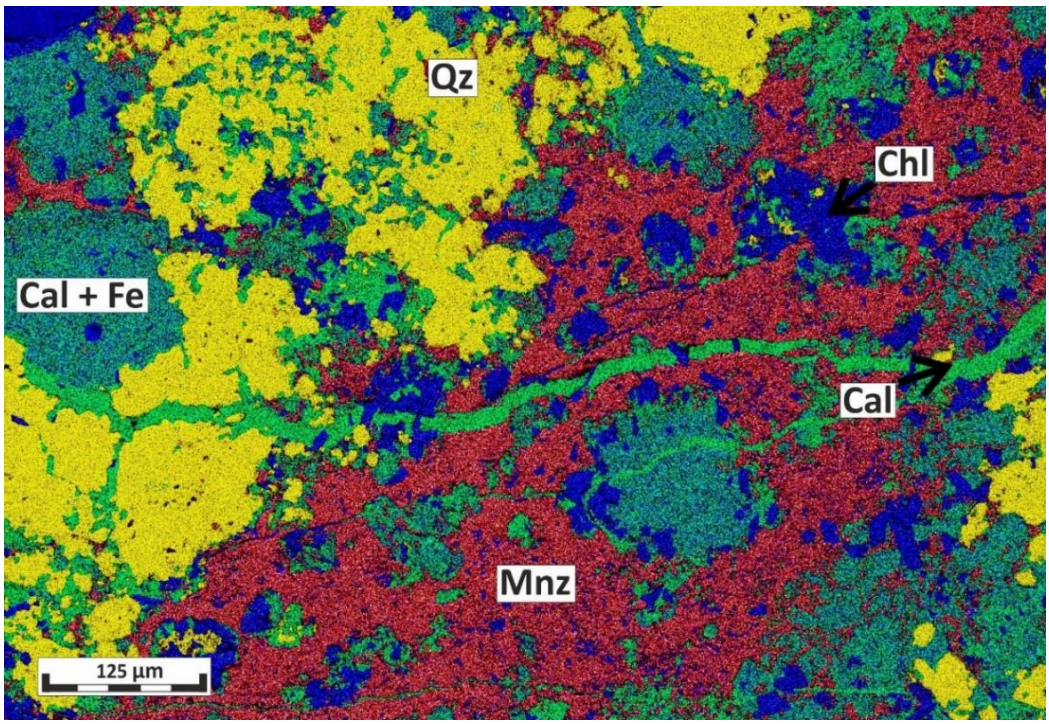

Figure 7-34: The enlarged combined EDS element map of Fig. 7-33 shows fine-grained monazite-(Ce) forming around chlorite and calcite. The calcite has many inclusions of tiny (< 5 µm) Fe-oxides giving the phase a bluish tint. A later generation of inclusion-free calcite veins crosscut the other phases and has a more turquoise colouration. (16-82-FE). Cal – Calcite, Chl – Chlorite, Fe – Fe-oxide, Mnz – Monazite-(Ce) and Qz – Quartz.

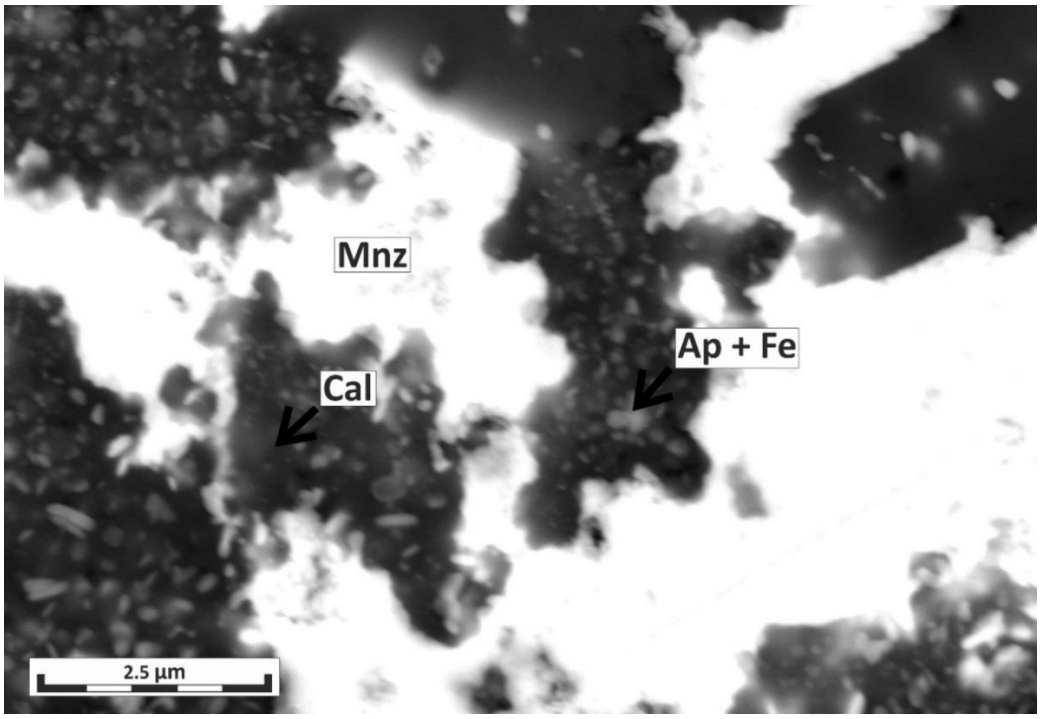

Figure 7-35: The enlarged combined BES-SEM image shows monazite-(Ce) in intergrowth with the inclusion-rich calcite. Spot analysis do not provide a reliable chemical composition of the inclusion due to their small crystal size, but the analyses showed that besides Fe-oxide, a Ca-P phase has to be present. This phase is likely to be apatite. (16-82-FE). Ap – Apatite, Cal – Calcite, Fe – Fe-oxide and Mnz – Monazite-(Ce).

7.1.7 Other vein types

Table 7-2: Vein types of the Fen transect with their mineral composition, host rock and detected REE-minerals. ✚ – ✚ ✚ ✚ = rarely – common ✚Th = REE mineral contains Th Gr = Chloritised Granite Gneiss; Fl = Fluorite mineralisation; C1 = Dolomite-Carbonatite; C2 = Chlorite-bearing Dolomite-Carbonatite.

	Rock type	Synchysite-(Ce)	Bastnäsite-(Ce)	Monazite-(Ce)
V1: Chlorite vein (+ Fe-Dol)	Gr			
V2: Quartz vein (± Sph)	Gr			
V3: Apatite vein (+Qz, Brt)	Fl	✚Th		
V4: Fe-Dolomite vein (Py, Qz, Cal, Brt, Na-Fsp)	Fl	✚		
V5: Calcite-Dolomite-Barite vein	C1	✚ ✚ ✚		
V6: Quartz vein (Ap, Fe, Chl, Ba-Fsp, Fl)	C1	✚	✚ ✚	
V7: Pyrite-Ankerite vein (Qz, Cal, Fe, Brt)	C1	✚	✚	
V8: Apatite-Barite vein (Qz, Cal, Dol, Chl, Na-Fsp)	C1	✚ ✚ ✚Th		✚Th
V9: Quartz-Fe-oxide vein (Chl, Ba-Fsp, Fl, Cal, Ap)	C2	✚Th ✚Th		
V10:Fe-Dolomite-Ankerite vein	C1, C2			
V11: Rødbergite vein (Qz, Cal, Fe, Py, Mnz, Chl, Ap, Brt, F-Fsp	Gr, C1, C2	✚Th		✚Th ✚Th ✚Th

A wide range of veins is distinguished within the Fen transect (Tab. 7-2). Although they vary in terms of their mineral composition and texture, it is possible to simplify and summarise the veins into categories.

Broadly speaking they are either apatite-dominated, quartz-dominated or carbonate-dominated (Fig. 7-36) with additional amounts of pyrite, Fe-oxide, chlorite, barite, fluorite, synchysite-(Ce), bastnäsite-(Ce), monazite-(Ce), barian orthoclase, orthoclase and accessory thorite, sphalerite, galena and chalcopyrite.

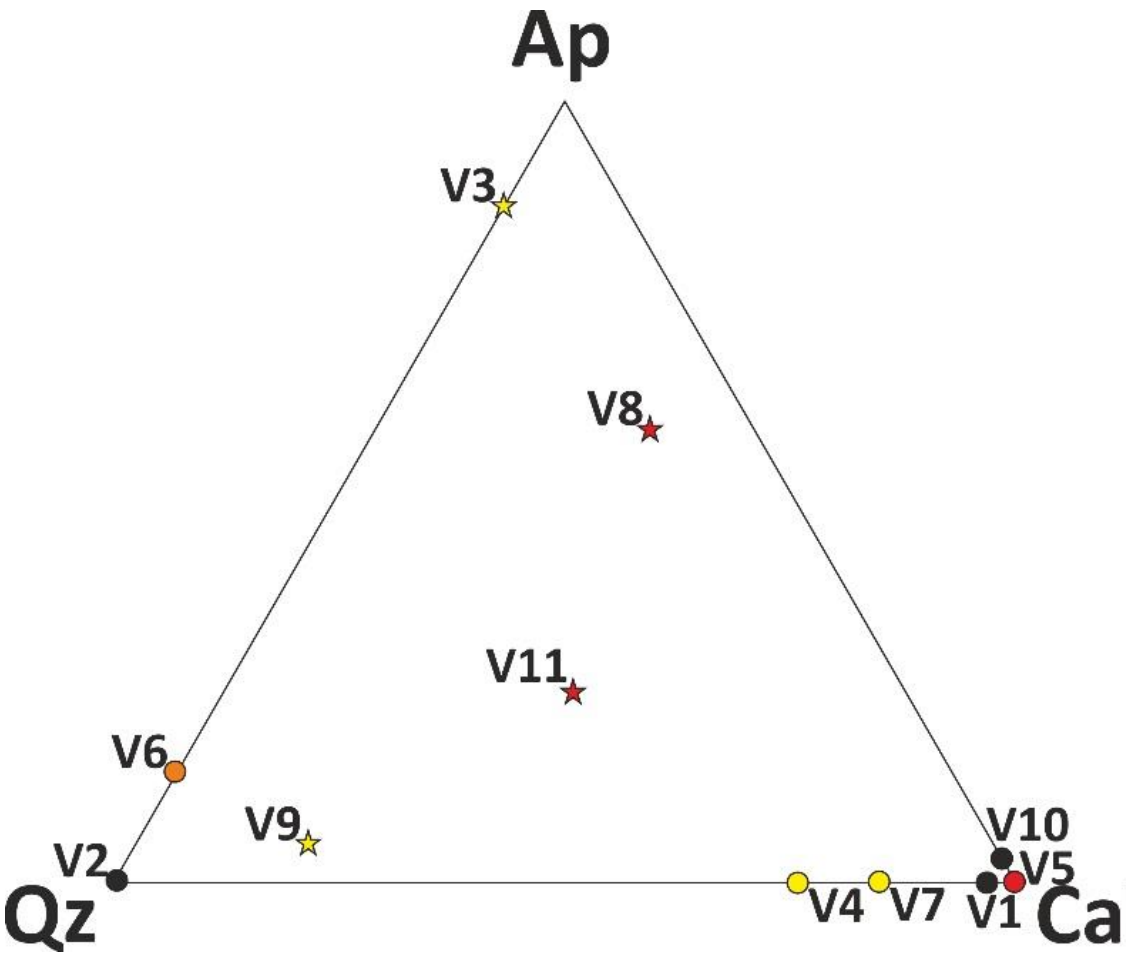

Figure 7-36: Fen transect vein classification based on the relative amount of Qz = quartz, Cab = carbonate and Ap = apatite. ● ● ● ● = no REE-minerals to many REE-minerals ☆ = REE-mineral contains Th.

7.2 Geochemical results

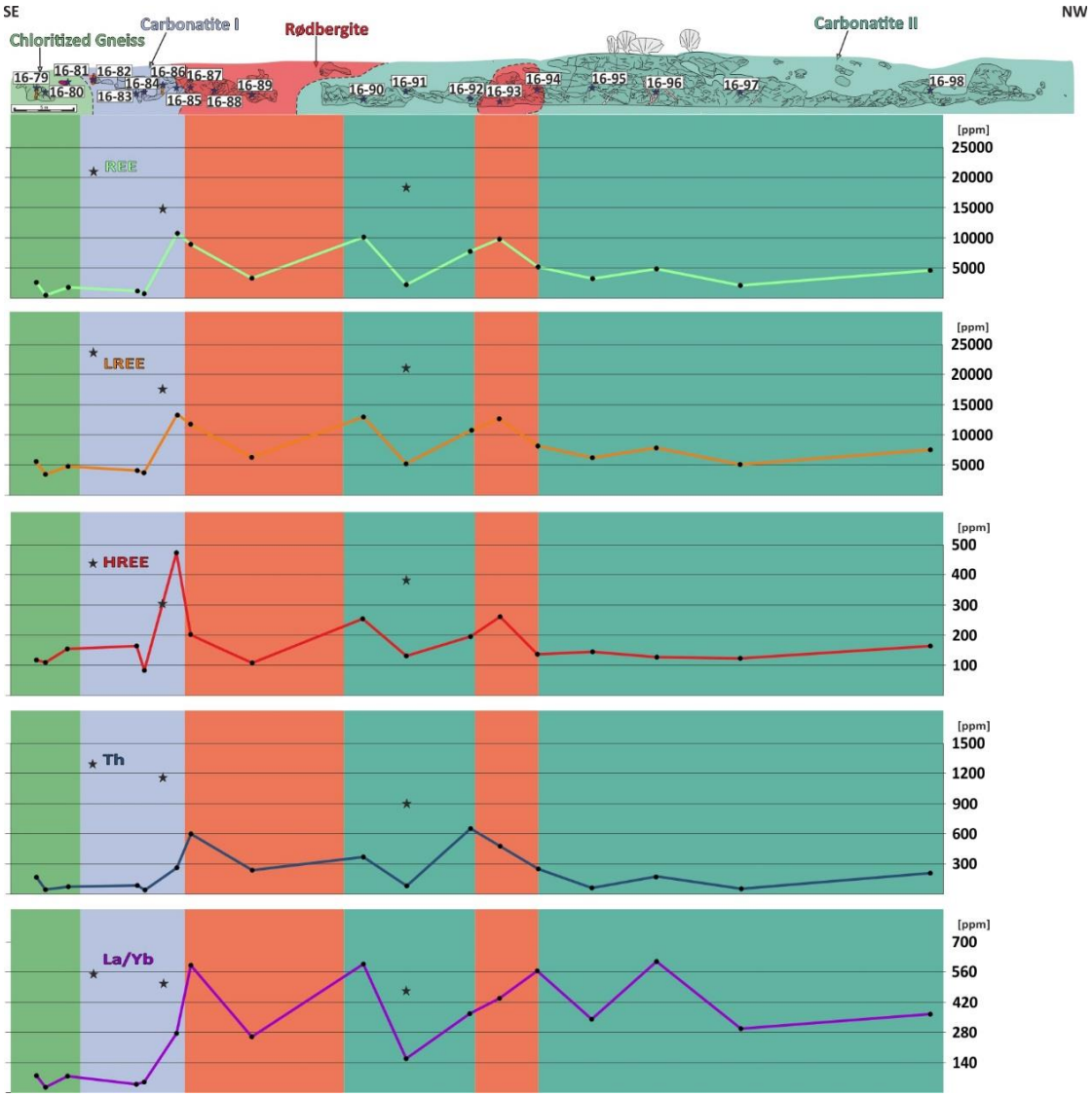

Figure 7-37: Sketch of the Fen Road transect, which is divided into four different zones: rødbergite (red), carbonatite II —chlorite-bearing dolomite-carbonatite (turquoise), carbonatite I — dolomite-carbonatite (blue) and chloritised granitic gneiss (green) For each sampling point, the concentration of REE, LREE, HREE and Th is plotted exactly below the sampling location. Additionally, the last plot shows the ratios of La/Yb as an indicator for LREE to HREE fractionation. Three vein samples are excluded from the trend line and are represented with the ★ symbol.

The REE concentration along the Fen transect (Fig. 7-37) varies from ca. 500 ppm REE in chloritised granitic gneiss to a rødbergite vein with ca. 21,000 ppm (2.1 wt%) of REE.

Table 7-3: Average concentration of REE, LREE, HREE, Th and La/Yb for the main rock types of Fen transect.

		REE [ppm]	**LREE** [ppm]	**HREE** [ppm]	**Th** [ppm]	**La/Yb**
Chloritized Gneiss	(n=1)	478	369	109	42	27
Fluorite-rich Carbonatite	(n=1)	1807	1653	154	71	77
Dolomite-Carbonatite (SE)	(n=2)	918	794	124	60	45
Dolomite-Carbonatite (NW)	(n=1)	4871	4745	127	177	612
Chlorite-bearing Dolomite-Carbonatite	(n=7)	5835	5622	213	240	390
Rødbergite	(n=5)	8393	8191	203	545	474
Rødbergite vein	(n=3)	14729	14413	316	791	441

The average REE concentration of dolomite-carbonatite from the SE is 918 ppm (Tab. 7-3). Locally the REE concentration can be significantly higher (up to 4871 ppm REE) due to the presence of REE-mineral bearing vein types V6 and V7 (Fig. 7-15). Chlorite-bearing dolomite-carbonatite has an average REE concentration of 5835 ppm, which is the highest observed REE concentration in lithotypes, unaffected by red rødbergitisation, at the Fen Road transect. The REE concentration of chlorite-bearing dolomite-carbonatite is ca. 6 times higher than the REE concentration of chlorite-free dolomite-carbonatite. Rødbergite and rødbergite veins have an average REE concentration of 8393 ppm and 14729 ppm, respectively (Tab. 7-3).

All of the samples are strongly enriched in LREE relative to HREE, which is illustrated by the ratio of La/Yb » 1 and is seen in the negative slope of the REE-normalized plot (Fig. 7-38).

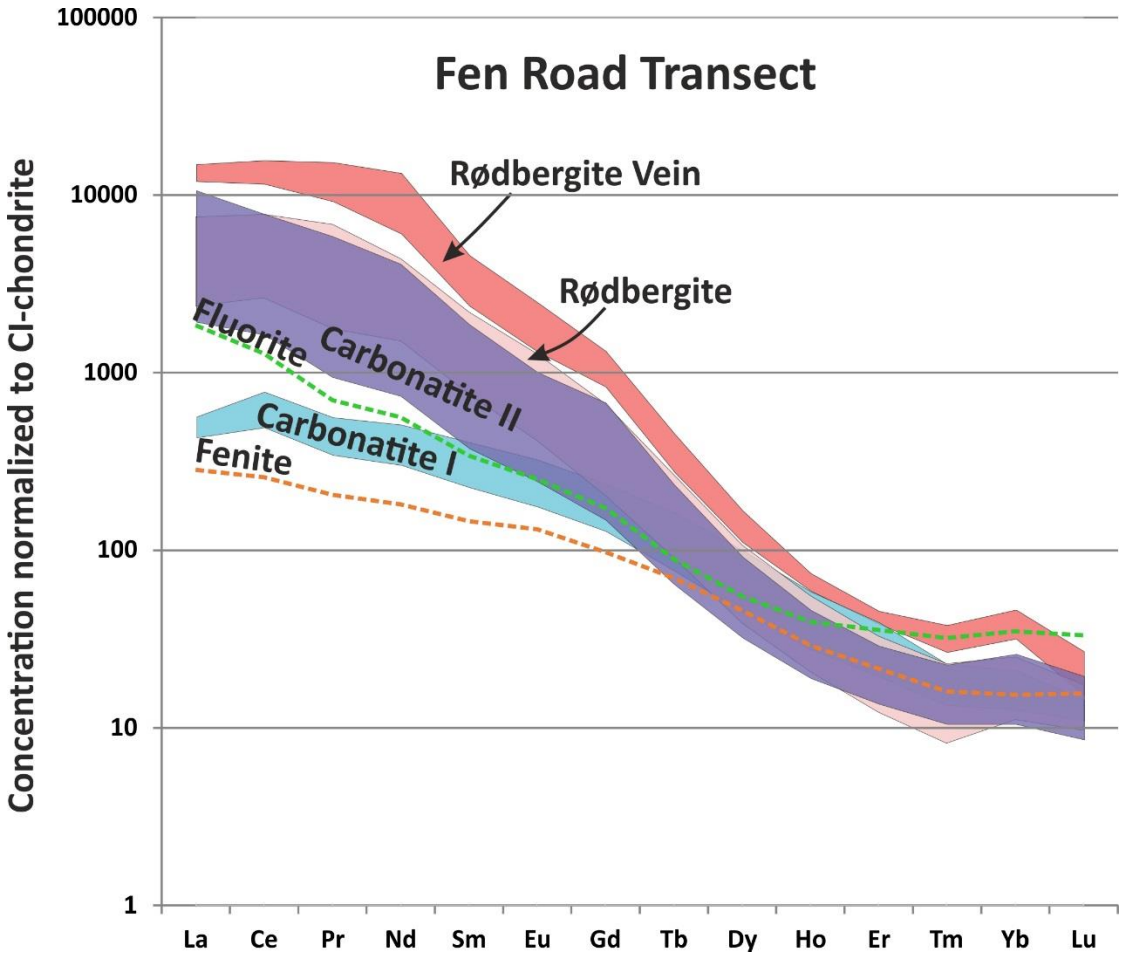

Figure 7-38: REE concentrations normalised to CI1-chondrite values from McDonough and Sun (1995). The range of REE normalised values is represented in coloured boxes for rødbergite veins (n = 3), rødbergite (n = 4), carbonatite I (dolomite-carbonatite) (n = 2) and carbonatite II (chlorite-bearing dolomite-carbonatite) (n = 6) samples. Additionally, two dashed lines represent samples of fenite as well as fluorite mineralisation, respectively. The diagram shows a strong LREE enrichment relative to HREE in various degrees for all the rock types. While the boxes largely overlap for HREE, the values for LREE spread strongly with magnitudes between carbonatite I samples and rødbergite veins. There are no Ce or Eu anomalies present but a positive Yb anomaly for rødbergite veins and to a lesser degree for carbonatite II. The Yb anomaly is likely to be an artefact of an unidentified spectral overlap.

A positive correlation between La/Yb ratio and REE concentration (Tab. 7-4) and furthermore a positive correlation between HREE and REE (Tab. 7-4) suggest that the process which concentrated REE lead to an absolute enrichment of LREE and HREE and a relative enrichment of LREE compared to HREE in the sample. Additionally, this is supported by the chondrite-normalised diagram (Fig. 7-38). In the HREE range, the curve is relatively flat and narrow while the LREE section of the graph has a steep curve with larger variations in concentration levels. Interestingly, the highest La/Yb is in a dolomite-

carbonatite sample from the NW part of the section which is unaffected by Fe-oxide alteration but has a high density of REE-mineral bearing veins (V6 & V7). The presence of the REE-mineral-bearing veins caused a significant increase in LREE, while the HREE concentrations remained unaffected and are at the same level as in an unveined dolomite-carbonatite from the SE (Fig. 7-38). The concentration of Th in the Fen Road transect correlates positively with the concentration of REE and correlates slightly better with LREE than with HREE (Tab. 7-4). The highest concentrations of Th are in rødbergite veins, rødbergite and chlorite bearing dolomite-carbonatite (Tab. 7-3).

The geochemical data show strong enrichment of REE, especially LREE and Th, during rødbergitisation.

***Table 7-4**:* Correlation matrix of REE, LREE, HREE, Th and La/Yb for the Fen Road transect.

	TREE	*LREE*	*HREE*	*Th*	*La/Yb*
TREE	-				
LREE	1.00	-			
HREE	0.88	0.88	-		
Th	0.93	0.93	0.72	-	
La/Yb	0.45	0.45	0.25	0.42	-

7.3 Discussion

7.3.1 Original and alteration mineral assemblage

The mineral composition of unaltered dolomite-carbonatite and chlorite-bearing dolomite-carbonatite includes magmatic and early-postmagmatic minerals (Table 7-5). Carbonatites are significantly more susceptible to changes in their original magmatic texture than silicate rocks, and their evolution commonly involves a variety of post-magmatic processes, including exsolution and subsolidus re-equilibration with carbothermal-derived fluids (Broom-Fendley et al., 2016; Chakhmouradian et al., 2015b). Therefore, magmatic minerals, e.g., apatite, carbonate and pyrite, are likely to change.

Table 7-5: The original- and alteration mineral assemblages of dolomite-carbonatite and chlorite-bearing dolomite-carbonatite in comparison to the minerals common in a rødbergite.

	Original Mineral Assemblage (magmatic - early postmagmatic)	**Alteration Mineral Assemblage** (postmagmatic - rødbergitisation)
Dolomite-Carbonatite	Apatite Dolomite-Ankerite Pyrite Columbite	Ankerite-Dolomite Barite Quartz Chlorite Bastnäsite-(Ce), Synchysite-(Ce) Monazite-(Ce)
Chlorite-bearing Dolomite Carbonatite	Dolomite-Ankerite Pyrite	Ankerite Apatite Fe-oxide Chlorite Quartz Barite Fluorite Bastnäsite-(Ce), Synchysite-(Ce)
Rødbergite + Rødbergite Veins		Calcite Fe-oxide Quartz Pyrite Chlorite Barite Apatite Monazite-(Ce)

For instance, apatite-carbonate layering in dolomite-carbonatite is a common feature in carbonatites worldwide (Chakhmouradian et al., 2017) and indicates a cumulate

formation or late magmatic solidification (flow foliation). The alignment of pyrite in the same layers could be the result of coprecipitation during crystallisation (Fig. 7-13). Alternatively, a subsolidus deformation event could have been responsible for creating oriented layers of apatite and pyrite. However, these layers are not present in chlorite-bearing dolomite-carbonatite or rødbergite. Another observed feature is the fine irregular network of ferroan dolomitic to ankeritic veinlets in dolomite-carbonatite and chlorite-bearing dolomite-carbonatite (Fig. 7-13; Fig. 7.14; Fig. 7-15). It is unclear, if this feature developed in an early postmagmatic stage, or as part of a later alteration process. The fluorite mineralisation is a special case of carbonatite alteration. The texture of individual dolomite crystals and dolomite patches within the fluorite mineralisation described earlier (Fig. 7-7), indicates a replacement of carbonatite by a fluorite-rich solution. Later apatite veins crosscut the fluorite mineralisation but do not affect the individual dolomite crystals and are further crosscut but dolomite veins (Fig. 7-7). The dolomite veins cross-cut most of the apatite but are interrupted by the centre of the apatite vein. This could be explained by a sequence of initial apatite, followed by dolomite and finally barite-quartz vein. The barite-quartz vein used the same pathway as the apatite vein and caused a reopening of the apatite vein.

The REE concentration of dolomite-carbonatite is roughly six times less the REE concentration of chlorite-bearing dolomite-carbonatite. This significant difference in REE concentration is the result of a magmatic or hydrothermal enrichment or a combination of both processes. There is a general trend in carbonatite systems worldwide from an early calciocarbonatite to magnesiocarbonatite to an evolved ferrocarbonatite (please refer to chapter 3) (Woolley and Kempe, 1989). The evolutionary trend is usually associated with an increase in REE at the same time

because REE behave as incompatible elements in a carbonatite system (Woolley and Kempe, 1989). In the Fen transect the prevalent carbonate species in dolomite-carbonatite and chlorite-bearing dolomite-carbonatite is ferroan dolomite with an observed significant increase of the (Fe+Mn)/Mg ratio from ca. 0.16 for dolomite-carbonatite (Fig. 7-13), to 0.48 in chlorite-bearing dolomite-carbonatite (Fig. 7-23). Although the (Fe+Mn)/Mg ratio is based on semiquantitative LAM EDX-SEM analysis, the increase in (Fe+Mn)/Mg ratio in ferroan dolomite is significant. In case the increase in Fe is the result of magmatic evolution, the REE concentration should have increased at the same time. Alternatively, the increase in Fe could be the result of chloritisation. The chlorite-bearing dolomite-carbonatite comprises a high amount of chlorite, Fe-oxides, apatite and quartz (Fig. 7-23; Tab. 7-1). Based on their texture and mineral characteristics, these minerals belong to the alteration mineral assemblage (Fig. 7-24 & Tab. 7-5). The hydrothermal fluid responsible for the alteration mineral assemblage must have been enriched in Fe in order to form Fe-oxide and chlorite and could have caused an increase of Fe in the groundmass carbonates. The REE minerals present in chlorite-bearing dolomite-carbonatite are stacked sheets of synchysite-(Ce) and bastnäsite-(Ce) (Fig. 7-24 & Fig. 7-26). Although they are associated with the alteration mineral assemblage, they occur as partly replaced, subhedral and poikilitic crystals. This texture is significantly different from the usual fine intergrowth texture of hydrothermal REE-minerals observed in the rest of the Fen road transect (Fig. 7-10; Fig. 7-16; Fig. 7-20). Nevertheless, this type of REE-fluorocarbonates is exclusively associated with a hydrothermal chlorite-Fe-oxide-apatite mineral assemblage, which indicates a hydrothermal origin for the REE-fluorocarbonates as well.

The minerals of the alteration assemblage (chlorite, apatite, quartz and Fe-oxide) in chlorite bearing dolomite-carbonatite are also an essential part in the rødbergite fluid as well as other vein fluids (Fig. 7-32). The similarities of the minerals assemblages draws a possible link between chloritisation and hydrothermal REE-mineralisation and rødbergitisation. The rødbergitisation at the Fen Road transect altered dolomite-carbonatite and chlorite-bearing dolomite-carbonatite into red rødbergite, while simultaneously enriching the rock in REE and Th (Fig. 7-37; Fig. 7-38). The similarities between chloritisation and rødbergitisation indicate a genetic link. It is possible that the chemical alteration halo of the rødbergitisation fluid goes beyond the red coloured rødbergite. The lack of red colouration normally associated with the Fe-oxide precipitation might not be an absolute criterion for the alteration of the rock by rødbergitisation fluids —Fe-oxides are also part of the alteration mineral assemblage associated with the chloritisation.

7.3.2 Hydrothermal Rare Earth Mineralisation

All REE minerals observed in the Fen Road transect are of hydrothermal origin. This makes hydrothermal processes especially important for the REE enrichment at the Fen Road transect.

The rødbergite veins are the fluid feeder system for a more widespread rødbergitisation of carbonatite. Since rødbergite veins are the source of REE enrichment in the rødbergitisation process, it makes sense that they show the highest concentration of REE (Fig. 7-38; Tab. 7-3). Rødbergite veins are not the only REE-mineral bearing veins in the Fen transect. From the 11 different vein types described for the Fen transect, including rødbergite veins, REE-minerals were detected in eight of the vein types (please

refer to chapter 7.1.7; Tab. 7-2). Contrary to rødbergite veins, the other REE-mineral bearing veins are thinner and range between 50 µm in case of Fe-dolomite-ankerite veins (V10; Fig. 7-14) and 5 mm for apatite veins (V3; Fig. 7-7). Additionally, the main REE carrier of V3, V4, V5, V6, V7, V8, V9 and V10 are REE-fluorocarbonates in contrast to the monazite-(Ce) dominated rødbergite veins (Tab. 7-2). The REE concentration varies between the different vein types. The presence of V5, V6 and V8 will significantly enhance the REE-concentration of a rock unit. The REE concentration of the dolomite-carbonatite sample 16-96-FE (Fig. 7-15) is 5x above the average REE-concentration of dolomite carbonatite (918 ppm) due to the presence of V6 and V7 (Tab. 7-3). Although rødbergite veins are not the only vein-type to enhance the REE-concentration of a rock unit, they are more potent due to their greater thickness (5 – 15 cm).

There are three major attributes influencing the overall REE budget of samples at the Fen transect A) the density of veining B) the rock type before rødbergitisation and C) rødbergitisation. Rødbergite veins or rødbergite altered chlorite bearing dolomite-carbonatite with a high density of veining are the most promising targets for a high REE concentration.

The main REE-mineral in rødbergite veins is monazite-(Ce) with minor amounts of REE-fluorocarbonates. Monazite-(Ce) generally coprecipitates with chlorite, embedded in a groundmass of inclusion-rich (Fe-oxide and apatite) calcite, which is preferentially in vicinity of pyrite (Fig. 7-33; Fig 7-34). At the rim of rødbergite veins, the mix of calcite, Fe-oxide and monazite-(Ce) penetrates the wall rock along a network of ferroan dolomite and ankerite veinlets. This network of Fe-dolomite veinlets (V10) is present in most of the carbonatites at the Fen road transect and is likely to be the path for the more pervasive distal rødbergitisation. Besides the main REE-carrier monazite-(Ce),

minor amounts of REE-fluorocarbonates occur within the same cluster or micro-vein. Monazite-(Ce) and REE-fluorocarbonates are interchangeable depending on the physicochemical parameters at a given moment, and small local changes can lead to the change of the prominent REE-phase (Fig. 7-21). Monazite-(Ce) as the major REE phase is restricted to rødbergite veins. All the other types of REE-mineral bearing veins are dominated by synchysite-(Ce) and bastnäsite-(Ce).

REE-fluorocarbonates are genetically associated with the alteration mineral assemblage and are often in intergrowth with apatite, Fe-oxide, barite, chlorite, quartz, ankerite and calcite. They are present in three different forms:

A) In fluorite mineralisation as clusters of synchysite-(Ce) embedded in calcite with minor quartz and barite. Texturally very similar to monazite-(Ce) mineralisation in rødbergite veins (Fig. 7-9; Fig. 7-10; Fig. 7-11).

B) As subhedral to anhedral aggregates in various kinds of calcite-dolomite-quartz-apatite-barite veins (Fig. 7-16; Fig. 7-17; Fig. 7-19; Fig. 7-20; Fig. 7-21).

C) As partly corroded-looking subhedral, occasionally poikilitic, stacks of bastnäsite-(Ce) and synchysite-(Ce) within apatite-Fe-oxide replacement fronts in chlorite-bearing dolomite-carbonatite (Fig. 7-24; Fig. 7-25; Fig. 7-26; Fig. 7-27).

7.3.3 REE stability in the hydrothermal fluid of the Fen Road transect

Based on the different styles of alteration mineral assemblages (Tab.7-2), which are associated with REE-minerals, the alteration mineral assemblages cannot be the result of a single hydrothermal fluid. The different styles of hydrothermal alteration were caused either by different fluid pulses generated by different sources and processes or by multiple hydrothermal cycles triggered by the same process that generated a variety

of fluids, which changed due to progressive interaction with the wall rock or a combination of both scenarios.

The alteration mineral assemblage of rødbergite and rødbergite veins is more oxidised compared to the unaltered mineral assemblage (Tab. 7-5), which is underpinned by the higher concentration of Fe-oxides within the rødbergite and rødbergite veins (Fig. 7-32), and by the presence of the sulphate mineral barite (Fig. 7-39). The oxidised nature of the rødbergite fluid must have been acquired outside of the Fen complex. This notion is confirmed by strontium and oxygen isotopic analysis presented by Andersen (1984) that shows the fluid involved in rødbergite formation had high $^{87}Sr/^{86}Sr$ ratios as well as elevated $\partial^{18}O$ and therefore was at least partly equilibrated with Precambrian quartzofeldspathic gneisses outside of the Fen Complex, and possibly with groundwater.

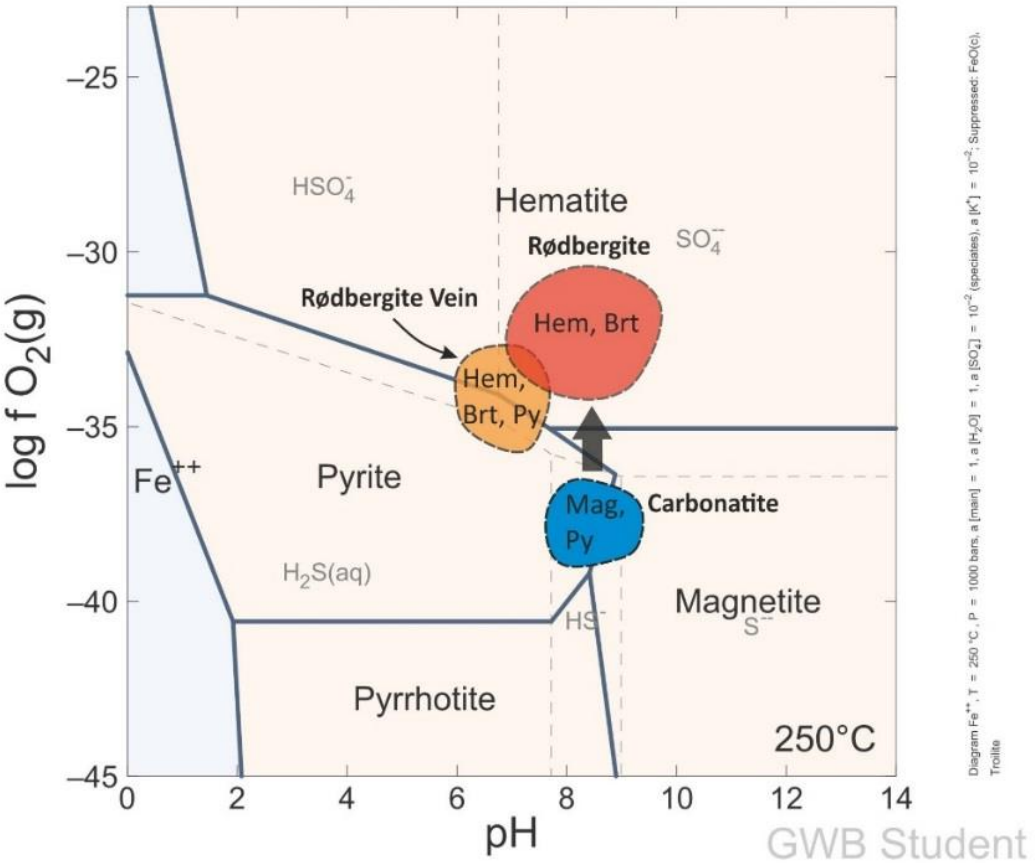

Figure 7-39: Stability diagram of Fe-minerals depending on pH and fO_2 at 250°C. Dashed lines mark the stability fields of S- specification. During the hydrothermal alteration of the carbonatite (blue), the unaltered mineral assemblage of magnetite and pyrite oxidised to hematite and barite, forming rødbergite (red). Rødbergite veins are comprised of barite, hematite as well as pyrite, which required more acidic conditions than rødbergite. The plot was modelled using the Geochemical Workbench Student edition V12.0 and the following parameters: T = 250°C; p = 1000 bar; $a[Fe^{2+}] = 1$; $a[H_2O] = 1$; $a[SO_4^{2-}] = 10^{-2}$ (speciation enabled); $a[K^+] = 10^{-2}$; troilite supressed

This suggests that the fluids involved in the REE mineralisation in the Fen Complex were not simply evolved melt-like hydrous fluids; such late-magmatic fluids often play a critical role in producing high grades in REE-resources (Bodeving et al., 2017; Duraiswami and Shaikh, 2014; Smith et al., 2016; Wall and Mariano, 1996).

While rødbergite veins frequently contain pyrite and Fe-oxide together (Fig. 7-32; Fig. 7-33; Fig. 7-34), other REE-mineral bearing veins show a high concentration of pyrite with very little or no Fe-oxides (V4; V7; Tab. 7-2). There is no evidence that a fluid producing a REE-mineral bearing pyrite-dolomite vein is more oxidised than an unaltered

carbonatite with essentially the same mineral paragenesis. Rather than assuming there is a separate reduced fluid able to mobilise REE, the presence of pyrite indicates the range of redox potential from a reduced fluid to an oxidised fluid. The progressive interaction of the oxidised external fluid with the carbonatite decreases the oxygen fugacity of the fluid. Therefore, even an initial oxidising fluid can create a reduced mineral paragenesis further down the evolution. It is important to realise that the hydrothermal alteration generally happens in multiple pulses. The carbonatite wall rock less chemically buffers the second pulse of fluid, and the redox-boundary is shifted from the fluid source further into the wall rock. In case the pathway of the fluid changes into primary carbonatite, the whole cycle starts again. In that way, it is possible to produce a range of different veins while having reduced and oxidised mineral assemblages at the same time (Fig. 39).

In summary, the hydrothermal fluid causing rødbergitisation is an externally derived oxidising fluid. The fluid contains a variable concentration of Ca, Mg, Fe, Si, Ba, S, P, F, C and REE, although some of these elements, e.g., REE were acquired via interaction with the Fen Complex intrusives. The fluid preferentially forms calcite, dolomite-ankerite, barite, quartz, apatite, Fe-oxide, pyrite and chlorite (Tab.7-2). REE minerals are found in both oxidising and more reducing conditions with synchysite-(Ce) and bastnäsite-(Ce) being the dominant REE carrier in reduced environments (V3, V4, V5, V6, V7, V8, V9 and V10), and monazite-(Ce) preferentially found under more oxidizing conditions (V11).

7.3.4 REE mobilisation and precipitation

The REE from the hydrothermal fluid are coming from the dissolution of REE-minerals (e.g. REE-fluorocarbonates) or REE-bearing minerals (e.g. calcite, dolomite-ankerite and apatite) from the unaltered carbonatite mineral assemblage. Carbonatite is a more fertile source for REE than the surrounding gneiss or other rock types of the Fen Complex. Chlorite-bearing dolomite-carbonatite contains partly corroded stacks of REE-fluorocarbonate in contact with a Fe-oxide-apatite cluster (Fig. 7-26). This indicates a dissolving potential of REE-fluorocarbonates by an oxidising fluid.

The mobilisation of the REE into solution is most efficiently accomplished by fluoride, sulphate and chloride ligands to form stable REE complexes in hydrothermal fluids at 200 - 400 °C in geological environments (Williams-Jones and Migdisov, 2014; Williams-Jones et al., 2012), with REE-sulphate complexes dominating at temperatures >300 °C in weakly acidic fluids (Migdisov and Williams-Jones, 2014). The presence of barite as part of the alteration mineral assemblage in rødbergite and six from eight REE-mineral bearing veins (Tab. 7-2) suggests an important role for sulphate complexes in REE mobilisation, especially under oxidising environments. The fine intergrowth between barite and REE-minerals (Fig. 7-9; Fig. 7-13; Fig. 7-21) indicates coprecipitation of these phases and underlines the importance of sulphate complexing. The breakdown of original sulfides in unaltered carbonatites after being in contact with the oxidising hydrothermal fluid is the most likely source for sulphate in the fluid. Additionally, fluoride might play a role as a complexing agent for REE ions, especially in reduced environments because fluoride can be form stable REE complexes with no sulphate present. The association of apatite (Fig. 7-27; Fig. 7-35) and fluorite (Fig. 7-10; Fig. 7-16) with REE-minerals and the presence of fluorite (V6; V9) and apatite (V3; V6; V8; V9; V11)

in REE-mineral bearing veins illustrates the importance of fluoride ligands for the REE-mineralisation. Chlorite and calcite with Fe-oxides inclusions are also a common coprecipitation for REE-minerals (Fig. 7-10; Fig. 7-20; Fig. 7-34). The precipitation of REE-minerals can be triggered by decreasing the stability of these complexes. Experimental studies have demonstrated that the stabilities of REE-fluoride, -sulphate and -chloride complexes decrease strongly with decreasing temperature and increasing pH (Migdisov and Williams-Jones, 2014; Williams-Jones and Migdisov, 2014; Williams-Jones et al., 2012). Therefore, cooling of the hydrothermal fluid, or reaction with carbonate host rocks leading to a pH-increase in the fluid, are possible mechanisms for triggering precipitation of REE-minerals from aqueous solutions.

7.3.5 A comparison between Bjørndalen and Fen Road

Bjørndalen was the first site for a detailed investigation of the formation of rødbergite with 27 samples taken on a length of 30 m and the extensive use of SEM on these samples. The Fen Road transect has a length of 60 m with 19 samples taken along this transect and a fraction of the SEM time used compared to the investigation of the Bjørndalen transect. Nevertheless, lessons learned from the Bjørndalen transect were applied on the Fen Road transect for a more efficient and resourceful approach in collecting data. Therefore, the comparison between those two data sets is possible because both are based on reliable and representative data collection.

The rock types chloritised granitic gneiss, fluorite-rich carbonatite and chlorite-bearing dolomite-carbonatite are not part of the Bjørndalen transect sensu stricto. While the dark chlorite-bearing dolomite-carbonatite and chloritised granitic gneiss are not present in the surrounding area, fluorite mineralisation is present proximal to the

Bjørndalen transect. Similarly to the Fen road transect, the fluorite mineralisation occurs at the contact between wall rock (fenite) and carbonatite. A brief investigation of the fluorite mineralisation in Fenite proximal (< 20 m) to the Bjørndalen transect failed to detect REE-minerals, in contrast to the fluorite mineralisation with synchysite-calcite clusters found at the Fen Road transect (Fig. 7-9).

The level of REE concentration is on a similar level (± 1000 ppm) for unaltered dolomite-carbonatite of both transects (Fig. 6-40; Tab. 7-3). The dark coloured chlorite-bearing dolomite-carbonatite, which does not occur at the Bjørndalen transect, has a higher average REE concentration with 5800 ppm (Tab. 7-3). The REE level for rødbergite is significantly higher for the Fen transect. Rødbergite veins which do not occur in the Bjørndalen transect are thicker than REE-mineral bearing veins within the Bjørndalen transect and have the highest concentration of REE of all the analysed samples (Fig. 7-37). The process of rødbergitisation created a transitional alteration of carbonatite to rødbergite at the Bjørndalen transect (Fig. 6-1). A similar progressive alteration was not be observed at the Fen Road transect. The observed red colouration of the rødbergitisation seems to be rather sharp with a narrow halo of higher barite, chlorite and Fe-oxide concentration in the contact zone to carbonatite (Fig. 7-12B; Fig. 7-18). Veins also play an important role in the overall REE budget in both transects. Besides the REE-rich rødbergite veins, there are many different vein types with REE minerals in the Fen transect and Bjørndalen transect. For instance, the eastern transitional rødbergite from the Bjørndalen transect shows an increase of REE relative to the western transitional rødbergite by a factor of 10 (Fig. 6-40). Intense veining of the eastern transitional rødbergite causes this increase in REE. Similarly, the NW dolomite-carbonatite (16-95-FE) of the Fen transect has two different REE-mineral bearing sets of

veins and a REE concentration that is five times higher than the average dolomite-carbonatite from the Fen Road transect (Tab. 7-3). Apatite relics in rødbergite and transitional rødbergite from the Bjørndalen transect provide an effective way to precipitation clusters of monazite-(Ce) (Fig. 6-37; Fig. 6-38). Samples of the Fen Road transect do not show a similar trap mechanism, which might be for the following reason:

a) It was not sampled or not accessible for sampling.
b) The prevalent REE-minerals at the Fen Road transect are REE-fluorocarbonates rather than monazite-(Ce). The precipitation mechanism of REE-fluorocarbonates is less affected by the addition of P into the hydrothermal system.

REE-fluorocarbonates are the main carrier for REE at Fen Road transect, whereas monazite-(Ce) dominated mineralisation is prominent in the Bjørndalen transect. However, for REE-mineralisation associated with rødbergitisation at the Fen Road transect (e.g. rødbergite veins) the main REE-carrier is monazite-(Ce) (Fig. 7-33).

The REE-mineral bearing veins of both transects have a similar mineral composition consisting of calcite, dolomite, quartz and barite ± Fe-oxide and apatite (Tab. 7-1; Fig. 6-36). Barian phlogopite, which is typical of the alteration mineral assemblage of the Bjørndalen transect (Fig. 6-26), is not present at the Fen Road transect. Instead, chlorite is omnipresent as the dominant alumosilicate (Fig. 7-34).

Both transects show a strong LREE enrichment relative to HREE due to hydrothermal processes. While the Bjørndalen transect shows a decoupling of HREE and LREE (Fig. 6-40), this was not detected at the Fen transect. The Fen transect demonstrates a strong positive correlation of LREE, HREE and Th (Tab. 7-4).

Apatite veins from the fluorite mineralisation of the Fen Road transect have the same texture as those from the rødbergite of the Bjørndalen transect (Fig. 7-7; Fig. 6-37). In both cases, the thick apatite veins incorporate minerals from the host rock and preserve the orientation of these minerals. This evidence suggests, therefore, a metasomatic replacement of the rock by apatite. The centre of the metasomatic vein is, in both cases, a quartz-barite mix (Fig. 7-7; Fig. 6-37). The apatite zone is either part of a quartz-barite vein envelope or a preceding vein generation.

7.3.6 Rare Earth mineralisation model for the Fen transect

Similar to the Bjørndalen transect, the findings described for the Fen Road are not consistent with the model of Andersen (1984; 1986) for the REE-mineralisation in rødbergite of the Fen Complex. The following is a REE mineralisation model based solely on the Fen Road section. After evaluating all the data, including the Gruveåsen transect, chapter 10 will illustrate a unifying REE mineralisation model.

The REE mineralisation of the Fen transect is the result of multiple stages:

1. **Fractional Crystallisation or Chloritisation?**

   The Fen Road transect has two different types of carbonatites with significantly different REE concentrations. The groundmass carbonates of chlorite-bearing dolomite-carbonatite (Fig. 7-23) have a higher concentration of Fe and Mn relative to Mg than the groundmass carbonates of dolomite-carbonatite (Fig. 7-13). This is generally a sign of a more evolved carbonatite magma. REE are incompatible elements in evolving carbonatite systems and enrich with continuing fractional crystallisation. However, during chloritisation Fe is added

to the system and could potentially increase the Fe-content of the groundmass carbonate as well. Based on textural evidence, the chloritisation of chlorite-bearing dolomite-carbonatite is a hydrothermal alteration process. Chlorite is in general associated with a fine network of Fe-oxide, apatite and REE-minerals (Fig. 7-23; Fig. 7-24). Although the REE-minerals are only found in this mineral assemblage, which links them genetically (spatially) to the chloritisation, the texture suggests a more complex relationship. The REE-minerals are partly corroded subhedral, occasionally poikilitic, stacks of bastnäsite-(Ce) and synchysite-(Ce) (Fig. 7-24; Fig. 7-25; Fig. 7-26). This texture does not support a coprecipitation of REE minerals with the chlorite mineral assemblage and has not been observed for any other hydrothermal REE minerals within the Fen Road transect. However, the spatial association and texture indicate a relationship between hydrothermal process and REE mineralisation. The relative effect of fractional crystallisation and chloritisation on the REE enrichment is hard to quantify.

2. Rødbergitisation

Rødbergitisation at the Fen Road transect is a hydrothermal alteration of dolomite-carbonatite and chlorite-bearing dolomite-carbonatite caused by oxidising fluid penetrating the rock through crystal boundaries and rødbergite veins. Rødbergitisation caused the formation of monazite-(Ce), which correlates to a substantial increase of REE in the rock to an average of 8393 ppm in rødbergite (Tab. 7-3). The generally higher REE level of Fen Road rødbergite compared to Bjørndalen rødbergite is because the REE source for the rødbergite

fluid is chlorite-bearing dolomite-carbonatite rather than dolomite-carbonatite. Chlorite-bearing dolomite-carbonatite is, because of its higher REE concentration, a more fertile REE source than dolomite-carbonatite, resulting in higher REE concentration in the rødbergite fluid.

Alternatively, the hydrothermal alteration is at a level for increased REE precipitation. There is necessarily an area of REE leaching and an area of REE precipitation. The higher REE concentration of the Fen Road rødbergite compared to the Bjørndalen rødbergite could be due to a position in the volume of hydrothermal alteration, which is in a more effective zone of REE precipitation.

3. Veining

Multiple generations of REE-mineral (either synchysite-(Ce) or bastnäsite-(Ce)) bearing veins are part of the Fen Road transect (Tab. 7-2). Although the mineral composition varies, most of the veins incorporate the following minerals: barite, apatite, chlorite, Fe-oxide, calcite and dolomite.

The lack of cross-cutting relationships makes it impossible to establish relative timing. Additionally, it is important to note that the same minerals in different proportions make up the rødbergite veins. Therefore, it is likely that some of these veins represent different stages in the evolution of the rødbergitisation fluid. Pyrite-dominated veins represent a more reduced fluid chemistry than the oxidised rødbergite veins.

7.4 Conclusion

Research on the Fen Road transect showed that the combination of a detailed mineralogical and geochemical investigation is necessary to understand the complex history of REE-mineralisation. The comparison between the Bjørndalen transect and the Fen transect revealed some fundamental commonalities with an additional layer of complexity. There are five major key points:

a) Rødbergite, chlorite-bearing dolomite-carbonatite and none-rødbergite REE-mineral bearing veins show similar mineral and geochemical characteristics (Tab. 7-1; Tab. 7-2), which points to a common source.

b) The REE concentration of the chlorite-bearing dolomite-carbonatite is significantly higher than the REE concentration of dolomite-carbonatite or any other rock type (excluding rødbergite) of the Fen Complex (Tab. 7-3).

c) The hydrothermal formation of rødbergite from carbonatite caused an 8-fold and 1.5-fold average increase in REE concentration of for dolomite-carbonatite and chlorite-bearing dolomite-carbonatite, respectively (Tab. 7-3). Rødbergite veins yield the highest REE concentration, which is 21-fold and 4-fold higher than the average dolomite-carbonatite and chlorite-bearing dolomite-carbonatite, respectively. This increase in REE is caused by the formation of hydrothermal synchysite-(Ce), bastnäsite-(Ce) and monazite-(Ce) (Fig. 7-16; Fig. 7-24; Fig. 7-33).

d) The externally derived oxidising hydrothermal fluid, causing the rødbergitisation, produced a range of different mineral paragenesis with the following key minerals: calcite, dolomite-ankerite, barite, quartz, apatite, Fe-oxide, pyrite and chlorite (Tab. 7-2; Fig. 7-36). The ongoing reaction of the oxidising external fluid

with the reducing carbonatite host rock creates variable reaction conditions – from a carbonatite dominated reducing environment to a more oxidising environment in equilibrium towards the external fluid. REE minerals are found in both oxidising and reducing condition with synchysite-(Ce) and bastnäsite-(Ce) being the dominant REE carrier in reduced environments, and monazite-(Ce) preferentially found under oxidising conditions.

e) The REE mineralisation at the Fen Road transect is similar to the Bjørndalen transect with regards to the following exceptions: The REE-rich chlorite-bearing dolomite-carbonatite from Fen Road transect does not have an equivalent at the Bjørndalen transect and is a major reason for the significantly higher level of REE concentration in the Fen Road rødbergite compared to the Bjørndalen rødbergite. REE-fluorocarbonates are significantly more abundant at the Fen Road transect compared to the monazite-(Ce) dominated Bjørndalen transect. Finally, there were no observed apatite traps concentrating REE at the Fen Road transect.

8 Gruveåsen Transect

This chapter will focus on the effect of hydrothermal rødbergite-type alteration on REE and Th concentrations in different lithofacies within the Gruveåsen transect. The samples for this study were acquired along the Grønvoldvegen road following the northern side of Gruveåsen mining area. Along a length of ca. 850 m, 40 samples were collected, from which 25 samples were further chemically analysed. The Gruveåsen transect displays a greater variation of lithotypes compared to the other sites investigated in the Fen Complex and allowed for an investigation and visualisation of the REE distribution on a larger scale compared to the Bjørndalen transect or Fen Road transect.

8.1 Rock types

Figure 8-1 illustrates the distribution of the lithofacies and sample points at the Gruveåsen transect. The original map by Bergstøl and Svinndal (1960) had to be modified to represent the identified rock type of the sample along the Grønvoldvegen road. A detailed investigation to further map the extent of these newly defined lithological units across a wider area in the Fen Complex was not carried out.

The Gruveåsen transect can be broadly divided into three parts. The western part is mainly comprised of carbonatites; the central part is a heterogeneous mix of carbonatite, damtjernite and rødbergite; and the eastern part comprises brecciated fenite, rødbergite and gneiss.

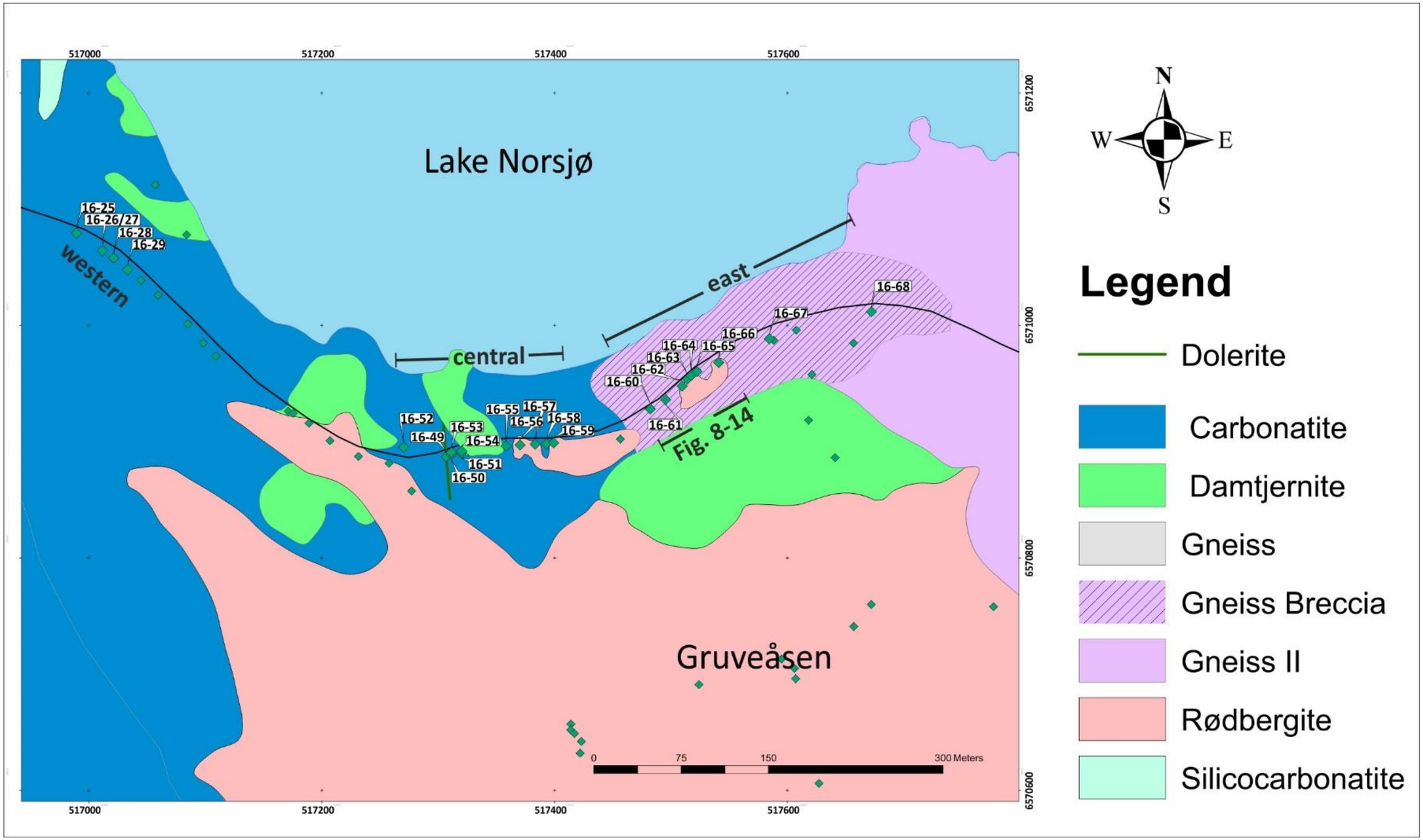

Figure 8-1: Simplified geological map of the Gruveåsen transect, which is located along the Grønvoldvegen road between the Gruveåsen mining district and lake Norsjø. Sampling points are marked by a green spot. Sampling points which were included in the study of the Gruveåsen transect are annotated. Map was modified after Bergstøl and Svinndal (1960).

The following subchapter summarises the main characteristics for the rock types of the Gruveåsen transect. The Gruveåsen transect is important for the understanding of rødbergitisation because all the major rock types (lithofacies), e.g., carbonatite, damtjernite and fenite underwent rødbergitisation. In the central part of the Gruveåsen area, around the Gruveåsen hill, it is generally not possible to identify the protolith of rødbergite because the alteration completely obliterated any feature of the former rock, whereas, at the Gruveåsen transect, which represents the outer zone of the rødbergitisation, remnants of unaltered rock are partially preserved. Contrary to the Bjørndalen- and Fen Road transect, the identification of the mineral species relies exclusively on field observation. With the experience gained from work on the other parts of the Fen Complex, it was possible to identify the main mineral composition.

8.1.1 Carbonatite

The carbonatite of the Gruveåsen transect is a leucocratic to mesocratic rock with a general increase of dark minerals from the west to the centre of the transect. The light coloured groundmass is composed of different proportions of white, beige, slightly blueish and reddish patches, which comprise of carbonate minerals and apatite (Fig. 8-2). There is no preferred orientation within the groundmass visible. Minor amounts (1-5 Vol-%) of pyrite are present in the form of irregularly shaped clusters. Rusty coloured coating around the pyrites is a sign for incipient oxidation of pyrite. There are minor amounts of euhedral, small, black crystals of magnetite and columbite. Fine irregular veins, clusters and patches of chlorite are the cause of the dark colouration of some carbonatite samples (Fig. 8-3) — comparable to the chlorite-bearing dolomite-carbonatite from the Fen Road transect. Samples are often heterogeneous with white

and grey parts of mixed carbonate-apatite and dark parts of chlorite-magnetite in close proximity. Additionally, the sharp edges of some compartments are textural evidence for brecciation and incorporation of older carbonatite.

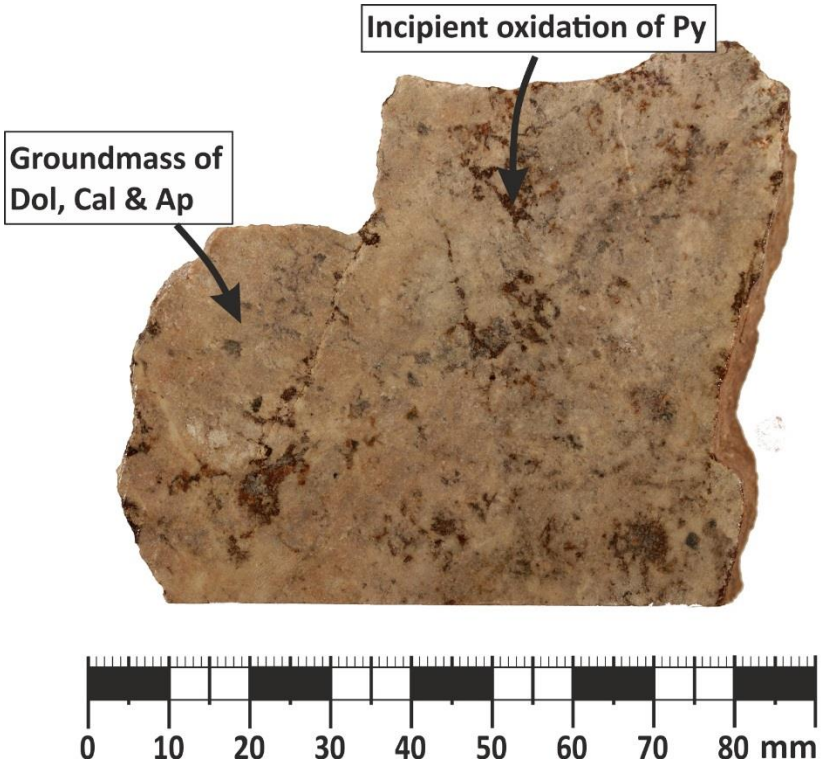

Figure 8-2: Photo of a leucocratic carbonatite hand specimen with incipient signs of oxidation (16-25-FE). Ap – Apatite, Cal – Calcite, Dol – Dolomite and Py – Pyrite.

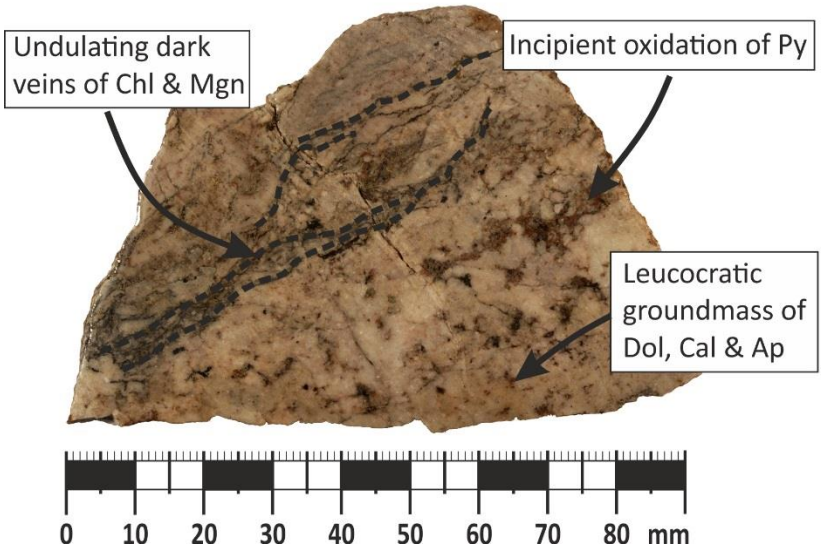

Figure 8-3: Photo of a mesocratic carbonatite hand specimen with dark veins and schlieren of chlorite and magnetite illustrated by the black dashed line (16-27-FE).

Occasionally, carbonatite samples display a noticeable higher density, which due to a higher content of pyrite and magnetite, generally associated with the chlorite veinlet network.

8.1.2 Dolerite

One dolerite dyke cross-cuts the rocks in the centre of the Gruveåsen transect. The dyke is 25 cm wide and strikes N-S (356-81-W). The dolerite dyke is comprised of white to yellowish feldspar lath-shaped phenocrysts (ca. 2 mm) showing a slightly preferred orientation in the dark, fine-grained groundmass (Fig. 8-4). Additionally, there are angular to rounded light-coloured clast, possibly carbonatite xenoliths. The dolerite cross-cuts lithotypes mildly affected by the rødbergite alteration process, but is itself unaffected, and therefore post-dates the alteration.

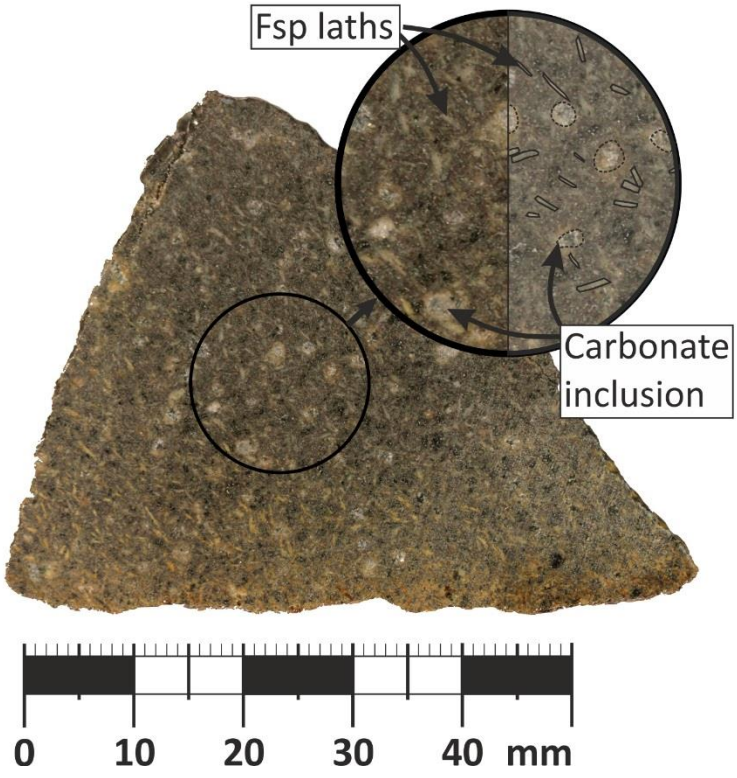

Figure 8-4: Photo of a porphyritic dolerite dyke with oriented laths of plagioclase and rounded grey inclusions of carbonate (16-49-FE).

8.1.3 Calcitic Ultramafic Lamprophyre

The classic damtjernite from the type locality Damtjern occurs as a porphyritic intrusive dyke with phlogopite, amphibole and pyroxene phenocrysts in a black to slightly greenish silicate groundmass with magmatic carbonate. Damtjernite occurs in multiple localities throughout the Fen Complex and exhibits a characteristic dark colouration with reflective phlogopite phenocryst. However, the ultramafic lamprophyre at the Gruveåsen transect has ambiguous properties, placing it between a classic damtjernite and a mesocratic carbonatite. Ultramafic lamprophyre from the Gruveåsen transect has a porphyritic texture with phlogopite phenocrysts (Fig. 8-5), which are less abundant and smaller (< 1 cm) compared to a classic damtjernite. The grey fine-grained carbonate groundmass of ultramafic lamprophyre incorporates rounded and fragmented aggregates of carbonate.

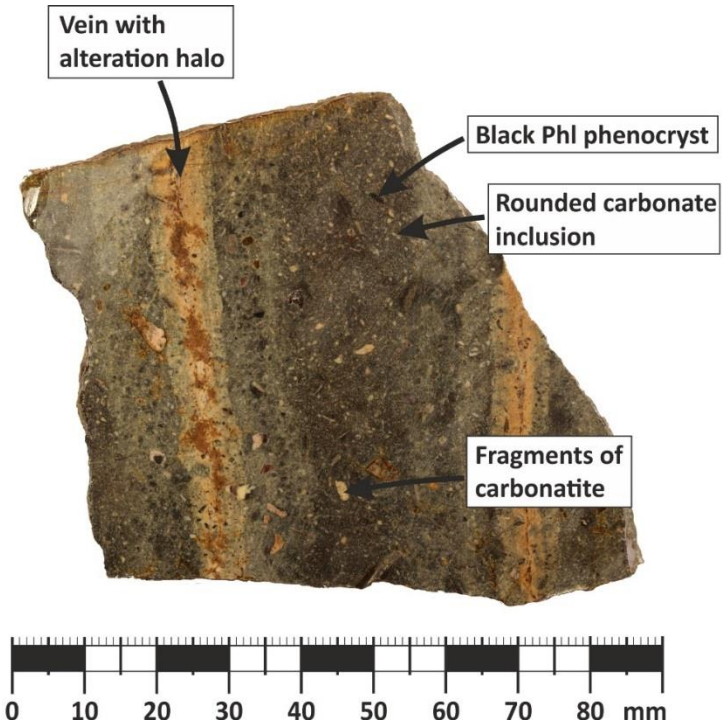

Figure 8-5: Photo of a calcitic ultramafic lamprophyre with phlogopite phenocrysts and carbonate fragments. There are two veins cutting through the lamprophyre with a centre of pastel coloured alteration surrounded by a narrow halo of bleached groundmass (16-55-FE).

The colour and the appearance of the groundmass resemble those of the darker varieties of the mesocratic carbonatite, especially those specimens with minor amounts of phlogopite phenocrysts. Loose specimen of classic damtjernite along the Gruveåsen transect and the occurrence of damtjernite north of the Gruveåsen transect towards Lake Norsjø indicate a possible genetic relationship of the ultramafic lamprophyre to classic damtjernite. The ultramafic lamprophyre resembles the C-lamprophyres — nepheline- and alkali feldspar-free with 25–50 vol. % modal carbonate — described by Dahlgren (1994). According to the classification of ultramafic lamprophyres, the C-lamprophyres correspond to aillikites (Tappe et al., 2005). Without proper mineralogical analyses of multiple sets of these Gruveåsen ultramafic lamprophyres, it is not possible to distinguish between an aillikites and a calcitic damtjernite. Therefore, the rock unit will be referred to as a calcitic ultramafic lamprophyre.

The close spatial occurrence of damtjernite, carbonatite and calcitic ultramafic lamprophyre, which looks like a transitional rock type between damtjernite and carbonatite, must have prompted Sæther (1957) to create a model of the formation of rauhaugite by the replacement of damtjernite (chapter 4). Furthermore, the presence of possible carbonate enclaves as a form of carbonatitic magma blob in a silicate-ultramafic magma indicates a genetic link between an ultramafic parental magma (damtjernite) and the formation of an evolved carbonatitic magma through magma unmixing. To test the magma-unmixing hypothesis, a representative sample number of damtjernite, carbonatite and calcitic ultramafic lamprophyre in close vicinity could be analysed for trace elements, and Sr and Nd isotopes. A separate analysis of the carbonatite enclaves, the calcitic ultramafic lamprophyre, carbonatite and damtjernite would show the genetic relationship between those lithotypes. The process of magma

unmixing will not affect the ratios of $^{87}Sr/^{86}Sr$ and $^{143}Nd/^{144}Nd$ and lead to similar isotopic ratios for all the analysed samples, which shows the genetic relations between the different lithotypes (Zaitsev and Bell, 1995). At the same time, magma unmixing will have a significant effect on the trace element data. Additionally, a study of oxygen isotopes will allow reconstructing the temperature of the different magmas and more importantly, help to identify any postmagmatic alteration event.

8.1.4 Fenite & Gneiss

According to the geological map N50 of the NGU (Geological Survey of Norway) the easternmost 150 m of the Gruveåsen transect is mapped as gneiss, which is in direct contact with the rødbergite unit without the formation of fenite in-between. The absence of fenite on the eastern margin of the Fen Complex is in accordance with every geological map of the Fen Complex. Nevertheless, the identified rock units at the easternmost 200 m of the Gruveåsen transect are not simple gneisses.

Foliated Gneiss: The least altered rock sample collected from the very end of the Gruveåsen transect (east) is a foliated gneiss. The foliated gneiss comprises bright layers of medium grain sized quartz and feldspar, which are interrupted by layers of dark blueish and greenish minerals (Fig. 8-6). Small veins of Fe-oxide cut through the foliated gneiss and partly join the dark layers. The dark minerals are likely to be amphibole and chlorite, although a reliable mineral identification requires a microscopic analysis.

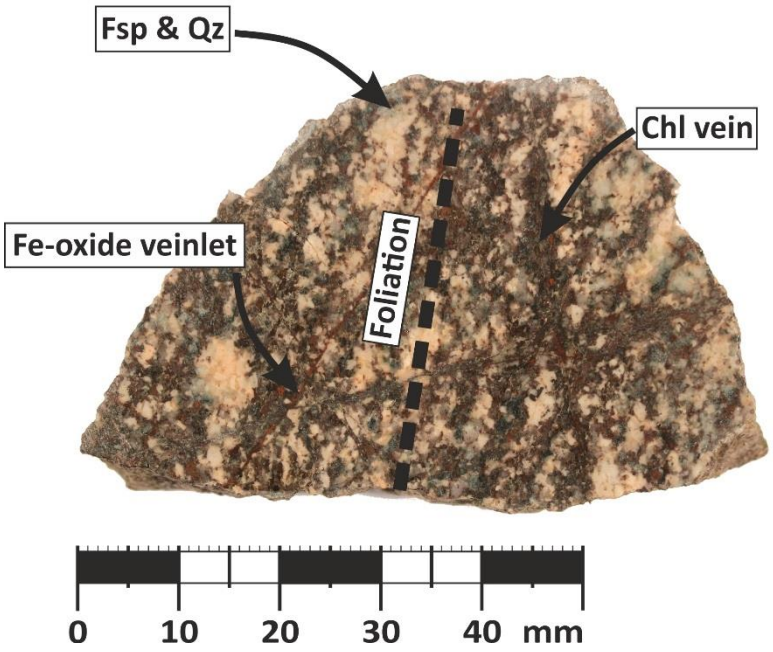

Figure 8-6: Photo of a foliated gneiss with light quartzofeldspatic areas and darker cross-cutting amphibole-phlogopite areas. Additionally, there is a fine network of randomly oriented red veinlets. (16-68-FE).

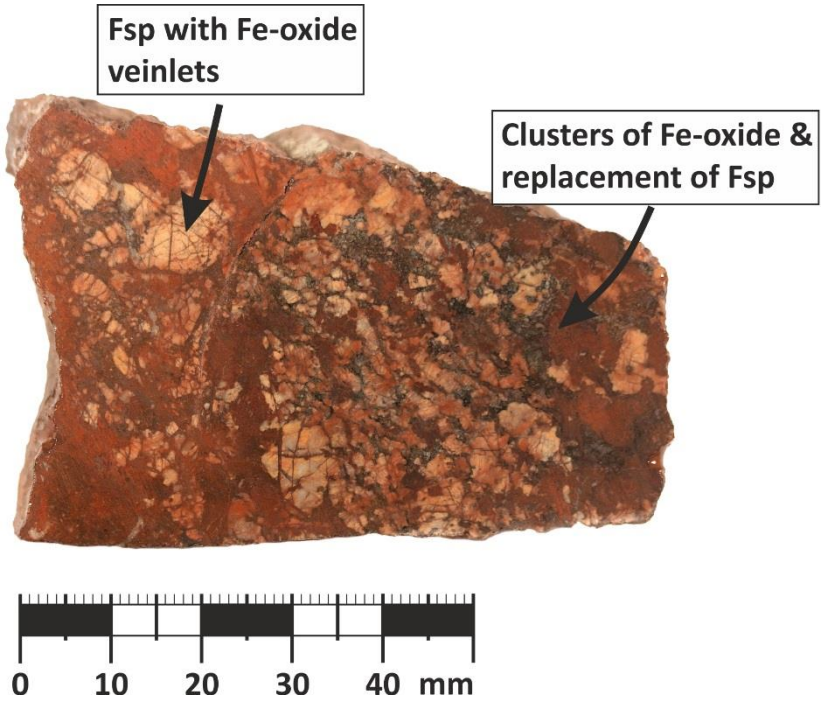

Figure 8-7: Photo of fenite, which is brecciated and partly replaced by a network and clusters of Fe-oxide (16-49-FE).

Brecciated Fenite: Moving west towards the centre of the Gruveåsen transect, the foliated gneiss becomes a massive brecciated fenite (Fig. 8-7). The brecciation was caused by a network of a millimetre to decimetre thick veins of Fe-oxide, chlorite and minor calcite — quartz is absence from the rock. Partly fenite is largely replaced by

rødbergite leaving remnants of altered feldspar and metamorphic layering. Occasionally, phenocrysts of chlorite, or a pseudomorph after dark mica phenocrysts, are part of the rødbergite groundmass surrounding clusters of brecciated fenite (Fig. 8-8). The presence of chlorite phenocrysts indicates the brecciation of fenite by former calcitic ultramafic lamprophyre or damtjernite, which in turn was altered to rødbergite. Xenolith of rødbergite within the altered calcitic ultramafic lamprophyre suggests at least two events of rødbergitisation with the emplacement of calcitic ultramafic lamprophyre in between. Additionally, 50 cm wide carbonatite sill cross-cuts through the brecciated fenite. The multiple brecciations created large (> 2m) blocks of brecciated fenite.

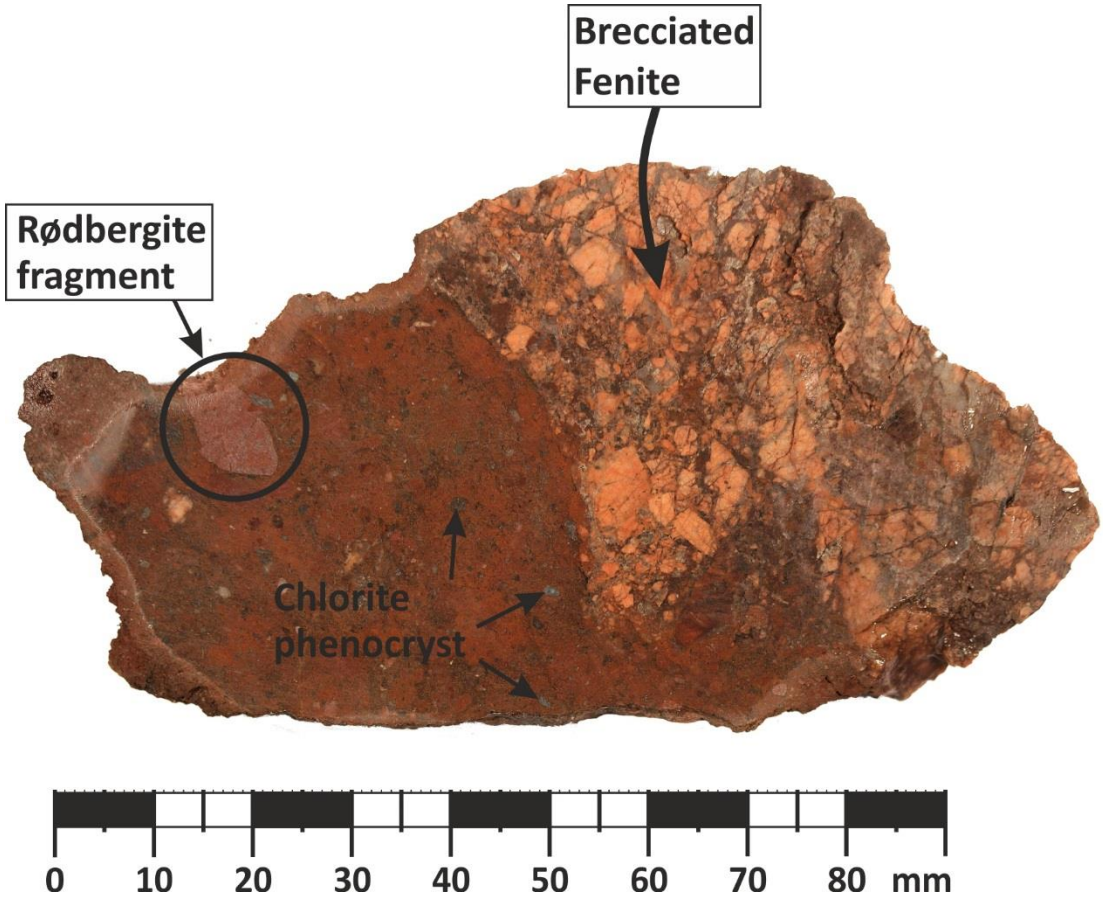

Figure 8-8: Photo of brecciated fenite in a rødbergite groundmass with chlorite phenocrysts (16-62-FE). A fragment of older rødbergite is incorporated into the rødbergite groundmass.

8.1.5 Explosive Damtjernite Breccia

A rock unit with varies different types and sizes of angular xenoliths is located in the middle of the brecciated fenite (Fig. 8-9). The collected hand specimen contains unaltered foliated and unfoliated gneiss, fenite, different types of carbonatite and rødbergite. The groundmass is greyish to greenish and contains smaller angular xenoliths, rounded aggregates and a few brown phlogopite phenocrysts. The variety and concentration of xenoliths within the breccia is the result of an explosive reaction. The presence of phlogopite phenocrysts indicates damtjernite magma to be the source of this explosive event.

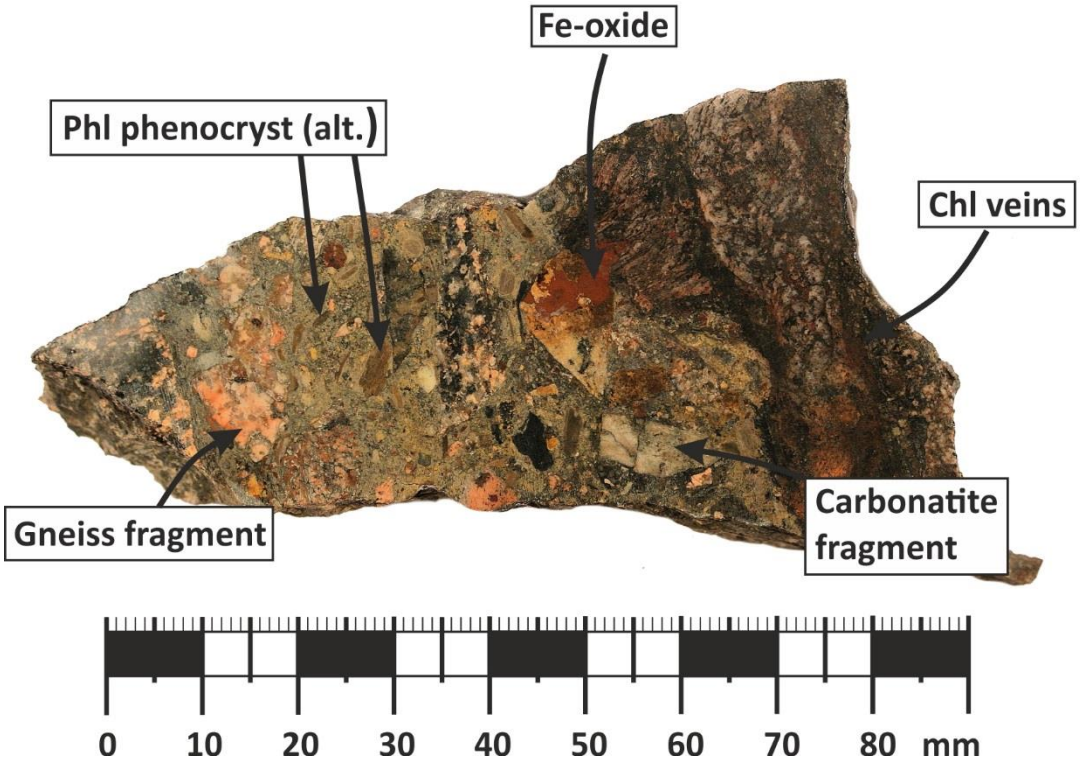

Figure 8-9: Photo of an explosive lamprophyric breccia. The sample has a greenish groundmass with bronze coloured phlogopite phenocrysts and comprises a variety of xenoliths, e.g., fenite, gneiss, carbonatite, rødbergite and dark veins (16-65-FE).

8.1.6 Rødbergite

Massive rødbergite was analysed from the central and eastern section of the Gruveåsen transect. Proximal to the eastern rødbergite outcrop are the remnants of an old iron ore mine. In general, mining activities left numerous deep, long and narrow pits within the Gruveåsen area (Fig. 8-10), which show a preferred orientation of NW-SE. Locally the Fe-exploitation left elliptical shaped cavities of up to 40 m in length. At the old iron mine adjacent to the Gruveåsen transect are three different types of rødbergite present, i.e., a massive fine crystalline variety, one type with schlieren in different shades of red, and one type with rather circular clusters and nests of different shades of red.

Figure 8-10: A)-D) Remnants of Fe-mines at Gruveåsen hill. A) The largest mining cavity at Gruveåsen hill B)-D) Other remnants generally resemble narrow (<5 m), steep and long (up to 100 m) canyons

The alteration process forming the massive rødbergite unit affected the adjacent rock units and the influence of Fe-oxide (patches and veinlets) can be traced until the eastern end of the Gruveåsen transect (Fig. 8-6). The brecciated fenite, NE of the rødbergite, is characterised by a high density of veinlets, veins and flakes of Fe-oxide that occasionally transform into massive rødbergite (Fig. 8-11). Locally, rødbergite samples collected at the eastern end of the Gruveåsen transect show layering, which indicates the replacement of a foliated gneiss (Fig. 8-12).

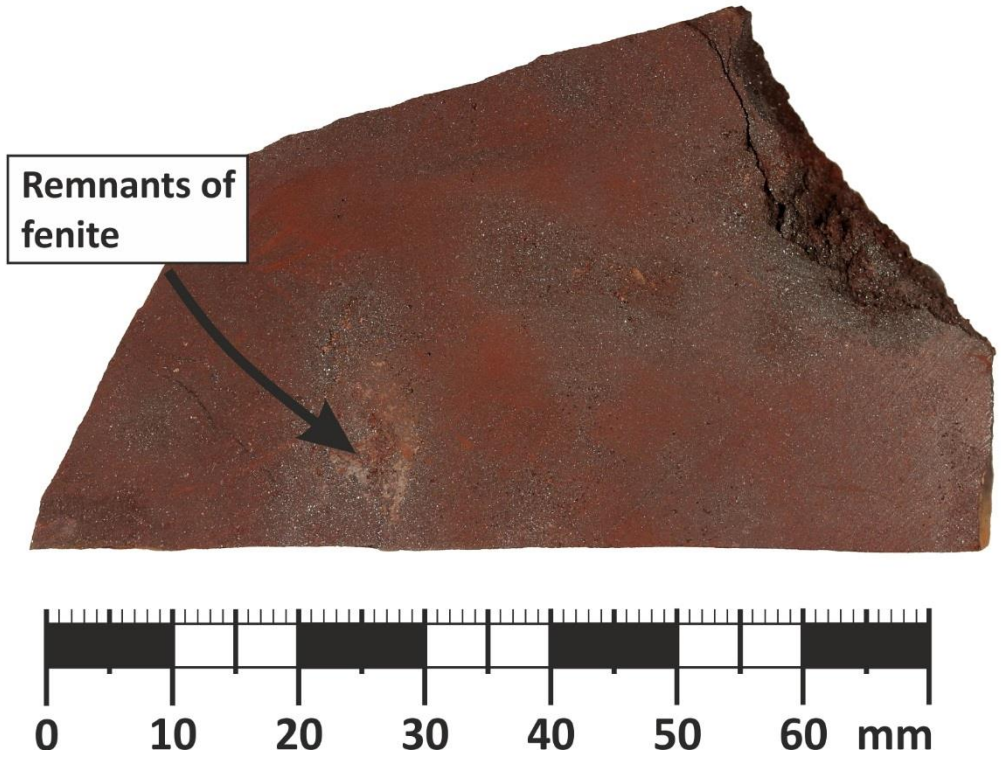

Figure 8-11: Photo of a dark red rødbergite with remnants of fenite surrounded by a porous metallic halo. (16-66-FE).

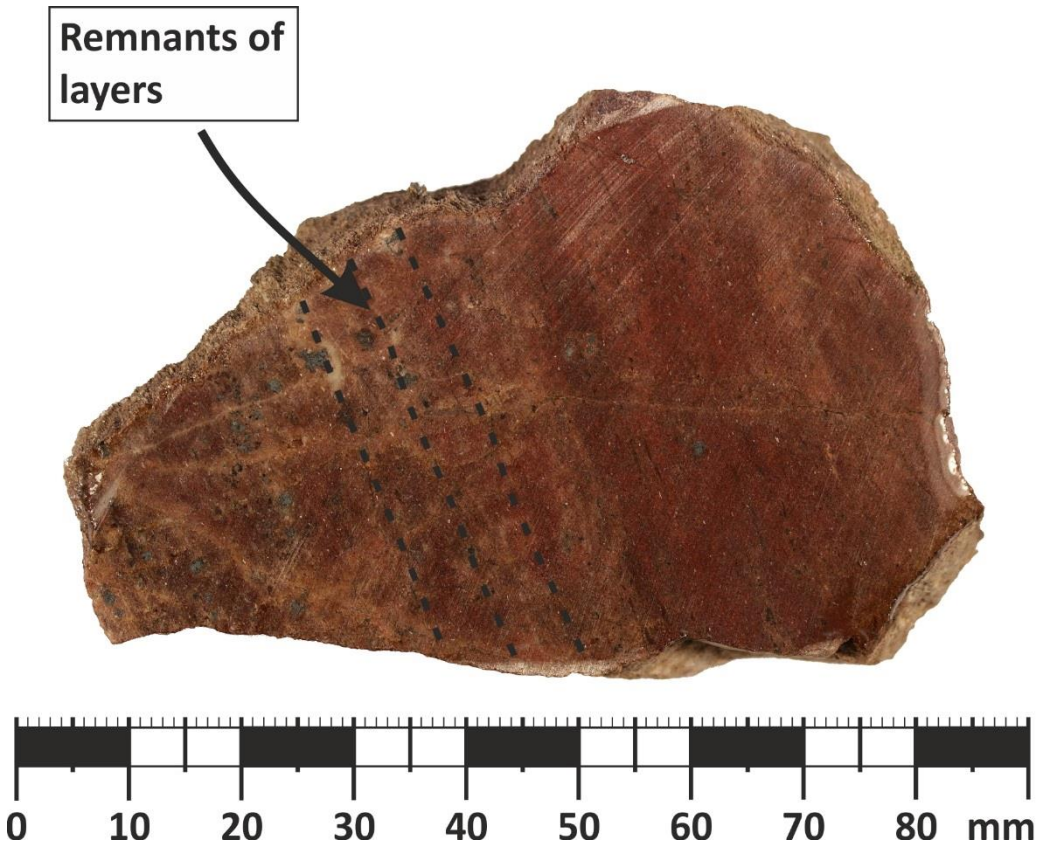

Figure 8-12: Photo of a rødbergite with remnants of oriented layers of foliated gneiss (16-67-FE).

The damtjernite and carbonatite units southwest of the rødbergite unit are less intensely fractured by rødbergitisation and are more extensively replaced. One group of rødbergite samples contain phenocrysts of chlorite pseudomorphs after phlogopite surrounded by a red groundmass, which points to calcitic ultramafic lamprophyre or damtjernite as being one of the protoliths before rødbergitisation (Fig. 8-8; Fig. 8-13).

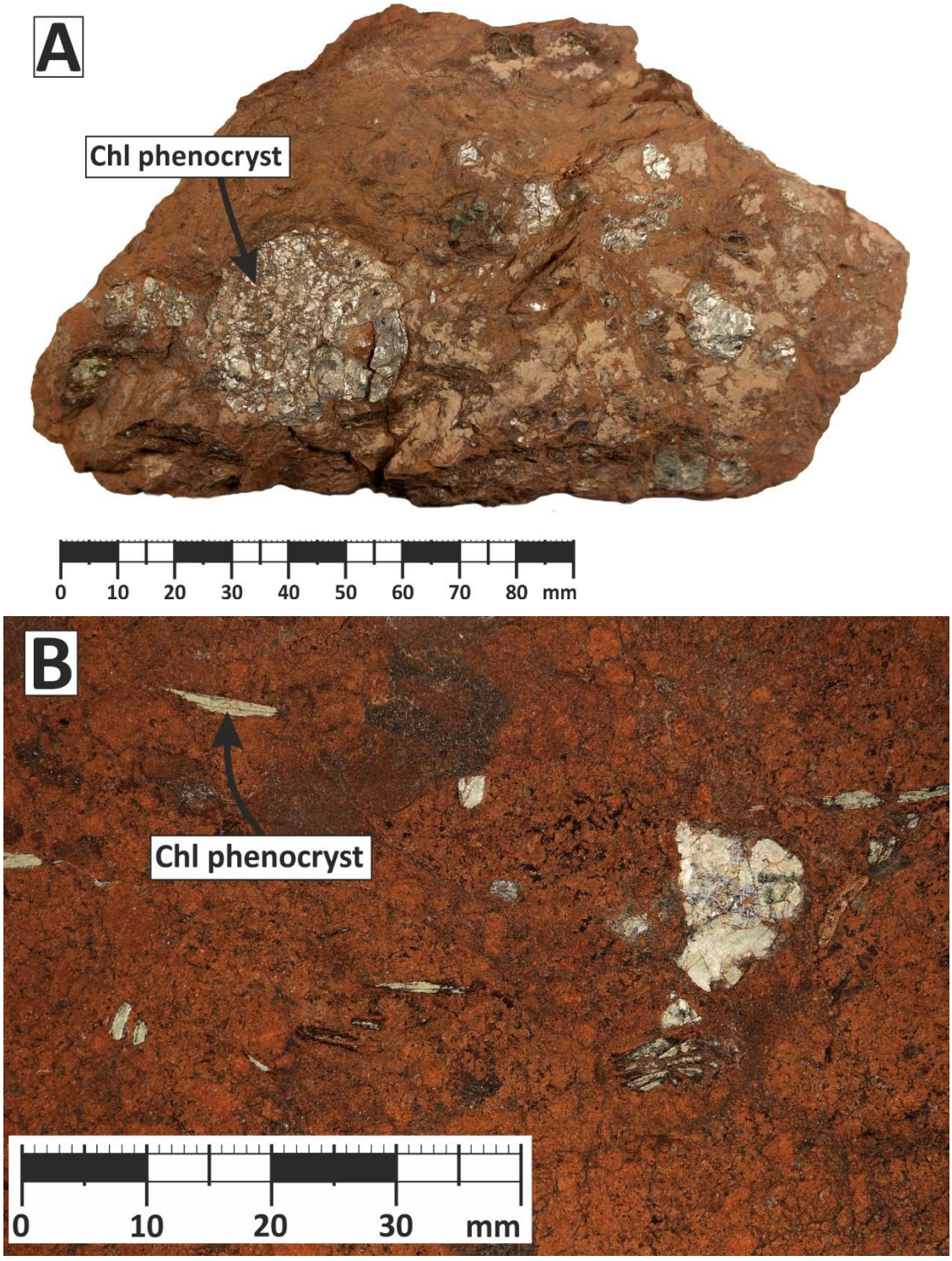

Figure 8-13: (A) Photo of a rødbergite specimen with a porphyritic texture of rounded chlorite phenocrysts. (B) Polished surface of the same specimen, is showing differently oriented stacks of silverish chlorite phenocrysts in a groundmass of rødbergite (16-57-FE).

8.2 Bulk REE and Th concentrations

The measurements of bulk REE and Th concentrations measured by ICP-MS after sodium-peroxide sintering (please refer to chapter 5 for details about the method) reveals variations in the distribution of REE, LREE, HREE, Th and La/Yb along the Gruveåsen transect, which correlates with the type of protolith. The concentration of total REE ranges from 155 ppm in a foliated gneiss to 22,538 ppm in a rødbergite vein (Fig. 8-14; Tab. 8-1).

Table 8-1: Average concentration and range of REE, LREE, HREE, Th and La/Yb for the main rock types of Gruveåsen transect.

			REE [ppm]	**LREE** [ppm]	**HREE** [ppm]	**Th** [ppm]	**La/Yb**
Carbonatite	(n=11)	Average	7236	6913	322	549	243
		Range	1900-17685	1786-17285	114-712	114-886	39-47
Rødbergite	(n=6)	Average	4762	4475	287	398	73
		Range	155-11811	118-11376	38-602	64-903	14-155
Rødbergite vein	(n=3)	Average	11577	11236	342	1443	354
		Range	420-22538	303-21971	116-567	119-3152	15-524
Fe-ore	(n=1)		7254	6341	913	574	33
Calcitic Ultramafic Lamprophyre	(n=1)		1586	1450	136	63	70
Explosive Damtjernite Breccia	(n=1)		1483	1124	359	396	15
Fenite	(n=3)	Average	477	361	116	77	14
		Range	341-669	204-575	94-137	10-103	44-75
Gneiss	(n=1)		230	180	50	25	13
Dolerite	(n=1)		335	286	49	8	28

The range in REE and Th concentration along the transect mirrors the diverse nature of rock types described in section 8.1. Additionally, the enrichment of REE, LREE, HREE and Th do not necessarily correlate with each other. The distribution of LREE and REE is almost identical along the transect, which is expressed by a perfect correlation of the two variables (Tab. 8-2). A very strong or perfect correlation is not surprising because LREE constitute an average of 94% of the REE budget. Th shows a strong positive correlation with REE. The distribution of HREE is slightly different and shows a strong positive correlation with REE and a moderately strong positive correlation with Th (Tab. 8-2).

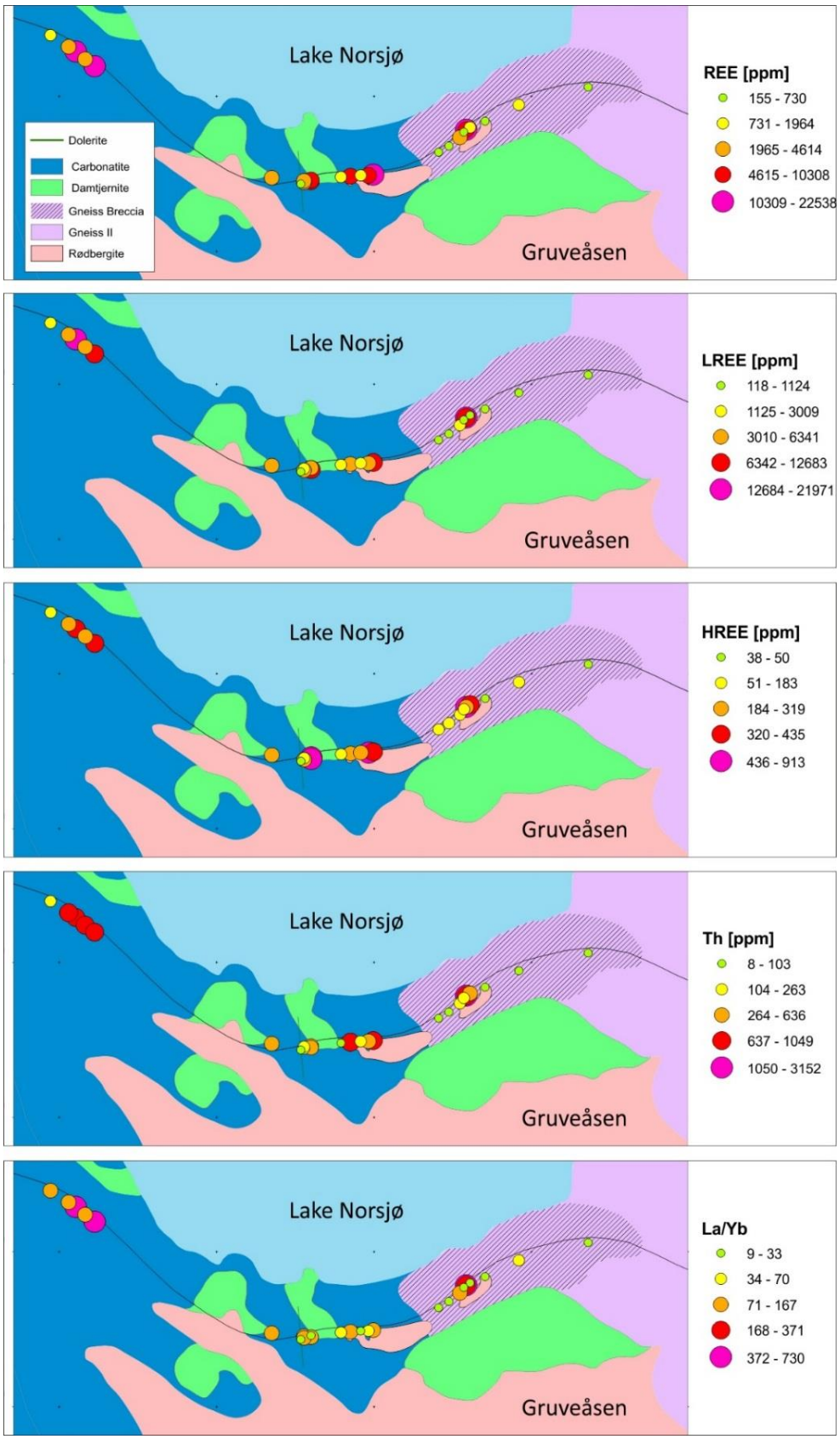

Figure 8-14: Element concentration distribution of REE, LREE, HREE, Th and La/Yb along the Gruveasen transect. The analysed data were categorised into five classes using the Jenks-Caspall-Algorithm for generating natural breaks.

Table 8-2: Correlation matrix of REE, LREE, HREE, Th and La/Yb for the Gruveåsen transect.

	REE	LREE	HREE	Th
REE	-			
LREE	1.00	-		
HREE	0.62	0.60	-	
Th	0.84	0.84	0.52	-
La/Yb	0.86	0.87	0.28	0.64

The transect is divided into a western, a central and an eastern section. REE and Th systematics are discussed for each of these sections separately.

The western part of the Gruveåsen transect is comprised of carbonatite (n=5). The westernmost sample of the transect (16-25-FE) has the lowest concentration of LREE, HREE and Th (Fig. 8-2). Going eastward, the following four samples are on average elevated in HREE and Th by a factor of three and seven respectively. LREE are elevated as well but differ stronger than HREE or Th. The sample 16-27-FE has the highest LREE concentration with 17,285 ppm, which corresponds to a 10-fold enrichment (Appendix IV). The samples enriched in LREE, HREE and Th appear much darker due to a higher proportion of chlorite and magnetite. Additionally, sample 16-27-FE has a high proportion of black veinlets, similar in appearance to REE-mineral bearing veins from the Bjørndalen transect (Fig. 8-3; Fig. 6-13).

The central part of the Gruveåsen transect is comprised of carbonatite (n=5), rødbergite (n=4), dolerite (n=1) and a calcitic ultramafic lamprophyre (n=1) (Fig. 8-1). The carbonatite samples from the central part are similar to the western part of the transect in terms of optical appearance, as well as LREE and HREE concentrations.

Carbonatite (16-54-FE) adjacent to a rødbergite vein exhibits an ochre-beige colouration, and yields elevated LREE and Th concentrations and the highest concentration of HREE (913 ppm) within the Gruveåsen transect. Rødbergite samples exhibit variable concentrations of LREE, HREE and Th, and show the highest LREE and Th concentrations in the central section. Rødbergite 16-57-FE is the alteration product of a calcitic ultramafic lamprophyre or damtjernite and has the lowest concentrations of LREE, HREE and Th within the central rødbergite group. Rødbergite sample 16-56-FE is comprised partly of pure hematite/magnetite ore and therefore especially enriched in Th (903 ppm). Sample 16-55-FE is a calcitic ultramafic lamprophyre with small vein alteration and shows relatively low concentrations of LREE, HREE and Th, which are slightly less than in the rødbergitised calcitic ultramafic lamprophyre sample (16-57-FE). The dolerite dyke stands out with its relatively low concentration of LREE (286 ppm), HREE (49 ppm) and Th (8 ppm) (Tab. 8-1).

The eastern part of the Gruveåsen transect is mainly comprised of brecciated fenite (Fig. 8-7; Fig. 8-8) and gneiss (Fig. 8-6) with several rødbergite veins and lenses of massive rødbergite (Fig. 8-11), and is characterised by a low average REE concentration of less than 1,000 ppm (Fig. 8-14; excluding 16-64-FE). The foliated gneiss (Fig. 8-6) from the eastern end of the Gruveåsen transect is the sample least affected by the rødbergite alteration and has a relatively low REE concentration of 230 ppm. The next sample (collected 90 m apart) along the transect is a rødbergite with a remnant of a gneissic foliation (Fig. 8-12), which indicates that the protolith was most likely a foliated gneiss. The REE concentration of 961 ppm is relatively low for a rødbergite but four-times as much as the REE concentration of the foliated gneiss (Tab. 8-1).

The following rødbergite sample along the Gruveåsen transect has relics of brecciated fenite (Fig. 8-11) and with 155 ppm the lowest REE concentration of the Gruveåsen transect, which is below the average upper crustal REE concentration of 170 ppm (Rudnick and Gao, 2003). The brecciated and strongly altered fenites 16-60/61/63-FE (Fig. 8-15) have elevated but still relatively low REE concentrations (341 ppm – 669 ppm). The only exception is a rødbergite sample 16-62-FE with 3,148 ppm REE and a rødbergite vein 16-64-FE (Fig. 8-15). The REE concentration of the rødbergite vein is with 22,538 ppm the highest concentration of Gruveåsen transect.

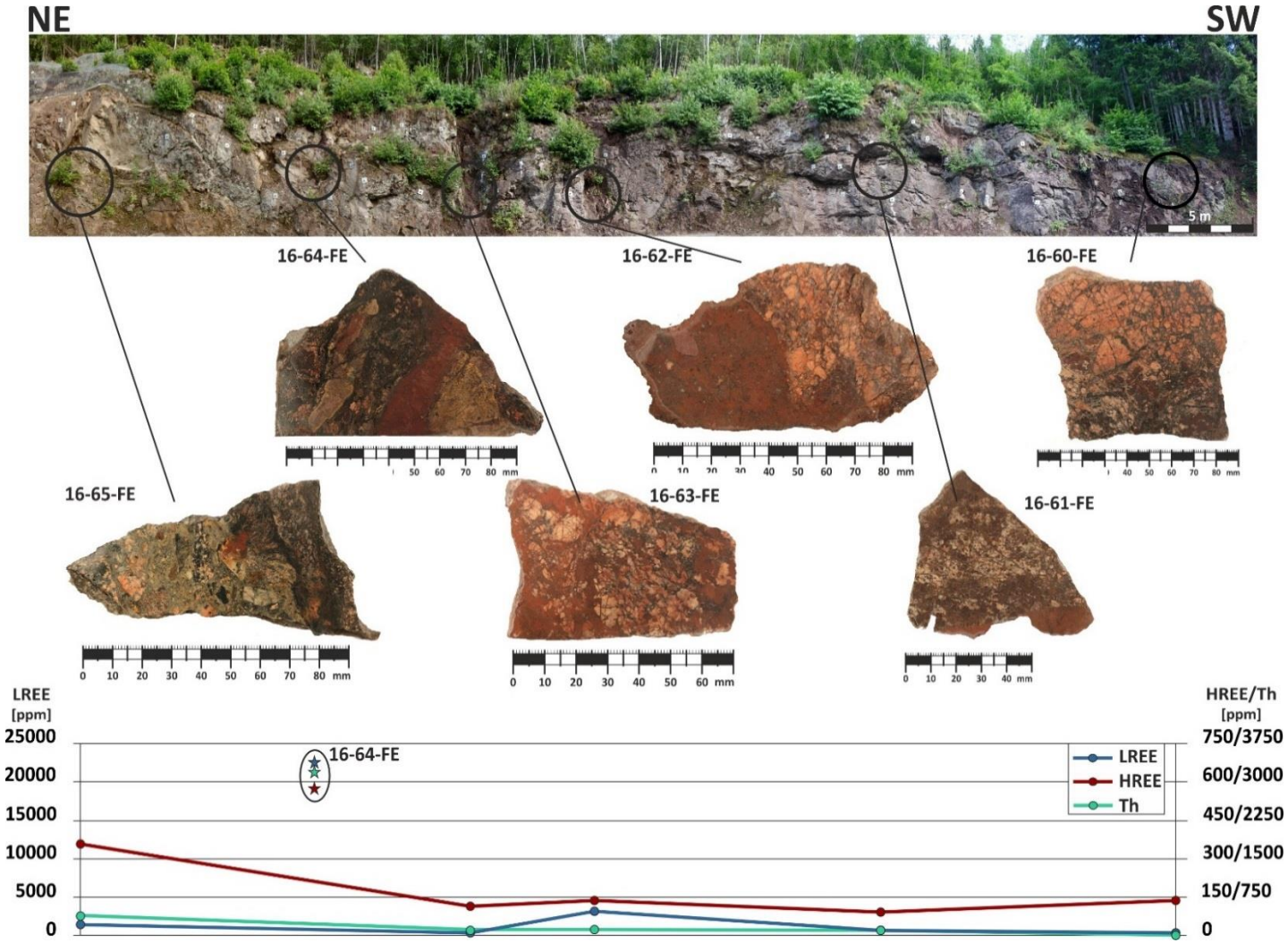

Figure 8-15: The 50 m long central part of the Gruveasen transect comprises samples of brecciated fenite, rødbergite and explosive lamprophyric breccia. The concentration of LREE, HREE and Th are plotted below the location of the sample. The diagram is showing a relatively low level of the three parameters with a strong spike of LREE, HREE and Th for vein composition of 16-64-FE.

The chondrite-normalised REE concentration diagrams show negative slopes for the samples of the Gruveåsen transect because LREE are relatively enriched to HREE (Fig. 8-16). The relative enrichment of LREE is significantly more pronounced in carbonatites, rødbergite and rødbergite veins compared to gneiss and fenite. Within the LREE-enriched rock types, the effect is in general stronger for samples with a relatively high REE concentration. Within the group of carbonatites, the chondrite-normalised plots show very similar values for the last four HREE Ho-Lu and more variable values for the lighter REE (Fig. 8-16A). The most significant difference of the graphs occurs from Gd to Ho and results in a change from an asymptotic trend for lower REE carbonatites to a sigma trend in higher REE carbonatites. Sample 16-58-FE has an exceptionally high HREE concentration and appears to be an outlier. The chondrite-normalised plot for rødbergite samples enriched in REE show a similar trend than the group of carbonatites while also having samples with a very low REE concentration and a relatively flat trend (Fig. 8-16B). Especially, rødbergite samples collected distal to the main rødbergite zone within fenite and gneiss show flatter curves and lower REE concentrations. The Fe-ore sample (16-54-FE) has the highest level of HREE and has a maximum in Pr and Nd enrichment and a negative Ce anomaly (Fig. 8-16D). Rødbergite veins show a similar REE distribution to rødbergite, but exhibit a straight to weakly asymptotic trend in contrast to the sigmoidal trend of rødbergite (Fig. 8-16C). The lithotypes dolerite, gneiss and brecciated fenite with Fe-oxide mineralisation have low REE concentrations relative to rødbergite and carbonatite with relatively flat curves (Fig. 8-16E). The calcitic ultramafic lamprophyre (16-55-FE) with veins has a similar curve than a low REE carbonatite sample.

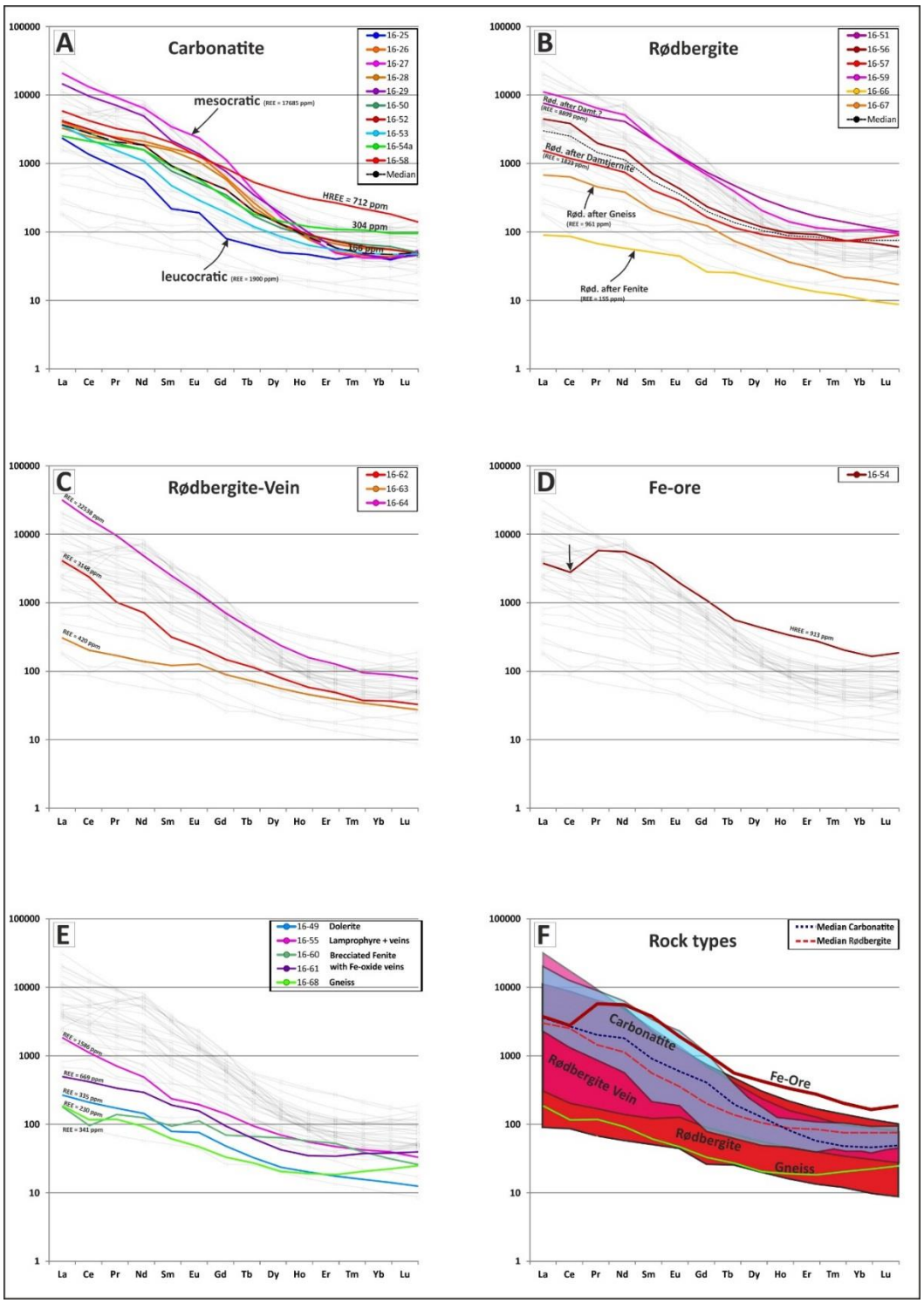

Figure 8-16: REE concentrations of the Gruveåsen transect samples normalised to CI1-chondrite values from McDonough and Sun (1995). A) Carbonatites have high REE concentration and show a strong LREE to HREE enrichment, which is more pronounced in mesocratic carbonatite than in the leucocratic variety. B) Rødbergite samples show a great variety of REE concentration ranging from low level to high levels of REE enrichment. They show a strong LREE to HREE enrichment but with higher HREE concentration compared to carbonatite samples. C) Rødbergite veins show a similar trend to rødbergite samples but have a more gradual increase in slope and the highest REE concentration of all samples. D) Fe-ore has a less steep slope with relatively high HREE values and a Ce anomaly. E) Dolerite, calcitic ultramafic lamprophyre and gneiss samples show a LREE to HREE enrichment with relatively low REE concentrations compared to A to D. F) Plot showing the relation between the prominent rock types and the medians for carbonatite and rødbergite

8.3 Discussion

8.3.1 Chloritisation

The carbonatites of Gruveåsen transect yield a high capacity for REE mineralisation with two samples containing more than 10,000 ppm REE (Fig. 8-15). Although there was no sign for rødbergitisation, which would have been an explanation for the high REE contents, the samples show signs of post-magmatic alteration. The western end of the Gruveåsen transect is marked by a leucocratic carbonatite with a REE concentration of 1,900 ppm and no obvious signs of alteration (Fig. 8-2). Compared to the first sample the rest of the carbonatites are mesocratic and relatively dense, associated with a higher amount of chlorite, magnetite and pyrite, while simultaneously having a much higher REE concentration (Fig. 8-16A). Chlorite, magnetite and pyrite are forming schlieren, patches and veinlets indicating a hydrothermal origin of these minerals (Fig. 8-3). Additionally, a majority of the carbonatites are brecciated, which further underlines the presence of a fluid phase. All the evidence suggest a link between the alteration mineral assemblage of chlorite, magnetite and pyrite with the enrichment in REE by a factor of 2 to 9 (Tab. 8-1).

8.3.2 Rødbergitisation at Gruveåsen transect

The process of rødbergitisation cannot only alter, replace and completely obliterate the original texture of carbonatite (Fig. 6-22; Fig. 7-28) but has the same effect on gneiss/fenite and calcitic ultramafic lamprophyre. The complete alteration to rødbergite does not allow a reliable reconstruction of the protolith. Nevertheless, textural evidence in chapter 8.1 indicates different degrees of rødbergitisation for gneiss, fenite and calcitic ultramafic lamprophyre (Fig. 8-7; Fig. 8-11; Fig. 8-12). The presence of relics with the original texture helped to reconstruct the protolith.

The variation in REE concentration for rødbergite and rødbergite veins ranges from the lowest to the highest value for the Gruveåsen transect – 155 ppm to 22,538 ppm (Fig. 8-16B; Fig. 8-16C). While rødbergite situated adjacent to carbonatite and/or calcitic ultramafic lamprophyre has systematically high REE values, REE concentrations in rødbergite and rødbergite veins in fenite and gneiss show large variations with a significantly lower average REE content. This indicates an important role of the host rock for both REE concentration and mineralisation during rødbergitisation. Two aspects of the host rock are of general significance a) being a fertile source for REE and b) being a potential trap for REE. Brecciated fenite altered by rødbergitisation (16-61-FE; REE = 661 ppm) showed the general potential for fenite to trap REE and proved the existence of fenite samples elevated in REE. It is however not possible to quantify the efficiency of incorporating/trapping REE within fenite, and it is likely to be less than in carbonate-bearing rock, e.g., carbonatite and calcitic ultramafic lamprophyre. Additionally, the presence of rødbergite veins – highly enriched in REE – proved the possible existence of an REE-mineralisation within fenite (Fig. 8-15).

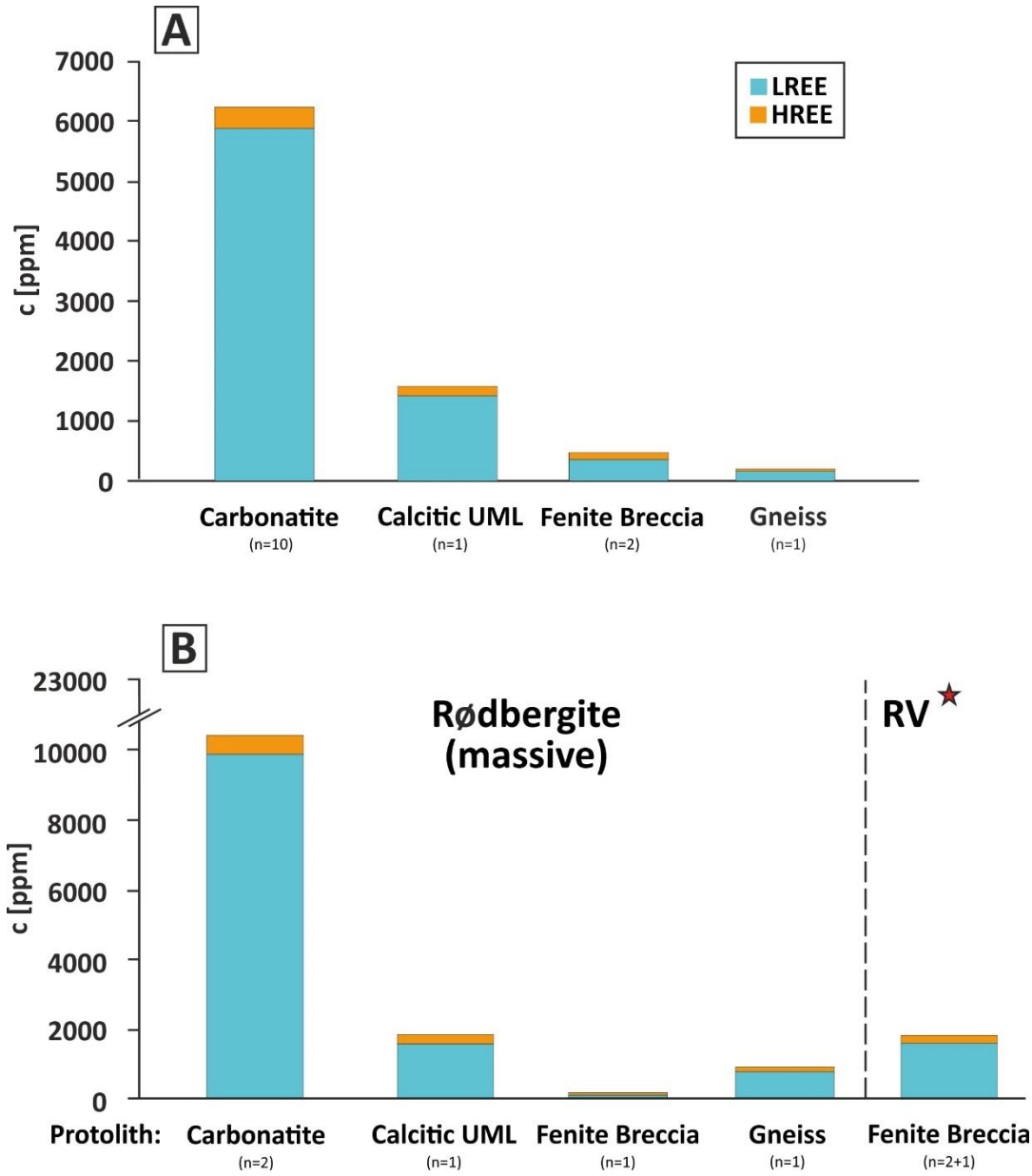

Figure 8-17: (A) Cumulative average LREE and HREE concentration for carbonatite, calcitic UML, fenite breccia and gneiss. (B) Cumulative average LREE and HREE concentration of rødbergite samples divided into protoliths. Additionally, the cumulative average LREE and HREE concentration of rødbergite veins in fenite breccias are illustrated. One rødbergite vein (red star) was excluded from the average calculation due to the high values of REE. The similar relative distribution of REE between (A) and (B) illustrates a connection between the REE concentration of the rock and the REE concertation of its rødbergitised rock variety.

Nevertheless, the generally low REE concentration of rødbergite samples in the eastern part of Gruveåsen transect strongly suggest a link between the REE concentration of the host rock and a potential REE-mineralisation in areas altered by rødbergitisation (Fig. 8-17).

For most of the rødbergite samples in the eastern part of the transect, fenite and gneiss are the host rock as well as the source rock at the same time. The redistribution of the REE through rødbergitisation fluids was a local process, and more fertile sources were not part of the hydrothermal cell or were too far away for effective transport of REE.

Contrary to the general low REE concentration of rødbergite samples collected from the eastern part of the Gruveåsen transect, is one rødbergite vein containing the highest REE concentration of all the samples of the Gruveåsen transect (Fig. 8-15). This rødbergite vein (16-64-FE; REE = 22,538 ppm) is 4 and 8 m apart from other rødbergite veins with relatively low REE concentrations. The surrounding source rock is fenite in all three cases. This REE-rich vein might be connected to a deeper fault providing fluid from a deeper but fertile source (e.g. carbonatite). In this case, fenite could have had an enhancing effect on the REE concentration within the vein, due to its more inert chemical composition. Besides altered fenite, the vein also contains clasts of beige carbonatite, which suggest the availability of carbonatite in the hydrothermal system. Additionally, the vein is in proximity to an explosive damtjernite breccia (Fig. 8-15), which might enhance fluid permeability or could provide fertile REE sources.

The high REE concentration of rødbergite veins and rødbergite samples show the general capacity for rødbergite fluid to transport REE and enrich an area in REE. The curve for the median chondrite-normalised diagrams for rødbergite has a strong negative slope due to a stronger LREE relative to HREE enrichment of the rock (Fig. 8-16B). The curve for the median chondrite-normalised diagram for carbonatite has a similar trend with a stronger LREE enrichment relative to HREE than rødbergite (Fig. 8-16A). The rødbergite median has a higher concentration for the five heaviest REE (Ho, Er, Tm, Yb, Lu) compared to the carbonatite median (Fig. 8-16F). However, within the

group of Fe-oxide mineralised rocks, there is a distinct variation in the $(La/Yb)_N$ ratio with a general decrease in the following order: rødbergite vein (160) > rødbergite (49) > Fe-ore vein (23). Fe-ore veins contain relatively high HREE concentrations (921 ppm) while having low La/Yb ratios (Tab. 8-1).

The geometry and orientation of the mining pits at the Gruveåsen area (Fig. 8-10) confirm the preferred orientation of the Fe-vein mineralisation discussed by Sæther (1957) and Andersen (1983). The parallel set of Fe vein-type ore bodies with the same orientation can be traced until the centre of the Fen Complex (Fig. 8-18). Therefore, a regional stress field must have been the cause of the formation of a set of parallel faults or fractures, which the rødbergite fluids then used as the preferred fluid pathway.

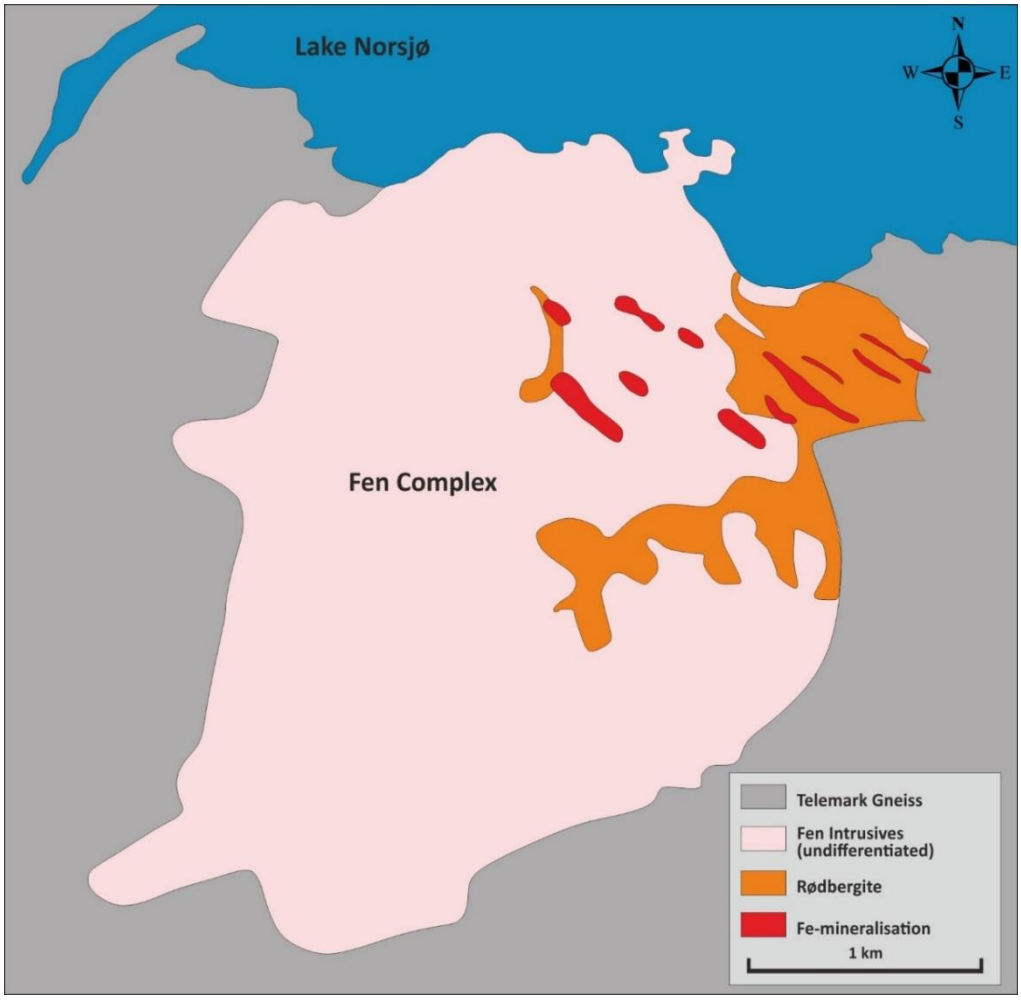

Figure 8-18: Simplified geological map of the Fen Complex showing the extent of rødbergite and the preferred orientation of Fe-vein mineralisation at the centre of rødbergite (Sæther, 1957).

8.3.3 REE Fluid Chemistry

The formation of rødbergite was the result of the hydrothermal alteration of a protolith by a REE-bearing oxidising fluid. The oxidising conditions did not affect the cerium concentration of rødbergite or rødbergite veins. However, the chondrite-normalised plots for REE show a negative cerium anomaly in one Fe-ore vein (Fig. 8-16). The hydrothermal fluid must have caused the oxidation of Ce^{3+} to Ce^{4+} in the REE source rock. In a hydrothermal system, Ce^{4+} is less soluble than Ce^{3+} and remains in the REE source rock, resulting in a negative cerium anomaly in the Fe-ore vein. The fact that a cerium anomaly is missing in rødbergite or rødbergite veins and only occurs in the Fe-ore vein indicates especially oxidising conditions during the formation of the Fe-ore vein. These conditions can be achieved by overcoming the redox buffer of the host rock through, e.g., multiple events of hydrothermal alteration.

The presence of magnetite and pyrite in the alteration process (Fig. 8-3), which causes an REE enrichment in carbonatite of the Gruveåsen transect, indicates a more reducing environment relative to the rødbergitisation. In both types of alteration, the fluid contains REE, Th and Fe. There might be a link between the two types of alteration, showing the evolution from a reduced environment of pyrite and magnetite mineralisation to a more oxidised environment of red Fe-oxides precipitation. This evolution could be the result of the decreasing chemical buffer ability of the reduced host rock and an increasing equilibration to atmospheric conditions, which produces oxidising hydrothermal fluid.

8.4 Conclusions

The analysis of the effect of rødbergite-type hydrothermal alteration on different lithofacies presented in this chapter, in particular on the bulk rock REE concentrations, revealed five key conclusions:

a) An alteration of carbonatite by less oxidising fluids is characterised by the formation of chlorite, magnetite and pyrite (Fig. 8-3). The altered carbonatite is darker, denser and displays a 9-fold enrichment of REE and 8-fold enrichment of Th, relative to the unaltered igneous carbonatite (Tab 8-1).

b) An oxidising fluid producing a red Fe-mineralisation and an associated enrichment in REE and Th in the host rock caused the rødbergitisation.

c) The process of rødbergitisation completely replaced every major rock type along the transect — calcitic ultramafic lamprophyre, carbonatite, fenite and gneiss (Fig. 8-7; Fig. 8-8; Fig. 8-11; Fig. 8-12; Fig. 8-13). In turn, the REE concentration of the underlying host rock before rødbergitisation influenced the REE concentration of rødbergite (Fig. 8-17). This highlights the importance of local redistribution of REE for the most part of rødbergite formation, rather than the transport of REE over a long distance. However, a minority of rødbergite veins contradict these observations; these veins are evidence for long-range transport of REE, which have been provided by a more distal, probably deeper source (Fig. 8-15). This led to the formation of rødbergite veins, highly enriched in REE, within a host rock low in REE concentration.

d) Both alteration processes involve the transport and subsequently enrichment of REE, Fe and Th via a hydrothermal fluid. Therefore, the processes might be genetically linked and represent endmembers on a range of redox potentials rather than two separate processes.

9 Geochronology

This chapter will review previously reported geochronology and present new (U)-Th-Pb radio-isotopic geochronology for the emplacement of the carbonatite-peralkaline Fen Complex in Norway and the formation of hydrothermal monazite-(Ce) in altered carbonatite – classified as rødbergite. The aim is to create a deeper understanding of the REE-mineralisation processes in rødbergite and elaborate on underlying geological processes, which initiated the hydrothermal alteration.

The relative intrusive ages of the Fen Complex rock suite has been established using the cross-cutting relationship of the rocks in the field and drill cores. The ijolite rock sequence is considered the oldest intrusive unit within the Fen Complex and the main source for high alkaline fluids causing the fenitisation of the gneiss country rock (Kresten and Morogan, 1986). They were followed by carbonatite dykes and ring dykes that overlapped with the intrusion of damtjernite dykes (Mitchell and Brunfelt, 1975). Finally, phonolite dykes (tinguaite), which are affiliated with the Fen magmatism, intruded adjacent to the Fen Complex (Bergstøl, 1979).

To date, geochronology of the different rock types is sparse, imprecise and does not encompass all key magmatic events (Tab. 9-1). For instance, the emplacement of the ijolite suite has not been dated so far. More importantly, for this thesis, though, there has been no attempt to date the hydrothermal REE-mineralisation associated with rødbergitisation. Because the REE-minerals were identified as magmatic minerals by the former researcher (Andersen, 1984; Andersen, 1986), there was no reason to assume a different age between carbonatite emplacement and the formation of the REE-minerals. The best emplacement age for the Fen Complex magmatism itself is derived from a

single Ar-Ar age of a damtjernite 60 km outside of the Fen Complex, which is thought to be coeval with the carbonatite-damtjernite magmatism of the Fen Complex (Meert et al., 1998). The same laboratory dated a phonolite dyke 10 km SW of the Fen Complex.

***Table 9-1**:* Currently available age constraints for the different evolutionary stages of the Fen Complex. Updated with new unpublished age dates (*) for the carbonatite emplacement and formation age of hydrothermal monazite-(Ce). 1 - Andersen and Taylor (1988); 2 – Dahlgren (1994); 3 – Meert et al. (1998); 4 – Andersen and Sundvoll (1987); 5- Verschure et al. (1983).

Stage 1. Intrusion of Fen Complex	
Stage 1A. Alkaline magmatism & main fenitization	
not dated	——
Stage 1B. Carbonatite Intrusion	
Th-Pb age of zircons (**new**)	576 ± 10*
Pb-Pb WR ages of carbonatites	539 ± 14[1]
Revised regression w/o high-U samples	573 ± 60[2]
Stage 1C. Damtjernite Intrusion	
Rb-Sr isochron biotites	578 ± 24[2]
Ar/Ar age of biotite	589.1 ± 1[3]
Stage 1D. Phonolite dikes	
Rb-Sr isochron biotites	550 ± 7[4]
Revised regression w/o altered biotites	583 ± 41[2]
Ar/Ar age of biotite	578.3 ± 1.6[3]
Stage 2. Rødbergite and related REE-Mineralisation	
U-Pb age monazite-(Ce) **(new)**	272 ± 5*
Th-Pb age monazite-(Ce) **(new)**	272 ± 4*
Stage 3. Dolerite dikes associated with Oslo rift	
K-Ar WR age	253 ± c.20[5]

This phonolite dyke is 10 Myr younger than the damtjernite, which indicates the age range of the protracted nature of magmatism. Unaltered dolerite dykes in the Fen Complex are associated with the Oslo Rift and show a Carboniferous to Early Permian Age (Verschure et al., 1983).

As discussed in chapter 6 the formation of rødbergite is the product of a post-magmatic alteration. The formation of rødbergite has not been dated so far, which in turn means the timing of REE-mineralisation associated with the formation of rødbergite is unclear. In order to establish a reliable age for the Fen Complex magmatism in relation to the REE-mineralisation of the rødbergite in-situ U-Th-Pb analysis was performed on zircon and monazite from the Fen Complex by LA-ICPMS the NERC Isotope Geosciences Laboratory (NIGL), British Geological Survey, Keyworth, UK in collaboration with Dr Simon Tapster. At the time this thesis was written, the geochronology project was still in progress. Nevertheless, robust preliminary data was included for the benefits of the proposed REE-model.

9.1 Samples for Dating

Zircons are one of the most common accessory minerals used in determining the age of a rock, due to its chemical resistance to alteration, the minerals high closure temperature and the normally high concentrations of the parent element U. The generally low U concentration of the zircons, which was typically below 10 ppm in sample TS650a and below 1 ppm for 15-83-FE, is a challenge in dating zircons from the Fen Complex (Appendix VII). Zircons with the same characteristics are described for a number of carbonatite-alkaline-kimberlite systems, e. g., Kovdor alkaline–ultramafic complex (Rodionov et al., 2012), Miaoya carbonatite complex (Ying et al., 2017) and

Bayan Obo REE–Nb–Fe deposit (Campbell et al., 2014), which is a common feature for zircons in carbonatite-peralkaline complexes (Ying et al., 2017). This effect is caused by the preferential incorporation of Th and U in minerals at the early stages of the carbonatite complex formation such as in pyrochlore (Rodionov et al., 2012). Hence producing zircons with low U, which causes problems for geochronology (Amelin and Zaitsev, 2002). Additionally, high common Pb concentration of the selected zircons due to their inclusion-rich nature presented another issue for U-Pb dating. In order to obtain reliable age constrains for the emplacement of the Fen Complex, Th-Pb dating was applied instead of the more common and well-established U-Pb isotopic system for zircons.

Zircons were selected form carbonatites from two different localities 2 km apart. Sample 15-83-FE is from the intensely studied Bjørndalen transect, and sample TS650a is from the Tufte tunnel (Fig. 5-1). Sample 15-83-FE is a dolomite carbonatite with signs of initial alteration (Fig. 6-1). In contrast to transitional rødbergite of the Bjørndalen transect, 15-83-FE still shows a preferred orientation of carbonate layers, pyrite and apatite. The zircons are present as a few relatively large subhedral clusters of polycrystalline stumpy zircons with up to 5 mm in size and contain a high concentration of dolomite inclusion (Fig. 9-1). The origin of the zircons is not purely magmatic and exhibits signs of recrystallisation (either hydrothermal or late magmatic). Nevertheless, the coeval formation of dolomite and zircon indicates that the zircon age is likely to be close to the formation age of the rock.

The main REE-mineral in rødbergite and transitional rødbergite from the Bjørndalen transect is hydrothermal monazite-(Ce). In general, monazite-(Ce) contains Th and U to various degrees, which can be used for U-Th-Pb dating.

Monazite-(Ce) is present at the Bjørndalen transect in the form of veins, around apatite-relics and interstitial areas in the groundmass (Fig. 6.36; Fig. 6.38, Fig. 6.16). Based on textural evidence, these three mineralisation styles are caused by precipitation from a REE-rich hydrothermal fluid.

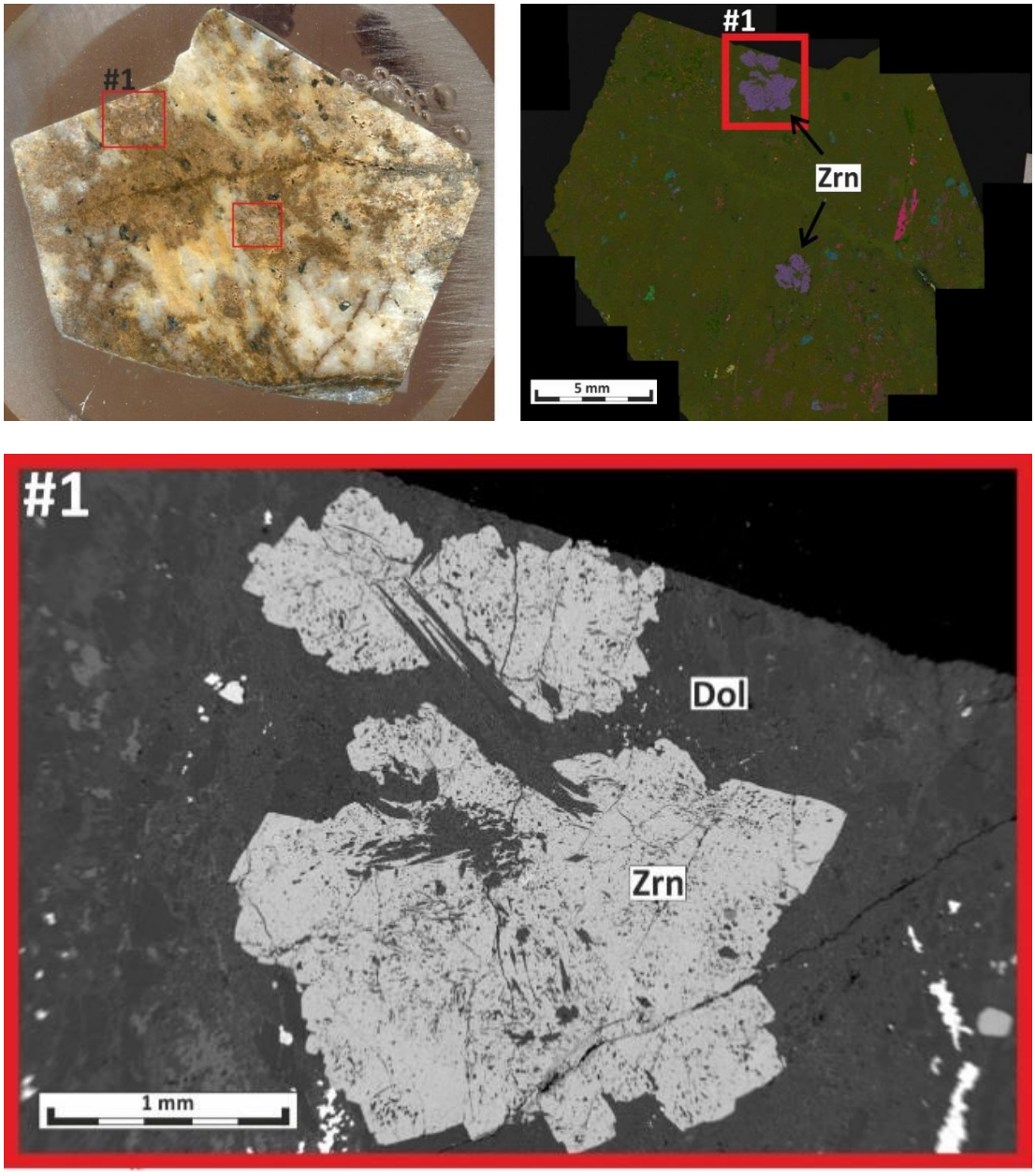

Figure 9-1: Photo (upper left) of a polished block of transitional carbonatite with zircons marked with a red box. Combined large-area EDS mosaic (upper right) of the same block with zircons coloured in purple. Blown up BSE image of the #1 red box zircon from the upper right picture. Note the poikiloblastic texture of the zircon crystal with dolomite inclusion (15-83-FE). Dol – Dolomite & Zrn – Zircon.

However, a magmatic origin of interstitial monazite-(Ce) cannot be ruled out completely, while a postmagmatic formation of hydrothermal monazite-(Ce) is the only explanation for the apatite replacement texture and monazite-(Ce) bearing veins. Additionally, monazite-(Ce) is associated and intergrown with barite, phlogopite, calcite and apatite, which makes it technically challenging to analyse monazite-(Ce) without acquiring a mixed signal.

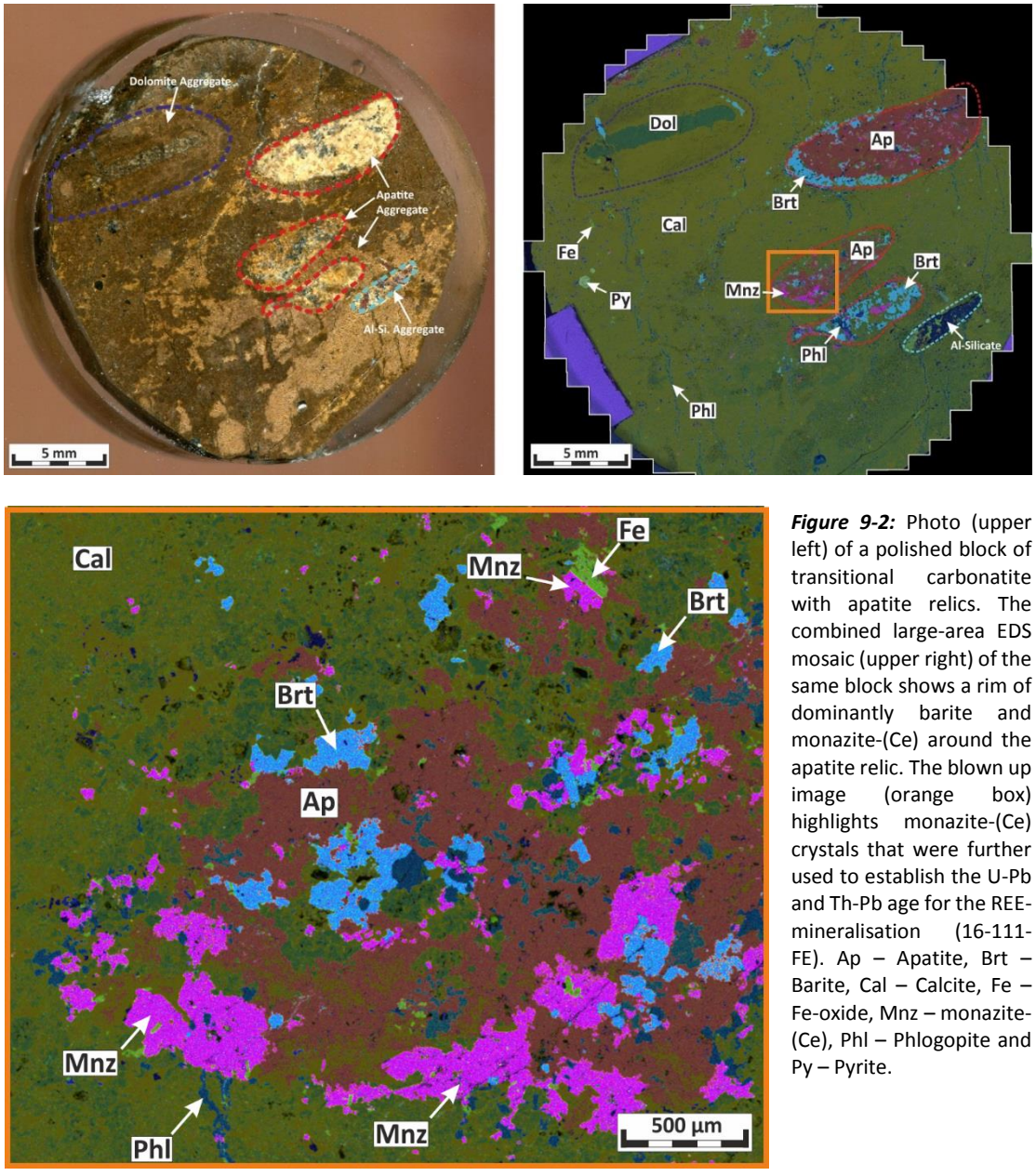

Figure 9-2: Photo (upper left) of a polished block of transitional carbonatite with apatite relics. The combined large-area EDS mosaic (upper right) of the same block shows a rim of dominantly barite and monazite-(Ce) around the apatite relic. The blown up image (orange box) highlights monazite-(Ce) crystals that were further used to establish the U-Pb and Th-Pb age for the REE-mineralisation (16-111-FE). Ap – Apatite, Brt – Barite, Cal – Calcite, Fe – Fe-oxide, Mnz – monazite-(Ce), Phl – Phlogopite and Py – Pyrite.

Therefore a large (500-µm) monazite-(Ce) crystal from an apatite replacement zone was chosen for further LA-ICPMS work because the monazite-(Ce) has a clear hydrothermal origin and the interference of other mineral phases can be minimised due to its size (Fig. 9.2). The selected monazite-(Ce) is part of a transitional rødbergite (16-111-FE) from the Bjørndalen transect and was analysed for U-Th-Pb isotopic data.

9.2 LA-ICP-MS U-Th-Pb Geochronology Results

The low U concentration of the analysed zircons in combination with their high concentration of common Pb made date interpretation based on U-Pb isotopes unreliable. Fortunately, much higher Th concentrations (500-9000 ppm) enabled the use of the Th-Pb isotopic system. However, the correction for common Pb was not completely possible. Nevertheless, the Th-Pb isotopic age from two samples are in agreement: TS650a: 565.2 +- 7.1 (n=13 of 14; MSWD 1.4) and 15-83d Th-Pb: 576 +-10 (n=8 of 9; MSWD 1.4) (Fig. 9.3). Monazite-(Ce) from sample 16-111-FE were dated using U-Pb and Th-Pb isotopic system. Monazites exhibited high common Pb with a lower intercept of the line of Discordia yielding a U-Pb age of 259 +- 77 Ma (n=15, MSWD= 1.8) (Fig. 9.4). Additionally, the U-Pb Concordia plot identified monazite-(Ce) analysis most affected by common lead. Three analysis were rejected because their ellipses — representing the analysis — were not in agreement with the Discordia (Fig. 9.4). After the rejection of the three analyses most affected by common Pb, a Th-Pb weighted mean age of 279.2 +-3.4 Ma (n=12; MSWD =1.8) was obtained (Fig. 9.5).

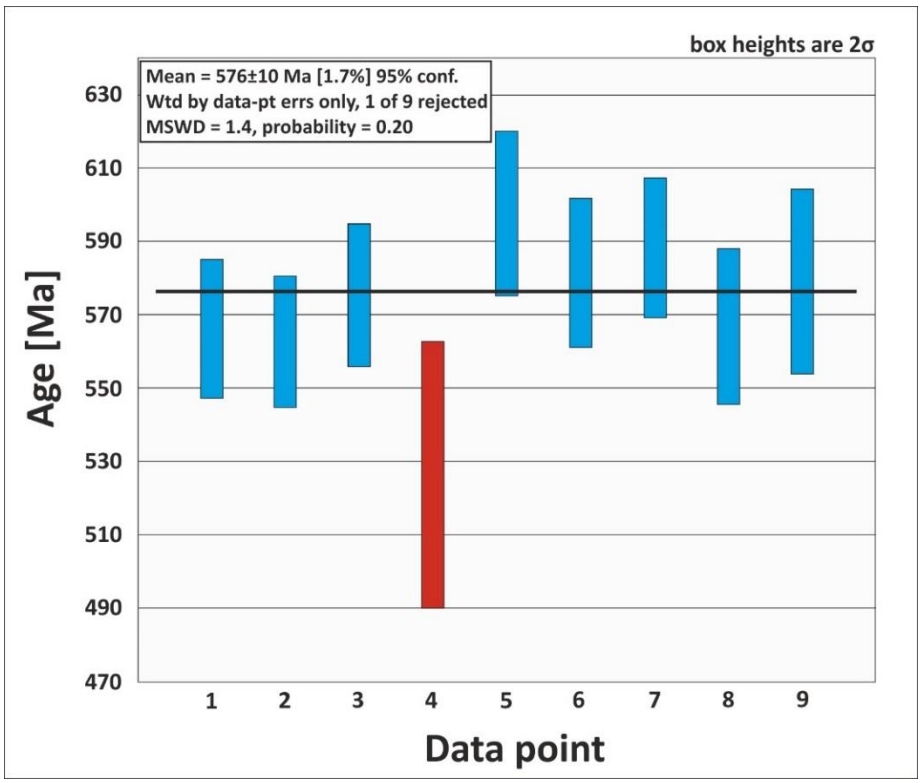

Figure 9-3: Th-Pb isotopic age of zircon 576 +- 10 Ma was calculated using 8 of 9 analyses (15-83d-Fe).

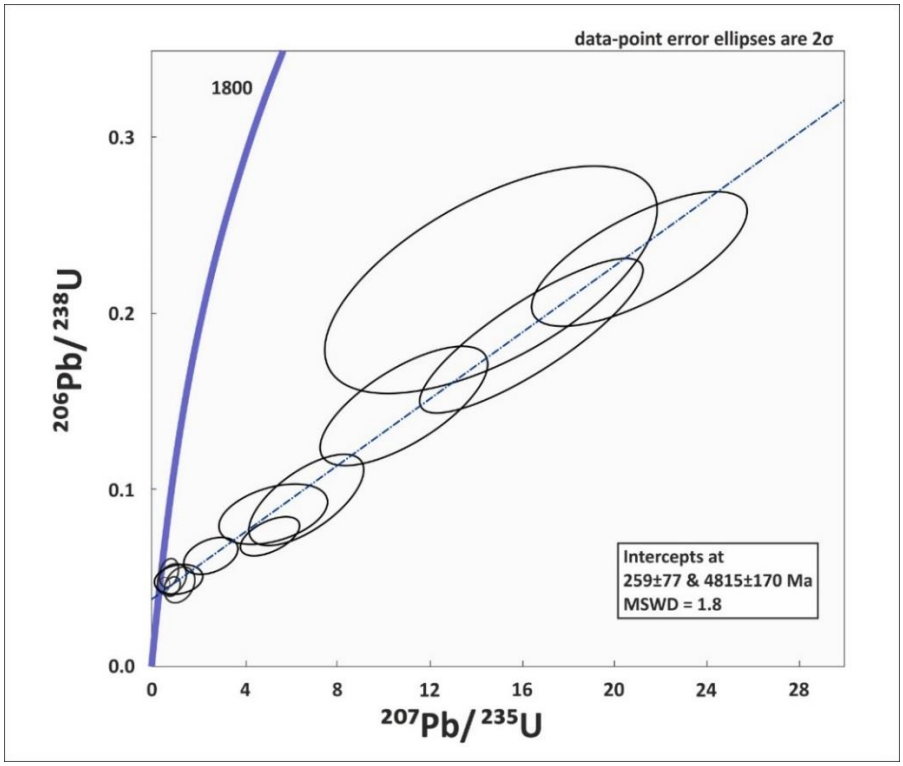

Figure 9-4: U-Pb Concordia diagram with Discordia yielding a U-Pb isotopic monazite age of 259 +- 77 Ma (16-111-FE). Additionally, the Discordia helped to identify monazite crystals with a high content of common Pb.

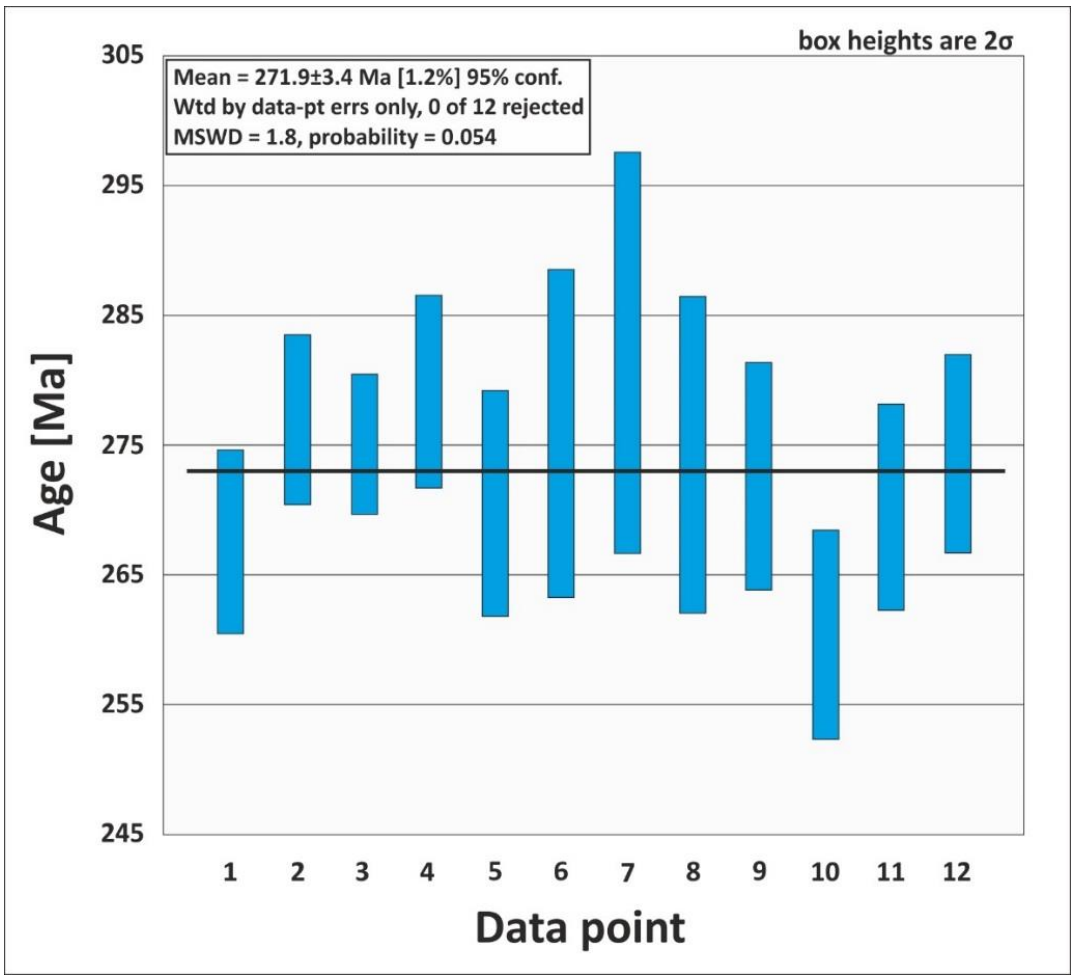

Figure 9-5: Th-Pb isotopic age of monazite-(Ce) 279.2 +-3.4 Ma was calculated using 12 analyses (16-111-FE).

9.3 Fen Complex Geochronology Discussion

Zircons from carbonatite yielded a Th-Pb age of ~570 Ma, which confirms an Ediacaran to Cambrian intrusive age for the Fen Complex acquired by earlier age date analyses of Fen Complex carbonatite (Andersen and Taylor, 1988; Dahlgren, 1994). This age coincides with the breakup of Rodinia and the opening of the Iapetus Ocean from 620 – 550 Ma (Pease et al., 2008), which was described in chapter 4.2 and 4.3. Strictly speaking, the emplacement of the Fen Complex happened during a minor extensional activity during the drift phase and separation of Baltica from Greenland (Meert et al., 1998).

The isotopic age of the apatite replacement zone of hydrothermal monazite-(Ce) is significantly younger and cannot be genetically associated with the magmatic emplacement of the Fen Complex. However, the Fen Complex is less than 20 km away from the magmatic rock sequence of the Oslo Graben. The Oslo Graben, part of the Oslo Rift, is described as a high-volcanicity continental rift system similar to the East African Rift System (Sundvoll and Larsen, 1994). The magmatic activity of the Oslo Graben extends from 308 Ma to 245 Ma (Larsen et al., 2008; Sundvoll and Larsen, 1994). The isotopic age of monazite-(Ce) 272.9 Ma ± 3.4 Ma coincides with the mature stage of the Oslo rift (288 Ma – 265 Ma), characterised by central volcanos and caldera collapse (Larsen et al., 2008). More importantly, the emplacement of dolerite dykes (253 Ma ± 20 Ma) at Fen and the monazite mineralisation in rødbergite are within the uncertainty of their isotopic ages, which links Permian magmatic activity at Fen with the REE-mineralisation event. The prolonged magmatic activity of ~63 Myr of the Oslo Graben fitted spatially and temporally with the isotopic age of the monazite-(Ce) and had the potential to provide the necessary hydrothermal fluid circulation. Therefore, it is likely that the magmatic activity of the Oslo Graben triggered the circulation of the hydrothermal fluid at the Fen Complex.

Geochronology provides an important constraint on the REE-mineralisation model. There are two end member explanations for the isotopic ages of the hydrothermal monazite-(Ce) crystals. Either: 1) a hydrothermal event caused the resetting of the isotopic signature of the monazite-(Ce) crystals or 2) the hydrothermal fluid caused the precipitation of new monazite-(Ce) at 272.9 Ma ± 3.4 Ma. In this context, it is crucial to understand if the hydrothermal fluid was forming new monazite-(Ce) or if the hydrothermal fluid partly or fully reset the isotopic signature of much older, potentially

magmatic (~570 Ma) monazite. In other words, is the REE mineralisation caused by an event linked to the formation of the Fen Complex that was subsequently masked as a new mineralisation event, or is it a REE mineralisation event caused by a much younger process linked to the Oslo rift? It is important to note that in both cases, the observed textures demand the presence of hydrothermal fluid.

Scenario 1 requires a reset of the isotopic age of monazite-(Ce). The closure temperature of monazite is reasonably well established by Cherniak et al. (2004), however, isotopic resetting can be greatly expedited in the presence of fluid through the dissolution of older monazite-(Ce) and reprecipitation to younger monazite-(Ce) (Harlov et al., 2005; Rasmussen and Muhling, 2007; Teufel and Heinrich, 1997). Therefore, it is likely that a fluid that was able to mobilise monazite at the minimum of the crystal scale would have to have been present at ~270 Ma. However, partial resetting would generate a variation of isotopic data and mixed analyses of both initial and reset isotopic ages. The data exhibit characteristics of a single statistical population (as identified by a statistically acceptable MSWD), this suggest that a partial resetting of pre-existing monazite is less probable as a possible explanation for the isotopic signature of monazite-(Ce) and lends itself to the formation of hydrothermal monazite at 272.9 Ma ± 3.4 Ma.

This is further supported when the textural evidence of monazite formation is also taken into account. Textures such as monazite-(Ce) bearing veins, monazite-(Ce)-apatite replacement zones or monazite-(Ce) in interstitial groundmass space (Fig. 6-16, Fig. 6-17, Fig. 6-28, Fig. 6-36, Fig. 6-38) indicate that the fluid responsible for the monazite ages at 272.9 Ma ± 3.4 Ma was also responsible for the significant event of REE re-mobilisation and precipitation that generated REE mineralisation at Fen.

Therefore on the basis of a link between the monazite geochronology and the significant hydrothermal alteration at Fen, it is plausible that following emplacement of the Fen complex at ~570 Ma, rødbergitisation and REE redistribution did not take place until 300 Myr later, when the magmatic expression of the Oslo rift occurred, injecting dolerite dykes into the region and causing the hydrothermal circulation required for REE mobilisation.

For the practical reason and to ensure a monomineralic signal, the LA-ICP-MS analysis was done on the largest (> 500 µm) monazite-(Ce) crystal within sample 16-111-FE (Fig. 9-2). However, the REE-mineralisation event, which caused the formation of the large monazite-(Ce) crystals, might not be the same event, which precipitated smaller monazite-(Ce) crystals or monazite bearing veins. Although the mineral paragenesis and texture of large monazite-(Ce) crystal are the same as for the smaller monazite-(Ce) crystals, the question of representation has to be addressed. Future geochronology will encompass the analysis of different sizes as well as textures of monazite-(Ce) from a variety of samples and locations. This will identify the potential existence of multiple REE-mineralisation events and clarify if the age of large monazite-(Ce) crystals is representative for the whole of the hydrothermal monazite-(Ce) population. Furthermore, accurate WDS trace element analysis and mapping of monazite-(Ce) will clarify the existence of potential zonation within the monazite-(Ce) crystals and/or the presence of multiple monazite-(Ce) population. Trace element signature is especially important to ensure the representation of very small (< 100 µm) monazite-(Ce) crystals, where reliable geochronology will be more prone to errors due to mixed signals.

9.4 Age Dating Conclusions

The chapter on age dating revealed two important points. First, Th-Pb dating of zircons from two different carbonatite locations established an age for the emplacement of the Fen Complex carbonatite at ~570 Ma and hence supported the broad Ediacaran temporal bracket for the Fen complex intrusion as indicated by earlier indirect constraints from comparable magmatic activity in the region. Second, the robust Th-Pb age at 272.9 Ma ± 3.4 Ma from hydrothermal monazite in REE-rich transitional rødbergite, is significantly (~300 Myr) younger than the Fen Complex magmatism. Textural and geochronological evidence indicates that the Oslo rift (308 Ma – 245 Ma Larsen et al. (2008)) is the cause for the hydrothermal overprint and the hydrothermal REE-mineralisation of the Fen Complex.

10 REE Mineralisation Model

In this chapter, a synthesis is put forward combining the REE mineralisation model of the Bjørndalen transect with the observations made at the Fen Road transect and Gruveåsen transect. The aim is to create an REE-mineralisation model, which can be applied to the whole of the Fen Complex and incorporates possible local REE-mineralisation anomalies from different sampling sites.

The previous model for the formation of rødbergite and the associated REE-mineralisation describes a progressive residual enrichment of insoluble REE-minerals by leaching and removal of the carbonate minerals during hydrothermal alteration (Andersen, 1984). For a more detailed explanation of the REE-mineralisation model by Andersen (1984), please refer to chapter 4.4.1.

As already pointed out in Marien et al. (2018), the findings made in the course of the present project and reported in this thesis are not fully consistent with the previous model of Andersen (1984). The main contradictory points are:

a) The main REE carrier-mineral changes during rødbergitisation from synchysite-(Ce) in unaltered carbonatite (Fig. 6-8; Fig. 6-12)to monazite-(Ce) in rødbergite and rødbergite veins (Fig. 6-16, Fig. 6-17, Fig. 6-18; Fig. 6-28; Fig. 7-33). Therefore rødbergitisation has to involve the dissolution of REE-minerals in the unaltered carbonatite (Fig. 6-12) and formation of new hydrothermal REE-minerals, which is contrary to idea of preservation of insoluble REE-phases during rødbergitisation Andersen (1984).
b) REE-mineral bearing veins contribute a substantial amount of REE to the total REE content of various lithotypes e.g. transitional rødbergite, rødbergite of the

Bjørndalen transect (Fig. 6-36) and dolomite carbonatite, chlorite-bearing dolomite carbonatite and rødbergite of the Fen Road transect (Tab. 7-2; Fig. 7-15; Fig. 7-16; Fig. 7-17). Samples with a high density of REE mineral bearing veins (Fig. 7-15 – 16-96-FE; Fig. 6-36 – 15-93-FE; Fig. 8-3 – 16-27-FE) have an increased REE-concentration compared to unveined samples from the same rock unit of 16x to 5x5 respectively (Fig. 6-40; Tab. 7-3). Rødbergite veins at the Fen Road transect (Tab. 7-3) and Gruveåsen transect (Tab. 8-1) show the highest REE concentrations detected in this project. Additionally, melanocratic carbonatite (Fig. 8-3), from the Gruveåsen transect, with a high concentration of dark veins show 10x more REE than adjacent leucocratic carbonatite (Fig. 8-2). These observations support the mobilisation of REE during rødbergitisation and indicate the importance of hydrothermal processes for the REE mineralisation.

c) The Bjørndalen transect (chapter 6.2), the Fen Road transect (chapter 7.2) and at the Gruveåsen transect (chapter 8.2) show an REE enrichment in rødbergite relative to the adjacent protolith by more than an order of magnitude. For instance, the difference in REE concentration between a transitional rødbergite (15-93-FE – REE = 14161ppm) and an unaltered carbonatite (15-85-FE – REE = 864 ppm) of the Bjørndalen transect is by a factor of 16.39. In order to achieve a 16-fold residual enrichment, a major volume reduction by 93.75% is required in a purely passive enrichment model. Such an order of volume reduction would cause an intense brecciation and a formation of porous rocks. This could not be confirmed by field observations (e.g. Fig. 6-13). A representative batch of rødbergite samples from the Bjørndalen transect showed porosity of 2-3 Vol% without any signs of brecciation (Fig. 5-5). Brecciation was only observed in rocks

of the Gruveåsen transect and is not related to an increase in REE. For the majority of the samples, there is no evidence of a major volume reduction during rødbergitisation and no connection to an increase in REE. Hence, a passive enrichment via volume reduction cannot be the major cause for the REE enrichment.

d) Several rødbergite samples show the preservation of original magmatic textures (Fig. 6-38; Fig. 7-13; Fig. 8-7; Fig. 8-11). The replacement of foliated gneiss by rødbergite occasionally preserved the metamorphic foliation within the rødbergite (Fig. 8-12). The rødbergitisation of damtjernite caused the alteration of phlogopite to chlorite while preserving the original magmatic flow texture in some cases (Fig. 8-13). The preservation of magmatic texture in rødbergite is not consistent with massive volume reduction. Volume reduction would necessarily cause brecciation, which in turn disrupts the original rock textures.

e) Th-Pb dating of zircons from two different carbonatite locations established a robust age for the emplacement of the Fen Complex carbonatite of 550 Ma ± 10 Ma (please refer to chapter 9.4). Hydrothermal monazite from REE-rich transitional rødbergite gave U-Pb and Th-Pb ages of 272 Ma ± 5 Ma and 272 Ma ± 10 Ma respectively, which is coincident with the main magmatic stage of the Oslo rift formation (Larsen et al., 2008). The hydrothermal REE-mineralisation of the Fen Complex is likely to be associated with Oslo rift magmatism and hydrothermal fluid circulation rather than with the Fen Complex magmatism itself.

To explain the observations made at the three localities, a new REE model is proposed which combines elements of Andersen's (1984) model with new evidence from the Bjørndalen, Fen Road and Gruveåsen transects.

10.1 Source and Host Rock

The observations and evidence related to the source rock and host rock are listed in Tab. 10-1 and Tab. 10-2. Source and host rock are described in the same chapter because evidence suggests a link between the two.

Zones of intense fluid-rock interaction are marked by massive red rødbergite. Rocks of moderate fluid-rock interaction are marked by beige-ochre massive transitional rødbergite (Fig. 6-40)). Although transitional rødbergite forms a distinct zone around massive red rødbergite of the Bjørndalen transect, it is not present at the Fen Road transect and occurs very rarely at the Gruveåsen transect. In general, areas affected by rødbergitisation have sharp rather than gradual boundaries (Fig. 7-12B). In addition to massive rødbergite, there are mineralogically similar rødbergite veins with a red-whitish colouration (Fig. 7-30). Rødbergite veins have a thickness of 1 to 10 cm and show a very narrow chemical influence on the surrounding host rock. Replacement zones and relics of protolith in rødbergite show that any of the following calcite-dolomite-ankerite-chlorite carbonatite (Fig. 6-22; Fig. 7-28), calcite damtjernite (Fig. 8-14), brecciated fenite (Fig. 8-7) and foliated gneiss (Fig. 8-12) can be completely replaced by rødbergite. These rock types display a variety of average REE concentrations ranging from 230 ppm to 7,769 ppm for foliated gneiss and chlorite carbonatite, respectively (Tab. 8-1). Rødbergite created by the replacement of these host rocks tends to be significantly enriched in REE but is influenced by the REE concentration of the host rock at the same

time. This is the reason for the large concentration range in REE for the rødbergite of the Gruveåsen transect from 155 ppm to 11,811 ppm because rødbergite replaced rocks that are very low in REE, e.g. gneiss, and REE fertile rocks, e.g. carbonatite and ultramafic lamprophyre. The Fen transect largely consists of dolomite-ankerite-chlorite carbonatite, which is the most fertile REE source rock. Rødbergite of the Fen transect is largely the product of replacement of REE-rich carbonatite and contains an average of 8393 ppm REEs – the highest average of any rock type analysed in this study (Tab. 7-3). Only rødbergite veins have higher average REE concentrations. The correlation between total REE concentration in host rocks and REE concentration in rødbergite veins are less distinctive than for host rock and rødbergite.

REE concentrations in rødbergite are variable at the Gruveåsen transect and are partially controlled by the replaced- and surrounding protolith. The close relationship between the REE concentration of the rødbergite and the adjacent host rock implies a local redistribution of REE (Fig. 8-17). However, it is difficult to quantify the exact distance between sites of leaching and sites of reprecipitation because the vertical extent of the rock types in the Fen Complex is unknown. There is one notable exception of a REE-rich rødbergite vein in a low REE level host rock (16-64-FE - Fig. 8-15).

It is plausible that the REE concentration of the rødbergite is partly dependent on the REE-concentration of the alteration fluid. At the same time, the REE concentration of the rødbergite correlated with the REE concentration of the surrounding host rock. This connection means that the source rock for the REE component of the alteration fluid is likely to come from the same rock unit as the host rock.

Therefore, the rødbergite fluid is not limited to carbonatites but must be able to leach the REE carriers in the different host rocks. The dominant REE minerals in the investigated carbonatites are REE-fluorocarbonates. The rødbergite fluid can dissolve REE-fluorocarbonates in order to enrich the REE concentration of the fluid. Unaltered carbonatite from the Bjørndalen transect showed evidence of the replacement of REE-fluorocarbonates by a Fe-oxide rich fluid, which indicates the ability of rødbergite fluid to leach REE-fluorocarbonates (Fig. 6-12).

Table 10-1: Summary of source rock properties for the Bjørndalen-, Fen Road- and Gruveåsen transect.

Bjørndalen Transect	Fen Road Transect	Gruveåsen Transect
Leaching Mechanism Replacement of REE-fluorocarbonates from primary carbonatites by Fe-oxide indicates the ability of rødbergite fluids to dissolve REE-fluorocarbonates and shows a possible leaching mechanism for a deeper REE source by rødbergite fluids.	**Host Rock fertility** The high level of average REE concentration (8393 ppm) in rødbergite from the Fen Road transect relative to the average REE concentration (5130 ppm) in rødbergite from the Bjørndalen transect, is possibly connected to the higher average REE level of the surrounding carbonatite at the Fen Road (5835 ppm) compared to Bjørndalen (1429 ppm). In case rødbergite fluid obtains its REE content from leaching of proximal rocks, a more fertile host rock would lead to a higher REE concentration in the fluid, which in turn leads to a higher REE concentration in rødbergite formed by this fluid. **Leaching Mechanism** The main REE-carrier in dolomite-ankerite-chlorite carbonatite are REE-fluorocarbonates. If there is a connection between the host rock REE concentration and the REE concentration of the adjacent rødbergite, the leaching of REE-fluorocarbonates must be possible. The rødbergite fluid must be able to dissolve REE-fluorocarbonates in order to enrich in REE and subsequently form hydrothermal monazite-(Ce).	**Host Rock fertility** There is clear evidence for a link between the REE concentration of rødbergite and the surrounding host rock. Rødbergites with relict texture of gneiss and fenite are having significantly lower average REE concentrations (558 ppm) compared to average REE concentrations (6864 ppm) of rødbergite proximal to carbonatite and damtjernite. **Local Redistribution** The link between the REE budget of most rødbergite and rødbergite veins with their surrounding host rock suggest a local redistribution of REE for the main part of the formation of rødbergite. Rødbergite veins are partly provided by a deeper source and are occasionally highly enriched despite a low REE concentration in their host rock.

Table 10-2: Summary of host rock properties for the Bjørndalen-, Fen Road- and Gruveåsen transect.

Bjørndalen Transect	Fen Road Transect	Gruveåsen Transect
Rock Types The host rock is a dolomite-calcite carbonatite. **Signs of Rødbergitisation** Zones of intense fluid-rock interaction are marked by red rødbergite. The alteration progressively weakens towards unaltered areas of primary carbonatite. Zones of moderate fluid-rock interaction are marked by beige-ochre coloured transitional rødbergite.	**Rock types** The host rocks are a dolomite-ankerite carbonatite and a dolomite-ankerite-chlorite carbonatite. The carbonate matrix of the dolomite-ankerite-chlorite carbonatite has a higher Fe concentration and is significantly enriched in REE (5835 ppm) compared to the dolomite-ankerite carbonatite (918 ppm). **Signs of Rødbergitisation** Zones of intense fluid-rock interaction are marked by red rødbergite. Rødbergite veins show a narrow zone (<10 cm) of host rock alteration.	**Rock types** The host rocks are carbonatites (dolomite-calcite with varying amount of chlorite), calcitic damtjernite, brecciated fenite and foliated gneiss. Rock types in order of descending average REE concentration, foliated gneiss (230 ppm), brecciated fenite (505 ppm), calcitic damtjernite (1586 ppm), carbonatite without chlorite (1900 ppm) and chlorite-rich carbonatite (7769 ppm). **Signs of Rødbergitisation** Zones of intense fluid rock interaction are marked by red rødbergite. Rødbergite veins show a narrow zone (<10 cm) of host rock alteration.

10.2 Fluid chemistry

The observations and evidence related to the fluid chemistry are listed in Tab. 10-3. The alteration mineral assemblage of rødbergite at the Bjørndalen transect and rødbergite veins at the Fen Road transect indicates that the hydrothermal rødbergite fluid was rich in O_2, Ca, Fe, Ba, REE, Th, CO_3, S and F. The alteration mineral assemblage is more oxidised than the unaltered mineral assemblage, which indicates an oxidised fluid. The oxidised character of the fluid must have been acquired outside of the Fen Complex. Andersen (1984) presented strontium and oxygen isotopic data which shows high $^{87}Sr/^{86}Sr$ ratios and elevated $\partial^{18}O$ for the fluid and further suggests that the fluids involved in the REE mineralisation of the Fen Complex were not simply evolved melt-like hydrous fluids. The rødbergite fluids were hydrothermal and had at least partly equilibrated with Precambrian quartzofeldspathic gneisses outside of the Fen Complex, and possibly with groundwater (Andersen, 1984).

However, the rødbergitisation process occurs in multiple stages indicated by the presence of many different vein generations with similar but changing mineral assemblages. The different mineral assemblages are the result of changing physicochemical conditions of the hydrothermal fluid, e.g., change in T of the fluid, dissolution/reprecipitation of minerals and ongoing fluid-rock interaction. The host rock equilibrated with the external hydrothermal fluid and became more oxidised while simultaneously losing its ability to buffer the hydrothermal fluid.

Table 10-3: Summary of hydrothermal fluid properties for the Bjørndalen-, Fen Road- and Gruveåsen transect.

Bjørndalen Transect	Fen Road Transect	Gruveåsen Transect
Fluid Chemistry Rødbergite fluid is an oxidising fluid, which is rich in SO42- and minor F-. The fluid can mobilise and transport Th and REE in solution and contains a high amount of Ba and Fe. High 87Sr/86Sr ratios indicate an external fluid source. Multiple generations of veins suggest a change in the physicochemical properties of the hydrothermal fluid. Especially the change in redox conditions can be seen by the formation of hydrothermal pyrite.	**Fluid Chemistry** Rødbergite fluid is an oxidising fluid, which is rich in SO42- and minor F-. The fluid can mobilise and transport Th and REE in solution and contains a high amount of Ba and Fe. Multiple generations of veins suggest a change in the physicochemical properties of the hydrothermal fluid. The change in redox conditions can be seen by the formation of hydrothermal pyrite in rødbergite. Rødbergite veins always contain idiomorphic pyrite simultaneously with Fe-oxide.	**Fluid Chemistry** Rødbergite fluid is an oxidising fluid, which can mobilise and transport Th and REE in solution and contains a high amount of Fe.

10.3 REE Mineralisation

The observations and evidence related to the REE mineralisation are listed in Tab. 10-4. The formation of rødbergite alters and replaces the original mineral assemblage of the host rock. The typical alteration mineral assemblage comprises various amounts of Fe-oxide, barite, chlorite, calcite, quartz, barian phlogopite and ferroan dolomite to ankerite with minor amounts of apatite, REE-minerals and barian orthoclase (Fig. 6-23; Fig. 6-25; Fig. 6-36; Fig. 7-32).

Present REE-minerals are in descending order: monazite-(Ce), synchysite-(Ce), bastnäsite-(Ce) and allanite-(Ce). Monazite-(Ce) is the main REE-mineral in interstitial areas, veins and aggregates within rødbergite and transitional rødbergite at the Bjørndalen transect but it is less common at the Fen Road transect. There is no evidence for mineralised apatite relics at the Fen Road transect and REE-fluorocarbonates dominate the different generations of REE-mineral veins. At the same time, these veins have little or no Fe-oxide and can have considerable amounts of pyrite. There is a connection between the redox potential during mineralisation of a vein and the prevalent REE-mineral, with the formation of monazite-(Ce) under more oxidising conditions and the precipitation of REE-fluorocarbonates under less oxidising conditions. The similarity of mineralisation textures of monazite-(Ce) and REE-fluorocarbonates suggests a flexible change in the mode of precipitation, which occasionally happens within the same sample.

The hydrothermal REE-minerals form in multiple different ways:

a) As irregular aggregates (nm to mm range) of monazite finely intergrown with calcite as part of rødbergite veins (Fig. 7-33; Fig. 7-34; Fig. 7-35) and texturally similar synchysite blades (< 5 µm in length) and sheets (ca. 250 µm) intergrown with calcite surrounded by fluorite (Fig. 7-10; Fig. 7-11).
b) Within a fine pervasive network of Fe-oxide and carbonate along grain boundaries (Fig. 6-16; Fig. 6-28; Fig. 6-31) (<5 µm).
c) Subhedral to euhedral crystals (>500 µm) surrounded by calcite with tiny (5 – 25 µm) inclusions of blade-shaped apatite (Fig. 6-18).
d) In intergrowth with minerals of the alteration assemblage (100 – 500 µm), e.g., barite (Fig. 6-8; Fig. 6-17; Fig. 6-19), chlorite (Fig. 7-20), quartz (Fig. 7-16) and hematite (Fig. 7-25).
e) As part of REE-mineral bearing veins (Fig. 6-36).
f) As apatite relic (Fig. 6-29; Fig. 6-38; Fig. 6-39).

The replacement of apatite-dolomite relics of unaltered carbonatite (f) by the rødbergite fluid triggered the precipitation of monazite-(Ce). These relics function as an REE trap for the REE-bearing fluid and lead to a concentration of monazite-(Ce) in rocks with apatite relics and a high density of REE-mineral bearing veins (Fig. 6-29; Fig. 6-38; Fig. 6–39). The REE mineralisation mechanism (f) was only identified at the Bjørndalen transect. Without a SEM analysis, it is not possible to identify this style of REE-mineralisation that is why it could not have been detected at the Gruveåsen transect. For further details of the lack of apatite replacement REE-mineralisation at the Fen Road transect, please refer to chapter 7.3.5.

The Bjørndalen transect has a distinct enrichment of HREE and Th in the centre of intense fluid-rock interaction (red rødbergite) (Fig. 6-40). Zones of LREE enrichment occur in the western transitional rødbergite, which has the highest density of REE-minerals veins. The Gruveåsen transect shows a different trend with congruent zones of LREE and Th and a separation of HREE (Fig. 8-14). Samples with an exceptionally high concentration of HREE are veins of pure Fe-oxide ore (Tab. 8-1). The Fen Road transect does not show separation with congruent zones of LREE, HREE and Th enrichment. The process of pervasive massive oxidisation of unaltered protolith to red rødbergite does not necessarily lead to different zones of LREE, HREE and Th enrichment. For different zones to occur, additional processes have to be involved. For instance, the formation of LREE-veins caused LREE enrichment, and the formation of pure Fe-oxide veining caused an enrichment of HREE. Furthermore, samples with an unproportioned amount of Th relative to LREE and HREE exist, but further mineralogical studies are required for an explanation.

Table 10-4: Summary of REE-mineralisation properties for the Bjørndalen-, Fen Road- and Gruveåsen transect.

Bjørndalen Transect

REE Mineralisation

Besides minor amounts of allanite-(Ce) and synchysite-(Ce), the precipitation of hydrothermal monazite-(Ce) is the main reason for an enrichment in REE in rødbergite and transitional rødbergite. The mineralisation occurs along with a fine, pervasive, irregular network of micro veins, as part of multiple generations of veins and around apatite relics. Therefore the overall REE concentration is a combination of the density of the pervasive network of REE-mineral bearing veins and the presence of apatite-dolomite relics. The average REE enrichment in rødbergite is 5-fold compared to the primary carbonatite with a maximum of a 10 -fold enrichment.

Apatite Traps

The replacement of primary apatite-dolomite relics by rødbergite fluid triggered the precipitation of monazite-(Ce). These relics function as a REE trap for the REE-bearing fluid and lead to a concentration of monazite-(Ce) in rocks with apatite relics and a high density of REE-mineral bearing veins

REE-Mineral bearing Veins

There are two generations of REE-mineral bearing veins:

a) Monazite-(Ce) vein (Ba-bearing phlogopite, barite ± chlorite and hematite)

b) Allanite-(Ce) ± REE-fluorocarbonate (calcite ± barite, dolomite)

HREE/LREE/Th Distribution

The relative enrichment of HREE, LREE and Th are variable throughout the Bjørndalen transect due to different element mobilities and the density of the REE-vein networks. Zones of Th and HREE enrichment are proximal to the centre of intense fluid-rock interaction (red rødbergite). Zones of LREE enrichment are defined by the presence of REE-minerals veins, which concentrate in the western transitional rødbergite.

Fen Road Transect

REE Mineralisation

The precipitation of hydrothermal synchysite-(Ce), bastnäsite-(Ce) and monazite-(Ce) is the main reason for an enrichment in REE in rødbergite, rødbergite veins and altered carbonatite. The mineralisation occurs along with a fine, pervasive, irregular network of micro veins, as part of multiple generations of veins and thicker (1-10 cm) rødbergite veins. The average REE enrichment in rødbergite is 9-fold compared to the dolomite-ankerite carbonatite, and 1.4-fold compare to dolomite-ankerite-chlorite carbonatite with a maximum of a 23 -fold enrichment and 4 -fold enrichment respectively.

Chloritisation

Secondary dark chlorite mineralisation in chlorite-rich dolomite-ankerite carbonatite is associated with Fe-oxide, apatite and REE-fluorocarbonates. The texture of the REE-fluorocarbonates is ambiguous, and it is not clear if REE-fluorocarbonates are formed or replaced during the chlorite mineralisation. The average REE concentration for chlorite bearing carbonatites (5835 ppm) is much higher compared to the REE concentration of chlorite free carbonatites (985 ppm).

Rødbergite Veins

Rødbergite veins are 1-10 cm thick and represent the feeder veins for the rødbergitisation. They are mainly comprised of Fe-oxide and variable proportion of quartz, calcite, pyrite, monazite-(Ce) with minor chlorite, apatite, barite, K-feldspar and synchysite-(Ce). Interestingly they contain Fe-oxide and FeS_2 simultaneously and also have monazite-(Ce) and synchysite-(Ce) at the same time. This might indicate local variations in the physicochemical properties of the fluid. Rødbergite veins have the highest REE concentration of all rock types.

REE-Mineral bearing Veins

Multiple generations of synchysite-(Ce) and bastnäsite-(Ce) bearing veins are present in rocks of the Fen Road transect. The veins are made of variable amounts of barite, apatite, chlorite, Fe-oxide, calcite and dolomite. This mineral assemblage is similar to rødbergite veins indicating a genetic relationship between REE-bearing veinlets and thicker rødbergite veins. REE-minerals are found in both oxidising and reducing condition with synchysite-(Ce) and bastnäsite-(Ce) being the dominant REE carrier in reduced environments, and monazite-(Ce) preferentially found under oxidising conditions.

Gruveåsen Transect

REE Mineralisation

The formation of rødbergite is either massive or in the form of rødbergite veins. The average REE enrichment in rødbergite ranges from 0.5 to 3-fold compared to their adjacent host rocks with a maximum of 95-fold.

Chloritisation

A secondary alteration of carbonatite by less oxidising fluids is characterised by the formation of chlorite, magnetite and pyrite. The altered carbonatite is darker, denser and associated by a 9-fold enrichment of REE and 8-fold enrichment of Th, relative to the primary igneous carbonatite. Both chloritisation and rødbergitisation, involve the transport and subsequently enrichment of REE, Fe and Th via a hydrothermal fluid. Therefore, these alteration processes might be genetically linked and could represent endmembers on a range of redox potential rather than two separate processes.

HREE/LREE/Th Distribution

The enrichment of LREE and Th shows similar patterns and have a strong positive correlation. The enrichment of HREE is slightly different and has a maximum in Fe-ore mineralisation.

10.4 Chloritisation-Rødbergitisation

The chloritisation of carbonatite and minor amounts of gneiss was observed at the Fen Road transect and Gruveåsen transect. For Further information, please refer to chapter 8 section 8.1.1, 8.1.4 and 8.3.1. The chloritisation of the host rock occurs by veinlet infiltration and along grain boundaries and causes a black colouration and an increase in density of the rock (Fig. 8-3). Thicker veins of chlorite could be observed in gneiss of the Fen Road transect (Fig. 8-6). The main alteration minerals are chlorite and magnetite with minor amounts of pyrite. The increasing amount of dark mineral phases is accompanied by an increase in REE and Th concentration (Fig. 8-16A; Tab. 8-1). The REE concentration in chloritised carbonatite is relatively high with an average REE concentration of 5,835 ppm and 7,769 ppm for the Fen Road transect and Gruveåsen transect respectively. The chloritised gneiss of the Fen Road has a low REE and Th concentration and comprises no pyrite or magnetite that makes it distinctly different from chloritised carbonatites (Fig. 7-4).

It is important to note that the process of chloritisation and rødbergitisation are very similar in terms of trace element concentration (REE & Th enrichment), REE chondrite normalised patterns (Fig. 8-16), alteration texture (via veins, veinlets and grain boundaries) and the presence of Fe-oxide. Chlorite is a common constituent in the rødbergite mineral paragenesis and occasionally, intergrown with monazite-(Ce) (Fig. 7-36), which shows a connection between REE-mineralisation and chlorite formation. Carbonatites from the Gruveåsen transect show a positive correlation between the amount of chlorite (dark schlieren) and the REE concentration. The characteristic difference between a rødbergitised carbonatite and a chloritised carbonatite is their colour due to different contents of hematite, magnetite and chlorite. The alteration

mineral assemblage in zones of chloritisation (magnetite and pyrite) indicates a more reduced environment compared to Fe-oxide (hematite or goethite) and pyrite assemblage in rødbergite. Chlorite and hematite are in general a common hydrothermal alteration assemblage. The giant hydrothermal hematite deposits Carajás (Brazil), Hamersley (Australia), Krivoy Rog (Ukraine), Quadrilátero Ferrífero (Brazil), Bailadila (India) and Thabazimbi (South Africa) all show wall-rock alteration of hematite-chlorite paragenesis (± carbonate) (Dalstra and Guedes, 2004). Additionally, hypogene hematite-carbonatite formation in BIFs coincides with wall rock intensely altered with carbonate, chlorite and talc (Dalstra and Guedes, 2004).

It is common for a hydrothermal fluid to change its physicochemical properties during fluid-rock interaction. The fO_2 of the initial hydrothermal fluid will decrease with progressing interaction with Fen rock intrusives, e.g., carbonatite. Therefore, it is likely that chloritisation and rødbergitisation represent two end members of the same hydrothermal alteration process. However, there is no evidence in the field, linking both processes to the same hydrothermal event. Rødbergite shows a gradual transition into carbonatite (transitional rødbergite) or displays sharp boundaries to the unaltered host rock. An actual transition into a chloritised rock (± magnetite and pyrite) has not been documented. Therefore, rødbergitisation and chloritisation are defined as two separate processes.

10.5 Implications for REE-Exploration

At the end of chapter 6 about the Bjørndalen transect, a preliminary model was introduced, and several predictions were made for REE-exploration. Data gathered from the Fen Road transect, and Gruveåsen transect is used to test these predictions and develop new insights.

So far, the existence of separate zones rich in LREE, HREE or Th, which is described in chapter 6.3.7, are a unique feature of the Bjørndalen area, and such segmentation is not obvious along the Gruveåsen or Fen Road transect. While the absence of proof is not the proof of absence, along the Fen Road and Gruveåsen transects rødbergitisation created a coupled enrichment of LREE, HREE and Th (Fig. 6-40). The results suggest that a clear decoupling in the behaviour of LREE, HREE and Th only occurs in areas with a high density of REE-mineral-bearing veins, or Fe-ore veins. REE-mineral-bearing veins cause a LREE enrichment relative to HREE and Th (please refer to chapter 6, sample 15-93-FE, Fig. 6-35; Fig. 6-40; chapter 7, sample 16-96-FE, Fig. 7-15; Tab. 7-3 Dolomite-Carbonatite (NW); chapter 8 - Fig. 8-14 La/Yb) and Fe-ore veins have the same effect for the enrichment of HREE (please refer to chapter 8, sample 16-54, Fig. 8-16 D). In order to find a zone of selective enrichment, one of these vein types must be present in a sufficiently high abundance.

Because the formation of rødbergite is caused by an external REE-rich fluid, the formation of rødbergite derived from other protoliths than carbonatite was predicted in chapter 6.3.7. The Gruveåsen transect showed the potential formation of rødbergite from any available precursor rock. At the same time, a correlation between the REE concentration of the resultant rødbergite and the REE concentration of the surrounding host rock (protolith) suggested a rather localised (< 50 m) mobilisation of REE (Fig. 8-17), which lowered the probability of forming REE-rich rødbergite in a REE-poor host rock. However, it is likely that high REE level rødbergite veins or REE-mineral-bearing veins occur within low REE level host rock due to their ability to transport REE over a larger distance (Fig. 8-15).

The rocks with the highest REE concentration and the best potential for REE exploration are chlorite-rich carbonatite, rødbergite and rødbergite veins. Rødbergite has the highest variation in REE concentration due to the dependency on REE concentrations of the surrounding host rock. The host rock influence on rødbergite veins is less strong, and rødbergite veins typically show very high REE concentrations. Chlorite-rich carbonatites have a less variable high REE concentration. The REE concentration increases with an increasing proportion of dark mineral phases.

Additionally, rock samples with a high density of veins and/or the presence of apatite relics are more likely to be enriched in REE. Even unaltered lithotypes originally low in REE can be greatly enriched in REE, if REE-mineral-bearing veins are present, as was shown for transitional rødbergite at the Bjørndalen transect (Fig. 6-40). Another telling example was collected during a sampling campaign in the Søve tunnel in the western part of the Fen Complex. In the middle of a long on-going sequence (270 m) of unaltered carbonatite, a specimen with a high density of dark veins was collected, and the analysed REE concentration showed a 10-fold increase compared to the surrounding host rock carbonatites. The REE-mineralisation of a country rock such as the gneiss is possible if fluid pathways were available, and a close look at the prevalent fault systems will present an idea of potentially mineralised areas. A reddish hematised rock type has been observed outside of the Fen Complex (Andersen, 1989a), which is evidence for the hematisation event extending beyond the borders of the Fen Complex. However, the REE-mineralisation of the country rock is not likely to be greater than the REE-mineralisation within the Fen Complex, due to the more proximal distance to the REE-source.

10.6 Similar REE-Mineralisation worldwide

The REE-mineralisation associated with the rødbergitisation of the Fen Complex is an exceptional case of a carbonatite-related hydrothermal REE-deposit. Several REE-deposits worldwide show similarities to the Fen Complex e.g., the hydrothermal Red REE-rich Veins (RRV) of the Bachu Carbonatite (Cheng et al., 2018), the heavily altered HREE-enriched carbonatite dykes of the Huanglongpu district (Smith et al., 2018), the REE-rich ferrocarbonatite-breccia of Kuge in Kenya (Onuonga et al., 1997), the Th-rich hydrothermal altered shear zone at Sarfartoq in Greenland (Bedini and Rasmussen, 2018). The implementation of the major findings of this thesis will enhance the understanding of these REE-deposits.

The nearest equivalent to the Fe-ore veins and rødbergite of the Fen Complex are the ironstone veins of the Gifford Creek Ferrocarbonatite Complex (GFC) in Western Australia (Pirajno et al., 2014). The GFC comprises dykes, sills and veins of ferrocarbonatite that are associated with complex and irregular distributed zones of fenite together with a swarm of ironstone (hematite, magnetite and goethite) veins. Pirajno et al. (2014) obtained an average U-Pb age of 1075 ± 35 Ma for the GFC, which is within the range of ages for the Warakuna Large Igneous Province. Monazite from the fenite of the ironstone yielded a younger age of 1050 ± 25 Ma, which is interpreted as the second phase of carbonatite magmatism. During this second phase, a pull-apart structure formed and reactivated the carbonatite system, which resulted in the emplacement of a swarm of sinuous ironstone veins (Pirajno et al., 2014). The genetic model of the ironstones of GFC is based on a dissolution of primary of Fe-bearing minerals and multiple stages of redistributing of Fe in the form of magnetite, hematite and goethite. For the formation of REE-minerals Pirajno et al. (2014) refer to Andersen

(1984), which suggests a magmatic origin with passive enrichment during hematisation. However, if the REE were, in fact, mobile, similar to the result of this thesis for the Fen Complex, this would change the perspective for the REE-exploration. A REE-mineralised horizon would not be restricted to the ironstone and ferrocarbonatite but instead could extend in the proximity (<100 m) of the centre of hematisation, depending on the permeability of the surrounding rock. Especially host rocks rich in carbonate and/or apatite are of major importance because they are more susceptible to hydrothermal alteration and are more effective in destabilising REE-complexes compared to granitic host rocks. Additionally, the GFC has single veins and not overlapping zones of multiple alteration cells; this makes a decoupling of HREE and LREE during hydrothermal alteration, comparable to the Bjørndalen transect, more likely. In fact, according to Pirajno et al. (2014), most of the REE-mineralisation is hosted in the fenitic halos, which indicates a hydrothermal origin of REE-minerals. The Fenites of GFC surround ferrocarbonatites as well as ironstones. A link between the hematisation events of the ironstone associated with a hydrothermal REE-mineralisation is therefore already indicated.

Carbonatites from the east-northeast-trending Cape Cross lineament in northern Namibia Kalkfeld, Ondurakorume and Onsongombo all show hematite ore associated with radioactivity (Verwoerd, 1966). The Fe- and Th-mineralisation style is very similar to that of the Fen Complex. Therefore, a hydrothermal mobilisation of REE similar to the Fen Complex can be anticipated, and features like REE-mineral bearing veins, LREE-HREE enriched zones and apatite-traps are likely to be present. Additionally, the application of remote sensing (radioactive – and electromagnetic radiation) could help to localise hidden Fe-Th-REE mineralised systems within the whole Cape Cross lineament.

The apatite Seligdar deposit in Russia is one of many similar apatite deposits within the Nimnyrskaya apatite zone, which is about 400 km long (Prokopyev et al., 2017). The origin of the Seligdar deposit is still subject of an ongoing debate. According to Prokopyev et al. (2017), the deposit is a hydrothermally altered and metamorphosed dolomite carbonatite, which subsequently altered the primary mineralogy of apatite, dolomite and magnetite to a rødbergite-like paragenesis of quartz, calcite, monazite-(Ce), xenotime-(Y), hematite, thorite, sulphates and sulphides. Chloride brines caused the remobilisation of REE and Th into hydrothermal monazite and subsequently evolved into oxidised carbonate-ferrous solution forming sulphates, monazite-(Ce) and hematite (Prokopyev et al., 2017). Analogous to the hydrothermal REE-mineralisation of the Fen Complex the focus of REE-exploration should be on understanding the fluid pathways (faults, vein generations) and to map potential zones of HREE, LREE and Th separations especially because HREE-minerals (xenotime-(Y)) and LREE-minerals (monazite-(Ce)) are present. The application of remote sensing would help to identify hidden mineralised pathways (electromagnetic) of hematised or magnetised ore veins. Additionally, radioactivity surveys could help to identify potential REE-mineralised areas on a regional scale of the Nimnyrskaya apatite zone. The occurrence of platform sediments in the Nimmyrskaya apatite zone could be beneficial for REE-mineralisation. Carbonate sediments are more effective in the destabilisation of REE-complexes than metamorphic rocks. REE^{3+} bearing hydrothermal fluid originating from the alteration of apatite deposits will neutralise in contact with platform sediments and precipitate REE-minerals.

The Hoidas Lake deposit in northern Saskatchewan is characterised by LREE-rich diopside-allanite veins and various generations of apatite breccia veins (Halpin, 2010). According to Pandur et al. (2016), the source of the mineralisation is most likely a carbonatite or syenitic intrusion. Locally the REE-mineralisation got redistributed by an oxidising hydrothermal fluid causing a chlorite-hematite alteration with secondary monazite, REE carbonatites, REE-Sr carbonates and allanite veins (Pandur et al., 2016). The mineralisation style shows many similarities to the REE-mineral bearing veins of the Fen Complex, e.g. LREE-enriched, associated with hematite, chlorite and barite, caused by an oxidising fluid. Therefore, the application of remote sensing (radioactive – and electromagnetic radiation) might identify a mineralised root system — analogue to the hematite and magnetite ore bodies of the Fen Complex. Similar to the HREE-dominated Fe-ore veins, apatite veins and central rødbergite zones of the Fen Complex, a central and deeper part of alteration is more likely to be enriched in HREE, due to less mobile nature of HREE compared to LREE.

The main findings of this thesis will help to change the perspective on some REE-deposits and extend the range of features that are important for REE-exploration, especially in hydrothermal systems enriched in REE, Fe and Th.

10.7 Economic evaluation

To properly decide if the exploitation of a deposit is economically viable is a complex process that requires much experience and has to take various types of information (geological, economic, legal) into account. Generally, this analysis is achieved in a feasibility study. The following analysis is based on the author's best knowledge and does not claim to be on the same level as a feasibility study.

Under the current situation and knowledge, the exploitation of REE from the hydrothermal REE-mineralisation of the Fen Complex appears unlikely.

First, the deposit is mainly enriched in LREE, which are less economically viable than HREE. Second, although some parts of the REE-mineralisation show the low concentration of Th, the majority of the REE-enriched rock has Th concentrations between 500 – 1500 ppm. The concentration process of REE-minerals and later beneficiation of the REE would produce a Th-rich concentrate. The proper disposal or storage would produce additional costs for the mining business. Third, the cost of building a mine solely for the production of REE is relatively high with respect to the world market value of REE. Most of the worldwide REE are mined as a by-product. Fourth, the average hourly labour cost in Norway is relatively high and with 50 € almost twice as high as the average hourly labour cost of the UK (27.4 €) or the average hourly labour cost of the EU with28 € (Eurostat, 2018). Fifth, Europe has large quantities of waste material with considerable REE-concentrations e.g. 2.7 billion tonnes (Klauber et al., 2011) of red mud with REE concentration of less than 1 wt% (Binnemans et al., 2015), apatite dumps from fertilizer production and Fe-extraction from Kiruna type mineralisation (Al-Thyabat and Zhang, 2015; Binnemans et al., 2015). From an environmental point of view, it appears better to reuse dumps than open new mines.

Depending on the mineralogical characteristic of the waste material, it is potentially also economically more feasible to reprocess old dumps to extract REE.

Although the hydrothermal REE-mineralisation associated with rødbergite shows the highest potential for REE enrichment within the Fen Complex, it might be economically more viable to mine the Nb-rich calciocarbonatite (søvite of the Tufte tunnel). The calciocarbonatite of the Tufte tunnel could potentially deliver the following commodities: Nb from pyrochlore or columbite, P from apatite, calcite, Fe from magnetite and REE from monazite-(Ce) and REE-fluorocarbonates — especially, calciocarbonatite with REE-mineral bearing veins near rødbergite. Even though the REE concentration is below the rødbergitised or chloritised lithotypes, the combination of multiple commodities could make REE extraction feasible.

On the other hand, if Th becomes a useful commodity (Th-molten salt reactor technology) instead of expensive waste product, rødbergite becomes a valuable Th-REE-ore. Additionally, discoveries of REE-mineralisation at the Fen Complex are still possible. The elongated hematite ore bodies grade into magnetite bodies in the more central area of the Fen Complex. The magnetite mineralisation represents different pH and fO2 conditions during the Fe-mineralisation. However, it is unclear how LREE, HREE and Th mineralisation are influenced by these parameters during hydrothermal alteration.

10.8 Conclusion

The REE-mineralisation of the Fen Complex is a REE-enrichment process triggered by the alteration with external hydrothermal fluids (Fig. 10-1). These fluids migrate along zones of structural weakness into the rocks of the Fen Complex and cause the dissolution and

oxidation of the carbonatite. The heat source, caused the circulation of the hydrothermal fluid, is supplied by an upwelling of hot mantle material during the formation of the Oslo rift. The reacted hydrothermal fluid was rich in Ca^{2+}, Mg^{2+}, $Fe^{2+/+3}$, K^{+}, Ba^{+}, REE^{3+}, Th^{4+}, CO_3^{2-}, SO_4^{2-} and F^{-} due to the dissolution of the unaltered mineral assemblage, e.g., carbonates, pyrite, apatite and REE-fluorocarbonates (Fig. 6-12). The ascending hydrothermal fluid has caused a local redistribution of those elements along major NNW-SSE to NW-SE oriented fault zones (Andersen, 1983) and surrounding areas (see chapter 4) where the hydrothermal flow was most concentrated massive narrow veins of hematite/magnetite ore formed (Fig. 8-10). Hydrothermal fluid further invades the wall rock via veinlets, rødbergite veins and through pervasive migration along crystal boundaries (Fig. 6-16; Fig. 6-36; Fig. 7-32). The hydrothermal alteration has caused large-scale oxidation of carbonatite to rødbergite. Although rødbergite has preferentially formed by the replacement of carbonatite, evidence for the rødbergitisation of damtjernite, fenite and gneiss was observed (Fig. 8-7; Fig. 8-11; Fig. 8-12). The alteration mineral assemblage is characterised by varying amounts of Fe-oxide, barite, calcite, chlorite, quartz, phlogopite, ferroan dolomite-ankerite and with minor amounts of apatite, REE-minerals and barian orthoclase. Monazite-(Ce), synchysite-(Ce) and bastnäsite-(Ce) are the most common hydrothermal REE-minerals and are part of the veinlet, vein assemblage and interstitial areas in rødbergite (Tab. 7-2). The hydrothermal REE-minerals are commonly in intergrowth with barite, calcite, chlorite or phlogopite (Fig. 6-17; Fig. 6-28; 7-34).

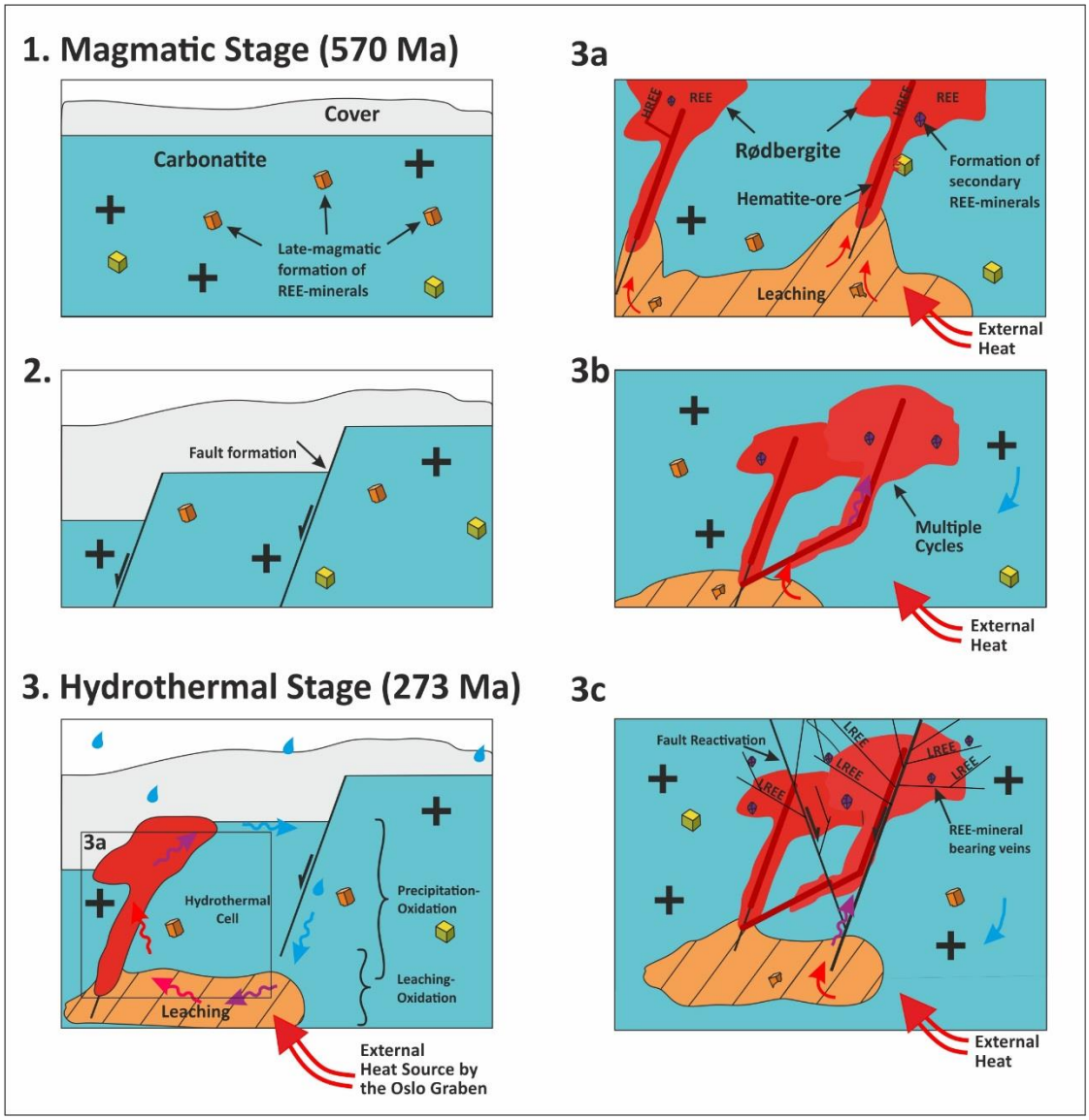

Figure 10-1: Simplified evolutionary stages of REE-mineralisation at the Fen Complex. **1.** Emplacement of the magmatic Fen carbonatite around 570 Ma. Formation of REE-minerals during late-magmatic processes within the carbonatite. **2**. Fracturing and faulting of the solidified carbonatite. **3**. External heat from the Oslo rift activates a hydrothermal cell at 273 Ma. The hydrothermal cell is circulated meteoric water along deep faults into the magmatic rock sequence, which is causing the oxidation of carbonatite. **3a** The hydrothermal alteration of the carbonatite caused the breakdown of unaltered mineral assemblage (e.g., REE-minerals) and formation of hydrothermal REE-minerals from the altered mineral assemblage. The REE redistribution caused REE enriched zones in rødbergite with a narrow zone of HREE enrichment along the hydrothermal pathways. **3b** Multiple cycles of rødbergite formation. **3c** LREE-rich veins formed within the rødbergite and unaltered carbonatite during the last stage of the hydrothermal alteration.

Additionally, monazite concentrates as a replacement halo around apatite relics from unaltered carbonatite (Fig. 6-38; Fig. 6-39). Thorium is mainly incorporated in monazite, REE-fluorocarbonates or forms the Th-mineral thorite. The precipitation of REE-minerals during rødbergitisation caused a general enrichment of REE and Th in the replaced host rocks by up to 23 times of the original REE concentration (Fig. 6-40; Fig. 7-37; Tab. 7-3; Tab. 8-1). The REE concentration within rødbergite varies strongly (Tab. 8-1) and is positively influenced by the presence of veinlets, rødbergite veins and apatite relics. Furthermore, the REE-level of rødbergite is related to the REE concentration of the surrounding host rock and is especially high for chlorite-rich carbonatite (Fig. 8-17). During the evolution of the passage of the hydrothermal fluid, the physicochemical properties of the system were constantly changing, which caused multiple sets of cross-cutting veins and overprinting rødbergitisation events. Figure 10-2 is a simplified geological cross-section of the Fen Complex and shows the formation of rødbergite relative to the rest of the Fen Complex.

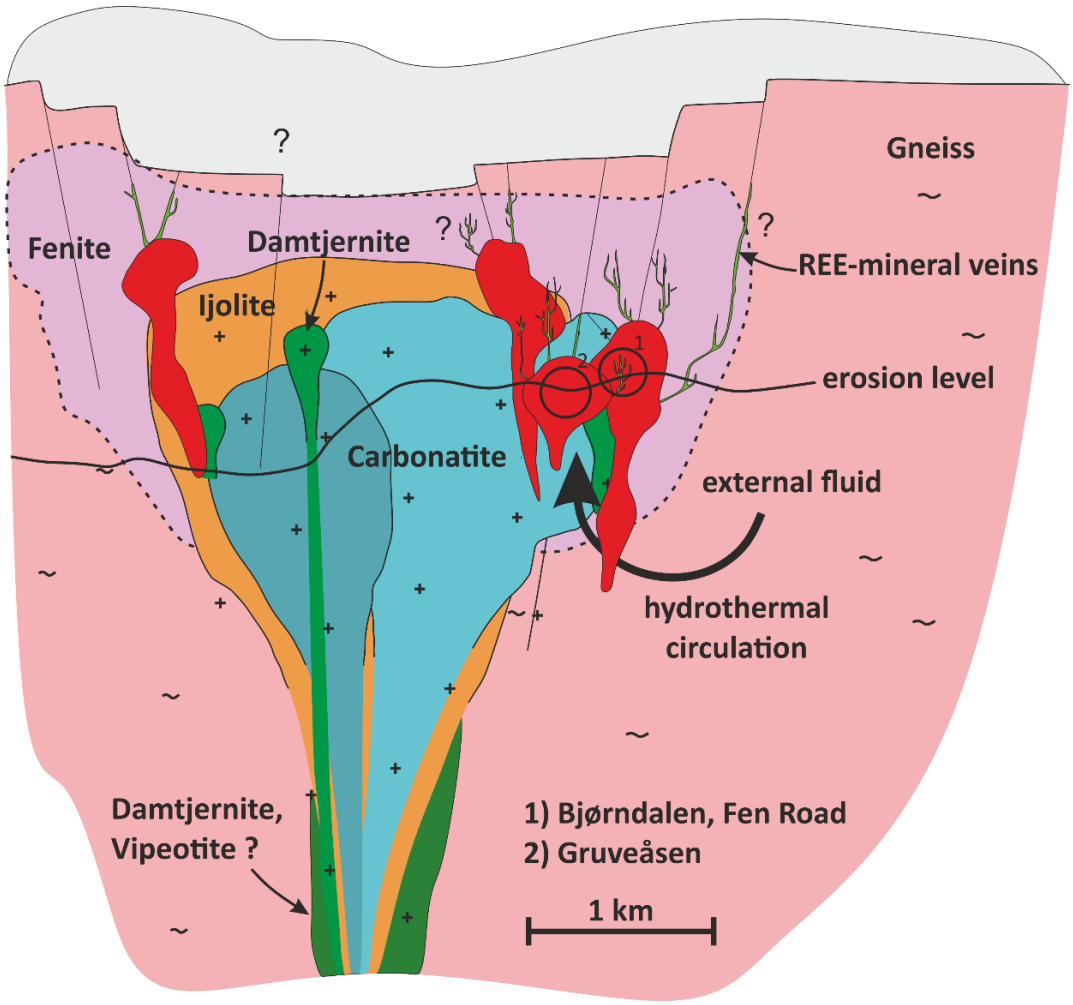

Figure 10-2: Schematic cross-section of the Fen Complex. Hydrothermal alteration of external fluid along fault zones is causing rødbergitisation of the carbonatites. The alteration is preferentially located at the outer rim of the complex with REE-mineral-veins extending beyond the rødbergitisation as part of a feeder structure. Location 1 is mainly rødbergite with REE-mineral bearing veins and represents Bjørndalen- and Fen Road transect. Location 2 comprises a larger part of the complex with carbonatite, chloritised carbonatite, damtjernite and rødbergite, which represents the Gruveåsen transect.

11 Final Conclusion & Future Research

The Fen Complex in south Norway is with 484 Mt of Rare Earth Oxides (REO) at 0.93 wt% one of the largest REE resources in Europe and object of ongoing mineral exploration. However, the last period of intense research about the origin of the REE-mineralisation at the Fen Complex was done in the 1980s by Andersen. Due to the recent challenges regarding a secure supply of REE for the European market, this project set out to investigate the nature of the REE-mineralisation at the Fen Complex. The aim was to use a combination of geochemical data and high-resolution imaging to create an improved model of the REE-mineralisation and to provide companies a tool to strengthen their exploration campaigns.

The major findings of this study are:

a) Rødbergite is a hydrothermally altered red alteration product from different kinds of protoliths (gneiss, fenite, carbonatite and damtjernite).
b) The rødbergitisation of the protoliths caused an enrichment in REE concentrations in varying degrees (up to 23-fold of the original REE concentration), depending on the REE level of the protolith, REE-mineral/rødbergite vein density and the presence of apatite relics.
c) The precipitation of hydrothermal REE-minerals (monazite-(Ce), bastnäsite-(Ce), synchysite-(Ce) and allanite) dominated in LREE — and not the residual enrichment of insoluble original REE-minerals — caused the increase in REE concentration.

d) The increase in REE concentration is associated with a variable increase in Th, which is mainly incorporated in monazite-(Ce), REE-fluorocarbonates and rarely in thorite.

e) Th-Pb geochronology on zircons from two different carbonatite locations established an age for the emplacement of the Fen Complex carbonatite at ~570 Ma, an age that is in accordance with previous Rb-Sr and Ar/Ar dating of damtjernites that are coeval with the carbonatites.

f) According to Th-Pb ages of 272.9 Ma ± 3.4 Ma from hydrothermal monazite in REE-rich transitional rødbergite, the hydrothermal REE-mineralisation in rødbergite is significantly younger than the emplacement of the Fen Complex and indicates the Oslo rift as the main heat source for the hydrothermal rødbergitisation.

The project identified rødbergitisation as an effective process for REE enrichment due to the precipitation of hydrothermal REE-minerals. However, there is evidence at the Fen Road transect and Gruveåsen transect for a spatial association between rødbergite and chlorite-bearing dolomite-carbonatite. Rødbergitisation and chloritisation are similar processes as both are hydrothermal processes, which in general increase the REE and Th concentration of protoliths and precipitate, among others, Fe-oxides, pyrite and chlorite. Chloritisation — or the formation of grønnbergite as an equivalent to rødbergite — is potentially a more reduced version of rødbergitisation as the hydrothermal fluid penetrated deeper into the reduced intrusive rock of the Fen Complex (Fig. 11-1). The evolution towards a reduced and more alkaline fluid could explain the formation of magnetite bodies in the extension of hematite veins (Fig. 11-2).

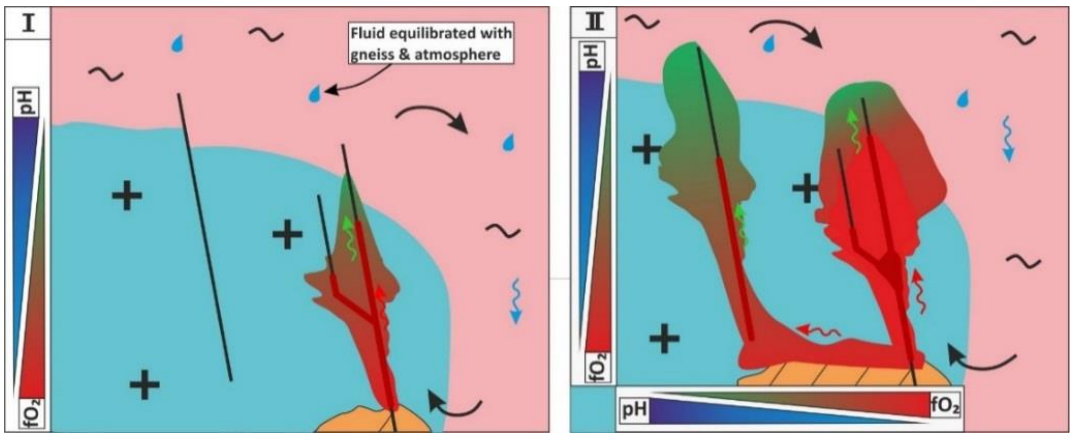

Figure 11-1: Schematic sketch of the vertical change in pH and fO_2 of hydrothermal fluid along faults due to reaction with the carbonatite (stage I). A vertical change in fluid properties is accompanied by a horizontal change from the periphery of the Fen Complex to a more central part of the complex. (stage II). Red areas indicate oxidised conditions (rødbergite) while the green parts represent more reduced conditions associated with chlorite-magnetite mineralisation.

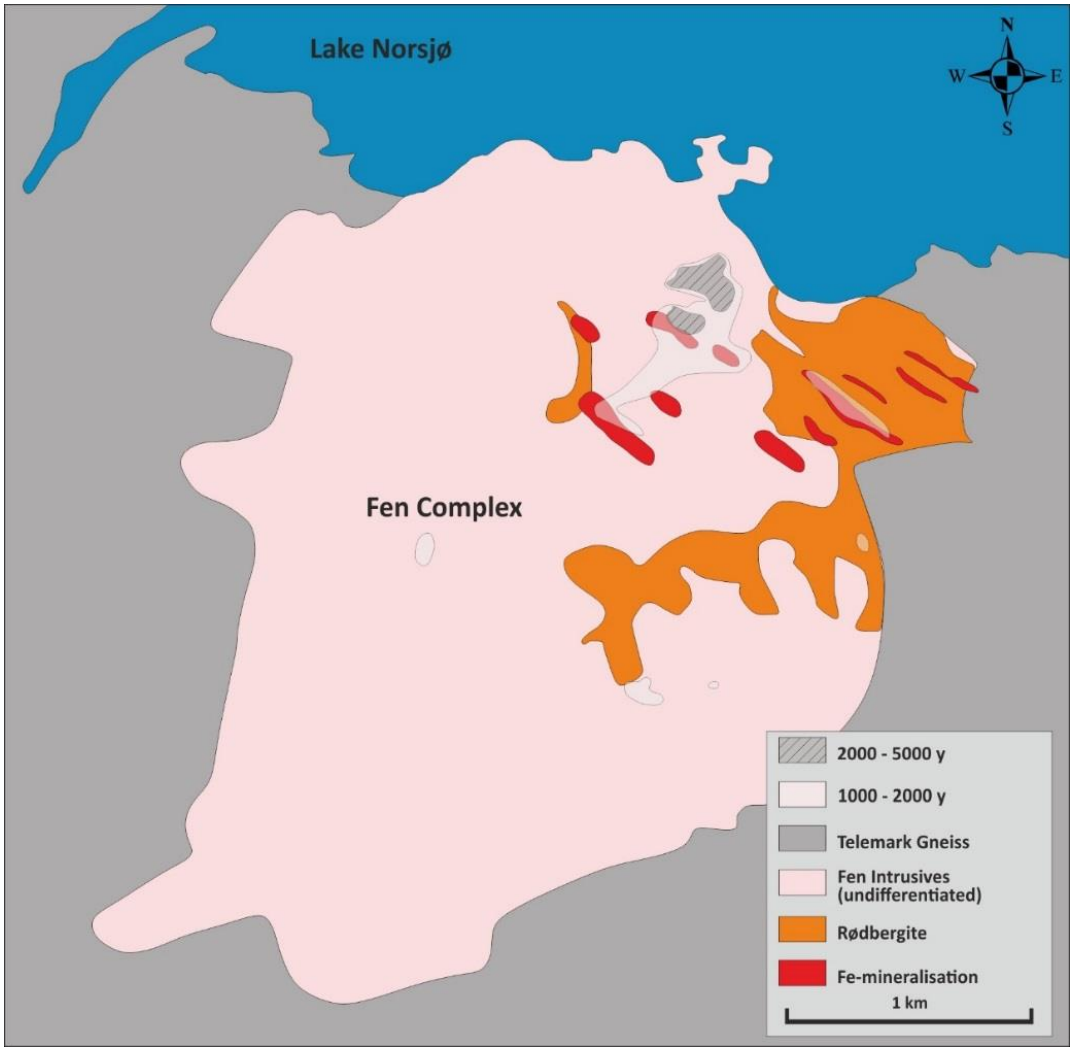

Figure 11-2: Simplified geological map of the Fen Complex showing the extent of rødbergite and the distribution of Fe-ore zones. The Fe-mineralisation overlaps partly with zones of magnetic intensity (unit is γ = 1 nT) calculated by Sæther (1957) indicating the presence of magnetite bodies.

A mineralogical and geochemical investigation should address the connection between rødbergite, chlorite-bearing dolomite-carbonatite and magnetite ores with focus on REE-mineralisation, Th concentration (potentially low around magnetite mineralisation) and other potentially interesting mineralisation, e.g. sphalerite, galena and chalcopyrite. Alternatively, evidence suggests that chloritisation is limited to dolomite-ankerite carbonatite and therefore might be a late- to post-magmatic alteration process unique to the Fe-rich carbonatite units.

The presence of postmagmatic pyrite is evidence for the hydrothermal fluid to have been equilibrated to atmospheric conditions. Based on the stability diagram of Fe-minerals, the formation of pyrite requires a pH below 9 (Fig. 11-3). A hydrothermal fluid in equilibrium with a carbonatite ranges between pH of 11.5 and 13 and would form magnetite under reducing conditions rather than pyrite. A hydrothermal fluid equilibrated with atmospheric CO_2 concentration is having a significantly lower pH in equilibrium with carbonatite and might be essential to the formation of pyrite (Langmuir, 1997). This supports the idea that the rødbergitisation fluid derived from meteoric water. Further modelling based on fluid inclusion data is necessary to check this hypothesis.

Additionally, more research is needed to investigate the nature of corroded alternating stack of REE-fluorocarbonates at the Fen Road transect, which could be part of the original- or alteration mineral assemblage.

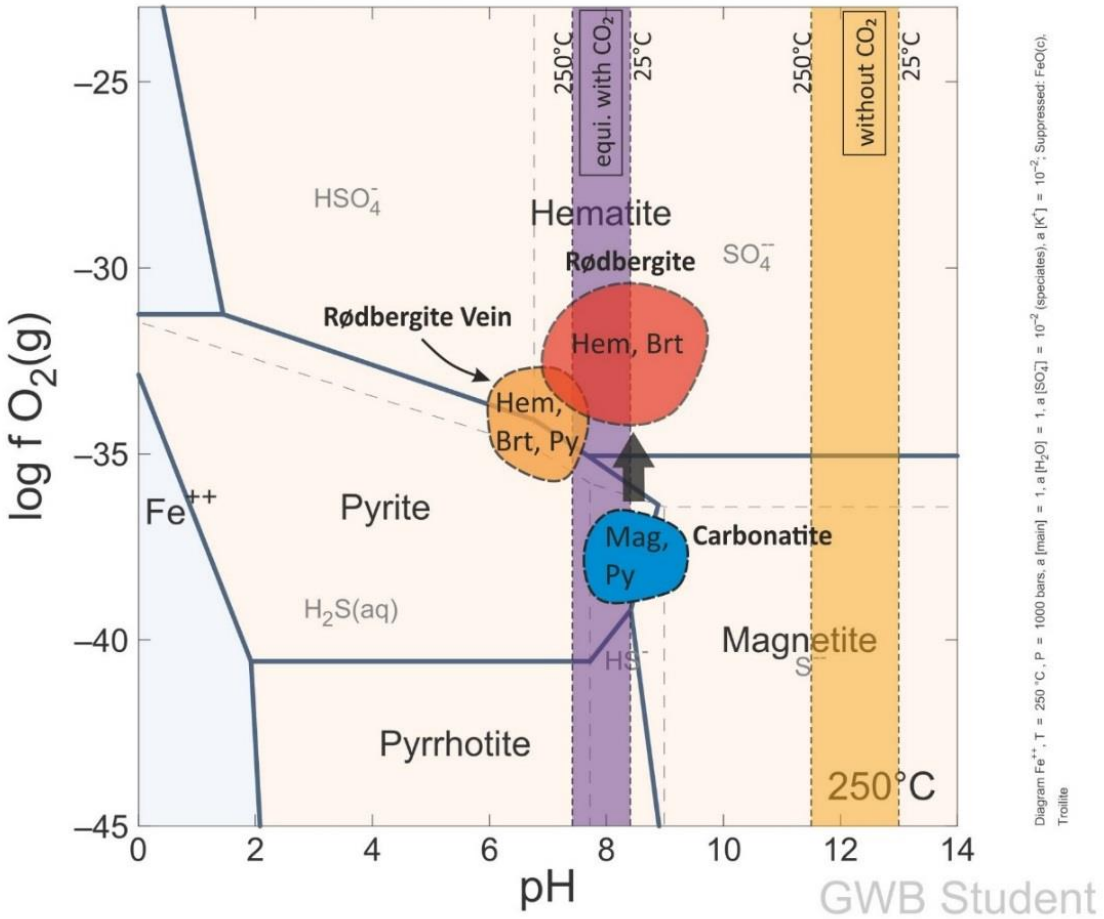

Figure 11-3: Stability diagram of Fe-minerals depending on pH and fO_2 at 250°C. The pH of a hydrothermal fluid in equilibrium with carbonatite is marked by a yellow box. The purple box represents the pH level of a hydrothermal fluid in equilibrium with carbonatite and atmospheric CO_2 concentrations. The hydrothermal fluid forming rødbergite veins had to be equilibrated with atmospheric CO_2 conditions in order to have been able to form pyrite. For details about the construction of the phase diagram, see the caption of figure 7.41.

To this point, the isotopic age of the REE-mineralisation was only calculated for samples from the Bjørndalen transect. To verify that the Permian age of the mineralisation, which coincides with the formation of the Oslo rift, is not an outlier, monazite-(Ce) from the Fen Road -and Gruveåsen transect should be analysed.

The Fen Road transect and especially the Gruveåsen transect display a correlation between the REE-concentration of rødbergite and the REE concentration of the former

protolith. One particular rødbergite vein in a host rock of brecciated fenite has a very high concentration of REE despite being surrounded by rock and vein with a low level of REE. This might be due to an adjacent unexposed host rock with a high level of REE, or due to the unique nature of this vein. A detailed mineralogical investigation is needed to clarify this case.

Apparent xenoliths of rødbergite occur locally in brecciated rødbergitised damtjernite and make the connection between rødbergite and REE-mineralisation more complex than initially thought. Was the Fen Complex subject of multiple events of rødbergitisation? How much time passed between these different rødbergitisation events (Ediacaran to Permian)? Are some of the damtjernite magmatism post-Ediacaran? Was there more than one event of hydrothermal REE-mineralisation, and were any additional mineralisation events necessarily associated with rødbergitisation? A better constrain about the geochronology of the REE minerals at different transects in combination with more mineralogical work targeting these rødbergite xenoliths will help to address these questions.

Rødbergitisation and chloritisation show a clear link between hydrothermal Fe-mineralisation, Th-mineralisation and REE-mineralisation. There are some properties which cause the mobilisation of REE — a group of elements which were regarded to be resistant against hydrothermal mobilisation of any kind — and Th and Fe at the same time (plus S, Ba, P, Ca, Mg, Si and Al). This is not just the case for the Fen Complex but can also be seen for other carbonatite associated complexes, e.g., Bayan Obo and even other types of deposits, e.g. IOCG or Kiruna-type deposits. Future research should also identify the common denominator as well as the differences in these types of deposits.

Finally, yet importantly, rødbergitisation and chloritisation are crucial processes to understand the REE-mineralisation of the Fen Complex. These processes involve common minerals and are happening under rather normal hydrothermal conditions. Nevertheless, they are rarely reported as key processes in other REE-mineralised carbonatites. Due to their similarity to typical hydrothermal mineral assemblages, it is unlikely that rødbergitisation and chloritisation are unique REE-mineralisation processes of the Fen Complex. Some carbonatite complexes report similar mineral parageneses that indicates processes like rødbergitisation to be the reason for the REE-mineralisation. For example, Bayan Obo, China (Drew et al., 1990), Lueshe, DR Congo (Maravic and Morteani, 1980), Buru and Tuge, Kenya (Onuonga et al., 1997), Sarfartôq, Greenland (Secher and Larsen, 1980). Therefore, future research should focus on recognising rødbergitisation and chloritisation related processes at other carbonatite complexes and similar REE-mineralisations worldwide and apply the findings of this thesis in order to improve the understanding of the REE-mineralisation of the respective complex.

REFERENCES

21st North, 2011. R1 - Fen Carbonatite complex - Summary of historic work and data.

21st North, 2014a. The Fen rare earth element deposit, Ulefoss, South Norway.

21st NORTH, 2014b. THE FEN RARE EARTH ELEMENT DEPOSIT, ULEFOSS, SOUTH NORWAY - Executive summary regarding deposit significance

Agence France-Presse, 2010. High-seas collisions trigger Japan-China spat.

Åhäll, K.-I. and Connelly, J.N., 2008. Long-term convergence along SW fennoscandia: 330m.y. of proterozoic crustal growth. Precambrian Research, 161(3-4): 452-474.

Ahall, K.I., Connelly, J.N. and Brewer, T.S., 2000. Episodic rapakivi magmatism due to distal orogenesis?: Correlation of 1.69-1.50 Ga orogenic and inboard, "anorogenic" events in the Baltic Shield. Geology, 28(9): 823-826.

Åhäll, K.I. and Gower, C.F., 1997. The Gothian and Labradorian orogens: Variations in accretionary tectonism along a late Paleoproterozoic Laurentia-Baltica margin. Gff, 119(2): 181-191.

Aksnes, S.S. and Årtveit, J.T., 2014. Fen – From Volcanism to Wealth. Søve Mines and Norsk Bergverk Ltd. 1951-65. In: G.N. GEOPARK (Editor).

Al-Thyabat, S. and Zhang, P., 2015. In-line extraction of REE from Dihydrate (DH) and HemiDihydrate (HDH) wet processes. Hydrometallurgy, 153: 30-37.

Al Ali, S., 2016. Mineralogy and mineral processing to optimise recovery of synchysite-(Ce) and ap atite from carbonatite at Songwe Hill, Malawi. , University of Exeter.

Ali, S., 2014. Social and Environmental Impact of the Rare Earth Industries. Resources, 3(1): 123-134.

Amelin, Y. and Zaitsev, A.N., 2002. Precise geochronology of phoscorites and carbonatites. Geochimica et Cosmochimica Acta, 66(13): 2399-2419.

ammrf, A.M.M.R.F., 2014. MyScope training for advanced research, Microanalysis Training module, pp. 63.

Andersen, T., 1983. Iron ores in the Fen central complex, Telemark (S. Norway): Petrography, chemical evolution and conditions of equilibrium. Norsk. Geol. Tidsskr., 63.

Andersen, T., 1984. Secondary processes in carbonatites: petrology of “rødberg” (hematite-calcite-dolomite carbonatite) in the Fen central complex, Telemark (South Norway). Lithos, 17: 227-245.

Andersen, T., 1986. Magmatic fluids in the Fen carbonatite complex, S.E. Norway. Contributions to Mineralogy and Petrology, 93(4): 491-503.

Andersen, T., 1987a. Mantle and crustal components in a carbonatite complex, and the evolution of carbonatite magma: Ree and isotopic evidence from the fen complex, southeast Norway. Chemical Geology: Isotope Geoscience section, 65(2): 147-166.

Andersen, T., 1987b. A model for the evolution of hematite carbonatite, based on whole-rock major and trace element data from the Fen complex, southeast Norway. Applied Geochemistry, 2(2): 163-180.

Andersen, T., 1989a. Carbonatite-related Contact Metasomatism in the Fen Complex, Norway: Effects and Petrogenetic Implications. Mineralogical Magazine, 53(372): 395-414.

Andersen, T., 1989b. A model for the evolution of hematite carbonatite, based on whole-rock

major and trace element data from the Fen complex, southeast Norway. Mineralogical Magazine, 53(372): 20.

Andersen, T., 1991. Temperature-HF Fugacity Trends During Crystallization of Calcite Carbonatite Magma in the Fen Complex, Norway. Mineralogical Magazine, 55(378): 81-94.

Andersen, T. and Qvale, H., 1986. Pyroclastic Mechanisms for Carbonatite Intrusion: Evidence from Intrusives in the Fen Central Complex, Se Norway. The Journal of Geology, 94(5): 762-769.

Andersen, T. and Sundvoll, B., 1987. Strontium and neodymium isotopic composition of an early tinguate (mepheline microsyenite) in the Fen complex, Telemark, Southeast Norway: age and petrogenetic implications. NGU Bulletin, 409: 29-34.

Andersen, T. and Taylor, P.N., 1988. Pb isotope geochemistry of the Fen carbonatite complex, S.E. Norway: Age and petrogenetic implications. Geochimica et Cosmochimica Acta, 52(1): 6.

Anell, I., Thybo, H. and Artemieva, I.M., 2009. Cenozoic uplift and subsidence in the North Atlantic region: Geological evidence revisited. Tectonophysics, 474(1-2): 78-105.

Arzamastsev, A.A., Glaznev, V.N., Arzamastseva, L.V., Bea, F. and Montero, P., 2001. Kola alkaline province in the Paleozoic: evaluation of primary mantle magma

composition and magma generation conditions. Russian Journal of Earth Sciences, 3(1): 1-32.

Arzamastsev, A.A., Yakovenchuk, V., Pakhomovsky, Y. and Ivanyuk, G., 2008. The Khibina and Lovozero alkaline massifs: Geology and unique mineralization, 33 IGC excursion No 47

Bailey, D.K., 1989. Peralkaline igneous rocks. 436-437.

Banks, D.A., Yardley, B.W.D., Campbell, A.R. and Jarvis, K.E., 1994. REE composition of an aqueous magmatic fluid: A fluid inclusion study from the Capitan Pluton, New Mexico, U.S.A. Chemical Geology, 113(3-4): 259-272.

Bao, Z. and Zhao, Z., 2008. Geochemistry of mineralization with exchangeable REY in the weathering crusts of granitic rocks in South China. Ore Geology Reviews, 33(3-4): 519-535.

Barker, D.S., 1989. Field Realtions of Carbonatites. In: K. Bell (Editor), Carbonatites. Genesis and Evolution. Unwin Hyman, London, pp. 31.

Barth, T.F.W. and Ramberg, I.B., 1966. The Fen circular complex. In: O.F. Tuttle and J. Gittins (Editors), Carbonatites. Wiley-Interscience, New York, pp. 225-57.

Bearden , J.A., 1967. X-ray Wavelengths Review Of Modern Physics, 39(1): 47.

Bédard, J.H., 2006. Trace element partitioning in plagioclase feldspar. Geochimica et Cosmochimica Acta, 70(14): 3717-3742.

Bedini, E. and Rasmussen, T.M., 2018. Use of airborne hyperspectral and gamma-ray spectroscopy data for mineral exploration at the Sarfartoq carbonatite complex, southern West Greenland. Geosciences Journal, 22(4): 641-651.

Behrens, A., Giljum, S., Kovanda, J. and Niza, S., 2007. The material basis of the global economy. Ecological Economics, 64(2): 444-453.

Bell, K., Blenkinsop, J., Cole, T.J.S. and Menagh, D.P., 1982. Evidence from Sr isotopes for long-lived heterogeneities in the upper mantle. Nature, 298(5871): 251-253.

Bell, K., Blenkinsop, J., Kwon, S.T., Tilton, G.R. and Sage, R.P., 1987. Age and radiogenic isotopic systematics of the Borden carbonatite complex, Ontario, Canada. Canadian Journal of Earth Sciences, 24(1): 24-30.

Bell, K., Kjarsgaard, B.A. and Simonetti, A., 1998. Carbonatites--Into the Twenty-First Century. Journal of Petrology, 39(11-12): 1839-1845.

Bell, K. and Simonetti, A., 2009. Source of parental melts to carbonatites–critical isotopic constraints. Mineralogy and Petrology, 98(1-4): 77-89.

Bergstøl, S., 1979. Tinguaite dikes adjacent to the Fen alkaline complex in Telemark, Norway. Norwegian Journal of Geology, 59(2): 10.

Bergstøl, S. and Svinndal, S., 1960. The carbonatite and per-alkaline rocks of the Fen area, Norges geologiske undersøkelse.

Bingen, B., Mansfeld, J., Sigmond, E.M.O. and Stein, H., 2002. Baltica-Laurentia link during the Mesoproterozoic: 1.27 Ga development of continental basins in the Sveconorwegian Orogen, southern Norway. Canadian Journal of Earth Sciences, 39(9): 1425-1440.

Bingen, B., Nordgulen, Ø., Sigmond, E.M.O., Tucker, R., Mansfeld, J. and Högdahl, K., 2003. Relations between 1.19–1.13 Ga continental magmatism, sedimentation and metamorphism, Sveconorwegian province, S Norway. Precambrian Research, 124(2-4): 215-241.

Bingen, B., Skar, O., Marker, M., Sigmond, E.M.O., Nordgulen, O., Ragnhildstveit, J., Mansfeld, J., Tucker, R.D. and Liegeois, J.P., 2005. Timing of continental building in the Sveconorwegian orogen, SW Scandinavia. Norwegian Journal of Geology, 85(1-2): 87-116.

Bingen, B., Stein, H.J., Bogaerts, M., Bolle, O. and Mansfeld, J., 2006. Molybdenite Re–Os dating constrains gravitational collapse of the Sveconorwegian orogen, SW Scandinavia. Lithos, 87(3-4): 328-346.

Binnemans, K. and Jones, P.T., 2015. Rare Earths and the Balance Problem. Journal of Sustainable Metallurgy, 1(1): 29-38.

Binnemans, K., Jones, P.T., Blanpain, B., Van Gerven, T. and Pontikes, Y., 2015. Towards zero-waste valorisation of rare-earth-containing industrial process residues: a critical review. Journal of Cleaner Production, 99: 17-38.

BIOCHEMISTRY, 2017. FIGURE 18.4 Simplified schematic of ICP-MS instrumentation.

Bjarnason, I.Þ., 2008. An Iceland hotspot saga. JÖKULL(58): 3-16.

Bloomberg, 2015. content.icicidirect.com/mailimages/RareEarth.htm. Access Date: 21/01/2018.

Bodeving, S., Williams-Jones, A.E. and Swinden, S., 2017. Carbonate–silicate melt immiscibility, REE mineralising fluids, and the evolution of the Lofdal Intrusive Suite, Namibia. Lithos, 268-271: 383-398.

Bogdanova, S.V., Bingen, B., Gorbatschev, R., Kheraskova, T.N., Kozlov, V.I., Puchkov, V.N. and Volozh, Y.A., 2008. The East European Craton (Baltica) before and during the assembly of Rodinia. Precambrian Research, 160(1-2): 23-45.

Bogdanova, S.V., Page, L.M., Skridlaite, G. and Taran, L.N., 2001. Proterozoic tectonothermal history in the western part of the East European Craton: 40Ar/39Ar geochronological constraints. Tectonophysics, 339(1-2): 39-66.

Bokhari, S.N.H. and Meisel, T.C., 2016. Method Development and Optimisation of Sodium Peroxide Sintering for Geological Samples. Geostandards and Geoanalytical Research.

Bowen, N.L., 1924. The Fen area in Telemark, Norway. American Journal of Science, s5-8(43): 1-11.

Brassinnes, S., Balaganskaya, E. and Demaiffe, D., 2005. Magmatic evolution of the differentiated ultramafic, alkaline and carbonatite intrusion of Vuoriyarvi (Kola Peninsula, Russia). A LA-ICP-MS study of apatite. Lithos, 85(1-4): 76-92.

Brewer, T.S., Ahall, K.I., Darbyshire, D.P.F. and Menuge, J.F., 2002. Geochemistry of late Mesoproterozoic volcanism in southwestern Scandinavia: implications for Sveconorwegian/Grenvillian plate tectonic models. Journal of the Geological Society, 159(2): 129-144.

British Geological Survey, 2011. Rare Earth Elements Mineral Profile, British Geological Survey, Nottingham, United Kingdom.

British Geological Survey, 2012. Risk List 2012 - An update to the supply risk index for elements or element groups that are of economic value, pp. 12.

Brøgger, W.C., 1921. Die Eruptivgesteine des Kristianiagebietes, IV. Das Fengebiet in Telemark, Norwegen, 494 pp.

Broom-Fendley, S., Brady, A.E., Wall, F., Gunn, G. and Dawes, W., 2017a. REE minerals at the Songwe Hill carbonatite, Malawi: HREE-enrichment in late-stage apatite. Ore Geology Reviews, 81: 23-41.

Broom-Fendley, S., Styles, M.T., Appleton, J.D., Gunn, G. and Wall, F., 2016. Evidence for dissolution-reprecipitation of apatite and preferential LREE mobility in carbonatite-derived late-stage hydrothermal processes. American Mineralogist, 101(3): 596-611.

Broom-Fendley, S., Wall, F., Spiro, B. and Ullmann, C.V., 2017b. Deducing the source and composition of rare earth mineralising fluids in carbonatites: insights from isotopic (C, O, 87Sr/86Sr) data from Kangankunde, Malawi. Contributions to Mineralogy and Petrology, 172(11-12).

Bühn, B., 2001. Rare-earth element systematics of carbonatitic fluorapatites, and their significance for carbonatite magma evolution. Contributions to Mineralogy and Petrology, 141(5): 572-591.

Campbell, G.A., 2014. Rare earth metals: a strategic concern. Mineral Economics, 27(1): 21-31.

Campbell, L.S., Compston, W., Sircombe, K.N. and Wilkinson, C.C., 2014. Zircon from the East Orebody of the Bayan Obo Fe–Nb–REE deposit, China, and SHRIMP ages for carbonatite-related magmatism and REE mineralization events. Contributions to Mineralogy and Petrology, 168(2).

Chakhmouradian, A.R. and Mitchell, R.H., 1998. Lueshite, pyrochlore and monazite-(Ce) from apatite-dolomite carbonatite, Lesnaya Varaka complex, Kola Peninsula, Russia. Mineralogical Magazine, 62(6): 769-782.

Chakhmouradian, A.R., Mumin, A.H., Demény, A. and Elliott, B., 2008. Postorogenic carbonatites at Eden Lake, Trans-Hudson Orogen (northern Manitoba, Canada): Geological setting, mineralogy and geochemistry. Lithos, 103(3-4): 503-526.

Chakhmouradian, A.R., Reguir, E.P., Couëslan, C. and Yang, P., 2016. Calcite and dolomite in intrusive carbonatites. II. Trace-element variations. Mineralogy and Petrology, 110(2-3): 361-377.

Chakhmouradian, A.R., Reguir, E.P., Kressall, R.D., Crozier, J., Pisiak, L.K., Sidhu, R. and Yang, P., 2015a. Carbonatite-hosted niobium deposit at Aley, northern British Columbia (Canada): Mineralogy, geochemistry and petrogenesis. Ore Geology Reviews, 64: 642-666.

Chakhmouradian, A.R., Reguir, E.P. and Zaitsev, A.N., 2015b. Calcite and dolomite in intrusive carbonatites. I. Textural variations. Mineralogy and Petrology, 110(2-3): 333-360.

Chakhmouradian, A.R., Reguir, E.P., Zaitsev, A.N., Couëslan, C., Xu, C., Kynický, J., Mumin, A.H. and Yang, P., 2017. Apatite in carbonatitic rocks: Compositional variation, zoning, element partitioning and petrogenetic significance. Lithos, 274-275: 188-213.

Chakhmouradian, A.R. and Wall, F., 2012. Rare Earth Elements: Minerals, Mines, Magnets (and More). Elements, 8(5): 333-340.

Chakhmouradian, A.R. and Zaitsev, A.N., 2012. Rare Earth Mineralization in Igneous Rocks: Sources and Processes. Elements, 8(5): 347-353.

Chao, E.C.T., Back, J.M., Minkin, J.A., Tatsumoto, M., Junwen, W., Conrad, J.E., McKee, E.H., Zonglin, H., Qingrun, M. and Shengguang, H., 1997. Sedimentary carbonate-hosted giant Bayan Obo REE-Fe-Nb ore deposit of Inner Mongolia, China; a

cornerstone example for giant polymetallic ore deposits of hydrothermal origin. 2143.

Charalampides, G., Vatalis, K.I., Apostoplos, B. and Ploutarch-Nikolas, B., 2015. Rare Earth Elements: Industrial Applications and Economic Dependency of Europe. Procedia Economics and Finance, 24: 126-135.

Chen, W., Honghui, H., Bai, T. and Jiang, S., 2017. Geochemistry of Monazite within Carbonatite Related REE Deposits. Resources, 6(4): 51.

Cheng, Z., Zhang, Z., Aibai, A., Kong, W. and Holtz, F., 2018. The role of magmatic and post-magmatic hydrothermal processes on rare-earth element mineralization: A study of the Bachu carbonatites from the Tarim Large Igneous Province, NW China. Lithos, 314-315: 71-87.

Cherniak, D.J., Watson, E.B., Grove, M. and Harrison, T.M., 2004. Pb diffusion in monazite: a combined RBS/SIMS study. Geochimica et Cosmochimica Acta, 68(4): 829-840.

Claverie, A. and Mouis, M., 2012.

Condie, K.C., 2016. Earth as an Evolving Planetary System. Elsevier.

Cook, N.J., Ciobanu, C.L., O'Rielly, D., Wilson, R., Das, K. and Wade, B., 2013. Mineral chemistry of Rare Earth Element (REE) mineralization, Browns Ranges, Western Australia. Lithos, 172-173: 192-213.

Cordeiro, P.F.O., Brod, J.A., Dantas, E.L. and Barbosa, E.S.R., 2010. Mineral chemistry, isotope geochemistry and petrogenesis of niobium-rich rocks from the Catalão I carbonatite-phoscorite complex, Central Brazil. Lithos, 118(3-4): 223-237.

Couture, A.R., 2000. CASINO - Software.

Cullers, R.L. and Graf, J.L., 1984. Rare earth elements in igneous rocks of the continental crust: predominantly basic and ultrbasic rocks. In: P. Henderson (Editor), Developments in Geochemistry, Vol. 2: Rare earth element geochemistry. Elsevier, Amsterdam, pp. 237-274.

Dahlgren, S., 1994. Late proterozoic and Carboniferous ultramafic magmatism of carbonatitic affinity in southern Norway. Lithos, 31(3-4): 141-154.

Dahlgren, S., 2004. Nordagutu, bedrock geology map 1713 IV, scale 1: 50,000. Nor. Geol. Unders.

Dalou, C., Koga, K.T., Hammouda, T. and Poitrasson, F., 2009. Trace element partitioning between carbonatitic melts and mantle transition zone minerals: Implications for the source of carbonatites. Geochimica et Cosmochimica Acta, 73(1): 239-255.

Dalstra, H. and Guedes, S., 2004. GIANT HYDROTHERMAL HEMATITE DEPOSITS WITH Mg-Fe METASOMATISM: A COMPARISON OF THE CARAJAS, HAMERSLEY, AND OTHER IRON ORES. Economic Geology, 99(8): 1793-1800.

Dalton, J.A. and Presnall, D.C., 1998. The Continuum of Primary Carbonatitic-Kimberlitic Melt Compositions in Equilibrium with Lherzolite: Data from the System CaO-MgO-Al2O3-SiO2-CO2 at 6 GPa. Journal of Petrology, 39(11-12): 1953-1964.

Daly, R.A., 1914. Igneous Rocks and Their Origin. McGraw-Hill.

Dawson, J.B., 1962. The geology of Oldoinyo Lengai. Bulletin Volcanologique, 24(1): 349-387.

Dawson, J.B., Garson, M.S. and Roberts, B., 1987. Altered former alkalic carbonatite lava from Oldoinyo Lengai, Tanzania: Inferences for calcite carbonatite lavas. Geology, 15(8): 765.

Deady, E., Richard, S. and Goodenough, K.M., 2017. Research and development for the Rare Earth Element supply chain in Europe., EUrare.

DERA, 2017. DERA-Rohstoffiste 2016. In: D.R.i.d.B.f.G.u. Rohstoffe (Editor), Berlin, pp. 116.

Dobson, D.P., Jones, A.P., Rabe, R., Sekine, T., Kurita, K., Taniguchi, T., Kondo, T., Kato, T., Shimomura, O. and Urakawa, S., 1996. In-situ measurement of viscosity and density of carbonate melts at high pressure. Earth and Planetary Science Letters, 143(1-4): 207-215.

Dowman, E., Wall, F., Treloar, P.J. and Rankin, A.H., 2018. Rare-earth mobility as a result of multiple phases of fluid activity in fenite around the Chilwa Island Carbonatite, Malawi. Mineralogical Magazine, 81(06): 1367-1395.

Drew, L.J., Qingrun, M. and Weijun, S., 1990. The Bayan Obo iron-rare-earth-niobium deposits, Inner Mongolia, China. Lithos, 26(1-2): 43-65.

Duraiswami, R. and Shaikh, T., 2014. Fluid-rock interaction in the Kangankunde Carbonatite Complex, Malawi: SEM based evidence for late stage pervasive hydrothermal mineralisation. Open Geosciences, 6(4).

Ebbing, J., Afework, Y., Olesen, O. and Nordgulen, Ø., 2005. Is there evidence for magmatic underplating beneath the Oslo Rift? Terra Nova, 17(2): 129-134.

Eldholm, O., Thiede, J. and Taylor, E., 1989. Evolution of the Vøring Volcanic Margin. 104.

Elliott, H.A.L., Wall, F., Chakhmouradian, A.R., Siegfried, P.R., Dahlgren, S., Weatherley, S., Finch, A.A., Marks, M.A.W., Dowman, E. and Deady, E., 2018. Fenites associated with carbonatite complexes: A review. Ore Geology Reviews, 93: 38-59.

Ernst, R.E. and Bell, K., 2009. Large igneous provinces (LIPs) and carbonatites. Mineralogy and Petrology, 98(1-4): 55-76.

European Commission, 2014. Report on critical raw materials for the EU. Report of the Ad-hoc Working Group on Defining Critical Raw Materials, pp. 41.

European Commission, 2016. Assessment of potential bottlenecks along the materials supply chain for the future deployment of low-carbon energy and transport technologies in the EU. In: J.S.f.P. Report (Editor), pp. 196.

European Commission, 2017. Study on the review of the list of Critical Raw Materials, pp. 93.

Eurostat, 2018. eurostat Statitics explained - Hourly labour costs. https://ec.europa.eu/eurostat/statistics-explained/index.php?title=Hourly labour costs#Hourly labour costs ranged between EUR.C2.A05.4 and 43.5 in 2018, accessed 03. May 2019.

Evans, E.H. and Giglio, J.J., 1993. Interferences in inductively coupled plasma mass spectrometry. A review. Journal of Analytical Atomic Spectrometry, 8(1): 1.

Fan, H.-R., Yang, K.-F., Hu, F.-F., Liu, S. and Wang, K.-Y., 2016. The giant Bayan Obo REE-Nb-Fe deposit, China: Controversy and ore genesis. Geoscience Frontiers, 7(3): 335-344.

Faul, H., Elmore, P.L.D. and Brannock, W.W., 1959. Age of the Fen carbonatite (Norway) and its relation to the intrusives of the Oslo region. . Geochimica et Cosmochimica Acta, 17: 153-156.

Feng, M., Xu, C., Kynicky, J., Zeng, L. and Song, W., 2016. Rare earth element enrichment in Palaeoproterozoic Fengzhen carbonatite from the North China block. International Geology Review, 58(15): 1940-1950.

Fowler, J.W., Alpert, B.K., Bennett, D.A., Doriese, W.B., Gard, J.D., Hilton, G.C., Hudson, L.T., Joe, Y.I., Morgan, K.M., O'Neil, G.C., Reintsema, C.D., Schmidt, D.R., Swetz, D.S., Szabo, C.I. and Ullom, J.N., 2017. A reassessment of absolute energies of the x-ray L lines of lanthanide metals. Metrologia, 54(4): 494-511.

Fraunhofer IMWS, 2018. Substitution, Effizienz, Recycling: Ergebnisse des Leitprojekts »Kritikalität Seltener Erden«.

Fredrich, J.T., Evans, B. and Wong, T.-F., 1989. Micromechanics of the brittle to plastic transition in Carrara marble. Journal of Geophysical Research: Solid Earth, 94(B4): 4129-4145.

Freestone, I.C., 1989. Liquid immiscibility. 281-283.

Friedrichsen, H., 1968. Sauerstoffisotopen einiger minerale der Karbonatite des Fengebietes. Süd Norwegen. Lithos, 1(1): 70-75.

Friel, J.J. and Lyman, C.E., 2006. Tutorial Review: X-ray Mapping in Electron-Beam Instruments. Microscopy and Microanalysis, 12(01): 2-25.

Gea Norvegica Geopark, 2018. Simplified geological map of Vestfold and Telemark.

Gee, D.G., Fossen, H., Henriksen, N. and Higgins, A.K., 2008. From the early Paleozoic platforms of Baltica and Laurentia to the Caledonide Orogen of Scandinavia and Greenland. Episodes, 31(1): 44-51.

Giebel, R.J., Gauert, C.D.K., Marks, M.A.W., Costin, G. and Markl, G., 2017. Multi-stage formation of REE minerals in the Palabora Carbonatite Complex, South Africa. American Mineralogist, 102(6): 1218-1233.

Gittins, J., 1989. The origin and evolution of carbonatite magmas. In: K. Bell (Editor), Carbonatites. Genesis and Evolution. Unwin Hyman, London, pp. 580–599.

Gittins, J. and Harmer, R.E., 2003. Myth and reality in the carbonatite - silicate rock "association". PERIODICO di MINERALOGIA, 72: 19-26.

Gittins, J., Harmer, R.E. and Barker, D.S., 2005. The bimodal composition of carbonatites: Reality or misconception? Lithos, 85(1-4): 129-139.

Goldstein, J.I., Newbury, D.E., Echlin, P., Joy, D.C., Lyman, C.E., Lifshin, E., Sawyer, L. and Michael, J.R., 2003. Scanning Electron Microscopy and X-Ray Microanalysis. Springer US.

Goodenough, K.M., Deady, E., Wall, F., Shaw, R.A. and Lusty, P., 2014. THE IMPORTANCE OF TECTONIC SETTING IN ASSESSING EUROPEAN RARE EARTH POTENTIAL, ERES2014: 1st European Rare Earth Resources Conference, Milos.

Goodenough, K.M., Schilling, J., Jonsson, E., Kalvig, P., Charles, N., Tuduri, J., Deady, E.A., Sadeghi, M., Schiellerup, H., Müller, A., Bertrand, G., Arvanitidis, N., Eliopoulos, D.G., Shaw, R.A., Thrane, K. and Keulen, N., 2016. Europe's rare earth element resource potential: An overview of REE metallogenetic provinces and their geodynamic setting. Ore Geology Reviews, 72: 838-856.

Goodenough, K.M., Wall, F. and Merriman, D., 2017. The Rare Earth Elements: Demand, Global Resources, and Challenges for Resourcing Future Generations. Natural Resources Research, 27(2): 201-216.

Gregg, J.M., Bish, D.L., Kaczmarek, S.E., Machel, H.G. and Hollis, C., 2015. Mineralogy, nucleation and growth of dolomite in the laboratory and sedimentary environment: A review. Sedimentology, 62(6): 1749-1769.

Griffin, W.L., 1973. Lherzolite nodules from the Fen alkaline complex, Norway. Contributions to Mineralogy and Petrology, 38(2): 135-146.

Griffin, W.L., O'Reilly, S.Y., Abe, N., Aulbach, S., Davies, R.M., Pearson, N.J., Doyle, B.J. and Kivi, K., 2003. The origin and evolution of Archean lithospheric mantle. Precambrian Research, 127(1-3): 19-41.

Griffin, W.L. and Taylor, P.N., 1975. The Fen Damkjernite: Petrology of a "central-complex kimberlite". Physics and Chemistry of the Earth, 9: 163-177.

Groves, D.I. and Vielreicher, N.M., 2001. The Phalabowra (Palabora) carbonatite-hosted magnetite-copper sulfide deposit, South Africa: an end-member of the iron-oxide copper-gold-rare earth element deposit group? Mineralium Deposita, 36(2): 189-194.

Guzmics, T., Zajacz, Z., Kodolányi, J., Halter, W. and Szabó, C., 2008. LA-ICP-MS study of apatite- and K feldspar-hosted primary carbonatite melt inclusions in clinopyroxenite xenoliths from lamprophyres, Hungary: Implications for significance of carbonatite melts in the Earth's mantle. Geochimica et Cosmochimica Acta, 72(7): 1864-1886.

Haggerty, S.E. and Fung, A., 2006. Orbicular oxides in carbonatitic kimberlites. American Mineralogist, 91(10): 1461-1472.

Halpin, K.M., 2010. The characteristics and origin of the Hoidas Lake REE deposit. University of Saskatchewan, Saskatoon, Canada, pp. 173.

Hamilton, D.L., Freestone, I.C., Dawson, J.B. and Donaldson, C.H., 1979. Origin of carbonatites by liquid immiscibility. Nature, 279: 52-54.

Hammouda, T., Chantel, J. and Devidal, J.-L., 2010. Apatite solubility in carbonatitic liquids and trace element partitioning between apatite and carbonatite at high pressure. Geochimica et Cosmochimica Acta, 74(24): 7220-7235.

Hammouda, T., Moine, B.N., Devidal, J.L. and Vincent, C., 2009. Trace element partitioning during partial melting of carbonated eclogites. Physics of the Earth and Planetary Interiors, 174(1-4): 60-69.

Harlov, D.E. and Förster, H.-J., 2004. Fluid-induced nucleation of (Y+REE)-phosphate minerals within apatite: Nature and experiment. Part II. Fluorapatite. American Mineralogist, 88(8-9): 1209-1229.

Harlov, D.E., Wirth, R. and Förster, H.-J., 2005. An experimental study of dissolution–reprecipitation in fluorapatite: fluid infiltration and the formation of monazite. Contributions to Mineralogy and Petrology, 150(3): 268-286.

Hatch, G.P., 2012. Dynamics in the Global Market for Rare Earths. Elements, 8(5): 341-346.

Hatert, F. and Burke, E.A.J., 2008. The Ima-Cnmnc Dominant-Constituent Rule Revisited and Extended. The Canadian Mineralogist, 46(3): 717-728.

Heincke, B.H., Smethurst, M.A., Bjørlykke, A., Dahlgren, S., Rønning, J.S. and Mogaard, J.O., 2008. Airborne gamma-ray spectrometer mapping for relating indoor radon

concentrations to geological parameters in the Fen region, southeastNorway. In: T. Slagstad (Editor), Geology for Society, Geological Survey of NorwaySpecial Publication, pp. 131-143.

Henderson, I.H.C. and Ihlen, P.M., 2004. Emplacement of polygeneration pegmatites in relation to Sveco-Norwegian contractional tectonics: examples from southern Norway. Precambrian Research, 133(3-4): 207-222.

Henderson, P., 1996. The rare earth elements: introduction and review. In: A.P. Jones, F. Wall and C.T. Williams (Editors), Rare Earth Minerals, Chemistry, origin and ore deposits. The Mineralogical Society Series. Chapman & Hall, London.

Hogarth, D.D., 1989. Pyrochlore, Apatite and Amphibole: Distinctive Minerals in Carbonatite. In: K. Bell (Editor), Carbonatites. Genesis and Evolution. Unwin Hyman, London, pp. 105–148.

Högbom, A.G., 1895. Über das Nephelinsyenitgebiet auf der Insel Alnö. Geologiska Föreningen i Stockholm Förhandlingar, 17(2): 100-158.

Hornig-Kjarsgaard, I., 1998. Rare Earth Elements in Sovitic Carbonatites and their Mineral Phases. Journal of Petrology, 39(11-12): 2105-2121.

Humphreys, E.R. and Niu, Y., 2009. On the composition of ocean island basalts (OIB): The effects of lithospheric thickness variation and mantle metasomatism. Lithos, 112(1-2): 118-136.

Humphris, S.E., 1984. The Mobility of the Rare Earth Elements in the Crust. 2: 317-342.

Ihlen, P.M., Schiellerup, H., Gautneb, H. and Skår, Ø., 2014. Characterization of apatite resources in Norway and their REE potential — A review. Ore Geology Reviews, 58: 126-147.

Ionov, D. and Harmer, R.E., 2002. Trace element distribution in calcite–dolomite carbonatites from Spitskop: inferences for differentiation of carbonatite magmas and the origin of carbonates in mantle xenoliths. Earth and Planetary Science Letters, 198(3-4): 495-510.

Johansson, Å., Bogdanova, S. and Čečys, A., 2006. A revised geochronology for the Blekinge Province, southern Sweden. GFF, 128(4): 287-302.

Jones, A.P., Genge, M. and Carmody, L., 2013. Carbonate Melts and Carbonatites. Reviews in Mineralogy and Geochemistry, 75(1): 289-322.

Jordens, A., Cheng, Y.P. and Waters, K.E., 2013. A review of the beneficiation of rare earth element bearing minerals. Minerals Engineering, 41: 97-114.

Joy, D.C., 1991. The theory and practice of high-resolution scanning electron microscopy. Ultramicroscopy, 37(1-4): 216-233.

Kanazawa, Y. and Kamitani, M., 2006. Rare earth minerals and resources in the world. Journal of Alloys and Compounds, 408-412: 1339-1343.

Karlstrom, K.E., Åhäll, K.-I., Harlan, S.S., Williams, M.L., McLelland, J. and Geissman, J.W., 2001. Long-lived (1.8–1.0 Ga) convergent orogen in southern Laurentia, its extensions to Australia and Baltica, and implications for refining Rodinia. Precambrian Research, 111(1-4): 5-30.

Kim, E.-J., Shin, D., Shin, S., Nam, H.-T. and Park, S., 2015. Skarn zonation and rock physical properties of the Wondong Fe-Pb-Zn polymetallic deposit, Korea. Geosciences Journal, 19(4): 587-598.

Klauber, C., Gräfe, M. and Power, G., 2011. Bauxite residue issues: II. options for residue utilization. Hydrometallurgy, 108(1-2): 11-32.

Klemme, S. and Dalpé, C., 2003. Trace-element partitioning between apatite and carbonatite melt. American Mineralogist, 88(4): 639-646.

Kogarko, L.N., Williams, C.T. and Woolley, A.R., 2002. Chemical evolution and petrogenetic implications of loparite in the layered, agpaitic Lovozero complex, Kola Peninsula, Russia. Mineralogy and Petrology, 74(1): 1-24.

Kono, Y., Kenney-Benson, C., Hummer, D., Ohfuji, H., Park, C., Shen, G., Wang, Y., Kavner, A. and Manning, C.E., 2014. Ultralow viscosity of carbonate melts at high pressures. Nature Communications, 5: 5091.

Krasnova, N., Petrov, T.G., Balaganskaya, E.G., Garcia, D., Moutte, J., Zaitsev, A.N. and Wall, F., 2004. Introduction to phoscorites : occurence, composition, nomenclature and petrogenesis. In: B. The Mineralogical Society of Great and Ireland (Editors), Phoscorites and Carbonatites from Mantle to Mine: the Key Example of the Kola Alkaline Province.

Kravchenko, S.M. and Pokrovsky, B.G., 1995. The Tomtor alkaline ultrabasic massif and related REE-Nb deposits, northern Siberia. Economic Geology, 90(3): 676-689.

Kresten, P. and Morogan, V., 1986. Fenitization at the Fen complex, southern Norway. Lithos, 19(1): 27-42.

Krneta, S., Ciobanu, C.L., Cook, N.J., Ehrig, K. and Kontonikas-Charos, A., 2017a. Rare Earth Element Behaviour in Apatite from the Olympic Dam Cu–U–Au–Ag Deposit, South Australia. Minerals, 7(8): 135.

Krneta, S., Cook, N.J., Ciobanu, C.L., Ehrig, K. and Kontonikas-Charos, A., 2017b. The Wirrda Well and Acropolis prospects, Gawler Craton, South Australia: Insights into evolving fluid conditions through apatite chemistry. Journal of Geochemical Exploration, 181: 276-291.

Lahtinen, R., Korja, A. and Nironen, M., 2005. Chapter 11 Paleoproterozoic tectonic evolution. 14: 481-531.

Langmuir, D., 1997. Aqueous Environmental Geochemistry. Prentice Hall, New Jersey.

Larsen, B.T., Olaussen, S., Sundvoll, B. and Heeremans, M., 2008. The Permo-Carboniferous Oslo Rift through Six Stages and 65 Million Years. Episodes, 31(1): 52-58.

Laznicka, P., 1999. Quantitative relationships among giant deposits of metals. Economic Geology, 94(4): 455-473.

Le Bas, M.J., 1989. Diversification of carbonatite. In: K. Bell (Editor), Carbonatites. Genesis and Evolution. Unwin Hyman, London, pp. 428–432.

Le Bas, M.J., 2008. Fenites Associated with Carbonatites. The Canadian Mineralogist, 46(4): 915-932.

Le Maitre, R.W., Streckeisen, A., Zanettin, B., Le Bas, M.J., Bonin, B. and Bateman, P., 2002. Igneous Rocks. A Classification and Glossary of Terms. Recommendations of the International Union of Geological Sciences Subcommission on the Systematics of Igneous Rocks. Cambridge University Press.

Lee, W.J. and Wyllie, P.J., 1998. Processes of Crustal Carbonatite Formation by Liquid Immiscibility and Differentiation, Elucidated by Model Systems. Journal of Petrology, 39(11-12): 2005-2013.

Liao, Y., 2018 Practical Electron Microscopy and Database.

Liu, W., Etschmann, B., Migdisov, A., Boukhalfa, H., Testemale, D., Müller, H., Hazemann, J.-L. and Brugger, J., 2017. Revisiting the hydrothermal geochemistry of

europium(II/III) in light of new in-situ XAS spectroscopy results. Chemical Geology, 459: 61-74.

Long, K.R., Van Gosen, B.S., Foley, N.K. and Cordier, D., 2010. The principal rare earth elements deposits of the United States—A summary of domestic deposits and a global perspective: U.S. Geological Survey Scientific Investigations Report 2010–5220. 96.

Lottermoser, B.G., 1990. Rare-earth element mineralisation within the Mt. Weld carbonatite laterite, Western Australia. Lithos, 24(2): 151-167.

Louvel, M., Bordage, A., Testemale, D., Zhou, L. and Mavrogenes, J., 2015. Hydrothermal controls on the genesis of REE deposits: Insights from an in situ XAS study of Yb solubility and speciation in high temperature fluids (T<400°C). Chemical Geology, 417: 228-237.

Lynas Corporation Ltd., 2007. Lynas acquires new rare earths resource in Malawi: Press release dated September 6, 2007.

Machacek, E. and Kalvig, P., 2016. Assessing advanced rare earth element-bearing deposits for industrial demand in the EU. Resources Policy, 49: 186-203.

Maravic, H.v. and Morteani, G., 1980. Petrology and geochemistry of the carbonatite and syenite complex of Lueshe (N.E. Zaire). Lithos, 13(2): 159-170.

Mariano, A., 1989. Nature of economic mineralization in carbonatites and related rocks. In: D.R. Bell (Editor), Carbonatites: genesis and evolution. Unwin Hyman Ltd., London, pp. 27.

Marien, C., 2014. Mineralogische Charakterisierung von Karbonatitproben aus der Bohrung WisBAW 768/78 des Ultramafit-Karbonatit-Komplexes Delitzsch, Martin-Luther-Universität Halle-Wittenberg, 119 pp.

Marien, C., Dijkstra, A. and Wilkins, C., 2016a. REE mobility during the alteration of Carbonatite and their economic potential, EGU, Vienna.

Marien, C., Dijkstra, A. and Wilkins, C., 2016b. Rødbergite – a potential source for REE within the Fen Complex, Norway., 2nd European Mineralogical Conference, Rimini.

Marien, C., Dijkstra, A.H. and Wilkins, C., 2018. The hydrothermal alteration of carbonatite in the Fen Complex, Norway: mineralogy, geochemistry, and implications for rare-earth element resource formation. Mineralogical Magazine, 82(S1): S115-S131.

Marks, M.A.W., Hettmann, K., Schilling, J., Frost, B.R. and Markl, G., 2011. The Mineralogical Diversity of Alkaline Igneous Rocks: Critical Factors for the Transition from Miaskitic to Agpaitic Phase Assemblages. Journal of Petrology, 52(3): 439-455.

McDonough, W.F. and Sun, S.-S., 1995. The composition of the Earth. Chemical Geology, 120(3-4): 223–253.

McMenamin, M.A. and McMenamin, D.L.S., 1990. The emergence of animals : the Cambrian breakthrough. Columbia University Press, New York, x, 217 p. pp.

Meert, Joseph G., Torsvik, Trond H., Eide, Elizabeth A. and Dahlgren, S., 1998. Tectonic Significance of the Fen Province, S. Norway: Constraints From Geochronology and Paleomagnetism. The Journal of Geology, 106(5): 553-564.

Meija, J. and Caruso, J.A., 2004. Deconvolution of isobaric interferences in mass spectra. Journal of the American Society for Mass Spectrometry, 15(5): 654-658.

Menzies, M. and Murthy, V.R., 1980. Mantle metasomatism as a precursor to the genesis of alkaline magmas-isotopic evidence. Am. J. Sci, 280: 622-638.

Michaut, C., Jaupart, C. and Mareschal, J.-C., 2009. Thermal evolution of cratonic roots. Lithos, 109(1-2): 47-60.

Migdisov, A.A. and Williams-Jones, A.E., 2014. Hydrothermal transport and deposition of the rare earth elements by fluorine-bearing aqueous liquids. Mineralium Deposita, 49(8): 987-997.

Migdisov, A.A., Williams-Jones, A.E. and Wagner, T., 2009. An experimental study of the solubility and speciation of the Rare Earth Elements (III) in fluoride- and chloride-bearing aqueous solutions at temperatures up to 300°C. Geochimica et Cosmochimica Acta, 73(23): 7087-7109.

Mitchell, R.H., 2005. Carbonatites and Carbonatites and Carbonatites. The Canadian Mineralogist, 43(6): 2049-2068.

Mitchell, R.H. and Brunfelt, A.O., 1974. Scandium, cobalt and iron geochemistry of the Fen alkaline complex, southern Norway. Earth and Planetary Science Letters, 23(2): 189-192.

Mitchell, R.H. and Brunfelt, A.O., 1975. Rare earth element geochemistry of the Fen alkaline complex, Norway. Contributions to Mineralogy and Petrology, 52(4): 247-259.

Mitchell, R.H. and Crocket, J.H., 1972. Isotopic Composition of Strontium in Rocks of the Fen Alkaline Complex, South Norway. Journal of Petrology, 13(1): 83-97.

Mitchell, R.H. and Kjarsgaard, B.A., 2010. Experimental Studies of the System Na2CO3-CaCO3-MgF2 at 0{middle dot}1 GPa: Implications for the Differentiation and Low-temperature Crystallization of Natrocarbonatite. Journal of Petrology, 52(7-8): 1265-1280.

Moine, B.N., Grégoire, M., O'Reilly, S.Y., Delpech, G., Sheppard, S.M.F., Lorand, J.P., Renac, C., Giret, A. and Cottin, J.Y., 2004. Carbonatite melt in oceanic upper mantle beneath the Kerguelen Archipelago. Lithos, 75(1-2): 239-252.

Moldoveanu, G.A. and Papangelakis, V.G., 2012. Recovery of rare earth elements adsorbed on clay minerals: I. Desorption mechanism. Hydrometallurgy, 117-118: 71-78.

Moldoveanu, G.A. and Papangelakis, V.G., 2016. An overview of rare-earth recovery by ion-exchange leaching from ion-adsorption clays of various origins. Mineralogical Magazine, 80(01): 63-76.

Montero Mining & Exploration Ltd., 2018. Wigu Hill, Tanzania.

Moore, M., Chakhmouradian, A.R., Mariano, A.N. and Sidhu, R., 2015. Evolution of rare-earth mineralization in the Bear Lodge carbonatite, Wyoming: Mineralogical and isotopic evidence. Ore Geology Reviews, 64: 499-521.

Mörner, N.-A., 1977. Past and present uplift in Sweden: Glacial isostasy, tectonism and bedrock influence. Geologiska Föreningen i Stockholm Förhandlingar, 99(1): 48-54.

Mosar, J., Lewis, G. and Torsvik, T., 2002. North Atlantic sea-floor spreading rates: implications for the Tertiary development of inversion structures of the Norwegian–Greenland Sea. Journal of the Geological Society, 159(5): 503-515.

Nelson, D.R., Chivas, A.R., Chappell, B.W. and McCulloch, M.T., 1988. Geochemical and isotopic systematics in carbonatites and implications for the evolution of ocean-island sources. Geochimica et Cosmochimica Acta, 52(1): 1-17.

Neumann, E.-R., Wilson, M., Heeremans, M., Spencer, E.A., Obst, K., Timmerman, M.J. and Kirstein, L., 2004. Carboniferous-Permian rifting and magmatism in southern Scandinavia, the North Sea and northern Germany: a review. Geological Society, London, Special Publications, 223(1): 11-40.

NGU, 2017. Simplified Geological Map of Scandinavia.

Nickel, E.H., 1992. Solid solutions in mineral nomenclature. The Canadian Mineralogist, 30: 231-234.

Onuonga, I.O., Fallick, A.E. and Bowden, P., 1997. The recognition of meteoric-hydrothermal and supergene processes in volcanic carbonatites, Nyanza Rift, western Kenya, using carbon and oxygen isotopes. Journal of African Earth Sciences, 25(1): 103-113.

Orris, G. and Grauch, R.I., 2002. Rare Earth Element Mines, Deposits, and Occurrences. USGS.

Owens, C.L., Nash, G.R., Hadler, K., Fitzpatrick, R.S., Anderson, C.G. and Wall, F., 2018. Zeta potentials of the rare earth element fluorcarbonate minerals focusing on bastnäsite and parisite. Advances in Colloid and Interface Science, 256: 152-162.

Pan, Y. and Fleet, M.E., 1995. Site preference of rare earth elements in fluorapatite. American Mineralogist, 80: 329-335.

Pan, Y. and Fleet, M.E., 2002. Composition of the Apatite-Group Minerals: Substitution Mechanisms and Controlling Factors. In: M.J. Kohn, J.F. Rakovan and J.M. Hughes

(Editors), Phosphates. Geochemical, geobiological, and materials importance. Mineralogical Society of America (Reviews in mineralogy and geochemistry, v. 48), Washington DC, pp. 13–49.

Pandur, K., Ansdell, K.M., Kontak, D.J., Halpin, K.M. and Creighton, S., 2016. Petrographic and Mineral Chemical Characteristics of the Hoidas Lake Deposit, Northern Saskatchewan, Canada: Constraints on the Origin of a Distal Magmatic-Hydrothermal REE System. Economic Geology, 111(3): 667-694.

Parthemore, C., 2011. Elements of Security: Mitigating the Risks of U.S. Dependence on Critical Minerals. In: C.f.a.N.A. Security (Editor), Washington DC.

Pease, V., Daly, J.S., Elming, S.Å., Kumpulainen, R., Moczydlowska, M., Puchkov, V., Roberts, D., Saintot, A. and Stephenson, R., 2008. Baltica in the Cryogenian, 850–630Ma. Precambrian Research, 160(1-2): 46-65.

Petibon, C.M., Kjarsgaard, B.A., Jenner, G.A. and Jackson, S.E., 1998. Phase Relationships of a Silicate-bearing Natrocarbonatite from Oldoinyo Lengai at 20 and 100 MPa. Journal of Petrology, 39(11-12): 2137-2151.

Pilet, S., Baker, M.B. and Stolper, E.M., 2008. Metasomatized Lithosphere and the Origin of Alkaline Lavas. Science, 320(5878): 916-919.

Pirajno, F., González-Álvarez, I., Chen, W., Kyser, K.T., Simonetti, A., Leduc, E. and leGras, M., 2014. The Gifford Creek Ferrocarbonatite Complex, Gascoyne Province, Western Australia: Associated fenitic alteration and a putative link with the ~1075Ma Warakurna LIP. Lithos, 202-203: 100-119.

Poorter, R.P.E., 1972. PRELIMINARY PALAEOMAGNETIC RESULTS FROM THE FEN CARBONATITE COMPLEX, S. NORWAY. Earth and Planetary Science Letters, 17: 194-198.

Potter, N.J., Kamenetsky, V.S., Simonetti, A. and Goemann, K., 2017. Different types of liquid immiscibility in carbonatite magmas: A case study of the Oldoinyo Lengai 1993 lava and melt inclusions. Chemical Geology, 455: 376-384.

Prokopyev, I.R., Doroshkevich, A.G., Ponomarchuk, A.V. and Sergeev, S.A., 2017. Mineralogy, age and genesis of apatite-dolomite ores at the Seligdar apatite deposit (Central Aldan, Russia). Ore Geology Reviews, 81: 296-308.

Ramberg, I.B., 1973. Gravity studies of the Fen complex, Norway, and their petrological significance. Contributions to Mineralogy and Petrology, 38(2): 115-134.

Rasmussen, B. and Muhling, J.R., 2007. Monazite begets monazite: evidence for dissolution of detrital monazite and reprecipitation of syntectonic monazite during low-grade regional metamorphism. Contributions to Mineralogy and Petrology, 154(6): 675-689.

Reeder, R.J. and Dollase, W.A., 1989. Structural variation in the dolomite-ankerite solid-solution series: An X-ray, Miissbauer, and TEM study. American Mineralogist, 74: 1159-1167.

Rodionov, N.V., Belyatsky, B.V., Antonov, A.V., Kapitonov, I.N. and Sergeev, S.A., 2012. Comparative in-situ U–Th–Pb geochronology and trace element composition of baddeleyite and low-U zircon from carbonatites of the Palaeozoic Kovdor alkaline–ultramafic complex, Kola Peninsula, Russia. Gondwana Research, 21(4): 728-744.

Rollinson, H.R., 1993. using geochemical data: evaluation, presentation, interpretation Prentice Hall.

Roskill, 2016. Rare earths: Global industry, markets and outlook, Roskill, London, UK.

Ruberti, E., Enrich, G.E.R., Gomes, C.B. and Comin-Chiaramonti, P., 2008. Hydrothermal Ree Fluorocarbonate Mineralization at Barra Do Itapirapua, a Multiple Stockwork Carbonatite, Southern Brazil. The Canadian Mineralogist, 46(4): 901-914.

Rubie, D.C. and Gunter, W.D., 1983. The role of speciation in alkaline igneous fluids during fenite metasomatism. Contributions to Mineralogy and Petrology, 82(2-3): 165-175.

Rudnick, R.L. and Gao, S., 2003. Composition of the Continental Crust. Treatise on Geochemistry, 3: 1-64.

Ryabchikov, I.D. and Hamilton, D.L., 1993. Interaction of carbonate-phosphate melts with mantle peridotites at 20-35 kbar. S.Afr.J.GeoI., 96(3): 143-148.

Sæther, E., 1957. The alkaline rock province of the Fen area in southern Norway, 1. Videnskapselsk, Trondheim, 148 pp.

Salvi, S. and Williams-Jones, A.E., 1996. The role of hydrothermal processes in concentrating high-field strength elements in the Strange Lake peralkaline complex, northeastern Canada. Geochimica et Cosmochimica Acta, 60(11): 1917-1932.

Schiellerup, H., Ihlen, P.M., Dahlgren, S., Müller, A. and Schilling, J., 2017. REE OCCURRENCES IN NORWAY, WITH SPECIAL EMPHASIS ON MINERALIZATIONS HOSTED BY APATITE-RICH INTRUSIONS, ERES 2017, Santorini, Greece.

Schilling, J., 2013. Petrography, mineralogy and whole-rock data of the major litholgies of the Fen Complex, Geological Survey of Norway.

Secher, K., Heaman, L.M., Nielsen, T.F.D., Jensen, S.M., Schjøth, F. and Creaser, R.A., 2009. Timing of kimberlite, carbonatite, and ultramafic lamprophyre emplacement in the alkaline province located 64°–67° N in southern West Greenland. Lithos, 112: 400-406.

Secher, K. and Larsen, L.M., 1980. Geology and mineralogy of the Sarfartôq carbonatite complex, southern West Greenland. Lithos, 13(2): 199-212.

Shannon, R.D., 1976. Revised effective ionic radii and systematic studies of interatomic distances in halides and chalcogenides. Acta Crystallographica Section A, 32(5): 751-767.

Sharygin, V.V., Kamenetsky, V.S., Zaitsev, A.N. and Kamenetsky, M.B., 2012. Silicate–natrocarbonatite liquid immiscibility in 1917 eruption combeite–wollastonite nephelinite, Oldoinyo Lengai Volcano, Tanzania: Melt inclusion study. Lithos, 152: 23-39.

Sievers, H. and Tercero, E.L., 2012. European dependence on and concentration tendencies of the material production POLINARES working paper, 14.

Simonetti, A., Goldstein, S.L., Schmidberger, S.S. and Viladkar, S.G., 1998. Geochemical and Nd, Pb, and Sr Isotope Data from Deccan Alkaline Complexes--Inferences for Mantle Sources and Plume-Lithosphere Interaction. Journal of Petrology, 39(11-12): 1847-1864.

Slabunov, A.I., Lobach-Zhuchenko, S.B., Bibikova, E.V., Sorjonen-Ward, P., Balangansky, V.V., Volodichev, O.I., Shchipansky, A.A., Svetov, S.A., Chekulaev, V.P., Arestova, N.A. and Stepanov, V.S., 2006. The Archaean nucleus of the Fennoscandian (Baltic) Shield. Geological Society, London, Memoirs, 32(1): 627-644.

Smith, F.H. and Adams, L.H., 1923. The system calcium oxide-carbon dioxide. Journal of the American Chemical Society, 45: 1167-1184.

Smith, M., Kynicky, J., Xu, C., Song, W., Spratt, J., Jeffries, T., Brtnicky, M., Kopriva, A. and Cangelosi, D., 2018. The origin of secondary heavy rare earth element enrichment in carbonatites: Constraints from the evolution of the Huanglongpu district, China. Lithos, 308-309: 65-82.

Smith, M.P., Campbell, L.S. and Kynicky, J., 2015. A review of the genesis of the world class Bayan Obo Fe–REE–Nb deposits, Inner Mongolia, China: Multistage processes and outstanding questions. Ore Geology Reviews, 64: 459-476.

Smith, M.P., Henderson, P. and Peishan, Z., 1999. Reaction relationships in the Bayan Obo Fe-REE-Nb deposit Inner Mongolia, China: implications for the relative stability of rare-earth element phosphates and fluorocarbonates. Contributions to Mineralogy and Petrology, 134(2-3): 294-310.

Smith, M.P., Moore, K., Kavecsánszki, D., Finch, A.A., Kynicky, J. and Wall, F., 2016. From mantle to critical zone: A review of large and giant sized deposits of the rare earth elements. Geoscience Frontiers, 7(3): 315-334.

Starmer, I.C., 1993. The Sveconorwegian Orogeny in southern Norway, relative to deep crustal structures and events in the North Atlantic Proterozoic Supercontinent Norsk Geologisk Tidsskrift, 73: 109-132.

Steff and ARTE, 2015. Diagram of a scanning electron microscope with English captions.

Stoppa, F. and Schiazza, M., 2013. An overview of monogenetic carbonatitic magmatism from Uganda, Italy, China and Spain: Volcanologic and geochemical features. Journal of South American Earth Sciences, 41: 140-159.

Sundvoll, B. and Larsen, B.T., 1994. Architecture and early evolution of the Oslo Rift. Tectonophysics, 240(1-4): 173-189.

Svinndal, S., 1967. Undersøkelser efter sjeldne jordartselementer (RE) I Fensfeltet, Ulefoss., pp. 23.

Svinndal, S., 1968. Undersøkelser efter sjeldne jordartselementer (RE) I Fensfeltet, Ulefoss., pp. 42.

Svinndal, S., 1973. Thorium Fensfeltet. , pp. 28.

Tappe, S., 2006. Genesis of Ultramafic Lamprophyres and Carbonatites at Aillik Bay, Labrador: a Consequence of Incipient Lithospheric Thinning beneath the North Atlantic Craton. Journal of Petrology, 47(7): 1261-1315.

Tappe, S., Foley, S.F., Jenner, G.A. and Kjarsgaard, B.A., 2005. Integrating Ultramafic Lamprophyres into the IUGS Classification of Igneous Rocks: Rationale and Implications. Journal of Petrology, 46(9): 1893-1900.

Teufel, S. and Heinrich, W., 1997. Partial resetting of the U・Pb isotope system in monazite through hydrothermal experiments: An SEM and U・Pb isotope study. Chemical Geology, 137(3-4): 273-281.

Thomas, R., 2013. Practical guide to ICP-MS : a tutorial for beginners. Practical spectroscopy. CRC Press, Taylor & Francis Group, Boca Raton, xxvii, 418 pages pp.

Thornberry, R.-T. and Smith, D.-W., 2018. H.R. 5515 – National Defense Authorization Act for Fiscal Year 2019. In: E.O.O.T.P.-O.O.M.A. BUDGET (Editor), pp. 9.

Tomkeieff, S.I., 1958. The petrochemistry of the Oslo-Fen petrographical province. Geochimica et Cosmochimica Acta, 14: 165.

Tucker, M.E. and Wright, V.P., 1990. Carbonate Sedimentology. Blackwell Scientific Publication, Boston, 482 pp.

Tyler, G., 2004. Ionic charge, radius, and potential control root/soil concentration ratios of fifty cationic elements in the organic horizon of a beech (Fagus sylvatica) forest podzol. Science of The Total Environment, 329(1-3): 231-239.

U.S. Department of Energy, 2011. Critical Materials Strategy, pp. 190.

USGS, 1996. Mineral commodity summary on REE In: USGS (Editor).

USGS, 2012. Mineral commodity summary on REE In: USGS (Editor).

USGS, 2017. Mineral commodity summary on REE In: USGS (Editor).

Verschure, R.H. and Maijer, C., 2005. A new Rb-Sr isotopic parameter for metasomatism, and its application in a study of pluri-fenitized gneisses around the Fen ring complex, South Norway. NGU Bulletin, 445: 45-71.

Verschure, R.H., Maijer, C., Andriessen, P.A.M., Boelrijk, N.A.I.M., Hebeda, E.H., Priem, H.N.A. and Verdurmen, E.A.T., 1983. Dating Explosive Volcanism Perforating the Precambrian Basement in Southern Norway. Norges geologiske undersøkelse, 380(70): 16.

Verwoerd, W., J., 1966. South African Carbonatites And Their Probable Mode of Origin. Annale Universiteit van Stellenbosch, 41(2): 118.

Viola, G., Henderson, I.H.C., Bingen, B. and Hendriks, B.W.H., 2011. The Grenvillian–Sveconorwegian orogeny in Fennoscandia: Back-thrusting and extensional shearing along the “Mylonite Zone”. Precambrian Research, 189(3-4): 368-388.

Vogt, J.H.L., 1910. Jernmalm og jernverk. Norges Geologiske Undersøkelse, 51.

Vogt, J.H.L., 1918. JERNMALM OG JERNVERK. Norges geologiske undersøkelse, 85.

Wall, F., 2014. Rare earth elements. In: G. Gunn (Editor), Critical Metals Handbook. Wiley-Blackwell, pp. 312-339.

Wall, F. and Mariano, A.N., 1996. Rare earth minerals in carbonatites: a discussion centred on the Kangankunde Carbonatite, Malawi. In: A.P. Jones, F. Wall and C.T. Williams (Editors), Rare Earth Minerals Chemistry, origin and ore deposits. The Mineralogical Society Series, pp. 34.

Wall, F., Rollat, A. and Pell, R.S., 2017. Responsible Sourcing of Critical Metals. Elements, 13(5): 313-318.

Weidendorfer, D., Schmidt, M.W. and Mattsson, H.B., 2016. Fractional crystallization of Si-undersaturated alkaline magmas leading to unmixing of carbonatites on Brava Island (Cape Verde) and a general model of carbonatite genesis in alkaline magma suites. Contributions to Mineralogy and Petrology, 171(5).

White, W.M., 2013. Geochemistry. Wiley-Blackwell.

Williams-Jones, A.E. and Migdisov, A.A., 2014. Rare Earth Element Transport and Deposition by Hydrothermal Fluids. Acta Geologica Sinica - English Edition, 88(s2): 472-474.

Williams-Jones, A.E., Migdisov, A.A. and Samson, I.M., 2012. Hydrothermal Mobilisation of the Rare Earth Elements - a Tale of "Ceria" and "Yttria". Elements, 8(5): 355-360.

Williams-Jones, A.E., Samson, I.M. and Olivo, G.R., 2000. The Genesis of Hydrothermal Fluorite-REE Deposits in the Gallinas Mountains, New Mexico. Economic Geology, 95(2): 327-341.

Wilson, M., Neumann, E.R., Davies, G.R., Timmerman, M.J., Heeremans, M. and Larsen, B.T., 2004. Permo-Carboniferous magmatism and rifting in Europe: introduction. Geological Society, London, Special Publications, 223(1): 1-10.

Wood, B.J., Kiseeva, E.S. and Matzen, A.K., 2013. Garnet in the Earth's Mantle. Elements, 9(6): 421-426.

Woolley, A.R., 1989. THE SPATIAL AND TEMPORAL DISTRIBUTION OF CARBONATITES. In: K. Bell (Editor), Carbonatites. Genesis and Evolution. Unwin Hyman, London, pp. 15–37.

Woolley, A.R. and Bailey, D.K., 2012. The crucial role of lithospheric structure in the generation and release of carbonatites: geological evidence. Mineralogical Magazine, 76(2): 259-270.

Woolley, A.R. and Kempe, D.R.C., 1989. Carbonatites: nomenclature, average chemical composition, and element distribution. In: K. Bell (Editor), Carbonatites. Genesis and Evolution. Unwin Hyman, London, pp. 1-14.

Woolley, A.R. and Kjarsgaard, B.A., 2008a. CARBONATITE OCCURRENCES OF THE WORLD: MAP AND DATABASE. In: G.S.o. Canada (Editor).

Woolley, A.R. and Kjarsgaard, B.A., 2008b. Paragenetic Types of Carbonatite as Indicated by the Diversity and Relative Abundances of Associated Silicate Rocks: Evidence from a Global Database. The Canadian Mineralogist, 46(4): 741-752.

Wyllie, P.J., Jones, A.P. and Deng, J., 1996. Rare earth elements in carbonatite-rich melts from mantle to crust. In: A.P. Jonas, F. Wall and C.T. Williams (Editors), Rare earth minerals. Chemistry, origin and ore deposits. Mineralogical Society series. Chapman & Hall, London, pp. 77–98.

Wyllie, P.J. and Lee, W.J., 1998. Model System Controls on Conditions for Formation of Magnesiocarbonatite and Calciocarbonatite Magmas from the Mantle. Journal of Petrology, 39(11-12): 1885-1893.

Wyllie, P.J. and Tuttle, O.F., 1960. The System CaO-CO2-H2O and the Origin of Carbonatites. Journal of Petrology, 1(1): 1-46.

Xu, C., Campbell, I.H., Allen, C.M., Huang, Z., Qi, L., Zhang, H. and Zhang, G., 2007. Flat rare earth element patterns as an indicator of cumulate processes in the Lesser Qinling carbonatites, China. Lithos, 95(3-4): 267-278.

Xu, C., Kynicky, J., Chakhmouradian, A.R., Campbell, I.H. and Allen, C.M., 2010. Trace-element modeling of the magmatic evolution of rare-earth-rich carbonatite from the Miaoya deposit, Central China. Lithos, 118(1-2): 145-155.

Yang, X.-Y., Sun, W.-D., Zhang, Y.-X. and Zheng, Y.-F., 2009. Geochemical constraints on the genesis of the Bayan Obo Fe–Nb–REE deposit in Inner Mongolia, China. Geochimica et Cosmochimica Acta, 73(5): 1417-1435.

Yang, X.J., Lin, A., Li, X.-L., Wu, Y., Zhou, W. and Chen, Z., 2013. China's ion-adsorption rare earth resources, mining consequences and preservation. Environmental Development, 8: 131-136.

Ying, Y., Chen, W., Lu, J., Jiang, S.-Y. and Yang, Y., 2017. In situ U–Th–Pb ages of the Miaoya carbonatite complex in the South Qinling orogenic belt, central China. Lithos, 290-291: 159-171.

Zaitsev, A. and Bell, K., 1995. Sr and Nd isotope data of apatite, calcite and dolomite as indicators of source, and the relationships of phoscorites and carbonatites from the Kovdor massif, Kola peninsula, Russia. Contributions to Mineralogy and Petrology, 121(3): 324-335.

APPENDIX

I Sample list

Key			
Carbonatite		**Ultramafic Lamprophyre**	
C1	Calcite-carbonatite	D	Damtjernite
C2	Dolomite-carbonatite		
C3	Chlorite-bearing dolomite-carbonatite	**Rødbergite**	
C	Carbonatite	R	Rødbergite
		Rv	Rødbergite dike
Silicocarbontite		O	Fe_xO_y (high grade)
SC	Silicocarbonatite	Pv	Pyrite-vein
SC1	Holaite		
SC2	Käsenite	**Metamorphic rocks**	
		S	Schist
Ijolite		G	Gneiss
Ijo1	Urtite		
Ijo2	Ijolite	**Others**	
Ijo3	Melteigite	F	Fenite
Ijo4	Vipetoite	Bsn	Basanite
		Fl	Fluorite-mineralisation
Dikes		Ch	Chlorite-mineralisation
Dk1	Dolerite	U	Unknown
Dk2	Phonolite		
Dk3	Tinguaite		
Dku	Dike unknown		

Sample	Locality	easting (32V)	northing	Rocktype
15-01-FE	1	515975	6571409	C1
15-02-FE	2	516088	6571453	U
15-03-FE	3	516166	6571509	D
15-04-FE	3	516166	6571509	C1, D
15-05-FE	3	516166	6571509	C1
15-06-FE	3	516166	6571509	D
15-07-FE	3	516166	6571509	C1
15-08-FE	3	516166	6571509	C1, D
15-09-FE	5	516521	6571506	C
15-10-FE	5	516521	6571506	C1
15-11-FE	6	516627	6571387	D
15-12-FE	7	516728	6571276	C2 or R
15-13-FE	7	516728	6571276	C2 or R
15-14-FE	8	516814	6571398	D
15-15-FE	8	516814	6571398	D
15-16-FE	10	517044	6571497	C1, C2
15-17-FE	12	517180	6569828	D
15-18-FE	12	517180	6569828	D
15-19-FE	12	517180	6569828	D
15-20-FE	13	517144	6568987	D
15-21-FE	13	517144	6568987	C1, D, F
15-22-FE	15	517489	6570901	R

Sample	Locality	easting (32V)	northing	Rocktype
15-23-FE	15	517489	6570901	R
15-24-FE	15	517489	6570901	R
15-25-FE	16	517326	6570888	Dk1
15-26-FE	17	517670	6569601	D
15-27-FE	17	517670	6569601	D
15-28-FE	17	517670	6569601	D
15-29-FE	17	517670	6569601	D
15-30-FE	17	517670	6569601	F
15-31-FE	17	517670	6569601	R
15-32-FE	18	517578	6569614	D
15-33-FE	18	517578	6569614	C2, R
15-34-FE	18	517578	6569614	D
15-35-FE	19	515597	6570288	SC1
15-36-FE	20	515647	6570260	SC1
15-37-FE	21	515257	6570858	SC2
15-38-FE	22	515426	6569408	N1
15-39-FE	22	515426	6569408	N2
15-40-FE	22	515426	6569408	N3
15-41-FE	22	515426	6569408	N3
15-42-FE	23	515458	6569185	N3
15-43-FE	22	515426	6569408	N3
15-44-FE	24	515952	6569231	N3?
15-45-FE	25	515833	6569292	N3?
15-46-FE	26	515798	6569269	D
15-47-FE	27	514940	6568795	Dk2?
15-48-FE	28	514850	6568400	D, R
15-49-FE	28	514850	6568400	D,R
15-50-FE	29	516831	6569595	V
15-51-FE	29	516831	6569595	V
15-52-FE	29	516831	6569595	V
15-53-FE	29	516831	6569595	V
15-54-FE	29	516831	6569595	V
15-55-FE	30	517657	6570985	R
15-56-FE	30	517657	6570985	R
15-57-FE	31	517621	6570958	R
15-58-FE	31	517621	6570958	Chl
15-59-FE	33	517641	6570886	R
15-60-FE	34	514662	6573874	R
15-61-FE	34	514662	6573874	S
15-62-FE	34	514662	6573874	Dk3
15-63-FE	34	514662	6573874	Dk3
15-64-FE	34	514662	6573874	Dk3
15-65-FE	35	516276	6571323	D
15-66-FE	36	516525	6571289	C2
15-67-FE	37	516521	6571257	U

Sample	Locality	easting (32V)	northing	Rocktype
15-68-FE	38	516449	6571168	C2
15-69-FE	38	516449	6571168	C2
15-70-FE	38	516449	6571168	C2
15-71-FE	39	516472	6571004	D
15-72-FE	40	516471	6570983	D
15-73-FE	41	516469	6570966	C2, D
15-74-FE	42	516479	6570927	C2, R
15-75-FE	42	516479	6570927	R
15-76-FE	42	516479	6570927	C2, R
15-77-FE	42	516479	6570927	C1, R
15-78-FE	42	516479	6570927	D
15-79-FE	43	517431	6570105	C2, R
15-80-FE	43	517431	6570105	R
15-81-FE	43	517431	6570105	C2, R
15-82-FE	44	517503	6569609	C2
15-83-FE	44	517503	6569609	C2
15-84-FE	44	517503	6569609	C2
15-85-FE	44	517503	6569609	C2
15-86-FE	44	517503	6569609	C2, R
15-87-FE	44	517503	6569609	Chl
15-88-FE	44	517503	6569609	R
15-89-FE	44	517503	6569609	R
15-90-FE	44	517503	6569609	C2, R
15-91-FE	44	517503	6569609	C2, R
15-92-FE	44	517503	6569609	C2
15-93-FE	44	517503	6569609	C2
15-94-FE	44	517503	6569609	C2, R
16-01-FE	45	516010	6571470	C1
16-02-FE	46	516172	6571456	U
16-03-FE	47	516239	6571550	C1
16-04-FE	47	516239	6571550	C1
16-05-FE	47	516239	6571550	C1
16-06-FE	48	516474	6571515	C1, F
16-07-FE	48	516474	6571515	C1, F
16-08-FE	48	516474	6571515	C1
16-09-FE	48	516474	6571515	C1
16-10-FE	48	516474	6571515	C1
16-11-FE	48	516474	6571515	U, C1
16-12-FE	49	517457	6570902	0
16-13-FE	50	517608	6570996	F
16-14-FE	51	517681	6569591	D
16-15-FE	51	517681	6569591	R, D
16-16-FE	52	517523	6569604	Chl
16-17-FE	52	517523	6569604	C2, R
16-18-FE	52	517523	6569604	C2

Sample	Locality	easting (32V)	northing	Rocktype
16-19-FE	52	517523	6569604	C2, R
16-20-FE	52	517523	6569604	C2, R
16-21-FE	52	517523	6569604	C2
16-22-FE	52	517523	6569604	R
16-23-FE	52	517523	6569604	R
16-24-FE	53	517561	6569578	F, R
16-25-FE	55	516989	6571080	C2
16-26-FE	55	517012	6571064	C3
16-27-FE	55	517012	6571064	C3
16-28-FE	55	517021	6571058	C3
16-29-FE	55	517033	6571048	C3
16-30-FE	55	517045	6571039	C
16-31-FE	55	517060	6571026	C
16-32-FE	55	517085	6571001	C
16-33-FE	55	517098	6570985	C
16-34-FE	55	517109	6570974	C
16-35-FE	55	517171	6570926	D
16-36-FE	55	517176	6570924	D
16-37-FE	55	517189	6570916	R
16-38-FE	55	517207	6570901	R
16-39-FE	55	517232	6570887	R
16-40-FE	55	517258	6570881	R
16-41-FE	55	517277	6570858	R
16-30-FE-A	56	517423	6570642	O
16-31-FE-A	56	517414	6570657	R
16-32-FE-A	56	517423	6570642	R
16-33-FE-A	56	517414	6570657	R
16-34-FE-A	56	517414	6570657	R
16-35-FE-A	57	517414	6570652	R?
16-36-FE-A	57	517417	6570649	R?
16-37-FE-A	57	517422	6570632	R?
16-38-FE-A	58	517524	6570691	C
16-39-FE-A	58	517524	6570691	R
16-40-FE-A	59	517607	6570696	R
16-41-FE-A	59	517595	6570713	C
16-42-FE	59	517606	6570705	R
16-43-FE	59	517627	6570606	O
16-44-FE	61	517672	6570760	C, R
16-45-FE	62	517657	6570741	Dku
16-46-FE	64	517898	6570652	R?
16-47-FE	65	517777	6570758	O
16-48-FE	66	517839	6570783	F, R
16-49-FE	67	517307	6570887	Dk1
16-50-FE	67	517311	6570889	C2
16-51-FE	67	517320	6570890	D

Sample	Locality	easting (32V)	northing	Rocktype
16-52-FE	67	517270	6570895	C3
16-53-FE	67	517311	6570891	C3
16-54-FE	67	517320	6570892	C3, R
16-55-FE	67	517358	6570896	D, R
16-56-FE	67	517370	6570897	O, R
16-57-FE	67	517383	6570898	R
16-58-FE	67	517393	6570898	C3
16-59-FE	67	517399	6570899	R
16-60-FE	67	517482	6570928	F, R
16-61-FE	67	517495	6570936	F
16-62-FE	67	517509	6570947	F, R
16-63-FE	67	517514	6570954	R
16-64-FE	67	517517	6570957	F
16-65-FE	67	517522	6570960	F
16-66-FE	67	517541	6570968	R
16-67-FE	67	517584	6570989	C, F, Gn
16-68-FE	67	517672	6571012	Gn
16-69-FE	68	515857	6571344	C, S
16-70-FE	68	515857	6571344	C, S
16-71-FE	68	515857	6571344	R
16-72-FE	68	515857	6571344	C
16-73-FE	68	515857	6571344	R, C
16-74-FE	68	515857	6571344	C
16-75-FE	68	515857	6571344	C, R
16-76-FE	68	515857	6571344	R
16-77-FE	68	515857	6571344	C, R
16-78-FE	69	517440	6569918	R?
16-79-FE	70	517500	6569969	C, Rv
16-80-FE	70	517500	6569971	C
16-81-FE	70	517500	6569974	Fl
16-82-FE	70	517500	6569980	Rv
16-83-FE	70	517500	6569984	C2,Rv
16-84-FE	70	517500	6569986	C2
16-85-FE	70	517499	6569992	C2
16-86-FE	70	517499	6569994	Rv
16-87-FE	70	517497	6569998	R
16-89-FE	70	517494	6570014	R
16-90-FE	70	517483	6570034	C3
16-91-FE	70	517480	6570040	C3, Rv
16-92-FE	70	517472	6570049	C3
16-93-FE	70	517469	6570053	R
16-94-FE	70	517459	6570064	R
16-95-FE	70	517448	6570077	C3
16-96-FE	70	517433	6570098	C2
16-97-FE	70	517421	6570113	C3

Sample	Locality	easting (32V)	northing	Rocktype
16-98-FE	70	517407	6570130	C3
16-99-FE	71	517057	6571121	R
16-100-FE	72	517084	6571078	R, C
16-101-FE	72	517084	6571078	C
16-102-FE	52	517523	6569604	C
16-103-FE	52	517523	6569604	C
16-104-FE	52	517523	6569604	R
16-105-FE	73	517073	6570052	D
16-106-FE	74	516879	6569893	D
16-107-FE	74	516879	6569893	C2
16-108-FE	75	517136	6569658	D
16-109-FE	75	517136	6569658	D, C2
16-110-FE	52	517523	6569604	C1, R
16-111-FE	52	517523	6569604	C1, R
16-112-FE	52	517523	6569604	R
16-113-FE	76	515581	6568933	Ijo
16-114-FE	77	537467	6566762	Bsn
16-115-FE	78	537705	6567415	Bsn
TUFTE Tunnel				
TS 100	68	515857	6571344	F
TS 150	68	515857	6571344	F
TS 200	68	515857	6571344	F
TS 250	68	515857	6571344	F
TS 275	68	515857	6571344	C
TS 300	68	515857	6571344	C, SC
TS 350	68	515857	6571344	C
TS 400	68	515857	6571344	C, R
TS 450	68	515857	6571344	C, R
TS 462	68	515857	6571344	C
TS 500	68	515857	6571344	C
TS 520	68	515857	6571344	Pv
TS 552	68	515857	6571344	C
TS 600	68	515857	6571344	C
TS 642	68	515857	6571344	C
TS 650	68	515857	6571344	SC
TS 700	68	515857	6571344	C
TS 750	68	515857	6571344	SC
TS 793	68	515857	6571344	R
TS 800	68	515857	6571344	C
TS 850	68	515857	6571344	C
TS 900	68	515857	6571344	C
TS 958	68	515857	6571344	C
TS 970 + 20	68	515857	6571344	SC
TS 1000	68	515857	6571344	C, SC

II Sample Reduction

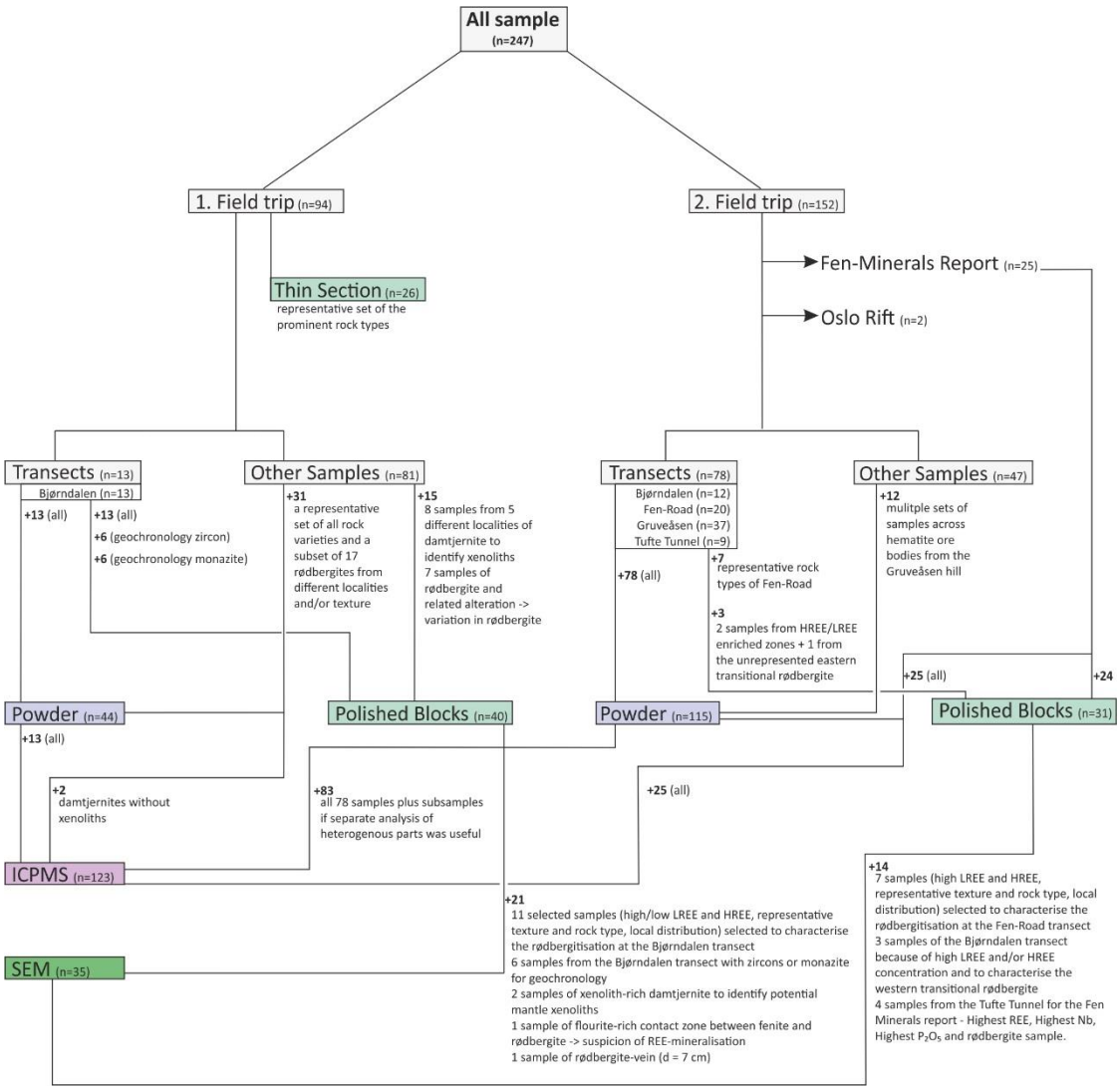

Figure A-1: Chart illustrating the sample number and criteria for the different sample preparation steps: thin section; sample powder; polished blocks; ICPMS and SEM.

III Sample Preparation (detailed)

- all samples were cut in half using a diamond saw;
- the two halves were then separated into one archive piece for storage and one working piece for further sample processing;
- one thin slice was cut from the working piece to represent the overall texture of the rock;
- approximately 100 g of rock material was cut to smaller blocks (< 2cm) for further crushing to produce rock powder, and a larger representative block was cut from every sample to produce polished blocks for microscopic analysis; 30 μm

Thin Section

- thin section was ordered with standard thickness of 30 μm and polished for further use in the Scanning Electron Microscope;
- the majority of the samples were prepared as polished blocks — polished blocks are a quicker and cheaper way of preparing samples for the Scanning Electron Microscope compared to thin sections;

Polished Block Preparation

- liquid resin (EPO Flo resin) and a liquid hardener (EPO Flo hardener) are mixed together in a ratio of 10:3 (by weight) and slowly stirred with a wooden toothpick for at least 2 min to ensure homogenisation;

- before mounting the sample chip into a 3 cm round plastic tube with a removable bottom, a release agent was spread on the inner wall of the mould;
- the chip was put into the mould and the resin mix was poured slowly over the sample to avoid trapping of air bubbles;
- the mould was placed on a hotplate at 60°C and left for at least 2 days for curing;
- the cured resin block was grinded with a grinding plate to remove any sharp edges;
- the blocks was hand polish using two different sized diamond grinding paper attached to a polishing plate;
- preparation with diamond grinding paper was done for at least 4 min for each sample to ensure full exposure of the specimen surface;
- further polishing was done in two steps with a slurry of water and alumina with a grain size of 14 µm and 9 µm, respectively — between each step the sample and the plate were washed and sonicated to remove any remnants of the slurry;
- mechanical polishing involved 3 steps with diamond pastes with 6 µm, 3 µm and 1 µm grain sizes;
- diamond paste was put on a polishing glove together with lubricant Buehler MetaDi and spread on the glove using the sample itself;
- after each step the sample was washed, put into an ultrasonic bath to get rid of any remaining polishing paste, and dried with an airgun before moving to the next finer polishing step;

Rock Powder Preparation (<30 µm)

- bench-top jaw-crusher with adjustable aluminium-oxide ceramic plates was used to crush approximately 100 g material of each sample
- to protect the ceramic plates from abrasion, the rock chips were less than 3 cm in size and crushed in 3 to 5 steps, starting with the largest distance between the ceramic plates and finishing with slightly less than the smallest distance possible; the last crushing step ensured that the particle size was less than 0.5 mm and therefore small enough to be effectively milled with the agate mill;
- after each sample the two jaws were screwed off and rigorously washed with hot water and a brush — more resistant impurities were successfully removed using crushed quartz powder;
- the jaw crusher was cleaned with paper towels and dry-cleaned with the airgun;
- after every second sample and every rødbergite sample, broken chips of Cornish quartz pebbles were crushed in > 10 steps for cleaning purpose;
- crushed sample material was milled using the Retsch RS 100 vibratory disc mill, with an agate ring-and-puck mill to obtain a fine powder of less than 30 µm particle size;
    - after the agate ring broke the rock samples of the Gruveåsen transect were milled with a tungsten-carbide (WC) ring-and-puck mill;
- duration of milling was variable and could take up to 10 min at 700 rpm ($11.\overline{6}$ s^{-1}) for the agate mill and 2 min at 1400 rpm ($23.\overline{3}$ s^{-1}) for the WC mill;
- the mill was emptied on a blank sheet of paper and sticking material was scratched off the agate mill;

- common problems with the agate mill occurred with phlogopite- and Fe-oxide rich samples;
    - phlogopite is hard to crush because it bends easily and absorbs the impact;
    - in a similar way Fe-oxides coat the agate mill and every particle with an impact absorbing layer;
    - in both cases less material and longer mill time was required;

Carbon Coating

- any impurities on the sample surface were cleaned off using an analytical duster spray;
- a rotary-pumped carbon and sputter coating system with a carbon rod evaporation head was used to carbon coat the samples;
- for carbon coating, two carbon rods were sharpened with a special sharpener to get a spigot;
    - one spigot was then grinded to an anvil shape using a special tool and grinding paper with 600- and 1200-grit;
- both rods were clamped into the electrodes of the evaporation head making sure that the sharpened tips were in contact;
- after the sample was placed in the chamber, the evaporation head was closed tightly and the program “ramped carbon” was selected;
    - evacuation took between 10 to 30 min depending on the porosity and size of the sample;

- when the required vacuum was reached, a high current was applied stepwise on the carbon rods to produce thermal evaporation of carbon, which deposited on the sample;
    - to ensure an even coating the sample was placed on a rotating stage during the whole process.
- for various reasons large area maps were more prone to charging and therefore samples, which were supposed to be mapped entirely, were coated twice;

IV Transect Rare Earth Element Concentration

Bjørndalen transect

Rock type	Sample	REE [ppm]	LREE [ppm]	HREE [ppm]	Th [ppm]	$(La/Yb)_N$
Carbonatite	**15-82**	1434	1310	123	117.61	40
Carbonatite	**15-83**	1442	1302	140	219.74	28
Carbonatite	**15-84**	800	692	108	66.66	13
Carbonatite	**15-85**	867	764	104	34.32	14
Carbonatite	**16-18**	1621	1459	162	66.08	30
Carbonatite	**16-21**	1106	989	117	35.12	32
Rødbergite	**15-86**	2234	1821	413	284.53	15
Rødbergite	**15-87**	1606	1470	135	49.95	22
Rødbergite	**15-88**	3426	2867	558	773.10	9
Rødbergite	**15-88/2**	3119	2631	488	781.10	10
Rødbergite	**15-89**	5577	5323	254	986.83	67
Rødbergite	**15-90**	8669	8444	225	404.71	137
Rødbergite	**15-94**	11220	10577	643	928.49	43
Rødbergite	**16-104**	1284	1088	196	136.14	17
Rødbergite	**16-112**	8485	8142	343	751.84	86
Rødbergite	**16-16**	488	430	59	62.63	17
Rødbergite	**16-22**	6202	5778	423	919.80	39
Rødbergite	**16-23**	1272	758	514	376.68	2
Transitional Rødbergite	**15-91**	12976	12632	344	452.15	145
Transitional Rødbergite	**15-92**	8371	8116	256	626.91	111
Transitional Rødbergite	**15-93**	14214	13770	444	494.01	127
Transitional Rødbergite	**16-110**	7305	7036	270	366.48	115
Transitional Rødbergite	**16-111**	14207	13652	555	578.39	121
Transitional Rødbergite	**16-17**	817	715	102	25.21	17
Transitional Rødbergite	**16-19**	806	707	98	53.07	12
Transitional Rødbergite	**16-20**	1026	784	243	192.56	7
Transitional Rødbergite	**16-20/2**	1021	785	237	190.24	8

Fen Road transect

Rock type	Sample	REE [ppm]	LREE [ppm]	HREE [ppm]	Th [ppm]	$(La/Yb)_N$
Chlorite-bearing Dolomite-Carbonatite	**16-90**	9994	9808	186	364.75	407
Chlorite-bearing Dolomite-Carbonatite	**16-91C**	2153	2067	85	78.86	108
Chlorite-bearing Dolomite-Carbonatite	**16-92**	7668	7531	137	648.57	250
Chlorite-bearing Dolomite-Carbonatite	**16-95**	3156	3068	88	59.05	233
Chlorite-bearing Dolomite-Carbonatite	**16-97**	2049	1992	57	51.23	203
Chlorite-bearing Dolomite-Carbonatite	**16-98**	4534	4419	115	207.04	249
Chloritized gneiss	**16-80**	440	367	74	42.24	18
Dolomite-Carbonatite	**16-83**	1118	967	151	82.70	27
Dolomite-Carbonatite	**16-84**	684	612	72	37.26	34
Dolomite-Carbonatite	**16-85**	10627	10224	403	259.71	188
Dolomite-Carbonatite	**16-96**	4803	4715	88	176.14	416
Fluorite-rich Carbonatite	**16-81**	1773	1643	130	70.95	53
Rødbergite	**16-87**	8819	8659	160	593.91	403
Rødbergite	**16-89**	3223	3144	79	234.87	177
Rødbergite	**16-93**	9733	9520	213	483.21	300
Rødbergite	**16-94**	5136	5019	117	247.49	385
Rødbergite Vein	**16-82**	20746	20390	356	1286.85	374
Rødbergite Vein	**16-86**	14586	14354	232	1150.71	344
Rødbergite Vein	**16-91V**	18136	17864	272	894.82	322
Rødbergite Vein in Chloritized Gneiss	**16-79**	2547	2460	87	167.09	55

Gruveåsen transect

Rock type	Sample	REE [ppm]	LREE [ppm]	HREE [ppm]	Th [ppm]	$(La/Yb)_N$
Calcitic UML	**16-55**	1601	1462	139	65	47
Carbonatite	**16-25**	1917	1800	117	116	59
Carbonatite	**16-26**	4628	4336	292	847	91
Carbonatite	**16-27**	17358	16963	395	870	490
Carbonatite	**16-28**	3949	3651	298	814	60
Carbonatite	**16-29**	13142	12780	362	690	353
Carbonatite	**16-50**	3885	3639	246	266	60
Carbonatite	**16-52**	4482	4213	269	336	75
Carbonatite	**16-53**	3189	3003	186	251	76
Carbonatite	**16-54a**	3287	2979	308	383	26
Carbonatite	**16-58**	6655	5936	719	641	32
Dolerite	**16-49**	342	291	51	9	19
Explosive D-Breccia	**16-65**	1493	1132	361	399	10
Fenite Breccia	**16-61**	678	581	97	105	13
Fenite Breccia	**16-60**	341	205	137	10	6
Fe-ore	**16-54**	7308	6388	921	579	23
Gneiss	**16-68**	236	184	53	27	9
Rødbergite	**16-51**	9001	8357	644	376	65
Rødbergite	**16-56**	4803	4485	319	911	65
Rødbergite	**16-57**	1840	1617	224	167	19
Rødbergite	**16-59**	11953	11466	487	798	105
Rødbergite	**16-66**	160	120	40	92	9
Rødbergite	**16-67**	926	813	114	65	34
Rødbergite Vein	**16-62**	3214	3031	183	129	113
Rødbergite Vein	**16-63**	426	307	120	121	10
Rødbergite Vein	**16-64**	22715	22133	582	3175	356

V EDS-SEM Analysis

All analysis are normalised to 100%. Please consider this when working on minerals with a high concentration of OH, H, CO_3, e.g., calcite, dolomite, REE-fluorocarbonates and apatite.

EDS-SEM point analysis												
Element	Allanite											
	P6-59											
	[wt%]	s	[at%]	[wt%]	s	[at%]	[wt%]	s	[at%]	[wt%]	s	[at%]
O	33.9	0.5	60.3									
Si	14.6	0.3	14.7									
Fe	13.2	0.3	6.7									
Ce	12.4	0.5	2.5									
Al	8	0.2	8.4									
Ca	7.3	0.2	5.2									
La	5.5	0.4	1.1									
Nd	3.6	0.4	0.7									
Pr	1.5	0.4	0.3									

Element	Apatite											
	P6-4			P6-8			P6-19			P6-23		
	[wt%]	s	[at%]	[wt%]	s	[at%]	[wt%]	s	[at%]	[wt%]	s	[at%]
Ca	41.5	0.3	25.3	41.5	0.3	25.2	41.5	0.3	25.3	41.3	0.3	55.4
O	36.6	0.4	55.8	36.4	0.4	55.4	36	0.4	54.9	36.5	0.4	25
P	18.5	0.2	14.5	18.2	0.2	14.3	18.2	0.2	14.4	18.2	0.2	14.3
F	3.4	0.3	4.4	4	0.3	5.1	4.3	0.3	5.5	4.1	0.3	5.3
	P6-28			P6-47			P6-55			P6-62		
	[wt%]	s	[at%]	[wt%]	s	[at%]	[wt%]	s	[at%]	[wt%]	s	[at%]
Ca	43.1	0.3	26.8	42.6	0.3	26.3	44.3	0.3	28.2	40.4	0.9	25
O	33.7	0.4	52.4	35.2	0.4	54.3	30.8	0.3	49	35.8	1.2	55.4
P	19	0.2	15.3	18.9	0.2	15.1	20.3	0.2	16.7	16.8	0.5	13.4
F	4.2	0.3	5.5	3.4	0.3	4.4	4.6	0.2	6.1	3.7	1	4.8
Fe										3.2	0.3	1.4
	P7-3			P7-6			P7-16					
	[wt%]	s	[at%]	[wt%]	s	[at%]	[wt%]	s	[at%]			
Ca	41	0.7	24.7	41.6	0.4	25.3	42.1	0.5	25.8			
O	37.4	0.8	56.4	36.3	0.5	55.3	35.5	0.6	54.5			
P	17.4	0.4	13.5	18.2	0.2	14.3	18.5	0.3	14.7			
F	4.2	0.6	5.4	4	0.3	5.1	3.9	0.4	5			

Element	Barian Feldspar to Celsian											
	P6-41			P6-42								
	[wt%]	s	[at%]	[wt%]	s	[at%]	[wt%]	s	[at%]	[wt%]	s	[at%]
O	34.8	0.3	59.5	37.8	0.3	58.8						
Ba	29.4	0.2	5.9	17.6	0.2	3.2						
Si	19.2	0.1	18.7	24.4	0.2	21.6						
Al	13.5	0.1	13.7	12.1	0.1	11.1						
K	3.3	0.1	2.3	7.8	0.1	4.9						
Na				0.3	0.1	0.4						

EDS-SEM point analysis												
	Barite											
Element	P6-10			P6-16			P6-40			P6-45		
	[wt%]	s	[at%]	[wt%]	s	[at%]	[wt%]	s	[at%]	[wt%]	s	[at%]
Ba	62.2	0.3	19	65	0.3	21.7	62.3	0.3	19.1	62.7	0.3	19.3
O	23.9	0.3	62.7	20.2	0.2	58	23.8	0.3	62.6	23.8	0.2	62.8
S	13.9	0.1	18.2	13.7	0.1	19.7	13.9	0.1	18.3	13.5	0.10	17.9
Sr				1.1	0.1	0.6						
	P6-57			P7-10			P7-31			P7-34		
	[wt%]	s	[at%]	[wt%]	s	[at%]	[wt%]	s	[at%]	[wt%]	s	[at%]
Ba	67	0.3	23.4	64.4	0.2	20.8	63.8	0.5	20.4	67.7	0.3	24.5
O	18.5	0.2	55.4	21.7	0.2	60	22.1	0.4	60.4	17	0.2	52.9
S	13.5	0.10	20.1	13.9	0.1	19.2	14.1	0.2	19.3	14	0.1	21.6
Sr										0.90	0.1	0.50
Fe	0.6	0.10	0.5									
Ca	0.5	0.10	0.6							0.40	0.1	0.50

	Calcite											
Element	P6-5			P6-13			P6-20			P6-27		
	[wt%]	s	[at%]	[wt%]	s	[at%]	[wt%]	s	[at%]	[wt%]	s	[at%]
O	52.1	0.3	73.1	49.9	0.4	71.5	51	0.4	71.9	29.5	0.5	51.5
Ca	47.7	0.3	26.8	48.3	0.4	27.6	45.7	0.3	25.7	66.2	0.5	46.2
Mg	0.2	0	0.2	0.3	0.1	0.3	1.8	0.1	1.7	0.5	0.1	0.6
Fe				0.6	0.1	0.2	1	0.1	0.4	1.7	0.1	0.9
Mn				0.9	0.1	0.4	0.5	0.1	0.2	1.4	0.1	0.7
Sr										0.6	0.1	0.2
	P6-34			P7-5			P7-11					
	[wt%]	s	[at%]	[wt%]	s	[at%]	[wt%]	s	[at%]			
O	52.1	0.3	73.2	54.8	1.2	75.2	48.5	0.5	71.1			
Ca	46.5	0.3	26.1	45.2	1.2	24.8	43.9	0.4	25.7			
Mg	0.4	0.1	0.3									
Fe	0.4	0.1	0.2				6.5	0.3	2.7			
Mn	0.6	0.1	0.2				1	0.2	0.4			

	Chlorite					
Element	P7-1			P7-28		
	[wt%]	s	[at%]	[wt%]	s	[at%]
O	42.3	0.3	60.5	35.6	0.3	54.5
Fe	22.6	0.3	9.3	28.7	0.4	12.6
Si	14.1	0.1	11.5	13.8	0.2	12
Al	10.9	0.1	9.2	12.8	0.2	11.6
Mg	10.1	0.1	9.5	9.1	0.2	9.2

EDS-SEM point analysis												
Element	**Columbite**											
	P6-07			P6-12			P6-56 Nb-mineral			P7-15		
	[wt%]	s	[at%]	[wt%]	s	[at%]	[wt%]	s	[at%]	[wt%]	s	[at%]
Nb	51.2	0.4	20.7	53.5	0.4	59.2	25.3	0.4	7.4	51.8	1.5	20.8
O	27.9	0.5	65.5	23.8	0.4	23.0	45.8	0.5	78.1	27.5	1.4	64.3
Fe	15.4	0.2	10.4	16.9	0.2	12.0	6.7	0.3	3.3	14.2	1	9.5
Mn	1.2	0.1	0.8	1.2	0.1	0.9				3.1	0.7	2.1
Ti	2.5	0.1	1.9	4.0	0.1	3.4	2.2	0.1	1.3	1.5	0.4	1.1
Ca	0.2	0.1	0.2				9.3	0.2	6.3	1.2	0.3	1.1
Si							1.1	0.1	1.1	0.7	0.2	0.9
Ta	0.9	0.3	0.2									
Rh	0.4	0.2	0.2									
V	0.3	0.1	0.2	0.7	0.1	0.5						
Ce							6	0.3	1.2			
Y							3.2	0.3	1			
Al							0.4	0.1	0.4			

Element	**Dolomite to Ferroan Dolomite**											
	P6-6			P6-14			P6-18			P6-29		
	[wt%]	s	[at%]	[wt%]	s	[at%]	[wt%]	s	[at%]	[wt%]	s	[at%]
O	53.3	0.3	71.1	51.2	0.3	69	52.6	0.3	70.5	44.7	0.3	65.1
Ca	27.6	0.2	14.8	29.9	0.2	16.1	27.5	0.2	14.7	31.1	0.2	18.1
Mg	13.9	0.1	12.2	15.2	0.1	13.5	14.4	0.1	12.7	12.6	0.1	12.1
Fe	4.5	0.1	1.7	2.4	0.1	0.9	4.2	0.1	1.6	8.7	0.1	3.6
Mn	0.6	0.1	0.2	1.3	0.1	0.5	0.9	0.1	0.4	2.3	0.1	1
Sr							0.5	0.1	0.1	0.7	0.1	0.2
	P6-33			P6-38			P6-49					
	[wt%]	s	[at%]	[wt%]	s	[at%]	[wt%]	s	[at%]			
O	54.8	0.3	71.2	24.9	0.2	44.7	39.6	0.4	59.3			
Ca	28.3	0.2	14.7	44.3	0.2	31.8	44.3	0.3	26.4			
Mg	16.2	0.1	13.8	11.5	0.1	13.6	13.3	0.1	13.1			
Fe	0.4	0.1	0.2	16.4	0.3	8.4	0.9	0.1	0.4			
Mn	0.3	0.1	0.1	2.8	0.2	1.5	1.9	0.1	0.8			
	P7-2			P7-7			A7-1			P7-17		
	[wt%]	s	[at%]	[wt%]	s	[at%]	[wt%]	s	[at%]	[wt%]	s	[at%]
O	50.6	0.9	70.8	51.2	0.6	69.7	51.8	0.1	69.9	51.7	0.2	69.9
Ca	26.3	0.7	14.7	28	0.4	15.2	28.4	0.1	15.3	28.5	0.2	15.4
Mg	8.9	0.4	8.2	13.8	0.3	12.3	14.3	0.1	12.7	14.2	0.1	12.6
Fe	12.8	0.8	5.1	5.7	0.4	2.2	4.1	0.1	1.6	4.3	0.1	1.7
Mn				1.3	0.3	0.5	0.9	0.1	0.4	0.8	0.1	0.3
Si	0.8	0.2	0.6									
Al	0.6	0.2	0.5									
Mn							0.9	0.0	0.4			
Sr							0.5	0.0	0.1	0.5	0.1	0.1

EDS-SEM point analysis												
	Dolomite to Ferroan Dolomite											
Element	P7-18			P7-19			P7-20			P7-29		
	[wt%]	s	[at%]	[wt%]	s	[at%]	[wt%]	s	[at%]	[wt%]	s	[at%]
O	50.9	0.5	69.8	51.9	0.2	70.1	49	0.1	69.8	46.1	0.5	64.6
Ca	28.2	0.3	15.4	27.7	0.2	14.9	26.2	0.1	14.9	31.8	0.4	17.8
Mg	12.8	0.2	11.5	13.9	0.1	12.4	9.8	0.1	9.2	16.8	0.3	15.5
Fe	6.5	0.3	2.6	5.2	0.1	2	13.3	0.1	5.4	2.1	0.3	0.8
Mn	1.7	0.2	0.7	1.3	0.1	0.5	1.8	0.1	0.7	3.2	0.3	1.3
	P7-30			P7-38			P7-39					
	[wt%]	s	[at%]	[wt%]	s	[at%]	[wt%]	s	[at%]			
O	48.4	0.5	69.4	48.5	0.3	68.9	48.1	0.3	69.8			
Ca	27.8	0.4	15.9	27	0.2	15.3	25.5	0.2	14.8			
Fe	13.6	0.4	5.6	11.8	0.2	4.8	15.5	0.2	6.5			
Mg	9.1	0.2	8.6	11.1	0.1	10.3	7.6	0.1	7.3			
Mn	1	0.2	0.4	1.3	0.1	0.5	2.4	0.1	1			
Si							0.5	0	0.4			
Al							0.4	0	0.3			
Sr				0.4	0.1	0.1						

	Fe-Oxide											
Element	P6-22			P6-25			P6-35			P6-39		
	[wt%]	s	[at%]	[wt%]	s	[at%]	[wt%]	s	[at%]	[wt%]	s	[at%]
Fe	67.1	0.2	63.0	71.8	0.2	57.1	67.3	0.2	63.0	75.7	0.2	52.4
O	32.9	0.2	36.9	27.6	0.2	42.6	32.7	0.2	37.0	24.3	0.2	47.6
Ti				0.6	0.1	0.5						
	P6-50 Fe-Ox-Mnz Mix			P6-53			P6-58					
	[wt%]	s	[at%]	[wt%]	s	[at%]	[wt%]	s	[at%]			
Fe	28.9	0.3	19	67.8	0.2	39.4	65.8	0.3	38.9			
O	26.8	0.3	61.6	28.4	0.2	57.7	27.7	0.3	57.3			
Ti				1.7	0.1	1.1	3.2	0.1	2.2			
Ca	0.4	0.1	0.4	1.9	0.1	1.5	0.4	0.1	0.3			
V				0.3	0.1	0.2	0.9	0.1	0.6			
Ba							1.8	0.3	0.4			
P	8.1	0.1	9.7				0.2	0	0.2			
Ce	19.9	0.3	5.2									
La	7.9	0.3	2.1									
Nd	8.1	0.3	2.1									
	P7-24			P7-36								
	[wt%]	s	[at%]	[wt%]	s	[at%]						
Fe	72.4	0.2	42.9	73.8	0.2	45						
O	27.6	0.2	57.1	25.7	0.2	54.6						
Ti				0.6	0.1	0.4						

EDS-SEM point analysis												
Element	**Flourite**											
	P7-8			P6-03								
	[wt%]	s	[at%]	[wt%]	s	[at%]	[wt%]	s	[at%]	[wt%]	s	[at%]
Ca	53.1	0.2	64.8	53.5	0.3	64.8						
F	46.6	0.2	34.9	46.5	0.3	35.2						
Mg	0.3	0	0.3									

Element	**Phlogopite**											
	P6-44			P6-48			P6-61					
	[wt%]	s	[at%]	[wt%]	s	[at%]	[wt%]	s	[at%]	[wt%]	s	[at%]
O	40.4	0.2	51.9	36.4	0.3	51.6	37.3	1.1	52			
Si	20.8	0.1	17.7	20.2	0.2	16.3	21.3	0.6	17			
Mg	11.9	0.1	11.5	13.6	0.1	12.7	12.5	0.5	11.5			
Fe	8.6	0.2	3.7	7.8	0.1	3.2	9.4	0.6	3.8			
K	8.4	0.1	5.2	8.3	0.1	4.8	8.4	0.4	4.8			
Al	5	0.1	4.4	6.6	0.1	5.5	5.9	0.4	4.9			
F	4.6	0.2	5.5	4.6	0.3	5.5	5.2	1.1	6.1			
Ti	0.4	0.1	0.2									
Ba				2.4	0.1	0.4						

Element	**Pyrite**											
	P6-2			P6-21			P6-30					
	[wt%]	s	[at%]	[wt%]	s	[at%]	[wt%]	s	[at%]	[wt%]	s	[at%]
S	52.7	0.2	65.9	51.5	0.3	65.4	49.8	0.6	64.6			
Fe	47.3	0.2	33.9	46.7	0.3	34.1	45.4	0.5	33.8			
Mo							3.1	0.9	1.3			
Hg				1.5	0.4	0.3	1.7	0.4	0.4			
Ca				0.2	0.1	0.2						
	P7-9			P7-22								
	[wt%]	s	[at%]	[wt%]	s	[at%]						
S	49.9	0.7	59.5	51.8	0.8	65.1						
Fe	46.6	0.7	31.9	48.2	0.8	34.9						
O	3.6	0.4	8.5									

EDS-SEM point analysis												
Element	**Monazite**											
	P6-15			P6-24			P6-26			P6-37		
	[wt%]	s	[at%]	[wt%]	s	[at%]	[wt%]	s	[at%]	[wt%]	s	[at%]
Ce	32.1	0.5	9.4	32	0.4	9.3	31	0.4	9.2	35.7	0.5	13.4
O	25.3	0.4	64.6	25.5	0.3	64.8	24.7	0.3	63.7	15.4	0.2	50.6
La	14.5	0.4	4.3	13.2	0.3	3.9	18.2	0.3	5.4	18.8	0.5	7.1
P	13	0.2	17.1	13.1	0.2	17.2	13.1	0.2	17.5	12.9	0.2	21.9
Nd	9.2	0.4	2.6	12.6	0.4	3.5	9.8	0.3	2.8	11.4	0.5	4.2
Pr	3.4	0.4	1	3.2	0.4	0.9	2.6	0.4	0.8			
Th	1.7	0.3	0.3							4.4	0.3	1
Ca	0.7	0.1	0.7	0.4	0.1	0.4	0.6	0.1	0.6	1.4	0.1	1.8
	P6-43			P6-46			P6-51			P6-60		
	[wt%]	s	[at%]	[wt%]	s	[at%]	[wt%]	s	[at%]	[wt%]	s	[at%]
Ce	31	0.4	9.1	33.2	0.4	9.8	29.6	0.4	8.3	32.7	2.6	9.6
O	25.3	0.3	64.4	24.6	0.3	63.9	26.4	0.3	65.1	25	2.1	64.2
La	15.1	0.3	4.6	13	0.3	3.9	13.2	0.3	3.8	16.1	2.3	4.8
P	13	0.2	17	13.2	0.2	17.8	12.5	0.2	15.9	13.4	1.2	17.7
Nd	10	0.4	2.8	12.3	0.4	3.6	10.1	0.3	2.8	8.4	2.4	2.4
Pr	2.7	0.4	0.8	3.6	0.4	1	3.6	0.3	1	4.4	2.4	1.3
Th	1.6	0.2	0.3				1.6	0.2	0.3			
Ca	1.2	0.1	1.2				2.9	0.1	2.8			
	P7-35			P7-43								
	[wt%]	s	[at%]	[wt%]	s	[at%]						
Ce	31.5	0.5	9.7	29.5	0.5	9.1						
O	23	0.3	61.7	22.8	0.3	61.6						
La	18.1	0.4	5.6	8	0.4	2.5						
P	13.1	0.2	18.2	12.9	0.2	17.9						
Nd	9.8	0.5	2.9	16.3	0.5	4.9						
Pr	2.4	0.5	0.7	4.2	0.4	1.3						
Th	1.2	0.3	0.2	2.9	0.3	0.5						
Ca	0.9	0.1	1	0.7	0.1	0.8						
Sm				2.1	0.4	0.6						
Si				0.3	0.1	0.4						
S				0.3	0.1	0.4						

Element	**Quarz**											
	P6-31						P7-4			P7-21		
	[wt%]	s	[at%]	[wt%]	s	[at%]	[wt%]	s	[at%]	[wt%]	s	[at%]
O	50.9	0.2	64.1				49.9	0.3	63.8	50.1	0.9	63.8
Si	49.1	0.2	35.9				48.2	0.3	35.1	49.9	0.9	36.2
Fe							0.7	0.1	0.3			
Al							0.5	0.1	0.4			
Ca							0.4	0.1	0.2			
Mg							0.3	0.1	0.2			

EDS-SEM point analysis												
Element	**REE-fluorocarbonates**											
	P6-01 Parisite			P6-11 Synchysite			P6-32 Synchysite			P6-52 Bastnäsite		
	[wt%]	s	[at%]	[wt%]	s	[at%]	[wt%]	s	[at%]	[wt%]	s	[at%]
Ce	30.8	0.4	8.5	26	0.4	6.7	26.6	0.4	7.1	27.7	0.4	7.7
O	24.7	0.3	59.9	28.3	0.4	64.2	26	0.4	61.1	25.6	0.3	62.4
La	15.4	0.3	4.3	11.9	0.3	3.1	13.5	0.3	7.1	11.8	0.3	3.3
Nd	9.2	0.3	2.5	8.2	0.3	2.1	8.7	0.3	3.6	7.2	0.3	1.9
Ca	8.5	0.1	8.3	14.1	0.2	12.7	13.3	0.2	12.4	3.8	0.1	3.7
F	6.8	0.3	14	5.1	0.3	9.8	5.3	0.3	10.4	7.1	0.3	14.5
Pr	3.3	0.3	0.9	2.5	0.3	0.6	2.7	0.3	0.7	3.3	0.3	0.9
Al	1	0.1	1.4				0.2	0.1	0.3			
S	0.2	0.1	0.2									
Sm				1.6	0.3	0.4						
Gd				1.2	0.3	0.3						
Th				1.1	0.2	0.2	1.2	0.2	0.2			
Nb							0.5	0.2	0.2			
Si							0.2	0.1	0.3			
Fe							2	0.1	1.3	6	0.2	4.2
Th										7.5	0.3	1.3
	P6-54 Syn (mix signal)			P7-12 Bastnäsite			P7-13 Synchysite			P7-14 Synchysite		
	[wt%]	s	[at%]	[wt%]	s	[at%]	[wt%]	s	[at%]	[wt%]	s	[at%]
O	30.7	0.4	61	28.4	0.6	62.2	23.7	0.3	58.6	29.5	0.5	63.9
Ce	14.8	0.4	3.3	25.4	0.8	6.4	25.1	0.5	7.1	25.5	0.6	6.3
Ca	21.9	0.3	17.3	15.3	0.3	13.4	13.5	0.2	13.3	15.5	0.3	13.4
La	6.3	0.4	1.4	13.7	0.7	6.4	12.2	0.4	3.5	12.1	0.5	3
Nd	6.6	0.4	1.4	10.7	0.8	3.5	10.9	0.4	3	11.6	0.6	2.8
F	4.5	0.3	7.5	6.5	0.5	11.9	5.6	0.2	11.7	5.8	0.4	10.5
Pr	1.9	0.4	0.4				2.7	0.4	0.7			
Sm							2	0.4	0.5			
Fe	2.6	0.2	1.5				1.5	0.2	1.1			
Th							1.4	0.2	0.2			
Gd	1.7	0.4	0.3				1.3	0.4	0.3			
Si	0.4	0.1	0.5									
Y	3.8	0.3	1.3									
P	3.3	0.1	3.4									
Nb	1.6	0.2	0.5									
	P7-23 Bastnäsite			P7-25 Bastnäsite			P7-26 Syn-Bst			P7-27 Synchysite		
	[wt%]	s	[at%]	[wt%]	s	[at%]	[wt%]	s	[at%]	[wt%]	s	[at%]
O	18.7	0.3	55.1	19.8	0.3	56.3	22.5	0.3	58.2	20.1	0.3	53.8
Ce	32.9	0.5	11	34.5	0.5	11.2	30.9	0.5	9.1	26.8	0.5	8.2
Ca	1.1	0.1	1.3	1	0.1	1.2	6	0.1	6.2	16	0.2	17.1
La	16.3	0.4	5.5	16.1	0.4	5.3	14.4	0.4	4.3	14.1	0.4	4.4
Nd	16.5	0.5	5.4	14.8	0.5	4.7	13.9	0.5	4	13.3	0.4	4
F	7.9	0.2	19.6	8.2	0.2	19.7	7.2	0.2	15.7	5	0.2	11.3
Pr	4.2	0.5	1.4	3.3	0.5	1.1	3.2	0.5	0.9	3.1	0.4	0.9
Sm	2.3	0.4	0.7	2.2	0.4	0.7				1.5	0.4	0.4
Zr							1.4	0.2	0.6			
Si							0.6	0.1	0.8			

EDS-SEM point analysis												
Element	**REE-fluorocarbonates**											
	P7-32 Bastnäsite			P7-33 Synchysite			P7-37 Bastnäsite			P7-42 Syn-Bst		
	[wt%]	s	[at%]	[wt%]	s	[at%]	[wt%]	s	[at%]	[wt%]	s	[at%]
Ce	33.5	0.5	11.5	27.7	0.5	8	37.8	0.5	12.8	33.2	0.5	11.1
O	18.3	0.3	54.9	22.5	0.3	57.3	18.7	0.3	55.4	19.2	0.3	56.1
La	23.9	0.5	8.3	15.2	0.4	4.5	17.3	0.4	5.9	15.5	0.4	5.2
Nd	10.3	0.5	3.4	10.7	0.4	3	14.4	0.5	4.7	12.5	0.5	4
F	7.6	0.2	19.3	5.4	0.2	11.6	7.9	0.2	19.6	7.4	0.2	18.2
Th	1.4	0.3	0.3	1.6	0.3	0.3				4.2	0.3	0.8
Pr	2.8	0.5	1	2.3	0.4	0.7	3.5	0.5	1.2	3.8	0.5	1.3
Ca	0.8	0.1	0.9	14.5	0.2	14.7	0.3	0.1	0.4	1.9	0.1	2.2
Sm	1.4	0.4	0.4							1.5	0.5	0.5
Fe										0.7	0.2	0.6

Element	**Thorite**											
	P7-40			P7-41								
	[wt%]	s	[at%]	[wt%]	s	[at%]	[wt%]	s	[at%]	[wt%]	s	[at%]
Th	43.6	0.4	6.8	51.5	0.4	10.4						
O	34.1	0.4	77.1	20.3	0.3	59.4						
Si	5.1	0.1	6.6	6.8	0.1	11.4						
Fe	4.6	0.2	3	3.7	0.2	3.1						
Ce	3.4	0.3	0.9									
Ca	3	0.1	2.7	6	0.1	7						
Zr	2.6	0.3	1	9.1	0.4	4.7						
La	1.4	0.3	0.4									
Nd	1.2	0.3	0.3									
P	0.7	0.1	0.8	2	0.1	3.1						
Al	0.3	0.1	0.4	0.5	0.1	0.9						

Element	**Zircon**											
	P6-09			P6-36 Zrk+Xenotime								
	[wt%]	s	[at%]	[wt%]	s	[at%]	[wt%]	s	[at%]	[wt%]	s	[at%]
Zr	52.4	0.4	18.4	24.8	0.7	10.7						
O	31.6	0.4	63.3	18.5	0.3	45.5						
Si	16	0.2	18.2	9.4	0.2	13.2						
P				9.1	0.3	11.6						
Ca				3.3	0.1	3.2						
Fe				2.9	0.3	2						
Th				1.5	0.4	0.3						
Y				30.6	0.6	13.5						

VI Polished samples

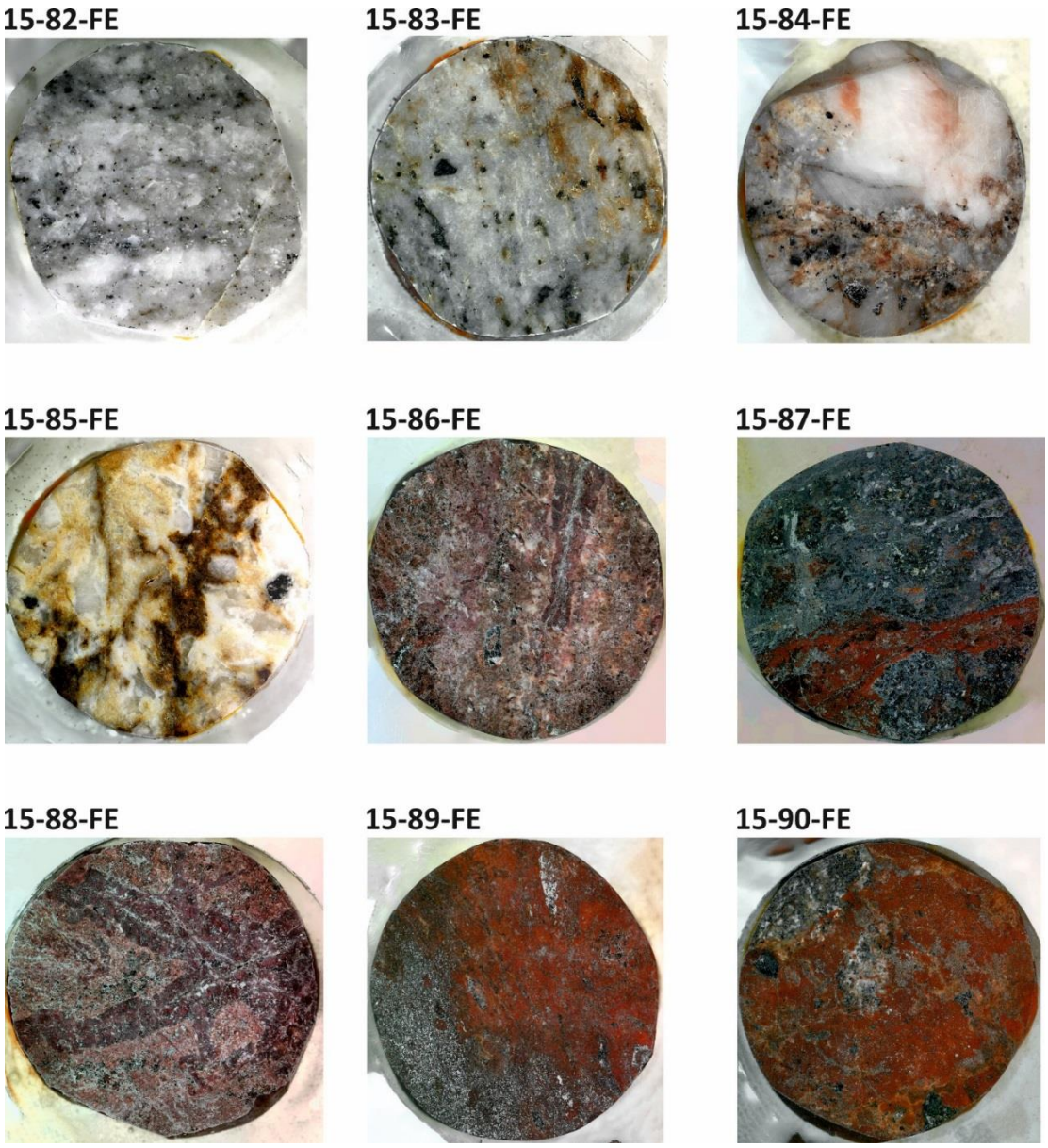

Figure A- 2: Polishes blocks from the Bjørndalen transect part 1.

15-91a-FE

15-92a-FE

15-93a-FE

15-93b-FE

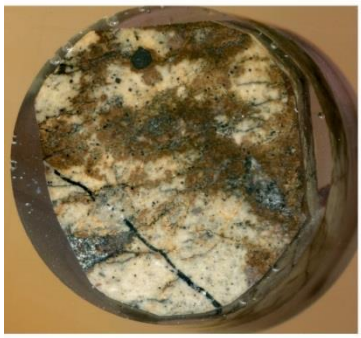

15-93-FE

15-94-FE

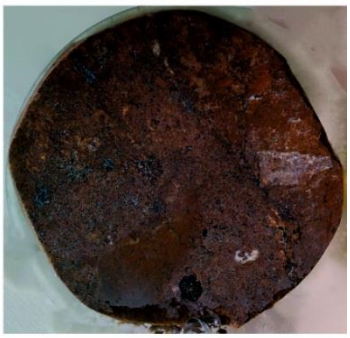

16-19-FE

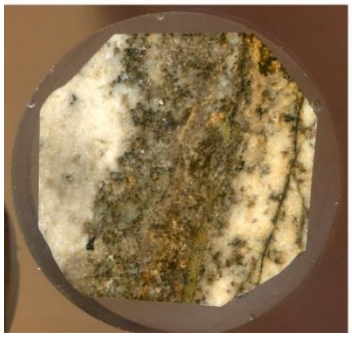

16-23-FE

16-111-FE

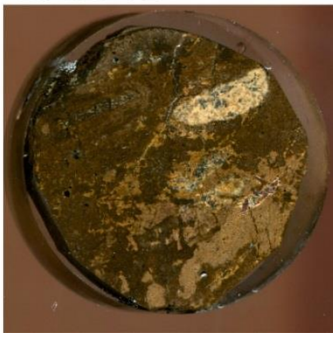

Figure A- 3: Polishes blocks from the Bjørndalen transect part 2.

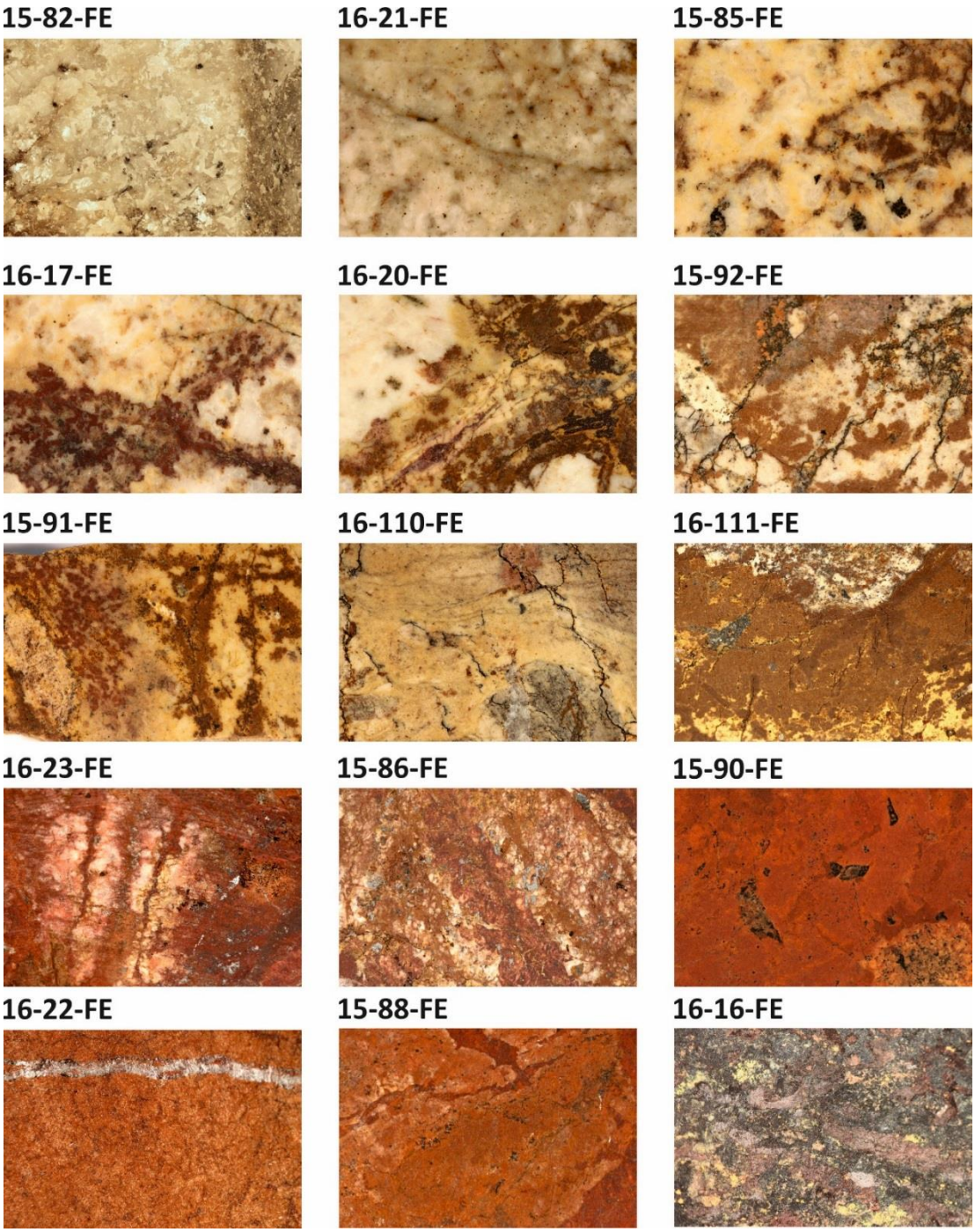

Figure A- 4: Polishes slices from the Bjørndalen transect.

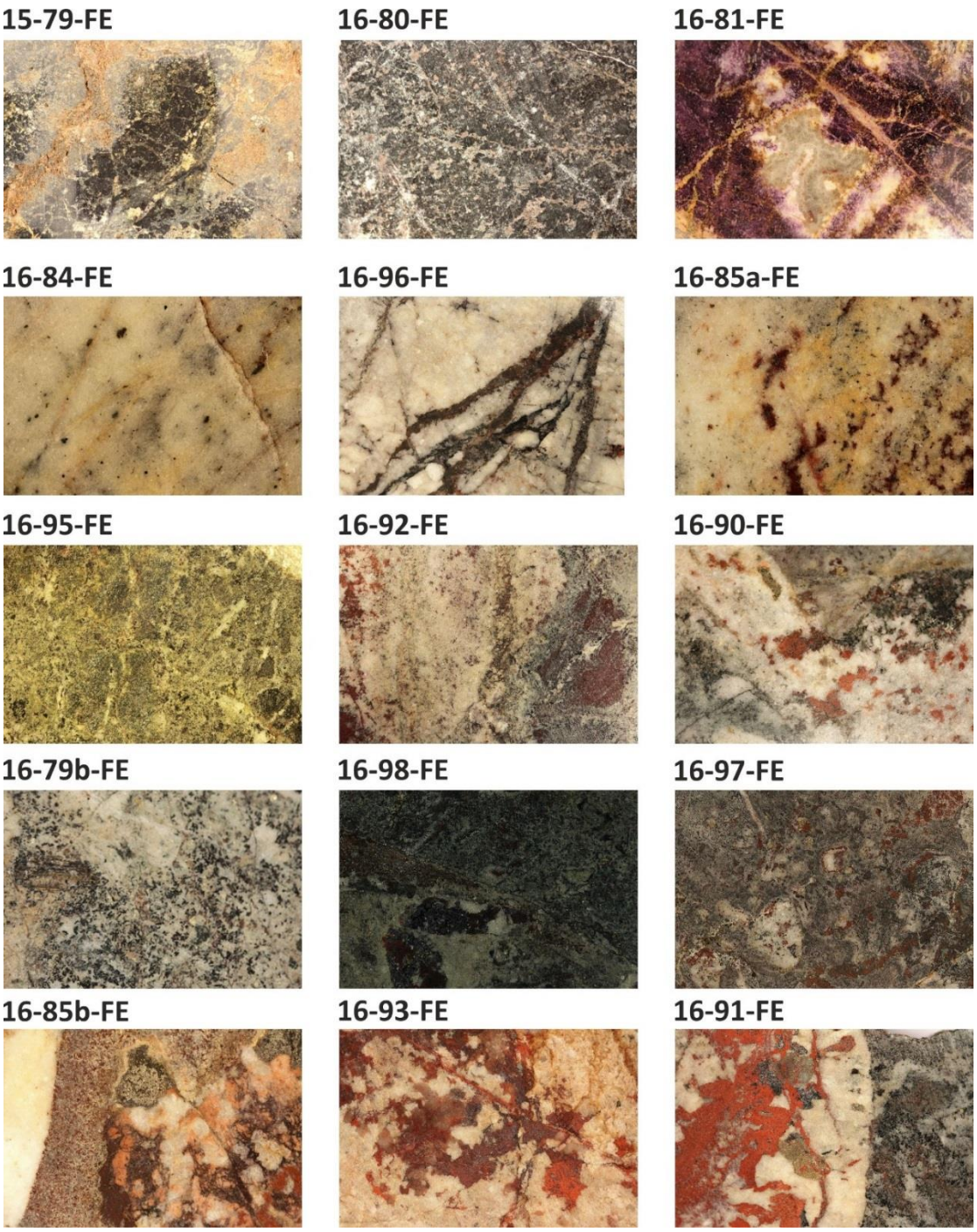

Figure A- 5: Polishes slices from the Fen Road transect part 1.

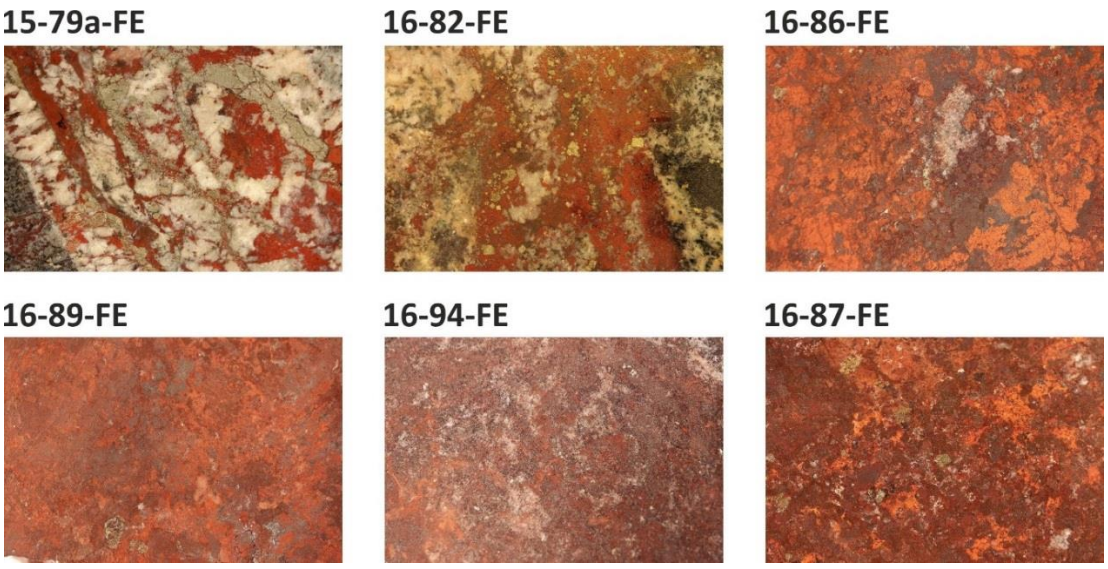

Figure A- 6 Polishes slices from the Fen Road transect part 2.

VII ICPMS chemical data table [dl in ppb, samples in ppm]

	Run I-IV	I 2	I 3	I 4	I 5	I 6	I 7	I 8	I 9	I 11	I 12	I 13	II 1
	dl [ppb]	**15-94**	**15-93**	**15-92**	**15-91**	**15-90**	**15-89**	**15-88**	**15-87**	**15-86**	**15-85**	**15-84**	**16-16**
Sc	0.05	59.46	50.22	50.02	44.83	47.77	47.74	22.68	13.60	7.07	2.02	2.08	19.45
V	-	-	-	-	-	-	-	-	-	-	-	-	-
Co	95.15	<dl	<dl	<dl	<dl	<dl	<dl	<dl	<dl	<dl	<dl	<dl	<dl
Y	1.50	288.14	190.97	100.65	126.28	80.62	110.27	269.56	46.66	214.37	50.19	50.58	26.73
Zr	4.63	869.63	384.28	235.82	230.45	214.85	153.79	253.93	207.72	634.60	52.36	71.03	162.70
Nb	34.75	1020.18	108.10	112.76	155.71	509.83	134.89	167.45	172.12	165.94	84.43	219.74	255.59
La	0.99	2704.77	3694.32	2164.08	3344.17	2368.23	1325.77	502.13	216.96	443.52	119.95	135.94	124.04
Ce	3.95	5211.88	6698.16	4056.03	6117.05	4170.14	2678.21	1308.20	350.35	876.45	425.56	354.78	137.96
Pr	0.38	549.98	706.17	435.37	651.45	439.94	295.48	178.69	225.39	81.58	40.67	33.82	27.27
Nd	1.31	1876.38	2414.35	1298.22	2269.95	1306.58	886.01	676.33	635.11	322.55	148.25	131.23	111.60
Sm	0.17	187.21	211.20	131.92	204.55	131.24	111.38	155.49	33.61	69.31	22.23	27.61	19.89
Eu	0.13	46.72	45.64	29.97	45.05	27.69	26.37	46.35	9.02	27.81	6.86	8.39	8.80
Gd	0.21	142.96	139.80	86.47	131.27	86.58	71.93	109.94	34.01	69.01	21.09	21.20	12.52
Tb	0.05	15.51	10.87	6.68	9.47	6.12	6.47	13.18	16.27	9.83	2.55	2.75	1.35
Dy	0.40	79.14	42.56	24.67	31.50	20.07	27.23	67.65	19.82	55.63	12.95	14.56	6.54
Ho	0.09	15.10	7.88	4.48	5.51	3.63	4.87	12.70	2.39	10.14	2.37	2.59	1.25
Er	0.33	47.16	26.37	15.47	19.55	13.26	15.50	38.96	7.26	27.16	6.73	7.31	4.16
Tm	0.05	6.26	3.04	1.89	2.26	1.61	1.96	5.36	0.93	3.35	0.88	0.99	0.64
Yb	0.33	42.93	19.83	13.30	15.67	11.73	13.41	35.93	6.81	20.66	5.87	7.00	4.87
Lu	0.04	5.91	2.79	2.01	2.32	1.78	2.02	5.06	1.19	2.83	0.87	1.04	0.77
Hf	0.21	7.19	4.37	3.56	3.24	2.49	3.60	3.90	9.76	4.84	0.84	1.39	7.54
Ta	0.84	7.59	<dl	<dl	<dl	2.80	<dl	<dl	<dl	29.60	30.34	1.95	1.45
Pb	-	-	-	-	-	-	-	-	-	-	-	-	-
Th	0.85	928.49	494.01	626.91	452.15	404.71	986.83	773.10	49.95	284.53	34.32	66.66	62.63
U	0.05	21.83	15.65	13.59	11.87	6.00	6.37	14.17	1.55	45.30	41.25	2.04	1.78

	Run I-IV	II 2	II 5	II 6	II 7	II 8	II 10	II 12	II 13	III 2	III 3	III 4
	dl [ppb]	**16-20**	**16-17**	**16-18**	**15-83**	**15-82**	**16-19**	**16-20/2**	**15-88/2**	**TS958**	**TS900**	**TS850**
Sc	0.05	8.20	1.69	2.95	5.94	1.53	2.92	7.75	19.96	4.44	11.21	3.68
V	-	-	-	-	-	-	-	-	-	-	-	-
Co	95.15	<dl	<dl	<dl	<dl	<dl	<dl	<dl	<dl	<dl	<dl	<dl
Y	1.50	133.15	51.82	75.97	62.88	53.55	47.19	128.91	232.01	30.50	55.69	39.87
Zr	4.63	66.14	58.15	36.56	1077.77	281.74	52.18	76.36	339.76	269.64	53.18	4.71
Nb	34.75	47.34	<dl	99.95	988.69	580.39	<dl	39.73	1875.66	5318.09	73.28	<dl
La	0.99	113.01	149.19	353.48	296.82	313.19	109.44	130.21	455.36	252.46	303.79	272.48
Ce	3.95	425.62	366.69	732.88	676.53	667.45	405.68	416.57	1234.22	595.78	652.70	538.71
Pr	0.38	40.54	38.52	68.39	58.90	60.55	36.20	39.50	161.34	60.53	66.27	51.54
Nd	1.31	159.70	133.64	252.59	220.13	223.38	129.81	154.79	601.60	231.49	257.00	192.25
Sm	0.17	31.99	20.05	38.34	38.05	35.04	19.65	31.12	137.25	35.18	43.10	29.79
Eu	0.13	12.77	6.43	13.16	11.44	10.84	6.35	12.39	41.21	10.15	13.33	8.81
Gd	0.21	35.07	18.77	34.70	31.97	31.34	18.71	34.54	97.63	28.98	38.82	26.11
Tb	0.05	5.51	2.35	4.28	3.91	3.72	2.39	5.40	11.64	2.93	4.38	2.85
Dy	0.40	32.84	12.38	21.97	19.47	17.54	12.67	32.20	59.72	11.77	19.24	12.66
Ho	0.09	6.09	2.32	3.92	3.36	2.90	2.36	5.97	11.25	1.70	2.91	2.01
Er	0.33	15.58	6.70	10.62	9.04	7.47	6.86	15.35	34.51	4.04	7.08	5.06
Tm	0.05	1.83	0.88	1.28	1.11	0.86	0.93	1.79	4.75	0.39	0.76	0.55
Yb	0.33	11.11	5.93	8.03	7.17	5.34	6.41	10.85	32.02	2.29	4.59	3.40
Lu	0.04	1.54	0.85	1.12	1.01	0.73	0.93	1.52	4.53	0.29	0.61	0.45
Hf	0.21	1.30	0.88	0.76	5.20	1.70	0.51	1.29	4.78	3.41	0.35	<dl
Ta	0.84	2.06	<dl	6.70	32.26	11.90	5.26	2.07	5.18	27.22	3.73	<dl
Pb	-	-	-	-	-	-	-	-	-	-	-	-
Th	0.85	192.56	25.21	66.08	219.74	117.61	53.07	190.24	781.10	96.94	33.57	9.64
U	0.05	15.87	7.20	73.38	5.76	20.63	32.36	15.35	12.85	2.09	1.37	0.45

	Run I-IV	III 5	III 6	III 7	III 8	III 10	III 11	III 12	III 13	III 14	IV 1	IV 2
	dl [ppb]	TS800	TS793	TS750	TS700	TS642	TS552	TS500	TS1000	TS650	16-22	16-21
Sc	0.05	3.37	7.33	7.81	14.07	4.38	13.15	11.96	5.36	7.04	67.68	2.31
V	-	-	-	-	-	-	-	-	-	-	-	-
Co	95.15	<dl	<dl	<dl	<dl	<dl	<dl	<dl	<dl	<dl	<dl	<dl
Y	1.50	59.81	86.36	3.84	66.97	15.30	6.69	5.87	54.52	45.96	214.08	57.14
Zr	4.63	82.98	50.18	9.51	216.42	<dl	7.45	12.29	147.44	1294.06	147.45	33.94
Nb	34.75	572.23	1553.70	1085.32	1070.50	71.57	87.78	53.89	128.24	349.96	695.89	355.31
La	0.99	396.67	1027.10	80.30	347.32	87.08	1524.79	2061.36	312.15	250.59	1468.06	283.71
Ce	3.95	784.36	2014.34	220.01	744.17	400.14	2302.46	2846.92	673.43	532.34	2827.96	431.24
Pr	0.38	72.94	227.25	24.81	73.35	45.33	205.70	243.40	67.50	53.93	316.24	51.02
Nd	1.31	265.45	761.47	109.41	279.50	192.19	510.83	609.81	257.75	213.24	1010.98	185.93
Sm	0.17	43.55	114.23	21.06	46.10	35.14	34.46	49.50	41.36	36.23	125.79	27.55
Eu	0.13	13.37	31.87	5.99	13.85	9.25	6.40	9.81	12.52	11.70	29.25	9.20
Gd	0.21	38.50	82.73	11.92	39.42	22.17	29.07	39.91	36.17	32.15	87.38	24.74
Tb	0.05	4.17	8.10	0.95	4.52	1.99	1.50	2.21	4.10	3.61	8.82	2.95
Dy	0.40	18.48	31.39	2.59	21.00	7.07	2.63	4.00	18.58	16.01	43.40	14.60
Ho	0.09	2.94	4.52	0.27	3.41	0.95	0.38	0.43	2.95	2.48	8.76	2.59
Er	0.33	7.62	11.32	0.67	8.62	2.19	1.95	1.96	7.47	6.21	28.28	7.06
Tm	0.05	0.87	1.12	<dl	0.95	0.17	0.14	0.08	0.84	0.69	3.80	0.91
Yb	0.33	5.61	7.04	0.34	5.78	1.01	1.13	0.67	5.34	4.33	25.32	6.07
Lu	0.04	0.78	0.98	0.05	0.76	0.14	0.21	0.15	0.74	0.61	3.57	0.93
Hf	0.21	0.74	1.13	<dl	2.19	0.37	0.33	0.36	2.12	12.78	2.70	1.24
Ta	0.84	27.86	25.51	172.02	25.77	<dl	<dl	<dl	6.54	95.54	3.96	90.95
Pb	-	-	-	-	-	-	-	-	-	-	-	-
Th	0.85	119.10	313.44	62.53	133.34	82.31	15.61	58.12	36.54	137.31	919.80	35.12
U	0.05	53.35	9.94	204.88	9.39	0.95	2.38	4.05	3.05	50.74	11.74	70.06

	Run I-IV	IV 3	IV 4	IV 5	IV 7	IV 10	IV 11	IV 12	IV 13	IV 14	Run VI	VI 1
	dl [ppb]	16-23	16-104	16-110	16-112	TS600	TS520	TS462	TS450r	TS450w	dl [ppb]	16-91V
Sc	0.05	17.20	7.85	48.17	61.31	16.71	35.74	1.57	22.01	8.55	0.03	45.51
V	-	-	-	-	-	-	-	-	-	-	0.12	40.56
Co	95.15	<dl	<dl	<dl	<dl	<dl	<dl	<dl	195.07	118.99	-	-
Y	1.50	292.22	96.32	107.54	144.26	24.71	11.43	27.55	71.53	5.35	0.07	55.94
Zr	4.63	167.35	95.80	135.69	206.80	<dl	9.68	<dl	1061.66	12.82	0.41	39.10
Nb	34.75	521.73	331.16	234.71	155.30	92.17	46.70	<dl	195.62	38.98	0.90	16.71
La	0.99	108.14	292.26	2348.45	2212.02	3819.38	3721.83	18.34	346.73	162.72	0.21	3465.15
Ce	3.95	335.69	452.70	2715.48	4033.22	6861.30	5829.14	35.10	736.93	356.67	0.25	8796.51
Pr	0.38	39.26	58.25	473.68	445.74	671.20	512.53	3.74	71.85	27.62	0.04	1081.18
Nd	1.31	189.07	228.57	1307.51	1275.24	1714.48	1245.56	13.92	274.87	87.33	0.13	3942.12
Sm	0.17	61.47	42.12	154.77	144.15	127.63	109.32	2.80	46.86	8.24	0.03	480.96
Eu	0.13	24.40	14.49	35.63	32.01	18.64	21.11	1.20	14.66	2.35	0.01	97.73
Gd	0.21	61.46	37.99	87.87	98.73	94.51	73.40	3.66	43.46	6.09	0.01	160.60
Tb	0.05	9.69	4.80	7.27	9.26	5.65	3.88	0.76	5.36	0.51	0.00	10.05
Dy	0.40	59.48	24.63	27.75	39.58	11.01	6.39	5.35	25.44	1.79	0.02	26.86
Ho	0.09	12.01	4.49	4.94	7.06	1.38	0.75	1.19	4.11	0.31	0.00	3.20
Er	0.33	36.56	12.86	16.23	21.44	5.75	3.78	3.79	10.38	0.92	0.01	6.58
Tm	0.05	5.09	1.73	1.99	2.63	0.30	0.22	0.62	1.28	0.13	0.00	0.88
Yb	0.33	32.66	11.52	13.90	17.56	1.93	1.55	4.44	8.73	0.85	0.03	7.31
Lu	0.04	4.43	1.69	2.19	2.51	0.37	0.41	0.71	1.35	0.18	0.00	0.57
Hf	0.21	3.92	1.42	2.37	3.68	<dl	<dl	<dl	7.42	<dl	0.02	0.61
Ta	0.84	<dl	74.50	2.12	2.61	<dl	<dl	<dl	4.92	<dl	0.02	0.08
Pb	-	-	-	-	-	-	-	-	-	-	0.88	10.11
Th	0.85	376.68	136.14	366.48	751.84	161.15	235.65	1.25	49.43	4.52	0.43	894.82
U	0.05	21.99	20.36	13.06	6.24	5.78	14.12	1.06	36.02	22.81	0.07	13.06

	Run VI	VI 3	VI 4	VI 5	VI 6	VI 7	VI 8	VI 10	VI 11	VI 12	VI 13	VI 14
	dl [ppb]	**16-81**	**16-95**	**16-82**	**16-83**	**16-85**	**16-87**	**16-98**	**16-91C**	**16-89**	**16-79**	**16-90**
Sc	0.03	15.95	45.83	36.14	8.83	19.91	19.64	38.01	36.39	24.83	21.46	26.79
V	0.12	38.00	109.89	75.28	17.04	24.13	59.78	90.86	68.76	129.87	62.68	36.62
Co	-	-	-	-	-	-	-	-	-	-	-	-
Y	0.07	69.26	24.37	67.62	64.56	171.60	32.24	26.12	30.22	22.66	21.75	49.22
Zr	0.41	357.39	46.13	173.34	8.43	45.13	119.38	150.09	45.94	62.59	10.05	77.39
Nb	0.90	75.90	642.78	66.29	26.27	53.35	44.37	176.91	49.94	39.82	10.76	106.15
La	0.21	448.42	738.79	2777.48	132.90	2938.46	1624.72	977.39	456.27	559.22	167.78	2516.12
Ce	0.25	798.89	1501.38	9454.38	473.64	4815.54	4329.60	2107.57	1004.50	1603.73	1250.95	4787.72
Pr	0.04	66.32	141.79	1395.21	51.61	519.11	571.58	207.97	97.31	162.56	158.38	540.88
Nd	0.13	262.65	575.28	5958.44	231.25	1603.82	1796.60	920.51	412.21	684.00	741.44	1647.54
Sm	0.03	51.91	89.15	666.98	59.42	279.76	277.55	168.33	79.30	110.81	116.97	260.57
Eu	0.01	14.46	21.81	137.53	18.05	67.28	59.12	37.09	17.67	23.20	24.28	55.38
Gd	0.01	28.53	43.41	215.36	42.93	125.24	91.04	62.26	34.06	37.58	44.71	93.65
Tb	0.00	3.20	3.27	16.52	5.78	14.01	8.30	5.03	2.97	3.19	3.92	8.52
Dy	0.02	13.92	10.19	40.37	24.28	53.49	20.21	13.74	9.83	9.45	10.80	22.42
Ho	0.00	2.22	1.24	4.00	3.22	7.82	1.99	1.50	1.39	1.13	1.21	2.53
Er	0.01	5.91	2.42	6.34	6.28	17.25	3.07	2.59	3.25	2.40	2.28	4.71
Tm	0.00	0.81	0.29	0.65	0.62	1.86	0.32	0.30	0.41	0.30	0.28	0.56
Yb	0.03	5.80	2.15	5.04	3.40	10.61	2.74	2.66	2.87	2.15	2.08	4.20
Lu	0.00	0.84	0.25	0.37	0.41	1.15	0.29	0.48	0.36	0.31	0.24	0.43
Hf	0.02	2.83	1.96	2.32	0.29	0.78	1.06	3.04	0.55	0.73	0.19	0.73
Ta	0.02	1.73	11.68	0.28	0.31	0.22	0.44	4.39	0.54	0.09	0.05	0.99
Pb	0.88	10.11	5.96	72.25	7.87	23.96	17.91	13.79	10.03	21.89	25.41	21.88
Th	0.43	70.95	59.05	1286.85	82.70	259.71	593.91	207.04	78.86	234.87	167.09	364.75
U	0.07	18.70	2.75	30.54	4.71	13.01	9.18	1.91	7.02	7.60	5.79	8.35

	Run VI	VI 15	VI 16	VI 17	VI 18	VI 19	VI 20	VI 22	VI 23	Run VII	VII 7	VII 8
	dl [ppb]	16-94	16-80	16-96	16-92	16-84	16-86	16-93	16-97	dl [ppb]	16-75r	16-73 ore
Sc	0.03	7.64	31.86	24.40	34.92	6.41	19.32	23.00	59.68	0.157	24.5	17.4
V	0.12	72.35	89.31	25.48	53.54	11.52	68.67	54.50	204.70	0.652	66.6	77.6
Co	-	-	-	-	-	-	-	-	-	-	-	-
Y	0.07	22.88	33.67	21.14	32.75	29.80	61.74	55.71	17.97	0.040	20.7	43.9
Zr	0.41	60.83	174.83	151.38	143.33	8.15	28.60	113.52	228.99	1.111	98.3	88.5
Nb	0.90	49.04	229.28	52.18	22.87	16.61	22.25	11.90	81.22	0.540	785.5	42.4
La	0.21	1012.57	69.24	1096.05	1241.13	101.00	3369.75	1776.77	503.47	0.051	8914.7	1425.5
Ce	0.25	2556.74	162.69	2419.60	3555.46	299.73	6994.84	4727.10	994.56	0.063	12016.7	2266.5
Pr	0.04	168.22	19.57	157.29	532.73	31.65	840.00	627.63	87.90	0.004	1021.8	157.9
Nd	0.13	1073.15	85.34	888.22	1875.11	136.34	2731.73	1993.37	336.58	0.043	2655.3	539.8
Sm	0.03	170.40	22.24	128.98	274.66	33.30	345.03	323.64	55.44	0.012	185.7	68.2
Eu	0.01	37.74	7.62	24.79	52.04	9.76	72.91	71.71	13.67	0.002	35.8	19.1
Gd	0.01	70.92	17.33	48.86	73.40	21.84	110.12	108.06	23.54	0.011	70.3	35.5
Tb	0.00	5.21	2.49	3.64	6.26	2.63	10.64	9.60	2.24	0.001	3.5	2.9
Dy	0.02	12.49	11.64	9.40	14.75	10.97	29.89	26.40	7.87	0.004	9.0	11.0
Ho	0.00	1.24	1.63	1.09	1.76	1.49	3.58	3.03	1.04	0.001	1.0	1.5
Er	0.01	1.99	3.56	2.04	3.51	3.08	7.37	5.40	2.18	0.003	1.5	3.6
Tm	0.00	0.20	0.41	0.24	0.44	0.33	0.92	0.56	0.26	0.000	0.2	0.5
Yb	0.03	1.79	2.57	1.79	3.37	2.02	6.65	4.03	1.69	0.007	1.5	3.4
Lu	0.00	0.24	0.40	0.13	0.37	0.27	0.65	0.43	0.21	0.000	0.2	0.5
Hf	0.02	0.67	2.99	1.18	1.81	0.20	0.48	1.09	7.38	0.047	1.4	1.0
Ta	0.02	0.25	1.03	1.72	0.09	0.07	0.08	0.06	2.67	0.021	12.4	0.9
Pb	0.88	3.37	30.61	10.04	17.51	6.38	23.48	15.37	10.15	0.272	12.4	10.2
Th	0.43	247.49	42.24	176.14	648.57	37.26	1150.71	483.21	51.23	0.047	186.6	82.0
U	0.07	4.90	73.37	5.63	12.14	1.55	19.32	9.69	5.12	0.040	10.6	6.4

	Run VII	VII 9	VII 10	VII 11	VII 12	VII 13	VII 14	VII 15	VII 16	VII 17	VII 18	VII 19
	dl [ppb]	16-73	16-73w	16-73r	16-75	16-73g	16-67	16-44	16-65	16-48	16-64	16-56
Sc	0.157	18.7	34.7	36.5	17.9	19.6	20.9	88.8	55.1	30.3	141.3	60.9
V	0.652	13.4	38.0	70.9	27.3	17.2	79.0	73.9	123.3	82.6	412.9	277.6
Co	-	-	-	-	-	-	-	-	-	-	-	-
Y	0.040	9.9	56.8	18.4	17.6	10.7	63.7	144.0	208.0	100.2	310.5	200.1
Zr	1.111	24.9	101.4	69.3	28.5	32.8	75.2	283.7	256.0	405.5	461.3	62.1
Nb	0.540	107.1	305.6	267.0	318.7	396.7	76.1	477.7	1576.1	642.0	54.4	242.1
La	0.051	2765.3	3322.4	4201.2	10964.4	2667.8	162.3	1182.3	195.9	138.7	7603.8	1080.9
Ce	0.063	4420.6	5482.5	7580.9	14692.0	4178.2	392.3	2126.3	568.6	179.4	10454.7	2384.0
Pr	0.004	416.3	588.7	820.3	1235.2	236.9	43.1	183.3	46.6	35.9	902.9	185.2
Nd	0.043	938.1	1638.0	2639.4	3112.9	859.8	174.6	788.0	243.1	155.9	2718.6	703.4
Sm	0.012	84.7	213.7	210.9	182.6	77.5	31.5	143.8	57.9	32.7	375.2	106.7
Eu	0.002	15.0	39.5	36.7	31.7	16.2	9.0	32.2	20.0	10.4	77.9	24.2
Gd	0.011	27.6	59.5	49.1	68.4	20.1	23.6	62.9	55.9	28.8	153.1	49.4
Tb	0.001	1.5	3.3	2.2	2.5	1.1	2.6	6.6	8.5	4.8	13.2	5.5
Dy	0.004	4.4	12.0	5.5	6.5	3.0	12.7	31.4	45.7	25.6	57.6	29.1
Ho	0.001	0.5	1.7	0.7	0.7	0.4	2.0	5.0	7.4	4.3	8.7	5.4
Er	0.003	0.8	3.8	1.2	1.1	0.6	4.7	12.0	17.8	11.0	20.2	14.7
Tm	0.000	0.1	0.5	0.2	0.1	0.1	0.5	1.5	2.2	1.4	2.4	1.9
Yb	0.007	0.8	3.8	1.4	1.1	0.8	3.2	9.3	13.3	8.3	14.5	11.4
Lu	0.000	0.1	0.5	0.2	0.2	0.1	0.4	1.1	1.8	1.1	1.7	1.5
Hf	0.047	0.3	1.1	1.0	0.4	0.6	0.6	5.5	4.1	8.8	10.7	0.7
Ta	0.021	0.5	7.1	0.6	12.6	0.7	0.1	3.3	2.9	3.1	0.1	0.4
Pb	0.272	6.9	7.4	11.3	5.2	8.3	6.5	24.3	18.7	63.3	23.3	17.5
Th	0.047	113.1	238.7	244.4	83.2	49.2	64.9	203.2	398.7	25.8	3175.2	910.6
U	0.040	4.1	15.8	7.2	17.1	3.7	1.9	1.3	6.7	1.4	8.5	2.1

	Run VIII-IX-X	VIII 13	VIII 14	VIII 15	VIII 16	VIII 17	VIII 18	VIII 19	VIII 20	VIII 21	VIII 22	IX 4
	dl [ppb]	16-46	16-41	16-43	16-45	16-36	16-52	16-40	16-55	16-49	16-50	16-54a
Sc	0.141	82.0	202.9	56.5	92.5	225.7	110.6	113.6	61.2	66.8	96.6	85.4
V	1.769	239.3	177.4	249.2	212.7	115.2	161.9	177.7	245.6	347.6	116.8	78.1
Co	-	-	-	-	-	-	-	-	-	-	-	-
Y	0.513	65.6	106.2	442.6	32.2	106.2	113.8	129.8	69.1	26.0	108.6	154.2
Zr	2.381	473.8	409.0	283.9	319.6	85.3	110.8	221.8	388.7	209.1	83.6	190.3
Nb	1.050	140.3	298.6	16.0	36.7	161.5	187.0	112.4	39.8	26.0	165.8	110.9
La	0.137	83.6	376.7	1470.2	56.9	914.0	1013.1	1046.0	438.0	63.3	884.0	602.0
Ce	0.294	171.0	865.8	3379.0	116.8	1883.7	1950.9	2041.6	683.5	127.2	1689.6	1297.1
Pr	0.045	22.0	117.4	450.6	16.2	246.6	220.1	266.3	67.7	17.5	188.2	173.5
Nd	0.093	66.9	539.4	2208.6	58.0	1075.1	854.7	1115.5	226.3	65.6	726.0	736.6
Sm	0.024	16.0	105.3	405.4	10.5	180.8	138.5	186.8	35.0	11.7	115.3	136.3
Eu	0.010	5.1	28.9	75.9	4.0	39.9	36.0	53.6	11.9	5.6	36.3	33.0
Gd	0.030	13.4	51.6	199.9	10.0	86.7	84.9	119.8	28.7	10.3	70.6	65.2
Tb	0.008	2.2	4.2	18.6	1.3	7.7	7.4	10.8	3.5	1.2	6.3	6.7
Dy	0.054	13.6	20.8	96.4	7.6	32.9	33.4	41.2	18.1	6.7	29.8	36.5
Ho	0.016	2.7	3.8	17.6	1.4	4.7	5.3	5.6	3.2	1.2	5.0	6.8
Er	0.053	8.6	11.2	43.3	3.8	10.5	12.3	11.2	7.9	3.1	12.4	18.1
Tm	0.011	1.4	1.7	5.2	0.5	1.5	1.5	1.3	1.0	0.4	1.6	2.7
Yb	0.063	10.0	12.0	27.3	3.2	9.2	9.1	7.9	6.3	2.2	9.9	15.6
Lu	0.011	1.5	1.8	3.2	0.5	1.3	1.2	1.1	0.8	0.3	1.2	2.4
Hf	0.620	29.9	24.0	12.9	11.9	5.9	7.5	14.9	10.8	7.5	6.1	37.4
Ta	0.028	1.2	3.2	0.2	2.5	1.1	2.0	1.2	1.1	1.8	1.1	0.8
Pb	31.650	284.2	20.8	19.2	21.1	15.4	41.8	9.8	8.2	18.2	11.8	32.2
Th	0.174	342.8	338.8	4201.6	28.2	664.9	336.5	232.8	64.7	8.9	265.7	383.3
U	0.004	1.8	1.0	23.0	1.3	3.9	2.6	2.3	2.8	1.2	5.2	12.1

	Run VIII-IX-X	IX 5	IX 6	IX 7	IX 10	IX 11	IX 12	IX 16	IX 17	IX 18	IX 19	IX 20
	dl [ppb]	**16-30**	**16-63**	**16-34**	**16-28**	**16-66**	**16-53**	**16-25**	**16-68**	**16-57**	**16-33**	**16-29**
Sc	0.141	45.3	28.6	149.0	40.2	34.7	28.0	44.5	17.6	48.7	94.9	41.2
V	1.769	147.8	116.4	52.6	71.0	75.0	140.6	42.9	69.2	161.0	109.3	44.5
Co	-	-	-	-	-	-	-	-	-	-	-	-
Y	0.513	151.0	67.2	195.6	112.2	21.5	96.8	65.9	29.0	126.8	257.5	123.6
Zr	2.381	85.4	81.9	121.6	91.3	22.2	173.9	72.5	1489.2	354.9	474.0	134.6
Nb	1.050	89.8	147.3	185.2	205.4	35.3	310.0	37.2	83.9	218.2	103.1	88.7
La	0.137	600.2	73.3	1321.9	787.3	21.5	861.9	558.6	44.9	372.6	1124.2	3512.2
Ce	0.294	2481.1	125.9	3141.0	1514.3	53.8	1406.6	847.0	71.6	731.3	3349.3	5947.9
Pr	0.045	557.8	17.4	457.8	193.1	8.0	148.0	83.9	12.6	90.2	615.0	654.8
Nd	0.093	3383.7	64.4	2535.2	863.6	26.5	497.4	267.3	42.1	344.4	3365.8	2262.1
Sm	0.024	495.6	18.4	460.2	230.8	7.6	71.8	32.6	9.2	60.9	585.5	320.5
Eu	0.010	70.6	7.4	85.2	62.1	2.6	17.1	11.0	3.1	17.0	106.5	82.2
Gd	0.030	116.4	19.0	125.3	116.8	6.2	39.2	16.8	7.5	34.0	172.0	154.1
Tb	0.008	3.9	2.7	6.5	8.4	1.0	4.5	2.4	1.1	4.3	9.5	12.7
Dy	0.054	30.3	14.9	36.1	33.0	5.9	22.3	13.4	5.9	23.9	49.3	47.4
Ho	0.016	5.2	2.6	6.4	4.8	1.0	3.7	2.8	1.2	4.6	8.0	5.6
Er	0.053	12.8	6.6	17.2	11.3	2.5	9.3	6.9	3.3	12.9	19.4	9.9
Tm	0.011	1.8	0.8	2.6	1.5	0.3	1.2	1.2	0.5	1.9	3.0	1.2
Yb	0.063	10.5	5.0	19.0	9.0	1.6	7.8	6.4	3.6	13.0	21.5	6.8
Lu	0.011	1.5	0.7	2.9	1.2	0.2	1.2	1.2	0.6	2.2	3.8	1.1
Hf	0.620	13.9	7.2	7.5	6.1	2.9	8.7	23.0	32.1	22.6	17.0	7.5
Ta	0.028	0.1	0.7	0.4	3.3	0.2	3.9	0.4	0.7	1.9	0.1	0.2
Pb	31.650	53.6	42.9	80.5	281.3	37.2	39.3	39.3	39.5	75.4	59.7	45.7
Th	0.174	1626.4	121.1	1379.6	814.0	92.1	250.9	115.7	26.6	167.1	2667.4	689.5
U	0.004	5.6	3.5	4.7	3.8	2.6	5.2	0.6	2.3	2.2	6.4	2.6

	Run VIII-IX-X	IX 21	IX 22	IX 23	IX 24	X 1	X 2
	dl [ppb]	16-26	16-27	16-37	16-38	16-42	16-54
Sc	0.141	50.0	29.9	96.6	53.1	74.9	106.9
V	1.769	46.6	32.2	149.6	67.0	62.3	209.4
Co	-	-	-	-	-	-	-
Y	0.513	96.4	92.9	201.2	47.2	309.5	476.1
Zr	2.381	81.9	132.6	373.7	443.1	403.3	66.2
Nb	1.050	60.5	97.8	202.2	220.5	671.2	381.7
La	0.137	982.7	4832.2	547.7	2140.6	395.7	900.3
Ce	0.294	1809.5	7788.5	956.8	3302.7	213.8	1719.7
Pr	0.045	232.1	829.8	127.0	356.2	127.5	540.5
Nd	0.093	983.9	2874.5	538.2	1091.0	629.7	2552.2
Sm	0.024	250.5	505.3	153.0	123.0	224.4	565.0
Eu	0.010	77.5	132.6	46.2	29.9	67.6	110.1
Gd	0.030	127.3	224.6	87.6	52.7	135.3	215.3
Tb	0.008	10.0	13.7	10.9	4.5	17.8	20.4
Dy	0.054	35.3	42.0	54.3	20.0	89.7	108.5
Ho	0.016	4.5	4.6	8.2	2.7	14.4	18.8
Er	0.053	8.9	8.1	19.6	5.8	35.8	44.9
Tm	0.011	1.1	1.0	2.6	0.8	4.5	5.1
Yb	0.063	7.3	6.7	17.3	5.1	25.1	26.9
Lu	0.011	1.3	1.3	3.4	1.0	4.1	4.6
Hf	0.620	5.1	6.0	13.5	17.7	13.0	4.0
Ta	0.028	0.7	0.5	1.8	1.1	9.7	1.1
Pb	31.650	154.2	263.4	45.5	31.9	12.4	40.0
Th	0.174	847.4	870.0	788.2	319.9	146.8	578.5
U	0.004	14.3	3.9	4.7	18.0	7.4	10.3

VIII Certified Reference Material

Table A- 1: Deviation in % of the analysis from CRMs from the values delivered by the CRM producer. *REE is an ore containing REEs, Zr and Nb from the Strange Lake deposit, Quebec, Canada. **ORE (OREAS 461) is an ore containing REE and represent a mixture from a barren siltstone and the lateritic Mount Weld deposit.

	Sc	Y	Zr	Nb	La	Ce	Pr	Nd	Sm	Eu	Gd	Tb	Dy	Ho	Er	Tm	Yb	Lu	Hf	Ta	Th	U
REE* CRM [ppm]	8	5480	19100	4050	1661	3960	435	1456	381	23.5	433	106.2	847	208	701	106	678	92.4	479	231	719	137
95% conf		130	700	150	32	70	8	25	8	0.8	10	4.4	19	9	26	2.9	22	3.8	14	13	26	5
Run **I-IV**																						
mean (n=4) [ppm]	17	5017	19332	3338	1656	3808	448	1438	355	25	453	124	985	234	807	122	797	105	553	205	834	158
95% conf	1	211	698	270	56	135	9	36	10	3	14	4	34	8	29	4	28	3	15	30	17	6
rel% error	108	-8	1	-18	0	-4	3	-1	-7	6	5	16	16	12	15	16	18	14	15	-11	16	15
Run **VI**																						
mean (n=3) [ppm]	29	4905	15939	1913	1597	4006	429	1259	351	22	418	99	851	203	726	107	705	95	402	119	965	148
95% conf	4	136	5060	1020	200	179	45	26	29	1	13	2	50	12	51	5	20	2	90	80	195	1
rel% error	259	-10	-17	-53	-4	1	-1	-14	-8	-7	-4	-7	0	-2	4	1	4	2	-16	-48	34	8
Run **VII**																						
mean (n=4) [ppm]	35	5931	30235	2036	1462	2855	386	1224	270	17	326	82	683	164	573	88	581	77	304	106	701	120
95% conf	5	563	2709	1064	232	923	65	168	32	2	36	8	68	16	54	8	52	7	60	73	209	10
rel% error	335	8	58	-50	-12	-28	-11	-16	-29	-27	-25	-22	-19	-21	-18	-17	-14	-17	-37	-54	-3	-13
Run **VIII-X**																						
mean (n=3) [ppm]	44	4745	31565	1952	1531	3655	422	1390	361	23	394	103	839	196	684	104	674	90	337	140	690	130
95% conf	9	198	6237	1019	86	201	25	59	17	1	13	3	36	7	26	4	28	4	145	74	32	7
rel% error	448	-13	65	-52	-8	-8	-3	-5	-5	-3	-9	-3	-1	-6	-2	-2	-1	-3	-30	-39	-4	-5
ORE CRM [ppm]**	38.8	91	603	1296	2690	3510	489	1629	220	46.7	100	9.08	34.8	4.56	8.80	0.89	4.39	0.52	14.1	25.1	210	4.79
95% conf	2.5	4.4	27	98	158	132	21	54	7	2.2	8	0.3	1.4	0.3	0.3	0.09	0.2	0.04	0.6	1.0	7	0.2
Run **VIII-X**																						
mean (n=3) [ppm]	43	82	1160	782	2565	3413	477	1615	208	46	102	8	33	4	11	1	5	1	18	19	190	4
95% conf	2	2	166	59	65	57	11	41	6	1	8	0	1	0	0	0	0	0	2	1	5	5
rel% error	10	-10	92	-40	-5	-3	-2	-1	-5	-2	2	-11	-4	-5	23	1	8	21	28	-25	-10	-7

IX Procedural Blanks & Acid Blanks

	Sc	Co	V	Y	Zr	Nb	La	Ce	Pr	Nd	Sm	Eu	Gd	Tb	Dy	Ho	Er	Tm	Yb	Lu	Hf	Ta	Pb	Th	U
Run I-IV A-blank																									
x	0.06	0.11	-	0.06	0.46	0.11	0.01	0.02	0.002	0.01	0.001	0.09	0.001	b.d.l.	0.001	b.d.l.	0.001	b.d.l.	0.001	b.d.l.	0.08	0.01	-	0.18	0.01
%RSD	15.45	8.34	-	4.18	7.64	11.59	10.66	2.95	7.16	33.00	45.88	4.05	49.50	-	32.06	-	-	53.69	50.93	-	7.29	2.75	-	1.52	11.90
Run I-IV P-blank																									
mean (n=5) [ppb]	0.06	54.61	-	0.35	1.93	7.05	0.36	1.41	0.14	0.44	0.06	0.05	0.07	0.01	0.09	0.02	0.07	0.01	0.07	0.01	0.11	0.22	-	0.42	0.02
sigma (ppb)	0.02	31.72	-	0.50	1.59	11.58	0.33	1.32	0.13	0.42	0.06	0.04	0.07	0.02	0.13	0.03	0.11	0.02	0.11	0.01	0.07	0.28	-	0.28	0.02
detection limit [ppb]	0.05	95.15	-	1.50	4.77	34.75	0.99	3.95	0.38	1.26	0.17	0.13	0.21	0.05	0.40	0.09	0.33	0.05	0.33	0.04	0.22	0.84	-	0.85	0.05
Run VI A-blank																									
x	0.06	-	14.16	0.001	0.03	0.004	0.01	0.03	0.003	0.01	0.001	0.002	0.002	b.d.l.	b.d.l.	b.d.l.	b.d.l.	b.d.l.	0.003	b.d.l.	0.001	b.d.l.	0.13	0.01	0.001
%RSD	5.46	-	4.20	19.60	27.06	6.77	5.65	5.43	32.31	23.24	86.62	24.92	36.34	-	-	-	-	-	28.49	-	1.21	-	6.34	18.21	13.02
Run VI P-blank																									
mean (n=3) [ppb]	0.07	-	0.62	0.04	0.27	0.38	0.11	0.24	0.03	0.13	0.02	0.01	0.02	0.002	0.01	0.002	0.005	0.001	0.02	0.0003	0.01	0.01	0.98	0.16	0.02
sigma (ppb)	0.01	-	0.04	0.02	0.14	0.30	0.07	0.08	0.01	0.04	0.01	0.00	0.01	0.001	0.01	0.001	0.004	0.001	0.01	0.0005	0.01	0.01	0.29	0.14	0.02
detection limit [ppb]	0.03	-	0.12	0.07	0.41	0.90	0.21	0.25	0.04	0.11	0.03	0.01	0.03	0.003	0.02	0.003	0.013	0.003	0.03	0.0014	0.02	0.02	0.88	0.43	0.07
Run VII A-blank																									
x	0.29	-	0.89	0.01	0.04	0.16	0.01	0.01	0.001	0.05	0.001	0.001	0.002	0.001	0.001	b.d.l.	0.001	0.001	0.01	b.d.l.	0.003	0.002	0.37	0.05	0.01
%RSD	4.28	-	2.38	25.45	18.47	4.99	13.86	14.72	20.74	20.23	34.32	19.57	19.35	78.42	15.91	-	52.41	69.17	13.36	-	17.61	30.32	3.07	6.68	20.14
Run VII P-blank																									
mean (n=3) [ppb]	0.25	-	0.74	0.04	2.00	0.33	0.05	0.09	0.01	0.05	0.01	0.003	0.009	0.001	0.007	0.002	0.005	0.001	0.010	0.001	0.04	0.01	0.61	0.07	0.02
sigma (ppb)	0.05	-	0.22	0.01	0.37	0.18	0.02	0.02	0.001	0.02	0.00	0.001	0.004	0.0005	0.001	0.0005	0.001	0.0001	0.002	0.0001	0.02	0.01	0.09	0.02	0.01
detection limit [ppb]	0.16	-	0.65	0.04	1.11	0.54	0.05	0.06	0.004	0.05	0.01	0.002	0.011	0.001	0.004	0.001	0.003	0.0004	0.007	0.0004	0.05	0.02	0.27	0.05	0.04
Run VIII-X A-blank																									
x	0.20	-	0.38	0.004	0.32	0.10	0.006	0.006	0.023	0.006	0.005	0.006	0.004	0.004	0.004	0.004	0.004	0.004	0.004	0.004	0.12	0.04	0.12	0.07	0.01
%RSD	0.01	-	0.01	0.001	0.10	0.01	0.0003	0.0001	0.001	0.001	0.001	0.001	0.001	0.001	0.001	0.0004	0.001	0.001	0.001	0.001	0.01	0.002	0.01	0.005	0.001
Run VIII-X P-blank																									
mean (n=4) [ppb]	0.09	-	2.04	0.14	2.86	0.40	0.09	0.17	0.04	0.08	0.01	0.005	0.01	0.003	0.02	0.004	0.01	0.003	0.02	0.003	0.18	0.01	6.92	0.08	0.008
sigma (ppb)	0.05	-	0.59	0.17	0.80	0.35	0.05	0.10	0.01	0.03	0.01	0.003	0.01	0.003	0.02	0.005	0.02	0.004	0.02	0.004	0.21	0.01	10.55	0.06	0.001
detection limit [ppb]	0.14	-	1.77	0.51	2.41	1.05	0.14	0.29	0.04	0.09	0.02	0.009	0.03	0.008	0.05	0.016	0.05	0.011	0.06	0.011	0.62	0.03	31.65	0.17	0.004